HAL
open science

Computational exploration of water adsorption and proton conduction in porous materials

Paulo Graziane Mendonça Mileo

To cite this version:

Paulo Graziane Mendonça Mileo. Computational exploration of water adsorption and proton conduction in porous materials. Material chemistry. Université Montpellier, 2018. English. NNT : 2018MONTS142 . tel-02288874

HAL Id: tel-02288874

https://theses.hal.science/tel-02288874

Submitted on 16 Sep 2019

HAL is a multi-disciplinary open access archive for the deposit and dissemination of scientific research documents, whether they are published or not. The documents may come from teaching and research institutions in France or abroad, or from public or private research centers.

L'archive ouverte pluridisciplinaire **HAL**, est destinée au dépôt et à la diffusion de documents scientifiques de niveau recherche, publiés ou non, émanant des établissements d'enseignement et de recherche français ou étrangers, des laboratoires publics ou privés.

THÈSE POUR OBTENIR LE GRADE DE DOCTEUR DE L'UNIVERSITÉ DE MONTPELLIER

En Chimie et Physico-chimie des Matériaux

École doctorale Sciences Chimiques Balard

Unité de recherche Institut Charles Gerhardt Montpellier (ICGM) – Equipe DAMP

COMPUTATIONAL EXPLORATION OF WATER ADSORPTION AND PROTON CONDUCTION IN POROUS MATERIALS

Présentée par Paulo Graziane Mendonça Mileo

Le 21 Décembre 2018

Sous la direction de Guillaume Maurin Directeur de thèse
Et de Sabine Devautour-Vinot co-Directrice de thèse

Devant le jury composé de

Pr. Jean DAOU, Professeur, IS2M, Université de Haute Alsace	Examinateur
Dr. Sabine DEVAUTOUR-VINOT, Maître de Conférences, ICGM, Université de Montpellier	co-Directrice de thèse
Pr. Jean-François DUFRECHE, Professeur, ICSM, Université de Montpellier	Examinateur
Dr. Aziz GHOUFI, Maître de Conférences, SPM, Université de Rennes 1	Rapporteur
Pr. Patrice MALFREYT, Professeur, ICCF, Université Clermont Auvergne	Rapporteur
Pr. Guillaume MAURIN, Professeur, ICGM, Université de Montpellier	Directeur de thèse
Pr. Nathalie STEUNOU, Professeur, ILV, Université de Versailles St Quentin en Yvelines	Examinateure

UNIVERSITÉ DE MONTPELLIER

Acknowledgements

As much as I wanted to individualise this page, as my colleges before me, I must firstly thank my supervisors. Dr. Guillaume Maurin and Dr. Sabine Devautour-Vinot really do deserve the greatest of thanks, since they have provided me with incredible support, encouragement and guidance in both the writing of this thesis and the work which preceded it.

I would also thank all members of the jury, Dr. A. Ghoufi and Dr. P. Malfreyt for having agreed to serve as rapporteurs, as well as Prof. N. Steunou, Prof. J. Daou and Prof. J.F. Dufreche for having accepted to serve as judges on the jury.

From the very moment I officially started this thesis, with the friends I made in Montpellier, throughout the time I have spent in the Institute ICGM at Université Montpellier, my spirits have been continually raised by the ubiquitous "too many people to mention".

This thesis was enriched significantly through helpful discussions with my co-workers Renjith S. Pillai and Mohammad Wahiduzzaman. The time spent talking with my colleagues working at the DAMP group was essential to address the difficult setting of simulations and the rationalization of the results obtained.

Away from work, special thanks go to my friends Rocio Semino, Mathieu Maas, Carla Vieira, Valentin Hetier, and Alliou Datta for their friendship and helping hand in the many moments I needed.

I would also like to acknowledge the program Science without Borders (*CsF*) from the Brazilian Government for the grant which has supported my livelihood and the conduction of my thesis.

Finally, thanks must go to my family. My father, who learned me principles of being a man and inspired me to always seek for the excellence; my mother, who has devoted all of herself to my development, especially after my father’s death; and my wife, Marianna, for the formidable and ever-engaging love she has devoted to me for more than one decade.

Table of contents

Introduction……..... 1

CHAPTER 1 – *Overview on the proton conduction and water adsorprtion in solids*…..... 11

Introduction…… 13

I. Solid state proton conductors…….. 14

I.1. Solid state proton conductors-based technology…….. 14

I.2 Classification of solid state proton conductors…….. 20

I.3. MOFs as novel solid state proton conductors……... 23

I.4. Evaluation of the Proton conductivity and microscopic mechanisms in play…….. 31

II. Materials for adsorption heat reallocation……. 37

II.1. Main technologies used in adsorption-based thermal devices……..... 37

II.2. General principles of adsorption-based heat transfer……...…... 37

II.3. Porous materials in water-based adsorption heat allocation devices……... 42

II.4. MOFs as water-adsorbent for refrigeration applications……. 44

Conclusion……. 51

References…….. 52

CHAPTER 2 – *Classical and quantum-based molecular simulations*…….. 73

Introduction…… 75

I. Classical Molecular Mechanics…….. 76

I.1. Statistical Mechanics-Ensembles…….. 76

I.2. Monte Carlo Simulations…….. 81

I.3. Molecular Dynamics simulations……. 86

I.4. Interatomic potentials……... 90

I.5. Microscopic description of porous materials…… 97

I.6. Microscopic description of the adsorbates…… 99

II. Quantum calculations…… 101

II.1. General aspects…… 101

II.2. Density functional theory…… 103

II.3. Illustrations of DFT applications to the description of solids……. 108

III. Ab Initio Molecular Dynamics……. 111

III.1. General aspects……... 111

III.2. Ehrenfest Molecular Dynamics…….. 112

III.2. Born-Oppenheimer Molecular Dynamics…….. 113

III.3. Car-Parrinello Molecular Dynamics…….. 114

References…….. 117

CHAPTER 3 – *Computational exploration of proton conduction in porous materials*…… 125
I. Introduction and contribution……. 127
II. MIL-163(Zr)…….. 133
III. KAUST-7'…… 140
IV. $Ti^{IV}Ti^{IV}(HPO_4)_4$……... 144
V. Conclusion……. 150
References…….. 151
Article 1…….. 155
Article 2…….. 165
Article 3…….. 177
CHAPTER 4 – *Computational exploration of water adsorption in MOFs*……... 185
I. Introduction and contribution……. 187
II. CUK-1(Me)……... 190
III. MOF-801(Zr)……... 199
IV. MIL-100(Fe)…… 214
V. Conclusion……. 227
References…….. 228
CHAPTER 5 – *Conclusion and perspectives*…… 231
Annexes……...……. 237

INTRODUCTION

In the last century, the unprecedented population growth and the progressive improvement of living standards have been pushing the environment to its limits, applying a substantial pressure into the natural resources and demanding ever-increasingly novel energy source. Such concerns have been the motivation of extensive efforts devoted to the development of novel and efficient materials designed for the production, distribution, storage and/or transformation of energy.

In this context, the development of solid-state proton conductors is of strategic interest. These materials are involved in many fields such as humidity sensors, membranes for water electrolyzers, redox-flow batteries and fuel cells. More specifically, this later technology, which allows the generation and storage of clean energy, integrates proton conductors as solid electrolytes to ensure an efficient proton transfer from the anode to the cathode. One of the remaining issues is that while the benchmark electrolyte material, i.e. Nafion shows high proton conduction performances under operating conditions it still suffers from high cost and a relatively poor mechanical stability. Such drawbacks still slow down the widespread development of this technology at much larger scale.

Adsorption-driven heat transfer (AHT) devices have also been increasingly envisaged as efficient technologies to be used for the exploitation of low-grade thermal energy sources such as solar plants and waste heat. The efficiency of such related AHT systems including adsorption heat pumps/chillers strongly depends on the adsorption/desorption performances of the adsorbents in terms of fluid uptake, shape of the corresponding adsorption isotherm and desorption kinetics as well as the choice of the adsorbent/fluid working pair. Although the most commonly employed adsorbent in AHT systems, i.e. the SAPO-34 zeolite, shows attractive adsorption uptake and high fluid affinity, its global performance is still not optimal mostly due to its energy-demanding desorption of the fluid. Therefore there is still considerable room for improving the adsorbent for this targeted technology.

These two applications have one fundamental aspect in common: the implication of water as fluid. While in the large majority of the solid-state proton conductors operating below 100°C, water has an indispensable role in assisting the proton propagation, in AHT devices this molecule is considered as the most appropriate working fluid. There is indeed a

need to gain a deeper knowledge on the behavior of water confined in the materials envisaged for these two applications for further developing refined solid electrolytes and adsorbents. This calls for an exploration at the microscopic scale of the organization and dynamics of the confined water as well as its interaction with the host framework that can be achieved by molecular simulations.

Molecular simulations integrate a large panel of techniques that can describe the system either at the electronic (quantum calculations) or the atomistic (classical calculations) levels. The treatment of periodic systems at the electronic level requires time-consuming calculations that still prevent the exploration of solids over long length/time. The classical simulations based on the use of forcefield to describe the interactions between all atoms constituting the system are commonly privileged to explore the adsorption and dynamics of confined fluid in porous materials using Monte Carlo and Molecular Dynamics simulations.

In this thesis, quantum- and force-field based simulations have been intertwined to gain insight at the microscopic scale into the water adsorption and the water-assisted proton-conduction mechanisms in a series of novel inorganic and hybrid porous materials that have been identified as excellent candidates for the two targeted applications. The selection of these materials results from a strong collaboration between our research team and two groups expert in the synthesis of porous materials (IMAP, Paris-ILV, Versailles, Dr. C. Serre & KAUST, Saudi Arabia, Prof. M. Eddaoudi) and one group specialized in the development of AHT applications (KRICT, Korea, Prof. J.S. Chang). The objective of this strong interplay between experimental and computational tools was to identify the key-features of the porous materials that drive their performances for the targeted applications.

Specifically, the following global strategy was devised to select the best water-mediated proton conduction materials. An experimental screening was first conducted on potentially attractive porous materials that incorporate diverse functional hydrophilic ligands with hydroxyl groups or sulfonic, phosphonic and carboxylic acid-based functions as proton sources [1–10] and different pore size and topology to create a percolated water hydrogen bonded network to favor an efficient proton-migration pathway [11–16]. The performances of these materials were then systematically evaluated in the group by Complex Impedance

Spectroscopy measurements in different temperatures (298 – 473K) and relative hydration levels (anhydrous - 95%RH). The main results are summarized in Figure 1 where we grouped the materials according to their constitutive main proton sources i.e. (i) grafted carboxylic functions, (ii) coordinated water molecules, (iii) terminal phosphate (POH) groups, (iv) μ-OH groups in the SBU, (v) coordinated acids, and (vi) hydroxyl groups present in the ligands.

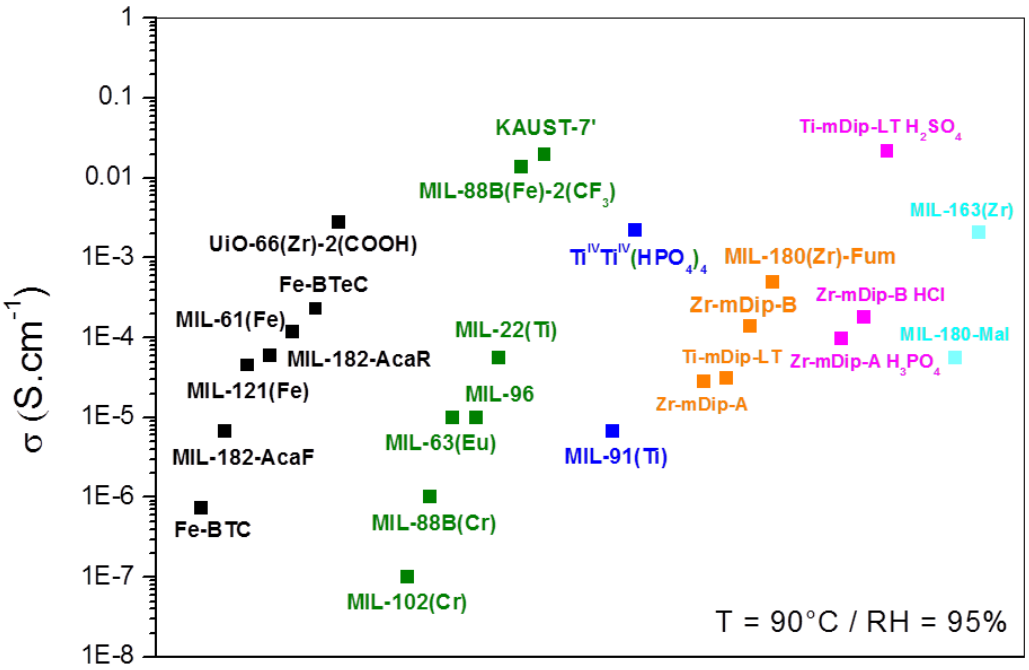

Figure 1 - Main materials screened experimentally by group with respect to their proton conductivity by complex impedance spectroscopy and their respective conductivity at 90°C and 95% RH. These materials were grouped according to their proton source, being: grafted carboxylic functions (black), coordinated water molecules (olive), terminal phosphate (POH) groups (blue), μ-OH groups in the SBU (orange), coordinated acids (magenta) and hydroxyl groups in the ligands (cyan).

The selection of water adsorbents suitable for AHT purposes was achieved in collaboration with the research group of Prof. J.S. Chang (KRICT) with the following criteria: (i) chemical and mechanical stability, (ii) a S-shaped water adsorption isotherm whose step occurs in a favorable region of relative pressure at ambient temperature ($0.05 < P/P_0 < 0.4$), (iii) negligeable hysteresis, and (iv) large water uptakes.

This group evaluated the Coefficient of Performances (COP) of a relatively large series of Metal Organic Framework materials under different refrigeration operating conditions to identify the most promising materials that can compete with the existing benchmark material (i.e. SAPO-34). As a typical illustration, Figure 2 reports a comparison of the COP of a series of materials at a low desorption temperature (70°C).

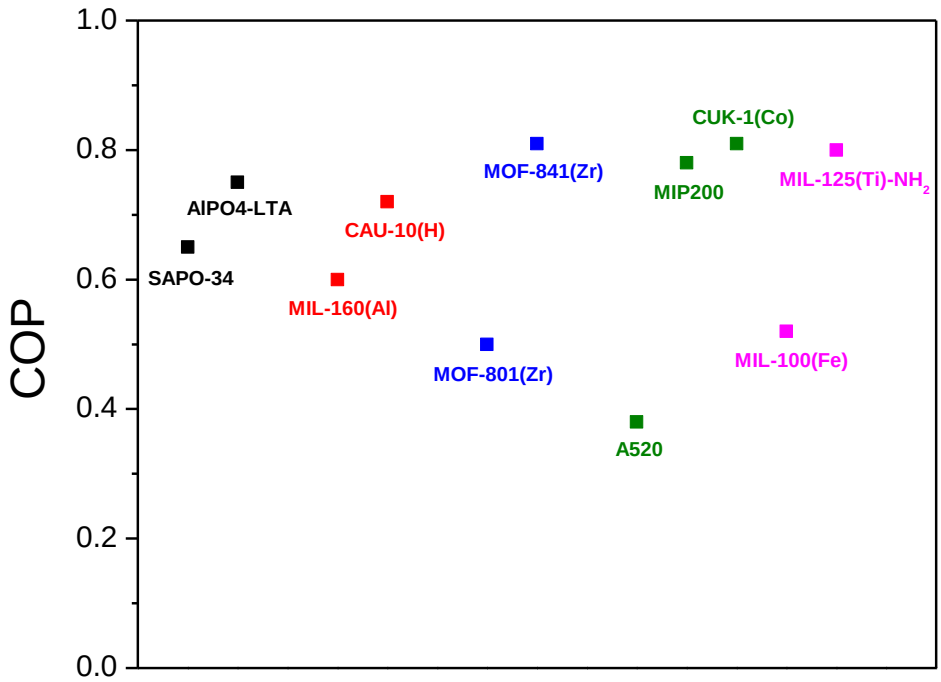

Figure 2 – Coefficient of performance (COP) at 343 K of a selection of MOFs recently studied for AHT applications compared with the benchmark materials in this field. In red, Al-based MOFs; in blue, Zr-based MOFs; in green, MOFs with 1D pores and μ-OH groups, and in magenta mesoporous MOFs.

The manuscript is thus constructed as follows:

The first chapter introduces the general principles and technologies involved in solid-state proton conductors and AHT applications. This is followed by the state of the art regarding the materials currently employed in both fields with a special emphasizes on the family of Metal Organic Framework materials that are one of the most recent classes of porous solids envisaged for such application.

The second chapter provides a brief description of the molecular simulation techniques (principles, inputs and outputs) that have been used in this work: (i) the Density Functional Theory applied here to geometry optimize the investigated solids at the electronic level, determine their atomic charges, evaluate the water/framework interaction energies and further derive accurate force field parameters, (ii) the classical molecular simulations including the Monte Carlo and Molecular Dynamics techniques used here to predict the water adsorption isotherm/energetics as well as to understand the water arrangement and (iii) the *Ab Initio* Molecular Dynamics used here to describe the proton migration mechanisms.

The third chapter presents the computational exploration of the water-assisted proton conduction mechanisms of three of the most promising materials that have been identified experimentally in Figure 1, i.e. two Metal Organic Frameworks namely MIL-163(Zr) and KAUST-7' as well as the Ti-phosphate ($Ti^{IV}Ti^{IV}(HPO_4)_4$).

The fourth chapter describes the simulations that have been conducted on three of the best Metal Organic Frameworks found experimentally for AHT applications (Figure 2): the series of CUK-1(Me) (Me = Ni, Co, Mg), the MOF-801(Zr) and the MIL-100(Fe).

Finally, the last chapter assembles the main conclusions of this work and the perspectives it offers while the annex provides the papers published on other adsorption-related topics.

REFERENCES

[1] A. Shigematsu, T. Yamada, H. Kitagawa, Wide Control of Proton Conductivity in Porous Coordination Polymers, J. Am. Chem. Soc. 133 (2011) 2034–2036. doi:10.1021/ja109810w.

[2] J.M. Taylor, K.W. Dawson, G.K.H. Shimizu, A water-stable metal-organic framework with highly acidic pores for proton-conducting applications, J. Am. Chem. Soc. 135 (2013) 1193–1196. doi:10.1021/ja310435e.

[3] M. Bazaga-García, R.M.P. Colodrero, M. Papadaki, P. Garczarek, J. Zoń, P. Olivera-Pastor, E.R. Losilla, L. León-Reina, M.A.G. Aranda, D. Choquesillo-Lazarte, K.D. Demadis, A. Cabeza, Guest Molecule-Responsive Functional Calcium Phosphonate Frameworks for Tuned Proton Conductivity, J. Am. Chem. Soc. 136 (2014) 5731–5739. doi:10.1021/ja500356z.

[4] P. Ramaswamy, N.E. Wong, B.S. Gelfand, G.K.H.H. Shimizu, A Water Stable Magnesium MOF That Conducts Protons over 10 –2 S cm –1, J. Am. Chem. Soc. 137 (2015) 7640–7643. doi:10.1021/jacs.5b04399.

[5] W.J. Phang, H. Jo, W.R. Lee, J.H. Song, K. Yoo, B. Kim, C.S. Hong, Superprotonic Conductivity of a UiO-66 Framework Functionalized with Sulfonic Acid Groups by Facile Postsynthetic Oxidation, Angew. Chemie Int. Ed. 54 (2015) 5142–5146. doi:10.1002/anie.201411703.

[6] F. Yang, H. Huang, X. Wang, F. Li, Y. Gong, C. Zhong, J.-R. Li, Proton Conductivities in Functionalized UiO-66: Tuned Properties, Thermogravimetry Mass, and Molecular Simulation Analyses, Cryst. Growth Des. 15 (2015) 5827–5833. doi:10.1021/acs.cgd.5b01190.

[7] D.D. Borges, S. Devautour-Vinot, H. Jobic, J. Ollivier, F. Nouar, R. Semino, T. Devic, C. Serre, F. Paesani, G. Maurin, Proton Transport in a Highly Conductive Porous Zirconium-Based Metal-Organic Framework: Molecular Insight, Angew. Chemie - Int. Ed. 55 (2016) 3919–3924. doi:10.1002/anie.201510855.

[8] P.G.M. Mileo, S. Devautour-Vinot, G. Mouchaham, F. Faucher, N. Guillou, A. Vimont, C. Serre, G. Maurin, Proton-Conducting Phenolate-Based Zr Metal–Organic Framework: A Joint Experimental–Modeling Investigation, J. Phys. Chem. C. 120 (2016) 24503–24510. doi:10.1021/acs.jpcc.6b04649.

[9] F. Yang, G. Xu, Y. Dou, B. Wang, H. Zhang, H. Wu, W. Zhou, J.-R. Li, B. Chen, A flexible metal–organic framework with a high density of sulfonic acid sites for proton conduction, Nat. Energy. 2 (2017) 877–883. doi:10.1038/s41560-017-0018-7.

[10] Z. Hassanzadeh Fard, N.E. Wong, C.D. Malliakas, P. Ramaswamy, J.M. Taylor, K. Otsubo, G.K.H. Shimizu, Superprotonic Phase Change to a Robust Phosphonate Metal–Organic Framework, Chem. Mater. 30 (2018) 314–318. doi:10.1021/acs.chemmater.7b04467.

[11] C. Dey, T. Kundu, R. Banerjee, Reversible phase transformation in proton conducting Strandberg-type POM based metal organic material, Chem. Commun. 48 (2012) 266–268. doi:10.1039/C1CC15162B.

[12] S.S. Bao, K. Otsubo, J.M. Taylor, Z. Jiang, L.M. Zheng, H. Kitagawa, Enhancing proton conduction in 2D Co-La coordination frameworks by solid-state phase transition, J. Am. Chem. Soc. 136 (2014) 9292–9295. doi:10.1021/ja505916c.

[13] S. Horike, D. Umeyama, M. Inukai, T. Itakura, S. Kitagawa, Coordination-Network-Based Ionic Plastic Crystal for Anhydrous Proton Conductivity, J. Am. Chem. Soc. 134 (2012) 7612–7615. doi:10.1021/ja301875x.

[14] M. Inukai, S. Horike, W. Chen, D. Umeyama, T. Itakura, S. Kitagawa, Template-directed proton conduction pathways in a coordination framework, J. Mater. Chem. A. 2 (2014) 10404–10409. doi:10.1039/C4TA01261E.

[15] J.M. Taylor, T. Komatsu, S. Dekura, K. Otsubo, M. Takata, H. Kitagawa, The Role of a Three Dimensionally Ordered Defect Sublattice on the Acidity of a Sulfonated Metal–Organic Framework, J. Am. Chem. Soc. 137 (2015) 11498–11506. doi:10.1021/jacs.5b07267.

[16] S.S. Park, A.J. Rieth, C.H. Hendon, M. Dincă, Selective Vapor Pressure Dependent Proton Transport in a Metal–Organic Framework with Two Distinct Hydrophilic Pores, J. Am. Chem. Soc. 140 (2018) 2016–2019. doi:10.1021/jacs.7b12784.

CHAPTER 1

Overview on the proton conduction and water adsorption in solids

Introduction

The objective here is to introduce the reader to the main concepts and technologies involved in solid-state proton conductors and adsorption-based heat pump/chiller applications.

The first part of the chapter deals with the area of solid-state proton conductors by first providing a general description of the three main technologies in which the proton conductors are used: fuel cells, redox-flow batteries and resistivity-based humidity sensors. These technologies show a large potential but they are still hampered by the fact that most of their proton-electrolytes materials are not ideally adapted to the operating conditions. The different classes of proton-conducting materials are then listed and described, including water containing systems, oxo acids, perovskite-like solids and hybrid materials, depending on their typical operating conditions and their driving forces involved in the proton conduction process. This is followed by a section on the promises of MOFs as new solid-state proton conductors in both anhydrous and hydrated conditions. Even though these materials have been discovered quite recently, due to their vast diversity of composition, topologies, and pore sizes, some of pure and composite superprotonic MOF materials have been discovered, with performances outpassing those of the benchmark Nafion™.

The second part of the chapter is dedicated to the description of water adsorbents for heat reallocation application, starting with a brief introduction to thermally-driven heat pumps and chillers. The use and principles of adsorption-based heat reallocation devices is then described, with the introduction of basic thermodynamic concepts including the operation and the calculation of the coefficient of performance, an important parameter that relates the input and useful heat of a thermic transformation process. A description of the main characteristics expected from an optimal adsorbent in heat allocation applications is further proposed as well as a list of benchmark materials that are currently commercialized. At this stage, MOFs are also presented as promising water adsorbents for heat transfer applications.

I. Solid state proton conductors

I.1. Solid state proton conductors-based technology

The investigation of solid state proton conductors was initiated early 1900s when ice was found as an electrical conductor [1], and continued specially in the 1950s with a focus on defective solids. At this stage, the proton conduction phenomenon was mostly explored from a fundamental perspective. This paradigm started to change in the 1960s with the use of Nafion, the first commercial proton conducting material, as a fuel cell electrolyte in the context of the Gemini and Apollo space programs [2]. Proton conductors have been envisaged so far for several applications including the energy production and storage with the use of ***fuel cells*** and ***redox-flow batteries***, as well as microionic devices such as ***humidity sensors*** [3] that are briefly described below:

(1) Fuel cells are devices that fundamentally turn the energy of chemical reactions to electrical energy. Differently from batteries, they can provide electrical power continuously, as long as a fuel, such as hydrogen, methanol, or light hydrocarbons are provided. Since hydrogen is the most common fuel encountered in fuel cells, here it will be considered as the default fuel. In this specific case, fuel cells imply the following global reaction:

$$2H_{2(g)} + O_{2(g)} \rightarrow 2H_2O_{(l)} \tag{1.1}$$

As shown in Figure 1.1, a fuel cell is made of main components, i.e. an anode, a cathode, an electrolyte and structural components (e.g. end plates). At the anode a catalyst oxidizes H_2 and splits it into protons (i.e. H^+) and free electrons (reaction 1.2). The electrons move through an external circuit, providing electrical power, while the protons flow through the electrolyte from the anode to the cathode. At the cathode, the electrons from the circuit and the protons from the electrolyte membrane promote the reduction of O_2 (reaction 1.3) into H_2O molecules.

$$Anode: 2\mathrm{H}_{2(\mathrm{g})} \rightarrow 4H^+{}_{(\mathrm{aq})} + 4e^- \tag{1.2}$$

$$Cathode: O_{2(\mathrm{g})} + 4\,H^+{}_{(aq)} + 4e^- \rightarrow 2\,H_2O_{(\mathrm{l})} \tag{1.3}$$

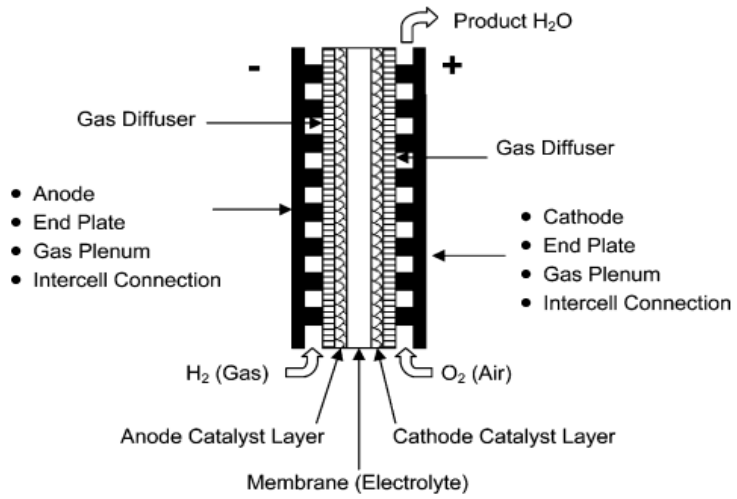

Figure 1.1 – Schematic representation of a fuel cell involving H_2(g) and O_2(g) (from ref. [4]).

One of the bottlenecks of this process occurs in the solid electrolyte. The corresponding membrane must ensure an efficient proton transfer from the anode to the cathode and at the same time it needs to be mechanically and thermally robust as well as resistant to the direct passage of gases from one electrode to the other (cross-over). In this context, two types of membranes are mainly envisaged. One to operate at low temperatures (< 100°C) for vehicles and mobile power applications and other at intermediary temperatures (100-300 °C) [5–7], avoiding the anode poisoning with impurities (e.g. CO) [8,9].

Nafion™ is the benchmark material used in low temperature (80 – 120°C) proton conducting membranes, even though it is a relatively old material, having been discovered in the 1960s. This material consists of a fluorinated hydrophobic backbone side-attached with hydrophilic sulfonic groups, forming channels (cf. Figure 1.2a) [10,11]. The hydration level of these channels drives its proton conductivity performance. For a low water content, the sulfonic polymer behaves as an insulator, as the water molecules are located only at the vicinities of the sulfonic groups, forming two separated hydrophobic and hydrophilic domains [11]. However, when saturated with water, conductivity values approach that of bulk aqueous electrolytes (~ 1×10^{-1} $S.cm^{-1}$ at 80 °C [12]) due to the formation of a well-developed percolated sulfonic-water network comprising channels filled with free water (cf.

Figure 1.2b) [11]. Indeed, Nafion™ exhibits both a high proton conductivity and a reasonable chemical stability at low temperatures.

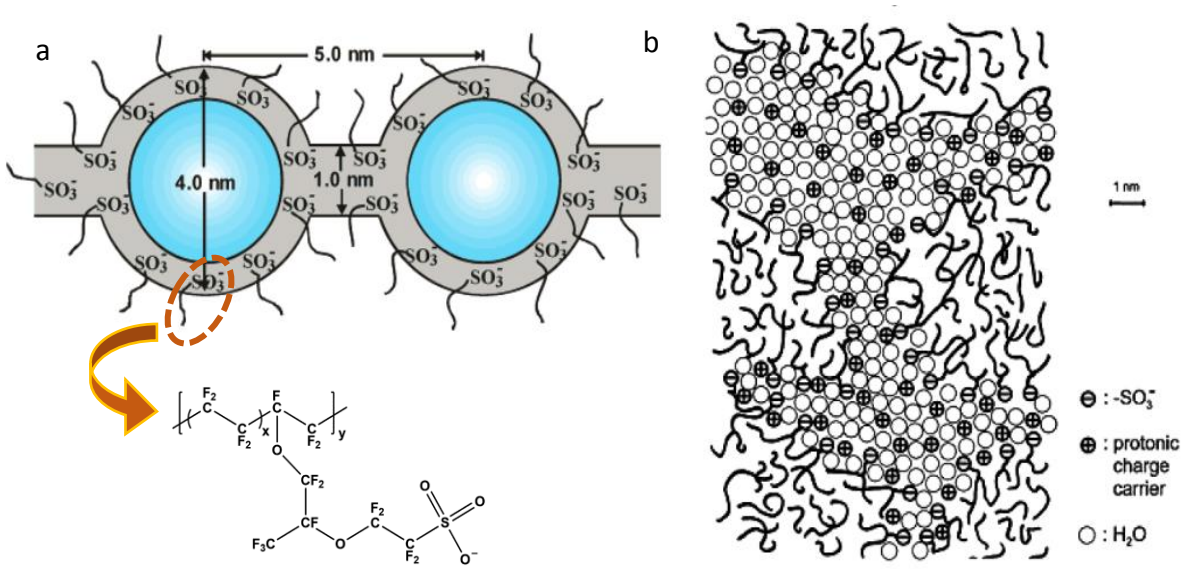

Figure 1.2 –Morphology description of Nafion™ as cluster channels, evidencing the hydrophobic backbone connected to hydrophilic chains (a), and clusters (b). Reproductions of ref. [10].

On the other hand, Nafion™ presents several drawbacks. The first is the strong dependence of its proton conduction performances on its hydration state, which does not meet the requirement of being used for temperatures significantly over 100 °C. Moreover, this material also displays a glass transition temperature at 125 °C which causes poor mechanical stability at higher temperatures [13]. Nafion™ also does not tolerate other cations than H^+, which are known to catalyze the polymer chain decomposition [14]. Additionally, it also shows an insufficient resistance to methanol crossover, which might be an important issue when methanol is used as fuel [11]. Finally, the cost of a Polymer Electrolyte Membrane (PEM) based on Nafion™ is prohibitively expensive due to their complex manufacturing processes. Therefore, there is still significant room for the development of new materials that may overcome all the limitations imposed by this material.

Table 1.1 summarizes the main types of fuel cells depending on the operating conditions, as well as their applicable properties and most common employed electrolytes.

Table 1.1 – Summary of the main types of solid state fuel cells based on proton conducting electrolytes, their respective most common employed electrolytes and operating conditions [15–17].

Type of fuel cell	Common Electrolyte	Operating Temp. (°C)	Power Density (mW/cm^2)	Fuel Efficiency (%)
Polymer Electrolyte Membrane Fuel Cell (PEMFC)	Nafion™	80 - 120	300 – 1000	45 – 60
Solid Acid Fuel Cell (SAFC)	$CsHPO_4$	230 - 280	130	55
Protonic Ceramic Fuel Cell (PCFC)	BCY[a], BCZY[b]	400 - 700	100 – 540	60 – 80

[a] BCY = yttrium-doped barium cerates. [b] yttrium-doped barium cerates zirconates.

(2) Redox flow batteries (RFBs) are recognized as one of the most realistic candidates amongst electrochemical technologies for energy storage in the range of several kW/kWh up to tens MW/MWh for stationary applications [18–20]. Compared to fuel cells, these batteries do not operate with gases that are consumed during their uses. Instead, they exploit the chemical energy inherent to redox processes of metal species in two liquid solutions to either store or produce energy according to their operating modes (cf. Figure 1.3). Another specificity of this technology versus fuel cells is its complete reversibility which allows to operate as a converter of electricity into chemical energy and vice-versa [21]. Since this system involves the use of liquid solutions, indeed it works at about room temperature. The reactions involved in the process are listed in Equations 1.4 and 1.5, where the direct equations occur in the charging mode and the inverse equations in the discharging mode. In these equations, the A and B species are placed at the anode and cathode respectively.

$$A^{n+} + xe^- \rightleftharpoons A^{(n-x)+} \tag{1.4}$$

$$B^{m+} - ye^- \rightleftharpoons B^{(m+y)+} \tag{1.5}$$

The four main RFB technologies are the Fe/Cr [22], the all-vanadium (VRB) [23,24], the V–Br [25] and the V–O_2 [26] cells. The representation of the components of each technology is expressed in terms of A^{n+}/B^{m+} pairs incorporated in Equations 1.4 and 1.5. They correspond to Cr^{3+}/Fe^{2+}, V^{3+}/VO^{2+}, VBr_3/Br^- and V^{3+}/H_2O [21] respectively. Unlike in PEMFCs, the redox-flow batteries have charge carriers transported through a membrane electrode assembly to maintain the electrical neutrality of the electrolyte solutions. In RFBs more attention must be paid on the membrane manufacturing, since it must (i) allow the crossing of charge equilibrium species, like protons (H^+) in the Vanadium redox-flow batteries, (ii) prevent the water transfer and consequent flooding of the half cells, (iii) be resistance upon the acid environment of the aqueous solutions of the positive and negative electrolyte solutions and (iv) prevent the crossing-over of the redox chemical species to avoid a short-circuit in the cell [27]. Since the power and energy density of RFBs is low compared to other storage technologies (limiting their use in mobile applications [21]), there is a crucial need to enhance the efficiency of their components, specially their membrane electrode assembly as well as the development of their overall design.

As in PEMFCs, perfluorinated membranes (like Nafion^{TM}) are the main Ion Exchange Membrane (IEM) used in RFB technologies [28–31]. In addition to the problems associated with Nafion^{TM} listed in the previous section, it is often required to modify the membrane with inorganic (e.g. SiO_2 [32], TiO_2 [33]) and organic (e.g. polyethylenimine [34], polypyrrole [35]) components in order to increase the ion selectivity of the membrane. Other non-fluorinated membranes are also employed in RFBs, such as (i) pore filled IEMs, which consist of ion-exchange resins (e.g. Amberlite CG 400 [36]) or polyelectrolytes (e.g. polystyrene sulfonate [37]) introduced in a polymeric matrix, (ii) sulfonated polymers [38], and (iii) inorganic materials (e.g. zeolites [39]).

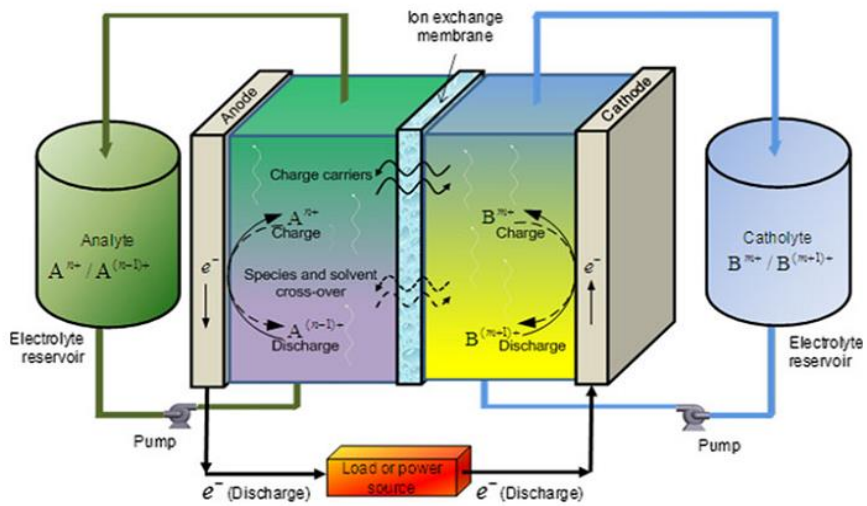

Figure 1.3 – Diagram scheme of a redox-flow battery taken from ref. [40]. Cylinders represent the reservoirs where the catholyte and analyte solutions are stored. The widths of the space membrane/cathode and membrane/anode where the charge and discharge reactions that place are exaggerated for clarity. Usually many of these anode/membrane/cathode are stacked adjacently in order to enhance the RFB power density.

(3) Finally, humidity sensors are involved in a wide range of domestic, e.g. air conditioning systems; medical, e.g. incubators and industrial applications, e.g. dehydrated food and textile mill [41]. Given their range of applications, an ideal humidity sensor should fit a certain range of requirements such as: good sensibility, fast response, good reproducibility, durability, resistance to contaminants, reliability in a broad range of temperatures, easy processing and low cost [41,42]. With the objective to fulfil such requirements, a wide variety of sensor mechanisms have been considered for humidity detection based on resistive, capacitive, optical, piezoresistive, gravimetric or magnetoelastic properties [41,43]. In the resistive-based mechanism, the difference in proton conductivity of a material between its anhydrous and hydrated states constitutes the driving force of the sensor. The current materials used in such sensors are ceramics (semiconductors), organic polymers and organic/inorganic hybrid materials [44]. However, these materials show some drawbacks. For ceramics, due to the chemisorption of OH^- at their surface, there is a reduction of their resistive potential with time, requiring them to be thermally activated to regenerate the sensor surface. This requires an additional heater to the system that increases the complexity of the overall system. Regarding polymers, they often present issues in terms of thermal and chemical stability and this limits their use in severe environments. Solid

oxides and zeolites have also been considered for this application however they also show limitations in terms of operating conditions since they require the need of oxidant atmosphere and temperatures over 400 ºC [45]. Therefore, optimal resistive-based sensors materials operating under harsh environment and medium temperatures are still lacking [45]. In Figure 1.4, a graphic representation of a resistivity-based humidity sensor is presented.

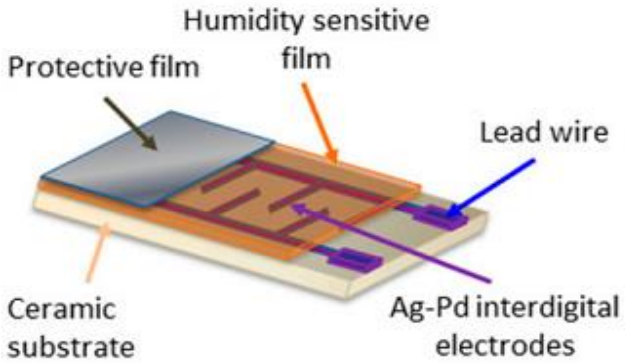

Figure 1.4 – Schematic representation of a humidity sensor (from ref. [46]).

I.2 Classification of solid state proton conductors

A common point of the three proton conducting technologies mentioned above is the need to improve their performances. This search is inevitably driven towards the discovery of new and more efficient proton conductors used as solid electrolytes that would make their respective processes more efficient. It is therefore of interest to first explore the proton conduction properties of the materials that can be envisaged as future solid electrolytes.

In this context, solid state materials may be classified into three major groups: insulators, protonic conductors and superprotonic conductors [47]. Insulators present conductivities lower than 10^{-10} S.cm^{-1}, protonic conductors show intermediary conductivities values that could reach 10^{-5} S.cm^{-1}, whereas superprotonic conductors show conductivity values of at least 10^{-4} S.cm^{-1}.

Another simple and technological-based approach consists of classifying these proton conducting materials into three categories depending on the operating conditions, i.e. low, medium and high temperature (cf. Table 1.1). The first family of materials operates below

100 °C and their proton conductivity depends on the Relative Humidity (RH), the higher RH allowing to ensure a high water concentration to assist the proton migration. The second group of materials operates between 100 and 190°C. In this range of temperature, conductivities beyond 10^{-3} $S.cm^{-1}$ can be reached with (i) materials with coordinated water (e.g. zirconium sulfoaryl phosphonates [48], sulfonated PEEK [49], acid-enriched PAMA [50] and PBI[1] [51]) maintained at high pressure (e.g. 6 atm [52]) in order to avoid the loss of water [53] and (ii) porous materials with protic solvents (e.g. imidazole, triazole [54,55]). The third set of materials presenting good proton conduction properties at high temperatures (usually above 400°C) are perovskite-like oxides (e.g. BCY [56], BCZY [57]) and lanthanum tungstate (LWO) [58,59].

A more classical and insightful classification suggested by Kreuer [60] assembles superprotonic materials, as shown in Figure 1.5, into four main categories: water containing systems, oxo-acid salt conductors, densely packed oxides and organic/inorganic systems:

(1) The first category includes a large diversity of standard materials such as layered solids [61,62], oxide hydrates [63,64], heteropolyacid [65], protonic β-aluminas [66,67], acidic phosphates and phosphonates [47,68–76], and hydrated acidic polymers [77,78]. The sulfonated fluorocarbon polymer Nafion™ is the most known component of this family of materials characterized by the highest proton conductivity. In these materials, the water molecules play a prominent role in the proton conduction mechanism, by dissociating and delocalizing protons from their active sites and by acting as a mediator for the proton transfer throughout the solid.

(2) The second category is made of salts of oxo-acids with sizeable cations (e.g. $CsHSO_4$, $RbHSO_4$) which exhibit a superprotonic behavior due to the formation of an orientationaly disordered phase called as superprotonic phase transition, at moderate temperatures – usually above 140 °C [79]. This phase transition appears to be related to the softer M–O bonds [80]. These materials do not require the existence of Brønsted acid sites or a structured proton network to manifest high conductivity [79] and they may be used in

[1] PEEK stands for polyether ether ketone, PAMA for polydiallydimethylammonium and PBI for polybenzimidazole.

tandem with intergranular oxides (e.g. SiO_2, Al_2O_3, Fe_2O_3, etc.) to enhance their mechanical properties [79].

(3) The third category encompasses a series of different densely packed oxides. These materials show as a common feature their robustness particularly at high temperatures and the conduction of proton by vacancies, either intrinsic or introduced by the involvement of dopants or chemical treatments [79]. Their use at low temperatures is however an issue, since they only present proton conduction at high temperatures. The perovskites (e.g. yttrium-doped $(Sr,Ba)CeO_3$ and $(Ba,Sr)ZrO_3$) are typical examples of this family of materials that show superprotonic behavior especially at high temperatures.

(4) The fourth category is formed by the association of organic and inorganic systems. One example is the combination of acids like H_2SO_4 and H_3PO_4 with organic systems incorporating basic functions such as triethylenediamine, hexamethylenetetramine and polyacrylamide [60]. Another is the blend of oxo-acids and polymers (e.g. polyacrylamide·$1.2H_2SO_4$). In this category, the driving force for the proton conduction is the synergy between the rich source of protons and a structured matrix for proton transmission provided by the inorganic acids and the polymers, respectively. This family also includes protic solvents such as heterocycles bases, imidazoles, alkyls and pyrazoles used in association with polymers or meso/microporous materials that enhance their proton conduction performances through confinement effects [81–83].

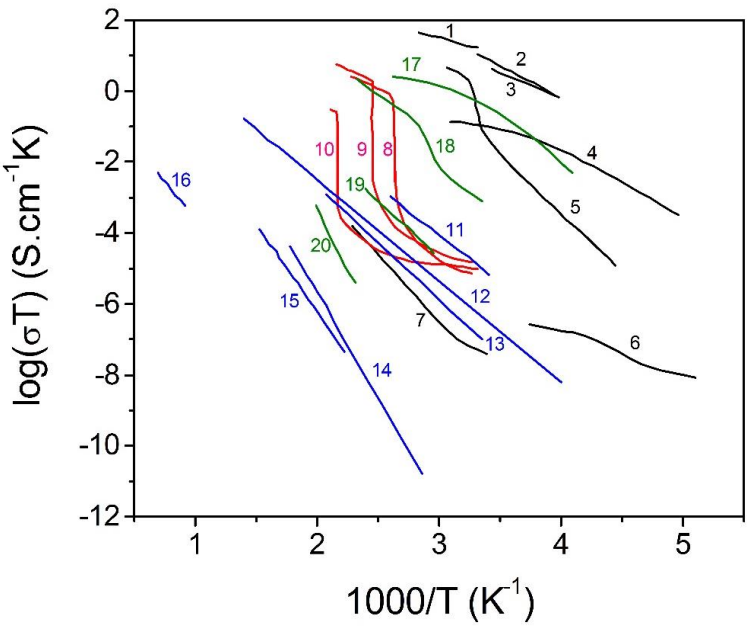

Figure 1.5 – Temperature dependence of the proton conductivity for the 4 different classes of proton conducting materials (adapted from ref. [60]). In black, water containing systems; in red, oxo-acids; in blue, densely packed oxides and in green inorganic/organic systems. The materials considered in this plot are the Nafion (1), $H_4SiW_{12}O_{40}\cdot 28H_2O$ (2), γ-Zr sulfophosphonates (3), $SnO_2\cdot nH_2O$ (4), $H_3UO_2AsO_4\cdot 3H_2O$ (5), ice (6), H_2O – β-alumina (7), $(Cs,Tl)HSO_4$ (8), $CsHSO_4$ (9), $RbHSO_4$ (10), Nd:$BaCeO_3$ (11), Y:ZrO_3 (12), Y:$SrCeO_3$ (13), $FeLiNbO_3$ (14), Ni:$KTaO_3$ (15), Y_2O_3 (16), polyacrylamide·$1.2H_2SO_4$ (17), poly(ethylene oxide) – NH_4ClO_4 blend (18), α-$Zr(HPO_4)_2$/0.75 pyrazole (19) and $Zr(PO_3(CH_2)_5COOH)_2$ (20).

I.3. MOFs as novel solid state proton conductors

Recent efforts in the development of new superprotonic materials have allowed the discovery of efficient proton conducting porous materials. Among them, one of the most recent class of porous materials, the metal-organic frameworks (MOFs) have been intensively explored over the last ten years for this targeted application.

The MOFs are hybrid porous materials that are formed by the assembly of organic linkers and inorganic nodes [84]. They are characterized by a wide range of pore sizes/shapes, topologies and chemical compositions [85,86] that make this family of solid highly tunable for diverse applications in the fields of gas storage/separation, catalysis, sensoring, biomedicine, and more recently as heat pump components and proton conductors [87–89].

Nevertheless, even though a large number of MOF structures have already been discovered [85], only a fraction of them are chemically and mechanically stable, easily scalable and low cost/low toxic, pre-requirements to be further promoted at the industrial-level. Considering particularly applications where the adsorption of water is directly involved such as water-mediated proton conduction or heat pumps, water stability is clearly of utmost importance. In a review reported in 2014, Burtch *et al.* [90] have defined four degrees of stability: thermodynamic stability (ThS), high kinetic stability (HK), low kinetic stability (LK), and unstable (Uns). ThS stability refers to materials that are stable over long-term exposure to aqueous solutions, HK to those stable under high RH but decompose after exposure to liquid water, LK to those stable only under low RH and Uns to those unstable upon any exposure of moisture. After a qualitative analysis over different 200 MOFs, Burtch *et al.* concluded that 10% of the MOFs show ThS, 60% HK, 20% LK and 10% Uns behaviors. Regarding the water-related applications, ThS or at least HK materials are required. This clearly indicates that only a fraction of existing MOFs can be considered for the targeted applications in this work and that a significant effort needs to be deployed to discover novel more robust architectures.

Yuan *et al.* [91] have correlated the stability of MOFs to the Pearson's hard/soft acid/base. In their rationalization, they schematically separated the organic linkers of MOFs in hard (carboxylates) and soft (azolates) Lewis basis and the metals coordinated to the linkers in hard (e.g. Al^{3+}, Cr^{3+}, Fe^{3+}, Ti^{4+}, Zr^{4+}) and soft (e.g. Co^{2+}, Ni^{2+}, Cu^{2+}, Zn^{2+}) Lewis acids. According to their observations, the association of Lewis bases with Lewis acids results in more stable materials as the strength of the coordination between metal and ligands is accordingly stronger. This overcomes the collapse of the architecture which most often occurs via the interaction between water molecules and the metal-ligand connection. Another observation pointed out in their work states that stability is also highly enhanced by the hindering of the metal-oxo clusters from water upon functionalization and the lability of the ligands where large and labile linkers introduce a higher degree of stress in the metal-ligand bonds than small and rigid ones [91]. Recent reviews from Serre *et al.* [92,93], confirmed the importance to consider highly-valent cations to form highly stable MOFs.

Some water stable MOFs have been often considered for proton conduction applications since compared to conventional materials they may offer great advantages in terms of tunable functionality, topology and pore size/shape, allowing the design of solids with a large variety of potential proton sources and an ordered arrangement of confined species acting as proton media. Diverse strategies have been devised to tailor the proton conductivity performances of MOFs via (i) the introduction of functional hydrophilic ligands with hydroxyl groups or sulfonic, phosphonic and carboxylic acid-based functions as proton sources, [94–103] (ii) the incorporation of guest molecules in the pores as proton transfer agents e.g., water, protic molecules or strong acids, [81,104–107] (iii) the design of anionic MOFs with proton donors as counter-ions in the pores [7,108–110] or (iv) the control of the pore size and topology to create a percolated hydrogen bonded network of the guest molecules [111–114]. Nevertheless, it is still difficult to rationalize all these approaches into optimal design strategies considering the myriad of topologies and chemical environments available in the different classes of MOFs. Consequently, much of the experimental research in this field is based on trial-and-error methodologies which are often unproductive. One way to change this perspective would be to acquire a deeper understanding of the mechanisms involved in the proton conducting MOF materials. The combination of molecular simulation and experiments have demonstrated to be a powerful strategy to elucidate the proton conduction mechanisms in MOFs although this has been applied only rarely so far [81,99–101,115–125].

Three main reviews have comprehensively enumerated the main proton conducting MOFs reported in the literature [86,126,127]. We updated this listing with the inclusion of novel MOFs recently reported for this application. Table 1.2 reports the full list of MOFs that display a superprotonic behavior ($\sigma > 10^{-4}$ S.cm^{-1}). We deliberatively made the choice to classify these materials as anhydrous and water-mediated proton conductors. We can notice that some of the reported materials reach the threshold value of 10^{-2} S.cm^{-1} at low temperature. This makes them very attractive as an alternative solution to the benchmark material (Nafion^{TM}).

Table 1.2 – Listing of anhydrous and water-mediated proton conducting MOFs, their topology, pore, guests, proton conductivity value and operating conditions published in the literature according to the reviews of Ramaswamy *et al.* [126], Meng *et al.* [86] and Li *et al.* [127]. Entries from 2014 forward were revised and new entries were added up to September 2018.

Materials	Features and topologies	Pore Guests	Conductivity ($S.cm^{-1}$)	Conditions	Ref.
		Anhydrous MOFs			
$(C_2N_2H_{10})(C_2N_2H_9)_2Cu_8Sn_3S_{12}$	3D framework with rhombicuboctahedron cages	HCl	3.62×10^{-2}	442 K	[128]
Cu^I-MOF	Interpenetrated 3D network with 1D channels (impregnated with acids)	Pz·6HCl [l]	2.17×10^{-2}	353 K	[129]
		Pz·$3H_2SO_4$ [l]	3.83×10^{-3}	353 K	
$[Zn(H_2PO_4)_2(C_2N_3H_3)_2]_n \cdot xH_3PO_4$	Stacked 2D sheets	H_3PO_4	4.6×10^{-3}	423 K	[130]
SA-EIMS@MIL-101 [a]	3D framework	SA, EIMS	1.89×10^{-3}	423 K	[131]
His@$[Al(OH)(ndc)]_n$ [b]	3D framework with 1D channels	Histamine	1.7×10^{-3}	423 K	[105]
EMIMCI@UiO-67(Zr) [c]	3D framework	EMIMCI	1.67×10^{-3}	473 K	[132]
UiO-67	3D framework	Imidazole	1.44×10^{-3}	393 K	[133]
$[Zn_3(H_2PO_4)_6](Hbim)$ [d]	1D chains templated by benzimidazole molecules	Benzimidazole	1.3×10^{-3}	393 K	[134]
$(Me_2NH_2)[Eu(L)]$ [e]	2D layered material	$(Me_2NH_2)^+$	1.25×10^{-3}	423 K	[135]
β-PCMOF-2$(Tz)_{0.45}$ [f]	3D honeycomb with 1D channels	1,2,4-Triazole	5×10^{-4}	423 K	[104]
$[Zn(HPO_4)(H_2PO_4)_2](ImH_2)_2$ [g]	1D chains	CF_3SO_3H	2.7×10^{-4}	383 K	[136]
FJU-31@Hq [h]	3D framework with 1D channels	Hydroquinone	2.65×10^{-4}	398 K	[137]
$[Zn(HPO_4)(H_2PO_4)_2](ImH_2)_2$ [g]	1D chains templated with Imidazolium cations	Imidazolium cations	2.5×10^{-4}	403 K	[138]
$[Zn(H_2PO_4)(HPO_4)] \cdot (H_2dmbim)_2$ [i]	1D chains	-	2×10^{-4}	463 K	[139]
EIMS-HTFSA@MIL-101 [j]	3D framework impregnated with ionic liquids	EIMS, HTFSA	2×10^{-4}	413 K	[140]
$(CH_3NH_3)_2Ag_4Sn_3S_8$	3D framework with 1D pores	CH_3NH_3	1.87×10^{-4}	463 K, anhydrous	[141]
$[Zn(H_2PO_4)_2(TzH)_2]_n$ [f]	2D	-	1.2×10^{-4}	423 K	[5]
$[H_3O]_2[Mn_7(\mu_3\text{-}OH)_4(SDBA)_6(H_2O)_4]\text{-}(H_2O)_2(DMF)_8\{[(Me_2NH_2)_3(SO_4)]_2[Zn_2(ox)_3]\}_n$ [k]	3D supramolecular structure	DMA^+, SO_4^{2}	1.0×10^{-4}	423 K	[7]
		Water Mediated MOFs			
H_2SO_4@MIL-101-SO_3H	3D framework	H_2O and H_2SO_4	1.82	343 K, 90% RH	[142]
Co-tri	1D structures	H_2O	1.49×10^{-1}	353 K, 98% RH	[110]
Co-tetra			4.15×10^{-2}		
Co-fdc			4.85×10^{-3}		
BUT-8(Cr)-SO_3H	3D framework with 1D pores	H_2O	1.27×10^{-1} (Cr)	353 K, 100% RH	[102]
PCMOF2$^1/_2$(Pz) [l]	3D honeycomb with 1D channels	Pz, H_2O	1.1×10^{-1}	358 K, 90% RH	[107]
PCMOF2$^1/_2$(Tz) [m]		Tz, H_2O	1.17×10^{-1}		
PCMOF2(Pz) [l]		Pz, H_2O	4.6×10^{-2}		
UiO-66-SO_3H	3D framework post-synthetically oxidized	H_2O	8.4×10^{-2}	353 K, 90% RH	[98]
CPM-103[a]	3D framework with cubic cavities	H_2O	5.8×10^{-2}	295 K, 98% RH	[143]
CPM-103b			4.8×10^{-2}		
Fe-CAT-5	3D extended metal catecholates framework	H_2O and DMA	5.0×10^{-2}	298 K, 98% RH	[144]
Ti-CAT-5			8.2×10^{-4}		
$[Sr(\mu_2\text{-}H_2PhIDC)_2(H_2O)_4] \cdot 2H_2O$ [n]	3D framework with irregular 1D pores	NH_3, H_2O	4.76×10^{-2}	363 K, 98% RH	[145]

$\{[Co_3(p\text{-}ClPhHIDC)_3(H_2O)_3]\cdot 6H_2O\}_n$ [o] $\{[Co_3(m\text{-}ClPhIDC)_2(H_2O)_6]\cdot 2H_2O\}_n$	3D framework with 1D pores	H_2O and NH_3 H_2O	4.25×10^{-2} 2.89×10^{-2} 2.47×10^{-4} 7.62×10^{-4}	373 K, 98% RH 363 K, 98% RH 373 K, 98% RH	[146]
$[H_3O]_2[Mn_7(\mu_3\text{-}OH)_4(SDBA)_6(H_2O)_4]\text{-}(H_2O)_2(DMF)_8\{[(Me_2NH_2)_3(SO_4)]_2[Zn_2(ox)_3]\}_n$ [j]	3D supramolecular structure	H_2O, DMA^+, SO_4^{2-}	4.2×10^{-2}	298K, 98% RH	[7]
H_2SO_4@MIL101 H_3PO_4@MIL101	3D micro and mesoporous	H_2O and H_2SO_4 H_2O and H_3PO_4	4.0×10^{-2} 6.0×10^{-2} 1.0×10^{-2} 2.5×10^{-4} 3.0×10^{-3}	296 K, 20% RH 353 K, 20% RH 423 K, 0.1% RH 296 K, 20% RH 423 K, 0.1 RH	[6]
$Co(DCDPP)\cdot 5H_2O$ [p]	3D framework with 1D pores	H_2O	3.9×10^{-2}	353 K, 97% RH	[147]
PCMOF-10	2D layered architecture	H_2O	3.55×10^{-2}	343 K, 95% RH	[97]
Cu^I-MOF	Interpenetrated 3D network with 1D channels (impregnated with acids)	$pz\cdot 3H_2SO_4$ $pz\cdot 6HCl$ $pz\cdot 2H_2PO_4$	3×10^{-2} 2.94×10^{-2} 1.25×10^{-2}	353 K, 95% RH 353 K, 95% RH 348 K, 95% RH	[129]
$Na_2[Eu(SDB)_2(COO)]\cdot 0.375DMF\cdot 0.4H_2O$ [q]	3D frameworks with 1D pores	H_2O	2.91×10^{-2}	363 K, 90% RH	[148]
VNU-15	3D framework	H2O, DMA	2.9×10^{-2}	368 K, 60% RH	[108]
H^+@Ni-MOF-74	3D framework with functionalized groups1D hexagonal pores	H_2O	2.2×10^{-2}	353 K, 60% RH	[149]
PCMOF2$^1/_2$	3D honeycomb with 1D channels	H_2O	2.1×10^{-2}	358 K, 90% RH	[150]
KAUST-7’	2D layers macromolecularly connected thrugh H-bonds	H_2O	2.0×10^{-2}	363K, 95% RH	[151]
Im@(NENU-3) Im-Cu(NENU-3)	3D framework	H_2O and Imidazole	1.82×10^{-2} 3.16×10^{-4}	343 K, 90% RH	[152]
VNU-23	3D framework with 1D pores	H_2O	1.79×10^{-2}	368 K, 85% RH	[153]
MROF-1	3D framework with 1D pores	H_2O	1.72×10^{-2}	343 K, 97% RH	[154]
$Mg_4(C_8O_4H_4)_4(C_5NOH_5)4Cs\cdot 7H_2O$	2D layered material	H_2O and Cs^+	1.61×10^{-2}	363 K, 90% RH	[155]
TETA@HPW-MIL101 [r]	3D framework impregnated	H_2O, TETA, and HPW	1.52×10^{-2}	353 K, 100% RH	[156]
Im-Fe-MOF Im@Fe-MOF Fe-MOF	3D franework with 2 cages	H_2O and Imidazole	1.21×10^{-2} 4.23×10^{-3} 1.25×10^{-4}	333 K, 98% RH	[81]
PCC-72	3D framework with 1D channels	H_2O	1.2×10^{-2}	368 K, 95% RH	[157]
CPM-102	3D framework with two types of 1D channels	H_2O and NH_4^+ cations	1.1×10^{-2}	295 K, 98% RH	[158]
$Cu(H_2spip)Cl_2\cdot H_2O$ [s] $Cu_2H_2(Hspip)_2Cl_4\cdot H_2O$ $Cu(Hspip)(HPO_4)\cdot H_2O$	2D layered materials	H_2O	1.09×10^{-2} 6.47×10^{-3} 6.90×10^{-4}	368 K, 97% RH	[159]
POM-OF	3D open framework with 1D helical channels	H_2O	1.04×10^{-2}	353 K, 75% RH	[160]
$(DMA)_3[Zr(HL)F_2]$ [t]	3D framework	H_2O	1.0×10^{-2}	353 K, 95% RH	[103]
$[Cu_2(phen)_2(AcO)_2(H_2O)_2][Al(OH)_6Mo_6O_{18}]$ $M(nH_2O)$ ($M^+ = H^+, Li^+, Na^+, K^+$)	3D framework with 1D pores	H_2O and M^+	$\sim 1 \times 10^{-2}$	290 K, 80% RH	[161]
$Zn_3(bpdc)_2(pdc)(DMF)\cdot 6DMF$ [u]	3D frameworks with 1D pores	H_2O and DMF	9.5×10^{-3}	333 K, 97% RH	[162]
JLU-Liu44	3D framework	H_2O and $Me_2NH_2^+$	8.4×10^{-3}	300 K, 98% RH	[163]
$(NH_4)_2(adp)[Zn_2(ox)_3]\cdot 3H_2O$ [v]	2D honeycomb layer with hydrophilic interlayer	H_2O and NH_4^+ ions	8×10^{-3}	298 K, 98% RH	[164]
$La(H_5DTMP)\cdot 7H_2O$ [x]	3D framework with small 1D channels	H_2O	8×10^{-3}	297 K, 98% RH	[165]
$[Him]_2Tb_2(ox)_4(H_2O)_2\cdot 2H_2O$ [y]	3D open frameworks	H_2O and	7.7×10^{-3}	353 K, 98% RH	[166]

$[Hmim]_2Eu_2(ox)4(H_2O)_2\cdot 2H_2O[Him]_2$ $Eu_2(ox)_4(H_2O)_2\cdot 2H_2O$		Imidazolium	7.1×10^{-3} 4.6×10^{-3}	353 K, 98% RH 343 K, 98% RH	
MOF-808	3D breathing framework	H_2O	7.58×10^{-3}	315 K, 99% RH	[167]
UiO-66	3D with defects created by addition of fatty acids	H_2O	6.93×10^{-3}	338 K, 95% RH	[168]
CaPiPhtA-NH_3	3D framework with 1D channels	H_2O and NH_3	6.6×10^{-3}	297 K, 98% RH	[96]
Ln-PCMOF-5 (Ln^{3+} = La, Ce, Pr, Nd, Sm, Eu, Gd)	3D pillared layer	H_2O	6.0×10^{-3} (La) 3.9×10^{-3} (Pr) 2.5×10^{-3} (La) 2.3×10^{-3} (Sm) 2.1×10^{-3} (Nd) 1.9×10^{-3} (Eu) 1.5×10^{-3} (Gd) 1.2×10^{-3} (Ce)	358 K, 95% RH 358 K, 95% RH 333 K, 98% RH 358 K, 95% RH 358 K, 95% RH 358 K, 95% RH 358 K, 95% RH 358 K, 95% RH	[169] [170]
VNU-17	3D framework with 1D pores	H_2O	5.90×10^{-3}	343 K, 85% RH	[171]
UiO-66	3D with defects created by vacancies of ligands	H_2O	5.62×10^{-3}	338 K, 95% RH	[114]
Na-HPAA Li-HPAA K-HPAA	1D framework Pillared layered "house of cards" structure 3D framework	H_2O	5.6×10^{-3} 1.1×10^{-4} 1.3×10^{-3}	297 K, 98% RH	[172]
$[Co^{II}(ox)(bphy)\cdot 0.2(DMF)]_n$ [z]	Concatenated "Star-of-David" 3D framework	H_2O	5.5×10^{-3}	353 K, 98% RH	[173]
$\{[Ln(L)(Ox)(H_2O)]_n\cdot xH_2O\}$ [aa] (Ln = Gd^{3+}, x =3)	2D stacked sheets forming a 1D pore	H_2O	4.7×10^{-3}	348 K, 95% RH	[122]
$H[Ln(H_2O)_4][MnV_{13}O_{38}]\cdot 9NMP\cdot 17H_2O$ (Ln = Ce, La; NMP = N-methyl-2-pyrrolidone)	3D framework with 1D channels	H_2O	4.68 × 10-3 (Ce) 3.46 × 10-3 (La)	334 K, 95% RH	[174]
$[Sm(H_2O)_5(CO_2CH_2NH_3)_2][Al(OH)_6Mo_6O_{18}]\cdot 10H_2O$	3D supramolecular framework with 1D channels	H_2O	4.53×10^{-3}	353 K, 95% RH	[175]
$\{[Co_3(DMPhIDC)_2(H_2O)_6]\cdot 2H_2O\}_n$ [ab] $\{[Co_3(m\text{-}BrPhIDC)_2(H_2O)_6]\cdot 2H_2O\}_n$	3D frameworks with 1D pores	H_2O and NH_3,	4.41×10^{-3} 5.07×10^{-4}	373K, 1.5M $NH_3\cdot H_2O$ 373K, 1.5M $NH_3\cdot H_2O$	[176]
$A_2[Cr_3O(OOCH)_6(etpy)_3]_2[\alpha\text{-}SiW_{12}O_{40}]\cdot nH_2O$ (A = Li, Na, K) [ac]	3D framework	H_2O, $Li^+/Na^+/K^+$	4.4×10^{-3} (Na^+) 1.9×10^{-3} (Li^+) 1.6×10^{-3} (K^+)	323 K, 95%	[177]
Cu-TCPP	2D layers	H_2O	3.9×10^{-3}	298 K, 98% RH	[178]
$(Me_2NH_2)[Eu(L)]$ [e]	2D layered material	H_2O and $(Me_2NH_2)^+$	3.76×10^{-3}	373 K, 98% RH	[135]
Cd-5TIA	3D framework with 1D channels	H_2O and DMA^+	3.6×10^{-3}	301 K, 98% RH	[179]
$(N_2H_5)[CeEu(C_2O_4)_4(N_2H_5)]\cdot 4H_2O$	3D framework with a double channel	H_2O	3.42×10^{-3}	298 K, 100% RH	[180]
In-IA-2D-1	2D layers	$[(CH_3)_2NH_2]^+$ and H_2O	3.4×10^{-3}	300 K, 98% RH	[181]
UiO-66-SO_3H UiO-66-$(COOH)_2$	3D framework with functionalized groups	H_2O	3.4×10^{-3} 1.0×10^{-3}	303 K, 97% RH	[99]
SCU-12	Ladder-like 3D framework formed from interconnnected 2D sheets	H_2O	2.9×10^{-3}	298 K, 98% RH	[182]
Cu^I-MOF	Interpenetrated 3D network with 1D channels (impregnated with several molecules)	H_2O, Tz H_2O, DEA H_2O, DMF H_2O, DMSO H_2O, pyridine H_2O, NB H_2O, DNB	2.89×10^{-3} 2.41×10^{-3} 1.89×10^{-3} 6.58×10^{-4} 1.45×10^{-3} 1.29×10^{-3} 1.02×10^{-3}	353 K, 95% RH 338 K, 95% RH 338 K, 95% RH 333 K, 95% RH 353 K, 95% RH 353 K, 95% RH 338 K, 95% RH	[183]
$\{[M(H_2O)_8][H(H_2O)_{2.5}](HINO)_4(PMo_{12}O_{40})\}_n$ (M = Co, Ni)	3D supramolecular framework with 1D channels	H_2O	2.83×10^{-3}	373 K, 98% RH	[184]
$[Nd(mpca)_2Nd(H_2O)_6Mo(CN)_8]\cdot nH_2O$ [ad]	3D framework with	H_2O	2.8×10^{-3}	294 K, 98% RH	[185]

	1D channels				
$[Me_2NH_2][Eu(ox)_2(H_2O)]\ 3H_2O$	3D framework with 1D pores	H_2O	2.73×10^{-3}	328 K, 95% RH	[186]
$V[Cr(CN)_6]_{2/3}\cdot zH_2O$ $Co[Cr(CN)_6]_{2/3}\cdot zH_2O$	3D Prussian blue analogues	H_2O	2.6×10^{-3} 1.6×10^{-3} 1.7×10^{-3} 1.3×10^{-3}	308 K, 100% RH 293K, 100% RH 308 K, 100% RH 293K, 100% RH	[187]
$\{[Cu(dmbipy)(H_2O)_3]_2[SiW_{12}O_{40}]\}\cdot 7H_2O$ [ae]	3D framework	H_2O	2.60×10^{-3}	373 K, 98% RH	[188]
$[\{(Zn_{0.25})_8(O)\}Zn_6(L)_{12}(H2O)_{29}\text{-}(DMF)_{69}(NO_3)_2]_n$ [af]	2D sheets interpenetrate forming 3-fold 1D channels	H_2O and DMF	2.3×10^{-3}	298 K, 95% RH	[189]
UiO-66-$(COOH)_2$	3D framework	H_2O	2.3×10^{-3}	363 K, 95% RH	[100]
$(Hpy)_2[Zn_2(ox)_3]\cdot H_2O$ [ag]	2D stacked layers	H_2O and pyridinium	2.2×10^{-3}	298 K, 98% RH	[190]
$[Eu_2(CO_3)(ox)_2(H_2O)_2]\cdot 4H_2O$	1D channels	H_2O	2.1×10^{-3}	423 K	[191]
Ni-BDP-COOH	3D framework with bipyramidal pores	H_2O	2.22×10^{-3}	353 K, 97% RH	[192]
MIL-163	3D framework with squared-shapped 1D channels	H_2O and DMA	2.1×10^{-3}	363 K, 95% RH	[101]
Cu-DSOA	3D framework with two hydrophilic channels	H_2O	1.9×10^{-3}	358 K, 98% RH	[193]
$(C_3N_2H_5)_4[MnCr_2(ox)_6]\cdot 5H_2O$	3D framework with 1D pores	H_2O and Imidazolium	1.86×10^{-3}	295 K, 88% RH	[194]
MOF-801	3D framework	H_2O	1.8×10^{-3}	298 K, 98% RH	[195]
$(C_2H_{10}N_2)[Mn_2(HPO_4)_3](H_2O)$	2D layered material	H_2O and ethylenediamine	1.64×10^{-3}	293 K, 99% RH	[196]
$MgH_6ODTMP\cdot 6H_2O$ [ah]	3D pillared framework with 2 types of 1D channels	H_2O	1.6×10^{-3}	292 K, 100% RH	[197]
$[Cu(p\text{-}IPhHIDC)]_n$ (p-IPhHIDC = 2-(p-N-imidazol-1-yl)-phenyl-1H-imidazole-4,5-dicarboxylicacid)	3D framework formed from association of 2D net-like structures	H_2O	1.51 × 10-3	373 K, 98% RH	[198]
NENU-530	3D framework with 1D channels	H_2O	1.5×10^{-3}	348 K, 98% RH	[199]
$[Cu_2(Htzehp)_2(4,4'\text{-bipy})]\cdot 3H_2O$ [ai]	2D layered material	H_2O	1.43×10^{-3}	353 K, 95% RH	[200]
$[Cp_3Zr_3(\mu_3\text{-}O)(\mu_2\text{-}OH)_3]_2L3\cdot 4Na\cdot 4H_2O$ [aj]	3D framework with cilindrical cavities	H_2O	1.41×10^{-3}	303 K, 98% RH	[201]
$\{Fe(ox)(H_2O)_2\}$	1D chain	H_2O	1.3×10^{-3}	298 K, 98% RH	[202]
PCMOF-17	3D framework with 1D squared shaped pores	H_2O	1.25×10^{-3}	298 K, 40% RH	[109]
$\{[M_2C_{l2}(BTC)_{4/3}]\cdot(Me_2NH_2)^+{}_2\cdot 4/3H_2O\}_n$ [ak] (M = Co, Mn)	Isostructural 3D network	H_2O and $(Me_2NH_2)^+$	1.19×10^{-3} (Co) 2.60×10^{-4} (Mn)	292 K, 65% RH	[203]
$(CH_3NH_3)_2Ag_4Sn_3S_8$	3D framework with 1D pores	H_2O and CH_3NH_3	1.14×10^{-3}	340 K, 99% RH	[141]
$[SmK(BPDSDC)(DMF)(H_2O)]\cdot x(solvent)$ [al]	3D framework with 1D channels	H2O and DMF	1.11×10^{-3}	353 K, 98% RH	[204]
$(NH_4)_4[MnCr_2(ox)_6]_3\cdot 4H_2O$	3D chiral (quartz-like) anionic framework	H_2O and NH_4^+ ions	1.1×10^{-3}	295 K, 96% RH	[205]
Cu(HL)L [am]	2D sheets connected supramolercularly forming a 3D framework	H_2O	1.08×10^{-3}	298 K, 97% RH	[206]
$[Co^{III}Ca^{II}(notpH_2)(H_2O)_2]ClO_4\cdot 4H_2O$ [an]	2D layered structure	H_2O and ClO_4^- anions	1.0×10^{-3}	298 K, 95% RH	[207]
$ZrF[H_3(O_3PCH_2NHCH_2NHCH_2COO)_2]$ $Zr_3H_8[(O_3PCH_2)_2NCH_2COO]_4\cdot 2H_2O$ $Zr[(O_3PCH_2)(HO_3PCH_2)NHCH_2COOH]_2\cdot 2H_2O$	1D chains connected in herringbone fashion 2 D layered structure 3D framework	H_2O	1.0×10^{-3} 1.0×10^{-3} 1.0×10^{-4}	413 K, 95% RH	[208]
$[Mn_4(C_{14}H_8O_6S)_4(DMA)_2]\cdot 3DMA$	3D framework with 1D channels	H_2O and DMA	8.7×10^{-4}	307 K, 98% RH	[209]
$Ca^{II}Cu^{II}{}_6[(S,S)\text{-alamox}]_3(OH)_2(H_2O)\}\cdot 32H_2O$ [ao]	3D framework with 1D channels	H_2O	8.60×10^{-4}	353 K, 95% RH	[121]
$Cu_4(L)_2(OH)_2(DMF)_2$ [ap]	3D framework with	H_2O, DMF	7.4×10^{-4}	368 K, 95% RH	[210]

	1D channels				
NKU-109	1D chains hydrogen bonded supramolecularly in 2D sheets	H_2O	5.87×10^{-4}	343 K, 75% RH	[211]
MIT-25	Micro-meoporous 3D framework	H_2O	5.1×10^{-4}	348 K, 95% RH	[119]
MFM-500(Ni)	2D layered structure	H_2O	4.5×10^{-4}	343 K, 98% RH	[212]
$\{[Zn(C_{10}H_2O_8)_{0.5}(C_{10}S_2N_2H_8)]\cdot 2H_2O]\}_n$	1D chains	H_2O	4.39×10^{-4}	353 K, 95% RH	[124]
JUK-2	2D layered structure	H_2O	4×10^{-4}	298 K, 70-90% RH	[213]
$[Zn(5\text{-sipH})(bpy)]\cdot DMF\cdot 2H_2O$ [aq]	2D layers stacked to form 1D channels	H_2O and DMF	3.9×10^{-4}	298 K, 60% RH	[214]
$Gd_3(H_{0.75}O_3PCHOHCOO)_4\cdot xH_2O$ (x = 15–16)	3D framework with oval-shaped 1D channels	H_2O	3.2×10^{-4}	294 K, 98% RH	[215]
$\{[Mn_2(DBIBA)_3]\cdot(NO_3)\cdot 3DMF\cdot 4H_2O\}_n$ [ar]	3D framework with 1D pores	H_2O	3.09×10^{-4}	343 K, 100% RH	[216]
$[H_3O][Mn_3\text{-}(\mu_3\text{-}OH)(SDBA)_3(H_2O)]\ (DMF)_5$ [as]	3D framework with 1D channels	H_2O, H_3O^+, and DMF	3.0×10^{-4}	307 K, 98% RH	[217]
Mg-BPTC [at]	3D framework with functionalized groups	H_2O	2.6×10^{-4}	373 K, 98% RH	[218]
$[H_2en]_4[Ni_5(OH)_3(trzS)_3(en)(H_2O)(B\text{-}\alpha\text{-}PW_9O_{34})]\cdot 6H_2O$ [au]	Nanotube-like 3D framework	H_2O and protonated amines	2.4×10^{-4}	358 K, 98% RH	[219]
$\{NEt_3(CH_2COOH)\}[MnCr(ox)_3]\cdot 2H_2O$ [av]	2D layer with Net3 groups in the interlayer space	H_2O and Alkyl groups	2.0×10^{-4}	298K, 80% RH	[220]
$[La_3L_4(H_2O)_6]Cl\cdot xH_2O$ [ax]	3D framework with 1D channels	H_2O	1.7×10^{-4}	383 K, 98% RH	[221]
$\{[Eu_3(bpydb)_3(HCOO)(OH)_2(DMF)\cdot 3DMF\cdot 2H_2O\}_n$ $\{[Tb_3(bpydb)_3(HCOO)(OH)_2(DMF)\cdot 3DMF\cdot H_2O\}_n$ [ay]	3D franework with two types of irregular 1D channels	H_2O	1.7×10^{-4} 1.1×10^{-4}	325 K, 95% RH 334 K, 95% RH	[222]
Tb-DSOA	3D framework with 1D channels	H_2O	1.66×10^{-4}	373 K, 98% RH	[223]
$\{H[Cu(Hbpdc)(H_2O)_2]_2[PM_{12}O_{40}]\cdot nH_2O\}$ (M = Mo, W and n = 7.5-8) [u] $[Cu(bpdc)(H_2O)]_n$ [u]	3D framework with 1D channels 1D chains connected supramolecularly into a 2D structure	H_2O	1.56×10^{-4} (W) 1.25×10^{-3} (Mo) 1.55×10^{-4}	373 K, 98% RH	[224]
$[CoCa(notpH_2)(H_2O)_2]Cl\cdot nH_2O$	2D layered material	H_2O and Cl^-	1.4×10^{-4}	298 K, 95% RH	[225]
$Zn[(HO_3PCH_2)_2N(H)\text{-}CH_2C_6H_4CH_2N(H)(CH_2PO_3H)_2(H_2O)_2]\cdot 2H_2O$	3D pillared framework with 1D channels	H_2O	1.39×10^{-4}	314 K, 98% RH	[226]
$\{[Zn(dmphen)(DMF)_2(H_2O)]_2[SiW_{12}O_{40}]\}\cdot 6H_2O$ [az]	3D hydrogen bonded network	H_2O	1.30×10^{-4}	373 K, 98% RH	[227]
TMOF-2	3D framework with defects	H_2O	1.23×10^{-4}	363 K, 98% RH	[228]
Ca-BTC-H_2O [at]	3D framework with 1D channels	H_2O	1.2×10^{-4}	298 K, 98%RH	[229]
$K_2(H_2adp)[Zn_2(ox)_3]\cdot 3H_2O$ [v]	2D layered structure	H_2O, adipic acid and K^+	1.2×10^{-4}	298 K, 98% RH	[230]
$[Co_3(HL)_3(H_2O)_6]_n\cdot 13n(H_2O)$ [ba]	1D chains	H_2O	1.2×10^{-4}	353 K, 95% RH	[231]
$\{[Cu_4(dpdo)_{12}][H(H_2O)_{27}(CH_3CN)_{12}][PW_{12}O_{40}]_3\}_n$ [bb]	3D framework with cubic cavities	H_2O	1.0×10^{-4}	373 K, 98% RH	[232]
$Zr(L)_2X_2H_2\cdot 5H_2O$ [bc] (X = H, Na^+, NH_4^+)	3D open framework bridged by cycloheyl	H_2O, Na^+, NH_4^+	1.0×10^{-4} (bulk, X = H)	353 K, 95% RH	[233]
$\{NH(prol)_3\}[M^{II}Cr^{III}(ox)_3]$ [bd] (M^{II} = Mn^{II}, Fe^{II}, Co^{II})	2D oxalate-bridged layers	$\{NH(prol)_3\}^+$ ions, H_2O	~ 1×10^{-4}	298 K, 75% RH	[234]

[a] SA = sulfate; EIMS = 1-(1-ethyl-3-imidazolium)propane-3-sulfonate). [b] His = Histamine; ndc = 1,4-naphtalenedicarboxylate. [c] EMIMCI = 1-Ethyl-3-methylimidazoliumChloride. [d] bim = Benzimidazole. [e] (H_4L=5-(phosphonomethyl)isophthalic acid) [f] Tz = 1,2,4-Triazole [g] ImH_2= monoprotonated imidazole. [h] Hq = Hydroquinone [i] H_2dmbim = protonated 5,6-dimethylbenzimidazole. [k] EIMS = 1-(1-ethyl-3-imidazolium)propane-3-sulfonate; HTFSA = N,N-bis(trifluorome-thanesulfonyl)amide [l] Pz = 1H-pyrazole. [m] Tz = 1H-1,2,4-triazole. [n] H_3PhIDC - 2-phenyl-4,5-imidazole dicarboxylic acid. [o] p-ClPhH_3IDC = 2-(p-chlorophenyl)imidazole-4,5-dicarboxylic acid; m-ClPhH_3IDC = 2-(m-chlorophenyl)imidazole-4,5-dicarboxylic acid. [p] H_2DCDPP = 4-carboxylphenyl)-10,20-di(4-pyridyl)porphyrin. [q] H_2SDB = 4,4'-sulfonyldibenzoic acid. [r] TETA = triethylenetetramine; HPW = $H_3PW_{12}O_{40}$. [s] H_2spip = 2-sulfophenylimidazo(4,5-f)(1,10)-phenanthroline. [t] H_6L = 2,4,6-tris(4-phosphonophenyl) pyridine. [u] bpdc = 4,4′-biphenyldicarboxylic acid; pdc = pyridine-3,5-dicarboxylate. [v] ox = oxalate; adp = adipic acid. [x] H_8DTMP = hexamethylenediamine-N,N,N',N'-tetrakis(methylenephosphonic acid). [y] im = imidazole; mim = methylimidazole; ox = oxalate. [z] bphy = 1,2-bi-s(4-pyridyl)hydrazine. [aa] H_2L = mucic acid; OxH_2= oxalic acid. [ab] DMPhIDC = 2-(3,4-

dimethylphenyl)-imidazole-4,5-dicarboxylic acid; m-BrPhH_3IDC = 2-(m-bromophenyl)-imidazole-4,5-dicarboxylic acid. [ac] etpy = 4-ethylpyridine. [ad] mpca = 5-methyl-2-pyrazinecarboxylate. [ae] dmbipy = 4,4′-dimethyl-2,2′-bipyridine. [af] H_2L = 1,3-bis(4-carboxyphenyl)imidazolium. [ag] py = pyridine; ox = oxalate. [ah] H_8ODTMP = octamethylenediamine-N,N,N′,N′-tetrakis(methylenephosphonic acid. [ai] H_3tzehp =N-[2-(1H-tetrazol-5-yl)ethyl]-L-hydroxyprolin. [aj] Cp = η^5-C_5H_5; NaH_2L = 1,2-bis(sodium-2-sulfonate-4-carboxyphenoxy)ethane. [ak] H_3BTC = benzene-1,3,5-tricarboxylic acid. [al] BPDSDC = biphenyl-3,3′-bisulfonyl-4,4′-dicarboxylic acid. [am] L = 4-(1H-imidazolyl) benzoic acid. [an] notpH_6 = 1,4,7-triazacyclononane-1,4,7-triyl-tris-methylenephosphonic acid. [ao] H_4-(S,S)-alamox =N,N′-bis((S)-2-propanoicacid)oxamide. [ap] L = 5-sulfoiso-phthalic acid. [aq] 5-sipH3= -sulfo-isophthalic acid; bpy = 4,4'-bipyridine; DMF = dimethyl formamide. [ar] DBIBAH = 3,5-di(1H-benzo[d]imidazol-1-yl)benzoic acid. [as] H_2SDBA = 4,4'-sulfonyldibenzoic acid. [at] (BPTC = 2,2′,6,6′-tetracarboxybiphenyl). [au] H_2trzS = 1H-1,2,4-Triazole-3-thiol; en = ethylenediamine. [av] Et = ethyl. [ax] L^{2-} = 4-(4H-1,2,4-triazol-4-yl)-phenylphosphonate. [ay] H_2bpydb = 4,4′-(4,4′-bipyridine-2,6-diyl) dibenzoic acid. [az] dmphen =4,7-dimethyl-1,10-Phenanthroline. [ba] H_3L = oxonic acid. [bb] H_3L = oxonic acid. [bc] L = cyclohexyl-N,N,N',N'-diamino-tetraphosphonate. [bd] NH(prol)$^{3+}$ = Tri(3-hydroxypropyl)ammonium.

In particular, MOFs based on phosphoric (H_3PO_4) and phosphonic (H_3PO_3) acids and more generally metal phosphonate materials [96,97,112,165,169,207,235–238] offer a prominent platform for the design of proton-conducting solids because the phosphonic acid groups both act as a proton source and contribute to a better thermal/water stability and oxidation resistance [239] compared to other protogenic species. However, in the design of phosphorous-based proton conductors, pure inorganic crystalline solids have also been considered because of their much higher thermally and chemically stability compared to metal phosphonate hybrid materials [240]. Therefore, metal(IV) phosphates have been extensively investigated, with a particular focus on titanium-, zirconium-, or silicon-based solids [48,241–245] due to their interesting proton conduction performances [47,61,69–76]. However, these materials are normally organized in chains or layers rather than in three-dimensional (3D) open-framework structures, which severely limits their potential as water-mediated solid proton conductors. Only a few three-dimensional metal(IV) phosphates showing an open framework have been reported to date [246–251], mostly due to the destruction of the framework upon the removal of structure-directing agents [250,251].

I.4. Evaluation of the Proton conductivity and microscopic mechanisms in play

The proton is a special case among the ions. Different from other cations, the proton is the only one without an electron shell. This makes it ultimately small, light, highly mobile and much more capable to polarize its surrounding environments. With an aqueous mobility approximately 9 times higher than that of Li^+ and 5 times higher than that of K^+ [252], the proton shows an unusual ability to move in the condensed matter. From an experimental point of view at the macroscopic scale, the performances of proton conducting materials are assessed by the measurement of their conductivity. The ionic conductivity (σ) is a variable which measures the motion of an ion from one site to the other through defects or assisted

molecules that create a specific pathway in the solid. The conductivity is expressed according to the Nernst-Einstein law (Equation 1.6) and holds a direct proportionality to the diffusion coefficient (D), the concentration of charge carriers (n) and the motional entropy (ΔS_m) and is inversely proportional to the temperature (T), according to Equation 1.6.

$$\sigma = \frac{\mathrm{nDe}^2 \Delta \mathrm{S_m}}{kT} \tag{1.6}$$

Where e and k are respectively the elementary charge and the Boltzmann constant. Taking into consideration that both D and n are thermally activated, Equation 1.6 may be expressed according to the enthalpies of formation (E_f) and diffusion (E_d), whose sum is assumed as the energy of activation (Ea) of the proton conduction process.

$$\sigma = \frac{n_0 D_0 e^2 \Delta S_m \exp\left(-\left(E_d + E_f\right)/_{kT}\right)}{kT} = \frac{n_0 D_0 e^2 \Delta S_m \exp\left(-E_a/_{kT}\right)}{kT} \tag{1.7}$$

At the microscopic level, during its pathway, the proton moves through the condensed matter via a charge-carrier. To date, only a handful of these carriers have been extensively considered to participate in the proton conduction mechanism: water (cf. Table 1.2), oxo-acid anions [7], oxo-acids [130], amine-based molecules (e.g. NH_3 [96], DMA [101]) , heterocycles (e.g. imidazole family compounds [54,134]) and oxide ions [252]. All these species share an important feature: their ability to form hydrogen bonds. Hydrogen bonds correspond to interactions between the hydrogen atoms and light and polarizable atoms, especially N, F and O. These interatomic forces may be also understood as the mutual organization of three kinds of atoms: a donor (D), a hydrogen (H) and an acceptor (A). A hydrogen bond is typically highly directional, with the angle D–H–A (see Figure 1.6) normally exceeding 150° in the case of water molecules [253]. The hydrogen bonding is characterized by an intermediate energy between dispersive and covalent interactions. In liquid water, this energy was estimated to be of 6.3 $kJ.mol^{-1}$ [254] whereas the energy of London and covalent interactions lies around a few $kJ.mol^{-1}$ and about 100 $kJ.mol^{-1}$ respectively [255]. Another important aspect of hydrogen bonds is their dynamic nature, the strength and the number of H-bonds fluctuating over time in a considered system [256].

These characteristics of the hydrogen bonds are of fundamental importance to gain a full understanding of the proton conduction mechanisms either in homogeneous or heterogeneous media.

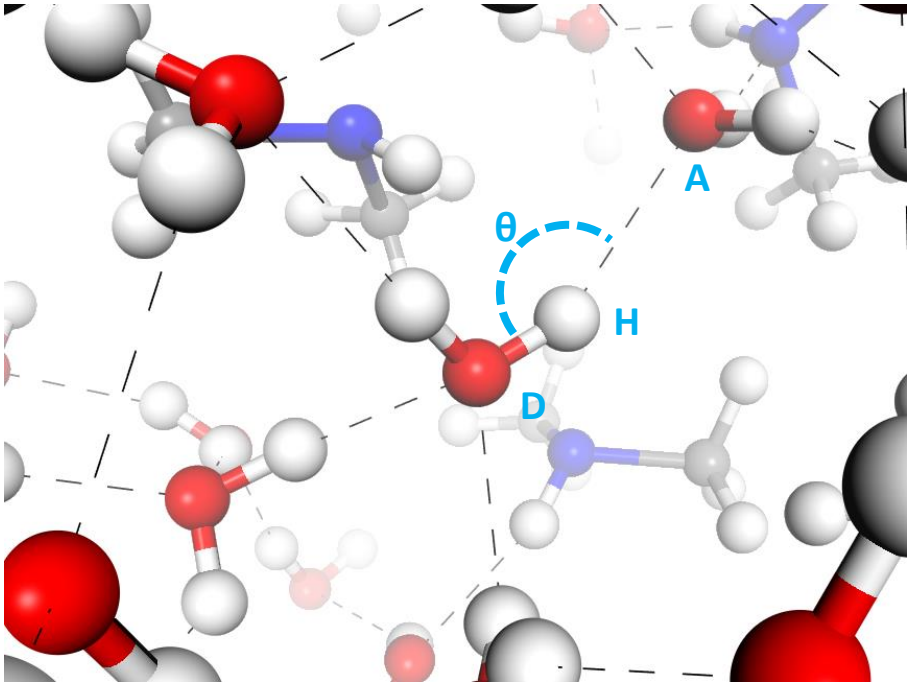

Figure 1.6 – Hydrogen bonds (dashed lines) in a system containing water and dimethylamine (DMA). Oxygen, nitrogen, carbon and hydrogen are identified with red, blue, gray and white colors, respectively. In light blue, atoms that participate to the hydrogen bond as donor (D), hydrogen (H), and acceptor (A) and the angle (θ) they establish [257].

There is a rich diversity of mechanisms associated with the mobility of the protons depending on the nature of the protonic charge carriers and the media through which they move, however they can be categorized into two main conduction mechanisms, namely the Grotthus and the vehicular mechanisms [258]. In the vehicular mechanism, the proton does not migrate as H^+ but bonded to a vehicle molecule (e.g. H_2O, NH_3, etc.) which acts as a Brønsted base [259] and moves through the medium by molecular diffusion. The Grotthus mechanism was suggested in the beginning of the 19th century, when von Grotthus postulated, after a series of observations on galvanic cells, that the proton transfer in aqueous solutions would occur from one molecule to the other, where each oxygen from one water molecule receives and passes one excess proton to the next molecule [260]. A very simple

schematic representation of the difference between the vehicular and Grotthus mechanism is given in Figure 1.7.

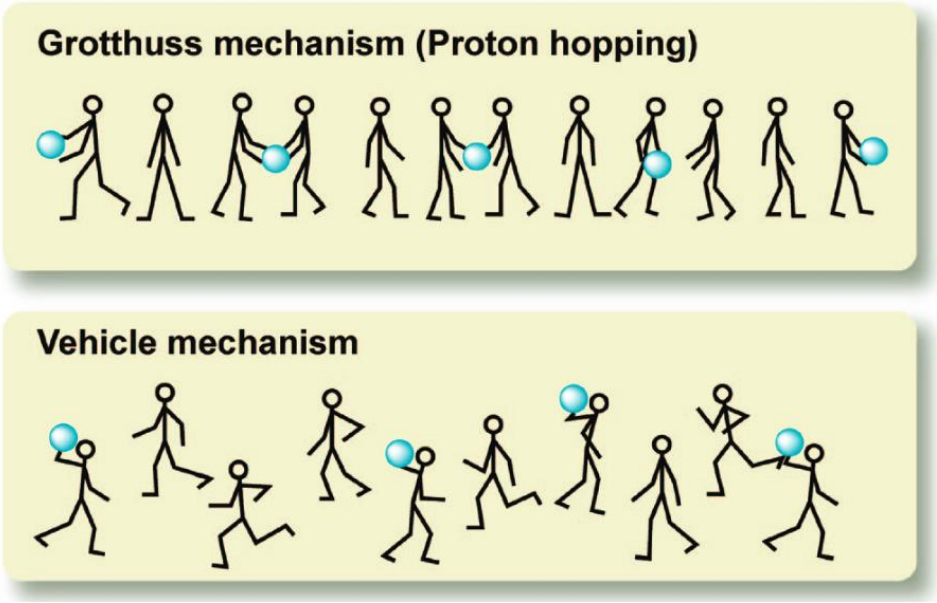

Figure 1.7 – Scheme of the Grotthus and vehicular proton transfer mechanisms in aqueous solutions (taken from ref. [261]).

With the advances made by the experimental and modelling techniques, the theoretical basis involved in the Grotthus mechanism has gained a deeper fundamental backbone. In contrast to the scheme initially proposed, the concept of proton transfer [262–266] is not based on the proton hopping from one molecule to the other in a subsequential hydrogen-bonded molecular chain, as it would result in an unfavorable electrostatic polarization of the chain [60,252,267]. The propagation of the proton in aqueous solution is based on the concept of "structure diffusion". This is illustrated in Figure 1.8. Initially, the proton is accommodated in an Eigen ion, formed by a core of H_3O^+ hydrogen bonded with three water molecules, in an effective $H_9O_4^+$ ion. When one of the neighbor molecules of the ion breaks one of its hydrogen bonds with the surrounding molecules, a Zundel ion, $H_5O_2^+$, is formed between the core molecule of the former Eigen ion and that water molecule whose hydrogen bond was broken. In this Zundel ion, the excess proton is directly solvated by two water molecules and is accommodated in a central short O–H--O bond where it fluctuates between the oxygen atoms almost adiabatically. In a third stage, the excess proton of this

Zundel species can be stabilized in another Eigen species upon the change in the potential energy caused by the formation of a new hydrogen bond (c.f. Figure 1.8). This dynamic between the central molecule of the Eigen ion and a surrounding water molecule which will constitute the subsequent Zundel ion is assigned to the terminology "special pair dance" [266] and to the global mechanism labeled as the Eigen-Zundel-Eigen (EZE) mechanism.

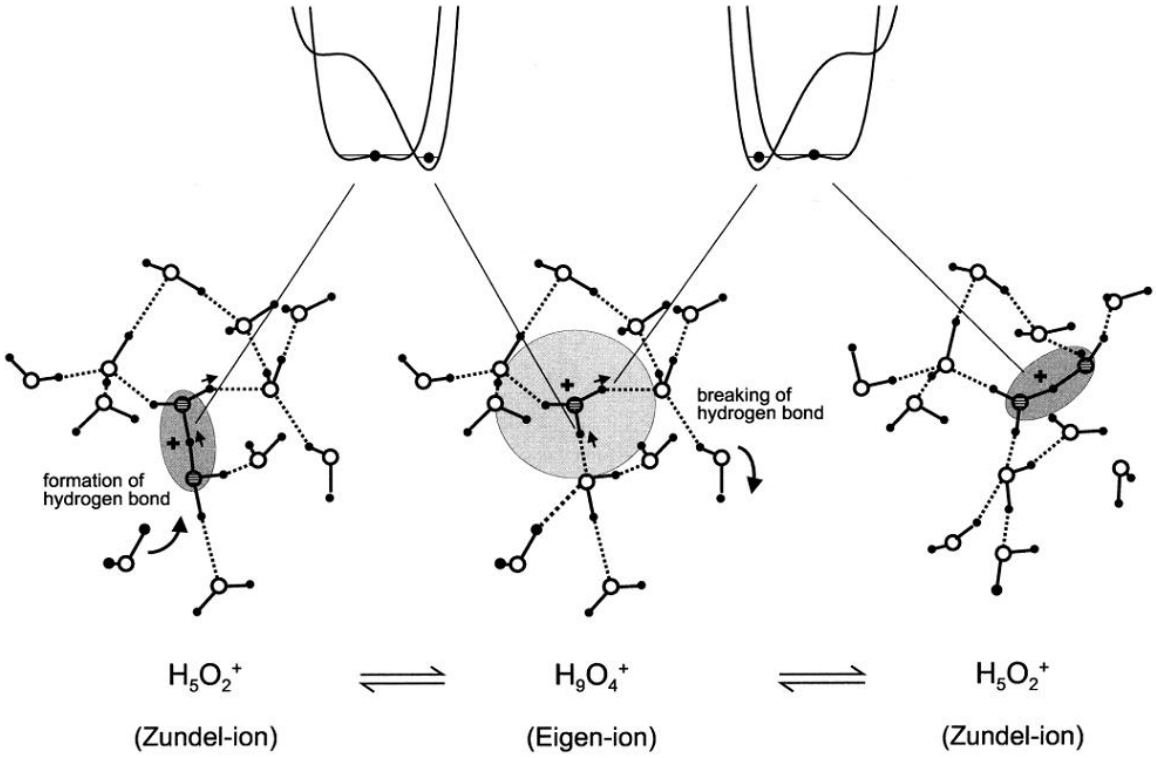

Figure 1.8 – Microscopic conduction mechanism of a proton in water [252]. The "structure diffusion" is highlighted in grey, with Zundel and Eigen ions shown respectively in dark and light grey. A schematic energy barrier assigned to the excess proton between two neighboring water molecules is also assigned and it shows the adiabatic nature of a proton transfer from a molecule to another under the context of a Zundel – Eigen transition.

There are several implications of the EZE mechanism. One of the most important is the low associated activation energy, usually below 0.4 eV. This drastically deviates with the vehicular mechanism that involves the displacement of bulkier ionic species, e.g. H_3O^+ and hence associated with a much higher activation energy. Another difference is that in overall the excess charge does not actually move in large extent, as the actual movements of the excess charges are just from the center of an elongated bond to a more compact bond. The

center of charge, or "structure" is however dislocated by a much longer distance, as seen in Figure 1.8, this would explain how even so small proton displacements may lead to a large overall charge transfer. Even though there is a clear differentiation between both the Grotthus mechanism and the vehicular mechanism, in real situations, both mechanisms can act together. For instance, in bulk water, due to the self-diffusion of the water molecules (D_{H2O} = 2.25 × 10^{-5} cm^2/s at room temperature), about 22% of the total conductivity in aqueous solutions is due to the vehicular mechanism [252].

The proton mobility has been modeled in different ways in other homogeneous media, such as in heterocycle species (e.g. imidazole), where the proton conduction pathway occurs along unidimensional hydrogen bonded chain of molecules with the proton transmitter media, in a Grotthus-like mechanism [252,268,269]. Interestingly, this mechanism has been shown to be even more efficient owing to the confinement of these molecules in porous materials [81,138].

Another interesting case happens with the consideration of phosphoric acid. In contrast to water, which has a high proton conductivity but a low concentration of protonic charge carriers, phosphoric acid shows a high proton mobility and a large concentration of proton carriers [252]. This component shows an unusual transmission of the charge defect at long distance involving up to 4 molecules [270,271] and most probably relates to the mechanism initially proposed with the proton conduction ensured by the formation of Grotthus chains.

Finally, differently from the proton conduction in hydrogen-bonded networks, the proton conduction in oxides may be seen like the propagation of an -OH defect, since the protons, as expected, are connected to the most electronegative atoms of the oxides by strong hydrogen bonds [272].

II. Materials for adsorption heat reallocation

II.1. Main technologies used in adsorption-based thermal devices

The use of energy from renewable sources is societally relevant since the fossil fuels reserves head to their inevitable depletion. Heat-driven chillers and heat pumps; thermal energy storage devices; or desiccant units have drawn attention in the last decades since they are able to efficiently transform and store energy in conjunction with green-energy sources such as low grade waste heat and solar thermal energy [273–275].

Conceptually, the difference between a heat pump and a chiller is that the former removes heat from a space making it cooler and rejecting heat to the environment while the latter extract heat from the surroundings and use it to provide useful heat. However, heat pumps can be used in both heating and cooling applications according to their settings while chillers are normally used for cooling water streams. Henceforth the term “heat pump” will be employed more generally as they encompass both heat transformation schemes.

Thermally-driven heat pumps are devices that are able to operate sustainably when supply and heating demands are in phase, e.g. in applications such as air conditioning, refrigeration and hot water production [89]. The main working principles for such devices are chemical reactions, absorption and adsorption. Adsorption heat pumps (AHPs) present over its competitors the advantages of a low temperature driving energy sources, the non-requirement of moving parts for the circulation of the working fluid, simplicity, and use of environmentally benign working fluids [276]. However their current relatively lower performance is still an essential drawback for a more extended development of this technology [89].

II.2. General principles of adsorption-based heat transfer

The working principle of an adsorption-driven heat pump technology can be understood as a composite of two cycles. In the working cycle, a working fluid leaves an evaporator taking energy (Q_{EVAP}) from the external environment and then it is further adsorbed into a porous material. As the adsorption phenomenon is spontaneous and exothermic, heat (Q_{ADS}) is consequently released to the exterior. In the regeneration cycle,

the saturated adsorbent is heated (Q_{DES}) in order to desorb the working fluid, which is then condensed, releasing heat (Q_{COND}) to the external environment. In Figure 1.9, both cycles and the involved heat transfers are representatively shown.

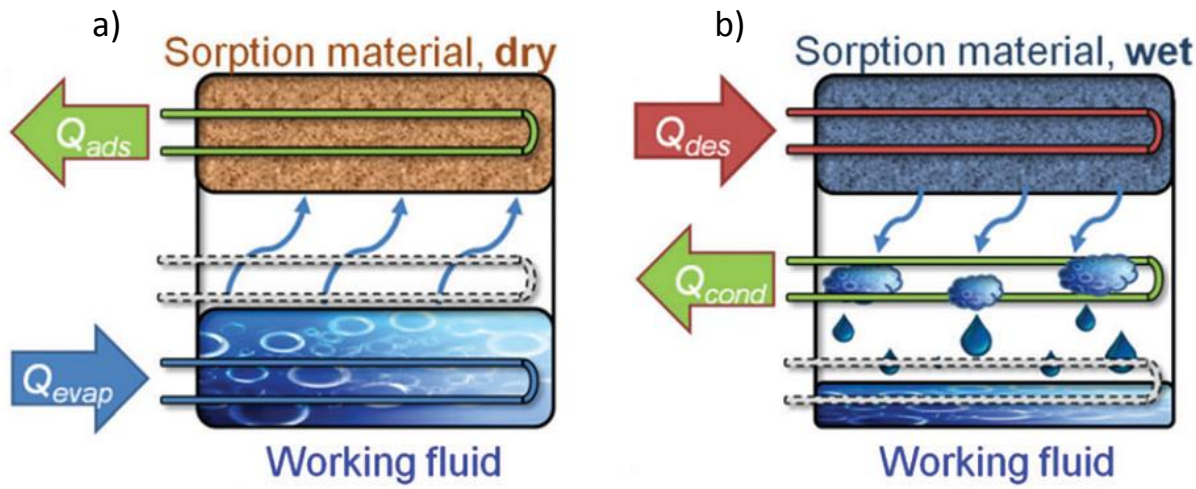

Figure 1.9 – Working scheme of the heat transfer (a) and regeneration (b) cycles of an adsorption heat pump (adapted from ref. [277]).

These cycles are in turn usually subdivided in two steps, as shown in the 4-step thermodynamic cycle represented in Figure 1.10. Starting from the beginning of the regeneration cycle, where the adsorbent is entirely saturated and the evaporator is disconnected from the condenser (point I), the first step consists of an increase of the isosteric heating of the adsorbent. This leads to an increase in the pressure of the evaporator (P_{EVAP}) to the level of the one in the condenser (P_{COND}) (point II). After this pressure level is reached, the regeneration goes on with the isobaric desorption stage, where the working fluid continues to be heated however now allowed to reach the condenser. At this point, heat (Q_{COND}) is released to the environment. This process, as well as the regeneration one, ends when the desorption temperature (T_{DES}) is reached (point III). Now under the context of the working cycle, the subsequent step consists of an isosteric cooling of the adsorbent isolated from the evaporator vessel until P_{EVAP} is reached again (point IV). In the final step, the adsorbent vessel is allowed to exchange mass with the evaporator and this leads to the capture of heat from the evaporator's environment (Q_{EVAP}) and the evaporation of the working fluid followed by its adsorption to the porous material and consequent release of heat to the environment (Q_{ADS}). Even though in a real working heat pump such discretized

steps may happen concomitantly, such partition of the process is especially useful for the modeling and subsequent performance evaluation of a heat pump.

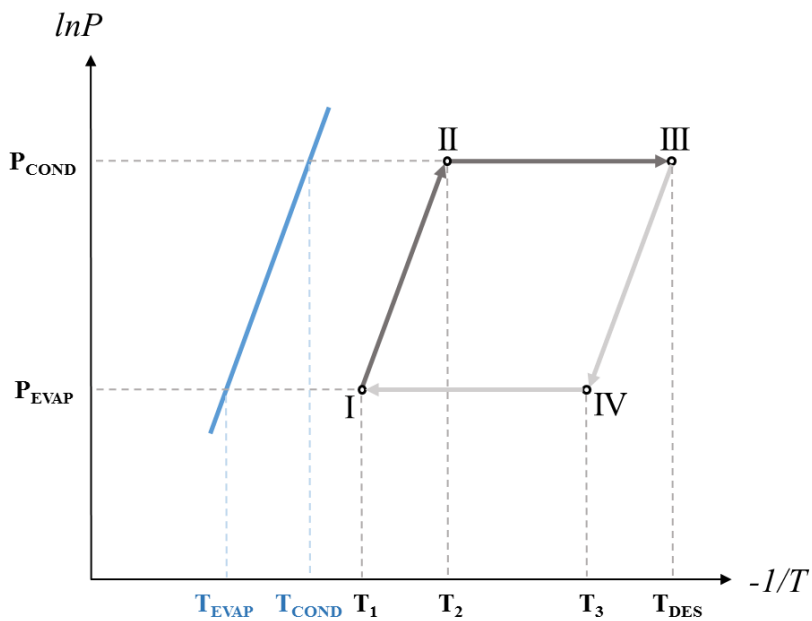

Figure 1.10 – Theoretical thermodynamic cycle of a heat pump cycle. In blue, the thermodynamic states of the working fluid at the evaporator and condenser.

As stated before, heat allocation devices may be used for both heating and cooling operations. For the former, the energy can be directly taken at high temperatures from the adsorbent heating (Q_{DES}) and at low temperature from the environment at the evaporator (Q_{EVAP}) level. This energy is then transferred at the condenser (Q_{COND}) and the adsorbent bed (Q_{ADS}) levels to the environment at the intermediate range of temperature. On the other hand, during cooling operations, the evaporator is responsible for the cooling effect, operating at temperatures lower than the ambient condition and ultimately using as input energy the heat of desorption (Q_{DES}). In this case, the heats-generated at intermediate temperature (Q_{COND} and Q_{ADS}) are discarded. These heat pump operation modes are schematically resumed in Figure 1.11.

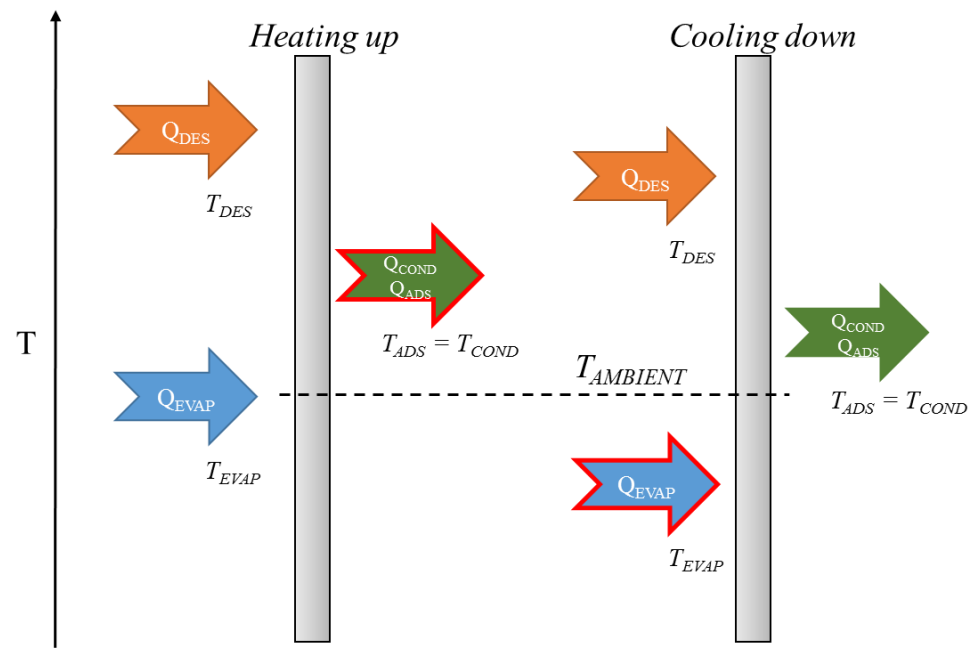

Figure 1.11 – Heats and temperatures associated with the operation of a heat pump in heating or cooling mode. The arrows outlined in red correspond to the useful heats associated with the operation of the heat pump in each mode (adapted from ref. [89]).

It is then evident that the useful heat is not the same in heating and cooling operations. While for the former, the heat of condensation and adsorption are the most important for their exploitation in the heating at an intermediate temperature, for the latter the heat extracted from the environment at a lower temperature is the core of the cooling operation. These concepts are of foremost importance in the assessment of the performance of an adsorption-based heat pump. Commonly, such assessment is made with the determination of the coefficient of performance (COP), an important parameter which relates the useful heat obtained from the heat pump with the heat provided in the regeneration of the adsorbent. Therefore, in adsorption heat pumps the COP is expressed as follows:

$$COP = \frac{Useful\ heat}{Heat\ of\ regeneration} \tag{1.8}$$

$$COP_H = \frac{-(Q_{COND}+Q_{ADS})}{Q_{DES}} \tag{1.9}$$

$$COP_C = \frac{Q_{EVAP}}{Q_{DES}} \tag{1.10}$$

Where COP_H and COP_C are the coefficients of performance respectively in heating and cooling operating modes. The minus sign in the useful heat comes to the convention that heats leaving the system are counted as negative while heats entering the system are counted as positive.

Considering the reversibility of the adsorption process and most commonly the absence of hysteresis phenomena in the adsorption of the working fluid, the heats of adsorption and desorption are similar in magnitude. Considering that the heat of adsorption is the driving force of the heat transferring, it must be in modulus larger than the heat of condensation. In terms of coefficient of performance of heating, it means that: $1 \leq COP \leq 2$. Then again, due to the inevitable heat losses and entropy gain associated with any heat transfer processes, the useful heat can only be smaller than the heat provided at a higher temperature. Again, in terms of the coefficient of performance, $COP \leq 1$.

Clearly, the calculation of the COP depends on the determination of the heats involved in the process. As it is not usual to measure directly such quantity, thermodynamical models are then employed. In general, these models are derived from some main assumptions, such as the absence of inert mass in the adsorption bed, the treatment of the working fluid as a liquid for the specific heat capacities and adsorption calculations, the fluid leaving the condenser and evaporator in saturated state and the fluid flowing from the condenser and evaporator is enthalpic [273]. Details on the development of this model can be found in the review article reported by de Lange *et al.* [89].

In the conception, dimensioning, modeling or even manufacturing of a heat pump as well as for any other fluid-based heat transfer device, the choice of the working fluid is primordial. A suitable working fluid for AHP applications must preferentially have a high enthalpy of evaporation and a high heat capacity to optimize heat transfers from evaporation and to store the largest amounts of energy per volume. In addition, the working fluid must be condensable under operating conditions and not be a threat to human health or to the environment. As it is usually the case for working fluids, only a handful of them fulfil all these requirements, e.g. water, methanol, ethanol and ammonia. Due to its superior enthalpy of evaporation and heat capacity, water is the most thermodynamically efficient fluid,

however ammonia and alcohols, with their higher vapor pressure, are more efficient in terms of mass transfer and consequently for cycle time perspectives. Contrarily to water, these working fluids can also be operated in temperatures below 0 °C. Alcohols show also the advantage to be potentially employed in materials with relatively large pores, without involving any hysteresis and showing high stability with respect to the adsorbents [278]. At the same time, ammonia is a much more toxic fluid and has already shown to raise stability concerns when used with certain adsorbents [279–281]. Ultimately, considering its availability and cost, water is undoubtedly the most appropriate working fluid in AHP applications. On the other hand, the bottleneck of the AHP technology lies in its core: the adsorbent material. Many attempts on improving the performance of AHPs have been carried out through combining different pairs of adsorbents and working fluids [274]. There is still a growing interest to discover novel porous materials with the optimal water-adsorption behavior to achieve outstanding coefficient of performances for the targeted applications.

II.3. Porous materials in water-based adsorption heat allocation devices

Similarly to the working fluid, the adsorbents to be used in an AHP must also address a multitude of criteria. First of all, the material must obviously be stable towards water either in its vapor or liquid state for a long time ensuring an efficient operation of the AHP during many sorption/desorption cycles. Moreover, these adsorbents must present a water adsorption enthalpy higher than the fluid's latent heat in order to ensure an efficient mass transfer from the evaporator to the adsorption bed. At the same time, such enthalpy must not be too high otherwise the temperature of regeneration would be high, what is usually at odds with the low powered heat sources that are envisaged to feed the heat pump. Furthermore, AHP adsorbent materials should also present a large water uptake (at least over 0.2 $g.g^{-1}$) [282] to both favor the portability of the sorption bed as well as to maximize the transferred heat per cycle in the heat pump. Such large uptake, however, is much preferably to occur all at once in a given pressure. This would allow the tuning of the water adsorption with the pressure of the evaporator and would favor the mass transfer process occurring in both vessels. Another prerequisite for an optimal operation of an AHP adsorbent is the full reversibility of the adsorption, or in other terms, the absence of hysteresis between the adsorption and the desorption branches. The presence of hysteresis is mostly assigned to the difficulty of

desorbing the fluid due to its capillary condensation in the pores of the adsorbent that would increase considerably the regeneration temperature and would add complexity to the overall process.

From a practical point of view, a preliminary assessment of the performances for potential AHP adsorbents consists of measuring/simulating their water adsorption isotherms as well as their cycling properties by performing a consecutive series of adsorption/desorption water adsorption isotherms. Besides the determination of the water uptakes at a given relative pressure, the water adsorption isotherm and in particular its shape is of high importance to assess the degree of hydrophilicity of the adsorbent. For highly hydrophilic materials, such as zeolites containing extra-framework cations, their water adsorption isotherms show a sharp increase in its uptake at very low pressure as a result of the high affinity between water and the extra-framework cations. On the other hand, in typically hydrophobic materials, like the standard carbonaceous materials, the amount adsorbed is negligible at lower and intermediary pressures and the water adsorption mostly occurs via a pore filling mechanism. Clearly, as stated before, neither of these extreme situations is desired for an AHP material, instead, a trade-off between them is highly looked-for. Such compromise can be obtained with water-adsorbents which show a S-shaped water isotherm with a negligible amount adsorbed at low pressures and a sharp step in the uptake leading to the saturation. Empirically, it has been determined that for real AHP applications this step should be located in the range of 0.05 [283] – 0.1 [284] < P/P_0 < 0.3 [284] – 0.4 [283]. For steps located at lower P/P_0, high desorption temperatures are required for the regeneration of the adsorption bed. On the other hand, for steps present at larger P/P_0, the difference between the low (evaporator) temperature and the intermediate (condenser/adsorption bed) becomes increasingly smaller, leading to the achievement of only minor temperature lifts [89].

With the recommercialization of AHPs in the early 1990's, silica gels were the first envisaged AHP adsorbents owing to their application as desiccants [285,286]. These materials can be employed in adsorption chillers which use low temperature heat (50 - 80 °C) [283]. However, even though silica gels show a relatively large water uptake, the linear profile of their water isotherms does not make them as highly efficient materials from a

thermodynamic standpoint. Zeolites and aluminophosphates were then further considered since they were the standard classes of materials used in the industry for catalysis and gas separation [287,288] and largely known for their hydrophilicity. Consequently, commercial materials such as the AQSOA^{TM} Z-series, especially the SAPO-34 zeolite (Z02) and partially iron-exchanged or pure $AlPO_4$-5 aluminophosphate (respectively, Z01 and Z05) emerged in the early 2000's and became the benchmark AHP adsorbents owing to their high cyclic stability to sorption cycles and their suitable water adsorption profile (see Figure 1.11). However, their total water uptakes are either still quite low (especially for the $AlPO_4$-5 materials) or their isotherms do not present a step in uptake as sharp as ideally expected. Furthermore, their water desorption requires high temperature treatment due to the strong interactions between water and their architectures. Carbonaceous materials also have been considered with some success as AHP adsorbents in most cases using ammonia [289], methanol [290,291] or ethanol [292,293] as working fluids.

II.4. MOFs as water-adsorbent for refrigeration applications

It thus appears that there is plenty of room for the development of new highly performant AHP materials. Following this trend, water stable MOFs have been envisaged as promising materials for adsorption heat applications. Compared to the standard materials used in AHP applications, MOFs present a much higher variety of composition, pore structure and topology, most often exhibiting high surfaces, pore volumes and more importantly a degree of hydrophobicity/hydrophilicity that can be tuned either *a priori* with the appropriate selection of the type of ligand and inorganic nodes constituting the MOF or *a posteriori*, with the decoration of the architectures with functional groups. Among them, the following materials, CAU-10(Al)-H, MIL-160(Al), Al-fumarate, CUK-1(M), MIP-200 (Zr), MIL-100(Fe), MOF-841(Zr), MOF-801(Zr) and MIL-125(Ti)-NH_2 have been reported as the best MOFs for such applications. A short description of their structures and water adsorption performances is reported below. In Figure 1.12, the crystal structures of these MOFs are presented.

(I) CAU-10(Al) is a MOF formed by 1D chains of cis-corner AlO_6-octahedra interconnected by isophthalate linkers and μ-OH groups, forming a tridimensional structure

with one-dimensional square-shaped pores of ~10 Å. This MOF has shown a favorable steep uptake at P/P_0 of 0.18 and a water uptake around 0.38 $g.g^{-1}$ at 298 K [294] that is preserved even after more than 700 cycles [295].

(II) MIL-160(Al) is a derivative of CAU-10(Al), the pristine terephthalate linker being substituted by the green 2,5-furandicarboxylate linker [296]. This material shows a favorable water adsorption isotherm with a higher hydrophilicity and less steep uptake occurring at P/P_0 ~ 0.07 and a superior water adsorption capacity (0.42 $g.g^{-1}$ at 303 K) as compared to CAU-10(Al).

(III) Al-fumarate (or A520) presents a rather high water adsorption capacity (~0.40 $g.g^{-1}$) at 303 K with a more hydrophobic behavior, with a gradual step occurring in $0.2 < P/P_0 < 0.3\text{-}0.4$ [297,298]. This framework has diamond-shaped one-dimensional pores formed from the association of corner-sharing Al^{III} octahedra chains bridged by μ_2-OH groups and fumarate ligands [299]. This MOF is isoreticular to the MIL-53 framework, a MOF with 1,4-benzenedicarboxylate (BDC) linkers, largely known for its flexibility and phase transitions between larger and narrow pores triggered by the temperature, pressure and adsorption stimuli. However, the Al-fumarate does not show a breathing behavior but rather only small local guest-induced structural rearrangements [299,300]. This is probably one of the main reasons of its robustness, being able to resist more than 4500 sorption cycles when grown on support with minor capacity losses (~13%) [301]. This also leads to a much less pronounced hysteresis compared to MIL-53. Incidentally, such high degree of hysteresis is one of the major factors that prevents the use of MIL-53 for AHP applications [89].

(IV) CUK-1(M) is made of the association of 1D chains of M^{II} (M = Mg, Co, Ni) edge- and vertex- sharing octahedral bridged by μ_2-OH groups and coordinated to 2,4-pyridinedicarboxylic acid (2,4-pdc) forming diamond-shaped 1D pores of ca. 13 Å sized [302]. The Ni and Co variants structure have shown similar water adsorption profiles, showing a sharp step in uptake near $P/P_0 = 0.1$. Interestingly, for the Mg variant the step is shifted towards a higher relative pressure ($P/P_0 = 0.2$). This interesting behavior allows the tailoring of the MOF according to the temperature lift desired in the AHP application, which

depends on the P/P_0 at which the adsorption step is observed by only changing the metal in the MOF, as explained in chapter 4.

(V) MIP-200 (Zr) is a framework which has 8-connected $Zr_6(\mu_3\text{-}O)(\mu_3\text{-}OH)_4$ secondary building units (SBUs) each connected with eight carboxylate and four terminal formate groups interconnected with H_4mdip (methylenediisophthalic acid) molecules. This association results in a framework with separated 1D hexagonal and triangular channels of respectively 13 and 6.8 Å. The water adsorption in this framework has shown a high water uptake (0.39 $g.g^{-1}$) at 303 K and $P/P_0 < 0.3$. This MOF has also shown satisfactory cyclability showing negligible uptake loss after 50 sorption cycles [303]. On the other hand, although the water uptake in the MIP-200 occurs in the AHP favorable $P/P_0 < 0.25$ range, it shows a double step with about half of its amount adsorbed in $P/P_0 < 0.05$, which requires higher desorption temperatures for its use in an AHP device.

(VI) MIL-125(Ti)-NH_2 is a framework having bipyramidal pores with dimensions of 14 and 18 Å formed by cyclic octamers of edge and corner-sharing $TiO_5(OH)$ octahedra linked to eight NH_2–BDC linkers each. This framework shows a steep single water uptake at $P/P_0 = 0.2$ and a high water uptake (0.55 $g.g^{-1}$) at 308 K and $P/P_0 < 0.3$ [304,305]. This framework although thermally stable up to 550 K has shown 17% of uptake loss after 40 water sorption cycles in considerably high desorption temperatures (413 K) [306] however, in lower desorption temperatures (353 K), the structural integrity is preserved and no adsorption losses is noticed after the sorption cycles [305].

(VII) MIL-100(Fe) is a framework formed from SBUs composed of trimers of Fe^{III} octahedral with terminal (-OH, F) groups and linked to each other by trimesate carboxylates [307]. The SBU – organic linkers' arrangement leads to the formation of supertetrahedra of *ca.* 9.5 Å. These supertetrahedra further assemble themselves into a MTN zeolitic architecture delimiting two mesoporous cages of 25 and 29 Å free apertures accessible through windows of 5.5 and 8.6 Å [308]. In its dry state, this framework has coordination unsaturated Fe^{III} sites (CUS) that allow the coordination of water molecules [309]. The water adsorption in this framework is characterized by a subtle initial gain in uptake in very low pressure followed by a gradual increase in the uptake up to ~ 0.1 $g.g^{-1}$ at $P/P_0 = 0.2$.

Subsequently, it is observed a two-stepped gain in the uptake up to the near saturation state at $P/P_0 > 0.4$. Although the water adsorption behavior in this framework is not ideal, the strikingly high water uptake (0.7 $g.g^{-1}$) and the solid stability are key factors to promote this material among the best MOFs for AHP applications. The corresponding water adsorption mechanism, showing the key role played by the CUS sites, will be further discussed in chapter 4.

(VIII) The two other zirconium-based MOFs that have been considered for AHP applications show the same kind of SBU, the $Zr_6(\mu_3\text{-}O)_4(\mu_3\text{-}OH)_4$. In one, MOF-841(Zr), each SBU is connected to eight 4,4′,4″,4‴-Methanetetrayltetrabenzoic (MTB) linkers forming a framework with octahedral-shaped cages of 11.6 Å diameter each. The water adsorption isotherm of this MOF at 298 K, shows a sharp step at $P/P_0 \sim 0.2$ with a relatively high water capacity (0.45 $g.g^{-1}$) [310]. Regarding MOF-801(Zr), the same SBU is coordinated to twelve fumarate linkers, forming three symmetry-independent cavities, two with similar diameter (4.8 and 5.6 Å) and tetrahedral shape and a third octahedral-shaped and larger diameter (7.4 Å). This MOF showed two distinct water adsorption isotherms according to its synthesis route: with a water uptake increasing from ~ 0.2 $g.g^{-1}$ to 0.3 $g.g^{-1}$, when single crystals and powders are considered respectively [310]. This distinct behavior, related to the presence of defects in this framework [311], will be detailed in chapter 4.

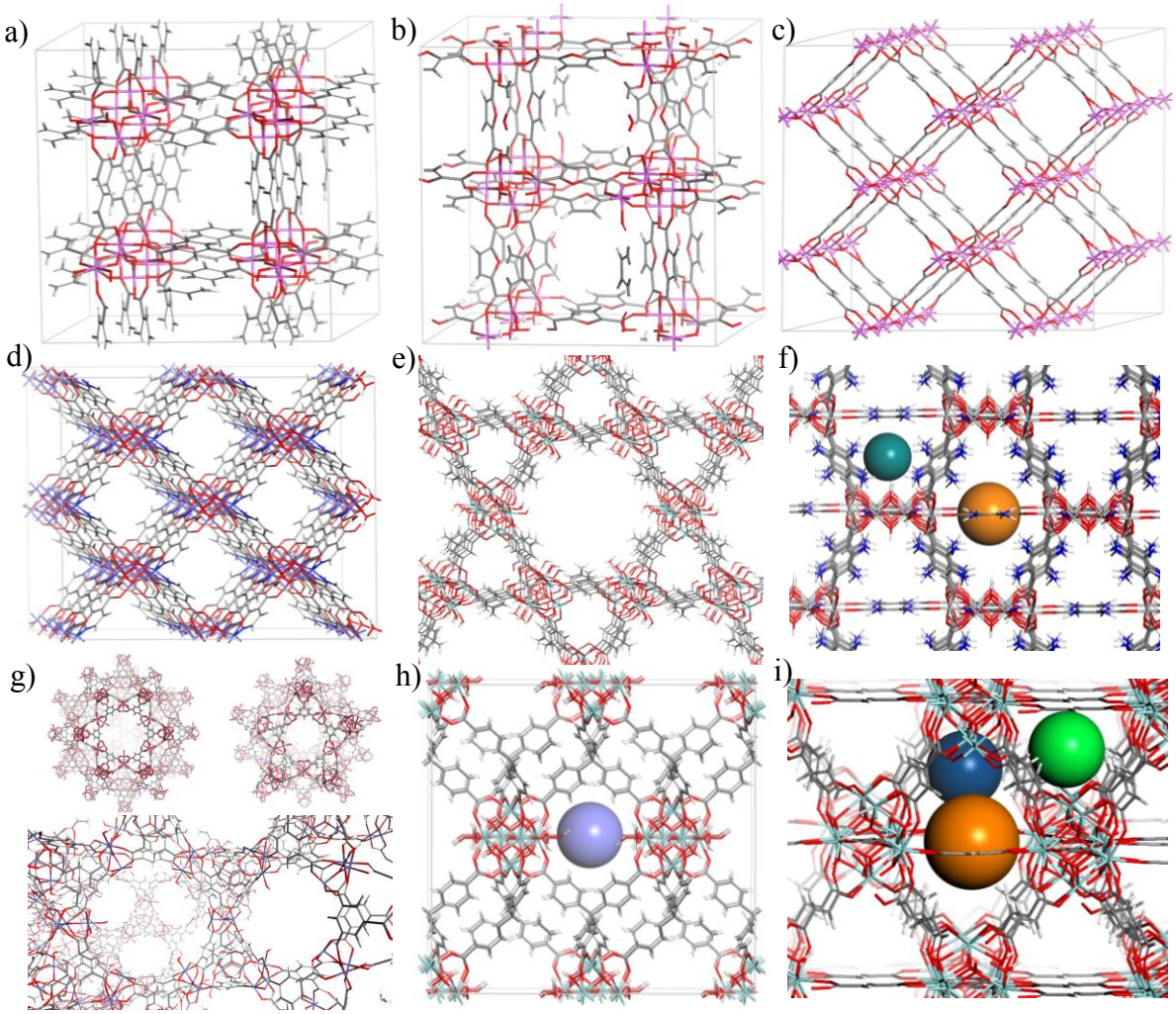

Figure 1.12 – Crystal structures of the MOFs CAU-10(Al) (a), MIL-160(Al) (b), Al-fumarate (c), CUK-1(Co) (d), MIP200 (e), MIL-125(Ti)-NH_2 (f), MIL-100(Fe) (g), MOF-841(Zr) (h), and MOF-801(Zr) (i). The C, H, O, N, Al, Fe, Zr, Ti and Co atoms are represented by grey, white, red, blue, pink, cyan, turquoise, silver, and indigo colors. Spheres of different colors are used to draw attention to the cages in the MIL-125(Ti)-NH_2, MOF-841(Zr), and MOF-801(Zr).

Figure 1.13 summarizes the water adsorption isotherms collected for this series of MOFs which are further compared with those of benchmark materials (AQSOA-Z01 ($AlPO_4$-5), AQSOA-Z02 (SAPO-34) and an activated carbon).

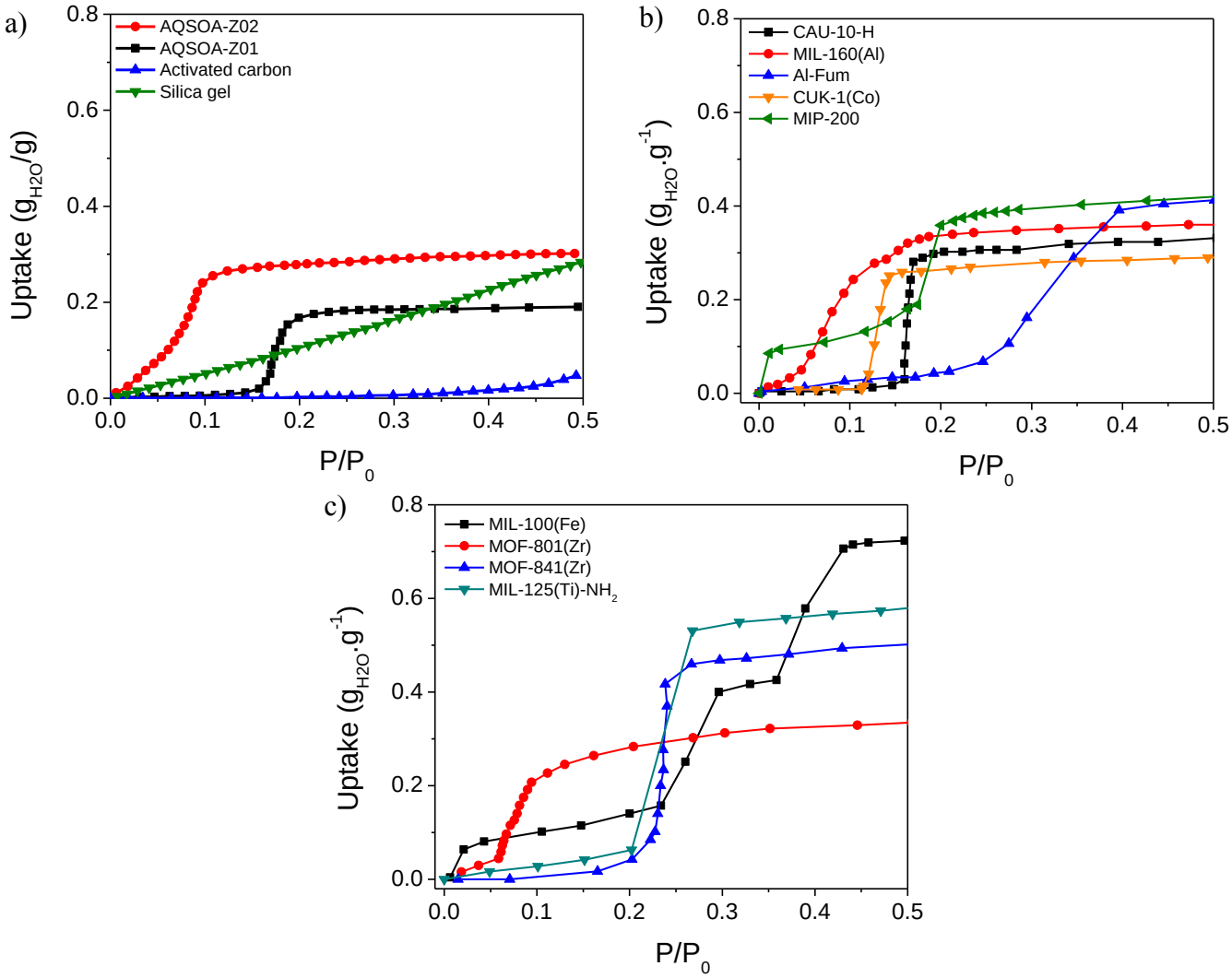

Figure 1.13 –Water adsorption isotherms of benchmark materials [89] at room temperature (a) compared with the MOFs' CAU-10(Al) [294], and MIL-160(Al) [312], Al-fumarate [297], CUK-1(Co) [313], MIP200 [303] at 303K (b and c).

Noteworthy, MOFs generally show a superior COP compared to benchmark solids when used for chilling rather than for heating applications [89]. Figure 1.13 compares the COP variation with the desorption temperature for six of these MOFs (CAU-10, MIL-160, A520, Co-CUK-1, MIP200, and MOF-801) and the AQSOA-Z02 (SAPO-34) benchmark material in the case of the chilling conditions, i.e. T_{EVAP} = 5 °C and T_{ADS} = 30 °C [89,298,303,313]. The MOF MIL-125(NH_2) also showed a similar COP (~ 0.80) for regeneration temperatures between 70°C and 90°C, however the COP curve was not reported [314]. Unfortunately, it is rather complex to make a consistent comparison of MOF/water

COP data since the considered evaporation/regeneration temperatures considerably vary from one study to another, or these data are not reported.

However, one can notice in Figure 1.14 that at least five MOFs (CAU-10, MIL-160, Co-CUK-1, NH_2-MIL-125, and MIP200) outperform the standard AHP adsorbent, especially at low desorption temperature. Noteworthy, for chilling applications the MOFs-water working pairs are placed among the best efficient pairs compared to other common and innovative working pairs based on activated carbons, silica, zeolites with water, ammonia or alcohols as fluids [89,278,315]. This emphasizes the great potential of this family of materials for further employment in adsorption-based heat transfer applications.

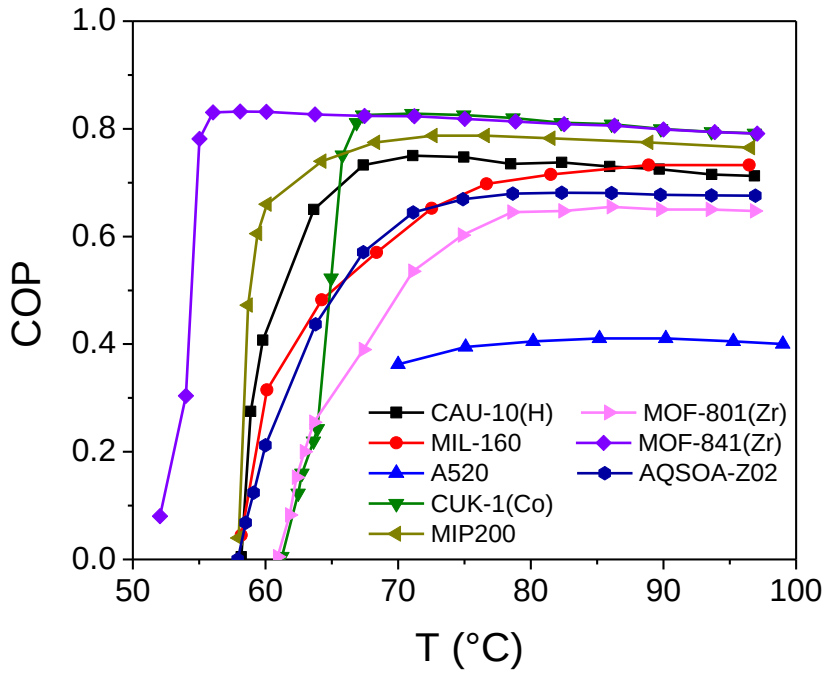

Figure 1.14 – Coefficients of performance in chilling conditions (T_{EVAP} = 5 °C and T_{ADS} = 30 °C) of the MOFs CAU-10(Al) (■), MIL-160(Al) (●), A520 (▲), CUK-1(Co) (▼), MIP200 (◀), and MOF-801 (▶) compared to the benchmark material AQSOA-Z02 (○) obtained from ref. [89,298,303,313].

Conclusion

Proton conduction and adsorptive-based heat reallocation technologies are much dependent respectively on the solid materials of the electrolyte membranes/sensors and the adsorption bed. MOFs have been pointed out as promising among the novel material designed for solid-state proton conduction and adsorption-based heat reallocation applications. As shown in this chapter, only a handful of these materials have been identified as potential competitors with respect with the benchmark solids in both fields of applications. While the effort devoted to the design of novel materials has been relatively successful so far employing trial and error or high-throughput screening, a better understanding of the mechanisms of the proton transport on the one hand and of the water adsorption on the other hand is still needed. This calls for a fundamental perception of the relations between the structure of these materials and their properties. Such insights can be developed from dual experimental modelling approaches that would ultimately tune the chemical and topological features of the MOFs architectures for an optimization of their performances. The following chapters are dedicated to the development of this strategy.

REFERENCES

[1] W.E. Ayrton, J. Perry, Ice as an Electrolyte. - Second Communication, Proc. Phys. Soc. London. 2 (1875) 171–182. doi:10.1088/1478-7814/2/1/320.

[2] M. Warshay, P.R. Prokopius, The fuel cell in space: yesterday, today and tomorrow, J. Power Sources. 29 (1990) 193–200. doi:10.1016/0378-7753(90)80019-A.

[3] P. Knauth, M.L. Di Vona, Solid state proton conductors : properties and applications in fuel cells, Wiley Subscription Services, Inc., A Wiley Company, Sussex, 2012.

[4] M. Winter, R.J. Brodd, What Are Batteries, Fuel Cells, and Supercapacitors?, Chem. Rev. 104 (2004) 4245–4270. doi:10.1021/cr020730k.

[5] D. Umeyama, S. Horike, M. Inukai, T. Itakura, S. Kitagawa, Inherent Proton Conduction in a 2D Coordination Framework, J. Am. Chem. Soc. 134 (2012) 12780–12785. doi:10.1021/ja304693r.

[6] V.G. Ponomareva, K.A. Kovalenko, A.P. Chupakhin, D.N. Dybtsev, E.S. Shutova, V.P. Fedin, Imparting high proton conductivity to a metal-organic framework material by controlled acid impregnation, J. Am. Chem. Soc. 134 (2012) 15640–15643. doi:10.1021/ja305587n.

[7] S.S. Nagarkar, S.M. Unni, A. Sharma, S. Kurungot, S.K. Ghosh, Two-in-One: Inherent Anhydrous and Water-Assisted High Proton Conduction in a 3D Metal-Organic Framework, Angew. Chemie Int. Ed. 53 (2014) 2638–2642. doi:10.1002/anie.201309077.

[8] A. Pozio, L. Giorgi, E. Antolini, E. Passalacqua, Electroxidation of H2 on Pt/C Pt–Ru/C and Pt–Mo/C anodes for polymer electrolyte fuel cell, Electrochim. Acta. 46 (2000) 555–561. doi:10.1016/S0013-4686(00)00625-3.

[9] Z. Qi, C. He, A. Kaufman, Poisoning of Proton Exchange Membrane Fuel Cell Cathode by CO in the Anode Fuel, Electrochem. Solid-State Lett. 4 (2001) A204. doi:10.1149/1.1414944.

[10] K.A. Mauritz, R.B. Moore, State of Understanding of Nafion, Chem. Rev. 104 (2004) 4535–4586. doi:10.1021/cr0207123.

[11] A. Kraytsberg, Y. Ein-Eli, Review of Advanced Materials for Proton Exchange Membrane Fuel Cells, Energy & Fuels. 28 (2014) 7303–7330. doi:10.1021/ef501977k.

[12] M. Casciola, G. Alberti, M. Sganappa, R. Narducci, On the decay of Nafion proton conductivity at high temperature and relative humidity, J. Power Sources. 162 (2006) 141–145. doi:10.1016/j.jpowsour.2006.06.023.

[13] H.-Y. Jung, J.W. Kim, Role of the glass transition temperature of Nafion 117 membrane in the preparation of the membrane electrode assembly in a direct methanol fuel cell (DMFC), Int. J. Hydrogen Energy. 37 (2012) 12580–12585. doi:10.1016/j.ijhydene.2012.05.121.

[14] N. Zamel, X. Li, Effect of contaminants on polymer electrolyte membrane fuel cells, Prog. Energy Combust. Sci. 37 (2011) 292–329. doi:10.1016/j.pecs.2010.06.003.

[15] S.J. Peighambardoust, S. Rowshanzamir, M. Amjadi, Review of the proton exchange membranes for fuel cell applications, Elsevier Ltd, 2010. doi:10.1016/j.ijhydene.2010.05.017.

[16] V. Evoen, Electrocatalysis in Solid Acid Fuel Cell Electrodes, California Institute of Technology, 2016.

[17] M. Marrony, Proton-Conducting Ceramics, Pan Stanford, 2015. doi:10.1201/b18921.

[18] P. Leung, A.A. Shah, L. Sanz, C. Flox, J.R. Morante, Q. Xu, M.R. Mohamed, C. Ponce de León, F.C. Walsh, Recent developments in organic redox flow batteries: A critical review, J. Power Sources. 360 (2017) 243–283. doi:10.1016/j.jpowsour.2017.05.057.

[19] P. Leung, X. Li, C. Ponce de León, L. Berlouis, C.T.J. Low, F.C. Walsh, Progress in redox flow batteries, remaining challenges and their applications in energy storage, RSC Adv. 2 (2012) 10125.

doi:10.1039/c2ra21342g.

[20] C. Ponce de León, A. Frías-Ferrer, J. González-García, D.A. Szánto, F.C. Walsh, Redox flow cells for energy conversion, J. Power Sources. 160 (2006) 716–732. doi:10.1016/j.jpowsour.2006.02.095.

[21] P. Alotto, M. Guarnieri, F. Moro, Redox flow batteries for the storage of renewable energy: A review, Renew. Sustain. Energy Rev. 29 (2014) 325–335. doi:10.1016/j.rser.2013.08.001.

[22] M. Skyllas-Kazacos, M.H. Chakrabarti, S.A. Hajimolana, F.S. Mjalli, M. Saleem, Progress in Flow Battery Research and Development, J. Electrochem. Soc. 158 (2011) R55. doi:10.1149/1.3599565.

[23] Z. He, Z. Li, Z. Zhou, F. Tu, Y. Jiang, C. Pan, S. Liu, Improved performance of vanadium redox battery using methylsulfonic acid solution as supporting electrolyte, J. Renew. Sustain. Energy. 5 (2013) 023130. doi:10.1063/1.4800202.

[24] E. Sum, M. Rychcik, M. Skyllas-kazacos, Investigation of the V(V)/V(IV) system for use in the positive half-cell of a redox battery, J. Power Sources. 16 (1985) 85–95. doi:10.1016/0378-7753(85)80082-3.

[25] H. Vafiadis, M. Skyllas-Kazacos, Evaluation of membranes for the novel vanadium bromine redox flow cell, J. Memb. Sci. 279 (2006) 394–402. doi:10.1016/j.memsci.2005.12.028.

[26] C. Menictas, M. Skyllas-Kazacos, Performance of vanadium-oxygen redox fuel cell, J. Appl. Electrochem. 41 (2011) 1223–1232. doi:10.1007/s10800-011-0342-8.

[27] H. Prifti, A. Parasuraman, S. Winardi, T.M. Lim, M. Skyllas-Kazacos, Membranes for Redox Flow Battery Applications, Membranes (Basel). 2 (2012) 275–306. doi:10.3390/membranes2020275.

[28] C.-H. Bae, E.P.. Roberts, R.A.. Dryfe, Chromium redox couples for application to redox flow batteries, Electrochim. Acta. 48 (2002) 279–287. doi:10.1016/S0013-4686(02)00649-7.

[29] M. Skyllas-Kazacos, G. Kazacos, G. Poon, H. Verseema, Recent advances with UNSW vanadium-based redox flow batteries, Int. J. Energy Res. 34 (2010) 182–189. doi:10.1002/er.1658.

[30] M. Skyllas-Kazacos, Novel vanadium chloride/polyhalide redox flow battery, J. Power Sources. 124 (2003) 299–302. doi:10.1016/S0378-7753(03)00621-9.

[31] F.-Q. Xue, Y.-L. Wang, W.-H. Wang, X.-D. Wang, Investigation on the electrode process of the Mn(II)/Mn(III) couple in redox flow battery, Electrochim. Acta. 53 (2008) 6636–6642. doi:10.1016/j.electacta.2008.04.040.

[32] J. Xi, Z. Wu, X. Qiu, L. Chen, Nafion/SiO2 hybrid membrane for vanadium redox flow battery, J. Power Sources. 166 (2007) 531–536. doi:10.1016/j.jpowsour.2007.01.069.

[33] X. Teng, Y. Zhao, J. Xi, Z. Wu, X. Qiu, L. Chen, Nafion/organic silica modified TiO2 composite membrane for vanadium redox flow battery via in situ sol–gel reactions, J. Memb. Sci. 341 (2009) 149–154. doi:10.1016/j.memsci.2009.05.051.

[34] Q. Luo, H. Zhang, J. Chen, P. Qian, Y. Zhai, Modification of Nafion membrane using interfacial polymerization for vanadium redox flow battery applications, J. Memb. Sci. 311 (2008) 98–103. doi:10.1016/j.memsci.2007.11.055.

[35] J. Zeng, C. Jiang, Y. Wang, J. Chen, S. Zhu, B. Zhao, R. Wang, Studies on polypyrrole modified nafion membrane for vanadium redox flow battery, Electrochem. Commun. 10 (2008) 372–375. doi:10.1016/j.elecom.2007.12.025.

[36] S.C. Chieng, M. Kazacos, M. Skyllas-Kazacos, Modification of Daramic, microporous separator, for redox flow battery applications, J. Memb. Sci. 75 (1992) 81–91. doi:10.1016/0376-7388(92)80008-8.

[37] X. Li, H. Zhang, Z. Mai, H. Zhang, I. Vankelecom, Ion exchange membranes for vanadium redox flow battery (VRB) applications, Energy Environ. Sci. 4 (2011) 1147. doi:10.1039/c0ee00770f.

[38] D. Chen, S. Wang, M. Xiao, Y. Meng, Synthesis and characterization of novel sulfonated poly(arylene

thioether) ionomers for vanadiumredox flow battery applications, Energy Environ. Sci. 3 (2010) 622–628. doi:10.1039/B917117G.

[39] Z. Xu, I. Michos, X. Wang, R. Yang, X. Gu, J. Dong, A zeolite ion exchange membrane for redox flow batteries, Chem. Commun. 50 (2014) 2416. doi:10.1039/c3cc47214k.

[40] A.Z. Weber, M.M. Mench, J.P. Meyers, P.N. Ross, J.T. Gostick, Q. Liu, Redox flow batteries: a review, J. Appl. Electrochem. 41 (2011) 1137–1164. doi:10.1007/s10800-011-0348-2.

[41] N. Yamazoe, Y. Shimizu, Humidity sensors: Principles and applications, Sensors and Actuators. 10 (1986) 379–398. doi:10.1016/0250-6874(86)80055-5.

[42] E. Traversa, Ceramic sensors for humidity detection: the state-of-the-art and future developments, Sensors Actuators B Chem. 23 (1995) 135–156. doi:10.1016/0925-4005(94)01268-M.

[43] Z. Chen, C. Lu, Humidity Sensors: A Review of Materials and Mechanisms, Sens. Lett. 3 (2005) 274–295. doi:10.1166/sl.2005.045.

[44] H. Farahani, R. Wagiran, M. Hamidon, Humidity Sensors Principle, Mechanism, and Fabrication Technologies: A Comprehensive Review, Sensors. 14 (2014) 7881–7939. doi:10.3390/s140507881.

[45] S. Achmann, G. Hagen, J. Kita, I. Malkowsky, C. Kiener, R. Moos, Metal-Organic Frameworks for Sensing Applications in the Gas Phase, Sensors. 9 (2009) 1574–1589. doi:10.3390/s90301574.

[46] A. Tripathy, S. Pramanik, J. Cho, J. Santhosh, N. Abu Osman, Role of Morphological Structure, Doping, and Coating of Different Materials in the Sensing Characteristics of Humidity Sensors, Sensors. 14 (2014) 16343–16422. doi:10.3390/s140916343.

[47] A. Potier, D.J. Jones, J. Roziere, P. Colomban, A. Novak, J.O. Thomas, I. Svare, P.G. Dickens, A.M. Chippindale, H. Iwara, F. Freund, I.A. Ryzhkin, H. Fuzellier, J. Conard, E.K. Andersen, I.G.K. Andersen, A. Clearfield, G. Alberti, M. Casciola, G. Pourcelly, C. Gavach, J.C. Lassegues, S. V. Bhat, R. Frech, J.C. Badot, K.-D. Kreuer, E. Skou, J.P. Korb, F. Devreux, R.C.T. Slade, P.S. Nicholson, N. Miura, N. Yamazoe, J. Guitton, C. Poinsignon, J.Y. Sanchez, O. Bohnke, Proton conductors, Cambridge University Press, Cambridge, 1992. doi:10.1017/CBO9780511524806.

[48] G. Alberti, Protonic conductivity of layered zirconium phosphonates containing —SO3H groups. III. Preparation and characterization of γ-zirconium sulfoaryl phosphonates, Solid State Ionics. 84 (1996) 97–104. doi:10.1016/S0167-2738(96)83011-6.

[49] Amir-Al-Ahmed, A.S. Sultan, S.M.J. Zaidi, Sulfonated Poly(Ether Ether Ketone) (SPEEK): A Promising Membrane Material for Polymer Electrolyte Fuel Cell, in: Ion Exch. Technol. I, Springer Netherlands, Dordrecht, 2012: pp. 437–451. doi:10.1007/978-94-007-1700-8_12.

[50] a. Bozkurt, M. Ise, K.D. Kreuer, W.H. Meyer, G. Wegner, Proton-conducting polymer electrolytes based on phosphoric acid, Solid State Ionics. 125 (1999) 225–233. doi:10.1016/S0167-2738(99)00179-4.

[51] R. He, Proton conductivity of phosphoric acid doped polybenzimidazole and its composites with inorganic proton conductors, J. Memb. Sci. 226 (2003) 169–184. doi:10.1016/j.memsci.2003.09.002.

[52] B. Bauer, D.J. Jones, J. Rozière, L. Tchicaya, G. Alberti, M. Casciola, L. Massinelli, A. Peraio, S. Besse, E. Ramunni, Electrochemical characterisation of sulfonated polyetherketone membranes, J. New Mater. Electrochem. Syst. 3 (2000) 93–98.

[53] G. Alberti, M. Casciola, Solid state protonic conductors, present main applications and future prospects, Solid State Ionics. 145 (2001) 3–16. doi:10.1016/S0167-2738(01)00911-0.

[54] A. Jankowska, A. Zalewska, A. Skalska, A. Ostrowski, S. Kowalak, Proton conductivity of imidazole entrapped in microporous molecular sieves, Chem. Commun. 53 (2017) 2475–2478. doi:10.1039/C7CC00690J.

[55] S.T. Günday, A. Bozkurt, W.H. Meyer, G. Wegner, Effects of different acid functional groups on proton conductivity of polymer-1,2,4-triazole blends, J. Polym. Sci. Part B Polym. Phys. 44 (2006) 3315–3322. doi:10.1002/polb.20956.

[56] J. Dailly, M. Marrony, BCY-based proton conducting ceramic cell: 1000 h of long term testing in fuel cell application, J. Power Sources. 240 (2013) 323–327. doi:10.1016/j.jpowsour.2013.04.028.

[57] Y. Yoo, N. Lim, Performance and stability of proton conducting solid oxide fuel cells based on yttrium-doped barium cerate-zirconate thin-film electrolyte, J. Power Sources. 229 (2013) 48–57. doi:10.1016/j.jpowsour.2012.11.094.

[58] A. Magrasó, Transport number measurements and fuel cell testing of undoped and Mo-substituted lanthanum tungstate, J. Power Sources. 240 (2013) 583–588. doi:10.1016/j.jpowsour.2013.04.087.

[59] C. Solís, V.B. Vert, M. Balaguer, S. Escolástico, S. Roitsch, J.M. Serra, Mixed Proton-Electron Conducting Chromite Electrocatalysts as Anode Materials for LWO-Based Solid Oxide Fuel Cells, ChemSusChem. 5 (2012) 2155–2158. doi:10.1002/cssc.201200446.

[60] K.-D. Kreuer, Proton Conductivity: Materials and Applications, Chem. Mater. 8 (1996) 610–641. doi:10.1021/cm950192a.

[61] A. Donnadio, M. Nocchetti, F. Costantino, M. Taddei, M. Casciola, F. da Silva Lisboa, R. Vivani, A Layered Mixed Zirconium Phosphate/Phosphonate with Exposed Carboxylic and Phosphonic Groups: X-ray Powder Structure and Proton Conductivity Properties, Inorg. Chem. 53 (2014) 13220–13226. doi:10.1021/ic502473w.

[62] J.C. Badot, A. Fourrier-Lamer, N. Baffier, P. Colomban, Phase transitions and dielectric relaxations in superionic protonic conductor HUP (H3OUO2PO4.3H2O) in the broad frequency range (10-2-1010 Hz), J. Phys. 48 (1987) 1325–1336. doi:10.1051/jphys:019870048080132500.

[63] S. Hara, S. Takano, M. Miyayama, Proton-Conducting Properties and Microstructure of Hydrated Tin Dioxide and Hydrated Zirconia, J. Phys. Chem. B. 108 (2004) 5634–5639. doi:10.1021/jp0370369.

[64] J. Bielecki, S.F. Parker, D. Ekanayake, S.M.H. Rahman, L. Börjesson, M. Karlsson, Short-range structure of the brownmillerite-type oxide Ba 2 In 2 O 5 and its hydrated proton-conducting form BaInO 3 H, J. Mater. Chem. A. 2 (2014) 16915–16924. doi:10.1039/C4TA03213F.

[65] S. Sachdeva, J.A. Turner, J.L. Horan, A.M. Herring, The Use of Heteropoly Acids in Proton Exchange Fuel Cells, in: A. Bocarsly, D.M.P. Mingos (Eds.), Fuel Cells Hydrog. Storage, Springer Berlin Heidelberg, Berlin, Heidelberg, 2011: pp. 115–168. doi:10.1007/430_2011_45.

[66] K.G. Frase, G.C. Farrington, J.O. Thomas, Proton Transport in the β/β" -Aluminas, Annu. Rev. Mater. Sci. 14 (1984) 279–295. doi:10.1146/annurev.ms.14.080184.001431.

[67] G.C. Farrington, J.L. Briant, Hydronium beta″ alumina: A fast proton conductor, Mater. Res. Bull. 13 (1978) 763–773. doi:10.1016/0025-5408(78)90038-7.

[68] A. Donnadio, M. Nocchetti, F. Costantino, M. Taddei, M. Casciola, F. Da Silva Lisboa, R. Vivani, A layered mixed zirconium phosphate/phosphonate with exposed carboxylic and phosphonic groups: X-ray powder structure and proton conductivity properties, Inorg. Chem. 53 (2014) 13220–13226. doi:10.1021/ic502473w.

[69] W. HOGARTH, S. MUIR, A. WHITTAKER, J. DINIZDACOSTA, J. DRENNAN, G. LU, Proton conduction mechanism and the stability of sol–gel titanium phosphates, Solid State Ionics. 177 (2007) 3389–3394. doi:10.1016/j.ssi.2006.10.015.

[70] E. Rodríguez-Castellón, J. Jiménez-Jiménez, A. Jiménez-López, P. Maireles-Torres, J.. Ramos-Barrado, D.. Jones, J. Rozière, Proton conductivity of mesoporous MCM type of zirconium and titanium phosphates, Solid State Ionics. 125 (1999) 407–410. doi:10.1016/S0167-2738(99)00202-7.

[71] G. ALBERTI, M. BRACARDI, M. CASCIOLA, Ionic conduction of γ-titanium phosphate in hydrogen

and alkali metal salt forms☆, Solid State Ionics. 7 (1982) 243–247. doi:10.1016/0167-2738(82)90055-8.

[72] G. Alberti, M. Casciola, Layered metalIV phosphonates, a large class of inorgano-organic proton conductors, Solid State Ionics. 97 (1997) 177–186. doi:10.1016/S0167-2738(97)00070-2.

[73] G. Alberti, U. Costantino, M. Casciola, S. Ferroni, L. Massinelli, P. Staiti, Preparation, characterization and proton conductivity of titanium phosphate sulfophenylphosphonate, Solid State Ionics. 145 (2001) 249–255. doi:10.1016/S0167-2738(01)00948-1.

[74] G. Alberti, M. Casciola, S. Cavalaglio, R. Vivani, Proton conductivity of mesoporous zirconium phosphate pyrophosphate, Solid State Ionics. 125 (1999) 91–97. doi:10.1016/S0167-2738(99)00162-9.

[75] J.M. Troup, A. Clearfield, Mechanism of ion exchange in zirconium phosphates. 20. Refinement of the crystal structure of .alpha.-zirconium phosphate, Inorg. Chem. 16 (1977) 3311–3314. doi:10.1021/ic50178a065.

[76] W.H.J. Hogarth, J.C. Diniz da Costa, J. Drennan, G.Q. (Max) Lu, Proton conductivity of mesoporous sol–gel zirconium phosphates for fuel cell applications, J. Mater. Chem. 15 (2005) 754–758. doi:10.1039/B413413N.

[77] A.E.C. Palmqvist, Synthesis of ordered mesoporous materials using surfactant liquid crystals or micellar solutions, Curr. Opin. Colloid Interface Sci. 8 (2003) 145–155. doi:10.1016/S1359-0294.

[78] P. Knauth, M.L. Di Vona, Proton Mobility in Hydrated Acidic Polymers: Consequences for Optimization of Proton Conductivity, ECS Trans. 50 (2013) 1037–1044. doi:10.1149/05002.1037ecst.

[79] J.W. Phair, S.P.S. Badwal, Review of proton conductors for hydrogen separation, Ionics (Kiel). 12 (2006) 103–115. doi:10.1007/s11581-006-0016-4.

[80] S.M. Haile, D.A. Boysen, C.R.I. Chisholm, R.B. Merle, Solid acids as fuel cell electrolytes, Nature. 410 (2001) 910–913. doi:10.1038/35073536.

[81] F.-M. Zhang, L.-Z. Dong, J.-S. Qin, W. Guan, J. Liu, S.-L. Li, M. Lu, Y.-Q. Lan, Z.-M. Su, H.-C. Zhou, Effect of Imidazole Arrangements on Proton-Conductivity in Metal–Organic Frameworks, J. Am. Chem. Soc. 139 (2017) 6183–6189. doi:10.1021/jacs.7b01559.

[82] J. Tritt-Goc, I. Jankowska, K. Pogorzelec-Glaser, R. Pankiewicz, P. Ławniczak, Imidazole-doped nanocrystalline cellulose solid proton conductor: synthesis, thermal properties, and conductivity, Cellulose. 25 (2018) 281–291. http://link.springer.com/10.1007/s10570-017-1555-8.

[83] G. Scharfenberger, W.H. Meyer, G. Wegner, M. Schuster, K.-D. Kreuer, J. Maier, Anhydrous Polymeric Proton Conductors Based on Imidazole Functionalized Polysiloxane, Fuel Cells. 6 (2006) 237–250. doi:10.1002/fuce.200500210.

[84] S.R. Batten, N.R. Champness, X.-M. Chen, J. Garcia-Martinez, S. Kitagawa, L. Öhrström, M. O'Keeffe, M. Paik Suh, J. Reedijk, Terminology of metal–organic frameworks and coordination polymers (IUPAC Recommendations 2013), Pure Appl. Chem. 85 (2013) 1715–1724. doi:10.1351/PAC-REC-12-11-20.

[85] P.Z. Moghadam, A. Li, S.B. Wiggin, A. Tao, A.G.P. Maloney, P.A. Wood, S.C. Ward, D. Fairen-Jimenez, Development of a Cambridge Structural Database Subset: A Collection of Metal-Organic Frameworks for Past, Present, and Future, Chem. Mater. 29 (2017) 2618–2625. doi:10.1021/acs.chemmater.7b00441.

[86] X. Meng, H.-N. Wang, S.-Y. Song, H.-J. Zhang, Proton-conducting crystalline porous materials, Chem. Soc. Rev. 46 (2017) 464–480. doi:10.1039/C6CS00528D.

[87] R.J. Kuppler, D.J. Timmons, Q.-R. Fang, J.-R. Li, T.A. Makal, M.D. Young, D. Yuan, D. Zhao, W. Zhuang, H.-C. Zhou, Potential applications of metal-organic frameworks, Coord. Chem. Rev. 253 (2009) 3042–3066. doi:10.1016/j.ccr.2009.05.019.

[88] H. Furukawa, K.E. Cordova, M. O'Keeffe, O.M. Yaghi, The chemistry and applications of metal-organic frameworks, Science (80-.). 341 (2013). doi:10.1126/science.1230444.

[89] M.F. de Lange, K.J.F.M. Verouden, T.J.H. Vlugt, J. Gascon, F. Kapteijn, Adsorption-Driven Heat Pumps: The Potential of Metal–Organic Frameworks, Chem. Rev. 115 (2015) 12205–12250. doi:10.1021/acs.chemrev.5b00059.

[90] N.C. Burtch, H. Jasuja, K.S. Walton, Water Stability and Adsorption in Metal–Organic Frameworks, Chem. Rev. 114 (2014) 10575–10612. doi:10.1021/cr5002589.

[91] S. Yuan, L. Feng, K. Wang, J. Pang, M. Bosch, C. Lollar, Y. Sun, J. Qin, X. Yang, P. Zhang, Q. Wang, L. Zou, Y. Zhang, L. Zhang, Y. Fang, J. Li, H.-C. Zhou, Stable Metal-Organic Frameworks: Design, Synthesis, and Applications, Adv. Mater. 1704303 (2018) 1704303. doi:10.1002/adma.201704303.

[92] T. Devic, C. Serre, High valence 3p and transition metal based MOFs, Chem. Soc. Rev. 43 (2014) 6097–6115. doi:10.1039/c4cs00081a.

[93] G. Maurin, C. Serre, A. Cooper, G. Férey, The new age of MOFs and of their porous-related solids, Chem. Soc. Rev. 46 (2017) 3104–3107. doi:10.1039/C7CS90049J.

[94] A. Shigematsu, T. Yamada, H. Kitagawa, Wide Control of Proton Conductivity in Porous Coordination Polymers, J. Am. Chem. Soc. 133 (2011) 2034–2036. doi:10.1021/ja109810w.

[95] J.M. Taylor, K.W. Dawson, G.K.H. Shimizu, A Water-Stable Metal–Organic Framework with Highly Acidic Pores for Proton-Conducting Applications, J. Am. Chem. Soc. 135 (2013) 1193–1196. doi:10.1021/ja310435e.

[96] M. Bazaga-García, R.M.P. Colodrero, M. Papadaki, P. Garczarek, J. Zoń, P. Olivera-Pastor, E.R. Losilla, L. León-Reina, M.A.G. Aranda, D. Choquesillo-Lazarte, K.D. Demadis, A. Cabeza, Guest Molecule-Responsive Functional Calcium Phosphonate Frameworks for Tuned Proton Conductivity, J. Am. Chem. Soc. 136 (2014) 5731–5739. doi:10.1021/ja500356z.

[97] P. Ramaswamy, N.E. Wong, B.S. Gelfand, G.K.H.H. Shimizu, A Water Stable Magnesium MOF That Conducts Protons over 10 –2 S cm –1, J. Am. Chem. Soc. 137 (2015) 7640–7643. doi:10.1021/jacs.5b04399.

[98] W.J. Phang, H. Jo, W.R. Lee, J.H. Song, K. Yoo, B. Kim, C.S. Hong, Superprotonic Conductivity of a UiO-66 Framework Functionalized with Sulfonic Acid Groups by Facile Postsynthetic Oxidation, Angew. Chemie Int. Ed. 54 (2015) 5142–5146. doi:10.1002/anie.201411703.

[99] F. Yang, H. Huang, X. Wang, F. Li, Y. Gong, C. Zhong, J.-R. Li, Proton Conductivities in Functionalized UiO-66: Tuned Properties, Thermogravimetry Mass, and Molecular Simulation Analyses, Cryst. Growth Des. 15 (2015) 5827–5833. doi:10.1021/acs.cgd.5b01190.

[100] D.D. Borges, S. Devautour-Vinot, H. Jobic, J. Ollivier, F. Nouar, R. Semino, T. Devic, C. Serre, F. Paesani, G. Maurin, Proton Transport in a Highly Conductive Porous Zirconium-Based Metal-Organic Framework: Molecular Insight, Angew. Chemie - Int. Ed. 55 (2016) 3919–3924. doi:10.1002/anie.201510855.

[101] P.G.M. Mileo, S. Devautour-Vinot, G. Mouchaham, F. Faucher, N. Guillou, A. Vimont, C. Serre, G. Maurin, Proton-Conducting Phenolate-Based Zr Metal–Organic Framework: A Joint Experimental–Modeling Investigation, J. Phys. Chem. C. 120 (2016) 24503–24510. doi:10.1021/acs.jpcc.6b04649.

[102] F. Yang, G. Xu, Y. Dou, B. Wang, H. Zhang, H. Wu, W. Zhou, J.-R. Li, B. Chen, A flexible metal–organic framework with a high density of sulfonic acid sites for proton conduction, Nat. Energy. 2 (2017) 877–883. doi:10.1038/s41560-017-0018-7.

[103] Z. Hassanzadeh Fard, N.E. Wong, C.D. Malliakas, P. Ramaswamy, J.M. Taylor, K. Otsubo, G.K.H. Shimizu, Superprotonic Phase Change to a Robust Phosphonate Metal–Organic Framework, Chem. Mater. 30 (2018) 314–318. doi:10.1021/acs.chemmater.7b04467.

[104] J.A. Hurd, R. Vaidhyanathan, V. Thangadurai, C.I. Ratcliffe, I.L. Moudrakovski, G.K.H. Shimizu, Anhydrous proton conduction at 150 °C in a crystalline metal–organic framework, Nat. Chem. 1 (2009) 705–710. doi:10.1038/nchem.402.

[105] D. Umeyama, S. Horike, M. Inukai, Y. Hijikata, S. Kitagawa, Confinement of mobile histamine in coordination nanochannels for fast proton transfer, Angew. Chemie - Int. Ed. 50 (2011) 11706–11709. doi:10.1002/anie.201102997.

[106] D.N. Dybtsev, V.G. Ponomareva, S.B. Aliev, A.P. Chupakhin, M.R. Gallyamov, N.K. Moroz, B.A. Kolesov, K.A. Kovalenko, E.S. Shutova, V.P. Fedin, High Proton Conductivity and Spectroscopic Investigations of Metal–Organic Framework Materials Impregnated by Strong Acids, ACS Appl. Mater. Interfaces. 6 (2014) 5161–5167. doi:10.1021/am500438a.

[107] S. Kim, B. Joarder, J.A. Hurd, J. Zhang, K.W. Dawson, B.S. Gelfand, N.E. Wong, G.K.H. Shimizu, Achieving Superprotonic Conduction in Metal–Organic Frameworks through Iterative Design Advances, J. Am. Chem. Soc. 140 (2018) 1077–1082. doi:10.1021/jacs.7b11364.

[108] T.N. Tu, N.Q. Phan, T.T. Vu, H.L. Nguyen, K.E. Cordova, H. Furukawa, High proton conductivity at low relative humidity in an anionic Fe-based metal–organic framework, J. Mater. Chem. A. 4 (2016) 3638–3641. doi:10.1039/C5TA10467J.

[109] B. Joarder, J.-B. Lin, Z. Romero, G.K.H. Shimizu, Single Crystal Proton Conduction Study of a Metal Organic Framework of Modest Water Stability, J. Am. Chem. Soc. 139 (2017) 7176–7179. doi:10.1021/jacs.7b03397.

[110] S.M. Elahi, S. Chand, W.-H. Deng, A. Pal, M.C. Das, Polycarboxylate-Templated Coordination Polymers: Role of Templates for Superprotonic Conductivities of up to 10 −1 S cm −1, Angew. Chemie Int. Ed. 57 (2018) 6662–6666. doi:10.1002/anie.201802632.

[111] C. Dey, T. Kundu, R. Banerjee, Reversible phase transformation in proton conducting Strandberg-type POM based metal organic material, Chem. Commun. 48 (2012) 266–268. doi:10.1039/C1CC15162B.

[112] S.S. Bao, K. Otsubo, J.M. Taylor, Z. Jiang, L.M. Zheng, H. Kitagawa, Enhancing proton conduction in 2D Co-La coordination frameworks by solid-state phase transition, J. Am. Chem. Soc. 136 (2014) 9292–9295. doi:10.1021/ja505916c.

[113] S. Horike, W. Chen, T. Itakura, M. Inukai, D. Umeyama, H. Asakura, S. Kitagawa, Order-to-disorder structural transformation of a coordination polymer and its influence on proton conduction, Chem. Commun. 50 (2014) 10241–10243. doi:10.1039/C4CC04370G.

[114] J.M. Taylor, T. Komatsu, S. Dekura, K. Otsubo, M. Takata, H. Kitagawa, The Role of a Three Dimensionally Ordered Defect Sublattice on the Acidity of a Sulfonated Metal–Organic Framework, J. Am. Chem. Soc. 137 (2015) 11498–11506. doi:10.1021/jacs.5b07267.

[115] F. Paesani, Molecular mechanisms of water-mediated proton transport in MIL-53 metal-organic frameworks, J. Phys. Chem. C. 117 (2013) 19508–19516. doi:10.1021/jp406163q.

[116] E. Eisbein, J.-O. Joswig, G. Seifert, Proton Conduction in a MIL-53(Al) Metal–Organic Framework: Confinement versus Host/Guest Interaction, J. Phys. Chem. C. 118 (2014) 13035–13041. doi:10.1021/jp5043969.

[117] N. Planas, J.E. Mondloch, S. Tussupbayev, J. Borycz, L. Gagliardi, J.T. Hupp, O.K. Farha, C.J. Cramer, Defining the Proton Topology of the Zr 6 -Based Metal–Organic Framework NU-1000, J. Phys. Chem. Lett. 5 (2014) 3716–3723. doi:10.1021/jz501899j.

[118] M. Liu, L. Chen, S. Lewis, S.Y. Chong, M.A. Little, T. Hasell, I.M. Aldous, C.M. Brown, M.W. Smith, C.A. Morrison, L.J. Hardwick, A.I. Cooper, Three-dimensional protonic conductivity in porous organic cage solids, Nat. Commun. 7 (2016) 12750. doi:10.1038/ncomms12750.

[119] S.S. Park, A.J. Rieth, C.H. Hendon, M. Dincă, Selective Vapor Pressure Dependent Proton Transport in

a Metal–Organic Framework with Two Distinct Hydrophilic Pores, J. Am. Chem. Soc. 140 (2018) 2016–2019. doi:10.1021/jacs.7b12784.

[120] E. Eisbein, J.-O. Joswig, G. Seifert, Enhanced proton-transfer activity in imidazole@MIL-53(Al) systems revealed by molecular-dynamics simulations, Microporous Mesoporous Mater. 216 (2015) 36–41. doi:10.1016/j.micromeso.2015.03.022.

[121] T. Grancha, J. Ferrando-Soria, J. Cano, P. Amorós, B. Seoane, J. Gascon, M. Bazaga-García, E.R. Losilla, A. Cabeza, D. Armentano, E. Pardo, Insights into the Dynamics of Grotthuss Mechanism in a Proton-Conducting Chiral bioMOF, Chem. Mater. 28 (2016) 4608–4615. doi:10.1021/acs.chemmater.6b01286.

[122] S. Biswas, J. Chakraborty, V. Singh Parmar, S.P. Bera, N. Ganguli, S. Konar, Channel-Assisted Proton Conduction Behavior in Hydroxyl-Rich Lanthanide-Based Magnetic Metal–Organic Frameworks, Inorg. Chem. 56 (2017) 4956–4965. doi:10.1021/acs.inorgchem.6b03147.

[123] S. Ling, B. Slater, Dynamic acidity in defective UiO-66, Chem. Sci. 7 (2016) 4706–4712. doi:10.1039/C5SC04953A.

[124] S. Sanda, S. Biswas, S. Konar, Study of Proton Conductivity of a 2D Flexible MOF and a 1D Coordination Polymer at Higher Temperature, Inorg. Chem. 54 (2015) 1218–1222. doi:10.1021/ic502098h.

[125] D. Gui, X. Dai, Z. Tao, T. Zheng, X. Wang, M.A. Silver, J. Shu, L. Chen, Y. Wang, T. Zhang, J. Xie, L. Zou, Y. Xia, J.J. Zhang, J.J. Zhang, L. Zhao, J. Diwu, R. Zhou, Z. Chai, S. Wang, Unique Proton Transportation Pathway in a Robust Inorganic Coordination Polymer Leading to Intrinsically High and Sustainable Anhydrous Proton Conductivity, J. Am. Chem. Soc. 140 (2018) 6146–6155. doi:10.1021/jacs.8b02598.

[126] P. Ramaswamy, N.E. Wong, G.K.H. Shimizu, MOFs as proton conductors – challenges and opportunities, Chem. Soc. Rev. 43 (2014) 5913–5932. doi:10.1039/C4CS00093E.

[127] A.-L. Li, Q. Gao, J. Xu, X.-H. Bu, Proton-conductive metal-organic frameworks: Recent advances and perspectives, Coord. Chem. Rev. 344 (2017) 54–82. doi:10.1016/j.ccr.2017.03.027.

[128] H. Bin Luo, L. Te Ren, W.H. Ning, S.X. Liu, J.L. Liu, X.M. Ren, Robust Crystalline Hybrid Solid with Multiple Channels Showing High Anhydrous Proton Conductivity and a Wide Performance Temperature Range, Adv. Mater. 28 (2016) 1663–1667. doi:10.1002/adma.201504591.

[129] S. Khatua, A.K. Bar, J.A. Sheikh, A. Clearfield, S. Konar, Achieving Amphibious Superprotonic Conductivity in a Cu I Metal-Organic Framework by Strategic Pyrazinium Salt Impregnation, Chem. - A Eur. J. 24 (2018) 872–880. doi:10.1002/chem.201704088.

[130] M. Inukai, S. Horike, T. Itakura, R. Shinozaki, N. Ogiwara, D. Umeyama, S. Nagarkar, Y. Nishiyama, M. Malon, A. Hayashi, T. Ohhara, R. Kiyanagi, S. Kitagawa, Encapsulating Mobile Proton Carriers into Structural Defects in Coordination Polymer Crystals: High Anhydrous Proton Conduction and Fuel Cell Application, J. Am. Chem. Soc. 138 (2016) 8505–8511. doi:10.1021/jacs.6b03625.

[131] H. Chen, S.-Y. Han, R.-H. Liu, T.-F. Chen, K.-L. Bi, J.-B. Liang, Y.-H. Deng, C.-Q. Wan, High conductive, long-term durable, anhydrous proton conductive solid-state electrolyte based on a metal-organic framework impregnated with binary ionic liquids: Synthesis, characteristic and effect of anion, J. Power Sources. 376 (2018) 168–176. doi:10.1016/j.jpowsour.2017.11.089.

[132] L.-H. Chen, B.-B. Wu, H.-X. Zhao, L.-S. Long, L.-S. Zheng, High temperature ionic conduction mediated by ionic liquid incorporated within the metal-organic framework UiO-67(Zr), Inorg. Chem. Commun. 81 (2017) 1–4. doi:10.1016/j.inoche.2017.04.019.

[133] S. Liu, Z. Yue, Y. Liu, Incorporation of imidazole within the metal–organic framework UiO-67 for enhanced anhydrous proton conductivity, Dalt. Trans. 44 (2015) 12976–12980. doi:10.1039/C5DT01667C.

[134] D. Umeyama, S. Horike, M. Inukai, S. Kitagawa, Integration of Intrinsic Proton Conduction and Guest-Accessible Nanospace into a Coordination Polymer, J. Am. Chem. Soc. 135 (2013) 11345–11350. doi:10.1021/ja4051668.

[135] Y.-S. Wei, X.-P. Hu, Z. Han, X.-Y. Dong, S.-Q. Zang, T.C.W. Mak, Unique Proton Dynamics in an Efficient MOF-Based Proton Conductor, J. Am. Chem. Soc. 139 (2017) 3505–3512. doi:10.1021/jacs.6b12847.

[136] S.S. Nagarkar, S. Horike, T. Itakura, B. Le Ouay, A. Demessence, M. Tsujimoto, S. Kitagawa, Enhanced and Optically Switchable Proton Conductivity in a Melting Coordination Polymer Crystal, Angew. Chemie Int. Ed. 56 (2017) 4976–4981. doi:10.1002/anie.201700962.

[137] Y. Ye, X. Wu, Z. Yao, L. Wu, Z. Cai, L. Wang, X. Ma, Q.H. Chen, Z. Zhang, S. Xiang, Metal-organic frameworks with a large breathing effect to host hydroxyl compounds for high anhydrous proton conductivity over a wide temperature range from subzero to 125°C, J. Mater. Chem. A. 4 (2016) 4062–4070. doi:10.1039/c5ta10765b.

[138] S. Horike, D. Umeyama, M. Inukai, T. Itakura, S. Kitagawa, Coordination-Network-Based Ionic Plastic Crystal for Anhydrous Proton Conductivity, J. Am. Chem. Soc. 134 (2012) 7612–7615. doi:10.1021/ja301875x.

[139] M. Inukai, S. Horike, W. Chen, D. Umeyama, T. Itakura, S. Kitagawa, Template-directed proton conduction pathways in a coordination framework, J. Mater. Chem. A. 2 (2014) 10404–10409. doi:10.1039/C4TA01261E.

[140] X.-L. Sun, W.-H. Deng, H. Chen, H.-L. Han, J.M. Taylor, C.-Q. Wan, G. Xu, A Metal-Organic Framework Impregnated with a Binary Ionic Liquid for Safe Proton Conduction above 100 °C, Chem. - A Eur. J. 23 (2017) 1248–1252. doi:10.1002/chem.201605215.

[141] H. Luo, M. Wang, J. Zhang, Z. Tian, Y. Zou, X. Ren, Open-Framework Chalcogenide Showing Both Intrinsic Anhydrous and Water-Assisted High Proton Conductivity, ACS Appl. Mater. Interfaces. 10 (2018) 2619–2627. doi:10.1021/acsami.7b17189.

[142] X.-M. Li, L.-Z. Dong, S.-L. Li, G. Xu, J. Liu, F.-M. Zhang, L.-S. Lu, Y.-Q. Lan, Synergistic Conductivity Effect in a Proton Sources-Coupled Metal–Organic Framework, ACS Energy Lett. 2 (2017) 2313–2318. doi:10.1021/acsenergylett.7b00560.

[143] Q.G. Zhai, C. Mao, X. Zhao, Q. Lin, F. Bu, X. Chen, X. Bu, P. Feng, Cooperative Crystallization of Heterometallic Indium-Chromium Metal-Organic Polyhedra and Their Fast Proton Conductivity, Angew. Chemie - Int. Ed. 54 (2015) 7886–7890. doi:10.1002/anie.201503095.

[144] N.T.T. Nguyen, H. Furukawa, F. Gándara, C.A. Trickett, H.M. Jeong, K.E. Cordova, O.M. Yaghi, Three-Dimensional Metal-Catecholate Frameworks and Their Ultrahigh Proton Conductivity, J. Am. Chem. Soc. 137 (2015) 15394–15397. doi:10.1021/jacs.5b10999.

[145] W. Chen, J. Wang, L. Zhao, W. Dai, Z. Li, G. Li, Enhancing proton conductivity of a highly water stable 3D Sr(II) metal-organic framework by exposure to aqua-ammonia vapor, J. Alloys Compd. 750 (2018) 895–901. doi:10.1016/j.jallcom.2018.04.087.

[146] X. Liang, B. Li, M. Wang, J. Wang, R. Liu, G. Li, Effective Approach to Promoting the Proton Conductivity of Metal–Organic Frameworks by Exposure to Aqua–Ammonia Vapor, ACS Appl. Mater. Interfaces. 9 (2017) 25082–25086. doi:10.1021/acsami.7b07635.

[147] H. Wu, F. Yang, X.-L. Lv, B. Wang, Y.-Z. Zhang, M.-J. Zhao, J.-R. Li, A stable porphyrinic metal–organic framework pore-functionalized by high-density carboxylic groups for proton conduction, J. Mater. Chem. A. 5 (2017) 14525–14529. doi:10.1039/C7TA03917D.

[148] X. Wang, Y. Wang, M.A. Silver, D. Gui, Z. Bai, Y. Wang, W. Liu, L. Chen, J. Diwu, Z. Chai, S. Wang, Superprotonic conduction through one-dimensional ordered alkali metal ion chains in a lanthanide-organic framework, Chem. Commun. 54 (2018) 4429–4432. doi:10.1039/C8CC00572A.

[149] W.J. Phang, W.R. Lee, K. Yoo, D.W. Ryu, B. Kim, C.S. Hong, pH-Dependent Proton Conducting Behavior in a Metal-Organic Framework Material, Angew. Chemie Int. Ed. 53 (2014) 8383–8387. doi:10.1002/anie.201404164.

[150] S. Kim, K.W. Dawson, B.S. Gelfand, J.M. Taylor, G.K.H. Shimizu, Enhancing Proton Conduction in a Metal–Organic Framework by Isomorphous Ligand Replacement, J. Am. Chem. Soc. 135 (2013) 963–966. doi:10.1021/ja310675x.

[151] P.G.M. Mileo, K. Adil, L. Davis, A. Cadiau, Y. Belmabkhout, H. Aggarwal, G. Maurin, M. Eddaoudi, S. Devautour-Vinot, Achieving Superprotonic Conduction with a 2D Fluorinated Metal–Organic Framework, J. Am. Chem. Soc. 140 (2018) 13156–13160. doi:10.1021/jacs.8b06582.

[152] Y. Ye, W. Guo, L. Wang, Z. Li, Z. Song, J. Chen, Z. Zhang, S. Xiang, B. Chen, Straightforward Loading of Imidazole Molecules into Metal-Organic Framework for High Proton Conduction, J. Am. Chem. Soc. 139 (2017) 15604–15607. doi:10.1021/jacs.7b09163.

[153] M. V. Nguyen, T.H.N. Lo, L.C. Luu, H.T.T. Nguyen, T.N. Tu, Enhancing proton conductivity in a metal–organic framework at T > 80 °C by an anchoring strategy, J. Mater. Chem. A. 6 (2018) 1816–1821. doi:10.1039/C7TA10148A.

[154] Y.H. Han, Y. Ye, C. Tian, Z. Zhang, S.W. Du, S. Xiang, High proton conductivity in an unprecedented anionic metalloring organic framework (MROF) containing novel metalloring clusters with the largest diameter, J. Mater. Chem. A. 4 (2016) 18742–18746. doi:10.1039/c6ta07939c.

[155] S. Shalini, S. Aggarwal, S.K. Singh, M. Dutt, T.G. Ajithkumar, R. Vaidhyanathan, 10000-Fold Enhancement in Proton Conduction by Doping of Cesium Ions in a Proton-Conducting Zwitterionic Metal-Organic Framework, Eur. J. Inorg. Chem. 2016 (2016) 4382–4386. doi:10.1002/ejic.201600364.

[156] X. Lai, Y. Liu, G. Yang, S. Liu, Z. Shi, Y. Lu, F. Luo, S. Liu, Controllable proton-conducting pathways via situating polyoxometalates in targeting pores of a metal–organic framework, J. Mater. Chem. A. 5 (2017) 9611–9617. doi:10.1039/C6TA10958F.

[157] L. Qin, Y.Z. Yu, P.Q. Liao, W. Xue, Z. Zheng, X.M. Chen, Y.Z. Zheng, A "Molecular Water Pipe": A Giant Tubular Cluster {Dy72} Exhibits Fast Proton Transport and Slow Magnetic Relaxation, Adv. Mater. 28 (2016) 10772–10779. doi:10.1002/adma.201603381.

[158] X. Zhao, C. Mao, X. Bu, P. Feng, Direct Observation of Two Types of Proton Conduction Tunnels Coexisting in a New Porous Indium–Organic Framework, Chem. Mater. 26 (2014) 2492–2495. doi:10.1021/cm500473f.

[159] M.-J. Wei, J.-Q. Fu, Y.-D. Wang, Y. Zhang, H.-Y. Zang, K.-Z. Shao, Y.-G. Li, Z.-M. Su, Highly tuneable proton-conducting coordination polymers derived from a sulfonate-based ligand, CrystEngComm. 19 (2017) 7050–7056. doi:10.1039/C7CE01589E.

[160] Q. Gao, X.L. Wang, J. Xu, X.H. Bu, The First Demonstration of the Gyroid in a Polyoxometalate-Based Open Framework with High Proton Conductivity, Chem. - A Eur. J. 22 (2016) 9082–9086. doi:10.1002/chem.201601233.

[161] H. Matsui, M. Tadokoro, Proton conduction through the nanochannel water in weak-acidic nanoporous crystals [Cu2(phen)2(AcO)2(H2O)2][Al(OH)6Mo6O18]M+(nH2O) (M+= H+, Li+, Na+, K+), Solid State Ionics. 285 (2016) 165–169. doi:10.1016/j.ssi.2015.09.020.

[162] X. Meng, M. Wei, H. Wang, H. Zang, Z. Zhou, Multifunctional luminescent Zn(<scp>ii</scp>)-based metal–organic framework for high proton-conductivity and detection of Cr^{3+} ions in the presence of mixed metal ions, Dalt. Trans. 47 (2018) 1383–1387. doi:10.1039/C7DT03932H.

[163] L. Zou, S. Yao, J. Zhao, D.-S. Li, G. Li, Q. Huo, Y. Liu, Enhancing Proton Conductivity in a 3D Metal–Organic Framework by the Cooperation of Guest [Me 2 NH 2] + Cations, Water Molecules, and Host Carboxylates, Cryst. Growth Des. 17 (2017) 3556–3561. doi:10.1021/acs.cgd.7b00512.

[164] M. Sadakiyo, T. Yamada, H. Kitagawa, Rational Designs for Highly Proton-Conductive Metal−Organic Frameworks, J. Am. Chem. Soc. 131 (2009) 9906–9907. doi:10.1021/ja9040016.

[165] R.M.P. Colodrero, P. Olivera-Pastor, E.R. Losilla, M.A.G. Aranda, L. Leon-Reina, M. Papadaki, A.C. McKinlay, R.E. Morris, K.D. Demadis, A. Cabeza, Multifunctional lanthanum tetraphosphonates: Flexible, ultramicroporous and proton-conducting hybrid frameworks, Dalt. Trans. 41 (2012) 4045. doi:10.1039/c2dt11992g.

[166] K. Wang, X. Qi, Z. Wang, R. Wang, J. Sun, Q. Zhang, In Situ Encapsulation of Imidazolium Proton Carriers in Anionic Open Frameworks Leads the Way to Proton-Conducting Materials, Eur. J. Inorg. Chem. 2017 (2017) 2295–2300. doi:10.1002/ejic.201700157.

[167] H.-B. Luo, M. Wang, S.-X. Liu, C. Xue, Z.-F. Tian, Y. Zou, X.-M. Ren, Proton Conductance of a Superior Water-Stable Metal–Organic Framework and Its Composite Membrane with Poly(vinylidene fluoride), Inorg. Chem. 56 (2017) 4169–4175. doi:10.1021/acs.inorgchem.7b00122.

[168] J.M. Taylor, S. Dekura, R. Ikeda, H. Kitagawa, Defect control to enhance proton conductivity in a metal-organic framework, Chem. Mater. 27 (2015) 2286–2289. doi:10.1021/acs.chemmater.5b00665.

[169] J.M. Taylor, K.W. Dawson, G.K.H. Shimizu, A water-stable metal-organic framework with highly acidic pores for proton-conducting applications, J. Am. Chem. Soc. 135 (2013) 1193–1196. doi:10.1021/ja310435e.

[170] N.E. Wong, P. Ramaswamy, A.S. Lee, B.S. Gelfand, K.J. Bladek, J.M. Taylor, D.M. Spasyuk, G.K.H. Shimizu, Tuning Intrinsic and Extrinsic Proton Conduction in Metal–Organic Frameworks by the Lanthanide Contraction, J. Am. Chem. Soc. 139 (2017) 14676–14683. doi:10.1021/jacs.7b07987.

[171] T.H.N. Lo, M. V. Nguyen, T.N. Tu, An anchoring strategy leads to enhanced proton conductivity in a new metal-organic framework, Inorg. Chem. Front. 4 (2017) 1509–1516. doi:10.1039/c7qi00350a.

[172] M. Bazaga-García, M. Papadaki, R.M.P. Colodrero, P. Olivera-Pastor, E.R. Losilla, B. Nieto-Ortega, M.Á.G. Aranda, D. Choquesillo-Lazarte, A. Cabeza, K.D. Demadis, Tuning Proton Conductivity in Alkali Metal Phosphonocarboxylates by Cation Size-Induced and Water-Facilitated Proton Transfer Pathways, Chem. Mater. 27 (2015) 424–435. doi:10.1021/cm502716e.

[173] Y.G. Huang, S.Q. Wu, W.H. Deng, G. Xu, F.L. Hu, J.P. Hill, W. Wei, S.Q. Su, L.K. Shrestha, O. Sato, M.Y. Wu, M.C. Hong, K. Ariga, Selective CO2Capture and High Proton Conductivity of a Functional Star-of-David Catenane Metal–Organic Framework, Adv. Mater. 29 (2017) 1–6. doi:10.1002/adma.201703301.

[174] J.-X. Wang, Y.-D. Wang, M.-J. Wei, H.-Q. Tan, Y.-H. Wang, H.-Y. Zang, Y.-G. Li, Inorganic open framework based on lanthanide ions and polyoxometalates with high proton conductivity, Inorg. Chem. Front. 5 (2018) 1213–1217. doi:10.1039/C8QI00108A.

[175] J. Miao, Y. Liu, Q. Tang, D. He, G. Yang, Z. Shi, S. Liu, Q. Wu, Proton conductive watery channels constructed by Anderson polyanions and lanthanide coordination cations, Dalt. Trans. 43 (2014) 14749–14755. doi:10.1039/c4dt01715c.

[176] R. Liu, L. Zhao, W. Dai, C. Yang, X. Liang, G. Li, A Comparative Investigation of Proton Conductivities for Two Metal−Organic Frameworks under Water and Aqua-Ammonia Vapors, Inorg. Chem. 57 (2018) 1474–1482. doi:10.1021/acs.inorgchem.7b02851.

[177] S. Uchida, R. Hosono, R. Eguchi, R. Kawahara, R. Osuga, J.N. Kondo, M. Hibino, N. Mizuno, Proton conduction in alkali metal ion-exchanged porous ionic crystals, Phys. Chem. Chem. Phys. 19 (2017) 29077–29083. doi:10.1039/C7CP04619G.

[178] G. Xu, K. Otsubo, T. Yamada, S. Sakaida, H. Kitagawa, Superprotonic Conductivity in a Highly Oriented Crystalline Metal–Organic Framework Nanofilm, J. Am. Chem. Soc. 135 (2013) 7438–7441. doi:10.1021/ja402727d.

[179] T. Panda, T. Kundu, R. Banerjee, Self-assembled one dimensional functionalized metal-organic nanotubes (MONTs) for proton conduction, Chem. Commun. 48 (2012) 5464–5466. doi:10.1039/c2cc31527k.

[180] K. Zhang, X. Xie, H. Li, J. Gao, L. Nie, Y. Pan, J. Xie, D. Tian, W. Liu, Q. Fan, H. Su, L. Huang, W. Huang, Highly Water-Stable Lanthanide-Oxalate MOFs with Remarkable Proton Conductivity and Tunable Luminescence, Adv. Mater. 29 (2017) 1701804. doi:10.1002/adma.201701804.

[181] T. Panda, T. Kundu, R. Banerjee, Structural isomerism leading to variable proton conductivity in indium(iii) isophthalic acid based frameworks, Chem. Commun. 49 (2013) 6197–6199. doi:10.1039/c3cc41939h.

[182] J. Shi, K. Wang, J. Li, H. Zeng, Q. Zhang, Z. Lin, Exploration of new water stable proton-conducting materials in an amino acid-templated metal phosphate system, Dalt. Trans. 47 (2018) 654–658. doi:10.1039/C7DT04125J.

[183] S. Khatua, A. Kumar Bar, S. Konar, Tuning Proton Conductivity by Interstitial Guest Change in Size-Adjustable Nanopores of a Cu I -MOF: A Potential Platform for Versatile Proton Carriers, Chem. - A Eur. J. 22 (2016) 16277–16285. doi:10.1002/chem.201601964.

[184] M.-L. Wei, P.-F. Zhuang, H.-H. Li, Y.-H. Yang, Crystal Structures and Conductivities of Two Organic-Inorganic Hybrid Complexes Based on Poly-Keggin-Anion Chains, Eur. J. Inorg. Chem. 2011 (2011) 1473–1478. doi:10.1002/ejic.201001144.

[185] Y. Gao, R. Broersen, W. Hageman, N. Yan, M.C. Mittelmeijer-Hazeleger, G. Rothenberg, S. Tanase, High proton conductivity in cyanide-bridged metal-organic frameworks: understanding the role of water, J. Mater. Chem. A. 3 (2015) 22347–22352. doi:10.1039/c5ta05280g.

[186] X. Wang, T. Qin, S.S. Bao, Y.C. Zhang, X. Shen, L.M. Zheng, D. Zhu, Facile synthesis of a water stable 3D Eu-MOF showing high proton conductivity and its application as a sensitive luminescent sensor for Cu2+ions, J. Mater. Chem. A. 4 (2016) 16484–16489. doi:10.1039/c6ta06792a.

[187] S. Ohkoshi, K. Nakagawa, K. Tomono, K. Imoto, Y. Tsunobuchi, H. Tokoro, High Proton Conductivity in Prussian Blue Analogues and the Interference Effect by Magnetic Ordering, J. Am. Chem. Soc. 132 (2010) 6620–6621. doi:10.1021/ja100385f.

[188] X. Wang, X. Duan, C. Kong, M. Wei, A complex based on a decorated Keggin-type cluster from Cu(II) and 4,4′-dimethyl-2,2′-bipyridine: synthesis, structure and proton conductivity, J. Coord. Chem. 69 (2016) 779–787. doi:10.1080/00958972.2016.1139105.

[189] S. Sen, N.N. Nair, T. Yamada, H. Kitagawa, P.K. Bharadwaj, High Proton Conductivity by a Metal–Organic Framework Incorporating Zn 8 O Clusters with Aligned Imidazolium Groups Decorating the Channels, J. Am. Chem. Soc. 134 (2012) 19432–19437. doi:10.1021/ja3076378.

[190] T. Yamada, T. Nankawa, High Proton Conductivity of Zinc Oxalate Coordination Polymers Mediated by a Hydrogen Bond with Pyridinium, Inorg. Chem. 55 (2016) 8267–8270. doi:10.1021/acs.inorgchem.6b01534.

[191] Q. Tang, Y. Liu, S. Liu, D. He, J. Miao, X. Wang, G. Yang, Z. Shi, Z. Zheng, High Proton Conduction at above 100 °C Mediated by Hydrogen Bonding in a Lanthanide Metal–Organic Framework, J. Am. Chem. Soc. 136 (2014) 12444–12449. doi:10.1021/ja5069855.

[192] T. He, Y.Z. Zhang, H. Wu, X.J. Kong, X.M. Liu, L.H. Xie, Y. Dou, J.R. Li, Functionalized Base-Stable Metal–Organic Frameworks for Selective CO2 Adsorption and Proton Conduction, ChemPhysChem. 18 (2017) 3245–3252. doi:10.1002/cphc.201700650.

[193] X.Y. Dong, R. Wang, J. Bin Li, S.Q. Zang, H.W. Hou, T.C.W. Mak, A tetranuclear Cu4(μ3-OH)2-based metal-organic framework (MOF) with sulfonate-carboxylate ligands for proton conduction, Chem. Commun. 49 (2013) 10590–10592. doi:10.1039/c3cc46226a.

[194] M. Mon, J. Vallejo, J. Pasán, O. Fabelo, C. Train, M. Verdaguer, S.I. Ohkoshi, H. Tokoro, K. Nakagawa, E. Pardo, A novel oxalate-based three-dimensional coordination polymer showing magnetic ordering and high proton conductivity, Dalt. Trans. 46 (2017) 15130–15137. doi:10.1039/c7dt03415f.

[195] J. Zhang, H.-J. Bai, Q. Ren, H.-B. Luo, X.-M. Ren, Z.-F. Tian, S. Lu, Extra Water- and Acid-Stable MOF-801 with High Proton Conductivity and Its Composite Membrane for Proton-Exchange Membrane, ACS Appl. Mater. Interfaces. (2018) acsami.8b09070. doi:10.1021/acsami.8b09070.

[196] H.R. Zhao, C. Xue, C.P. Li, K.M. Zhang, H. Bin Luo, S.X. Liu, X.M. Ren, A Two-Dimensional Inorganic-Organic Hybrid Solid of Manganese(II) Hydrogenophosphate Showing High Proton Conductivity at Room Temperature, Inorg. Chem. 55 (2016) 8971–8975. doi:10.1021/acs.inorgchem.6b01438.

[197] R.M.P.P. Colodrero, P. Olivera-Pastor, E.R. Losilla, D. Hernández-Alonso, M.A.G.G. Aranda, L. Leon-Reina, J. Rius, K.D. Demadis, B. Moreau, D. Villemin, M. Palomino, F. Rey, A. Cabeza, High proton conductivity in a flexible, cross-linked, ultramicroporous magnesium tetraphosphonate hybrid framework, Inorg. Chem. 51 (2012) 7689–7698. doi:10.1021/ic3007316.

[198] Z. Sun, S. Yu, L. Zhao, J. Wang, Z. Li, G. Li, A Highly Stable Two-Dimensional Copper(II) Organic Framework for Proton Conduction and Ammonia Impedance Sensing, Chem. - A Eur. J. 24 (2018) 10829–10839. doi:10.1002/chem.201801844.

[199] J. Li, X.-L. Cao, Y.-Y. Wang, S.-R. Zhang, D.-Y. Du, J.-S. Qin, S.-L. Li, Z.-M. Su, Y.-Q. Lan, The Enhancement on Proton Conductivity of Stable Polyoxometalate-Based Coordination Polymers by the Synergistic Effect of MultiProton Units, Chem. - A Eur. J. 22 (2016) 9299–9304. doi:10.1002/chem.201601250.

[200] R. Li, S.-H. Wang, X.-X. Chen, J. Lu, Z.-H. Fu, Y. Li, G. Xu, F.-K. Zheng, G.-C. Guo, Highly Anisotropic and Water Molecule-Dependent Proton Conductivity in a 2D Homochiral Copper(II) Metal–Organic Framework, Chem. Mater. 29 (2017) 2321–2331. doi:10.1021/acs.chemmater.6b05497.

[201] W. Xing, H. Li, X. Dong, S. Zang, Robust multifunctional Zr-based metal–organic polyhedra for high proton conductivity and selective CO 2 capture, J. Mater. Chem. A. 6 (2018) 7724–7730. doi:10.1039/C8TA00858B.

[202] T. Yamada, M. Sadakiyo, H. Kitagawa, High Proton Conductivity of One-Dimensional Ferrous Oxalate Dihydrate, J. Am. Chem. Soc. 131 (2009) 3144–3145. doi:10.1021/ja808681m.

[203] S.-J. Liu, C. Cao, F. Yang, M.-H. Yu, S.-L. Yao, T.-F. Zheng, W.-W. He, H.-X. Zhao, T.-L. Hu, X.-H. Bu, High Proton Conduction in Two Co II and Mn II Anionic Metal–Organic Frameworks Derived from 1,3,5-Benzenetricarboxylic Acid, Cryst. Growth Des. 16 (2016) 6776–6780. doi:10.1021/acs.cgd.6b00776.

[204] L.J. Zhou, W.H. Deng, Y.L. Wang, G. Xu, S.G. Yin, Q.Y. Liu, Lanthanide-Potassium Biphenyl-3,3′-disulfonyl-4,4′-dicarboxylate Frameworks: Gas Sorption, Proton Conductivity, and Luminescent Sensing of Metal Ions, Inorg. Chem. 55 (2016) 6271–6277. doi:10.1021/acs.inorgchem.6b00928.

[205] E. Pardo, C. Train, G. Gontard, K. Boubekeur, O. Fabelo, H. Liu, B. Dkhil, F. Lloret, K. Nakagawa, H. Tokoro, S.I. Ohkoshi, M. Verdaguer, High proton conduction in a chiral ferromagnetic metal-organic quartz-like framework, J. Am. Chem. Soc. 133 (2011) 15328–15331. doi:10.1021/ja206917z.

[206] B.-L. Liu, H.-Y. Zang, H.-Q. Tan, Y.-H. Wang, Y.-G. Li, Engineering the proton conductivity of metal–organic hybrid materials by varying the coordination mode of the ligand, CrystEngComm. 18 (2016) 3300–3305. doi:10.1039/C6CE00299D.

[207] S.S. Bao, N.Z. Li, J.M. Taylor, Y. Shen, H. Kitagawa, L.M. Zheng, Co-Ca Phosphonate Showing Humidity-Sensitive Single Crystal to Single Crystal Structural Transformation and Tunable Proton Conduction Properties, Chem. Mater. 27 (2015) 8116–8125. doi:10.1021/acs.chemmater.5b03897.

[208] M. Taddei, A. Donnadio, F. Costantino, R. Vivani, M. Casciola, Synthesis, crystal structure, and proton

conductivity of one-dimensional, two-dimensional, and three-dimensional zirconium phosphonates based on glyphosate and glyphosine, Inorg. Chem. 52 (2013) 12131–12139. doi:10.1021/ic4019597.

[209] S. Bhattacharya, A.J. Bhattacharyya, S. Natarajan, High proton mobility, solvent induced single crystal to single crystal structural transformation, and related studies on a family of compounds formed from Mn<inf>3</inf> Oxo-clusters, Inorg. Chem. 54 (2015) 1254–1271. doi:10.1021/ic5018517.

[210] X. Meng, S.Y. Song, X.Z. Song, M. Zhu, S.N. Zhao, L.L. Wu, H.J. Zhang, A tetranuclear copper cluster-based MOF with sulfonate-carboxylate ligands exhibiting high proton conduction properties, Chem. Commun. 51 (2015) 8150–8152. doi:10.1039/c5cc01732g.

[211] W.-H. Wang, Q. Gao, A. Li, Y. Jia, S.-Y. Zhang, J. Wang, Y. Zhang, X. Bu, A coordination compound featuring a supramolecular hydrogen-bonding network for proton conduction, Chinese Chem. Lett. 29 (2018) 336–338. doi:10.1016/j.cclet.2017.08.033.

[212] S. Pili, S.P. Argent, C.G. Morris, P. Rought, V. Garc??a-Sakai, I.P. Silverwood, T.L. Easun, M. Li, M.R. Warren, C.A. Murray, C.C. Tang, S. Yang, M. Schr??der, Proton Conduction in a Phosphonate-Based Metal-Organic Framework Mediated by Intrinsic "free Diffusion inside a Sphere," J. Am. Chem. Soc. 138 (2016) 6352–6355. doi:10.1021/jacs.6b02194.

[213] D. Matoga, M. Oszajca, M. Molenda, Ground to conduct: mechanochemical synthesis of a metal–organic framework with high proton conductivity, Chem. Commun. 51 (2015) 7637–7640. doi:10.1039/C5CC01789K.

[214] P. Ramaswamy, R. Matsuda, W. Kosaka, G. Akiyama, H.J. Jeon, S. Kitagawa, Highly proton conductive nanoporous coordination polymers with sulfonic acid groups on the pore surface, Chem. Commun. 50 (2014) 1144–1146. doi:10.1039/c3cc47980c.

[215] R.M.P. Colodrero, K.E. Papathanasiou, N. Stavgianoudaki, P. Olivera-Pastor, E.R. Losilla, M.A.G. Aranda, L. León-Reina, J. Sanz, I. Sobrados, D. Choquesillo-Lazarte, J.M. García-Ruiz, P. Atienzar, F. Rey, K.D. Demadis, A. Cabeza, Multifunctional luminescent and proton-conducting lanthanide carboxyphosphonate open-framework hybrids exhibiting crystalline-to-amorphous- to-crystalline transformations, Chem. Mater. 24 (2012) 3780–3792. doi:10.1021/cm302381k.

[216] R.A. Agarwal, High proton-conduction in a three-dimensional microporous coordination polymer of Mn(II), Inorg. Chem. Commun. 70 (2016) 115–117. doi:10.1016/j.inoche.2016.05.030.

[217] S. Bhattacharya, M. Gnanavel, A.J. Bhattacharyya, S. Natarajan, Organization of Mn-clusters in pcu and bcu networks: Synthesis, structure, and properties, Cryst. Growth Des. 14 (2014) 310–325. doi:10.1021/cg401587r.

[218] X.-Y. Dong, X.-P. Hu, H.-C. Yao, S.-Q. Zang, H.-W. Hou, T.C.W. Mak, Alkaline Earth Metal (Mg, Sr, Ba)–Organic Frameworks Based on 2,2′,6,6′-Tetracarboxybiphenyl for Proton Conduction, Inorg. Chem. 53 (2014) 12050–12057. doi:10.1021/ic5017593.

[219] G.J. Cao, J.D. Liu, T.T. Zhuang, X.H. Cai, S.T. Zheng, A polyoxometalate-organic supramolecular nanotube with high chemical stability and proton-conducting properties, Chem. Commun. 51 (2015) 2048–2051. doi:10.1039/c4cc08445d.

[220] M. Sadakiyo, H. Okawa, A. Shigematsu, M. Ohba, T. Yamada, H. Kitagawa, Promotion of low-humidity proton conduction by controlling hydrophilicity in layered metal-organic frameworks, J. Am. Chem. Soc. 134 (2012) 5472–5475. doi:10.1021/ja300122r.

[221] S. Begum, Z. Wang, A. Donnadio, F. Costantino, M. Casciola, R. Valiullin, C. Chmelik, M. Bertmer, J. Kärger, J. Haase, H. Krautscheid, Water-Mediated proton conduction in a robust triazolyl phosphonate metal-organic framework with hydrophilic nanochannels, Chem. - A Eur. J. 20 (2014) 8862–8866. doi:10.1002/chem.201402886.

[222] S. Yang, P.-P. Sun, Y. Yuan, C. Zhang, Q.-L. Wang, High proton conduction behavior in 12-connected 3D porous lanthanide–organic frameworks and their polymer composites, CrystEngComm. 20 (2018)

3066–3073. doi:10.1039/C8CE00476E.

[223] X.-Y. Dong, R. Wang, J.-Z. Wang, S.-Q. Zang, T.C.W. Mak, Highly selective Fe 3+ sensing and proton conduction in a water-stable sulfonate–carboxylate Tb–organic-framework, J. Mater. Chem. A. 3 (2015) 641–647. doi:10.1039/C4TA04421E.

[224] M. Wei, X. Wang, X. Duan, Crystal Structures and Proton Conductivities of a MOF and Two POM-MOF Composites Based on Cu II Ions and 2,2′-Bipyridyl-3,3′-dicarboxylic Acid, Chem. - A Eur. J. 19 (2013) 1607–1616. doi:10.1002/chem.201203154.

[225] S.S. Bao, Y.X. Wu, N.Z. Li, L.M. Zheng, Proton Conductivities Manipulated by the Counter-Anions in 2D Co-Ca Coordination Frameworks, Eur. J. Inorg. Chem. 2016 (2016) 4476–4482. doi:10.1002/ejic.201600203.

[226] R.M.P. Colodrero, G.K. Angeli, M. Bazaga-Garcia, P. Olivera-Pastor, D. Villemin, E.R. Losilla, E.Q. Martos, G.B. Hix, M.A.G. Aranda, K.D. Demadis, A. Cabeza, Structural variability in multifunctional metal xylenediaminetetraphosphonate hybrids, Inorg. Chem. 52 (2013) 8770–8783. doi:10.1021/ic400951s.

[227] C.-Y. Kong, X.-Y. Duan, J.-J. Lai, M.-L. Wei, Syntheses, Structures and Proton Conductivities of Two Complexes Based on Decorated Keggin-Type Clusters: {[M(dmphen)(DMF)2(H2O)]2[SiW12O40]}·6H2O (M = Cu and Zn; dmphen = 4,7-dimethyl-1,10-phenanthroline), J. Clust. Sci. 28 (2017) 1407–1420. doi:10.1007/s10876-016-1144-2.

[228] G. Zhang, H. Fei, Missing metal-linker connectivities in a 3-D robust sulfonate-based metal–organic framework for enhanced proton conductivity, Chem. Commun. 53 (2017) 4156–4159. doi:10.1039/C7CC01461A.

[229] A. Mallick, T. Kundu, R. Banerjee, Correlation between coordinated water content and proton conductivity in Ca-BTC-based metal-organic frameworks, Chem. Commun. 48 (2012) 8829–8831. doi:10.1039/c2cc34006b.

[230] M. Sadakiyo, T. Yamada, H. Kitagawa, Proton Conductivity Control by Ion Substitution in a Highly Proton-Conductive Metal–Organic Framework, J. Am. Chem. Soc. 136 (2014) 13166–13169. doi:10.1021/ja507634v.

[231] S. Goswami, S. Biswas, S. Konar, Concomitant spin-canted antiferromagnetic ordering and proton conduction in homometallic and homoleptic coordination polymers, Dalt. Trans. 44 (2015) 3949–3953. doi:10.1039/C4DT03575E.

[232] M. Wei, L. Chen, X. Duan, A porous Cu(II)-MOF containing [PW 12 O 40] 3− and a large protonated water cluster: synthesis, structure, and proton conductivity, J. Coord. Chem. 67 (2014) 2809–2819. doi:10.1080/00958972.2014.957689.

[233] F. Costantino, A. Donnadio, M. Casciola, Survey on the phase transitions and their effect on the ion-exchange and on the proton-conduction properties of a flexible and robust Zr phosphonate coordination polymer, Inorg. Chem. 51 (2012) 6992–7000. doi:10.1021/ic3009656.

[234] H. Ōkawa, A. Shigematsu, M. Sadakiyo, T. Miyagawa, K. Yoneda, M. Ohba, H. Kitagawa, Oxalate-Bridged Bimetallic Complexes {NH(prol) 3 }[MCr(ox) 3] (M = Mn II , Fe II , Co II ; NH(prol) 3 + = Tri(3-hydroxypropyl)ammonium) Exhibiting Coexistent Ferromagnetism and Proton Conduction, J. Am. Chem. Soc. 131 (2009) 13516–13522. doi:10.1021/ja905368d.

[235] J.M. Taylor, R.K. Mah, I.L. Moudrakovski, C.I. Ratcliffe, R. Vaidhyanathan, G.K.H. Shimizu, Facile Proton Conduction via Ordered Water Molecules in a Phosphonate Metal−Organic Framework, J. Am. Chem. Soc. 132 (2010) 14055–14057. doi:10.1021/ja107035w.

[236] R.M.P. Colodrero, K.E. Papathanasiou, N. Stavgianoudaki, P. Olivera-Pastor, E.R. Losilla, M.A.G. Aranda, L. León-Reina, J. Sanz, I. Sobrados, D. Choquesillo-Lazarte, J.M. García-Ruiz, P. Atienzar, F. Rey, K.D. Demadis, A. Cabeza, Multifunctional Luminescent and Proton-Conducting Lanthanide

Carboxyphosphonate Open-Framework Hybrids Exhibiting Crystalline-to-Amorphous-to-Crystalline Transformations, Chem. Mater. 24 (2012) 3780–3792. doi:10.1021/cm302381k.

[237] D. Grohol, M.A. Subramanian, D.M. Poojary, A. Clearfield, Synthesis, crystal structures, and proton conductivity of two linear-chain uranyl phenylphosphonates, Inorg. Chem. 35 (1996) 5264–5271. doi:10.1021/ic960332y.

[238] K.J. Gagnon, H.P. Perry, A. Clearfield, Conventional and Unconventional Metal–Organic Frameworks Based on Phosphonate Ligands: MOFs and UMOFs, Chem. Rev. 112 (2012) 1034–1054. doi:10.1021/cr2002257.

[239] M. Schuster, T. Rager, A. Noda, K.D. Kreuer, J. Maier, About the Choice of the Protogenic Group in PEM Separator Materials for Intermediate Temperature, Low Humidity Operation: A Critical Comparison of Sulfonic Acid, Phosphonic Acid and Imidazole Functionalized Model Compounds, Fuel Cells. 5 (2005) 355–365. doi:10.1002/fuce.200400059.

[240] P.G.M. Mileo, T. Kundu, R. Semino, V. Benoit, N. Steunou, P.L. Llewellyn, C. Serre, G. Maurin, S. Devautour-Vinot, Highly Efficient Proton Conduction in a Three-Dimensional Titanium Hydrogen Phosphate, Chem. Mater. 29 (2017) 7263–7271. doi:10.1021/acs.chemmater.7b01850.

[241] J.M. Troup, A. Clearfield, Mechanism of ion exchange in zirconium phosphates. 20. Refinement of the crystal structure of .alpha.-zirconium phosphate, Inorg. Chem. 16 (1977) 3311–3314. doi:10.1021/ic50178a065.

[242] D.M. Poojary, B. Shpeizer, A. Clearfield, X-Ray powder structure and Rietveld refinement of γ-zirconium phosphate, Zr(PO 4)(H 2 PO 4)·2H 2 O, J. Chem. Soc., Dalt. Trans. (1995) 111–113. doi:10.1039/DT9950000111.

[243] A. Clearfield, G.D. Smith, Crystallography and structure of .alpha.-zirconium bis(monohydrogen orthophosphate) monohydrate, Inorg. Chem. 8 (1969) 431–436. doi:10.1021/ic50073a005.

[244] G. Alberti, P. Cardini-Galli, U. Costantino, E. Torracca, Crystalline insoluble salts of polybasic metals—I Ion-exchange properties of crystalline titanium phosphate, J. Inorg. Nucl. Chem. 29 (1967) 571–578. doi:10.1016/0022-1902(67)80063-0.

[245] A.N. Christensen, E.K. Andersen, I.G.K. Andersen, G. Alberti, M. Nielsen, M.S. Lehmann, T. Tokii, X-Ray Powder Diffraction Study of Layer Compounds. The Crystal Structure of alpha-Ti(HPO4)2.H2O and a Proposed Structure for gamma-Ti(H2PO4)(PO4)).2H2O ., Acta Chem. Scand. 44 (1990) 865–872. doi:10.3891/acta.chem.scand.44-0865.

[246] D.M. Poojary, A.I. Bortun, L.N. Bortun, A. Clearfield, Synthesis and X-Ray Powder Structures of Three Novel Titanium Phosphate Compounds, J. Solid State Chem. 132 (1997) 213–223. doi:10.1006/jssc.1997.7470.

[247] S. Ekambaram, C. Serre, G. Férey, S.C. Sevov, Hydrothermal Synthesis and Characterization of an Ethylenediamine-Templated Mixed-Valence Titanium Phosphate, Chem. Mater. 12 (2000) 444–449. doi:10.1021/cm990492i.

[248] S. Ekambaram, S.C. Sevov, Organically templated mixed-valent Ti(III)/Ti(IV) phosphate with an octahedral-tetrahedral open framework, Angew. Chemie - Int. Ed. 38 (1999) 372–375. doi:10.1002/(SICI)1521-3773(19990201)38:3<372::AID-ANIE372>3.0.CO;2-P.

[249] Y. Fu, Y. Liu, Z. Shi, Y. Zou, W. Pang, Hydrothermal Synthesis and Structural Characterization of Two New Three-Dimensional Oxyfluorinated Titanium PhosphatesTi4(HPO4)2(PO4)4F2·C4N2H12·H2O and Ti4(HPO4)2(PO4)4F2·C2N2H10·H2O, J. Solid State Chem. 162 (2001) 96–102. doi:10.1006/jssc.2001.9360.

[250] Y. Liu, Z. Shi, Y. Fu, W. Chen, B. Li, J. Hua, W. Liu, F. Deng, W. Pang, Hydrothermal Synthesis and Structural Characterizatino of Three Organically Templated Titanium Phosphates: Ti2(HPO4)2(PO4)2.C2N2H10, Ti3(H2PO4)(HPO4)3.5(PO4)2.C2N2H10, and

Ti7(HPO4)6(PO4)6.C3N2H12, Chem. Mater. 14 (2002) 1555–1563.

[251] C. Serre, F. Taulelle, G. Ferey, Rational design of porous titanophosphates, Chem. Commun. (2003) 2755. doi:10.1039/b304703b.

[252] K.-D. Kreuer, S.J. Paddison, E. Spohr, M. Schuster, Transport in Proton Conductors for Fuel-Cell Applications: Simulations, Elementary Reactions, and Phenomenology, Chem. Rev. 104 (2004) 4637–4678. doi:10.1021/cr020715f.

[253] W.L. Jorgensen, Monte carlo results for hydrogen bond distributions in liquid water11Quantum and statistical mechanical studies of liquids, 9. Part 8 ref. [6]., Chem. Phys. Lett. 70 (1980) 326–329. doi:10.1016/0009-2614(80)85344-9.

[254] J.D. Smith, Energetics of Hydrogen Bond Network Rearrangements in Liquid Water, Science (80-.). 306 (2004) 851–853. doi:10.1126/science.1102560.

[255] L.H. Lee, Fundamentals of Adhesion, Springer US, New York, 1991.

[256] T. Steinel, J.B. Asbury, J. Zheng, M.D. Fayer, Watching Hydrogen Bonds Break: A Transient Absorption Study of Water, J. Phys. Chem. A. 108 (2004) 10957–10964. doi:10.1021/jp046711r.

[257] V.P. Voloshin, Y.I. Naberukhin, Proper and improper hydrogen bonds in liquid water, J. Struct. Chem. 57 (2016) 497–506. doi:10.1134/S0022476616030112.

[258] K. Kreuer, On the complexity of proton conduction phenomena, Solid State Ionics. 136–137 (2000) 149–160. doi:10.1016/S0167-2738(00)00301-5.

[259] K.-D. Kreuer, A. Rabenau, W. Weppner, Vehicle Mechanism, A New Model for the Interpretation of the Conductivity of Fast Proton Conductors, Angew. Chemie Int. Ed. English. 21 (1982) 208–209. doi:10.1002/anie.198202082.

[260] C.J.T. de Grotthuss, Sur la Décomposition de l'Eau et des Corps qu'Elle Tient en Dissolution à l'Aide de l'Electricité Galvanique, Ann. Chim. Phys. 58 (1806) 54–74.

[261] T. Ueki, M. Watanabe, Macromolecules in Ionic Liquids: Progress, Challenges, and Opportunities, Macromolecules. 41 (2008) 3739–3749. doi:10.1021/ma800171k.

[262] T. Ogawa, T. Aonuma, T. Tamaki, H. Ohashi, H. Ushiyama, K. Yamashita, T. Yamaguchi, The proton conduction mechanism in a material consisting of packed acids, Chem. Sci. 5 (2014) 4878–4887. doi:10.1039/C4SC00952E.

[263] Y.-L.S. Tse, C. Knight, G.A. Voth, An analysis of hydrated proton diffusion in ab initio molecular dynamics, J. Chem. Phys. 142 (2015) 014104. doi:10.1063/1.4905077.

[264] M.E. Tuckerman, On the Quantum Nature of the Shared Proton in Hydrogen Bonds, Science (80-.). 275 (1997) 817–820. doi:10.1126/science.275.5301.817.

[265] N. Agmon, The Grotthuss mechanism, Chem. Phys. Lett. 244 (1995) 456–462. doi:10.1016/0009-2614(95)00905-J.

[266] O. Markovitch, H. Chen, S. Izvekov, F. Paesani, G.A. Voth, N. Agmon, Special pair dance and partner selection: Elementary steps in proton transport in liquid water, J. Phys. Chem. B. 112 (2008) 9456–9466. doi:10.1021/jp804018y.

[267] D. Marx, Proton transfer 200 years after Von Grotthuss: Insights from ab initio simulations, ChemPhysChem. 7 (2006) 1849–1870. doi:10.1002/cphc.200600128.

[268] W. Tatara, M.J. Wójcik, J. Lindgren, M. Probst, Theoretical Study of Structures, Energies, and Vibrational Spectra of the Imidazole−Imidazolium System, J. Phys. Chem. A. 107 (2003) 7827–7831. doi:10.1021/jp030065z.

[269] F. Toda, K. Tanaka, C. Foces-Foces, A.L. Llamas-Saiz, H. Limbach, F. Aguilar-Parrilla, R.M.

Claramunt, C. López, J. Elguero, Intermolecular proton transfer in host–guest crystals: the case of pyrazole included in 1,1-di(2,4-dimethylphenyl)but-2-yn-1-ol, an X-ray and solid-state 13 C/ 15 N NMR study, J. Chem. Soc., Chem. Commun. (1993) 1139–1142. doi:10.1039/C39930001139.

[270] L. Vilčiauskas, M.E. Tuckerman, G. Bester, S.J. Paddison, K.-D. Kreuer, The mechanism of proton conduction in phosphoric acid, Nat. Chem. 4 (2012) 461–466. doi:10.1038/nchem.1329.

[271] L. Vilciauskas, S.J. Paddison, K.-D. Kreuer, Ab Initio Modeling of Proton Transfer in Phosphoric Acid Clusters, J. Phys. Chem. A. 113 (2009) 9193–9201. doi:10.1021/jp903005r.

[272] K.D. Kreuer, Perovskite Oxide for Solid Oxide Fuel Cells, Springer US, Boston, MA, 2009. doi:10.1007/978-0-387-77708-5.

[273] D.B. Boman, D.C. Hoysall, D.G. Pahinkar, M.J. Ponkala, S. Garimella, Screening of working pairs for adsorption heat pumps based on thermodynamic and transport characteristics, Appl. Therm. Eng. 123 (2017) 422–434. doi:10.1016/j.applthermaleng.2017.04.153.

[274] L.F. Cabeza, A. Solé, C. Barreneche, Review on sorption materials and technologies for heat pumps and thermal energy storage, Renew. Energy. 110 (2017) 3–39. doi:10.1016/j.renene.2016.09.059.

[275] F. Meunier, Solid sorption heat powered cycles for cooling and heat pumping applications, Appl. Therm. Eng. 18 (1998) 715–729. doi:10.1016/S1359-4311(97)00122-1.

[276] H. Demir, M. Mobedi, S. Ülkü, A review on adsorption heat pump: Problems and solutions, Renew. Sustain. Energy Rev. 12 (2008) 2381–2403. doi:10.1016/j.rser.2007.06.005.

[277] F. Jeremias, D. Fröhlich, C. Janiak, S.K. Henninger, Water and methanol adsorption on MOFs for cycling heat transformation processes, New J. Chem. 38 (2014) 1846. doi:10.1039/c3nj01556d.

[278] M.F. De Lange, B.L. van Velzen, C.P. Ottevanger, K.J.F.M. Verouden, L.-C.C. Lin, T.J.H. Vlugt, J. Gascon, F. Kapteijn, Metal–Organic Frameworks in Adsorption-Driven Heat Pumps: The Potential of Alcohols as Working Fluids, Langmuir. 31 (2015) 12783–12796. doi:10.1021/acs.langmuir.5b03272.

[279] D. Saha, S. Deng, Ammonia adsorption and its effects on framework stability of MOF-5 and MOF-177, J. Colloid Interface Sci. 348 (2010) 615–620. doi:10.1016/j.jcis.2010.04.078.

[280] I. Spanopoulos, P. Xydias, C.D. Malliakas, P.N. Trikalitis, A Straight Forward Route for the Development of Metal–Organic Frameworks Functionalized with Aromatic −OH Groups: Synthesis, Characterization, and Gas (N 2 , Ar, H 2 , CO 2 , CH 4 , NH 3) Sorption Properties, Inorg. Chem. 52 (2013) 855–862. doi:10.1021/ic302010e.

[281] C. Petit, S. Wrabetz, T.J. Bandosz, Microcalorimetric insight into the analysis of the reactive adsorption of ammonia on Cu-MOF and its composite with graphite oxide, J. Mater. Chem. 22 (2012) 21443. doi:10.1039/c2jm34973f.

[282] D. Fröhlich, E. Pantatosaki, P.D. Kolokathis, K. Markey, H. Reinsch, M. Baumgartner, M.A. van der Veen, D.E. De Vos, N. Stock, G.K. Papadopoulos, S.K. Henninger, C. Janiak, Water adsorption behaviour of CAU-10-H: a thorough investigation of its structure–property relationships, J. Mater. Chem. A. 4 (2016) 11859–11869. doi:10.1039/C6TA01757F.

[283] Y.I. Aristov, Challenging offers of material science for adsorption heat transformation: A review, Appl. Therm. Eng. 50 (2013) 1610–1618. doi:10.1016/j.applthermaleng.2011.09.003.

[284] F. Jeremias, A. Khutia, S.K. Henninger, C. Janiak, MIL-100(Al, Fe) as water adsorbents for heat transformation purposes—a promising application, J. Mater. Chem. 22 (2012) 10148–10151. doi:10.1039/C2JM15615F.

[285] L.W. Wang, R.Z. Wang, R.G. Oliveira, A review on adsorption working pairs for refrigeration, Renew. Sustain. Energy Rev. 13 (2009) 518–534. doi:10.1016/j.rser.2007.12.002.

[286] Y. Tashiro, M. Kubo, Y. Katsumi, T. Meguro, K. Komeya, Assessment of adsorption-desorption

characteristics of adsorbents for adsorptive desiccant cooling system, J. Mater. Sci. 39 (2004) 1315–1319. doi:10.1023/B:JMSC.0000013937.11959.6a.

[287] P. Payra, P.K. Dutta, R. Singh, R.F. Lobo, C.R.A. Catlow, D.S. Coombes, D.W. Lewis, J.C.G. Pereira, B. Slater, B. Subotic, J. Bronic, C.P. Grey, L. Kevan, O. Terasaki, T. Ohsuna, B. Smit, R. Krishna, J. Karger, S. Vasenkov, S.M. Auerbach, C. Li, Z. Wu, J. Sivaguni, J. Shallaja, V. Ramamurthy, K.B. Yoon, A. Walcarius, X. Rozanska, R.A. Santen, J.F. Haw, D.M. Marcus, S. Nalr, M. Tsapatsis, K. Hoffman, F. Marlow, M. Iwamoto, H. Yahiro, J. Izumi, H.S. Sherry, S. Sircar, A.L. Myers, K. Pavelic, M. Hadzija, Handbook of Zeolite Science and Technology, Marcel Dekker, Inc., New York, 2003. doi:10.1016/S1351-4180(04)00164-3.

[288] T.F. Degnan, Jr., Applications of zeolites in petroleum refing, Top. Catal. 13 (2000) 349–356. doi:10.1023/A:1009054905137.

[289] Z. Tamainot-Telto, S.J.J. Metcalf, R.E.E. Critoph, Y. Zhong, R. Thorpe, Carbon–ammonia pairs for adsorption refrigeration applications: ice making, air conditioning and heat pumping, Int. J. Refrig. 32 (2009) 1212–1229. doi:10.1016/j.ijrefrig.2009.01.008.

[290] R.Z. Wang, J.P. Jia, Y.H. Zhu, Y. Teng, J.Y. Wu, J. Cheng, Q.B. Wang, Study on a New Solid Absorption Refrigeration Pair: Active Carbon Fiber—Methanol, J. Sol. Energy Eng. 119 (1997) 214. doi:10.1115/1.2888021.

[291] Y. Hamamoto, K.C.A. Alam, B.B. Saha, S. Koyama, A. Akisawa, T. Kashiwagi, Study on adsorption refrigeration cycle utilizing activated carbon fibers. Part 1. Adsorption characteristics, Int. J. Refrig. 29 (2006) 305–314. doi:10.1016/j.ijrefrig.2005.04.008.

[292] I.I. El-Sharkawy, K. Kuwahara, B.B. Saha, S. Koyama, K.C. Ng, Experimental investigation of activated carbon fibers/ethanol pairs for adsorption cooling system application, Appl. Therm. Eng. 26 (2006) 859–865. doi:10.1016/j.applthermaleng.2005.10.010.

[293] I.I. El-Sharkawy, B.B. Saha, S. Koyama, J. He, K.C. Ng, C. Yap, Experimental investigation on activated carbon–ethanol pair for solar powered adsorption cooling applications, Int. J. Refrig. 31 (2008) 1407–1413. doi:10.1016/j.ijrefrig.2008.03.012.

[294] H. Reinsch, M.A. van der Veen, B. Gil, B. Marszalek, T. Verbiest, D. de Vos, N. Stock, Structures, Sorption Characteristics, and Nonlinear Optical Properties of a New Series of Highly Stable Aluminum MOFs, Chem. Mater. 25 (2013) 17–26. doi:10.1021/cm3025445.

[295] D. Fröhlich, S.K. Henninger, C. Janiak, Multicycle water vapour stability of microporous breathing MOF aluminium isophthalate CAU-10-H, Dalt. Trans. 43 (2014) 15300–15304. doi:10.1039/C4DT02264E.

[296] A. Cadiau, J.S. Lee, D. Damasceno Borges, P. Fabry, T. Devic, M.T. Wharmby, C. Martineau, D. Foucher, F. Taulelle, C.-H. Jun, Y.K. Hwang, N. Stock, M.F. De Lange, F. Kapteijn, J. Gascon, G. Maurin, J.-S. Chang, C. Serre, Design of Hydrophilic Metal Organic Framework Water Adsorbents for Heat Reallocation, Adv. Mater. 27 (2015) 4775–4780. doi:10.1002/adma.201502418.

[297] B. Bozbiyik, T. Van Assche, J. Lannoeye, D.E. De Vos, G. V. Baron, J.F.M. Denayer, Stepped water isotherm and breakthrough curves on aluminium fumarate metal–organic framework: experimental and modelling study, Adsorption. 23 (2017) 185–192. doi:10.1007/s10450-016-9847-0.

[298] E. Elsayed, R. AL-Dadah, S. Mahmoud, A. Elsayed, P.A. Anderson, Aluminium fumarate and CPO-27(Ni) MOFs: Characterization and thermodynamic analysis for adsorption heat pump applications, Appl. Therm. Eng. 99 (2016) 802–812. doi:10.1016/j.applthermaleng.2016.01.129.

[299] E. Alvarez, N. Guillou, C. Martineau, B. Bueken, B. Van de Voorde, C. Le Guillouzer, P. Fabry, F. Nouar, F. Taulelle, D. de Vos, J.-S. Chang, K.H. Cho, N. Ramsahye, T. Devic, M. Daturi, G. Maurin, C. Serre, The Structure of the Aluminum Fumarate Metal-Organic Framework A520, Angew. Chemie Int. Ed. 54 (2015) 3664–3668. doi:10.1002/anie.201410459.

[300] T. Loiseau, C. Serre, C. Huguenard, G. Fink, F. Taulelle, M. Henry, T. Bataille, G. Férey, A Rationale for the Large Breathing of the Porous Aluminum Terephthalate (MIL-53) Upon Hydration, Chem. - A Eur. J. 10 (2004) 1373–1382. doi:10.1002/chem.200305413.

[301] F. Jeremias, D. Fröhlich, C. Janiak, S.K. Henninger, Advancement of sorption-based heat transformation by a metal coating of highly-stable, hydrophilic aluminium fumarate MOF, RSC Adv. 4 (2014) 24073–24082. doi:10.1039/C4RA03794D.

[302] B. Saccoccia, A.M. Bohnsack, N.W. Waggoner, K.H. Cho, J.S. Lee, D.Y. Hong, V.M. Lynch, J.S. Chang, S.M. Humphrey, Separation of P-Divinylbenzene by selective room-temperature adsorption inside Mg-CUK-1 prepared by aqueous microwave synthesis, Angew. Chemie - Int. Ed. 54 (2015) 5394–5398. doi:10.1002/anie.201411862.

[303] S. Wang, J.S. Lee, M. Wahiduzzaman, J. Park, M. Muschi, C. Martineau-Corcos, A. Tissot, K.H. Cho, J. Marrot, W. Shepard, G. Maurin, J. Chang, C. Serre, A robust large-pore zirconium carboxylate metal–organic framework for energy-efficient water-sorption-driven refrigeration, Nat. Energy. (2018) 1–10. doi:10.1038/s41560-018-0261-6.

[304] M. Dan-Hardi, C. Serre, T. Frot, L. Rozes, G. Maurin, C. Sanchez, G. Férey, A New Photoactive Crystalline Highly Porous Titanium(IV) Dicarboxylate, J. Am. Chem. Soc. 131 (2009) 10857–10859. doi:10.1021/ja903726m.

[305] M. Sohail, Y.-N. Yun, E. Lee, S.K. Kim, K. Cho, J.-N. Kim, T.W. Kim, J.-H. Moon, H. Kim, Synthesis of Highly Crystalline NH 2 -MIL-125 (Ti) with S-Shaped Water Isotherms for Adsorption Heat Transformation, Cryst. Growth Des. 17 (2017) 1208–1213. doi:10.1021/acs.cgd.6b01597.

[306] F. Jeremias, V. Lozan, S.K. Henninger, C. Janiak, Programming MOFs for water sorption: amino-functionalized MIL-125 and UiO-66 for heat transformation and heat storage applications, Dalt. Trans. 42 (2013) 15967. doi:10.1039/c3dt51471d.

[307] P.L. Llewellyn, S. Bourrelly, C. Serre, A. Vimont, M. Daturi, L. Hamon, G. De Weireld, J. Chang, D. Hong, Y. Kyu Hwang, S. Hwa Jhung, G. Férey, High Uptakes of CO 2 and CH 4 in Mesoporous Metal□Organic Frameworks MIL-100 and MIL-101, Langmuir. 24 (2008) 7245–7250. doi:10.1021/la800227x.

[308] P. Horcajada, S. Surblé, C. Serre, D.-Y. Hong, Y.-K. Seo, J.-S. Chang, J.-M. Grenèche, I. Margiolaki, G. Férey, Synthesis and catalytic properties of MIL-100(Fe), an iron(III) carboxylate with large pores, Chem. Commun. 100 (2007) 2820–2822. doi:10.1039/B704325B.

[309] A. Vimont, J.-M. Goupil, J.-C. Lavalley, M. Daturi, S. Surblé, C. Serre, F. Millange, G. Férey, N. Audebrand, Investigation of Acid Sites in a Zeotypic Giant Pores Chromium(III) Carboxylate, J. Am. Chem. Soc. 128 (2006) 3218–3227. doi:10.1021/ja056906s.

[310] H. Furukawa, F. Gándara, Y.-B. Zhang, J. Jiang, W.L. Queen, M.R. Hudson, O.M. Yaghi, Water Adsorption in Porous Metal–Organic Frameworks and Related Materials, J. Am. Chem. Soc. 136 (2014) 4369–4381. doi:10.1021/ja500330a.

[311] J. Choi, L.-C. Lin, J.C. Grossman, Role of Structural Defects in the Water Adsorption Properties of MOF-801, J. Phys. Chem. C. 122 (2018) 5545–5552. doi:10.1021/acs.jpcc.8b00014.

[312] D. Damasceno Borges, P. Normand, A. Permiakova, R. Babarao, N. Heymans, D.S. Galvao, C. Serre, G. De Weireld, G. Maurin, Gas Adsorption and Separation by the Al-Based Metal–Organic Framework MIL-160, J. Phys. Chem. C. 121 (2017) 26822–26832. doi:10.1021/acs.jpcc.7b08856.

[313] J.S. Lee, J.W. Yoon, P.G.M. Mileo, K.H. Cho, J. Park, G. Maurin, H. Kim, S.M. Humphrey, M.F. de Lange, F. Kapteijn, J.-S. Chang, The porous metal-organic framework CUK-1 for heat allocation: toward green applications of natural refrigerant water, J. Mater. Chem. A. (2018).

[314] L.G. Gordeeva, M. V. Solovyeva, Y.I. Aristov, NH2 -MIL-125 as a promising material for adsorptive heat transformation and storage, Energy. 100 (2016) 18–24. doi:10.1016/j.energy.2016.01.034.

[315] A.A. Askalany, M. Salem, I.M. Ismael, A.H.H. Ali, M.G. Morsy, B.B. Saha, An overview on adsorption pairs for cooling, Renew. Sustain. Energy Rev. 19 (2013) 565–572. doi:10.1016/j.rser.2012.11.037.

CHAPTER 2

Classical and quantum-based Molecular simulations

Introduction

This chapter is written with the objective of presenting the main molecular simulation techniques that have been employed throughout my PhD to model the water adsorption and the proton migration in MOFs. I made the choice to introduce briefly the fundamental theory behind each major computational method aided by a minimal number of mathematical equations with the aim to provide just enough information to explain the computational strategy applied along the manuscript. The readers are referred to specialized books and review articles provided in each section to get more technical details.

The chapter is thus divided into three parts. The first one, named Classical Molecular Mechanics, presents the theoretical aspects of classical molecular simulations including Monte Carlo and Molecular Dynamics as well as the inputs required, i.e. microscopic models for both the MOF frameworks and the water, and the interatomic potentials (also called force field along the manuscript) to describe the MOF framework/water interactions. The second part focuses on the description of the main aspects involved in quantum calculations with a substantial stress on the Density Functional Theory method. The third part is finally dedicated to *Ab Initio* Molecular Dynamics, which was highly relevant in this work to model the proton dynamics.

I. Classical Molecular Mechanics

I.1. Statistical Mechanics-Ensembles

The description of the energetics states of matter is defined at the macroscopic scale by the laws of the thermodynamics. Elegantly, concepts such as heat and entropy are linked to measurable quantities such as pressure, volume, temperature and amount of particles without any reference to the description of the microscopic information of matter. The statistical mechanics complements the classical thermodynamics by giving a phenomenological background and bridging the macroscopic properties of a system to its microscopic constituents and their resulting interactions.

As a matter of fact, the number of particles present in a system is so huge, i.e. > 10^{23}, that the description of the macroscopic properties of a system via the microscopic characteristics of each particle seems very unlikely. Fortunately, most of the macroscopic observables of a system are not sensitive to microscopic details and therefore the properties of the system can be collectively derived. The collection of possible states of a system, considered all at once, which lead to a common set of macroscopic properties forms what we call an ensemble.

According to the statistical mechanics theory, it is possible to link each macroscopic property *A* to a microscopic function *a* that depends on the coordinates of each particle r in a similar way as for instance the temperature which is directly related to the average kinetic energy of the particles. In this sense, for an ensemble of N particles, a macroscopic property A can be calculated by an averaging procedure [1]:

$$A = \sum_i^N p_i a(r_i) = \langle a \rangle. \tag{2.1}$$

Where p_i is the probability of a given state $a(\boldsymbol{r}_i)$ with respect to the other states.

The classical laws of thermodynamics establish that a given system is defined when three of its fundamental variables (number of particles, energy, temperature, volume and chemical potential) are known since they are all linked by the fundamental equations of the thermodynamics expressed by Equation 2.2:

$$dS = \frac{1}{T}dE + \frac{P}{T}dV - \frac{\mu}{T}dN. \quad (2.2)$$

Where S is the entropy of the system, E its internal energy and μ its chemical potential. By analogy, the ensembles are also entirely defined by three among five fundamental variables: number of particles, energy, temperature, volume and chemical potential. Many ensembles can be envisaged by fixing three of these variables. Here, the main characteristics of the three most common ensembles, i.e. the microcanonical, canonical and grand canonical ensembles will be summarized.

Considering an ensemble with non-degenerated energy levels (N_U) denoted by Ω, each of these energetic levels shows a possible number of arrangements, $\omega(N_U)$. The total number of possible arrangements can be calculated using Equation 2.3:

$$\omega(N_E) = \frac{\omega(N_E^*)}{\Omega} = \frac{N!}{\prod_E N_E!} \quad (2.3)$$

where $\omega(N_E^*)$ is the most probable of these arrangements, which corresponds to the one with the largest number of states, N_U^* [2].

In the case of a closed system, i.e. a system which does not exchange neither matter nor energy, the number of particles, energy and volume are kept constant. Such a (NVE) ensemble is called as ***microcanonical ensemble***. In such a system, the internal energy can be obtained by summing the energy of the individual energy states $E = E_1 + E_2 + \ldots + E_N$. On the other hand, as shown by Equation 2.3 the total number of non-degenerated energy levels is expressed as a product. In order to treat additively the contributions of these levels, one shall consider the logarithm of Ω as follows:

$$ln\Omega(\mathrm{E}) = \ln\Omega_1(E_1) + ln\Omega_2(E_2) + \cdots + ln\Omega_N(E_N) \quad (2.4)$$

$$ln\Omega = lnN! - ln\prod_E N_E! = -N\sum_E \frac{N_E}{N} ln\frac{N_E}{N} = -N\sum_E P_E lnP_E \quad (2.5)$$

Since the redistribution of states over the particles is spontaneous, according to the second law of thermodynamics, the entropy, which is an extensive thermodynamic variable, should increase until thermodynamic equilibrium is reached. Boltzmann and Planck

established a relation between the number of degenerated states of a system and the entropy [2,3]. The so-obtained relation corresponds to the Boltzmann equation defined by Equation 2.6:

$$S(N,V,E) = k_B ln\Omega(\mathrm{N,V,E}). \tag{2.6}$$

Where k_B is the Boltzmann's constant whose value is 1.3806505(24) × 10^{-23} J.K^{-1}.

One basic assumption of the statistical mechanics applied to the microcanonical ensemble implies that all degenerated energy states of a system are equally probable, however the number of states that corresponds to a given distribution of energy depends strongly on the energy [2]. To find the most likely configuration (where $ln\Omega$ is maximized), the left hand side of Equation 2.4 is derived with respect to the energy (Equation 2.7). This expression corresponds to the definition of the thermodynamic beta (β) known as coldness, a fundamental thermodynamic quantity.

$$\beta(N,V,E)|_{equilibrium} = \left(\frac{\partial ln\Omega(\mathrm{E})}{\partial E}\right)_{N,V,E} = 0. \tag{2.7}$$

The incorporation of the partial derivative of the entropy with respect to the internal energy in Equation 2.2 allows the derivation of a relation between the variation of the number of non-degenerated states with the internal energy and the temperature in Equation 2.8:

$$\left(\frac{\partial S}{\partial E}\right)_{V,N} = \frac{1}{T} = k_B\beta \quad \rightarrow \quad \beta = \frac{1}{k_B T} \tag{2.8}$$

We can then define the ***canonical ensemble***. In this ensemble, the volume, temperature and number of particles are maintained fixed. Only the energy transfer is allowed between the system and its external environment. Considering a system (denoted as A) where the energy is allowed to be exchanged with a heat bath (denoted as B), the total energy is the sum of the energies of A and B. If the system A is set in one specific energy state U_i, the probability p_i to find the system A in state i at a temperature T is given by the Boltzmann distribution:

$$p_i = \frac{exp\left(-{}^{E_i}/_{k_B T}\right)}{\sum_i exp\left(-{}^{E_i}/_{k_B T}\right)} = \frac{exp\left(-{}^{E_i}/_{k_B T}\right)}{Q} \tag{2.9}$$

Where the term $Q = Q(N,V,T)$ is a normalization constant called canonical partition function, given by the sum over all the possible i states of the system A in the ensemble.

Coupling the Helmholtz free energy (F) definition ($F = E - TS$) with Equation 2.6, it is possible to derive Equation 2.10 for a system at constant temperature.

$$F = -k_B T lnQ \tag{2.10}$$

As shown below in Equation 2.11, the Helmholtz free energy is a characteristic state function of T, V and N, the same variables that are fixed in the canonical ensemble. Therefore, the Helmholtz free energy and consequently the partition function is the starting point for the complete treatment of the system.

$$dF = -SdT - PdV + \mu dN \tag{2.11}$$

The ***Grand Canonical ensemble*** refers to an expanded canonical system where not only the energy but also the number and nature of particles are allowed to be exchanged. In this case, the temperature T, the volume V and the chemical potential μ are fixed. The probability to find the system in a state i is given by Equation 2.12:

$$p_i = \frac{\exp(\beta(N_i\mu - E_i))}{Q'} = \frac{\exp(\beta(N_i\mu - E_i))}{\sum_i \exp(\beta(N_i\mu - E_i))}. \tag{2.12}$$

where Q' is the grand canonical partition function.

By analogy with the canonical ensemble, which considers the Helmholtz free energy related to the partition function, in the grand canonical ensemble the partition function is related to the grand potential (Φ_G), a function defined by Equation 2.13:

$$\Phi_G = -PV = F - \mu N. \tag{2.13}$$

By differentiating this function and combining it with Equation 2.11, it is possible to stress that the grand potential is a thermodynamic function of the variables μ, V and T (Equation 2.14).

$$d\Phi_G = dF - Nd\mu - \mu dN = -SdT - PdV - \langle N \rangle d\mu \tag{2.14}$$

Additionally, the fundamental relation of this grand canonical ensemble is given by Equation 2.15:

$$\Phi_G = -PV = -k_B lnQ' \tag{2.15}$$

As it can be seen from Equations 2.2 and 2.6 in the microcanonical ensemble, Equations 2.9 and 2.10 in the canonical ensemble, and Equations 2.12 and 2.15 in the grand canonical ensemble, the thermodynamic variables of each ensemble can be evaluated as partial derivatives of the entropy, the Helmholtz free energy and the grand potential respectively. Since each of these functions are defined from a microscopic perspective by means of their respective partition functions, it is then possible to characterize the macroscopic properties of each system by averaging their microscopic properties.

In general, the partition function of any ensemble can be expressed as an integral of the appropriate Hamiltonian of the ensemble over the coordinates and momenta of its constituent particles (Equation 2.16).

$$Q = \frac{1}{h^{3N}N!} \int dp^N dr^N \exp\left[-\beta\, \hat{H}\,(\boldsymbol{p}^N, \boldsymbol{r}^N)\right] \tag{2.16}$$

The thermodynamic observable $\langle A \rangle$ can be then obtained by Equation 2.17.

$$\langle A \rangle = \frac{\int dp^N dr^N A(\boldsymbol{p}^N, \boldsymbol{r}^N) exp\left[-\beta\, \hat{H}\,(\boldsymbol{p}^N, \boldsymbol{r}^N)\right]}{\int dp^N dr^N exp\left[-\beta\, \hat{H}\,(\boldsymbol{p}^N, \boldsymbol{r}^N)\right]} \tag{2.17}$$

The properties measured in a static manner through averages in the configurational space, are in real experiments evaluated by averages over time corresponding to the evolution of the system considered at thermodynamic equilibrium. The ergodic principle states that, for

a sufficiently long time, the time averaging (Equation 2.18) matches the configurational averaging described above.

$$\langle A \rangle = \lim_{t\to\infty} \int_0^t dt' A(r,t') \tag{2.18}$$

In the following sections, the implementation of this theoretical background in a computational perspective will be introduced with a brief explanation of the classical molecular simulation techniques employed in this thesis, i.e. Monte Carlo and Molecular Dynamics.

I.2. Monte Carlo Simulations

I.2.1. General aspects

In the previous section, Equation 2.17 was defined for an observable in a generic ensemble. Such an observable would require the evaluation of the function $A(\boldsymbol{p}^N,\boldsymbol{r}^N)$ for the total number of particles of the system by means of numerical quadrature. However, such a strategy is both impracticable and not enough accurate. Typically, for a system containing 100 particles and 5 mesh points it would require the evaluation of the integrand of 10^{210} points. In such conditions, besides the requirement of a huge computational effort, the large number of points to be averaged would result in high statistical errors. In light of these arguments, it becomes clear that the use of a sampling scheme such as the Monte Carlo method to evaluate the partition function (Equation 2.17) is required. However, a simple sampling scheme cannot be used to sample multidimensional integrals over the configurational space [4]. Fortunately, a careful look of Equation 2.17 reveals that the observable is not only an integral but a ratio of integrals.

There is a crucial need to select a reasonable number of representative points large enough to ensure an optimal exploration of the system thus allowing an accurate evaluation of the statistical average. This set of points, also called configuration, is described by a Maxwell Boltzmann distribution that is generated by the Metropolis method. Starting with an initial configuration randomly generated, the MC simulations consist of several millions of random trials/moves that allow an efficient sampling of the selected ensemble. The

corresponding random trials are accepted or rejected with appropriate criteria. These criteria are based on the Metropolis algorithm mentioned below at the core of the MC simulations.

Starting with an initial configuration denoted o (o for old) of the system $\boldsymbol{r}^N$ with a Boltzmann density probability of $\eta(o)$, the probability to move towards a new configuration with a Boltzmann density probability of $\eta(n)$ (n for new) is defined by $\pi(o \rightarrow n)$. In order to not perturb the equilibrium, the average number of accepted moves from o to n must be the same as the reverse. This is stated by the so-called balance equation (Equation 2.19):

$$\eta(o) \times \pi(o \rightarrow n) = \eta(n) \times \pi(n \rightarrow o). \tag{2.19}$$

The probability $\pi(o \rightarrow n)$ can be expressed as the probability of selecting the new configuration n , i.e. $\alpha(o \rightarrow n)$, multiplied by the probability of accepting it, acc(o → n).

$$\pi(o \rightarrow n) = \alpha(o \rightarrow n) \times acc(o \rightarrow n) \tag{2.20}$$

Considering a symmetric probability of selection from o to n and vice-versa in a NVE ensemble, Equation 2.19 turns to Equation 2.21:

$$\frac{acc(o \rightarrow n)}{acc(n \rightarrow o)} = \frac{\eta(n)}{\eta(o)} = exp[-\beta(U(n) - U(o))] \tag{2.21}$$

Where the potential energies $U(n)$ and $U(o)$ are calculated using predefined potential expressions.

The following o → n move is thus accepted with the following probability as defined by the Metropolis algorithm (Equation 2.22)

$$acc(o \rightarrow n) = \min\left(1, {\eta(n)}/{\eta(o)}\right) = \min(1, exp[-\beta\Delta U]). \tag{2.22}$$

The trial move is then accepted if the energy of the new configuration is lower than that of the old one. If this is not the case, the Boltzmann factor ($\exp(-\beta\Delta U)$) is calculated and a random number (*Ranf*) is generated in the interval [0,1]. If *Ranf* is higher than

$\exp(-\beta\Delta U)$, the new configuration is accepted, otherwise it is rejected and another trial move is attempted. This process continues for a certain number of steps (several millions) in order to generate an ensemble of configurations that obey to the Boltzmann statistical rule. Acceptance rates for each possible trial have to be judiciously adjusted in order to approach the equilibrium in a most efficient way. Usually, the acceptance rate is fixed to be about 40-50%. For accurate statistical results, the steps performed prior to equilibration have to be excluded in the analysis and the averages of interest be calculated over several millions of configurations.

In the typical MC simulations we used to explore our guest/host systems, the molecules of a given system are subjected to specific moves/trials in order to effectively sample the energy landscape of the ensemble. The most standard MC trials are thus the translation, rotation, insertion/deletion, partial/full regrow and identity change (in the case of a mixture of molecules).

The translation move is characterized by the displacement of the center of mass of a molecule by a random factor such as that:

$$\boldsymbol{r}(n) = \boldsymbol{r}(o) + \Delta r(Ranf - 0.5). \tag{2.23}$$

where Δr is the maximum displacement allowed. This parameter must be wisely chosen since for small displacements, the movement is more likely to be accepted however a larger number of steps is required for an efficient sampling of the phase space. In contrast for too large Δr values, the majority of the trial moves will be rejected. The Δr values are selected in such a way to respect the 40-50% probability acceptance of the trial moves however the most important parameter to take into consideration is the effective sampling of the configurational space [4].

The rotation move is considered for molecules with more than one interaction center and consists of assigning linear rotation transformations in the position vector with the rotation of one of the matrixes R_X, R_Y and R_Z such as its coordinates are rotated by an angle of $\Delta\theta$ along the x, y or z axis. For instance, for a rotation along the x axis, the rotational move can be expressed as Equation 2.24:

$$\boldsymbol{r}(n) = R_X.\boldsymbol{r}(o) = \begin{bmatrix} 1 & 0 & 0 \\ 0 & cos\Delta\theta & -sin\Delta\theta \\ 0 & sin\Delta\theta & cos\Delta\theta \end{bmatrix}.\boldsymbol{r}(o) \tag{2.24}$$

Again the choice of $\Delta\theta$ must be judicious in order to favor an adequate sampling.

The insertion trial which corresponds to the creation of a molecule placed in a random position and orientation also follows a Metropolis scheme. The acceptance probability of the new configuration is then given by Equation 2.25:

$$acc(o \rightarrow n) = \min\left(1, \frac{\beta f V}{N+1}\exp(-\beta\Delta U)\right) \tag{2.25}$$

Where f is the fugacity of the molecule, V is the volume of the simulation box.

The insertion trial may also be achieved with the Configurational-Bias Monte Carlo (CBMC) algorithm [5] when the standard Metropolis algorithm fails. This is for instance the case for molecules of large size to be incorporated in a relatively small porosity. First, the molecules are segmented in pre-defined beads. The first bead is then randomly inserted according to the Metropolis acceptance rule for an insertion move and the rest of molecule is then constructed by insertion trial moves obeying pre-defined intramolecular interactions. The construction of chain molecules according to their bonded potential is what attributes the "biased" factor in the CBMC algorithm.

The deletion trials are usually implemented with the random removal of a given molecule in a Metropolis scheme whose acceptance probability is given by Equation 2.26.

$$acc(o \rightarrow n) = \min\left(1, \frac{\beta f V}{N+1}\exp(-\beta\Delta U)\right) \tag{2.26}$$

In the regrowth move trial, similarly to the CBMC move, the molecules are discretized in beads and have these beads reorganized according to their intramolecular interactions. This reorganization can be done either by the removal of the molecule followed by their insertion with their beads randomly positioned (full regrowth) or the partial removal of some of the beads followed by their regrowth (partial regrowth).

The identity change is another trial implemented in the case of mixture of two or more molecules and this corresponds to a swap of molecules. The acceptance probability in a system of two molecules A and B is given by Equation 2.27:

$$P = \min\left\{1, \frac{f_B N_A}{f_A(N_B+1)} \exp(-\beta \Delta U)\right\} \tag{2.27}$$

Other trials can be also considered in MC simulations, some of them to calculate specific properties, such as the Widom insertion move [6], and some others to introduce biased potentials in order to map the configurational space of systems that present rare low-energy configurations such as in dense liquids or solids or macromolecular or polymeric systems [7,8].

I.2.2. Illustrations for the adsorption description in porous solids

MC simulations in the grand canonical ensemble, currently labeled as GCMC simulations, are frequently employed to assess the adsorption isotherms of a series of gases in a given porous solid once a thoughtful choice of the interacting potentials and microscopic models for both the adsorbent and the adsorbate (see sections I.4, I.5 and I.6) has been made. A comparison between the calculated total amount of adsorbed molecules and the corresponding experimental data needs to be carried out with caution. First, because in the simulations the porous material is assumed to be ideally activated, which is not always true from an experimental standpoint [9]. Moreover, during the simulation all the phase space of a unit cell is taken as available to be assessed even if the porosity is restricted by small windows or blocking molecules. To address this situation, it is usual to restrain the access of the adsorbate to parts of the porosity upon a blocking procedure.

Another important property calculated by GCMC calculations is the enthalpy of adsorption (ΔH_{ads}), commonly evaluated from the fluctuation of the number of molecules in the system and the potential energy U, as in Equation 2.28 [10]. The adsorption enthalpy may also be decoupled into adsorbate-adsorbate and adsorbent-adsorbate contributions, allowing to attribute the contributions of the surface-fluid and fluid-fluid interactions as a function of loading.

$$\Delta H_{ads} = RT - \frac{\langle U.N\rangle - \langle U\rangle\langle N\rangle}{\langle N^2\rangle - \langle N\rangle^2} \quad (2.28)$$

This method of calculation of the adsorption enthalpy assumes an ideal behavior of the gas phase and is dependent of a considerably large number of steps in order to achieve reliable results to this variable, especially at low coverage. The use of the mentioned Widom's insertion move applied in the canonical ensemble [6], a more recent and accurate strategy to obtain the heat of adsorption, allow to circumvent this limitation. The simulated adsorption enthalpy profile is then comparable with the experimental adsorption enthalpy profiles issued from microcalorimetry measurements performed in a wide range of pressures.

Beyond the prediction of the adsorption isotherms and enthalpies, MC simulations are valuable to gain insight on the microscopic mechanism involved and complement different types of experimental *in situ* measurements including infra-red spectroscopy and X-ray/neutron diffraction [11–13]. This analysis at the microscopic level is usually only assumed to be reliable when a reasonable agreement between simulated and experimental macroscopic properties (isotherms, enthalpies, etc.) is achieved. Such microscopic analysis is carried out using a collection of strategies such as (i) careful analysis of snapshots, (ii) construction of 2D density probability plots, and (iii) analysis of radial distribution functions (RDFs) between atom pairs of interest.

I.3. Molecular Dynamics simulations

I.3.1. Basic Principles

As mentioned in the section I.1, the ergodic principle states that the observables determined from the sampling and averaging of the configurational phase space in different ensembles can also be obtained by averaging over time with the implementation of molecular dynamics (MD) simulations. In this case, the MD simulations compute the evolution of the particles of a given system over time according to the classical Newton's equations of motion. As the observables are not averaged along a configurational space, different relations between the microscopic and macroscopic domains other than the partition functions must be applied in MD. One widespread consideration in classical many-body systems states for

instance that the temperature can be calculated from the definition of the equipartition principle [4]:

$$T(t) = \sum_{i=1}^{N} \frac{m_i v_i^2(t)}{k_B N_f} \tag{2.29}$$

Where N_f is the number of degrees of freedom ($N_f = N - 3$) for a tridimensional system with N particles with fixed total momentum, and m_i and v_i are respectively the mass and velocity of a particle i.

In a MD simulation, each atom of the system is randomly assigned to an initial velocity following most currently a Boltzmann distribution. The determination of the force acting on each atom is obtained by the gradient of the potential acting to each atom (Equation 2.30).

$$\boldsymbol{f}(\boldsymbol{r}) = -\nabla U(\boldsymbol{r}) \tag{2.30}$$

Once the forces are derived, they are integrated in the Newton's equations numerically over short-time steps via appropriate algorithms in order to generate the time-dependent trajectory of the system, a sequence of atomic positions with respect to time. Different integration algorithms exist, such as the Verlet [14,15], Leap Frog [16] and Beeman algorithms [17,18]. We used in this work the velocity Verlet algorithm [19] which integrates at the same time the positions and the velocities of the atoms based in Taylor expansions, as defined in Equations 2.31 and 2.32.

$$\boldsymbol{v}(t + \Delta t) \approx \boldsymbol{v}(t) + \frac{\boldsymbol{f}(t+\Delta t) + \boldsymbol{f}(t)}{2m} \Delta t + O(\Delta t^2) \tag{2.31}$$

$$\boldsymbol{r}(t + \Delta t) \approx 2\boldsymbol{r}(t) - r(t - \Delta t) + \frac{\boldsymbol{f}(t)}{m} \Delta t^2 + O(\Delta t^4) \tag{2.32}$$

The use of Taylor expansions in the integration of the equations of motion introduces invariably an associated error. As seen in the two previous equations, such an error is more important in the calculation of the velocities (error of Δt^2 order) than for the calculation of the positions (error of Δt^4 order). Since in Equation 2.32 the positions are calculated

independently from the velocity, the higher errors are then assigned to the calculation of the kinetic energy, directly obtained from the velocity [4].

The application of Verlet-like algorithms is straightforward for systems consisting of single-atoms (e.g. argon gas), however for molecules Eq. 2.31 and 2.32 are applied to their center of mass (COM), while their rotation around the COM are calculated considering the total torque exerted by the mutual interacting potential with the other molecules [20]. For more complex molecules which present bonded constraints, the positions of every constituting atom must be individually updated. In order to avoid bond breaking during this process, the positions of each atom are recalculated and corrected according to their intramolecular potentials. The most used algorithms to perform such corrections are the SHAKE [21] and RATTLE [22] algorithms.

As aforementioned, the Verlet algorithm although very precise and time reversible, is still derived from Taylor expansions and shows associated errors that depend of the timestep used. This means that (i) small timestep should be employed in order to avoid energy drifts in the system and (ii) for long times the trajectory of the particles may vary substantially from a real trajectory.

It is important to state that, similarly to MC calculations, the configurations in a MD simulation must be initially equilibrated and only after this initial stage, the averaging of the properties must be proceeded. In order to make the relaxation of the system easier and to minimize any numerical artifacts coming from injudicious initial configurations, it is common to employ velocity rescaling strategies [23] during the equilibration time. One way to circumvent a long equilibration stage is to use as an input a MC equilibrated configuration.

The particles in a standard MD simulation are treated as closed system with no external exchanges of energy or mass *i.e.* as a microcanonical ensemble. On the other hand, in a realistic perspective, considering a fixed number of particles, a given system is more likely to be found under isothermal (i.e. a NVT ensemble) or isobaric (i.e. a NPT ensemble) conditions. Different numerical strategies are applied to account for the external energies exchanges that allow a system to be either isothermal or isobaric. These numerical strategies

are respectively called thermostats and barostats. In the literature, the thermostats of Andersen [24], Berendsen [25], Langevin [26] and Nosé-Hoover [27–29], and the barostats of Berendsen [25] and Parrinello-Rahman [30] are commonly applied in MD simulations. For studying the adsorption in porous solid conducted in this work, the Nosé-Hoover thermostat was used to describe the NVT ensembles in MD simulations. This thermostat allows the generation of canonical distributions and a reliable description of the time-dependent properties of the system.

I.3.2. Illustrations for the adsorption description in porous solids

Diffusion in porous solids plays a crucial role in most adsorption processes, such as in membrane based applications, gas storage, and transport based devices (e.g. proton conduction electrolytes). MD has allowed the description of the diffusion of various adsorbates in porous materials at a detailed molecular level including the magnitude of the diffusivity and the mechanism for both translational and rotational motions within crystals [31,32]. A special application of this technique is to determine the self- (individual motions) or the transport-diffusivity (collective displacements) for the molecules with either incoherent or coherent cross section [10].

Different types of molecular diffusion can be extracted from equilibrium MD simulations usually realized in the canonical (NVT) or microcanonical (NVE) ensembles. The self-diffusivity, labelled as *Ds*, is calculated from the slope of the mean square displacement (MSD) of individual molecules with respect to time through the following Einstein relation (Equation 2.33):

$$D_s = \lim_{t\to\infty}\left\{\frac{1}{6t}\frac{1}{N}\langle\sum[r_i(t) - r_i(0)]^2\rangle\right\} \tag{2.33}$$

In this equation, a consideration of several trajectories generated from different starting configurations and an average over all time origin contributes to improve the statistics of the calculations. The observation time should be long enough to get a linear evolution of the MSD with time avoiding any anomalous diffusion regime such as the ballistic or the exclusion of mutual exchange regimes [10,33].

The transport or Fickian diffusivity, i.e. the collective dynamics, labelled as D_t, is also of great interest in real applications. It is defined as the proportional constant relating a macroscopic gradient in the chemical potentials of the adsorbate molecules to the flux generated by this gradient. Based on the linear response theory, this diffusivity is often expressed by Equation 2.34.

$$D_t = D_0 \left(\frac{\partial lnf}{\partial lnc}\right) \tag{2.34}$$

Where D_0 is the corrected diffusivity, or Maxwell–Stefan diffusivity, f and c are respectively the fugacity and the concentration of the adsorbate. The term ($\partial lnf/\partial lnc$), usually labelled as Γ, provides a measure of the adsorbate's density fluctuations at the equilibrium. It is referred to the thermodynamic correction factor which is usually estimated from the slope of the adsorption isotherm.

The corrected diffusivity can be calculated from the equilibrium MD simulations using an Einstein relation similar to Equation 2.33 which measures the MSD of the center of mass of the considered group of diffusive molecules denoted R, as indicated in Equation 2.35.

$$D_0 = N \lim_{t\to\infty} \left\{\frac{1}{6t}\frac{1}{N}\langle\sum[R_i(t) - R_i(0)]^2\rangle\right\} \tag{2.35}$$

The estimation of D_0 usually requires longer MD runs than for Ds as the statistical error is typically much larger than that for D_s, whose calculation offers the additional advantage of averaging over all molecules.

I.4. Interatomic potentials

The potential energy of a system can be analytically described as a sum of bonded and non-bonded energy terms:

$$U = U_{bonded} + U_{non-bonded} \tag{2.36}$$

These terms are represented by mathematical expressions which usually imply a set of adjustable parameters. We usually refer as a forcefield the analytical function and their associated parameters to describe the interactions in play for a given system.

The bonded interactions are most often represented by terms that account for the bond stretching, angle bending, torsion and improper (Equation 2.37).

$$U = (U_{stretching} + U_{bending} + U_{torsion} + U_{improper}) + (U_{dispersion} + U_{electrostatic}) \quad (2.37)$$

There are many mathematical expressions to represent such bonded interactions [34–36]. The most common functions used for the bond, angle and improper interactions are harmonic potentials and for the torsion interaction, a sum of cosine terms.

In the classical calculations conducted in this thesis, the adsorbate molecule (i.e. water) was considered as a rigid body, an approximation employed in the literature [37–40]. In this case, no bonded term was used for its microscopic description. Regarding the adsorbents, the inorganic material ($Ti^{IV}Ti^{IV}(HPO_4)_4$) excepted for which a partially flexible forcefield was considered (cf chapter 3), all solids were modelled as rigid frameworks, i.e. all atoms were considered fixed in their initial positions deduced from the X-ray diffraction data.

The non-bonded interactions are usually expressed by two terms respectively accounting for the electrostatic and the van der Waals interactions. The van der Waals interactions can be decomposed into two contributions: (i) one where the atoms are separated from each other and are mutually attracted due to the formation of permanent or induced dipoles and (ii) a second where the atoms are very close each other leading to an overlap of their electronic clouds causing a strong repulsion between the atoms. Generally speaking, the attracting potential also called dispersive contribution can be modeled by functions of r^{-6}, r^{-8} or r^{-10} accounting for dipole-dipole, dipole-quadrupole and quadrupole-quadrupole interactions, respectively. Furthermore, the repulsive contribution are commonly expressed by the Born-Mayer function (Ae^{-Br}) or by a r^{-12} term [10]. In this work, the popular 6-12 Lennard-Jones (LJ) and/or Buckingham potentials were used to describe the van der Waals interactions. The 6-12 LJ potential is described in Equation 2.38.

$$U_{ij}^{vdW} = \sum_i \sum_{j>i} 4\varepsilon_{ij} \left[\left(\frac{\sigma_{ij}}{r_{ij}}\right)^{12} - \left(\frac{\sigma_{ij}}{r_{ij}}\right)^{6} \right] \tag{2.38}$$

Where ε_{ij} is the Lennard-Jones energy well depth and σ_{ij} is the distance for which attractive and repulsive interactions cancel out. The cross term parameters for the pairs ij are obtained from the individual ε_i and σ_i parameters assigned to each atom or pseudo-atom which are related to their polarizability and size respectively. These cross term parameters ε_{ij} and σ_{ij} are usually obtained using mixing rules. In the case of the Lorentz-Berthelot mixing rule [41] these parameters are obtained as follows:

$$\sigma_{ij} = \frac{\sigma_i + \sigma_j}{2} \;\; and \; \varepsilon_{ij} = \sqrt{\varepsilon_i \varepsilon_j}. \tag{2.39}$$

The Buckingham potential is a variant of the LJ potential [42] where the repulsion term is represented by a more realistic exponential expression Ae^{-Br} (Equation 2.40) while the dispersion is represented by Cr^{-6}. Such a potential tends to drop to -∞ (cf. Figure 2.1) when the atom distance is close to zero. Usually this numerical artifact is corrected by the introduction of a hard sphere potential that assigns the potential value to +∞ for values of r_{ij} smaller than a critical r_{max} value.

$$\begin{cases} U_{ij}^{vdW} = Aexp(-Br_{ij}) - \frac{C}{{r_{ij}}^6} & r > r_{max} \\ U_{ij}^{vdW} = +\infty & r \leq r_{max} \end{cases} \tag{2.40}$$

Since this potential energy is represented by three parameters (*A*, *B*, *C*), it is more suitable than the LJ potential to represent interactions with sharp potential well profiles such as the ones involving the strong interactions between the guest molecules and the coordinatively unsaturated sites (CUS) in MOFs [43,44].

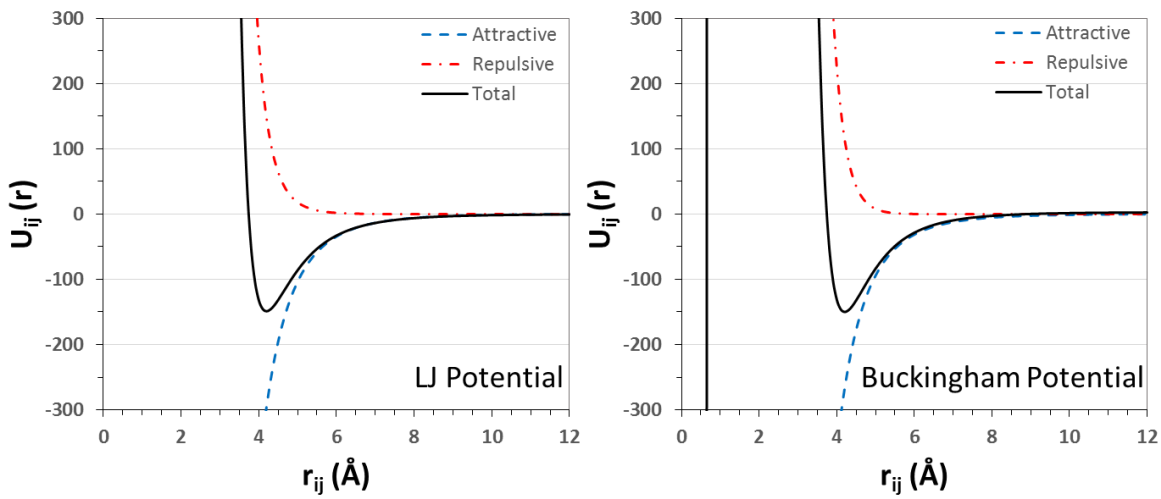

Figure 2.1 – Schematic Comparison between a LJ [45] and a Buckingham [46] potential to describe the non-bonded van der Waals interaction between two atoms. The energy profiles are coincident for the majority of the intermolecular distances (r_{ij}), however, for $r_{ij} \rightarrow 0$, the potential energy drops asymptotically to -∞.

The electrostatic interactions are often sufficiently reproduced by a classical Coulombic potential, as given in Equation 2.41.

$$U_{ij}^{electrostatic} = \sum_{i,j} \frac{1}{4\pi\varepsilon_0} \frac{q_i q_j}{r_{ij}} \tag{2.41}$$

Where q_i and q_j are the charges associated with interacting atoms i and j, and ε_0 is the vacuum permittivity.

Therefore, the total non-bonded potential is given by sum of the van der Waals and electrostatic terms:

$$U_{non-bonded} = U_{ij}^{vdW} + U_{ij}^{electrostatic} \tag{2.42}$$

In this work, the representation of the water/host interactions was described as follows:

(i) The interactions between water and all the atoms of the adsorbent framework with the exception of the CUS atoms were treated using a Coulombic term and a 12-6 LJ potential whose parameters were taken from generic forcefields.

(ii) The specific interactions between water and the CUS atoms were described with a Coulombic term and a Buckingham potential, whose repulsion (A and B) and dispersion (C) coefficients were fitted using quantum-calculations.

The overall non-bonded potentials considered in this work to describe the water/host interactions are summarized in Equation 2.43:

$$U(r_{ij}) = \begin{cases} \sum_{i,j} \frac{1}{4\pi\varepsilon_0} \frac{q_i q_j}{r_{ij}} + 4\varepsilon_{ij} \left[\left(\frac{\sigma_{ij}}{r_{ij}} \right)^{12} - \left(\frac{\sigma_{ij}}{r_{ij}} \right)^{6} \right], i \neq CUS \\ \sum_{i,j} \frac{1}{4\pi\varepsilon_0} \frac{q_i q_j}{r_{ij}} + \left[A e^{-\mathrm{B} r_{ij}} - \frac{\mathrm{C}}{{r_{ij}}^6} \right], i = CUS \end{cases} \tag{2.43}$$

In a system with many atoms, accounting the interactions of an atom with all the other atoms requires a huge numerical effort. Considering that only minor contributions of non-bonded interactions to the overall potential are obtained for large interatomic distances, it is usual to either truncate or shift the potential to a zero value after a cutoff distance (r_{cutoff}). Strictly speaking, different cutoff values should be tested and the shortest value from which no modification in the observables are noticed should be picked. However, the value of 12 Å is a default value normally employed in solid state.

Considering again the computational restraints imposed by even the most powerful machines, the amount of atoms that can be involved in the simulation of molecular systems could never attain the same order of magnitude of real systems (i.e. in the order of Avogadro's number). Furthermore, as seen in the previous sections, such large number of species is not even needed for the calculation of the observables of a system. However, the continuity of the real systems must be somehow represented even with a limited number of atoms. This continuity in a limited system can be achieved with the application of periodical boundary conditions in simulation cells. By propagating infinitively the simulation cell in the three *x*, *y*, *z* directions, the periodic conditions ensure the reproduction of an infinite system that corresponds to the conditions found in an ideal scenario where the material does not contain any defects and/or loss of crystallinity at a long range order. With the exception of the electrostatic interactions, the overall interacting energy would then be recalculated as follows [4]:

$$U_{ij} = \frac{1}{2}\sum_{i,j,n} U(|\boldsymbol{r}_{ij} + \boldsymbol{n}L|) \tag{2.44}$$

Where L is the length of the periodic cell (here, for convenience, considered cubic) and $\boldsymbol{n}$ is an arbitrary vector of three integer numbers.

One sensitive aspect of the periodic boundary conditions to be avoided concerns the possibility of a particle to interact with their own mirror image. In order to circumvent this problem, the shortest cell dimensions should be of at least double the size of the considered cutoff distance. Figure 2.2 shows the spurious interactions between a molecule and its mirror images coming for the injudicious choice of a cutoff larger than half of smallest of the unit cell units.

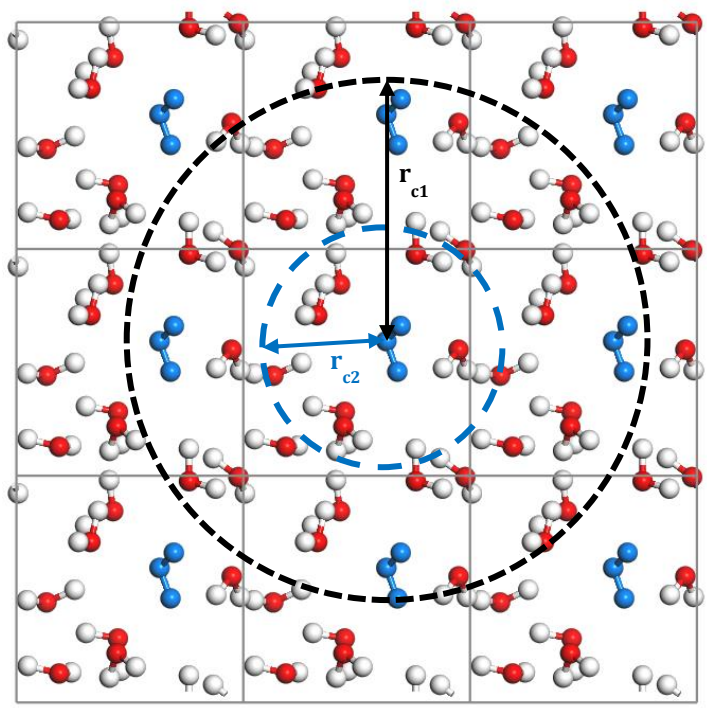

Figure 2.2 –Cubic periodic unit cell containing replicated in the *x* and *y* axis. Molecules in blue are mirror images of one another. The circles represent the interaction range for two cutoffs: one with the size of the unit cell dimension (r_{C_1} – black circle) and another with half the size of the unit cell dimension (r_{C_2} – blue circle).

As stated before, the electrostatic interactions are usually treated using a Coulombic potential. These interactions are taken into account with point charges introduced in charge centers that are (or not) coincident with the atomic centers. The possible relative dislocation

of the charge and atomic centers is not uncommon, being a usual way of representing the dipoles or quadrupoles of a given molecule.

Electrostatic interactions are also more sensitive to long-range order than the van der Waals interactions and they must be calculated for every periodic image as the truncation approximation usually causes significant numerical errors. The Ewald summation [47] is by far the most used method to account the electrostatic interactions in periodic systems and this method was applied in this work.

In the Ewald summation, the electrostatic potential is decomposed into short-range and long-range interactions that are treated in the real and Fourier spaces respectively. The use of the Fourier space allows the implementation of periodic boundary conditions. In this procedure, point charges are screened by a charge distribution of opposite charge normally expressed by a Gaussian of $\sqrt{2/\alpha}$ width, given by Equation 2.45. This charge distribution is then cancelled by another Gaussian distribution applied in the Fourier space which can be applied periodically (see Figure 2.3).

$$\rho^{Gaussian}(r) = -q_i \left(\frac{\alpha}{\pi}\right)^{\frac{3}{2}} \exp(-\alpha^2 r^2) \tag{2.45}$$

The Coulombic potential (U_c) in a periodic system, given by Equation 2.46 can then be expressed by three-term functions given by Equation 2.47.

$$U_C = \frac{1}{8\pi\varepsilon_0} \sum_i q_i \left(\sum_j \frac{q_j}{r_{ij}} + \sum_n \sum_j \frac{q_j}{|r_{ij}+nL|} \right) \tag{2.46}$$

$$U_C = \frac{1}{4\pi\varepsilon_0} \sum_i \sum_j \frac{q_i q_j erfc(\sqrt{\alpha} r_{ij})}{r_{ij}} + \frac{1}{2V_0\varepsilon_0} \sum_i \sum_j \sum_{k\neq 0} q_i q_j \frac{\cos(\boldsymbol{k}\cdot\boldsymbol{r}_{ij}) exp\left(-\frac{k^2}{4\alpha^2}\right)}{k^2} - \frac{\sqrt{\frac{\alpha}{\pi}}}{4\pi\varepsilon_0} \sum_i {q_i}^2 \tag{2.47}$$

Where $\boldsymbol{k}$ is a vector of the reciprocal space given by $\boldsymbol{k} = (2\pi/L)\boldsymbol{a}$, with $\boldsymbol{a}$ corresponding to the lattice vectors in the Fourier space. For convenience, the system is considered to be cubic with length L. V_0 is the volume of the unit cell.

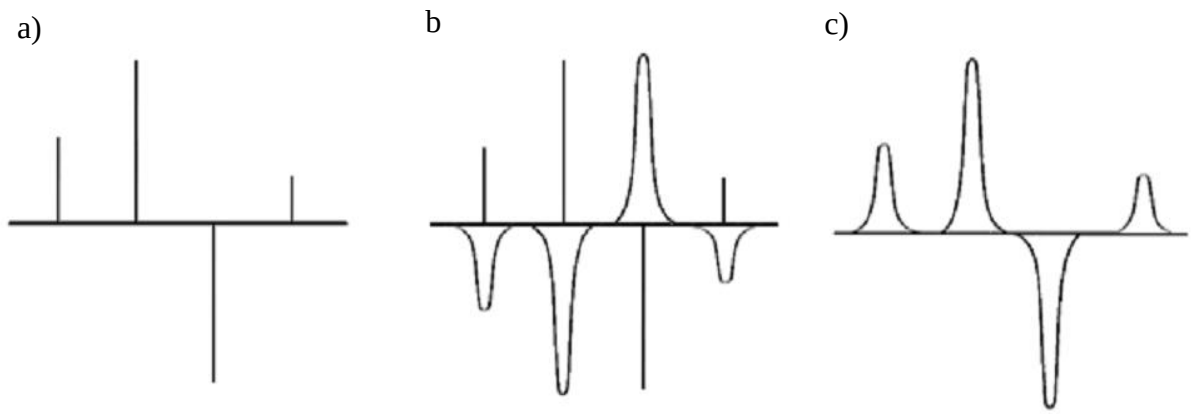

Figure 2.3 – The screening technique used in the Ewald summation procedure. Point charges (a) are screened by Gaussian charges distributions (b) in the real space. The Gaussian charge distributions in (b) are cancelled out by opposite charge distributions in the Fourier space (c).

The first term in Equation 2.47 corresponds to the summation of the density of charges $\rho_i^{Gaussian}(\boldsymbol{r})$ in the real space (Figure 2.3b). In this term, the complementary error function $erfc(\sqrt{\alpha}r_{ij})$ tends to zero for long distances and converges much more quickly than the r^{-1} function in Equation 2.46. The second term represents the opposite of the sum of the density of charges $\rho_i^{Gaussian}(\boldsymbol{r})$ in the Fourier space (Figure 2.3c). The third term is added to remove self-interaction energies of a given particle with itself contained in the second term [20].

I.5. Microscopic description of porous materials

The first pre-requirement to predict the adsorption properties of a porous solid consists of building a realistic atomistic description for this solid. The complexity of such a task strongly depends on whether (i) the considered adsorbent is crystalline or not, (ii) its framework is characterized by a chemical disorder or the positions of each atom type are well defined and (iii) its morphology/topology is experimentally controlled or not [10].

In crystalline materials, the relative positions of all atoms are generally experimentally resolved by the analysis of the X-ray powder diffraction (XRPD) data or can be also assisted computationally for the most complex system (poor crystallinity, large cell dimensions…). On the other hand, when chemical disorders are present, such as in the substitution of aluminum atoms by silicon atoms in aluminosilicalite forms, or in the cation distribution in certain zeolites, statistical approaches to distribute the different atoms based

on MC techniques [48,49] are usually recommended. More rarely, solid phases may also present changes in their reticulum dimensions caused by the adsorption of chemical species or by external stimuli (e.g. pressure, temperature, electric fields and light). Such behavior is observed in the swelling of clays and in the breathing of some MOFs [50].

In non-crystalline solids, an additional degree of complexity is involved in the atomic description of the system. This is seen in mesoporous silica solids, where a large range of morphologies and topologies is obtained and where sample-dependent (e.g. surface roughness and defects) play an important role in their adsorption properties. Microscopic models of these porous materials are usually made with reconstruction or mimetic approaches [10]. Activated carbons constitute another challenging class of materials to be modeled owing to their amorphous nature. Advances in understanding the microstructure of these materials such as the ordered graphite-like layers and other disordered elements [51] have allowed the construction of sophisticated slit-pore models [52,53].

In this work, we considered microscopic models for crystalline materials (MOFs and phosphates) that were already solved experimentally. These models were further geometry optimized at the Density Functional Theory level (see section II.3.2) to refine them and in particular to define the positions of the H-atoms which are not localized by XRD. As already mentioned, with the exception of the phosphate material, which was treated partially flexible with the consideration of a bonded-term potential to relax the -POH groups, all the materials were considered as rigid, i.e. with atoms fixed in their initial positions.

Each atom of these materials was treated by a single charged LJ center as it is usually operated in the field of porous materials. The LJ parameters in solid materials are usually taken from generic forcefields available in the literature, in particular the Universal (UFF) [54], DREIDING [55], and OPLS [56] force fields. These force fields contain LJ parameters for most of the atoms of the periodic table that are transferable for different types of materials, although the Universal force field is more usually applied for the modeling of inorganic systems while the DREIDING and OPLS force fields are more often used to describe the organic systems. In some inorganic components such as silicates, zeolites, phosphates and alumino-phosphates it is a common practice to assign LJ parameters to only the oxygen atoms of the framework since the other constitutive atoms are of much lower

polarizability [12,57–59]. Finally, the charges assigned to all atoms of these porous frameworks can be calculated by several methods including the charge equilibration (e.g. QEq [60] and Gasteiger [61]) or quantum calculation (e.g. Mulliken [62], ESP [63] and ChelpG [64]) approaches.

I.6. Microscopic description of the adsorbates

The microscopic models (interatomic potential parameters, charges, geometries) of the fluids are usually validated by a good agreement between their simulated and experimental intrinsic properties such as compressibility, density, dipole, and liquid vapor equilibrium (LVE) data. The latter is one the most reliable bases for the validation of a fluid model, even though experimental LVE data are often scarce for many systems.

The water molecule is probably one of the most representative examples of the variability of microscopic models reported in the literature. As shown in Table 2.1, a multitude of forcefields has been proposed for modeling the water properties, generally focusing in representing one particular physical parameter (e.g. density, critical parameters, radial distribution function, and melting or boiling temperatures).

In this work, three microscopic models were considered to represent the water molecules, the SPC, TIP4P-Ew and the TIP4P/2005 respectively.

The SPC model [39] is known to satisfactorily describe the structural and the diffusion properties of bulk liquid water at ambient conditions. In this three-site model, the partial charges are assigned to the center of the oxygen and hydrogen atoms while a single LJ interacting center is assigned to the oxygen atoms. The molecule is considered as rigid with a HOH angle of 109.47° and a O–H distance of 1.0 Å.

The TIP4P-Ew model is a four-site model used for water adsorption because of its good reproduction of bulk liquid properties [66]. In this model, point charges are placed in the hydrogen atoms and in a dummy atom placed in the bisection of the plane formed by the HOH angle and distant 0.1250 Å from the oxygen atom. The water's geometry is considered rigid with a HOH angle of 104.52° and a O–H distance of 0.9572 Å.

The TIP4P/2005 model is another four site model that was intensively validated to reproduce a variety of thermodynamic properties of water in a wide range of temperatures and pressures [38]. This model is very similar to the TIP4P-Ew, varying solely on the value of the point charges (cf. Table 2.1) and in the distance from the dummy atom to the oxygen atom (l_2 = 0.1546 Å).

Table 2.1 – Most representative forcefields used in the literature for the description of the water molecules including charges, LJ and geometric parameters associated with them. Figure taken from [65]

Model	Type	σ (Å)	ε (K)	L_1 (Å)	L_2 (Å)	q_1 (e)	q_2 (e)	θ (°)	ϕ (°)
SPC	1	3.166	78.178	1.00	-	+0.41	-0.82	109.47	-
SPC/E	1	3.166	78.178	1.00	-	+0.4238	-0.8476	109.47	-
PPC	2	3.234	72.160	0.9430	0.06	+0.5170	-1.0340	106.00	127.00
TIP3P	1	3.1506	76.542	0.9572	-	+0.4170	-0.8340	104.52	-
TIP4P	3	3.1536	77.937	0.9572	0.15	+0.52	-1.04	104.52	-
TIP4P-Ew	3	3.1643	81.900	0.9572	0.125	+0.5242	-1.0484	104.52	-
TIP4P/2005	3	3.1589	93.200	0.9572	0.1546	+0.5564	-1.1128	104.52	-
TIP5P	4	3.120	80.511	0.9572	0.70	+0.2410	-0.2410	104.52	109.47
TIP5P-Ew	4	3.097	89.579	0.9572	0.70	+0.2410	-0.2410	104.52	109.47

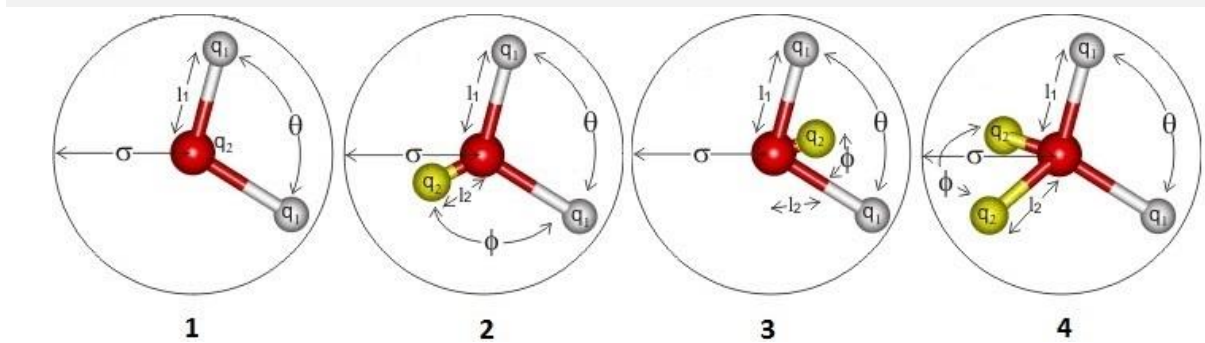

II. Quantum calculations

II.1. General aspects

The most elementary concept of quantum mechanics states that all the information of the electronic structure for a given system is contained in its wave function (Ψ). The knowledge of such a function allows a full description of the microscopic properties of a system. The Schrödinger equation allows the non-relativistic calculation of the wave function as follows:

$$\hat{H}\left|\Psi\left(\boldsymbol{r}_i, \boldsymbol{R}_j\right)\right\rangle = E_{el}\left|\Psi\left(\boldsymbol{r}_i, \boldsymbol{R}_j\right)\right\rangle \tag{2.48}$$

Where $\boldsymbol{r}$ and $\boldsymbol{R}$ are the coordinate vectors of electrons and nuclei respectively, $\hat{H}$ is the Hamiltonian and E_{el} is the associated electronic energy obtained from the eigenvalues of the wave function with respect to the Hamiltonian.

Strictly speaking, the Hamiltonian must account for both the kinetic and electrostatic energy contributions of both the nuclei and the electrons of the cloud, as well as the nuclei-electron interaction energy terms. This global expression is considerably simplified with the application of the Born-Oppenheimer approximation [67], which proposes the decoupling of the motions between nuclei and electrons because of their considerable mass difference. As a result of its much larger mass, the nuclei is much slower than the electrons and thus the electronic distribution evolves adiabatically according to the shifted position of the nuclei. With the consideration of this approximation, the application of the Schrödinger equation to the electrons leads to Equation 2.49.

$$\left[\sum_i^N \left(\frac{-\hbar^2 \nabla_i{}^2}{2m} + v(\boldsymbol{r}_i)\right) + \sum_{i<j} U\left(\boldsymbol{r}_i, \boldsymbol{r}_j\right)\right]\left|\Psi\left(\boldsymbol{r}_i, \boldsymbol{R}_j\right)\right\rangle = \epsilon\left(\boldsymbol{R}_j\right)\left|\Psi\left(r_i, \boldsymbol{R}_j\right)\right\rangle \tag{2.49}$$

Where $\hbar$ is the Dirac constant, U is the electron-electron interaction (usually a Coulombic potential), $v(\boldsymbol{r})$ an external potential generated by the nuclei, and ϵ the associated energy considering the position of the nuclei as a parameter.

This equation considers the energy of the electron clouds of a given system without considering the nuclear kinetic and repulsion energies. Consequently, ϵ in Equation 2.49

accounts for the contribution of the energy at the absolute zero. The total energy of a system must then be corrected with the nuclear kinetic and repulsion energies contributions.

The usual quantum-mechanical approach to the Schrödinger equation consists of specifying the potential $v(\boldsymbol{r})$ and incorporating it into this equation to determine the wave function $\Psi(\boldsymbol{r},\boldsymbol{r}_2,\ldots,\boldsymbol{r}^N)$. Any observable ($\hat{A}$) is then calculated as follows:

$$\langle \mathrm{A}(\boldsymbol{r})\rangle = \left\langle \Psi(\boldsymbol{r})\middle|\hat{A}(\boldsymbol{r})\middle|\Psi(\boldsymbol{r})\right\rangle \tag{2.50}$$

One of the observables that can be determined is the electronic density $\rho(\boldsymbol{r})$ that corresponds to the probability of finding one given electron of a system in a volume $d^3\mathbf{r}$. Applying Equation 2.50 for a many body system containing N electrons, the electronic density can be expressed by Equation 2.49:

$$\rho(\boldsymbol{r}) = N\int d^3r_2 \int d^3r_3 \ldots \int d^3r_N\, \Psi^*(\boldsymbol{r},\boldsymbol{r}_2,\ldots,\boldsymbol{r}_N)\Psi(\boldsymbol{r},\boldsymbol{r}_2,\ldots,\boldsymbol{r}_N) \tag{2.51}$$

Solving the Schrödinger equation for a many body system is an extremely complex and time consuming task even though supported by a range of specific methods such as the diagrammatic perturbation theory, built on the Feynman diagrams and Green's functions and the configuration interactions methods, based on the use of Slater determinants (e.g. Hartree-Fock method) [68]. One approximation to solve the Schrödinger equation is to consider the electronic density as a key variable from which all the other observables can be derived. This assumption is the foundation of the Density Functional Theory (DFT) discussed in the next section.

The mathematical description of the electronic density is generally done by the linear combination of functions used to represent each one of the atomic orbitals. These atom centered basis functions are also referred as basis sets and are mainly represented by functions of Gaussian- and Slater-type. These basis sets may be composed by one basis function (minimal basis set) or multiples basis functions (double-zeta, triple-zeta and etc.) per orbital.

Another way to describe the electronic density is to consider plane waves. These plane waves are periodic, delocalized and orthogonal functions evaluated in the reciprocal space that are more computationally efficient although they do not describe correctly regions where the electronic density is localized such as the nuclei neighborhood or electronic nodes. These functions are particularly used in periodic solid-state materials. Plane waves are particularly useful for the construction of pseudopotentials. These pseudopotentials are effective potentials constructed to replace the atomic all-electron potentials described by the basis sets. These potentials are constructed based on the assumption that the valence and core wave functions rarely overlap. Considering that the outer electrons are practically the only ones involved in the inter-atomic interactions, the contribution of the core electrons is neglected in the pseudopotential construction and the valence electrons are then described by pseudo-functions with significantly fewer nodes.

II.2. Density functional theory

Density Functional Theory (DFT) has been widely used to access the electronic description of a large diversity of systems and it is nowadays the main theoretical approach applied to explore the electronic-structure in material science. In this approach, the electronic density only depends on the spatial coordinates of the electrons. Fundamentally, the DFT is grounded in two theorems proposed by Hohenberg and Kohn [69].

The first theorem indicates that the electronic density $\rho(\boldsymbol{r})$ is not just a variable among others obtained after the solution of the Schrödinger equation, but instead it is a fundamental function from which the other observables of a system may be derived. It states that for each system, the external potential $v(\boldsymbol{r})$, and hence the total energy, is a bijective functional of the electron density $\rho(\boldsymbol{r})$. A consequence is that the energy functional can be written in terms of the external potential and the universal functional of $\rho(\boldsymbol{r})$, $F[\rho(\boldsymbol{r})]$, as described in Equation 2.52.

$$E_{el}[\rho(\boldsymbol{r})] = \int \rho(\boldsymbol{r}) v(\boldsymbol{r}) dr + F[\rho(\boldsymbol{r})] \tag{2.52}$$

$E_{el}[\rho(\boldsymbol{r})]$ is an observable of the Hamiltonian related to a wave function. Considering that the energy is a functional of $\rho(\boldsymbol{r})$, for a non-degenerated ground state, the wave function

$\Psi_0(\boldsymbol{r},\boldsymbol{r}_2,\ldots,\boldsymbol{r}_N)$ of such a state must minimize the expected value of the Hamiltonian and it is unique. Both conditions are only met if the wave function and the electronic density have a bijective relation between each other.

The second theorem states that the ground state energy is also a bijective function of $\rho(\boldsymbol{r})$ and reaches a minimum when $\rho(\boldsymbol{r})$ corresponds the ground state electronic density of the system. Therefore, for the ground state energy, the following equation can be written:

$$\frac{\delta E_{el}[\rho(\boldsymbol{r})]}{\delta\rho(\boldsymbol{r})} = 0 \tag{2.53}$$

Equation 2.52 can be further developed by expressing the energy term as the sum of the total electronic kinetic (T), internal (U) and external (V) potential energies (Equation 2.54), which are all functional of $\rho(\boldsymbol{r})$.

$$E_{el}[\rho(r)] = T[\rho(\boldsymbol{r})] + U[\rho(\boldsymbol{r})] + V[\rho(\boldsymbol{r})] = T[\rho(\boldsymbol{r})] + U[\rho(\boldsymbol{r})] + \int \rho(\boldsymbol{r})v(\boldsymbol{r})d^3r \tag{2.54}$$

In practice, one usually seeks the ground state energy of a collective system since this is the natural state in condensed matter. Considering a specified system for which $v(\boldsymbol{r})$ is known, the ground state energy, E_0 can be obtained with a certain and unique ground state electronic density ρ_0. Assuming that $v(\boldsymbol{r})$ depends on a certain parameter ζ, such as the distance or angle between two atoms in a solid, $E_0(\zeta)$ can be calculated for various values of ζ to find the one for which the ground state energy is at its minimum. This principle allows the calculation of a variety of important variables. For instance, this approach can be directly used in the determination of molecular and solid geometries, lattice constants, charge distributions, total energies, etc. Analyzing the change of $E_0(\zeta)$ with ζ makes possible the calculation of the compressibility, phonon spectra and bulk modulus in solids and vibrational frequencies in molecules. Finally, with the calculation of the total energy of a many-body system, the individual energy of its components and the interaction or dissociation energies can be calculated [68].

The DFT can be implemented in many ways. A coherent and practical procedure was proposed by Kohn and Sham [70]. The success of this approach is due to the use of a

referential non-interacting single-body system that is equivalent to the functional density of the actual many-body system.

In the Kohn-Sham approach, the kinetic term $T[\rho(\boldsymbol{r})]$ is divided into non-interacting $T_S[\rho(\boldsymbol{r})]$ and correlation $T_C[\rho(\boldsymbol{r})]$ terms while the internal electrostatic potential $U[\rho(\boldsymbol{r})]$ is divided into a Hartree interaction term $U_H[\rho(\boldsymbol{r})]$, an exchange term $U_X[\rho(\boldsymbol{r})]$ and a correlation term $U_C[\rho(\boldsymbol{r})]$. Grouping the terms corresponding to correlation and exchanges T_S, U_H and U_C in a single term, the exchange-correlation potential $E_{XC}[\rho(\boldsymbol{r})]$, Equation 2.54 can be rewritten as:

$$E[\rho] = T_S[\rho] + U_H[\rho] + E_{XC}[\rho] + V[\rho]. \tag{2.55}$$

Further, the non-interacting kinetic energy can be calculated in terms of single-particle orbitals (Φ_i^{KS}) as in Equation 2.56:

$$T_S[\rho] = \frac{-\hbar}{2m}\sum_i^N \int d^3r \Phi_i^{KS}(\boldsymbol{r})\nabla^2\Phi_i^{KS}(\boldsymbol{r}). \tag{2.56}$$

Since this expression is totally defined by single-particle orbitals and it is a functional of the electronic density, the electronic density must itself be defined by these orbitals, as stated below:

$$\rho(\boldsymbol{r}) = \sum_i^N f_i \left|\Phi_i^{KS}\right|^2. \tag{2.57}$$

Where f_i is the occupation of the i band state according to the Fermi-Dirac distribution.

Minimizing the energy in Equation 2.55 and combining it with Equation 2.53 leads to the following expression:

$$\frac{\delta E[\rho]}{\delta\rho} = \frac{\delta T_S[\rho]}{\delta\rho} + \frac{\delta U_H[\rho]}{\delta\rho} + \frac{\delta E_{XC}[\rho]}{\delta\rho} + \frac{\delta V[\rho]}{\delta\rho} = \frac{\delta T_S[\rho]}{\delta\rho} + v(\boldsymbol{r}) + v_H(\boldsymbol{r}) + v_{XC}(\boldsymbol{r}) = 0 \tag{2.58}$$

This equation is equivalent to the minimization of an energy expression of non-interacting electrons which undergo an external potential $v_S(r) = v(r) + v_H(r) + v_{XC}(r)$.

Therefore, one can calculate a many-body Schrödinger equation by solving the equations of a non-interacting (single-body) system of potential $v_s(\mathbf{r})$:

$$\left[\frac{-\hbar\nabla^2}{2m} + v_S(\boldsymbol{r})\right]\Phi_i^{KS}(\boldsymbol{r}) = \epsilon_i\Phi_i^{KS}(\boldsymbol{r}). \tag{2.59}$$

Considering several algebric relations, the total functional can be finally expressed as follows:

$$E_0 = \sum_i^N \epsilon_i - \frac{e^2}{2}\int d^3r d^3r' \frac{\rho_0(\boldsymbol{r})\rho_0(\boldsymbol{r}')}{|\boldsymbol{r}-\boldsymbol{r}'|} - \int d^3r v_{XC}(\boldsymbol{r})\rho_0(\boldsymbol{r}) + E_{XC}[\rho_0]. \tag{2.60}$$

Where the right hand side of this equation corresponds to the sum of the eigenvalues of Equation 2.58 (band energies), the mutual electrostatic interactions in the electron cloud, the effective many-body potential and the exchange-correlation energy respectively. All terms in this equation are exactly determined with the exception of the latter term which is currently estimated by several approaches such as the Local Density Approximation (LDA) [71,72], the Generalized Gradient Approximation (GGA) [73,74] and Hybrid methods [75]. Here are summarized the main characteristics of these methods.

The LDA approach considers that the exchange-correlation energy term depends only on the value of the electronic density at each point that is derived from the homogeneous electron gas model [76]. This approximation implies a smooth variation of the electronic density around a given particle. The application of LDA is thus valid to describe systems whose electronic density varies smoothly (i.e. homogeneous systems) while it fails in the situations where the density undergoes rapid changes, such as in molecules. The Perdew-Zunger (PZ) [71], Perdew-Wang (PW) [72] and Vosko-Wilk-Nusair (VWN) [77] are all common LDA functionals.

On the other hand, the GGA approach considers that the exchange-correlation energy depends not only on the electronic density but also on its gradient. This allows the successfully description of many systems characterized by heterogeneous electronic density distributions. The GGA functionals are usually a good trade-off between computational time

and accuracy. One of the most used GGA functional employed in the literature is the PBE functional [73], followed by others such as the PW91 [78] and BLYP [79,80].

Finally, the hybrid functional is constructed as a linear combination of the Hartree-Fock (HF) exact exchange functional with GGA and LDA functional. This approach has been widely employed for the calculation of molecular properties such as atomization energies, bond lengths and vibration frequencies [81]. The B3LYP [75,82] is the most popular hybrid functional used in the literature.

The determination of the ground state energy E_0 in Equation 2.59 proceeds with the first estimation of a set of electronic densities and Kohn-Sham orbitals with either localized atom-centered basis functions or plane waves. From this initial state, the Kohn-Sham Equation 2.58 is diagonalized and the resulting eigenvalues are used to determine the ground state energy from Equation 2.59 and a new electronic density using Equation 2.56. With the consideration of this new electronic density, Equation 2.58 can be again diagonalized. This process continues until a given convergence criteria (such as convergence in the electronic density or the ground state energy) is attained. This iterative process is known as the self-consistent field (SCF) method.

Among the diverse approaches used to estimate the exchange-correlation energy, the GGA is probably the most popular in computational chemistry since it demands moderate computational efforts and leads to results reasonably accurate as compared to the experimental data. On the other hand, such approximation becomes inaccurate when non-local interactions (e.g. dispersive interactions) have large contributions to the total electronic energy. In this case, the effects of non-local interactions can be taken into account via three main methods: (i) the vdW-DF method, which is based solely on the electronic density and does not rely on empirical terms, ii) the effective atom centered one-electron potential, an atom-centered potential that produces changes in the electronic charge density [83] and (iii) the semi-empirical approach which considers corrections via a $C_6 r^{-6}$ potential term, where C_6 is an empirical parameter [84]. This includes the DFT-D [85], DFT-D2 [86–88], DFT-D3 [89] and the Tkatchenko-Scheffler (TS) [90] approaches. The first two are very similar and have individual empirical parameters listed for most atoms of the periodic table and

interacting parameters calculated with mixing rules. DFT-D2 is the most popular approach, the corrected dispersion energy E_{DISP} is calculated according to Equation 2.61.

$$E_{DISP} = -s_6 \sum_i^{N_{AT}} \sum_{j>i}^{N_{AT}} \frac{C^{ij}{}_6}{R_{ij}^6} f_{DMP}(\boldsymbol{R}_{ij}) \tag{2.61}$$

Where s_6 is a scaling factor which depends on the considered functional (e.g. $s_{6PBE} = 0.75; s_{6BLYP} = 1.2; s_{6B3LYP} = 1.05$) and f_{DMP} is a dampening function which depends on the inter-atomic distance (R_{ij}), a fitting parameter $R^{ij}{}_{0,}$ and the van der Waals radii of the atoms in the system. The DFT-D3 approach is slightly more sophisticated since the corrected dispersion parameters not only depend on the atom types but also on the geometry of the system [83].

II.3. Illustrations of DFT applications to the description of solids.

II.3.1. Interaction energy

One of the most trivial applications of quantum calculations is the determination of the interaction energies between chemical species. Considering two interacting species A and B, the interaction energy is usually approximated with the following equation, where U_{inter} is the interaction energy, U_A and U_B are the respective energies of the isolated species A and B, and U_{AB} is the total energy of a system containing species A and B in interaction.

$$U_{inter} = U_{AB} - (U_A + U_B) \tag{2.62}$$

The calculations of the interaction energy for a range of separating A-B distances allow the plot of the interaction energy curve that is of particular interest to further derive force-field parameters using a fitting procedure (see section I.4). This approach has been widely employed in the case of diverse guest molecules in interaction with the coordinated unsaturated sites (CUS) in MOFs [43,44,91–93].

II.3.2. Geometry optimization

As stated before, quantum calculations are widely employed for geometry optimization by performing a systematic evaluation of the electronic energy of a system with

the variation of geometric parameters such as the mutual distances, angles and dihedrals between its constitutive atoms. Several numerical methods are used to find the global minimum of a system at the DFT level. The most popular algorithm implemented in the diverse Quantum Chemistry software packages is the Newton-Raphson method and its derivative (quasi-Newton methods). This method is characterized by its fast convergence, however the calculation of the Hessian matrix at each step turns it computationally expensive. The approximation of this matrix by the gradient history in the system is widely employed to enhance the computational efficiency of the optimization process as it is the case for the Broyden-Fletcher-Goldfarb-Shanno (BFGS) and Limited-memory BFGS methods [94]. Depending on the initial configuration of the system and the number of constituting atoms, the energy minimization can be a fastidious process. In order to better achieve convergence, other criteria than minimizing the total energy are usually employed in geometry optimization algorithms, such as the minimization of the average atom displacement and of the average individual force applied to the atoms.

II.3.3. Charge calculations

Another important use of quantum calculations is the estimation of atomic partial charges. Fundamentally, these charges are a useful simplification of the polarization of the electron distribution between bonded atoms. Under the framework of DFT calculations, atomic partial charges are often obtained by the population analysis of wave functions (e.g. Mulliken population analysis [62], natural population analysis [95], partitioning of electron density distributions (e.g. Bader [96], DDEC [97], CM5 [98], and Hirshfield [99] charges), or by a fitting of the electrostatic potential around a cluster, molecule or periodic structure (e.g. ESP, REPEAT charges). The Mulliken and ESP are the methods that were used in this thesis to determine the atomic partial charges of an investigated material. Assigning these partial charges to the atoms of a system permits determining the electrostatic potential on the classical calculations described in section I. These methods are then briefly detailed below.

In the Mulliken population analysis, the partial charge of the atom i is calculated as:

$$q_i = Z_i - \int \rho_i(\boldsymbol{r})dr \tag{2.63}$$

Where Z_i is the charge of the positively charged atom core and $\rho_i(\boldsymbol{r})$ is the electron density around the core of atom i.

In bonded systems, the Mulliken method assumes an equal distribution of the electron density among the pairs of the atoms to perform the integration indicated in Equation 2.63. This method, which can be directly applied to periodic systems, is relatively simple and computationally efficient, however it strongly depends on the geometry of the system and the basis set employed and it does not provide a good description of the degree of covalency in bonds [100].

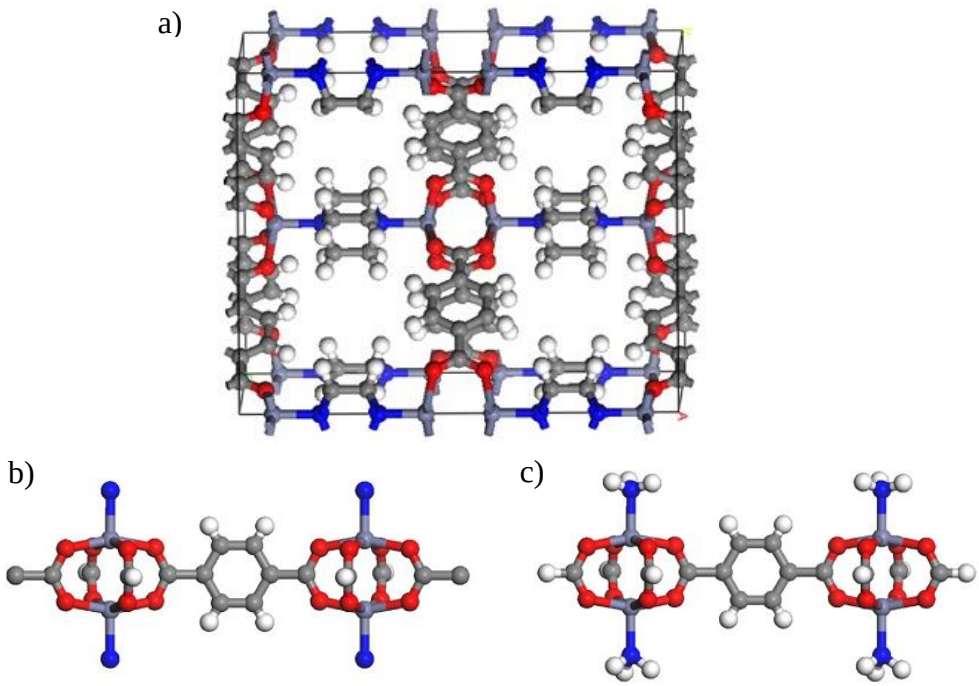

Figure 2.4 – Procedure to obtain a valid cluster model from a crystal for ESP charge calculations (adapted from [100]). From a periodic crystal model (a), a representative part of the framework is cut (b) and the dangling bonds resulting of this procedure are saturated with hydrogen atoms (c).

The derivation of electrostatic potential (ESP) charges is based on the iterative fitting of the atomic partial charges in a way that they generate an ESP grid as close as possible to a previously quantum-calculated ESP grid. There are several efficient methods to calculate ESP charges such as the CHELPG [64] and Merz-Kollman [101]. These methods can be applied directly to a molecule while in the case of periodic systems it is much less straightforward. In this case, representative clusters of the crystal are cut and further

saturated to avoid the presence of dangling bonds. The so-calculated charges are approximated as the global charges of the periodic system. It is common to use more than one cluster to extract reliable charges for each region of the periodic crystal. This is illustrated in Figure 2.4.

III. *Ab Initio* Molecular Dynamics

III.1. General aspects

As stated in section I.3, the classical MD simulations have been widely employed to investigate a wide range of materials however this approach does not allow the description of the bond breaking/forming that is of crucial importance when one aims to explore phenomena such as the dynamics and phase transitions of crystal systems [102–104], mechanical and chemical properties of polymeric systems [105–107], molecular and defect diffusion on semiconductors [108–111], and proton conduction [112–114]. Certainly, in complement to the reactive force-field (ReaxFF) [115–118] or empirical valence bond (EVB) [119,120]-based MD, the *Ab Initio* MD (AIMD) propose a way to circumvent these restrictions by evaluating the forces acting on the nuclei with the consideration of the electronic structure calculation performed on each step of the MD trajectories. In this way, the potential energy surface of the system is allowed to change on the course of the MD simulation. On the other hand, the overall MD principle is maintained such as the use of the integration algorithms (e.g. Verlet algorithm) for the configurational and the velocity update according to the Newton's equation of motion at each step, and the consideration of thermostats and barostats in the NVT and NPT ensembles respectively. The calculation of the electronic structure is carried out by solving the Schrödinger equation at each timestep. The two most popular approaches to perform such calculations are the Hartree-Fock and the DFT methods. The way in which the classic Newtonian mechanics equations are derived from the Schrödinger equation is not straightforward. According to how the quantum-classical coupling is made, AIMD simulations may be classified in three categories: Ehrenfest, Born-Oppenheimer and Car-Parrinello Molecular Dynamics.

III.2. Ehrenfest Molecular Dynamics

In the Ehrenfest MD scheme, the time-dependent electronic Schrodinger equation is solved "on the fly" as the nuclei are propagated using classical mechanics, as described in Equations 2.64 and 2.65 [121].

$$M_I \frac{\partial^2 \boldsymbol{R}_I(t)}{\partial t^2} = -\nabla_I \int \Psi^* H_e \Psi dr = -\nabla_I \langle H_e \rangle \tag{2.64}$$

$$i\hbar \frac{\partial \Psi}{\partial t} = \left[-\sum_i \frac{\hbar^2}{2m_e} \nabla^2 + v_{n-e}(\boldsymbol{r}_i, \boldsymbol{R}_I) \right] \Psi = H_e \Psi \tag{2.65}$$

Where H_e is the electronic Hamiltonian, $v_{n\text{-}e}$ is the potential exerted by the nuclei on the electrons, M_I and m_e and $\boldsymbol{R}_I$ and $\boldsymbol{r}_i$ are respectively the nuclei and electronic mass and positions.

The wave function Ψ can be expressed as a linear combination of different instantaneous electronic states Ψ_k:

$$\Psi(\mathrm{r}_i, R_I, t) = \sum_k c_k(t) \Psi_k(\mathbf{r}_i, \boldsymbol{R}_I). \tag{2.66}$$

Where the coefficient c_k are complex numbers whose norm describe the time evolution of the electronic population of the different Ψ_k electronic states [122]. For an adiabatic base of Ψ_k, obtained from the solution of the time-independent Schrodinger equation (Equation 2.48), Equations 2.64 and 2.65 can be rewritten as:

$$M_I \frac{\partial^2 \boldsymbol{R}_I(t)}{\partial t^2} = -\sum_k |c_k(t)|^2 \nabla_I E_k \tag{2.67}$$

$$i\hbar \frac{\partial c_k(t)}{\partial t} = c_k(t) E_k \tag{2.68}$$

The Ehrenfest MD allows a rigorous determination of the transitions between different Ψ_k electronic states within the framework of classical nuclear motion and the mean-field approximation to the electronic calculations [121]. If instead of a linear combination of different electronic states, only the wave function on the electronic ground state Ψ_0 is considered, these equations can be rewritten as follows:

$$M_I \frac{\partial^2 \boldsymbol{R}_I(t)}{\partial t^2} = -\nabla_I \langle \Psi_0 | H_e | \Psi_0 \rangle \tag{2.69}$$

$$i\hbar \frac{\partial \Psi_0}{\partial t} = H_e \Psi_0 \tag{2.70}$$

The Ehrenfest MD is the oldest method of resolution of AIMD on the fly and it is used only in very specific cases [122–124]. The solution of Equations 2.59 and 2.60 requires timesteps compatible with the relaxation time of the electrons, even though the electrons move much faster than the nuclei. Since most chemical processes are governed by the motion of the nuclei rather than by the motion of the electrons, this approach is clearly not ideal.

III.2. Born-Oppenheimer Molecular Dynamics

In the Born-Oppenheimer (BO) approximation, the motion of the nuclei is decoupled from the much faster motion of the electrons. In this case, at each timestep the electronic potential is calculated by solving the time-independent Schrodinger equation, and the position and momenta of the nuclei are recalculated with this electronic potential according to the classical dynamics equations. The electrons are then considered to move adiabatically as the nuclei translate over the system. In mathematical terms, this approach results in the following equations for the electronic ground state:

$$M_I \frac{\partial^2 \boldsymbol{R}_I(t)}{\partial t^2} = -\nabla_I \min_{\Psi_0} \langle \Psi_0 | H_e | \Psi_0 \rangle$$

(2.71)

$$H_e \Psi_0 = E_0 \Psi_0 \tag{2.72}$$

The right hand side of Equation 2.72 can be determined with the aid of the DFT formalism by making use of Kohn-Sham effective Hamiltonian [121], with $H_e = H_e^{KS}$.

Compared to the Ehrenfest MD, the BO-MD approximation allows the use of larger timesteps, as the nuclei are characterized by much larger relaxation times than the electrons. This made possible the description of entire trajectories of atoms and a more complete understanding of complex phenomena such as proton conduction [125].

On the other hand, since it is necessary to update the energetic landscape of the simulation cell at each timestep via quantum calculations, the computational cost associated with this technique is even larger than using the Ehrenfest MD scheme. The computational demand of BO-MD calculations restricts its use to describe processes with relaxation times in the order of a few picoseconds.

III.3. Car-Parrinello Molecular Dynamics

In the Car-Parrinello Molecular Dynamics (CPMD), the kinetic and configurational evolution of the electronic and the nuclei motions is described as a two-component classical problem instead of a coupled quantum-classical system. Such simplification is grounded on the difference on the timescale of the fast electronic and slow nuclei motions, for which the timescale gap is seen as a two-component adiabatical classical system with two energy scales [121]. The CPMD defines a fictitious mass μ to the electrons, giving them active degrees of freedom. This allows the classical treatment of the electronic movement, even though they are still submitted to the quantum forces dictated by the electronic Hamiltonian. The mathematical backbone of the CPMD theory is defined in the class of Lagrangians presented in Equation 2.73.

$$\mathcal{L} = \sum_I \frac{1}{2} M_I \frac{d\boldsymbol{R}_I(t)^2}{dt} + \sum_i \mu \langle \dot{\varphi}_i | \dot{\varphi}_i \rangle - \langle \Psi_0 | H_e | \Psi_0 \rangle + \sum_{i,j} (\langle \varphi_i | \varphi_j \rangle - \delta_{ij}) \tag{2.73}$$

In this equation, the first and second terms in the right hand side are assigned to the kinetic energy of the nuclei and orbitals, respectively. The third term corresponds to the potential energy of the electrons while the last term is assigned to the set of constraints imposed by the set of orbitals. Since the electronic energy $\langle \Psi_0 | H_e | \Psi_0 \rangle$ is a function of the nuclear positions and the wave function, the corresponding Newtonian equations of motion can be derived from the following associated Euler-Lagragian equations:

$$\frac{d}{dt} \frac{\partial L}{\partial \dot{R}_I} = \frac{\partial L}{\partial R_I} \tag{2.74}$$

$$\frac{d}{dt} \frac{\partial L}{\partial \dot{\varphi}_i^*} = \frac{\partial L}{\partial \varphi_i^*} \tag{2.75}$$

Applying these equations in conjunction with the effective one-particle Kohn-Sham Hamiltonians used in DFT and imposing the orthogonality constraint $\langle\varphi_i|\varphi_j\rangle = \delta_{ij}$ in the orbitals through Lagrange multipliers, the Car-Parrinello equations of motions can be obtained:

$$M_I \frac{\partial^2 \boldsymbol{R}_I(t)}{\partial t^2} = -\nabla_I \langle \Psi_0 | H_e^{KS} | \Psi_0 \rangle \tag{2.76}$$

$$\mu \frac{\partial^2 \boldsymbol{\varphi}_i(t)}{\partial t^2} = -H_e^{KS} \boldsymbol{\varphi}_i + \sum_j \Lambda_{ij} \boldsymbol{\varphi}_i \tag{2.77}$$

The resolution of this set of equations allows the determination of the time evolution of both the nuclei and the orbitals that depends on an initial self-consisted energy surface and the Kohn-Sham Hamiltonian. In contrast to the Ehrenfest MD, the CPMD method does not require small timesteps since the details of the electronic configuration are not scrutinized.

Following the two kinetic energy terms in the Equation 2.73, it is common to associate an instantaneous physical temperature to the nuclei, proportional to $\sum_I \frac{1}{2} M_I \dot{R}_I^2$, and a fictitious temperature to the electrons, proportional to $\sum_i \mu \langle \dot{\varphi}_i | \dot{\varphi}_i \rangle$. Following this, the term "cold electrons" corresponds to the electronic subsystem close to the instantaneous minimum of energy surface (Born-Oppenheimer) while "hot electrons" corresponds electrons that substantially deviate from these energetic hypersurface.

The major task in the CPMD method is to equilibrate the value of timestep and fictitious mass in order to respective allow a fast time evolution of the system and keep the electrons both cold for long time periods and following adiabatically the nuclear motion. A proper well converged and minimized Born-Oppenheimer hypersurface is also mandatory.

Even though the CPMD method is a mature technique whose fundamentals are well developed, the adjustable variables involved in its use require a certain level of maturity and even a degree of empiricism, especially for large systems with multiple chemical species (e.g. biological systems [126] and periodic solids with large unit cells [127]).

In this work, the water-mediated proton conductive mechanism was modeled using the Born-Oppenheimer MD approach, since the latter is reported as a suitable method when

transition metals are considered, as it was the case in the so-studied MOFs or inorganic phosphates solids [121].

REFERENCES

[1] Tuckerman ME. Statistical Mechanics: Theory and Molecular Simulation [Internet]. 2010. Available from: http://www.amazon.com/Statistical-Mechanics-Molecular-Simulation-Graduate/dp/0198525265.

[2] Vlugt TJH, van der Eerden JPJM, Dijkstra M, et al. Introduction to Molecular Simulation and Statistical Thermodynamics. Computer (Long. Beach. Calif). Delft; 2009.

[3] Sharp K, Matschinsky F. Translation of Ludwig Boltzmann's Paper "On the Relationship between the Second Fundamental Theorem of the Mechanical Theory of Heat and Probability Calculations Regarding the Conditions for Thermal Equilibrium" Sitzungberichte der Kaiserlichen Akademie d. Entropy [Internet]. 2015;17:1971–2009. Available from: http://www.mdpi.com/1099-4300/17/4/1971.

[4] Frenkel D, Smit B, Ratner MA. Understanding Molecular Simulation: From Algorithms to Applications. Phys. Today. 1997;50:66–66.

[5] Siepmann JI, Frenkel D. Configurational bias Monte Carlo: a new sampling scheme for flexible chains. Mol. Phys. [Internet]. 1992;75:59–70. Available from: http://www.tandfonline.com/doi/abs/10.1080/00268979200100061.

[6] Widom B. Some Topics in the Theory of Fluids. J. Chem. Phys. [Internet]. 1963;39:2808–2812. Available from: http://aip.scitation.org/doi/10.1063/1.1734110.

[7] Ungerer P, Tavitian B, Boutin A. Applications of Molecular Simulation in the Oil and Gas: Monte Carlo Methods. Paris: Editions Technip; 2005.

[8] Hehmeyer OJ, Arya G, Panagiotopoulos AZ, et al. Monte Carlo simulation and molecular theory of tethered polyelectrolytes. J. Chem. Phys. [Internet]. 2007;126:244902. Available from: http://aip.scitation.org/doi/10.1063/1.2747600.

[9] Yang Q, Wiersum AD, Jobic H, et al. Understanding the Thermodynamic and Kinetic Behavior of the CO 2 /CH 4 Gas Mixture within the Porous Zirconium Terephthalate UiO-66(Zr): A Joint Experimental and Modeling Approach. J. Phys. Chem. C [Internet]. 2011;115:13768–13774. Available from: http://pubs.acs.org/doi/10.1021/jp202633t.

[10] Rouquerol J, Rouquerol F, Sing KSW, et al. Adsorption by Powders and Porous Solids. 2nd ed. Academic Press; 2014.

[11] Maurin G, Llewellyn PL, Bell RG. Adsorption Mechanism of Carbon Dioxide in Faujasites: Grand Canonical Monte Carlo Simulations and Microcalorimetry Measurements. J. Phys. Chem. B [Internet]. 2005;109:16084–16091. Available from: http://pubs.acs.org/doi/abs/10.1021/jp052716s.

[12] Maurin G, Bourrelly S, Llewellyn PL, et al. Simulation of the adsorption properties of CH4 in faujasites up to high pressure: Comparison with microcalorimetry. Microporous Mesoporous Mater. [Internet]. 2006;89:96–102. Available from: http://linkinghub.elsevier.com/retrieve/pii/S1387181105004634.

[13] Llewellyn PL, Maurin G. Gas adsorption microcalorimetry and modelling to characterise zeolites and related materials. Comptes Rendus Chim. [Internet]. 2005;8:283–302. Available from: http://linkinghub.elsevier.com/retrieve/pii/S1631074804003157.

[14] Verlet L. Computer "Experiments" on Classical Fluids. I. Thermodynamical Properties of Lennard-Jones Molecules. Phys. Rev. [Internet]. 1967;159:98–103. Available from: https://link.aps.org/doi/10.1103/PhysRev.159.98.

[15] Levesque D, Verlet L. Molecular dynamics and time reversibility. J. Stat. Phys. [Internet]. 1993;72:519–537. Available from: http://link.springer.com/10.1007/BF01048022.

[16] Hockney RW, Eastwood JW. Computer Simulation Using Particles. Bristol: IOP Publishing; 1988.

[17] Schofield P. Computer simulation studies of the liquid state. Comput. Phys. Commun. [Internet]. 1973;5:17–23. Available from: http://linkinghub.elsevier.com/retrieve/pii/0010465573900040.

[18] Beeman D. Some multistep methods for use in molecular dynamics calculations. J. Comput. Phys. [Internet]. 1976;20:130–139. Available from:

http://linkinghub.elsevier.com/retrieve/pii/0021999176900590.

[19] Swope WC, Andersen HC, Berens PH, et al. A computer simulation method for the calculation of equilibrium constants for the formation of physical clusters of molecules: Application to small water clusters. J. Chem. Phys. [Internet]. 1982;76:637–649. Available from: http://aip.scitation.org/doi/10.1063/1.442716.

[20] Sanchez JMC. Molecular simulations in microporous materials: adsorption and separation. University Pablo de Olavide; 2010.

[21] Ryckaert J-P, Ciccotti G, Berendsen HJC. Numerical integration of the cartesian equations of motion of a system with constraints: molecular dynamics of n-alkanes. J. Comput. Phys. [Internet]. 1977;23:327–341. Available from: http://linkinghub.elsevier.com/retrieve/pii/0021999177900985.

[22] Andersen HC. Rattle: A "velocity" version of the shake algorithm for molecular dynamics calculations. J. Comput. Phys. [Internet]. 1983;52:24–34. Available from: http://linkinghub.elsevier.com/retrieve/pii/0021999183900141.

[23] Hermansson K, Lie GC, Clementi E. On velocity scaling in molecular dynamics simulations. J. Comput. Chem. [Internet]. 1988;9:200–203. Available from: http://doi.wiley.com/10.1002/jcc.540090303.

[24] Andersen HC. Molecular dynamics simulations at constant pressure and/or temperature. J. Chem. Phys. [Internet]. 1980;72:2384–2393. Available from: http://aip.scitation.org/doi/10.1063/1.439486.

[25] Berendsen HJC, Postma JPM, van Gunsteren WF, et al. Molecular dynamics with coupling to an external bath. J. Chem. Phys. [Internet]. 1984;81:3684–3690. Available from: http://aip.scitation.org/doi/10.1063/1.448118.

[26] Turq P, Lantelme F, Friedman HL. Brownian dynamics: Its application to ionic solutions. J. Chem. Phys. [Internet]. 1977;66:3039–3044. Available from: http://jcp.aip.org/resource/1/jcpsa6/v66/i7/p3039_s1?isAuthorized=no.

[27] Nosé S. A molecular dynamics method for simulations in the canonical ensemble. Mol. Phys. 1984;52:255–268.

[28] Nosé S. A unified formulation of the constant temperature molecular dynamics methods. J. Chem. Phys. [Internet]. 1984;81:511–519. Available from: http://link.aip.org/link/?jcp/81/511.

[29] Hoover WG. Canonical dynamics: Equilibrium phase-space distributions. Phys. Rev. A [Internet]. 1985;31:1695–1697. Available from: https://link.aps.org/doi/10.1103/PhysRevA.31.1695.

[30] Parrinello M, Rahman A. Polymorphic transitions in single crystals: A new molecular dynamics method. J. Appl. Phys. [Internet]. 1981;52:7182–7190. Available from: http://aip.scitation.org/doi/10.1063/1.328693.

[31] Jobic H, Theodorou DN. Quasi-elastic neutron scattering and molecular dynamics simulation as complementary techniques for studying diffusion in zeolites. Microporous Mesoporous Mater. [Internet]. 2007;102:21–50. Available from: http://linkinghub.elsevier.com/retrieve/pii/S1387181106005725.

[32] Greathouse JA, Cygan RT, Fredrich JT, et al. Molecular Dynamics Simulation of Diffusion and Electrical Conductivity in Montmorillonite Interlayers. J. Phys. Chem. C [Internet]. 2016;120:1640–1649. Available from: http://pubs.acs.org/doi/abs/10.1021/acs.jpcc.5b10851.

[33] Volgin I V., Larin S V., Abad E, et al. Molecular Dynamics Simulations of Fullerene Diffusion in Polymer Melts. Macromolecules [Internet]. 2017;50:2207–2218. Available from: http://pubs.acs.org/doi/10.1021/acs.macromol.6b02050.

[34] Feller SE, MacKerell AD. An Improved Empirical Potential Energy Function for Molecular Simulations of Phospholipids. J. Phys. Chem. B [Internet]. 2000;104:7510–7515. Available from: http://pubs.acs.org/doi/abs/10.1021/jp0007843.

[35] Jorgensen WL, Tirado-Rives J. Potential energy functions for atomic-level simulations of water and

organic and biomolecular systems. Proc. Natl. Acad. Sci. [Internet]. 2005;102:6665–6670. Available from: http://www.pnas.org/content/102/19/6665.abstract%5Cnhttp://www.pnas.org/content/102/19/6665.full.pdf.

[36] Erkoç Ş. Empirical many-body potential energy functions used in computer simulations of condensed matter properties. Phys. Rep. [Internet]. 1997;278:79–105. Available from: http://linkinghub.elsevier.com/retrieve/pii/S0370157396000312.

[37] Jorgensen WL, Chandrasekhar J, Madura JD, et al. Comparison of simple potential functions for simulating liquid water. J. Chem. Phys. [Internet]. 1983;79:926–935. Available from: http://aip.scitation.org/doi/10.1063/1.445869.

[38] Abascal JL, Vega C. A general purpose model for the condensed phases of water: TIP4P/2005. J. Chem. Phys. 2005;123:234505.

[39] Berendsen HJC, Grigera JR, Straatsma TP. The missing term in effective pair potentials. J. Phys. Chem. [Internet]. 1987;91:6269–6271. Available from: http://pubs.acs.org/doi/abs/10.1021/j100308a038.

[40] Rick SW. A reoptimization of the five-site water potential (TIP5P) for use with Ewald sums. J. Chem. Phys. [Internet]. 2004;120:6085–6093. Available from: http://aip.scitation.org/doi/10.1063/1.1652434.

[41] Lorentz HA. Ueber die Anwendung des Satzes vom Virial in der kinetischen Theorie der Gase. Ann. Phys. [Internet]. 1881;248:127–136. Available from: http://doi.wiley.com/10.1002/andp.18812480110.

[42] Buckingham RA. The Classical Equation of State of Gaseous Helium, Neon and Argon. Proc. R. Soc. A Math. Phys. Eng. Sci. [Internet]. 1938;168:264–283. Available from: http://rspa.royalsocietypublishing.org/cgi/doi/10.1098/rspa.1938.0173.

[43] Chen L, Morrison CA, Düren T. Improving Predictions of Gas Adsorption in Metal–Organic Frameworks with Coordinatively Unsaturated Metal Sites: Model Potentials, ab initio Parameterization, and GCMC Simulations. J. Phys. Chem. C [Internet]. 2012;116:18899–18909. Available from: http://pubs.acs.org/doi/10.1021/jp3062527.

[44] Yoon JW, Chang H, Lee S-J, et al. Selective nitrogen capture by porous hybrid materials containing accessible transition metal ion sites. Nat. Mater. [Internet]. 2016;16:526–531. Available from: http://www.nature.com/doifinder/10.1038/nmat4825.

[45] Sweatman MB, Quirke N. Characterization of Porous Materials by Gas Adsorption at Ambient Temperatures and High Pressure. J. Phys. Chem. B [Internet]. 2001;105:1403–1411. Available from: http://pubs.acs.org/doi/abs/10.1021/jp003308l.

[46] De Rocco AG, Halford JO. Intermolecular Potentials of Argon, Methane, and Ethane. J. Chem. Phys. [Internet]. 1958;28:1152–1154. Available from: http://aip.scitation.org/doi/10.1063/1.1744359.

[47] Ewald PP. Die Berechnung optischer und elektrostatischer Gitterpotentiale. Ann. Phys. [Internet]. 1921;369:253–287. Available from: http://doi.wiley.com/10.1002/andp.19213690304.

[48] Vitale G, Mellot CF, Bull LM, et al. Neutron Diffraction and Computational Study of Zeolite NaX: Influence of SIII‘ Cations on Its Complex with Benzene. J. Phys. Chem. B [Internet]. 1997;101:4559–4564. Available from: http://pubs.acs.org/doi/abs/10.1021/jp970393x.

[49] Maurin G, Senet P, Devautour S, et al. Combining the Monte Carlo Technique with 29 SI NMR Spectroscopy: Simulations of Cation Locations in Zeolites with Various Si/Al Ratios. J. Phys. Chem. B [Internet]. 2001;105:9157–9161. Available from: http://pubs.acs.org/doi/abs/10.1021/jp011789i.

[50] Vanduyfhuys L, Rogge SMJ, Wieme J, et al. Thermodynamic insight into stimuli-responsive behaviour of soft porous crystals. Nat. Commun. [Internet]. 2018;9:204. Available from: http://dx.doi.org/10.1038/s41467-017-02666-y.

[51] Franklin RE. Crystallite Growth in Graphitizing and Non-Graphitizing Carbons. Proc. R. Soc. A Math. Phys. Eng. Sci. [Internet]. 1951;209:196–218. Available from: http://rspa.royalsocietypublishing.org/cgi/doi/10.1098/rspa.1951.0197.

[52] Olivier JP. Improving the models used for calculating the size distribution of micropore volume of activated carbons from adsorption data. Carbon N. Y. 1998;36:1469–1472.

[53] McDonald-Wharry JS, Manley-Harris M, Pickering KL. Reviewing, Combining, and Updating the Models for the Nanostructure of Non-Graphitizing Carbons Produced from Oxygen-Containing Precursors. Energy & Fuels [Internet]. 2016;30:7811–7826. Available from: http://pubs.acs.org/doi/10.1021/acs.energyfuels.6b00917.

[54] Rappé AKK, Casewit CJJ, Colwell KSS, et al. UFF, a Full Periodic Table Force Field for Molecular Mechanics and Molecular Dynamics Simulations. J. Am. Chem. Soc. 1992;114:10024–10035.

[55] Mayo SL, Olafson BD, Iii W a G, et al. DREIDING: A Generic Force Field for Molecular Simulations. J. Phys. Chem. 1990;101:8897–8909.

[56] Jorgensen WL, Maxwell DS, Tirado-Rives J. Development and Testing of the OPLS All-Atom Force Field on Conformational Energetics and Properties of Organic Liquids. J. Am. Chem. Soc. [Internet]. 1996;118:11225–11236. Available from: http://pubs.acs.org/doi/abs/10.1021/ja9621760.

[57] Maurin G, Llewellyn P, Poyet T, et al. Influence of Extra-Framework Cations on the Adsorption Properties of X-Faujasite Systems: Microcalorimetry and Molecular Simulations. J. Phys. Chem. B [Internet]. 2005;109:125–129. Available from: http://pubs.acs.org/doi/abs/10.1021/jp0461753.

[58] Demontis P, Suffritti GB, Tilocca A. Diffusion and vibrational relaxation of a diatomic molecule in the pore network of a pure silica zeolite: A molecular dynamics study. J. Chem. Phys. [Internet]. 1996;105:5586–5594. Available from: http://aip.scitation.org/doi/10.1063/1.472398.

[59] Ndjaka JMB, Zwanenburg G, Smit B, et al. Molecular simulations of adsorption isotherms of small alkanes in FER-, TON-, MTW- and DON-type zeolites. Microporous Mesoporous Mater. 2004;68:37–43.

[60] Rappe AK, Goddard WA. Charge equilibration for molecular dynamics simulations. J. Phys. Chem. [Internet]. 1991;95:3358–3363. Available from: http://pubs.acs.org/doi/abs/10.1021/j100161a070.

[61] Gasteiger J, Marsili M. Iterative partial equalization of orbital electronegativity—a rapid access to atomic charges. Tetrahedron [Internet]. 1980;36:3219–3228. Available from: http://linkinghub.elsevier.com/retrieve/pii/0040402080801682.

[62] Mulliken RS. Electronic Population Analysis on LCAO–MO Molecular Wave Functions. I. J. Chem. Phys. [Internet]. 1955;23:1833–1840. Available from: http://aip.scitation.org/doi/10.1063/1.1740588.

[63] Heinz H, Suter UW. Atomic Charges for Classical Simulations of Polar Systems. J. Phys. Chem. B [Internet]. 2004;108:18341–18352. Available from: http://pubs.acs.org/doi/abs/10.1021/jp048142t.

[64] Breneman CM, Wiberg KB. Determining atom-centered monopoles from molecular electrostatic potentials. The need for high sampling density in formamide conformational analysis. J. Comput. Chem. [Internet]. 1990;11:361–373. Available from: http://doi.wiley.com/10.1002/jcc.540110311.

[65] Chaplin M. Water Models [Internet]. [cited 2018 Sep 12]. Available from: http://www1.lsbu.ac.uk/water/water_models.html.

[66] Horn HW, Swope WC, Pitera JW, et al. Development of an improved four-site water model for biomolecular simulations: TIP4P-Ew. J. Chem. Phys. [Internet]. 2004;120:9665–9678. Available from: http://aip.scitation.org/doi/10.1063/1.1683075.

[67] Born M, Oppenheimer R. Zur Quantentheorie der Molekeln. Ann. Phys. [Internet]. 1927;389:457–484. Available from: http://doi.wiley.com/10.1002/andp.19273892002.

[68] Capelle K. A bird's-eye view of density-functional theory. Brazilian J. Phys. [Internet]. 2006;36:1318–1343. Available from: http://www.scielo.br/scielo.php?script=sci_arttext&pid=S0103-97332006000700035&lng=en&nrm=iso&tlng=en.

[69] Hohenberg P, Kohn W. Inhomogeneous Electron Gas. Phys. Rev. [Internet]. 1964;136:B864–B871. Available from: https://link.aps.org/doi/10.1103/PhysRev.136.B864.

[70] Kohn W, Sham LJ. Self-Consistent Equations Including Exchange and Correlation Effects. Phys. Rev. [Internet]. 1965;140:A1133–A1138. Available from: https://link.aps.org/doi/10.1103/PhysRev.140.A1133.

[71] Perdew JP, Zunger A. Self-interaction correction to density-functional approximations for many-electron systems. Phys. Rev. B [Internet]. 1981;23:5048–5079. Available from: https://link.aps.org/doi/10.1103/PhysRevB.23.5048.

[72] Perdew JP, Wang Y. Accurate and simple analytic representation of the electron-gas correlation energy. Phys. Rev. B [Internet]. 1992;45:13244–13249. Available from: https://link.aps.org/doi/10.1103/PhysRevB.45.13244.

[73] Perdew JP, Burke K, Ernzerhof M. Generalized Gradient Approximation Made Simple. Phys. Rev. Lett. [Internet]. 1996;77:3865–3868. Available from: http://link.aps.org/doi/10.1103/PhysRevLett.77.3865.

[74] Perdew JP, Burke K, Ernzerhof M. Generalized Gradient Approximation Made Simple [Phys. Rev. Lett. 77, 3865 (1996)]. Phys. Rev. Lett. [Internet]. 1997;78:1396. Available from: http://link.aps.org/doi/10.1103/PhysRevLett.78.1396.

[75] Stephens PJ, Devlin FJ, Chabalowski CF, et al. Ab Initio Calculation of Vibrational Absorption and Circular Dichroism Spectra Using Density Functional Force Fields. J. Phys. Chem. [Internet]. 1994;98:11623–11627. Available from: http://pubs.acs.org/doi/abs/10.1021/j100096a001.

[76] Mahan GD. Homogeneous Electron Gas. Many-Particle Phys. [Internet]. Boston, MA: Springer US; 2000. p. 295–374. Available from: https://doi.org/10.1007/978-1-4757-5714-9_5.

[77] Vosko SH, Wilk L, Nusair M. Accurate spin-dependent electron liquid correlation energies for local spin density calculations: a critical analysis. Can. J. Phys. [Internet]. 1980;58:1200–1211. Available from: http://www.nrcresearchpress.com/doi/abs/10.1139/p80-159.

[78] Perdew JP, Chevary JA, Vosko SH, et al. Atoms, molecules, solids, and surfaces: Applications of the generalized gradient approximation for exchange and correlation. Phys. Rev. B [Internet]. 1992;46:6671–6687. Available from: https://link.aps.org/doi/10.1103/PhysRevB.48.4978.2.

[79] Lee C, Yang W, Parr RG. Development of the Colle-Salvetti correlation-energy formula into a functional of the electron density. Phys. Rev. B [Internet]. 1988;37:785–789. Available from: https://link.aps.org/doi/10.1103/PhysRevB.37.785.

[80] Becke AD. Density-functional exchange-energy approximation with correct asymptotic behavior. Phys. Rev. A. 1988;38:3098–3100.

[81] Perdew JP, Ernzerhof M, Burke K. Rationale for mixing exact exchange with density functional approximations. J. Chem. Phys. [Internet]. 1996;105:9982–9985. Available from: http://aip.scitation.org/doi/10.1063/1.472933.

[82] Kim K, Jordan KD. Comparison of Density Functional and MP2 Calculations on the Water Monomer and Dimer. J. Phys. Chem. [Internet]. 1994;98:10089–10094. Available from: http://pubs.acs.org/doi/abs/10.1021/j100091a024.

[83] Grimme S. Density functional theory with London dispersion corrections. Wiley Interdiscip. Rev. Comput. Mol. Sci. 2011;1:211–228.

[84] Dilabio GA, Otero-de-la-Roza A. Noncovalent interactions in density functional theory. In: Parril AL, Lipkowitz KB, editors. Rev. Comput. Chem. Vol. 29. 1st ed. John Wiley & Sons, Ltd; 2016. p. 1–97.

[85] Grimme S. Accurate description of van der Waals complexes by density functional theory including empirical corrections. J. Comput. Chem. [Internet]. 2004;25:1463–1473. Available from: http://doi.wiley.com/10.1002/jcc.20078.

[86] Grimme S. Semiempirical GGA-type density functional constructed with a long-range dispersion correction. J. Comput. Chem. [Internet]. 2006;27:1787–1799. Available from: http://doi.wiley.com/10.1002/jcc.20495.

[87] Jurečka P, Černý J, Hobza P, et al. Density functional theory augmented with an empirical dispersion

term. Interaction energies and geometries of 80 noncovalent complexes compared with ab initio quantum mechanics calculations. J. Comput. Chem. [Internet]. 2007;28:555–569. Available from: http://doi.wiley.com/10.1002/jcc.20570.

[88] Ortmann F, Bechstedt F, Schmidt WG. Semiempirical van der Waals correction to the density functional description of solids and molecular structures. Phys. Rev. B [Internet]. 2006;73:205101. Available from: https://link.aps.org/doi/10.1103/PhysRevB.73.205101.

[89] Grimme S, Antony J, Ehrlich S, et al. A consistent and accurate ab initio parametrization of density functional dispersion correction (DFT-D) for the 94 elements H-Pu. J. Chem. Phys. [Internet]. 2010;132:154104. Available from: http://aip.scitation.org/doi/10.1063/1.3382344.

[90] Tkatchenko A, Scheffler M. Accurate Molecular Van Der Waals Interactions from Ground-State Electron Density and Free-Atom Reference Data. Phys. Rev. Lett. [Internet]. 2009;102:073005. Available from: https://link.aps.org/doi/10.1103/PhysRevLett.102.073005.

[91] Fischer M, Gomes JRB, Jorge M. Computational approaches to study adsorption in MOFs with unsaturated metal sites. Mol. Simul. [Internet]. 2014;40:537–556. Available from: http://dx.doi.org/10.1080/08927022.2013.829228.

[92] Haldoupis E, Borycz J, Shi H, et al. Ab Initio Derived Force Fields for Predicting CO 2 Adsorption and Accessibility of Metal Sites in the Metal–Organic Frameworks M-MOF-74 (M = Mn, Co, Ni, Cu). J. Phys. Chem. C [Internet]. 2015;119:16058–16071. Available from: http://pubs.acs.org/doi/10.1021/acs.jpcc.5b03700.

[93] Campbell C, Ferreiro-Rangel CA, Fischer M, et al. A transferable model for adsorption in mofs with unsaturated metal sites. J. Phys. Chem. C. 2017;121:441–458.

[94] Williams M, Schwarz PA, Law BE, et al. Numerical Optimization [Internet]. Glob. Chang. Biol. Springer New York; 2006. Available from: http://www.biogeosciences-discuss.net/11/12733/2014/%5Cnhttp://www.deepdyve.com/lp/elsevier/the-reflex-project-comparing-different-algorithms-and-implementations-mUMVk0bx1v%5Cnhttp://books.google.co.uk/books/about/Numerical_Optimization.html?id=epc5fX0lqR.

[95] Reed AE, Weinstock RB, Weinhold F. Natural population analysis. J. Chem. Phys. [Internet]. 1985;83:735–746. Available from: http://aip.scitation.org/doi/10.1063/1.449486.

[96] Bader RFW. Atoms in Molecules. Encycl. Comput. Chem. [Internet]. Chichester, UK: John Wiley & Sons, Ltd; 2002. p. xviii, 438 p. Available from: http://doi.wiley.com/10.1002/0470845015.caa012.

[97] Manz TA, Sholl DS. Improved Atoms-in-Molecule Charge Partitioning Functional for Simultaneously Reproducing the Electrostatic Potential and Chemical States in Periodic and Nonperiodic Materials. J. Chem. Theory Comput. [Internet]. 2012;8:2844–2867. Available from: http://pubs.acs.org/doi/10.1021/ct3002199.

[98] Marenich A V., Jerome S V., Cramer CJ, et al. Charge Model 5: An Extension of Hirshfeld Population Analysis for the Accurate Description of Molecular Interactions in Gaseous and Condensed Phases. J. Chem. Theory Comput. [Internet]. 2012;8:527–541. Available from: http://pubs.acs.org/doi/10.1021/ct200866d.

[99] Hirshfeld FL. Bonded-atom fragments for describing molecular charge densities. Theor. Chim. Acta [Internet]. 1977;44:129–138. Available from: http://link.springer.com/10.1007/BF00549096.

[100] Hamad S, Balestra SRG, Bueno-Perez R, et al. Atomic charges for modeling metal–organic frameworks: Why and how. J. Solid State Chem. [Internet]. 2015;223:144–151. Available from: http://linkinghub.elsevier.com/retrieve/pii/S0022459614003521.

[101] Singh UC, Kollman PA. An approach to computing electrostatic charges for molecules. J. Comput. Chem. [Internet]. 1984;5:129–145. Available from: http://doi.wiley.com/10.1002/jcc.540050204.

[102] Tuckerman ME, Ungar PJ, VonRosenvinge T, et al. Ab initio molecular dynamics simulations. J. Phys. Chem. 1996;100:12878–12887.

[103] Ikeda T, Sprik M, Terakura K, et al. Pressure Effects on Hydrogen Bonding in the Disordered Phase of Solid HBr. Phys. Rev. Lett. [Internet]. 1998;81:4416–4419. Available from: https://link.aps.org/doi/10.1103/PhysRevLett.81.4416.

[104] Ruiz E, Payne MC. One-Dimensional Intercalation Compound 2 HgS·SnBr2: Ab Initio Electronic Structure Calculations and Molecular Dynamics Simulations. Chem. - A Eur. J. [Internet]. 1998;4:2485–2492. Available from: http://doi.wiley.com/10.1002/%28SICI%291521-3765%2819981204%294%3A12%3C2485%3A%3AAID-CHEM2485%3E3.0.CO%3B2-L.

[105] Meier RJ, van Doremaele GHJ, Iarlori S, et al. Ab Initio Molecular Dynamics Study of Metallocene-Catalyzed Ethylene Polymerization. J. Am. Chem. Soc. [Internet]. 1994;116:7274–7281. Available from: http://pubs.acs.org/doi/abs/10.1021/ja00095a034.

[106] Wallace DS, Stoneham AM, Hayes W, et al. Theory of defects in conducting polymers. I. Theoretical principles and simple applications. J. Phys. Condens. Matter [Internet]. 1991;3:3879–3903. Available from: http://stacks.iop.org/0953-8984/3/i=22/a=002?key=crossref.438ae562786d4286ec255766be108917.

[107] Hageman JCL, Meier RJ, Heinemann M, et al. Young Modulus of Crystalline Polyethylene from ab Initio Molecular Dynamics. Macromolecules [Internet]. 1997;30:5953–5957. Available from: http://pubs.acs.org/doi/abs/10.1021/ma9703721.

[108] Miyake T, Ogitsu T, Tsuneyuki S. Quantum Distributions of Muonium and Hydrogen in Crystalline Silicon. Phys. Rev. Lett. [Internet]. 1998;81:1873–1876. Available from: https://link.aps.org/doi/10.1103/PhysRevLett.81.1873.

[109] Wang C, Zhang Q-M. Amphoteric charge states and diffusion barriers of hydrogen in GaAs. Phys. Rev. B [Internet]. 1999;59:4864–4868. Available from: https://link.aps.org/doi/10.1103/PhysRevB.59.4864.

[110] Miyake T, Ogitsu T, Tsuneyuki S. First-principles study of the quantum states of muonium and hydrogen in crystalline silicon. Phys. Rev. B [Internet]. 1999;60:14197–14204. Available from: http://link.aps.org/doi/10.1103/PhysRevB.60.14197.

[111] Capaz RB, Assali LVC, Kimerling LC, et al. Mechanism for hydrogen-enhanced oxygen diffusion in silicon. Phys. Rev. B [Internet]. 1999;59:4898–4900. Available from: https://link.aps.org/doi/10.1103/PhysRevB.59.4898.

[112] Hassanali A, Prakash MK, Eshet H, et al. On the recombination of hydronium and hydroxide ions in water. Proc. Natl. Acad. Sci. [Internet]. 2011;108:20410–20415. Available from: http://www.pnas.org/cgi/doi/10.1073/pnas.1112486108.

[113] Devanathan R, Idupulapati N, Baer MD, et al. Ab Initio Molecular Dynamics Simulation of Proton Hopping in a Model Polymer Membrane. J. Phys. Chem. B [Internet]. 2013;117:16522–16529. Available from: http://pubs.acs.org/doi/10.1021/jp410229u.

[114] Mei HS, Tuckerman ME, Sagnella DE, et al. Quantum Nuclear ab Initio Molecular Dynamics Study of Water Wires. J. Phys. Chem. B [Internet]. 1998;102:10446–10458. Available from: http://dx.doi.org/10.1021/jp982623t.

[115] Chenoweth K, van Duin ACT, Goddard WA. ReaxFF Reactive Force Field for Molecular Dynamics Simulations of Hydrocarbon Oxidation. J. Phys. Chem. A [Internet]. 2008;112:1040–1053. Available from: http://pubs.acs.org/doi/abs/10.1021/jp709896w.

[116] van Duin ACT, Strachan A, Stewman S, et al. ReaxFF SiO Reactive Force Field for Silicon and Silicon Oxide Systems. J. Phys. Chem. A [Internet]. 2003;107:3803–3811. Available from: http://pubs.acs.org/doi/abs/10.1021/jp0276303.

[117] Nielson KD, van Duin ACT, Oxgaard J, et al. Development of the ReaxFF Reactive Force Field for Describing Transition Metal Catalyzed Reactions, with Application to the Initial Stages of the Catalytic Formation of Carbon Nanotubes. J. Phys. Chem. A [Internet]. 2005;109:493–499. Available from: http://pubs.acs.org/doi/abs/10.1021/jp046244d.

[118] Van Duin a. CT, Dasgupta S, Lorant F, et al. ReaxFF: A reactive force field for hydrocarbons. J. Phys.

Chem. A. 2001;105:9396–9409.

[119] Wu Y, Chen H, Wang F, et al. An Improved Multistate Empirical Valence Bond Model for Aqueous Proton Solvation and Transport †. J. Phys. Chem. B [Internet]. 2008;112:467–482. Available from: http://pubs.acs.org/doi/abs/10.1021/jp076658h.

[120] Warshel A, Weiss RM. An empirical valence bond approach for comparing reactions in solutions and in enzymes. J. Am. Chem. Soc. [Internet]. 1980;102:6218–6226. Available from: http://pubs.acs.org/doi/abs/10.1021/ja00540a008.

[121] Marx D, Hutter J. Ab Initio Molecular Dynamics [Internet]. Angew. Chemie Int. Ed. Cambridge: Cambridge University Press; 2009. Available from: http://books.google.com.hk/books?id=1Ijmiw_EchIC.

[122] Raynaud C. Dynamique moléculaire ab initio en base locale: principes et applications. Université Paul Sabatier - Toulouse III; 2005.

[123] Klein S, Bearpark MJ, Smith BR, et al. Mixed state `on the fly' non-adiabatic dynamics: the role of the conical intersection topology. Chem. Phys. Lett. [Internet]. 1998;292:259–266. Available from: http://linkinghub.elsevier.com/retrieve/pii/S0009261498006812.

[124] Garavelli M, Bernardi F, Olivucci M, et al. Product Distribution in the Photolysis of s-cis Butadiene: A Dynamics Simulation. J. Phys. Chem. A [Internet]. 2001;105:11496–11504. Available from: http://pubs.acs.org/doi/abs/10.1021/jp012058l.

[125] Choe Y-K, Tsuchida E, Ikeshoji T, et al. Nature of proton dynamics in a polymer electrolyte membrane, nafion: a first-principles molecular dynamics study. Phys. Chem. Chem. Phys. [Internet]. 2009;11:3892. Available from: http://xlink.rsc.org/?DOI=b819535h.

[126] Dal Peraro M, Ruggerone P, Raugei S, et al. Investigating biological systems using first principles Car–Parrinello molecular dynamics simulations. Curr. Opin. Struct. Biol. [Internet]. 2007;17:149–156. Available from: http://linkinghub.elsevier.com/retrieve/pii/S0959440X07000486.

[127] Schulte M, Frank I. Car-Parrinello simulations of Prussian blue: Structure, dynamics, and electronic properties. J. Phys. Chem. C. 2011;115:13560–13565.

CHAPTER 3

Computational exploration of Proton conduction in porous materials

I. Introduction and contribution

This chapter exposes the computational strategy and the corresponding specific tools that we developed to get insight into the water-mediated proton conduction in porous materials at the microscopic scale. This approach was applied to two MOFs, i.e. the 3D MIL-163 and the 2D KAUST-7', and one phosphate 3D material, namely the $Ti^{IV}Ti^{IV}(HPO_4)_4$, that were revealed during the course of the PhD as superprotonic conductors by complex impedance spectroscopy (CIS) measurements [1]. This joint simulation-experimental effort resulted in the publication of three articles provided at the end of this chapter.

Modelling the water-mediated proton conduction in porous media is a challenging task since this process usually involves several phenomena which occur concomitantly, such as the bond breaking/formation associated with the proton motion, the dynamics of other guest molecules, and the global or local structural rearrangements of the host framework that may take place in response to the dynamics of the protons. Different computational strategies have been employed to describe the water-mediated proton conduction mechanisms in MOF materials. They can be distinguished by the way that the interactions between the water and the host framework are determined.

(1) On the one hand, the potential energy has been modelled with classical forcefields that are implemented in Monte Carlo and Molecular Dynamics simulations. In most cases, the bond breaking/formation associated with the proton motion is not described and the proton conduction mechanism was discussed in light of the hydrogen bond network formed by the proton source and the proton carriers that defines a preferential pathway for the proton to migrate through the porosity of the solid. This approach was followed for instance in the work reported by Sanda *et al.* [2], who applied Monte Carlo calculations to explore the preferential arrangement of water molecules and their preferential interactions with carboxylate groups in two Zn-based MOFs with 1D and 2D topologies and correlated this information to their proton conduction properties. A similar strategy was followed by Yang *et al.* [3], who described by Monte Carlo the adsorption sites of water in the UiO-66 based MOFs, whose BDC linker was grafted with different polar functions. They suggested a plausible proton conduction mechanism in the best proton conductive MOFs, i.e. UiO-

66(Zr)-CO_2H and UiO-66(Zr)-SO_3H. On the other hand, unconventional methods such as the Empirical Valence Bond (EVB) [4,5] or the Reactive Forcefield (ReaxFF) [6] can describe the bond breaking/formation associated with the proton conduction. Using the EVB formalism, Paesani *et al.* [7] conducted MD simulations to characterize the structure, thermodynamics, and dynamics of the hydrated proton in the MOF MIL-53(Cr). A similar strategy was also followed by the group [8,9] to explore the proton migration mechanism in UiO-66(Zr)-$2CO_2H$.

(2) The potential energy surface has been also determined using quantum calculations. Although very accurate, these calculations demand high computation time. As a result, in some cases, these calculations were performed to determine the preferential arrangement of water by geometry optimization to further suggest proton migration pathways [10,11]. Such calculations have been also performed dynamically, under the formalisms of *Ab Initio* Molecular Dynamics (AIMD) techniques. This has been for instance reported in the work of Grancha *et al.* [12], who theoretically determined a complete cycle of proton motion through hydrogen bonds with as a starting point isolated clusters of water molecules whose relative positions were experimentally resolved in a *bio*MOF. In another work, Ling and Slater [13] correlated the proton conductivity of UiO-66 to the interaction of surrounding water molecules with vacant metal sites. In the work proposed by Eisben *et al.* [14,15], the role of the imidazole protic solvent confined in the pores of MOF MIL-53(Cr) was analyzed using AIMD simulations, which unambiguously correlated the increase of the proton conductivity performances with the adsorption of imidazole in the constrained environment.

Here, we used three different computational approaches, i.e. classical MC and MD as well as AIMD methods, to get insight on the water-mediated proton conduction mechanism in 3 porous materials.

(1) Typically, MC simulations in the Grand Canonical (μVT) ensemble were first conducted to predict the water adsorption isotherms that were further compared to the corresponding experimental data to validate the forcefield parameters to describe the interactions between water and the host frameworks. This was especially applied to $Ti^{IV}Ti^{IV}(HPO_4)_4$, as seen in section IV. The MC methodology was also applied with two

additional objectives. MC simulations in the Canonical (NVT) ensemble were performed to (i) determine the preferential conformation/distribution of water and/or inherent guest molecules and anticipate the possible proton conduction pathways in the anhydrous and hydrated states of the MIL-163(Zr) and (ii) generate starting configurations for subsequent MD calculations on the $Ti^{IV}Ti^{IV}(HPO_4)_4$ and KAUST-7'. All these MC simulations were carried out with a large number of steps (2×10^8 production steps preceded by 10^7 equilibration steps). This is particularly important since the computational description of the behavior of water in confined systems usually demands a large number of steps to achieve equilibrium. These MC simulations were conducted by considering the host frameworks with their atoms fixed in their initial positions. This assumption is often made when the pore dimensions of a given framework significantly exceed the kinetic diameters of the guest molecules and when the structure does not undergo any guest-induced structural transformations [16]. This approximation was applied to MIL-163(Zr) which shows a pore size much larger than the dimension of water. For porous solids with a higher degree of confinement, as the $Ti^{IV}Ti^{IV}(HPO_4)_4$ or the KAUST-7', this assumption needs to be taken with caution. There are some strategies to overcome this limitation under the theoretical backbone of the Monte Carlo calculations, such as the Hybrid Monte Carlo (GCMD) [17,18] or the Hybrid Osmotic Monte Carlo (HOMC) [19] methodologies. They generally rely on accurate bonded potentials forcefields to describe the flexibility of the framework. Here, we adopted two strategies to describe the structural relaxation of the framework: (i) the implementation of a flexible forcefield for the host framework in classical MD for $Ti^{IV}Ti^{IV}(HPO_4)_4$ and (ii) AIMD calculations for KAUST-7'.

(2) Classical MD calculations implementing a flexible force field were used to describe the local relaxation of the phosphate groups (POH) in the water-saturated $Ti^{IV}Ti^{IV}(HPO_4)_4$, with all the remaining structural atoms of the porous material kept fixed in their initial positions. The intramolecular parameters associated with the P–O and O–H bonds and the P–O–H angle were taken from a previous work dedicated to the modelling of Zr-phosphates [20]. The O–P–O–H torsional parameters were determined using a cosine potential with a constant force of 52 $kcal.mol^{-1}$, adjusted in order to achieve the usual average fluctuation of 30° during a MD run in the anhydrous material. This partially flexible model

makes sense considering that the expected lability of these functional groups is far superior to the ones of the other atoms of this inorganic material. These calculations were conducted with a large equilibration time (10 ns) and with the temperature kept constant using the Nose-Hoover thermostat [21–23]. These calculations allowed us to get a more realistic description of the H_2O distribution at the vicinity of the POH as well as in the pores.

(3) The AIMD approach was another strategy adopted to describe the structural rearrangements of the MOF framework in the presence of guests. This technique allowed us not only to study the behavior of the water molecules in a highly confined environment using a fully flexible model, but also gave insights on the proton conduction mechanism, since it describes the bond breaking/forming inherent to the proton conduction phenomena. This methodology was applied to describe the structural rearrangements of KAUST-7' and $Ti^{IV}Ti^{IV}(HPO_4)_4$ as well as the proton migration.

A complete portray of the water-mediated proton conduction in porous materials can be achieved by making use of analytical tools that indicate the level of connectivity and aggregation of the water molecules in the solid. In this thesis, two main analytical techniques were developed to study these variables to allow the analysis of the hydrogen bond network and the clustering effect. The hydrogen bond analysis is of importance since in all the studied systems, the low experimentally measured activation energies (Ea < 0.4 eV) strongly suggested that a Grotthus-based mechanism governs the proton migration (see chapter 1, section I.4). The clustering analysis, on the other hand, provides a measure of how extensive a continuous network of interacting water molecules can be obtained in the pores of the materials. This parameter is especially relevant to evaluate the maximum extension to which a proton transmission network can be achieved. In these calculations, hydrogen bonds are considered as the association of a donor (D) atom, a hydrogen (H) and an acceptor (A) atom, where both donor and acceptors may be any of the light electronegative atoms generally associated with H-bonds (N, O and F) (see chapter 1). In the literature, the criteria adopted to the definition of a hydrogen bond are somewhat general but usually based on the energy and the geometry of the hydrogen bonds [24]. With the energetic criteria, the hydrogen bond is defined when the mutual interaction energy between two molecules is higher than a threshold value [25,26], while the geometric criteria asserts that the hydrogen bond is determined by

the relative configuration of such neighboring molecules [25,27]. In this thesis, we used only the geometric criteria to determine the hydrogen bonds. They are then accounted when the D–A distance is below 3.5 Å and the angle formed between the D–H and the D–A vectors (A-D-H angle) is below 37° (i.e. a complementary angle of the one described in chapter 1, section I.4), a criterion compatible to what has been used in other works [25,27–30]. The validity of the distance criteria is usually tested by considering the peak position of the maximum of the radial distribution function of the donor and acceptor species, where usually a 3.5 Å distance is an acceptable value. The angle criteria, however, is more system dependent. In order to test the validity of such criteria, a screening of the probability density of species with D-A distance below 3.5 Å was performed. Typically Figure 3.1 reports the probability density plots of the interactions between water molecules and phenol groups and between the water molecules themselves in the case of water confined in MIL-163(Zr). Since the majority of the interactions are observed for acute values of A-D-H lesser than 37°, this angle was considered as an acceptable limit for describing the hydrogen bond interactions in the hydrated MIL-163(Zr). Such a preliminary analysis was then conducted for all solids prior to perform the hydrogen bond analysis.

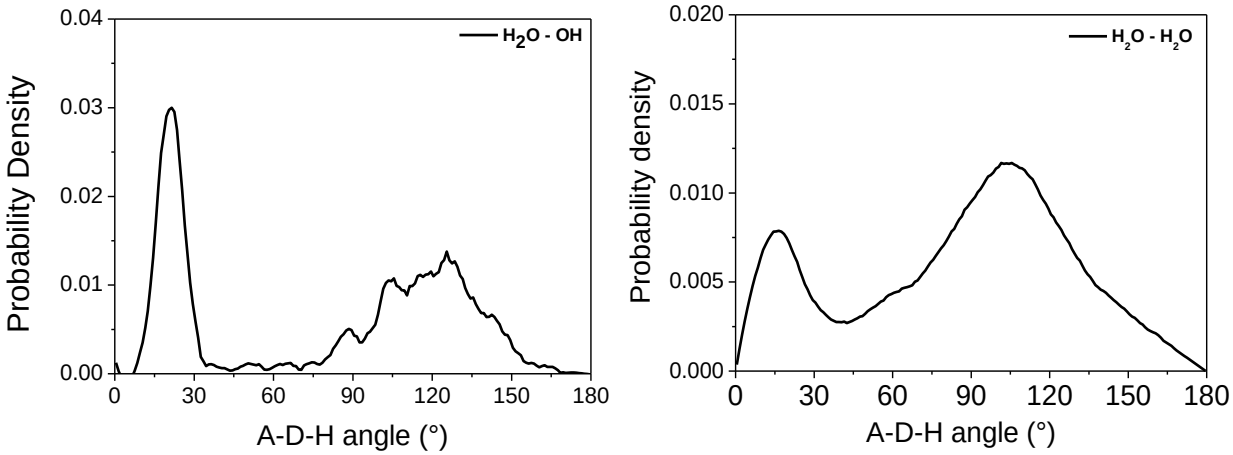

Figure 3.1. Distribution of the angles between the D-A vector and the D-H vector for donor-acceptor separated by a distance lower than 3.5 Å. These distributions are averaged over the MC configurations generated for the hydrated MIL-163(Zr). Interactions between H_2O and the phenol groups of the framework (see chapter 3, section II) (a) and with themselves (b) are evaluated.

Further, the main parameter that controls the definition of the water cluster is the critical cluster radius (CCR) corresponding to the maximum distance between two

neighboring water molecules used to determine that they are sufficiently close to each other to be considered part of the same cluster. It is thus possible to define the aggregation of water molecules in a continuous superstructure using a neighboring list algorithm [31]. In this thesis, we used a CCR of 3.1 Å, corresponding to the first interaction peak of the O – O RDF for liquid water [30]. This aggregation quantification was used to support the visual inspection of the molecules aggregation in representative snapshots.

In the following sections, we listed the main results obtained resulting from the application of the different simulations techniques and analytical tools described above to the microscopic description of the proton conduction mechanism in MIL-163(Zr), KAUST-7' and $Ti^{IV}Ti^{IV}(HPO_4)_4$.

II. MIL-163(Zr)

MIL-163(Zr) is a MOF with 12 Å (see pore size distribution in Figure 3.2) square-shaped 1D pores formed from the association of ZrO_8 edge-sharing polyhedra with four phenolic organic linker TzGal [5,5′-(1,2,4,5-tetrazine-3,6-diyl)bis(benzene-1,2,3-triol)], defining chains running along the [001] direction [32]. DMA (N,N-dimethylamine) is used as solvent in the synthesis procedure and stays as inherent guest molecules in the pores even after activation procedures. Since the phenol groups are the Brønsted acidic groups in this framework, they are considered as the main proton sources for the proton conduction observed in this material. Complex Impedance Spectroscopy measurements revealed that this structure shows a superprotonic conductivity ($\sigma_{90°C}$ = 2.1×10-3 S.cm-1) in its hydrated state, while the proton conduction is very low in the anhydrous state ($\sigma_{90°C}$ = 1.5×10-13 S.cm-1).

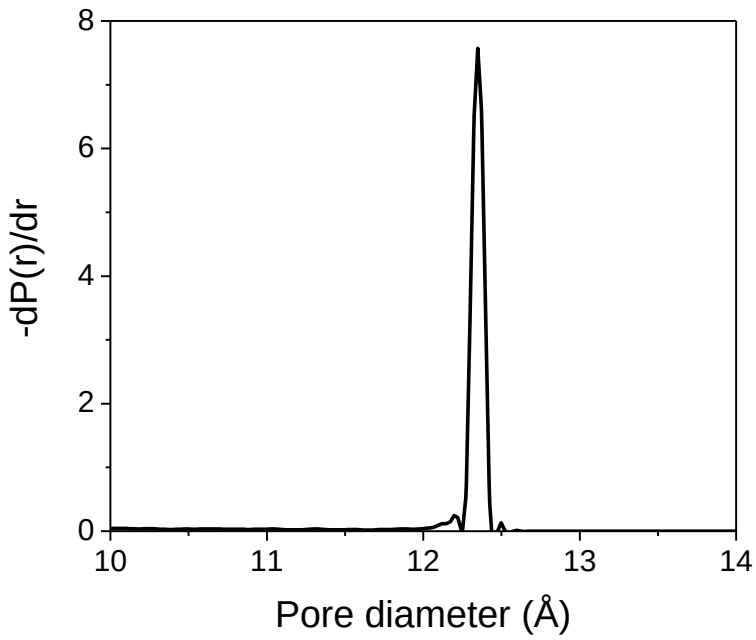

Figure 3.2 – Calculated pore size distribution of the DFT-optimized crystal structure of the MIL-163(Zr).

The DMA containing MOF framework was firstly investigated in the anhydrous and the water saturated states of the MOF using MC simulations in the canonical ensemble (NVT). These simulations revealed a difference in the organization of the DMA molecules in both cases. In the anhydrous state, these guest molecules are well-localized in the vicinity of the pore wall (cf. Figure 3.3a), each of them establishing hydrogen bonds with a single

phenol group (cf. Figure 3.4a). Furthermore these DMA molecules were found to be isolated from each other as shown by the characteristic separating distances between their carbon atoms (C_{DMA}) above 5 Å (Figure 3.4a). This scenario hampers the formation of a long-range hydrogen bond pathway for proton migration, limiting the proton transmission. This outcome explains the poor proton conductivity measured on the anhydrous MOF.

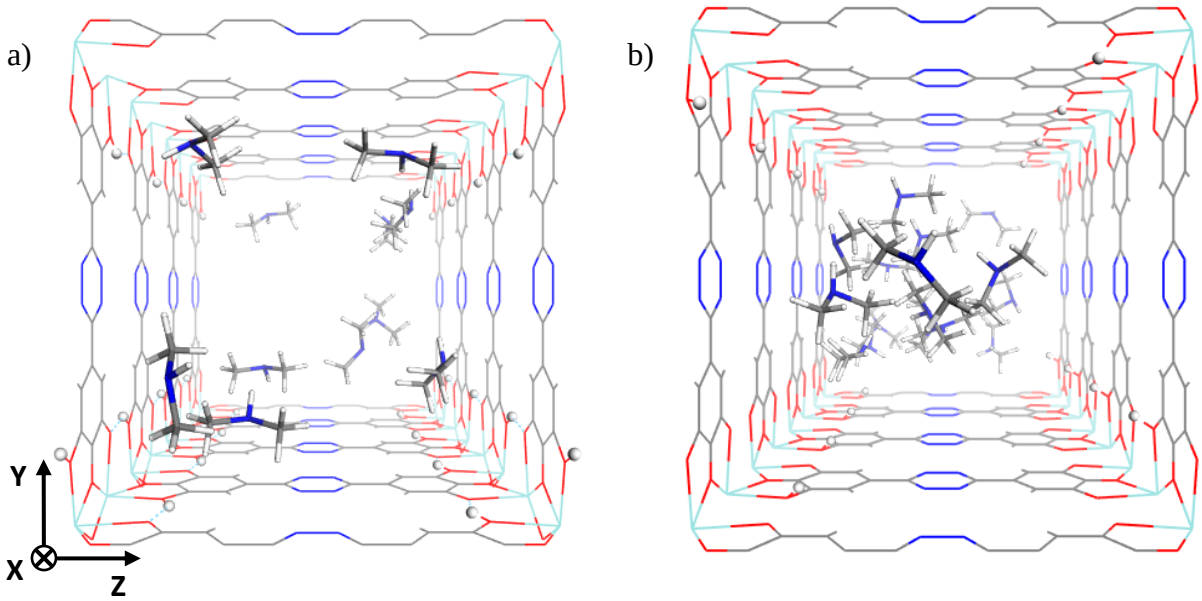

Figure 3.3 – Preferential arrangements of the DMA molecules in the pores of MIL-163(Zr) originated from MC calculations in the anhydrous (a) and water-saturated states (b) at 298 K. The water molecules are omitted for clarity. In grey, white, red, blue and indigo are represented atoms of C, H, O, N, and Zr respectively

In the water-saturated state, these DMA molecules are displaced by water molecules towards the center of the pores of the framework (cf. Figure 3.3b), suggesting that the interactions of the pore wall with H_2O are stronger than those with the DMA molecules. As observed in the radial distribution functions of Figure 3.4, these interactions between the MOF and the water molecules occur through hydrogen bonds via (i) the acid hydrogen of the phenol groups (H_{acid}) (cf. Figure 3.4b) and (ii) the nitrogen atoms of the pore linker (N_{linker}) (cf. Figure 3.4c).

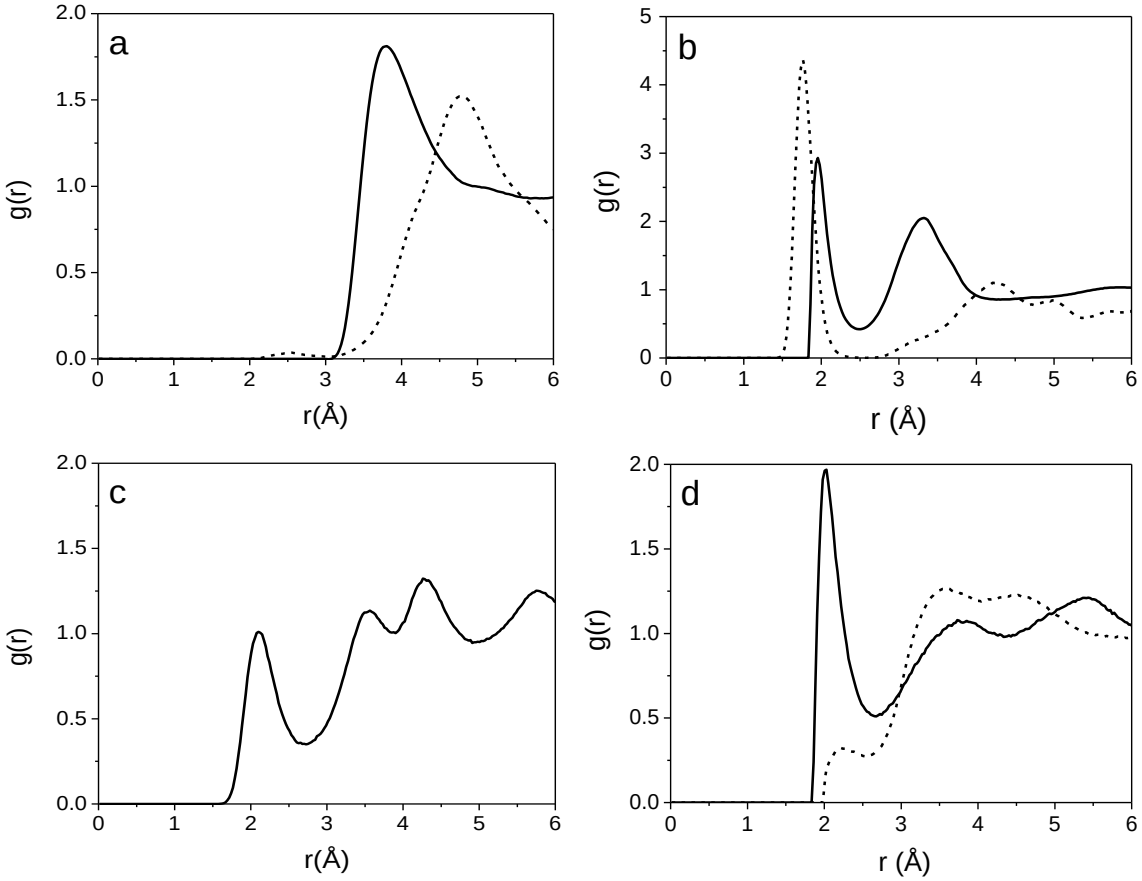

Figure 3.4 – Radial distribution functions for the pairs (a) $N_{DMA} – H_{acid}$ (solid lines) and $C_{DMA} – C_{DMA}$ (dashed lines) in the anhydrous framework and for the pairs (b) $O_{H2O} – H_{acid}$ (dashed lines) and $O_{H2O} – H_{H2O}$ (solid lines), (c) H_{H2O}-N_{linker}, and (d) $H_{DMA} – O_{H2O}$ (solid lines) and $H_{H2O} – N_{DMA}$ (dashed lines) in the hydrated MIL-163(Zr)

The water molecules arrange themselves in the pores forming extended hydrogen bonded clusters (cf. Figure 3.5a), with an average length of 15 molecules. This number is smaller than that predicted for other MOFs with 1D pores, such as MIL-53(Cr) and MIL-47(V) [33]. On the other hand, as seen in the histograms of Figure 3.5b, these clusters are constituted by both isolated clusters with a small number of molecules and by clusters with a larger number of molecules, resulting in the creation of a percolating pathway in the whole porosity investigated in the simulation cell. These percolating water clusters interconnect different phenol groups, in adjacent or opposite positons of the pore wall, creating an extended H-bonded network (cf. Figure 3.5c). In average, each water cluster interconnects ~4.5 of these phenol groups. This large number of phenol groups instantaneously

interconnected through hydrogen bonds favors the proton transmission from one hydrophilic group to the other.

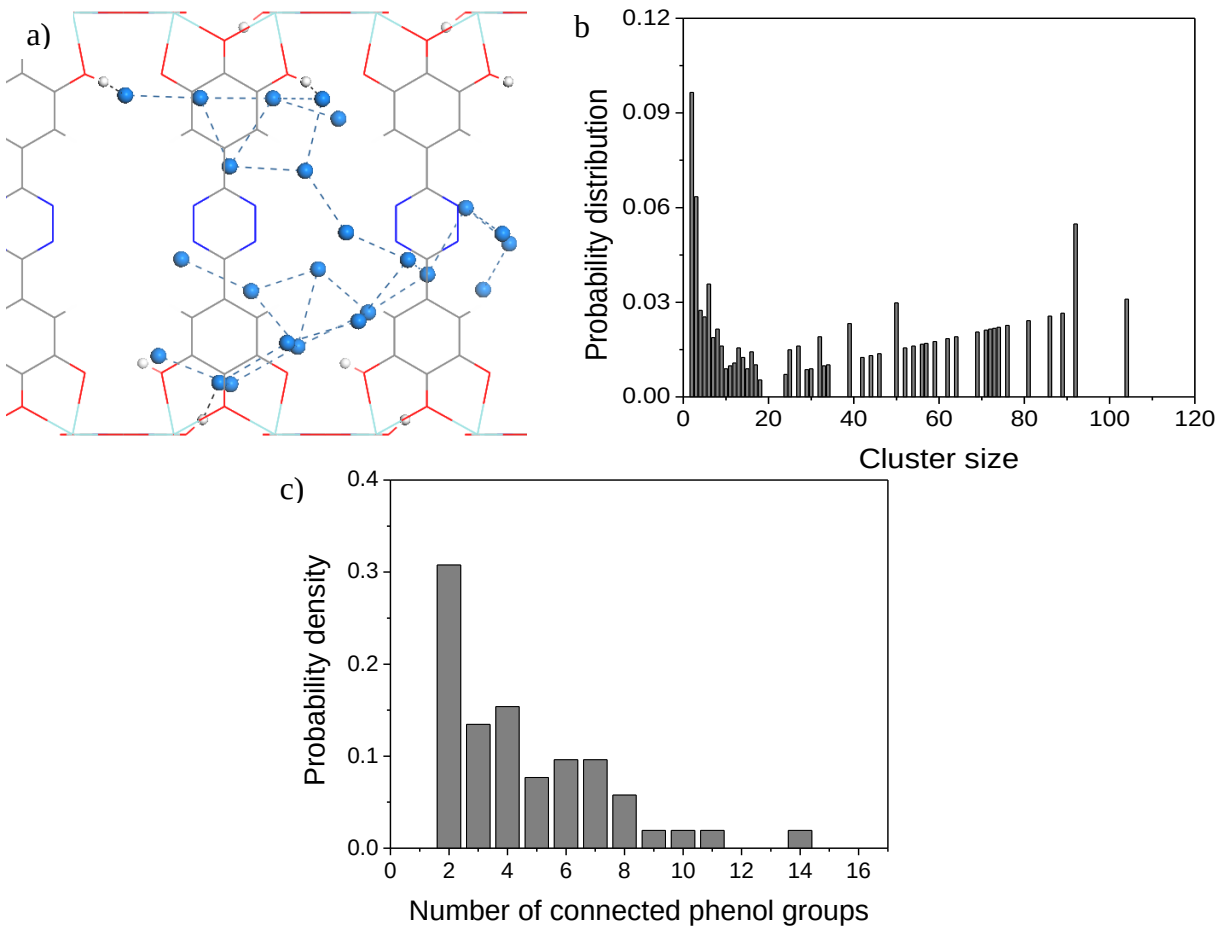

Figure 3.5 – (a) Representation of a typical cluster of water molecules (blue spheres) observed in snapshots obtained from MC calculations in the hydrated MIL-163(Zr) at 298 K, (b) probability distribution of the cluster sizes and (c) connectivity of the phenol groups in the clusters.

A hydrogen bond analysis of the hydrated MIL-163(Zr) allowed us to shed light on several key points of the H-bond network formed by the phenol groups, DMA and water molecules. One of them is that a large percentage (73.9%) of the phenol groups is engaged in hydrogen bonds, mainly with water molecules (66.6%) but also, in a smaller amount (7.3%), with the DMA molecules. Moreover, given the large number of water molecules per unit cell (32), the majority of the H-bonds in the hydrated MIL-163(Zr) results from H_2O – H_2O interactions. However, the total number of hydrogen bonds per water molecule (N_{HB}) is

relatively small (1.55) compared to what is observed in bulk water (3.6) [34]. Such low N_{HB} can be explained by (i) the relatively large pores of the MOF, which rather favor the association of the molecules between each other than with the framework, and (ii) the presence of the large DMA molecules in the pore, which, even though do not avoid the percolation of water molecules in large clusters, prevent them to acquire a larger degree of self-association.

In the hydrated state, we evidenced that in average, each DMA molecule is engaged in at least one H-bond with the water molecules. These molecules act mainly as H-donors (see Figure 3.6a), even though a certain H-acceptor character cannot be ruled out, as seen in the RDFs of Figure 3.4d. The clustering analysis on the MIL-163(Zr) has allowed us a further understanding of the role of the DMA molecules in the proton conduction. A comparison between the amount of phenol groups interconnected through a single water cluster in the fully hydrated MIL-163(Zr) in the presence and in the absence of DMA molecules revealed that, this amount is higher in the first case (cf. Figure 3.6b). The increase in the number of phenol groups connected by a single water cluster in the presence of the DMA molecules can be attributed to the higher number of water molecules in the vicinities of the pore wall in this situation, as they cannot effectively populate the pore center, partially occupied by DMA molecules.

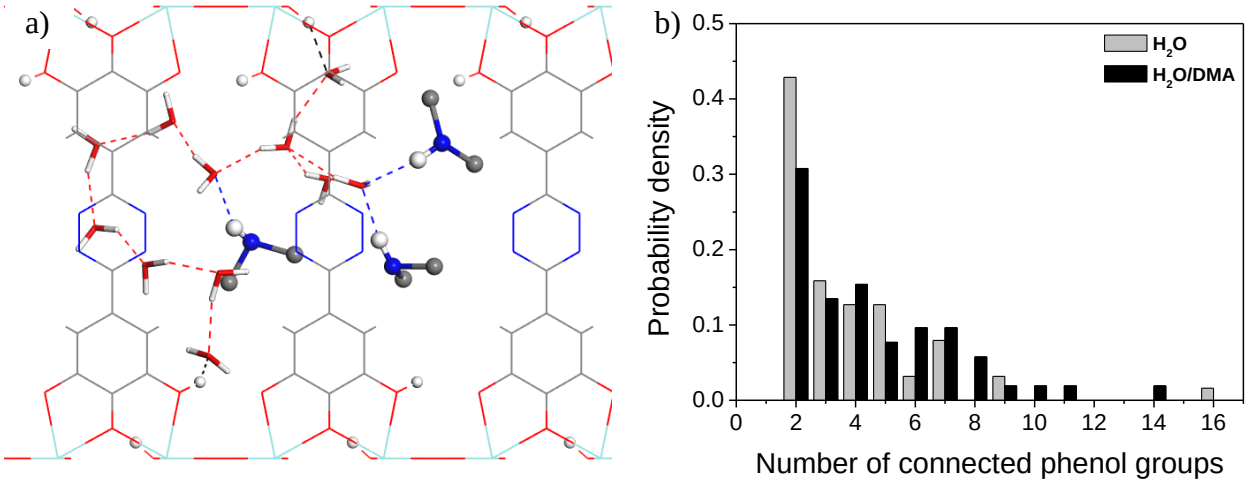

Figure 3.6 – Representation of a typical hydrogen bonded water chain interconnecting opposite phenol groups and the connection of DMA molecules to the chain observed in snapshots from MC calculations in the hydrated MIL-163(Zr) at 298 K (a) and probability density expressing the percentage of phenol groups interconnected via the water clusters in the hydrated MIL-163(Zr) with DMA molecules (black bars) and in their absence (grey bars) (b).

Finally, a careful analysis of the MC snapshots corresponding to the hydrated MIL-163(Zr) allowed us to characterize the water arrangement inside the pores of the MOF in chains and rings (Figure 3.7). Such geometry offers multiple 3D pathways for the proton motion along hydrogen bonds in the three directions from one hydrophilic group to another. Figure 3.6a thus illustrates a possible proton conduction pathway, where two phenol groups in opposite pore walls are connected by water molecules in a hydrogen bond chain, with DMA molecules connected to such chain. This hydrogen bond topology formed from interconnected water chains in a channel-like framework is quite similar to the one described by Grancha *et al.* [12] using a quantum Molecular Dynamics methodology. In their work, they describe the proton motion along hydrogen bonds as a Grottus-like mechanism. The extensive hydrogen bond networks interconnecting acidic phenol groups and the experimental energy of activation (Ea < 0.4eV) found for the proton conductivity in the hydrated MIL-163(Zr), indicate that such Grotthus-like mechanism also would be predominant in this MOF.

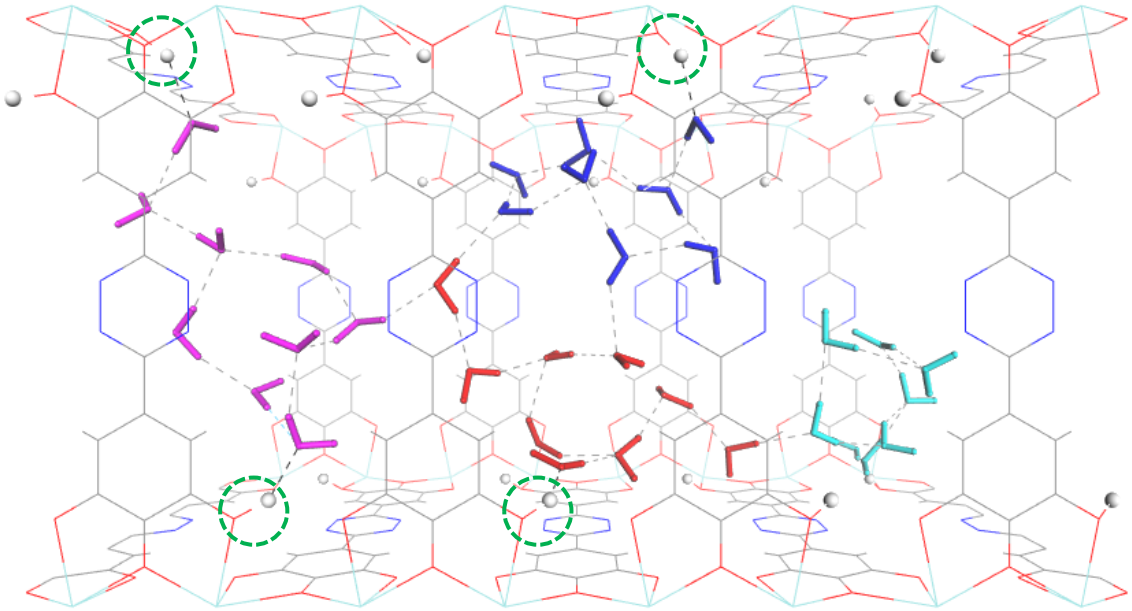

Figure 3.7 - Cluster of hydrogen bonded molecules of water interconnecting 4 phenol groups (highlighted in green dashed circles). The different water molecules which make part (or are closely associated) to one ring of H-bonded molecules are indicated by different colors.

III. KAUST-7'

KAUST-7' is a product of the structural change of the structural change of the 3D MOF KAUST-7 [35]. This new 2D MOF crystallizes in the space group C2/m and has a layered framework formed by the 6-fold coordination of Ni^{2+} atoms with bipyridine linkers in one axis, $(NbOF_4)^{2-}$ linkers in another and water molecules in the third axis (cf. Figure 3.8a). These layers are kept interconnected by hydrogen bonds between the coordinated water molecules and the fluorine atoms. The chemical formula of $NiNbOF_5(H_2O)_2$(pyr) was deduced from elemental analysis. This material was demonstrated to show a superprotonic behavior in the presence of water ($\sigma_{90°C} = 2.0\times10^{-2}$ S.cm^{-1}).

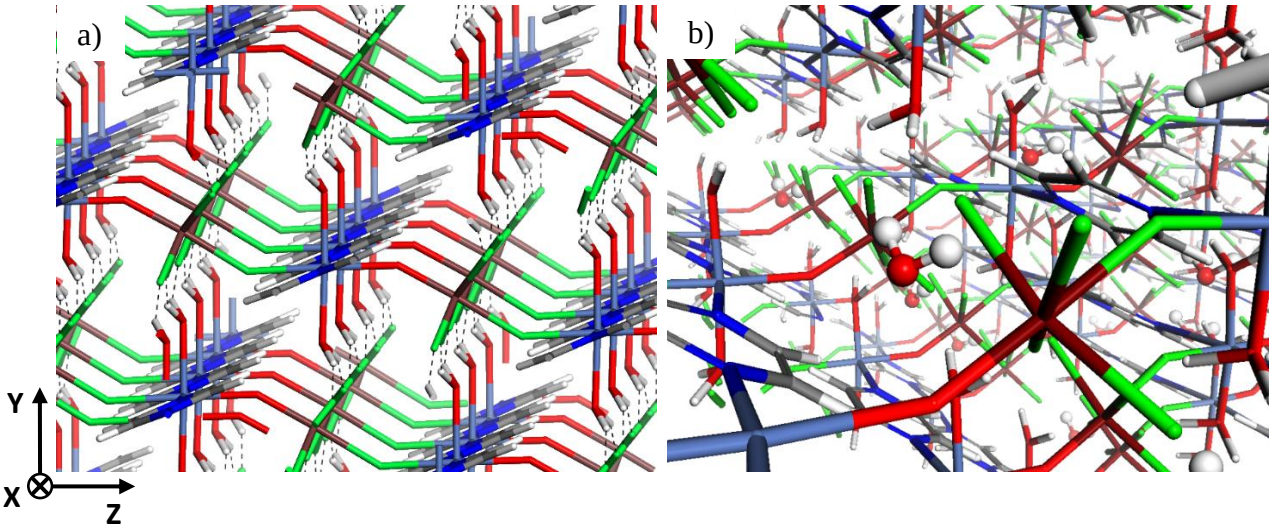

Figure 3.8 – (a) DFT optimized framework of the anhydrous 2D framework KAUST-7' characterized by hydrogen bonds (dashed black lines) established between fluorine atoms and H_2O molecules coordinated to metallic centers. (b) Details of the adsorption sites of the guest water molecules (ball and sticks) in the hydrated KAUST-7' framework (sticks). These water molecules are located between two opposite $(NbOF_4)^{2-}$ groups and two coordinated water molecules. C, H, N, O, F, Ni, and Nb atoms are represented in grey, white, blue, red, green, light blue and burgundy respectively.

As shown in the pore size distribution calculated for the DFT-optimized framework using the geometric parameters of the UFF forcefield to determine the atoms radius (cf. Figure 3.9), one can ascertain that this MOF contains extremely narrow pores, with accessible pores of the order of 2 Å. Considering that the water molecules have a kinetic diameter of 2.65 Å, local structural rearrangements are likely to occur in presence of water in

order to accommodate the water molecules within the porosity. Therefore, these rearrangements will be taken into account in the AIMD simulations carried out subsequently.

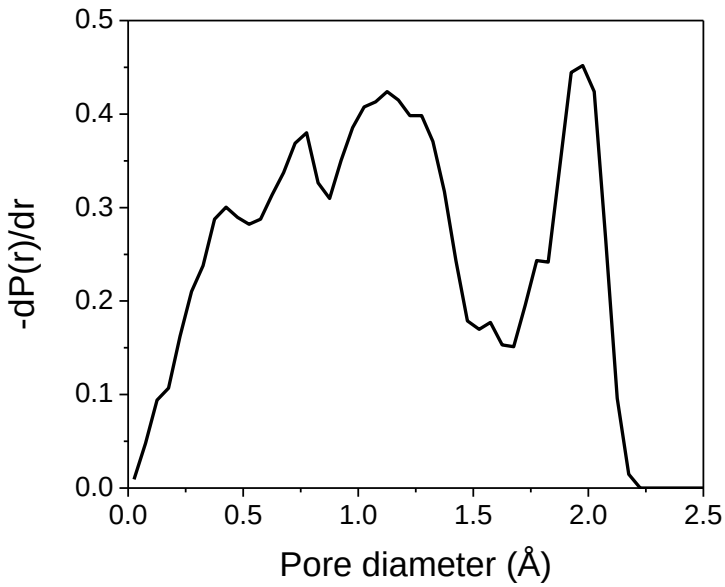

Figure 3.9 – Pore size distribution of the DFT-optimized structure of KAUST-7'.

MC simulations in the NVT ensemble were first run to determine the location of the adsorbed water molecules in the fully hydrated MOF framework with the water loading determined by both experimental TGA and volumetric measurements. These molecules were found to be highly localized in the space between two coordinated water molecules belonging respectively to two opposite neighboring layers of the framework (cf. Figure 3.8b). Equilibrium configurations obtained for the water-loaded structures issued from the MC calculations were then geometry optimized at the DFT level and further used as a starting point for AIMD runs. These AIMD simulations were run for 20 ps and revealed the formation of a hydrogen bond network involving the water adsorbed between the layers (H_2O_w), fluorine atoms (F) of the $(NbOF_4)^{2-}$ linkers and the water coordinated to Ni^{2+} atoms (H_2O_c). The RDFs extracted from these AIMD simulations (Figure 3.10) evidenced that the fluorine atoms interact with both the adsorbed and coordinated water molecules, however, comparing the RDFs of the pairs F – $H_w(H_2O_w)$ and F – $H_c(H_2O_c)$, their interaction with the latter seems stronger than with the former. These RDFs further evidenced that the adsorbed

water molecules also interact with the coordinated water molecules, via the H atom of the latter species, as seen in Figure 3.10.

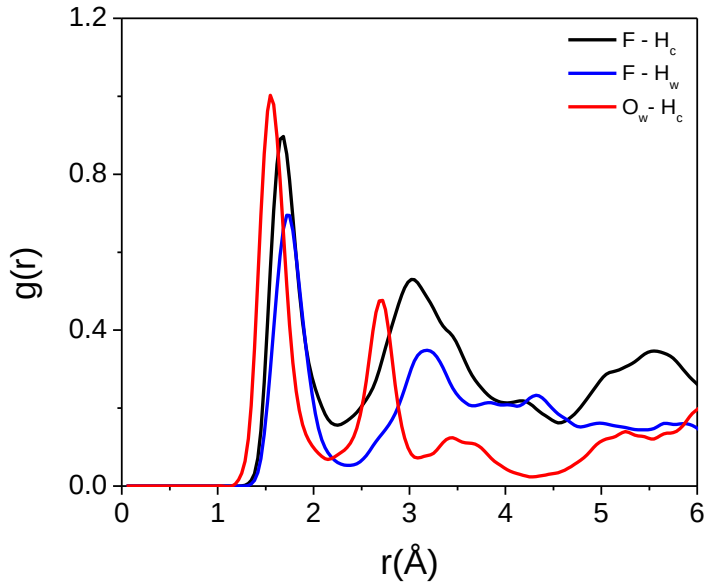

Figure 3.10 – Radial distribution functions of the interactions of the pairs F – $H_c(H_2O_c)$ (black line), F – $H_w(H_2O_w)$ (blue line), and $O_w(H_2O_w)$ – $H_c(H_2O_c)$ (red line) obtained from an AIMD simulation carried out in the fully hydrated KAUST-7' at 298K.

The AIMD simulations also revealed that the H-bond network is characterized by a continuous cleavage/formation of interactions between the H_2O_w, F and H_2O_c species. In particular, we revealed that the H_2O_w molecules have an important role as a bridging species, connecting different fluorine atoms and the H_2O_c molecules due to their higher degree of freedom to rotate, as shown by the higher amplitude of the average deviation angle of H_2O_w (37°) compared to that of H_2O_c (26°) (cf. Figure 3.11a and 3.11b). Such a global H_2O_w-assisted reorganization of the H-bond network in this framework generates favorable pathways for the proton propagation in a Grotthus-like mechanism and this is at the core of the excellent proton conduction properties observed in this material.

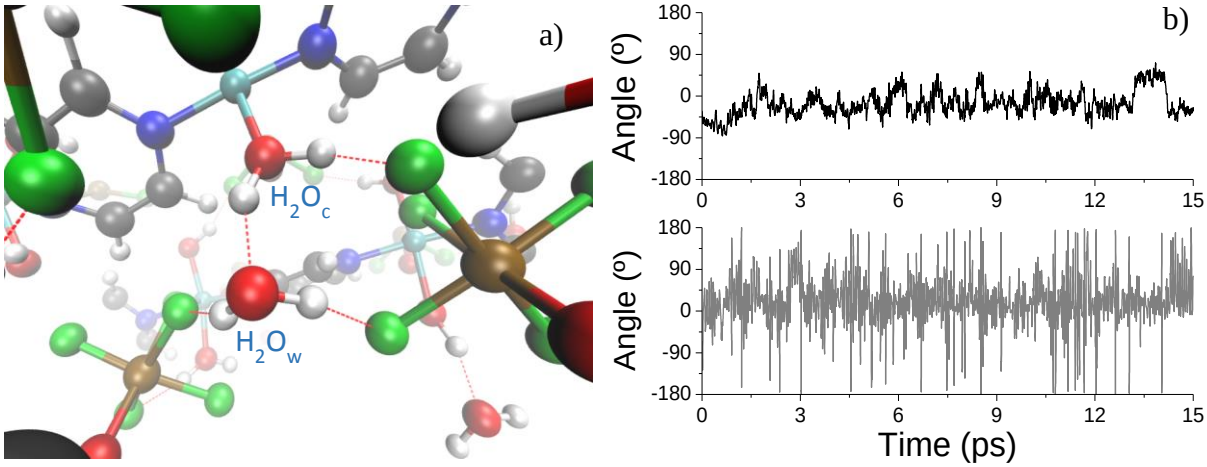

Figure 3.11 – Representative snapshot of a 15 ps AIMD simulation conducted at 298 K on the fully hydrated KAUST-7' framework, highlighting the H_2O_c and H_2O_w molecules hydrogen bonded (dashed lines) with each other and with fluorine atoms (a). Deviation angle in relation to the respective rotation axis of H_2O_w (grey line) and H_2O_c (black line) molecules (b).

The trajectory obtained by AIMD simulations on the water saturated KAUST-7' showed a relatively low average number of hydrogen bonds N_{HB} per water molecule (1.54), a value similar to that reported in the previous section for MIL-163(Zr) and rather low compared to the N_{HB} for bulk water [34]. The lower N_{HB} value in the KAUST-7' was attributed to (i) the adsorption of water molecules in highly 2D confined environment which make the hydrogen bonds greatly directional and (ii) the coordination of the water molecules to Ni^{2+} atoms. Once connected to the metals, the oxygen of these water molecules cannot act as hydrogen bond acceptors. We further evidenced that the extremely high confined environment of KAUST-7' prevents the association of water in clusters.

IV. $Ti^{IV}Ti^{IV}(HPO_4)_4$

$Ti^{IV}Ti^{IV}(HPO_4)_4$ is a titanium phosphate formed after the calcination of the mixed-valence titanium phosphate $Ti^{III}Ti^{IV}(HPO_4)_4$ [36]. This new material is made of corner-sharing octahedra and tetrahedral oxides centered by titanium and phosphorous atoms forming a 3D framework with 1D pores with 3 Å (pore 1), 6.5 Å (pore 2) and 4.6 Å (pore 3) cross-sectional diameters. These different pore sizes are easily identified through the inspection of the calculated pore size distribution presented in Figure 3.12 considering a DFT optimized framework. Both the smaller and larger pores are oriented towards the *x* axis, while the remaining pore is perpendicularly oriented and connects them to each other (see Figure 3.13). In fact, all the pores have roughly the same backbone and their dimensions depend on the concentration of POH groups they integrate. The smaller the pore, the richer it is in POH groups. Due to their acidity, these POH groups are considered as the main proton sources in this material.

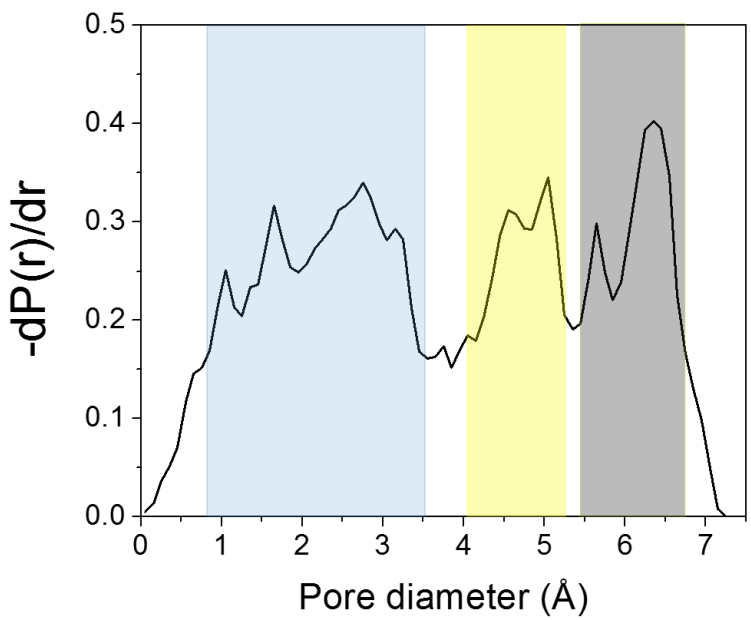

Figure 3.12 – Calculated Pore Size Distribution (PSD) of the crystal structure of $Ti^{IV}Ti^{IV}(HPO_4)_4$ with highlighted regions corresponding to the different pore types. In blue, the region related to pore 1; in yellow, the one assigned to pore 3; in gray, the one attributed to pore 2 (cf. Figure 3.13).

The conductivity of this material was demonstrated to show a large difference between the anhydrous state ($\sigma_{90°C}$ = 1.9×10^{-8} S.cm^{-1}) and the water-saturated state ($\sigma_{90°C}$ = 2.4×10^{-3} S.cm^{-1}), even if such difference (5 orders of magnitude) is smaller than the one observed for the MIL-163(Zr) and KAUST-7' (10 orders of magnitude).

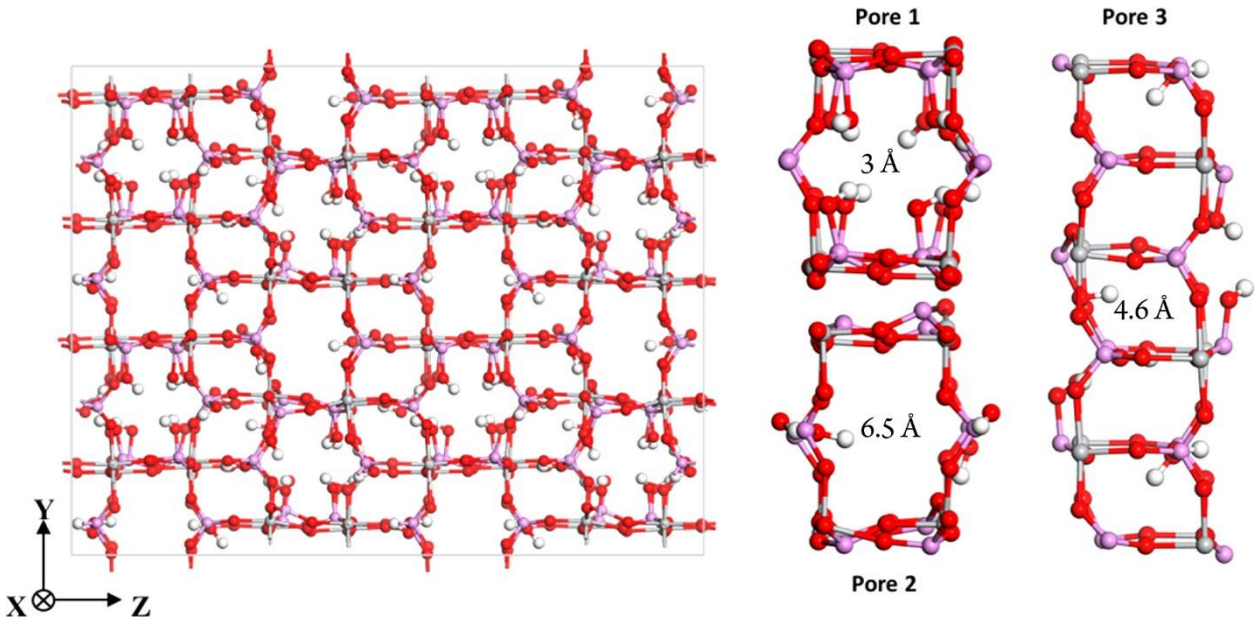

Figure 3.13 – Pore types identified in the $Ti^{IV}Ti^{IV}(HPO_4)_4$ framework. H, O, Ti, and P atoms are represented in white, red, grey, and pink respectively.

Since we did not find in the literature existing forcefields already validated to describe porous titanium phosphates, we constructed our own forcefield based on a set of potential parameters previously used to represent zeolites [37–39] and aluminium phosphates [40–42]. As it is usually the case for inorganic materials, while electrostatic contributions are considered for every atom of the framework, only the oxygen atoms are assumed to be relevant as van der Waals interacting sites, since the other constitutive atoms of the framework have a much lower polarizability. GCMC calculations using this microscopic description of the framework leads to a good description of the experimental water adsorption isotherm of $Ti^{IV}Ti^{IV}(HPO_4)_4$ using the SPC [43] water model. Fine adjustments of the LJ 12-6 geometric parameters (σ), which proved to be the most sensitive of the LJ 12-6 parameters in such a confined framework, allowed an excellent agreement between the simulation and experimental isotherms (cf. Figure 3.14). In table 3.1 the Lennard Jones

parameters assigned to the oxygen atoms of the framework and of the water atoms are summarized.

Table 3.1 – LJ 12-6 parameters assigned to the oxygen atoms of the $Ti^{IV}Ti^{IV}(HPO_4)_4$ framework and the water molecules derived from the SPC model [43].

	σ (Å)	**ε (K)**
Framework	2.629	120.0
Water	3.166	78.2

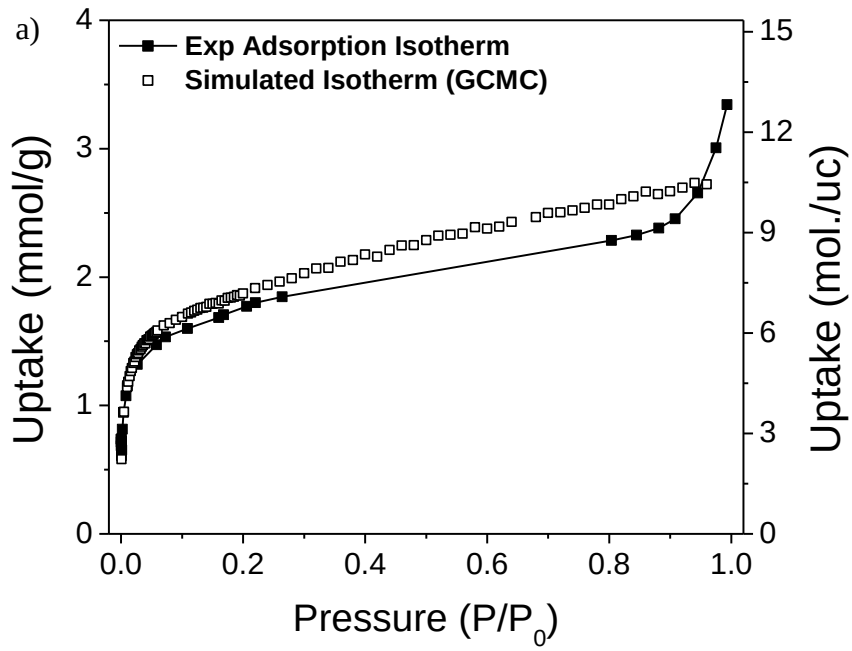

Figure 3.14 – Correspondence between the simulated (empty squares) and experimental (filled squares) adsorption isotherms of water in $Ti^{IV}Ti^{IV}(HPO_4)_4$. Simulated results were obtained from MC calculations using the forcefield developed in this work for the framework and the SPC model for the water molecules.

Once the forcefield was validated, we continued our study on the fully hydrated $Ti^{IV}Ti^{IV}(HPO_4)_4$ by evaluating the water arrangement in this framework, taking into account the local relaxation of the phosphate groups of the solid. This step was carried out using MD calculations that implemented a partially flexible structural model. In such model, the POH groups were considered flexible, while the rest of the framework was considered as rigid. The flexibility of the POH groups was modelled using harmonic potentials for the P-O and

O-H bonds and P-O-H angles obtained from the literature [20] and a cosine potential developed in this work for the O-P-O-H torsion angles.

The MD simulations evidenced that the water molecules interact with the POH groups by strong hydrogen bonds, as shown by the radial distribution functions (cf. Figure 3.15a) between the oxygen atoms of the POH groups (O_{POH}) and the oxygen atoms of the water molecules (O_W), whose equilibrium distance (2.4 Å) is shorter than the one predicted for the interactions between the water molecules (2.8 Å). These strong interactions suggests that the protons of POH are expected to be more easily transferred to a neighbor water molecule. Additionally, representative snapshots at the equilibrium show that the water molecules arrange themselves forming a percolating 3D hydrogen bond network that (i) encompasses all the pores of the framework in multiple directions (Figure 3.15b) and (ii) involves POH groups of pores 1 and 3.

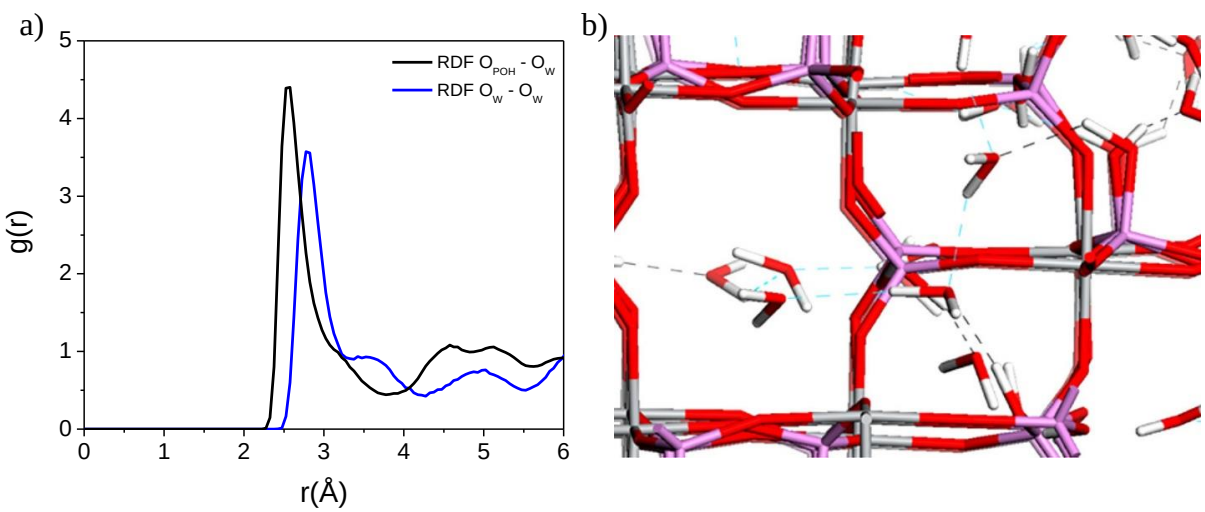

Figure 3.15 – (a) Comparison of the radial distribution functions for the pairs O_{POH} – O_w (black line) and O_w-O_w (blue line) for a 10 ns MD simulation of the fully hydrated $Ti^{IV}Ti^{IV}(HPO_4)_4$ at 298 K and (b) representative snapshot displaying the hydrogen bond pathway (dashed lines) formed from the association of water molecules and POH groups.

The connectivity of the water molecules in this network was evaluated by the number of hydrogen bonds per molecule (N_{HB}). The so-obtained value (3.10) is relatively high and close to the connectivity observed in bulk water (3.6) [34]. Such high connectivity can be related to the accommodation of water molecules in a highly hydrophilic environment with a

high level of confinement. However, in contrast to what was observed in the KAUST-7', the confinement of the water molecules in the $Ti^{IV}Ti^{IV}(HPO_4)_4$ is not at a level that restrains their degree of liberty to the point of restricting their hydrogen bond connectivity.

The extent of the hydrogen bond pathways observed through snapshots was quantitatively evaluated via the analysis of the probability density of the water cluster sizes in the hydrated framework (Figure 3.16a). Given the association of multiple POH groups in the H-bond pathway, we decided to account these groups as constituent species of the clusters. This analysis indicated a bimodal cluster distribution with both clusters of small size (up to 4 species), resulting from short-range coordination between water and POH groups, and clusters of larger size (from 5 to 25 species) resulting from the long ranging association of these species. The overall average cluster size was constituted by 9 species. A representative view of these clusters is shown in Figure 3.16b.

The relatively high level of percolation of the hydrogen bond network in the small pores of the Ti-phosphate, the active participation of the acidic POH groups contained in pores 1 and 3, as well as the H-bond connectivity of the water molecules in the pores offer an optimal configuration for the long-range proton motion throughout the solid.

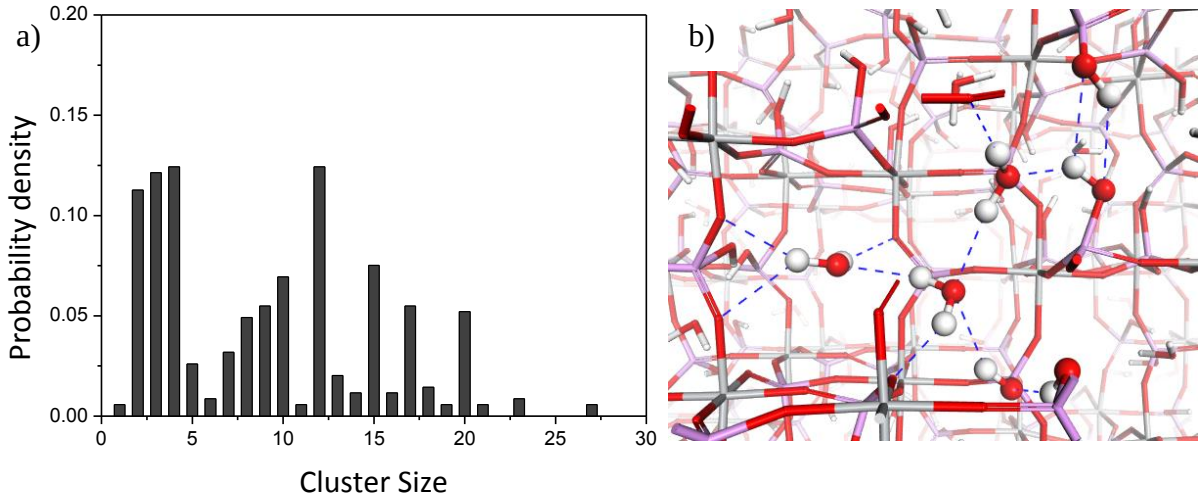

Figure 3.16 – (a) Cluster size density for the association of POH groups and water molecules at water saturation. (b) Example of a cluster of water molecules and POH groups formed in pore 3.

These conclusions were further complemented by the investigation of the mechanisms of proton transfer with the use of the AIMD technique. As already suggested in Figure 3.14, these calculations indicated that the proton migrate from a POH group in pore 1 through water molecules in pore 3 and pore 2, confirming that the percolating hydrogen bond network suggested by classical MD calculations is indeed a viable trail for a Grotthus-like proton conduction in the framework. In this particular mechanism, it was shown that (i) POH groups act as the proton source in this system with the spontaneous transfer of a proton from a POH group to a neighbor water molecule (Figure 3.17a), (ii) the movement of the hydronium ion toward a second water molecule, resulting in a distorted Zundel ($H_5O_2^+$) species stabilized by hydrogen bonds established with the framework atoms (Figure 3.17b-d), and (iii) the proton originating from the hydronium ion moves toward a bridging oxygen atom of the framework (Figure 3.17e) to form a bridging μ_2–OH function.

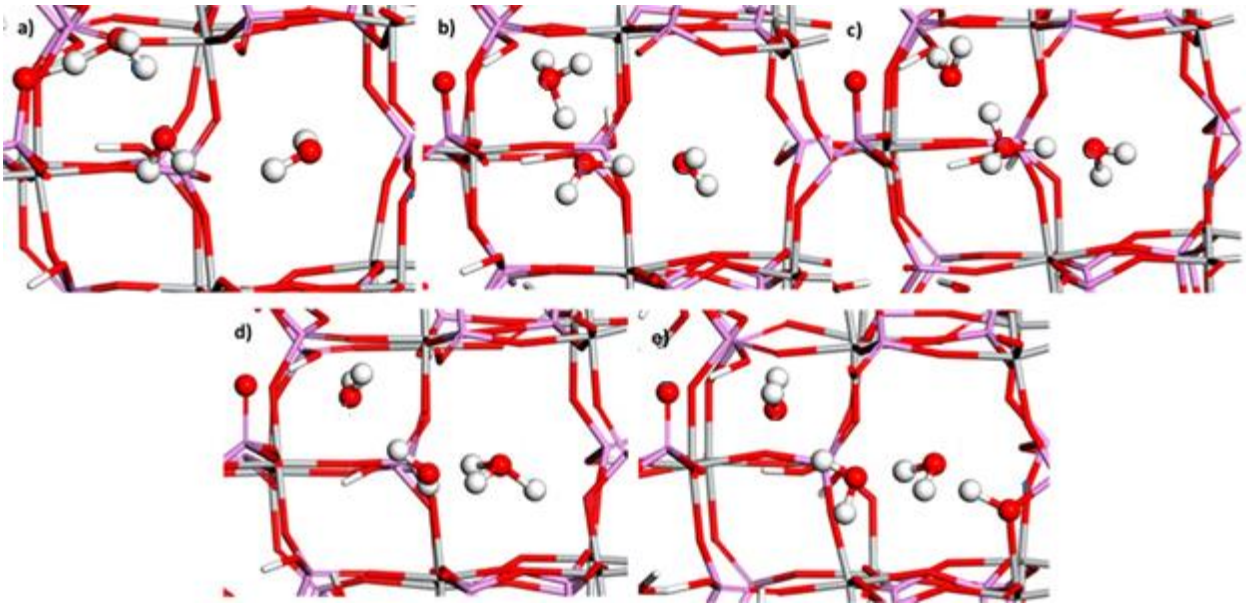

Figure 3.17 – Proton conduction mechanism in the water-saturated $Ti^{IV}Ti^{IV}(HPO_4)_4$, highlighting the transfer of a proton from the POH group in pore 1 to a water in pore 3 (a), the proton transfer equilibrium between two molecules in pore 3 and one in pore 2 (b, c, and d), and the transfer from a water molecule in pore 2 to a bridging oxygen in pore 2.

V. Conclusion:

This chapter describes the main computational techniques and the analytical tools we developed to get insight on the water arrangement and the resulting water-mediated proton migration mechanism in porous materials. This global methodology was applied to two MOFs, MIL-163(Zr) and KAUST-7', and the $Ti^{IV}Ti^{IV}(HPO_4)_4$ inorganic system that were initially identified as excellent proton-conducting materials using an experimental screening approach. Classical and quantum-calculations were coupled to evidence the formation of 3D-water hydrogen bonded network in the pores of these materials that provides the optimal conditions for transferring the proton at long distances via a Grotthus-mechanism. The local relaxation of the host framework had to be considered to accurately capture the rearrangement of water molecules in confined environment, while this is not so critical in the case of large pore materials. This was achieved by considering classical MD implementing flexible force field or AIMD simulations. The information gained from this study can be considered as a road-map to guide the choice of computational approaches to describe the proton conduction mechanisms in porous solids. Noteworthy, such a fundamental understanding has been only rarely achieved in the field of MOFs and we hope that this will pave the way towards a more systematic computational evaluation of the microscopic proton migration mechanism for the community working in this field, which mostly reports new materials with outstanding performances evidenced by experimental testing.

REFERENCES

[1] J.R. Macdonald, Impedance spectroscopy, Ann. Biomed. Eng. 20 (1992) 289–305. doi:10.1007/BF02368532.

[2] S. Sanda, S. Biswas, S. Konar, Study of Proton Conductivity of a 2D Flexible MOF and a 1D Coordination Polymer at Higher Temperature, Inorg. Chem. 54 (2015) 1218–1222. doi:10.1021/ic502098h.

[3] F. Yang, H. Huang, X. Wang, F. Li, Y. Gong, C. Zhong, J.-R. Li, Proton Conductivities in Functionalized UiO-66: Tuned Properties, Thermogravimetry Mass, and Molecular Simulation Analyses, Cryst. Growth Des. 15 (2015) 5827–5833. doi:10.1021/acs.cgd.5b01190.

[4] K. Park, W. Lin, F. Paesani, A Refined MS-EVB Model for Proton Transport in Aqueous Environments, J. Phys. Chem. B. 116 (2012) 343–352. doi:10.1021/jp208946p.

[5] Y. Wu, H. Chen, F. Wang, F. Paesani, G.A. Voth, An Improved Multistate Empirical Valence Bond Model for Aqueous Proton Solvation and Transport †, J. Phys. Chem. B. 112 (2008) 467–482. doi:10.1021/jp076658h.

[6] a. C.T. Van Duin, S. Dasgupta, F. Lorant, W. a. Goddard, ReaxFF: A reactive force field for hydrocarbons, J. Phys. Chem. A. 105 (2001) 9396–9409. doi:10.1021/jp004368u.

[7] F. Paesani, Molecular mechanisms of water-mediated proton transport in MIL-53 metal-organic frameworks, J. Phys. Chem. C. 117 (2013) 19508–19516. doi:10.1021/jp406163q.

[8] D.D. Borges, R. Semino, S. Devautour-Vinot, H. Jobic, F. Paesani, G. Maurin, Computational Exploration of the Water Concentration Dependence of the Proton Transport in the Porous UiO–66(Zr)–(CO 2 H) 2 Metal–Organic Framework, Chem. Mater. 29 (2017) 1569–1576. doi:10.1021/acs.chemmater.6b04257.

[9] D.D. Borges, S. Devautour-Vinot, H. Jobic, J. Ollivier, F. Nouar, R. Semino, T. Devic, C. Serre, F. Paesani, G. Maurin, Proton Transport in a Highly Conductive Porous Zirconium-Based Metal-Organic Framework: Molecular Insight, Angew. Chemie - Int. Ed. 55 (2016) 3919–3924. doi:10.1002/anie.201510855.

[10] M. Liu, L. Chen, S. Lewis, S.Y. Chong, M.A. Little, T. Hasell, I.M. Aldous, C.M. Brown, M.W. Smith, C.A. Morrison, L.J. Hardwick, A.I. Cooper, Three-dimensional protonic conductivity in porous organic cage solids, Nat. Commun. 7 (2016) 12750. doi:10.1038/ncomms12750.

[11] F.-M. Zhang, L.-Z. Dong, J.-S. Qin, W. Guan, J. Liu, S.-L. Li, M. Lu, Y.-Q. Lan, Z.-M. Su, H.-C. Zhou, Effect of Imidazole Arrangements on Proton-Conductivity in Metal–Organic Frameworks, J. Am. Chem. Soc. 139 (2017) 6183–6189. doi:10.1021/jacs.7b01559.

[12] T. Grancha, J. Ferrando-Soria, J. Cano, P. Amorós, B. Seoane, J. Gascon, M. Bazaga-García, E.R. Losilla, A. Cabeza, D. Armentano, E. Pardo, Insights into the Dynamics of Grotthuss Mechanism in a Proton-Conducting Chiral bioMOF, Chem. Mater. 28 (2016) 4608–4615. doi:10.1021/acs.chemmater.6b01286.

[13] S. Ling, B. Slater, Dynamic acidity in defective UiO-66, Chem. Sci. 7 (2016) 4706–4712. doi:10.1039/C5SC04953A.

[14] E. Eisbein, J.-O. Joswig, G. Seifert, Proton Conduction in a MIL-53(Al) Metal–Organic Framework: Confinement versus Host/Guest Interaction, J. Phys. Chem. C. 118 (2014) 13035–13041. doi:10.1021/jp5043969.

[15] E. Eisbein, J.-O. Joswig, G. Seifert, Enhanced proton-transfer activity in imidazole@MIL-53(Al) systems revealed by molecular-dynamics simulations, Microporous Mesoporous Mater. 216 (2015) 36–41. doi:10.1016/j.micromeso.2015.03.022.

[16] M.F. De Lange, J.J. Gutiérrez-Sevillano, S. Hamad, T.J.H. Vlugt, S. Calero, J. Gascon, F. Kapteijn, Understanding Adsorption of Highly Polar Vapors on Mesoporous MIL-100 (Cr) and MIL-101 (Cr): Experiments and Molecular Simulations, J. Phys. Chem. C. 117 (2013) 7613–7622. doi:10.1021/jp3128077.

[17] S. Duane, A.D. Kennedy, B.J. Pendleton, D. Roweth, Hybrid Monte Carlo, Phys. Lett. B. 195 (1987) 216–222. doi:10.1016/0370-2693(87)91197-X.

[18] B. Mehlig, D.W. Heermann, B.M. Forrest, Hybrid Monte Carlo method for condensed-matter systems, Phys. Rev. B. 45 (1992) 679–685. doi:10.1103/PhysRevB.45.679.

[19] A. Ghoufi, G. Maurin, Hybrid Monte Carlo Simulations Combined with a Phase Mixture Model to Predict the Structural Transitions of a Porous Metal-Organic Framework Material upon Adsorption of Guest Molecules, Society. 1 (2010) 6496–6502.

[20] G. Alberti, A. Grassi, G.M. Lombardo, G.C. Pappalardo, R. Vivani, Derivation of Force Field Parameters, and Force Field and Quantum Mechanical Studies of Layered α- and γ-Zirconium Phosphates, Inorg. Chem. 38 (1999) 4249–4255. doi:10.1021/ic9903937.

[21] S. Nosé, A molecular dynamics method for simulations in the canonical ensemble, Mol. Phys. 52 (1984) 255–268. doi:10.1080/00268978400101201.

[22] S. Nosé, A unified formulation of the constant temperature molecular dynamics methods, J. Chem. Phys. 81 (1984) 511–519. doi:10.1063/1.447334.

[23] W.G. Hoover, Canonical dynamics: Equilibrium phase-space distributions, Phys. Rev. A. 31 (1985) 1695–1697. doi:10.1103/PhysRevA.31.1695.

[24] C. Chen, W. Zhong Li, Y. Chen Song, L.D. Weng, N. Zhang, The Effect of Geometrical Criteria on Hydrogen Bonds Analysis in Aqueous Glycerol Solutions, J. Mol. Imaging Dyn. 01 (2011) 1–6. doi:10.4172/2155-9937.1000101.

[25] M. Matsumoto, Relevance of hydrogen bond definitions in liquid water, J. Chem. Phys. 126 (2007) 054503. doi:10.1063/1.2431168.

[26] D. Swiatla-Wojcik, Evaluation of the criteria of hydrogen bonding in highly associated liquids, Chem. Phys. 342 (2007) 260–266. doi:10.1016/j.chemphys.2007.10.009.

[27] E. Guàrdia, J. Martí, J.A. Padró, L. Saiz, A.V. Komolkin, Dynamics in hydrogen bonded liquids: water and alcohols, J. Mol. Liq. 96–97 (2002) 3–17. doi:10.1016/S0167-7322(01)00342-7.

[28] E. Guàrdia, J. Martí, L. García-Tarrés, D. Laria, A molecular dynamics simulation study of hydrogen bonding in aqueous ionic solutions, J. Mol. Liq. 117 (2005) 63–67. doi:10.1016/j.molliq.2004.08.004.

[29] R. Semino, J. Martí, E. Guàrdia, D. Laria, Excess protons in mesoscopic water-acetone nanoclusters, J. Chem. Phys. 137 (2012). doi:10.1063/1.4766201.

[30] W.L. Jorgensen, Monte carlo results for hydrogen bond distributions in liquid water11Quantum and statistical mechanical studies of liquids, 9. Part 8 ref. [6]., Chem. Phys. Lett. 70 (1980) 326–329. doi:10.1016/0009-2614(80)85344-9.

[31] M.P. Allen, D.J. Tildesley, Computer Simulation of Liquids, Oxford: Clarendon Pr, 1987.

[32] G. Mouchaham, L. Cooper, N. Guillou, C. Martineau, E. Elkaïm, S. Bourrelly, P.L. Llewellyn, C. Allain, G. Clavier, C. Serre, T. Devic, A Robust Infinite Zirconium Phenolate Building Unit to Enhance the Chemical Stability of Zr MOFs, Angew. Chemie - Int. Ed. 54 (2015) 13297–13301. doi:10.1002/anie.201507058.

[33] F. Salles, S. Bourrelly, H. Jobic, T. Devic, V. Guillerm, P. Llewellyn, C. Serre, G. Ferey, G. Maurin, Molecular Insight into the Adsorption and Diffusion of Water in the Versatile Hydrophilic/Hydrophobic Flexible MIL-53(Cr) MOF, J. Phys. Chem. C. 115 (2011) 10764–10776. doi:10.1021/jp202147m.

[34] A. Rastogi, A. K., S. Suresh, Hydrogen Bond Interactions Between Water Molecules in Bulk Liquid, Near Electrode Surfaces and Around Ions, in: Thermodyn. - Phys. Chem. Aqueous Syst., InTech, 2011. doi:10.5772/21074.

[35] A. Cadiau, K. Adil, P.M. Bhatt, Y. Belmabkhout, M. Eddaoudi, A metal-organic framework-based splitter for separating propylene from propane, Science (80-.). 353 (2016) 137–140. doi:10.1126/science.aaf6323.

[36] S. Ekambaram, C. Serre, G. Férey, S.C. Sevov, Hydrothermal Synthesis and Characterization of an Ethylenediamine-Templated Mixed-Valence Titanium Phosphate, Chem. Mater. 12 (2000) 444–449. doi:10.1021/cm990492i.

[37] G. Maurin, R.G. Bell, S. Devautour, F. Henn, J.C. Giuntini, Modeling the Effect of Hydration in Zeolite Na + −Mordenite, J. Phys. Chem. B. 108 (2004) 3739–3745. doi:10.1021/jp034151a.

[38] G. Maurin, P. Llewellyn, T. Poyet, B. Kuchta, Influence of Extra-Framework Cations on the Adsorption Properties of X-Faujasite Systems: Microcalorimetry and Molecular Simulations, J. Phys. Chem. B. 109 (2005) 125–129. doi:10.1021/jp0461753.

[39] P. Demontis, G.B. Suffritti, A. Tilocca, Diffusion and vibrational relaxation of a diatomic molecule in the pore network of a pure silica zeolite: A molecular dynamics study, J. Chem. Phys. 105 (1996) 5586–5594. doi:10.1063/1.472398.

[40] P. Demontis, J. Gulín González, G.B. Suffritti, A. Tilocca, Statics and Dynamics of Ethane Molecules in AlPO 4 -5: A Molecular Dynamics Simulation Study, J. Am. Chem. Soc. 123 (2001) 5069–5074. doi:10.1021/ja003940s.

[41] S.Y. Bhide, S. Yashonath, n -Pentane and Isopentane in One-Dimensional Channels, J. Am. Chem. Soc. 125 (2003) 7425–7434. doi:10.1021/ja0285868.

[42] S.Y. Bhide, S. Yashonath, Structure and Dynamics of Benzene in One-Dimensional Channels †, J. Phys. Chem. B. 104 (2000) 11977–11986. doi:10.1021/jp002626h.

[43] H.J.C. Berendsen, J.P.M. Postma, W.F. van Gunsteren, J. Hermans, Interaction Models for Water in Relation to Protein Hydration, in: Intermol. Forces, 1981: pp. 331–342. doi:10.1007/978-94-015-7658-1_21.

Article 1

THE JOURNAL OF PHYSICAL CHEMISTRY C

Article

pubs.acs.org/JPCC

Proton-Conducting Phenolate-Based Zr Metal–Organic Framework: A Joint Experimental–Modeling Investigation

P. G. M. Mileo,[†] S. Devautour-Vinot,[*,†] G. Mouchaham,[‡] F. Faucher,[§] N. Guillou,[‡] A. Vimont,[§] C. Serre,[‡] and G. Maurin[†]

[†]Institut Charles Gerhardt Montpellier, UMR-5253, Université de Montpellier, ENSCM, CNRS, Place E. Bataillon, Montpellier cedex 05, 34095 France

[‡]Institut Lavoisier, UMR CNRS 8180, Université de Versailles St. Quentin en Yvelines 45 avenue des Etats-Unis, Université Paris-Saclay, Versailles, 78035 France

[§]Laboratoire Catalyse et Spectrochimie, Normandie Université, ENSICAEN, UNICAEN, CNRS, 14000 Caen, France

Supporting Information

ABSTRACT: The proton-conduction performances of the chemically stable porous zirconium phenolate MIL-163 MOF were characterized for the first time by complex impedance spectroscopy. Whereas this large square-shaped channel-like MOF exhibits very poor conductivity under anhydrous conditions, measurements performed at 90 °C and 95% relative humidity evidenced a superprotonic behavior with a conductivity of 2.1×10^{-3} S·cm^{-1}, among the highest values reported so far for water-stable MOFs. This experimental investigation was further supported by Monte Carlo simulations to shed light on the effects of both the guest molecules (i.e., dimethylamine and water) and the acidic protons from the constitutive inorganic chains on the conduction properties of this porous hybrid solid. It was found that the water molecules form a three-dimensional hydrogen-bond network leading to the formation of multiple pathways that bridge the acidic Zr-bonded phenol groups of the organic linker, which act as a proton source. The dimethylamine molecules were revealed to form single hydrogen bonds with H_2O without leading to a disruption of the water hydrogen-bond network. This offers an optimal situation for the water-mediated transfer of protons over long distances at the origin of the good proton-conducting performance of MIL-163.

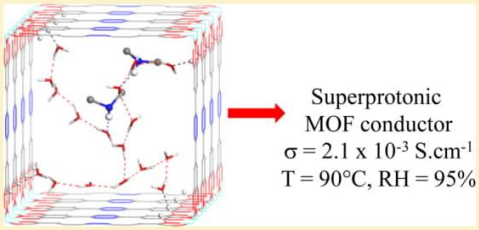

1. INTRODUCTION

To face growing global energy demands without the undesirable consequences inherent in the use of fossil fuels, considerable efforts have been dedicated toward the development of alternative energy production/storage solutions, among which fuel cells[1] and, to a lesser extent, redox flow batteries[2−4] have been intensively investigated so far. Ion-exchange membranes are key components in such technologies because they govern the performance of these systems and can represent up to 20% of the total cost of the devices.[4] In this context, a variety of electrolytes and solid-state proton conductors have been explored, including ceramic oxides,[5] oxoacids,[6] polymers,[7] and carbon nanotubes.[8] More recently, metal–organic frameworks (MOFs) have emerged as promising proton-conducting materials.[9−11] These crystalline porous hybrid solids combine tunable pore sizes with adjustable pore surface chemistries (metal, ligand) and thus offer a unique platform for the design of optimal materials for further use as fuel-cell electrolytes. The proton-conducting MOFs (PC-MOFs) reported so far have been classified into two families, namely, anhydrous (or water-free) and water-mediated PC-MOFs, which operate at $T > 100$ °C and $T \leq 100$ °C, respectively. The latter class of PC-MOFs typically relies on the combination of strong to moderate acidic functional groups grafted onto the pore wall to generate acidic protons, with appropriate topology/connectivity of the MOF structure to favor the formation of water hydrogen-bond pathways, a critical prerequisite for efficient proton transport. A series of hydrated PC-MOFs with superprotonic behavior under humidification has already been reported[12−21] as potential alternatives to the commercial benchmark Nafion. However, most of these MOFs still suffer from performance losses because of their insufficient hydrothermal stability when operating in humid environments. The design of highly water-stable MOFs with high proton-conduction performances is thus still challenging. This calls for the consideration of MOFs constructed from high-valence cations (3+ or 4+), which have been shown to be chemically and thermally robust.[22] Zirconium-based MOFs, especially those built from either Zr_6 oxo/hydroxo clusters (UiO-66, PCN-222, ...)[23,24] or zirconium oxide chains (MIL-140s)[25] are known to be remarkably stable, because of their strong Zr–ligand interactions. In this context, we very recently reported

Received: May 9, 2016
Revised: July 4, 2016
Published: July 12, 2016

ACS Publications © 2016 American Chemical Society

DOI: 10.1021/acs.jpcc.6b04649
J. Phys. Chem. C 2016, 120, 24503−24510

The Journal of Physical Chemistry C Article

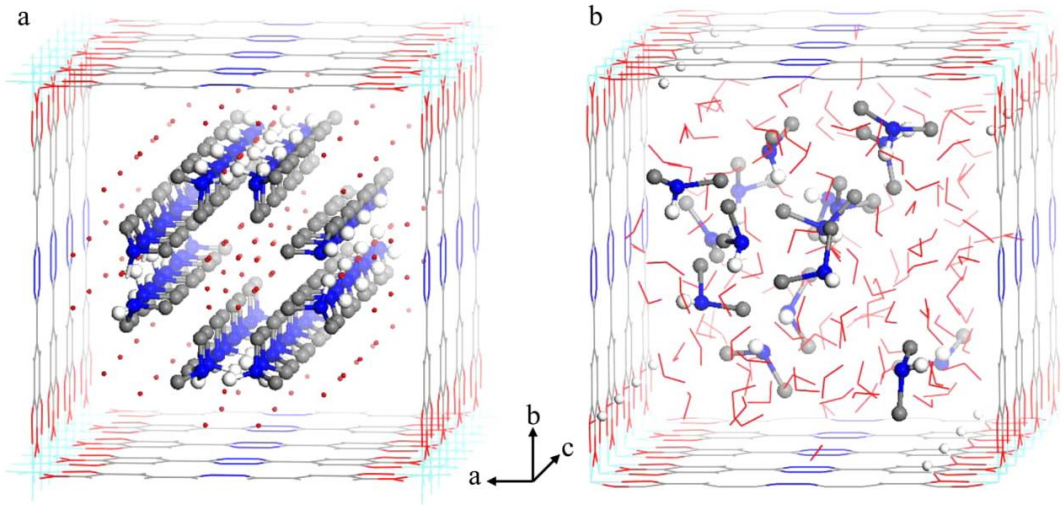

Figure 1. (a) Experimentally resolved crystal structure of hydrated MIL-163 and (b) representative snapshot of the Monte Carlo (MC) simulations performed at 25 °C for the saturation capacity of water and four dimethylamine molecules per unit cell. The atoms are represented as follows: Zr, light blue; C, gray; O, red; N, dark blue; and H, white. Perspective view in the *ab* plane. In panel b, note that DMA is represented by the united-atom model as selected in the MC simulations, and H_2O is described by red lines.

that the Zr-based UiO-66 grafted with two free carboxylic functions combines good water stability and high proton conductivity (2.1×10^{-3} S·cm^{-1}) at 90 °C and 95% relatively humidity, making this material a promising candidate for the targeted application.[26] Following these advances, we consider in this work one of the most recently developed Zr-based MOFs, namely, MIL-163 [$\{Zr_2(H_2\text{-}TzGal)_2\}\cdot(\text{solvent})_n$, where solvent = *N*,*N*-dimethylamine (DMA) and H_2O, TzGal =5,5′-(1,2,4,5-tetrazine-3,6-diyl)bis(benzene-1,2,3-triol)]. This is a phenolate-based MOF that exhibits a strongly enhanced chemical stability compared to all previously reported carboxylate Zr-based MOFs, as shown by its high stability in phosphate-containing simulated physiological media.[27] This MOF is built of edge-sharing ZrO_8 polyhedra connected by four linkers. Beyond its chemical stability, this square-shaped tunnel-like structure with a pore aperture of 12 Å (Figure 1a) displays optimal features for proton conduction, namely, the presence of (i) very acidic Zr-bonded phenol groups on the TzGal linker (as previously evidenced by ^{1}H solid-state NMR spectroscopy[27] and confirmed here by infrared spectroscopy using pyridine as a probe molecule; see Figure S1) that are expected to supply a source of protons and (ii) confined solvent molecules (DMA and water) that can act as conducting media in the pores. Note that the nitrogen atoms of Tz are known to show a very weak basic character[28] and the pK_a value of DMA, 10.73, is relatively low for a basic molecule. This supports the conclusion that both of these species are not involved in the conduction process. To verify the promise of this Zr-based MOF proton-conductivity measurements using complex impedance spectroscopy were performed on MIL-163 in its anhydrous and hydrated states up to 95% relative humidity. The performances of this MOF were further analyzed in light of the conclusions drawn from Monte Carlo simulations. This modeling effort allowed the exploration of the most preferential arrangement of the solvent molecules and the plausible formation of a hydrogen-bond network at the origin of the proton transport over long distances.

2. MATERIALS AND METHODS

2.1. Synthesis and Characterization. MIL-163 was synthesized according to the reported procedure.[27]

2.2. Proton-Conductivity Measurements. Impedance measurements were performed on a broadband dielectric spectrometer (Novocontrol Alpha Analyzer) over the frequency range from 1 Hz to 1 MHz with an applied ac voltage of 20 mV. Measurements were first collected from 150 to 25 °C on the anhydrous solid, obtained by in situ heating at 150 °C for 5 h [cf thermogravimetric analysis (TGA), Figure S2]. The powder sample was then introduced in a homemade cell and placed into an Espec Corp. SH-221 incubator to control the temperature (25 °C < T < 90 °C) and the relative humidity (RH = 95%). The solid was equilibrated for 24 h at the given T and RH values to ensure a constant water content before the impedance was recorded. About 75 mg of the powder sample was placed between two gold electrodes in a parallel-plate capacitor configuration with an annular Teflon spacer for insulation, allowing the use of the two-probe method for the electrical measurements. Resistivity was determined from the semicircle extrapolation in Nyquist plots. The conductivity was calculated considering $\sigma = 1/R \times l/S$, where R is the impedance (Ω); σ is the conductivity (S·cm^{-1}); and l and S are the sample thickness (cm) and surface area (cm^2), respectively.

2.3. Modeling. The experimental crystal structure of the fully hydrated MIL-163 was taken as the starting point.[27] Entrapped molecules were first removed, and missing hydrogen atoms were added on one-half of the *meta*-phenol groups of the ligand. The resulting structure was geometry-optimized at the density functional theory (DFT) level keeping the experimental unit cell parameters fixed. These calculations were performed using the Perdew−Burke−Ernzerhof (PBE) generalized gradient approximation (GGA) functional[29] combined with the double-numerical basis set containing polarization functions (DNP)[30] on all atoms as implemented in Dmol^3. The partial charge of each atom of MIL-163 was evaluated following an electrostatic potential (ESP) fitting strategy[31] that was applied

DOI: 10.1021/acs.jpcc.6b04649
J. Phys. Chem. C 2016, 120, 24503−24510

The Journal of Physical Chemistry C Article

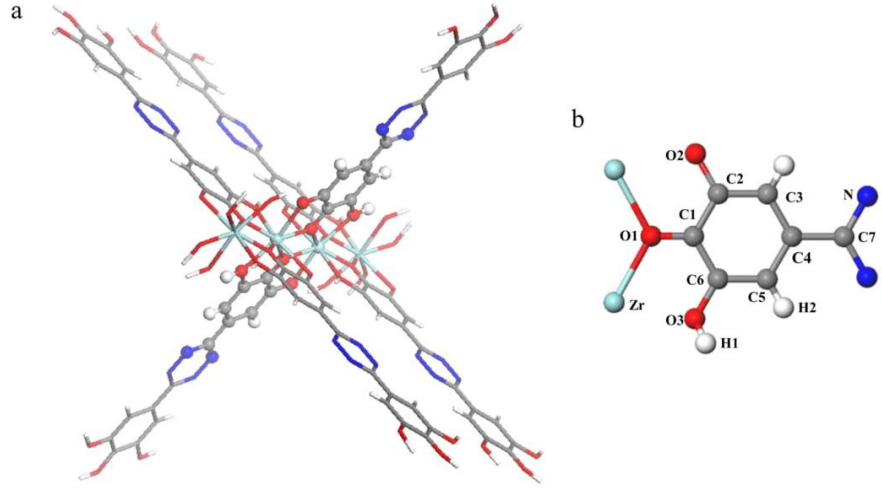

Figure 2. Selected cluster model for representing both inorganic and organic nodes of MIL-163. The color code is the same as in Figure 1a. (a) Atoms represented as balls considered for the extraction of the ESP charges and (b) their corresponding labels.

to a cluster cleaved from the optimized unit cell to model both the organic and inorganic nodes of the structure (see Figure 2). All terminations of this cluster were saturated with hydrogen atoms.

The resulting partial charges are reported in Table 1. This optimized structure was loaded with 4 dimethylamine and 32 water molecules per unit cell[27] and further geometry-relaxed using DFT calculations to refine the orientations of the acidic Zr-bonded phenol groups present in the TzGal linker. This step is of importance because it has been shown that guests usually induce significant local relaxation of the host MOF structures, including ligand flipping and/or tilting of the functional groups grafted on the ligand.[32−34] The resulting final structure model was considered for further Monte Carlo simulations. These calculations were performed in the *NVT* ensemble at 25 °C maintaining the structure rigid with a simulation box of 16 conventional unit cells (2 × 2 × 4) loaded with 64 dimethylamine (DMA) and 512 water molecules. To that end , 2.0×10^8 Monte Carlo steps following 10^7 steps for equilibration were performed. The interactions between the guest molecules and the MOF structure were described by a combination of site-to-site Lennard-Jones (LJ) contributions and Coulombic terms. The 12−6 LJ parameters for the atoms of the inorganic and organic moieties of the MOF were taken from the universal force field (UFF)[35] and DREIDING force field,[36] respectively. In addition, following the treatment employed in other well-known force fields,[37,38] the hydrogen atoms in the phenol and amino groups were considered to interact with the adsorbate molecules only through the

Table 1. ESP Partial Charges Considered for Each Atom of the MIL-163 Framework

atom type	charge (au)	atom type	charge (au)
Zr	1.851	C3	−0.101
N	−0.348	C4	−0.601
O1	−0.421	C5	−0.101
O2	−0.575	C6	0.198
O3	−0.538	C7	0.985
C1	−0.138	H1	0.499
C2	0.352	H2	0.106

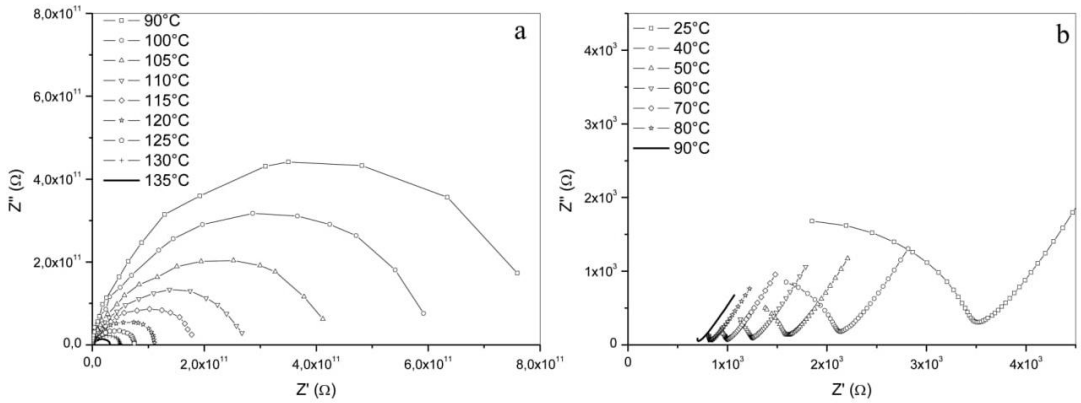

Figure 3. Nyquist representation of ac impedance spectra of (a) anhydrous MIL-163 from 90 to 135 °C and (b) hydrated MIL-163 from 25 to 90 °C.

DOI: 10.1021/acs.jpcc.6b04649
J. Phys. Chem. C 2016, 120, 24503−24510

Coulombic potential. The water molecules were represented by the TIP4P/2005 model,[39] and the DMA molecules were represented by the united-atom (UA) model previously reported by Schnabel et al.[40] All of the LJ cross-interaction parameters were determined by the Lorentz−Berthelot mixing rules. Short-range dispersion forces described by LJ potentials were truncated at a cutoff radius of 12 Å, whereas long-range electrostatic interactions were handled using the Ewald summation technique.

Finally, to gain insight into the arrangement of the guests in MIL-163, the guest−guest and guest−host radial distribution functions (RDFs), the density probability distributions for all of the guests, and the number of hydrogen bonds were obtained by averaging over hundreds of configurations generated during the MC simulations.

3. RESULTS AND DISCUSSION

3.1. Conductivity Measurements. The proton conductivity of MIL-163 was determined from the impedance measurements performed under anhydrous conditions at temperatures ranging from 150 to 25 °C. The real (Z') and imaginary (Z'') parts of the impedance are illustrated in the Nyquist plots in Figure 3a. These plots show a single distorted semicircle at high frequency, which represents grain-boundary and bulk-resistivity contributions, as are commonly observed for proton-conducting materials. At low frequency, the capacitive tail is characteristic of the blocking response of the gold electrodes, which clearly indicates that the conducting species are ionic, namely, H^+ ions. The total impedances were evaluated from the low-frequency-end intercept of the arc on the real axis. The proton conductivity, σ, was found to be 1.5×10^{-13} S·cm^{-1} at 90 °C, and it increased with temperature to reach 3.0×10^{-11} S·cm^{-1} at 150 °C.

The Arrhenius representation points to a thermally activated process of 1.20 eV (Figure 4). The very high activation energy combined with the low conductivity supports an inefficient proton transfer over long distances within the material. This is due to the lack of conducting media, because the acidic protons provided by MIL-163, namely, the neighboring phenol groups present in the organic linkers, are separated by distances of over 4 Å, which makes proton propagation highly unlikely without the involvement of an efficient charge carrier in the pores. This suggests that the DMA guest molecules are isolated from one another, resulting in a disrupted pathway for charge propagation.

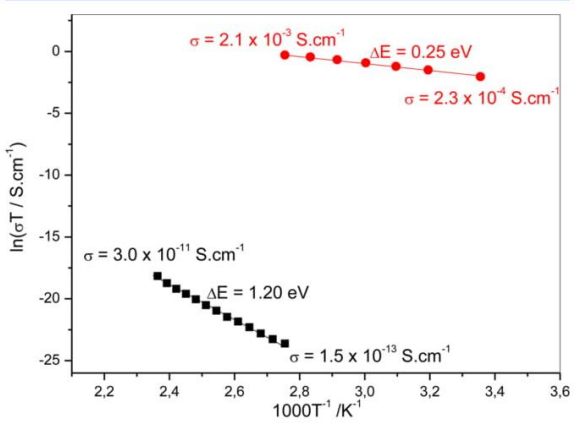

Figure 4. Arrhenius plot of anhydrous (black squares) and hydrated (red circles) MIL-163. The lines correspond to linear least-squares fits.

Most proton-conducting MOFs are reported under hydrated conditions, where water molecules aid the transport of protons. To investigate the impact of adsorbed water on the proton conductivity, impedance measurements were performed on hydrated MIL-163 (65% < RH < 95%) in the temperature range of 25−90 °C (see Figures S3 and S4 and Figure 3b). Note that the conductivity measurements obtained at 90 °C as a function of RH perfectly illustrate the acidic character of the protogenic groups of MIL-163[41] (see Figures S3 and S4). In addition, the evolution of the conductivity as a function of RH follows the increasing trend of water uptake deduced from the adsorption isotherm reported in ref 27, which supports the conclusion that the conductivity mainly occurs in the bulk. The Nyquist plots reported for RH = 95% reflect the fact that the hydrated sample exhibits a much lower resistance than the anhydrous solid, resulting in a linear tail end of a semicircle at the highest frequencies and a subsequent capacitive tail due to the ionic-blocking electrodes at lower frequencies. The total impedance was then extrapolated from the linear region to the Z' axis. The resulting total impedance ranged from 2.3×10^{-4} S·cm^{-1} at 25 °C to 2.1×10^{-3} S·cm^{-1} at 90 °C. This makes MIL-163 a superprotonic solid ($\sigma > 10^{-4}$ S·cm^{-1}).[42] Inspection of the powder X-ray diffraction pattern of the fully hydrated MIL-163 after the measurements confirmed its structural integrity (Figure S5). The so-obtained σ value at 90 °C is similar to the values collected for the best water-stable MOFs,[19−21] including the UiO-66(Zr)−$(CO_2H)_2$ that we recently reported.[26] Interestingly, this MOF shows a spectacular increase of the conductivity by 10 orders of magnitude from 0% to 95% RH at 90 °C, indicating that the presence of adsorbed water is critical for enhancing the conductivity performances of this solid and further emphasizing the key role of water molecules in assisting charge transfer through the proton-conducting pathways. Furthermore, this proton transfer involves an activation energy of 0.25 eV (Figure 4), which is among the lowest values reported so far for PC-MOFs.[9,10] This value falls into the 0.1−0.4 eV range that is usually related to a Grotthuss-like mechanism.[43,44] Referring to previous works on hydrated PC-MOFs, water is expected to serve as a mediator between the acidic protons provided by the phenol groups present in the TzGal linker. The low activation energy together with the high conductivity also suggests a high concentration of mediators in an ordered arrangement. This conclusion is supported by the large water uptake of the material at 25 °C (32 mmol·g^{-1}).[27] Monte Carlo simulations were further undertaken to gain insight into the arrangement of the confined water.

3.2. Modeling. As a preliminary step, we first validated the choice of microscopic model for the guests and host by obtaining good agreement between the preferential arrangements of both water and DMA molecules simulated by MC (Figure 1b) with those observed experimentally for hydrated MIL-163 (Figure 1a). In both cases, the DMA molecules are primarily distributed in the center of the pore and are thus screened from the pore walls by a layer of water molecules.

A careful analysis of the MC configurations indicated that the H_2O molecules are arranged in such a way that they interact with the MOF through (i) their oxygen atoms (O_w) and the proton (H_{acid}) of the acidic groups of the organic linker, resulting in a strong hydrogen bond, as shown by the short

DOI: 10.1021/acs.jpcc.6b04649
J. Phys. Chem. C 2016, 120, 24503−24510

The Journal of Physical Chemistry C Article

mean distance between the two atoms pairs [$d(O_w-H_{acid})$ = 1.80 Å; see RDFs in Figure 5a] and (ii) their protons atoms

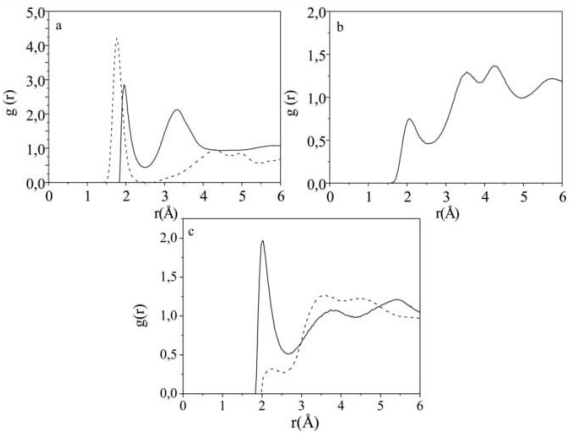

Figure 5. Radial distribution functions for the pairs (a) $O_w(H_2O)-H_{acid}$ (MIL-163) (dashed lines) and $O_w(H_2O)-H_w(H_2O)$ (solid lines), (b) $H_w(H_2O)-N(Tz)$, and (c) $H_{DMA}-O_w(H_2O)$ (solid lines) and $H_w(H_2O)-N_{DMA}$ (dashed lines) calculated from the average over the MC configurations considered for hydrated MIL-163 at 25 °C.

(H_w) and the N atom the TzGal linker with a mean distance of $d(H_w-N_{linker})$ = 2.10 Å (see RDF in Figure 5b) characteristic of a moderate interaction. The confined water molecules form a relatively strong three-dimensional hydrogen-bond network with a corresponding O_w-H_w mean distance of 1.95 Å (see RDF in Figure 5a), as short as those usually observed for water in the bulk state.[45] These whole observations remain the same when one considers a lower concentration of DMA i.e. 2 molecules/u.c. (see Figure S6). This emphasizes that the arrangements of water are not affected when DMA concentration varies from 2 to 4 molecules/u.c. This spatial distribution and the interactions at play are reminiscent of those commonly reported for water-mediated proton-conducting MOFs.[26]

A quantitative analysis of the number of hydrogen bonds per H_2O molecule was undertaken using the following criteria: $d(O_w-O_w)$ < 3.5 Å and angle formed between the intramolecular O−H vector (OH of the donor molecule) and the intermolecular O−O vector (O atoms of the donor and acceptor) less than 37°. This angle value was deduced from the distribution of the angles obtained for the confined water molecules in this MOF (see Figure S7). The total number of hydrogen bonds per H_2O molecule averaged over all generated MC configurations (1.55) was found to be significantly lower than that in bulk water (3.6)[39] because of the confinement generated by the porosity of the MOF (see Table S1). This value also remained lower than that we previously reported for UiO-66(Zr)−$(CO_2H)_2$ (2.40),[26] in relation with the one-dimensional tunnel-like topology of MIL-163 versus the three-dimensional cages of the pore structure of UiO-66(Zr)−$(CO_2H)_2$.

The resulting three-dimensional hydrogen-bond network in hydrated MIL-163 leads to the formation of clusters, implying up to 15 H_2O molecules (see SI), a number, which is smaller than previously observed for other one-dimensional-channel MOFs, such as MIL-53(Cr) and MIL-47(V).[46] These clusters are interconnected, and they create multiple pathways orientated along the three axes, as illustrated in Figure 6.

Such a resulting arrangement of water makes a bridge between two acidic groups present in adjacent or opposite pore walls. A quantitative analysis indicated that, on average, 4.5 phenol groups are connected to each other through the same water clusters (see Table S1). An illustration of this scenario is presented in Figure 7a,b in the *ab* and *bc* planes, respectively. The existence of such pathways offers an optimal situation for the water-mediated transfer of protons over long distances separating different organic linkers that act as a proton source in MIL-163. In addition, DMA mainly acts as a H-donor with a mean $O_w(H_2O)-H(DMA)$ distance of 2.0 Å, even though its H-acceptor character cannot be totally excluded, as suggested by the small contribution in the $H_w(H_2O)-N(DMA)$ RDF at

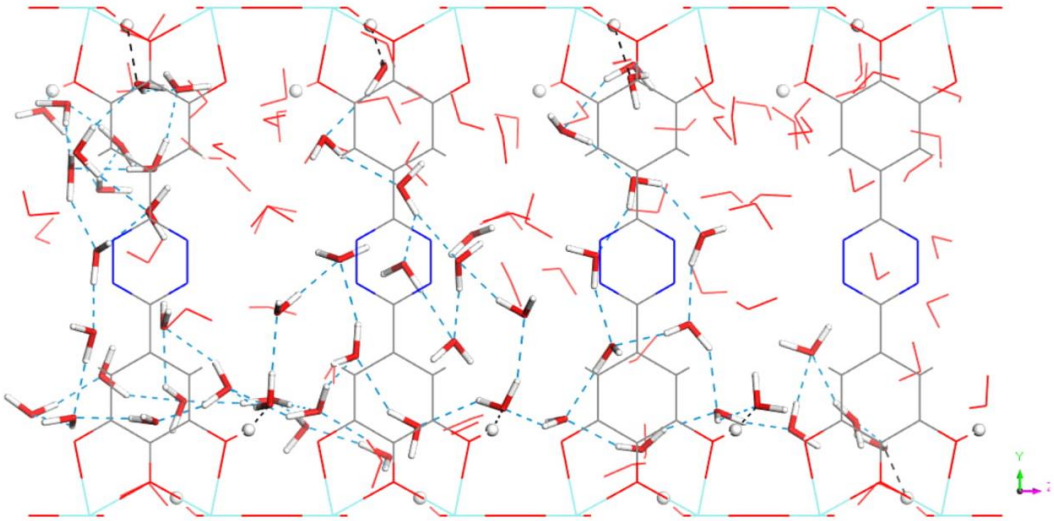

Figure 6. Illustration of the multiple hydrogen-bond pathways as evidenced by MC simulations performed at 25 °C for hydrated MIL-163. For the sake of clarity, DMA molecules have been omitted.

DOI: 10.1021/acs.jpcc.6b04649
J. Phys. Chem. C 2016, 120, 24503−24510

The Journal of Physical Chemistry C Article

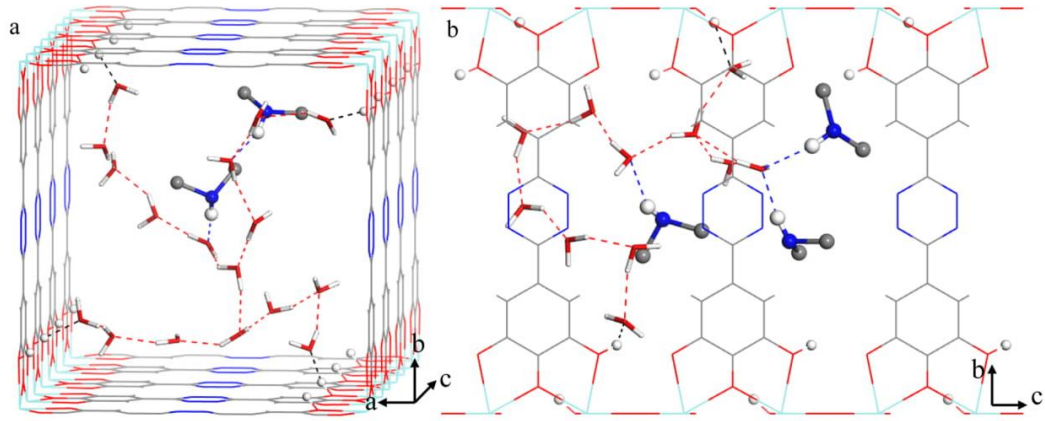

Figure 7. Illustrations of the preferential arrangement of water molecules as evidenced by MC simulations performed at 25 °C for hydrated MIL-163. The red dashed lines correspond to the hydrogen-bond network, and the blue dashed lines correspond to the interactions between DMA and water.

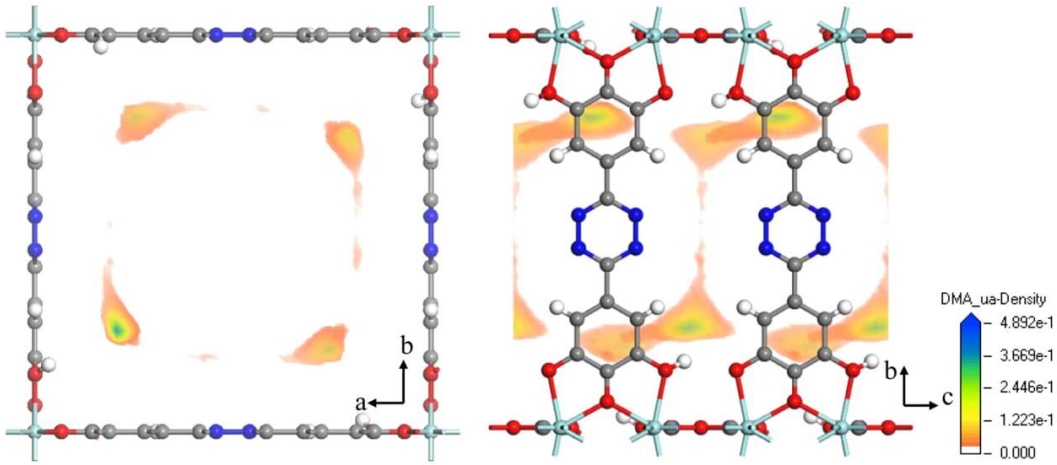

Figure 8. Two-dimensional density probabilities for DMA simulated by MC simulations at 25 °C for anhydrous MIL-163 in the (left) *ab* and (right) *bc* planes.

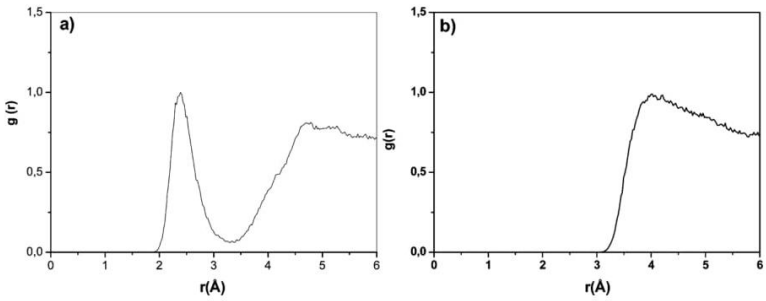

Figure 9. Radial distribution functions for the pairs (a) N_{DMA}–H_{acid} and (b) C_{DMA}–C_{DMA} calculated from the average over the MC configurations considered for anhydrous MIL-163 at 25 °C.

about 2.2 Å (see Figure 5c). Even though each dimethylamine molecule forms a single hydrogen bond through its H atoms (H_{DMA}) with the O atoms of water (O_w) (see Figure 7), the presence of these guest molecules does not lead to a disruption of the water hydrogen-bond network. This suggests that DMA does not have a detrimental effect on the conductivity performances of MIL-163.

MC simulations were further performed for MIL-163 in the absence of water molecules. As already reported, MIL-163 has a flexible framework and evolves upon dehydration from the aforementioned crystalline hydrated form to a dehydrated form

DOI: 10.1021/acs.jpcc.6b04649
J. Phys. Chem. C 2016, 120, 24503−24510

exhibiting broad and shifted diffraction peaks. For this reason, it was not possible to determine the structure of this activated form. Hence, in a first approximation, keeping the structure in its open form, the simulations on the anhydrous solid were carried out using the structure of the hydrated solid. It was found that whatever the considered DMA concentration, these guest molecules are localized at the corners of the structure (Figure 8, left and Figure S9), primarily interacting with the phenol groups of the linker, as shown by the relatively short distances separating the N atoms of diamine (N_{DMA}) and the H_{acid} atoms of the phenol groups of the organic linker [$d(N_{DMA}-H_{acid})$ = 2.70 Å; see the corresponding RDF in Figure 9a and Figure S10].

These molecules are isolated from each other, however, along the three axes, as illustrated in Figure 8 (right), consistent with guest–guest interacting distances of greater than 3.70 Å (see the RDF for the diamine–C_{DMA} carbon–carbon atom pair in Figure 9b and Figure S10). This latter observation supports the absence of a possible pathway for charge migration over long distances, leading to a poor conductivity of the sample in its anhydrous state, as measured experimentally.

4. CONCLUSIONS

The recently reported robust MIL-163 zirconium phenolate-based MOF was found to exhibit a relatively high conductivity of 2.1×10^{-3} S·cm^{-1} at 90 °C and 95% relative humidity. It was found that the square-shaped channel-like structure of this MOF allows the formation of a three-dimensional hydrogen-bond network, resulting in the creation of multiple pathways that offer an optimal scenario for the water-mediated transfer of protons supplied by the phenol groups present in the organic linker. Interestingly, these preferential pathways are not affected by the presence of the guest DMA molecules that tend to form single hydrogen bonds with water. Such proton-conduction performances coupled with the exceptional chemical robustness of this porous hybrid solid make it a promising candidate in the field of solid-state proton conduction.

■ ASSOCIATED CONTENT

Supporting Information

The Supporting Information is available free of charge on the ACS Publications website at DOI: 10.1021/acs.jpcc.6b04649.

Infrared spectra, thermogravimetric analysis, and powder X-ray diffraction patterns of the synthesized MIL-163 sample; complementary impedance data; and details of the calculations of the hydrogen bonds (PDF)

■ AUTHOR INFORMATION

Corresponding Author

*E-mail: sabine.devautour-vinot@umontpellier.fr. Tel.: +33 4 67 14 33 00.

Author Contributions

G.Mo. synthesized and characterized the MOF sample; F.F. and A.V. performed the infrared characterization; P.G.M.M., S.D.-V., and G.M. performed the conductivity measurements and the Monte Carlo simulations and wrote the manuscript.

Notes

The authors declare no competing financial interest.

■ ACKNOWLEDGMENTS

P.G.M.M. thanks the National Counsel of Technological and Scientific Development (CNPQ) for a scholarship, G.Ma. thanks the Institut Universitaire de France for its support, and G.Mo. thanks the LabEx CHARMMMAT for a postdoctoral fellowship.

■ REFERENCES

(1) Bagotsky, V. S. *Fuel Cells: Problems and Solutions*, 2nd ed.; John Wiley & Sons, Inc.: Hoboken, NJ, 2012.

(2) Badwal, S. P. S.; Giddey, S. S.; Munnings, C.; Bhatt, A. I.; Hollenkamp, A. F. Emerging Electrochemical Energy Conversion and Storage Technologies. *Front. Chem.* **2014**, *2*, 79.

(3) Alotto, P.; Guarnieri, M.; Moro, F. Redox Flow Batteries for the Storage of Renewable Energy: a Review. *Renewable Sustainable Energy Rev.* **2014**, *29*, 325–335.

(4) Soloveichik, G. L. Flow Batteries: Current Status and Trends. *Chem. Rev.* **2015**, *115*, 11533–11558.

(5) Kreuer, K. D. Proton-Conducting Oxides. *Annu. Rev. Mater. Res.* **2003**, *33*, 333–359.

(6) Boysen, D. A.; Uda, T.; Chisholm, C. R. I.; Haile, S. M. High-Performance Solid Acid Fuel Cells Through Humidity Stabilization. *Science* **2004**, *303*, 68–70.

(7) Mauritz, K. A.; Moore, R. B. State of Understanding of Nafion. *Chem. Rev.* **2004**, *104*, 4535–4586.

(8) Jheng, L.-C.; Huang, C.-Y.; Hsu, S. L-C. Sulfonated MWNT and Imidazole Functionalized MWNT/Polybenzimidazole Composite Membranes for High-Temperature Proton Exchange Membrane Fuel Cells. *Int. J. Hydrogen Energy* **2013**, *38*, 1524–1534.

(9) Horike, S.; Umeyama, D.; Kitagawa, S. Ion Conductivity and Transport by Porous Coordination Polymers and Metal–Organic Frameworks. *Acc. Chem. Res.* **2013**, *46*, 2376–2384.

(10) Ramaswamy, P.; Wong, N. E.; Shimizu, G. K. H. MOFs as Proton Conductors – Challenges and Opportunities. *Chem. Soc. Rev.* **2014**, *43*, 5913–5932.

(11) Yoon, M.; Suh, K.; Natarajan, S.; Kim, K. Proton Conduction in Metal–Organic Frameworks and Related Modularly Built Porous Solids. *Angew. Chem., Int. Ed.* **2013**, *52*, 2688–2700.

(12) Kim, S.; Dawson, K. W.; Gelfand, B. S.; Taylor, J. M.; Shimizu, G. K. H. Enhancing Proton Conduction in a Metal–Organic Framework by Isomorphous Ligand Replacement. *J. Am. Chem. Soc.* **2013**, *135*, 963–966.

(13) Dong, X. Y.; Wang, R.; Li, J. B.; Zang, S.-Q.; Hou, H.-W.; Mak, T. C. W. A Tetranuclear $Cu_4(\mu_3\text{-}OH)_2$-Based Metal–Organic Framework (MOF) with Sulfonate–Carboxylate Ligands for Proton Conduction. *Chem. Commun.* **2013**, *49*, 10590–10592.

(14) Panda, T.; Kundu, T.; Banerjee, R. Structural Isomerism Leading to Variable Proton Conductivity in Indium(III) Isophthalic Acid Based Frameworks. *Chem. Commun.* **2013**, *49*, 6197–6199.

(15) Taddei, M.; Donnadio, A.; Costantino, F.; Vivani, R.; Casciola, M. Synthesis, Crystal Structure, and Proton Conductivity of One-Dimensional, Two-Dimensional, and Three-Dimensional Zirconium Phosphonates Based on Glyphosate and Glyphosine. *Inorg. Chem.* **2013**, *52*, 12131–12139.

(16) Nagarkar, S. S.; Unni, S. M.; Sharma, A.; Kurungot, S.; Ghosh, S. K. Two-in-One: Inherent anhydrous and Water-Assisted High Proton Conduction in a 3D Metal–Organic Framework. *Angew. Chem., Int. Ed.* **2014**, *53*, 2638–2642.

(17) Sadakiyo, M.; Yamada, T.; Honda, K.; Matsui, H.; Kitagawa, H. Control of Crystalline Proton-Conducting Pathways by Water-Induced Transformations of Hydrogen-Bonding Networks in a Metal–Organic Framework. *J. Am. Chem. Soc.* **2014**, *136*, 7701–7707.

(18) Bazaga-García, M.; Colodrero, R. M. P.; Papadaki, M.; Garczarek, P.; Zoń, J.; Olivera-Pastor, P.; Losilla, E. R.; León-Reina, L.; Aranda, M. A. G.; Choquesillo-Lazarte, D.; et al. Guest Molecule-Responsive Functional Calcium Phosphonate Frameworks for Tuned Proton Conductivity. *J. Am. Chem. Soc.* **2014**, *136*, 5731–5739.

DOI: 10.1021/acs.jpcc.6b04649
J. Phys. Chem. C 2016, 120, 24503–24510

(19) Yang, F.; Huang, H.; Wang, X.; Li, F.; Gong, Y.; Zhong, C.; Li, J. R. Proton Conductivities in Functionalized UiO-66: Tuned Properties, Thermogravimetry Mass, and Molecular Simulation Analyses. *Cryst. Growth Des.* **2015**, *15*, 5827−5833.
(20) Phang, W. J.; Jo, H.; Lee, W. R.; Song, J. H.; Yoo, K.; Kim, B.-S.; Hong, C. S. Superprotonic Conductivity of a UiO-66 Framework Functionalized with Sulfonic Acid Groups by Facile Postsynthetic Oxidation. *Angew. Chem., Int. Ed.* **2015**, *54*, 5142−5146.
(21) Ramaswamy, P.; Wong, N. E.; Gelfand, B. S.; Shimizu, G. K. H. A Water Stable Magnesium MOF That Conducts Protons over 10^{-2} S cm^{-1}. *J. Am. Chem. Soc.* **2015**, *137*, 7640−7643.
(22) Devic, T.; Serre, C. High Valence 3p and Transition Metal Based MOFs. *Chem. Soc. Rev.* **2014**, *43*, 6097−115.
(23) Cavka, J. H.; Jakobsen, S.; Olsbye, U.; Guillou, N.; Lamberti, C.; Bordiga, S.; Lillerud, K. P. A New Zirconium Inorganic Building Brick Forming Metal Organic Frameworks with Exceptional Stability. *J. Am. Chem. Soc.* **2008**, *130*, 13850−13851.
(24) Feng, D.; Gu, Z.-Y.; Li, J.-R.; Jiang, H.-L.; Wei, Z.; Zhou, H.-C. Zirconium-Metalloporphyrin PCN-222: Mesoporous Metal−Organic Frameworks with Ultrahigh Stability as Biomimetic Catalysts. *Angew. Chem., Int. Ed.* **2012**, *51*, 10307−10310.
(25) Guillerm, V.; Ragon, F.; Dan-Hardi, M.; Devic, T.; Vishnuvarthan, M.; Campo, B.; Vimont, A.; Clet, G.; Yang, Q.; Maurin, G.; et al. A Series of Isoreticular, Highly Stable, Porous Zirconium Oxide Based Metal−Organic Frameworks. *Angew. Chem., Int. Ed.* **2012**, *51*, 9267.
(26) Damasceno Borges, D.; Devautour-Vinot, S.; Jobic, H.; Ollivier, J.; Nouar, F.; Semino, R.; Devic, T.; Serre, T.; Paesani, F.; Maurin, G. Proton Transport in a Highly Conductive Porous Zirconium-Based Metal−Organic Framework: Molecular Insight. *Angew. Chem., Int. Ed.* **2016**, *55*, 3919−3924.
(27) Mouchaham, G.; Cooper, L.; Guillou, N.; Martineau, C.; Elkaim, E.; Bourrelly, S.; Llewellyn, P. L.; Allain, C.; Clavier, G.; Serre, C.; et al. A Robust Infinite Zirconium Phenolate Building Unit to Enhance the Chemical Stability of Zr MOFs. *Angew. Chem., Int. Ed.* **2015**, *54*, 13297−13301.
(28) Clavier, G.; Audebert, P. s-Tetrazines as Building Blocks for New Functional Molecules and Molecular Materials. *Chem. Rev.* **2010**, *110*, 3299−3314.
(29) Perdew, J. P.; Burke, K.; Ernzerhof, M. Generalized Gradient Approximation Made Simple. *Phys. Rev. Lett.* **1996**, *77*, 3865−3868.
(30) Hehre, W. J.; Ditchfield, J. A.; Pople, J. A. Self-Consistent Molecular Orbital Methods. XII. Further Extensions of Gaussian-Type Basis Sets for Use in Molecular Orbital Studies of Organic Molecules. *J. Chem. Phys.* **1972**, *56*, 2257−2261.
(31) Heinz, H.; Suter, U. W. Atomic Charges for Classical Simulations of Polar Systems. *J. Phys. Chem. B* **2004**, *108*, 18341−18352.
(32) Benoit, V.; Pillai, R. S.; Orsi, A.; Normand, P.; Jobic, H.; Nouar, F.; Billemont, P.; Bloch, E.; Bourrelly, S.; Devic, T.; et al. MIL-91(Ti), a Small Pore Metal−Organic Framework which Fulfils Several Criteria: an Upscaled Green Synthesis, Excellent Water Stability, High CO_2 Selectivity and Fast CO_2 Transport. *J. Mater. Chem. A* **2016**, *4*, 1383−1389.
(33) Pillai, R. S.; Benoit, V.; Orsi, A.; Llewellyn, P. L.; Wright, P. A.; Maurin, G. Highly Selective CO_2 Capture by Small Pore Scandium-Based Metal−Organic Frameworks. *J. Phys. Chem. C* **2015**, *119*, 23592−23598.
(34) Maurin, M. Role of Molecular Simulations in the Structure Exploration of Metal−Organic Frameworks: Illustrations through Recent Advances in the Field. *C. R. Chim.* **2016**, *19*, 207−215.
(35) Rappe, A. K.; Casewit, C. J.; Colwell, K. S.; Goddard, W. A.; Skiff, W. M. UFF, a Full Periodic Table Force Field for Molecular Mechanics and Molecular Dynamics Simulations. *J. Am. Chem. Soc.* **1992**, *114*, 10024−10035.
(36) Mayo, S. L.; Olafson, B. D.; Goddard, W. A. DREIDING: a Generic Force Field for Molecular Simulations. *J. Phys. Chem.* **1990**, *94*, 8897−8909.
(37) Jorgensen, W. L.; Maxwell, D. S.; Tirado-Rives, J. Development and Testing of the OPLS All-Atom Force Field on Conformational Energetics and Properties of Organic Liquids. *J. Am. Chem. Soc.* **1996**, *118*, 11225−11236.
(38) Wick, C. D.; Stubbs, J. M.; Rai, N.; Siepmann, J. I. Transferable Potentials for Phase Equilibria. Primary, Secondary, and Tertiary Amines, Nitroalkanes and Nitrobenzene, Nitriles, Amides, Pyridine, and Pyrimidine. *J. Phys. Chem. B* **2005**, *109*, 18974−18982.
(39) Abascal, J. L. F.; Vega, C. A General Purpose Model for the Condensed Phases of Water: TIP4P/2005. *J. Chem. Phys.* **2005**, *123*, 234505−234512.
(40) Schnabel, T.; Vrabec, J.; Hasse, H. Molecular Simulation Study of Hydrogen Bonding Mixtures and New Molecular Models for Mono- and Dimethylamine. *Fluid Phase Equilib.* **2008**, *263*, 144−159.
(41) Donnadio, A.; Nocchetti, M.; Costantino, F.; Taddei, M.; Casciola, M.; da Silva Lisboa, F.; Vivani, R. A Layered Mixed Zirconium Phosphate/Phosphonate with Exposed Carboxylic and Phosphonic Grops: X-ray Powder Structure and Proton Conductivity Properties. *Inorg. Chem.* **2014**, *53*, 13220−13226.
(42) Colomban, P. *Proton Conductors: Solids, Membranes, and Gels—Materials and Devices*; Cambridge University Press: Cambridge, U.K., 1992.
(43) de Grotthuss, C. J. T. Sur la Décomposition de l'Eau et des Corps qu'Elle Tient en Dissolution à l'Aide de l'Electricité Galvanique. *Ann. Chim.* **1806**, *58*, 54−74.
(44) Kreuer, K. D.; Rabenau, A.; Weppner, W. A New Model for the Interpretation of the Conductivity of Fast Proton Conductors. *Angew. Chem., Int. Ed. Engl.* **1982**, *21*, 208−209.
(45) Jorgensen, W. L.; Jenson, C. Temperature Dependence of TIP3P, SPC, and TIP4P Water from NPT Monte Carlo Simulations: Seeking Temperatures of Maximum Density. *J. Comput. Chem.* **1998**, *19*, 1179−1186.
(46) Salles, F.; Bourrelly, S.; Jobic, H.; Devic, T.; Guillerm, V.; Llewellyn, P. L.; Serre, C.; Férey, G.; Maurin, G. Molecular Insight into the Adsorption and Diffusion of Water in the Versatile Hydrophilic/Hydrophobic Flexible MIL-53(Cr) MOF. *J. Phys. Chem. C* **2011**, *115*, 10764−10776.

DOI: 10.1021/acs.jpcc.6b04649
J. Phys. Chem. C 2016, 120, 24503−24510

Article 2

CHEMISTRY OF MATERIALS

Article

pubs.acs.org/cm

Highly Efficient Proton Conduction in a Three-Dimensional Titanium Hydrogen Phosphate

Paulo G. M. Mileo,[†] Tanay Kundu,[‡] Rocio Semino,[†] Virginie Benoit,[§] Nathalie Steunou,[‡] Philip L. Llewellyn,[§] Christian Serre,[∥] Guillaume Maurin,[†] and Sabine Devautour-Vinot*[,†]

[†]Institut Charles Gerhardt Montpellier, UMR 5253 CNRS, UM, ENSCM, Université Montpellier, Place E. Bataillon, 34095 Montpellier cedex 5, France

[‡]Institut Lavoisier, UMR CNRS 8180, Université de Versailles St-Quentin en Yvelines, 45 Avenue des Etats-Unis, 78035 Versailles Cedex, Université Paris-Saclay, France

[§]Aix Marseille Univ, CNRS, MADIREL, Marseille, France

[∥]Institut des Matériaux Poreux de Paris, FRE 2000 CNRS, Ecole Normale Supérieure, Ecole Supérieure de Physique et de Chimie Industrielles, PSL Research University, 75005 Paris, France

Supporting Information

ABSTRACT: Force field-based and ab initio molecular dynamics simulations are combined with impedance spectroscopy experiments to reveal the high proton conduction performance of a three-dimensional titanium phosphate $Ti^{IV}Ti^{IV}(HPO_4)_4$ under humidity and further elucidate the microscopic mechanism at the origin of the proton transport throughout the porosity of this solid. The molecular simulations revealed that the POH groups in the structure act as a proton source, and the proton is transported from one pore to another through the hydrogen bond network formed by water molecules and the bridging O of the solid. Propitiously, besides its superprotonic behavior with a conductivity of 1.2×10^{-3} S cm^{-1} at room temperature and 95% relative humidity, this material is one of the best porous solids reported to date in terms of efficiency for proton transfer with a resulting activation energy (0.13 eV) as low as that reported for Nafion commercially used as electrolyte membrane in fuel cells. Furthermore, this solid shows a spectacular increase of the conductivity by 9 orders of magnitude at 90 °C when the relative humidity goes from 0 to 95%. This makes $Ti^{IV}Ti^{IV}(HPO_4)_4$ as a potential candidate for humidity sensor applications.

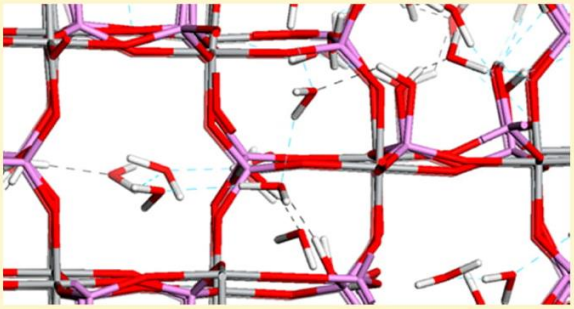

■ INTRODUCTION

Solid-state proton conductors are of central interest for many technological innovations. This includes the fields of hydrogen and humidity sensors; membranes for water electrolyzers; and most importantly, fuel cells where an efficient electrochemical energy conversion is expected to pave the way toward a reduced dependence on oil and a decrease of pollution. Recently, some materials of the family of metal–organic frameworks (MOFs) and porous coordination polymers (PCPs) have emerged as promising systems with high proton conduction performances at low and intermediate temperatures.[1–5] In particular, MOFs based on phosphoric and phosphonic acids and more generally metal phosphonate materials[6–29] offer a prominent platform for the design of proton-conducting solids because the phosphonic acid groups in addition to acting as a proton source contribute to a better thermal/water stability and oxidation resistance[30] compared to other protogenic species (sulfonic or carboxylic acids). In addition, multidimensional hybrid frameworks can be formed when metal ions are coordinated to phosphonate groups owing to their three oxygen atoms, which can act potentially as proton donor as well as proton acceptor to form a strong hydrogen-bond network.

However, porous phosphonate hybrid solids are less encountered in the literature compared to their carboxylate-based counterparts because of the less predictable coordination chemistry of phosphonate linkers and the larger diversity of possible coordinating modes, which lead to the formation of nonporous layered structures.[31,32] In the quest for designing phosphate-based proton conductors, pure inorganic crystalline solids have been also envisaged because they are much more thermally and chemically stable than the metal phosphonate hybrid materials. In this context, metal(IV) phosphates have been extensively investigated, with a particular focus on titanium-, zirconium-, or silicon-based solids.[33–37] However, these materials are chains or layer-like systems rather than

Received: May 5, 2017
Revised: August 21, 2017
Published: August 21, 2017

ACS Publications © 2017 American Chemical Society

DOI: 10.1021/acs.chemmater.7b01850
Chem. Mater. 2017, 29, 7263–7271

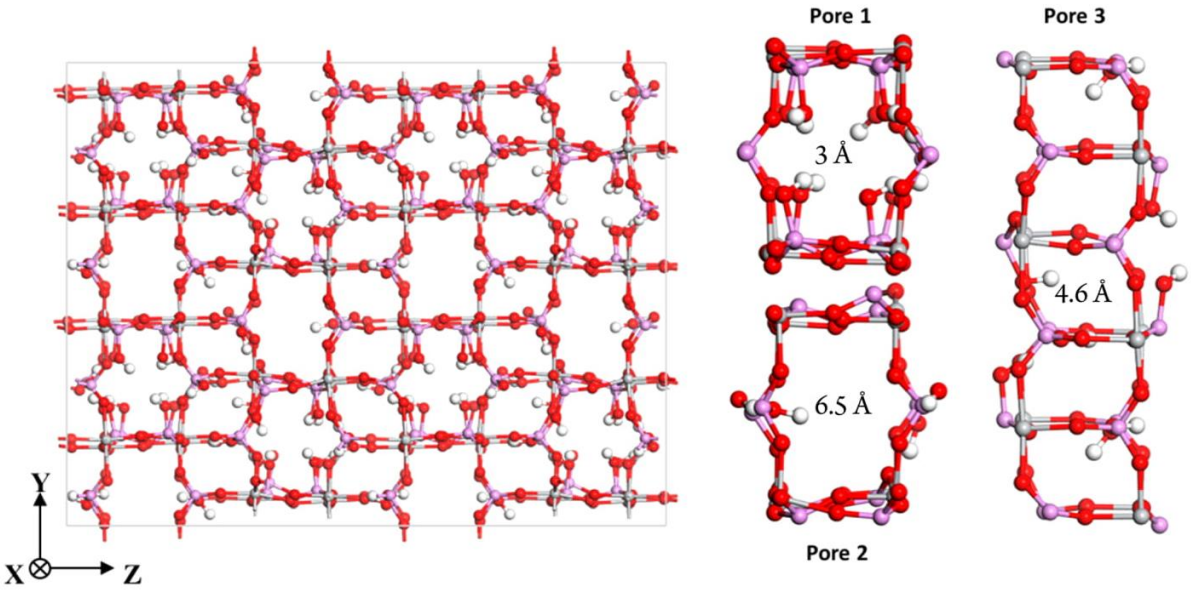

Figure 1. DFT-optimized structure of $Ti^{IV}Ti^{IV}(HPO_4)_4$ with the details of its pore network (pores 1, 2, and 3). The atoms are represented as follows: P, pink; C, gray; O, red; and H, white. The dimensions of each pore obtained from the pore size distribution analysis of the crystal structure (see the Supporting Information), are also provided. The representation is provided in the *yz* plane.

three-dimensional (3D) open-framework structures, and this limits their use as water-mediated solid proton conductors. As a typical illustration, the Zr(IV) phosphates are mostly structurally related to either $Zr(HPO_4)_2{\cdot}H_2O$ (α-ZrP)[33] or to $Zr(PO_4)$-$(H_2PO_4){\cdot}2H_2O$ (γ-ZrP).[34] In a similar way, the titanium phosphate compounds such as the α-$Ti(HPO_4)_2{\cdot}H_2O$[35,36] and γ-$Ti(H_2PO_4)(PO_4){\cdot}2H_2O$ show layered structures.[37] In contrast, only a few three-dimensional Ti- or Zr-based phosphate showing an open framework have been reported to date.[38−46] Note that most of these 3D open-framework structures lack accessible porosity because, unlike for zeolites or aluminophosphates, the removal of the structure-directing agents leads to the destruction of the framework.[42,43] The mixed-valence titanium phosphate,[40] i.e., $Ti^{III}Ti^{IV}(HPO_4)_4{\cdot}C_2N_2H_9{\cdot}H_2O$, is one of the rare examples of phosphate materials that contain microporous channels accommodating ethylenediamine cations and water molecules.

When calcined at 600 °C for 10 h in air flow, this solid is transformed into a new narrow pore phase, i.e. $Ti^{IV}Ti^{IV}(HPO_4)_4$, with a similar pore network, resulting from the simultaneous departure of the ethylenediamine molecules and the oxidation change of Ti^{III} to Ti^{IV} to ensure the electroneutrality of the system. The structure of this 3D titanium phosphate shows some similarities with that of τ-$Zr(HPO_4)_2$.[47]

As shown in Figure 1, $Ti^{IV}Ti^{IV}(HPO_4)_4$ is made of corner-sharing octahedra and tetrahedra of oxygens centered by titanium and phosphorus atoms, respectively, resulting in the creation of three distinct one-dimensional (1D)-type channels. The smallest pore (pore 1, 3.0 Å diameter, cf Figure 1) contains most of the phosphorus-centered tetrahedra, whose terminal hydroxyl groups pointing toward the center of the channel are expected to be hydrogen-bonded to each other. This pore is interconnected through pore 3 (4.6 Å diameter) to a larger pore 2 (6.5 Å diameter) that is almost free of P−OH groups. This ultramicroporous solid was shown to be nonporous upon N_2 adsorption; however, its ability to adsorb water makes it promising for proton conductivity applications owing to the large concentration of POH groups present at its pore surface.

The present paper aims at exploring the proton conduction performance of this three-dimensional open framework titanium phosphate $Ti^{IV}Ti^{IV}(HPO_4)_4$ under controlled temperature and relative humidity using complex impedance spectroscopy. A spectacular increase of the proton conductivity by 9 orders of magnitude was observed from 0 to 95% of relative humidity up to a value of 1.2×10^{-3} S cm^{-1} at room temperature. Force field-based and ab initio molecular dynamics (MD) simulations were further combined to shed light on the proton-transport mechanism at the microscopic level. This computational approach particularly explored the topology of the water hydrogen-bond network within the porous solid and the proton transfer throughout the solid.

■ EXPERIMENTAL SECTION

Synthesis and Characterization. $Ti^{IV}Ti^{IV}(HPO_4)_4$ was synthesized according to the previously reported procedure (see the Supporting Information for details about the synthesis).[40] The synthesis of this Ti phosphate proceeds in two steps, starting with the hydrothermal synthesis of the mixed valence $Ti^{III}Ti^{IV}(HPO_4)_4{\cdot}C_2N_2H_9{\cdot}H_2O$, followed by its calcination at 600 °C, thereby leading to $Ti^{IV}Ti^{IV}(HPO_4)_4$. The full characterization of $Ti^{IV}Ti^{IV}(HPO_4)_4$ is provided in the Supporting Information. This showed that the so-obtained calcined sample corresponds to the $Ti^{IV}Ti^{IV}(HPO_4)_4$ phase in the presence of traces of the as-synthesized $Ti^{III}Ti^{IV}(HPO_4)_4{\cdot}C_2N_2H_9{\cdot}H_2O$ (Figure S1).

Proton Conductivity Measurements. Impedance measurements were performed on a broadband dielectric spectrometer, Novocontrol alpha analyzer over a frequency range from 1 Hz to 1 MHz with an applied ac voltage of 20 mV. Measurements were first collected from 473 to 298 K on the anhydrous solid, obtained by a preliminary in situ heating at 473 K for 5 h (cf TGA, Figure S3). The sample was then introduced in a homemade cell and placed into an Espec Corp. SH-221 incubator to control the temperature ($298 < T$ (K) < 363) and the relative humidity (RH = 95%). The solid was equilibrated for 48 h at

DOI: 10.1021/acs.chemmater.7b01850
Chem. Mater. 2017, 29, 7263−7271

given T and RH values to ensure fixed water content before recording the impedance. The measurements were performed using powders. The consideration of pellets led to similar data (see the Supporting Information). Resistivity was determined from both the semicircle extrapolation method and the fitting of the Nyquist plots using equivalent circuit models. As shown in the Supporting Information, both procedures converge toward similar R values. The conductivity was calculated considering $\sigma = \frac{1}{R} \times \frac{l}{S}$, where R is the resistance (Ω) and σ is the conductivity ($S \cdot cm^{-1}$); l and S are the sample thickness (cm) and surface area (cm^2), respectively. The activated energy associated with the proton transport process was deduced from the linear fitting of $\ln(\sigma T)$ versus $1/T$, according to the Nernst−Einstein equation $[\sigma(T)) = \sigma_0/T \exp(-E_a/kT)]$.

Water Adsorption Isotherm. The behavior with respect to water vapor was investigated at 298 K (Belsorb-max, MicrotracBEL). Around 66 mg of sample was outgassed at 473 K (ramp of 1 °C/min) for 16 h under secondary vacuum (10^{-6} mbar). The water adsorption measurement was limited at a relative pressure $p/p^0 = 0.989$. To ensure that equilibrium was reached, for each p/p^0, the time dependence of the volume variation ΔV was fixed to be below 1 $cm^3\,g^{-1}\,s^{-1}$. As a result, the equilibrium time varies for each p/p^0 and 1 week was required to collect the adsorption isotherm, consistent with the small-pore nature of the microporous material $Ti^{IV}Ti^{IV}(HPO_4)_4$.

■ MODELING SECTION

Microscopic Models for the Framework and Water. $Ti^{IV}Ti^{IV}(HPO_4)_4$ was modeled using the crystal structure solved previously using X-ray powder diffraction data.[40] This structural model was saturated by the missing hydrogen atoms on the POH groups and was further geometry optimized at the density functional theory (DFT) level while keeping the experimental cell parameters fixed. These calculations were performed on a unit cell containing 13 water molecules corresponding to the water saturation capacity as measured by adsorption experiments. The PBE GGA functional[48,49] was combined with the use of Gaussian basis set and pseudopotential as implemented in the CP2K package.[50,51] The triple-ζ valence plus two polarization (TZV2P) basis set[52] was used for the H, O, and P atoms, while Ti was treated using the double-ζ valence plus polarization (DZVP) basis set.[53] The pseudopotentials used for all of the atoms were those derived by Goedecker, Teter, and Hutter.[54,55] A relative cutoff of 500 Ry and a convergence criterion for the self-consistent field interactions of 10^{-6} were employed. The van der Waals effects interactions were taken into account via the use of semi-empirical dispersion corrections as implemented in the DFT-D3 method. The resulting structural model was further used for all the force field-based calculations. The DFT-optimized structure of the 1D-type channel $Ti^{IV}Ti^{IV}(HPO_4)_4$ is illustrated in Figure 1.

Water was described by the SPC model[56] corresponding to a 3 charged Lennard-Jones (LJ) sites microscopic representation with a O−H bond length of 1.0 Å and a H−O−H angle of 109.47°. The interactions between $Ti^{IV}Ti^{IV}(HPO_4)_4$ and water were thus modeled using a van der Waals 12−6 LJ contribution and a Coulombic term. Similarly to the cases of silicates and other phosphonates materials,[57−59] here only the oxygen atoms of the framework were considered as LJ interacting sites, while all atoms of the framework contribute to the electrostatic interactions. The atomic partial charges for all atoms of the framework were further obtained by fitting the electrostatic potential from a single point energy calculation with Dmol^3 [60,61] on a cluster model appropriately cut from the periodic structure. These calculations were also based on the PBE functional and the double numerical basis set containing polarization functions (DNP).[62] The corresponding LJ force field parameters and atom charges of $Ti^{IV}Ti^{IV}(HPO_4)_4$ were implemented in the grand canonical Monte Carlo (GCMC) simulations.

GCMC simulations were carried out at 298 K to predict the adsorption behavior of water in $Ti^{IV}Ti^{IV}(HPO_4)_4$. The simulation box was made of 8 DFT-optimized unit cells (2 × 2 × 2) maintaining the atoms fixed in their initial positions. Short-range dispersion forces described by LJ potentials were truncated at a cutoff radius of 12 Å, while the Ewald summation approach was used to estimate the Coulombic contribution. For each state point, 2×10^8 Monte Carlo steps after 10^7 equilibration steps have been used. The adsorption enthalpy at low coverage ΔH for water was calculated using the revised Widom's test particle insertion method.[63] To shed light on the configurational distribution of the adsorbed species in $Ti^{IV}Ti^{IV}(HPO_4)_4$, the density probability of water within the porosity was calculated from the configurations generated from the GCMC calculations.

Molecular Dynamics Simulations. MD simulations were further carried out in the *NVT* ensemble using the Nosé−Hoover thermostat[64,65] with a total simulation time of 10 ns and a time step of 0.5 fs. These calculations were conducted using the software DL_POLY 4[66] considering 5 different starting configurations preliminarily generated by Monte Carlo simulations. The MD simulations were performed using a partially flexible framework for $Ti^{IV}Ti^{IV}(HPO_4)_4$ that allowed the POH to freely orientate upon water adsorption. The intramolecular potential parameters for the P−O and O−H bonds, as well as for the P−O−H angle were taken from a previous work dedicated to the modeling of zirconium phosphates.[67] For the intramolecular O−P−O−H torsion parameter, we used a cosine potential with a constant force of 52 kcal/mol in order to achieve the usual average fluctuation of the torsion angle of about 30° during a MD run conducted without any water inside the pores. These MD simulations were performed for the saturation regime, i.e., 13 water molecules per unit cell. The water arrangement in the pores was carefully analyzed based on the plot of the radial distribution functions between water/water and water/POH and the calculations of the number of hydrogen bonds per water assuming the following criteria: two H_2O molecules are considered as hydrogen bonded if the distance between their oxygen atoms is shorter than 3.5 Å and the angle formed between the intramolecular O−H vector (OH of donor molecule) and the intermolecular O−O vector (O atoms of donor and acceptor) is less than 37°. These criteria are the same we used previously to describe the H-bond network in other MOFs.[68,69] The total number of hydrogen-bond per H_2O was averaged over all the generated MD configurations.

Ab Initio Molecular Dynamics Simulations. Born−Oppenheimer first-principles MD simulations were performed for one unit cell of $Ti^{IV}Ti^{IV}(HPO_4)_4$ loaded with 13 water molecules using the CP2K package and the same level of description mentioned above for the geometry optimization. As in aqueous systems, the proton shuffling and hopping phenomena occur in a time scale of only several femtoseconds and a few picoseconds, respectively.[70] Indeed, these simulations were run with a time step of 1 fs for 15 ps at 298 K, in order to collect enough statistics to describe the main features of the microscopic proton conduction mechanism summarized in Table S3.

DOI: 10.1021/acs.chemmater.7b01850
Chem. Mater. 2017, 29, 7263−7271

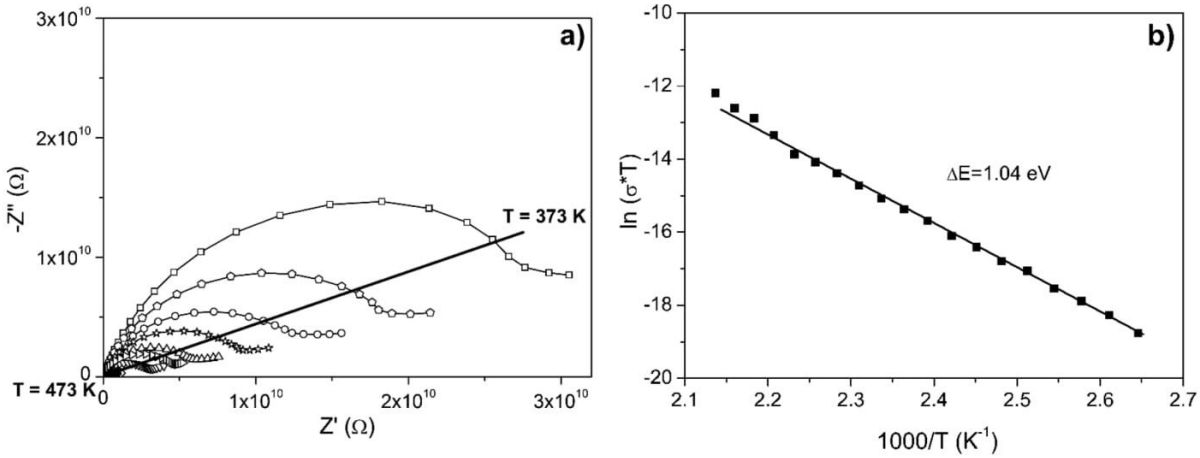

Figure 2. (a) Nyquist plot for the anhydrous $Ti^{IV}Ti^{IV}(HPO_4)_4$ measured at different temperatures (363 < T (K) < 473) and 0% RH. (b) Corresponding Arrhenius plot of the conductivities of the anhydrous $Ti^{IV}Ti^{IV}(HPO_4)_4$. The line corresponds to the linear least-squares fit.

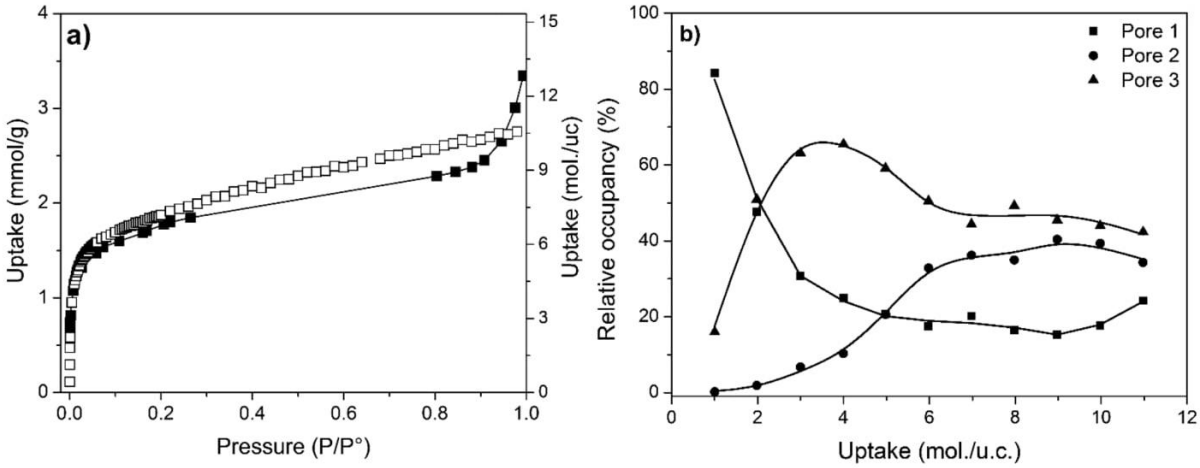

Figure 3. (a) Experimental (black squares) and GCMC simulated (open squares) adsorption isotherms of water in $Ti^{IV}Ti^{IV}(HPO_4)_4$ at 298 K. (b) Evolution of the relative water occupancy of pores 1 (squares), 2 (circles), and 3 (triangles) simulated by GCMC simulations at room temperature as a function of the water uptake. Lines are guides for the eye.

■ RESULTS AND DISCUSSION

Figure 2a shows the Nyquist plot as a function of temperature for the anhydrous $Ti^{IV}Ti^{IV}(HPO_4)_4$, i.e., for RH = 0%. The semicircle represents the bulk and grain boundary impedances, and the small tail at low frequency is indicative of the accumulation of ionic charges, i.e., proton species, at the blocking electrode interface. One notes that the tail is poorly pronounced in relation with the very low conductivity values, as illustrated by the Arrhenius plot in Figure 2b.

The conductivity increases from 5.0×10^{-3} S cm^{-1} at 363 K to 1.9×10^{-8} S cm^{-1} at 473 K, associated with a very high activation energy of 1.04 eV. This range of values evidences that the anhydrous solid does not allow an efficient proton propagation. Assuming that the acidic protons of $Ti^{IV}Ti^{IV}(HPO_4)_4$ stem from −POH groups present in relatively large concentration, this means that the proton transfer between these groups is highly limited without the presence of a charge carrier.

As a further step, it was first checked that $Ti^{IV}Ti^{IV}(HPO_4)_4$ adsorbs water by collecting the adsorption data at room temperature. Figure 3a evidences that the experimental adsorption isotherm is of type I with a sudden increase of the water uptake at low relative pressure as expected for hydrophilic microporous materials. The saturation capacity of water is around 3.0 mmol·g^{-1}, corresponding to ≈13 water molecules per unit cell (u.c.) confined in the pores of this material. This experimental adsorption isotherm was well reproduced by GCMC simulations, thus validating the microscopic model as well as the force field parameters we considered to describe $Ti^{IV}Ti^{IV}(HPO_4)_4$, the water molecules, and their interactions. These calculations confirmed that the material is highly hydrophilic, as evidenced by a high simulated adsorption enthalpy of −75 kJ mol^{-1} at low coverage.

The GCMC simulations revealed that at very low loading ([H_2O] < 0.5 mmol g^{-1}), the water molecules preferentially occupy pore 1 because this pore contains the larger concentration of POH groups that act as polar hydrogen bonding sites for the water molecules (see Figure 3b). Once the

DOI: 10.1021/acs.chemmater.7b01850
Chem. Mater. 2017, 29, 7263−7271

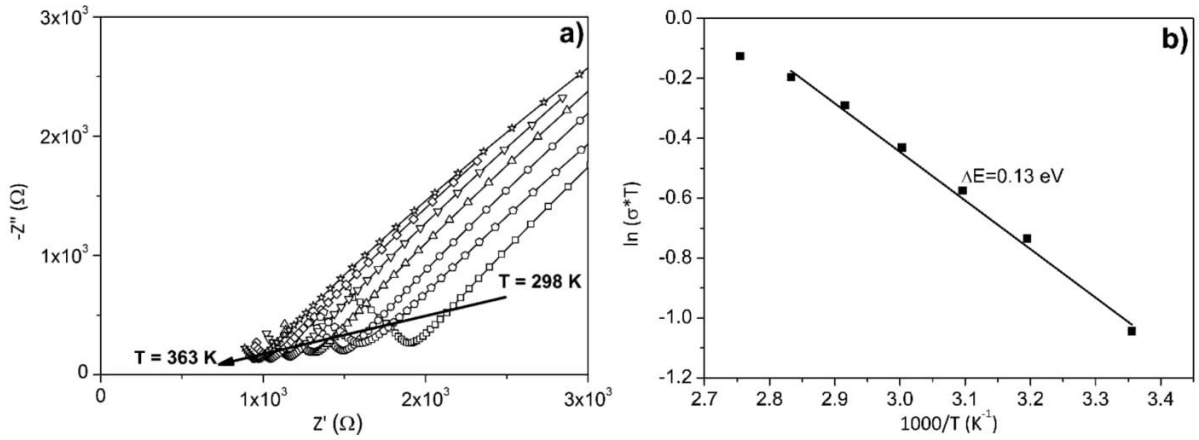

Figure 4. (a) Nyquist plot for $Ti^{IV}Ti^{IV}(HPO_4)_4$ measured at different temperatures (298 < T (K) < 363) and 95% RH. (b) Corresponding Arrhenius plot of the conductivities of the hydrated $Ti^{IV}Ti^{IV}(HPO_4)_4$. The line corresponds to the linear least-squares fit.

water loading reaches 0.5 mmol g^{-1}, pores 1 and 3 are equally filled, while pore 2 is still empty. For 0.75 mmol $g^{-1} \leq [H_2O] \leq 1.5$ mmol g^{-1}, the relative occupancy of pores 1 and 3 decreases in favor of the steadily occupancy of pore 2. Finally, at high water loadings ($[H_2O] \geq 1.5$ mmol g^{-1}), the relative occupancy of the three pores is roughly constant, consistent with a pore-filling process. This observation further evidences that despite the very narrow pore size of $Ti^{IV}Ti^{IV}(HPO_4)_4$ (3.5 Å), the water molecules enter all cavities of the solid and thus offer an optimal scenario for a potential transport of protons throughout all the accessible porosity of the solid.

Impedance measurements were further recorded at 95% RH for temperatures ranging from 298 to 363 K. The inspection of the XRPD pattern of the fully hydrated $Ti^{IV}Ti^{IV}(HPO_4)_4$ after the conductivity measurement confirmed that the solid maintains its crystal structure under this operating condition (Figure S7). The corresponding Nyquist plots are shown in Figure 4a. Compared to the response of the anhydrous solid, the hydrated $Ti^{IV}Ti^{IV}(HPO_4)_4$ exhibits such low impedances that semicircles are not observed, resulting in a linear tail end of semicircles at high frequency and a subsequent capacitive tail due to the ionic-blocking electrodes at lower frequencies. The total impedance was then extrapolated from the linear region to the real axis. The resulting total conductivity ranges from 1.2×10^{-3} S cm^{-1} at 298 K to 2.4×10^{-3} S cm^{-1} at 363 K. Complementary impedance measurements were performed on the pure as-synthesized $Ti^{III}Ti^{IV}(HPO_4)_4 \cdot C_2N_2H_9 \cdot H_2O$ material that revealed a conductivity performance 2 orders of magnitude lower at 298 K/RH 95% ($\sigma = 4.5 \times 10^{-5}$ S cm^{-1}, see the Supporting Information) than the value measured for the calcined sample ($\sigma = 1.2 \times 10^{-3}$ S cm^{-1}). This result clearly evidences that the traces of $Ti^{III}Ti^{IV}(HPO_4)_4 \cdot C_2N_2H_9 \cdot H_2O$ are not responsible for the high proton conductivity recorded for the calcined sample that can be thus undoubtedly attributed to the $Ti^{IV}Ti^{IV}(HPO_4)_4$ response.

Interestingly, the conductivity value at 298 K remains the same over 8 days of hydration (Figure S6). This conductivity largely outperforms the crystalline α-ZrP ($\sigma \approx 10^{-5}$–10^{-6} S cm^{-1}) recorded under the same conditions of T and RH[71] and spans in the same range as the best superprotonic materials (>10^{-3} S cm^{-1}) including not only phosphonate metal solids and MOFs[8–10,12,14,15,17,20,27,29] but also 2D layered phosphonates[72–74] or amorphous solids.[71,75] The corresponding activation energy of 0.13 eV (Figure 4b) is the lowest one observed for phosphate-phosphonate metal-based solids and more interestingly is similar to the value reported for Nafion.[76,77] This evidences a very efficient proton transfer in the pores of the solid and strongly emphasizes the key role of water, as shown by the spectacular increase of the conductivity by 9 orders of magnitude at 90 °C when RH evolves from 0 to 95%.

To shed light on the central role of water in the proton conduction mechanism, force field-based MD simulations were performed to analyze the preferential conformation of the confined water in the fully hydrated material. These calculations evidenced the formation of hydrogen bonds between water and the terminal POH groups of $Ti^{IV}Ti^{IV}(HPO_4)_4$ as well as between the water molecules themselves, as illustrated in the respective (O_{POH}–O_w and O_w–O_w) radial distribution functions (see Figure 5) which show peaks below 2.8 Å characteristic of strong hydrogen bonds. The total number of hydrogen bonds per water molecules (3.1) is significantly higher than the value we previously obtained in MOFs, i.e., MIL-163 (1.55)[69] and UiO-66(Zr)-$(CO_2H)_2$ (2.40),[68] and is

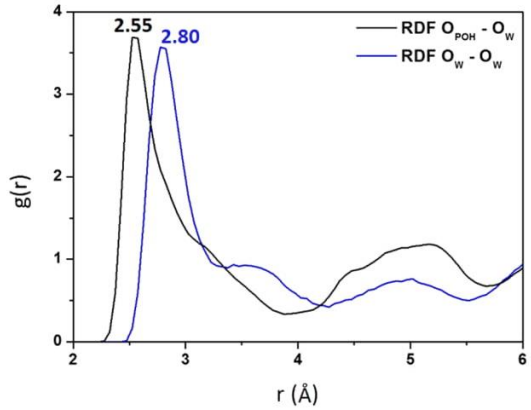

Figure 5. Radial distribution functions for the pairs O_{POH}–O_W (black line) and O_W–O_W (blue line) calculated from the average over the MD configurations considered for $Ti^{IV}Ti^{IV}(HPO_4)_4$ at 298 K and under water saturation.

DOI: 10.1021/acs.chemmater.7b01850
Chem. Mater. 2017, 29, 7263–7271

only slightly below the value reported for bulk water (3.6).[78] This suggests that the water molecules are involved in multidirectional interactions in this highly confined material. It was further evidenced that the water molecules and POH groups form aggregates starting from dimers to clusters involving up to 25 species (comprising H_2O molecules and POH groups), while the mean size of the clusters comprises 9 hydrogen-bonded species (see Figure S11).

These observations support the existence of a 3D percolating network of confined water and POH groups, as illustrated in Figure 6. The spatial arrangement of the guest molecules

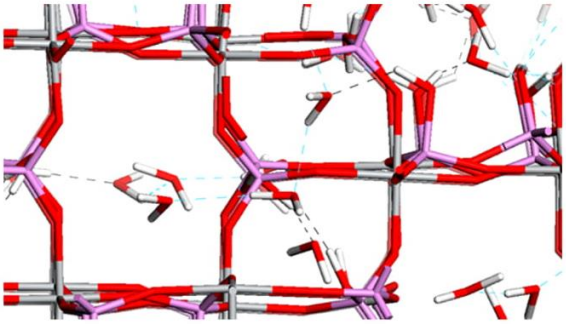

Figure 6. Illustration of the multiple hydrogen-bond pathways along pores 1, 2 and 3, resulting in the connection of the water molecules with the terminal POH groups (black dashed line) and with neighboring water molecules (blue dashed line), as evidenced by MD simulations performed at 298 K for the hydrated $Ti^{IV}Ti^{IV}(HPO_4)_4$.

creates multiple pathways that link pores 1, 2, and 3 through the interconnected water molecules. In addition, the acidic protons of the POH groups located in pore 1 are also involved in these pathways, thus offering an optimal situation for the long-range transfer of the acidic protons throughout the entire solid via the water molecules as the charge carrier.

Such a 3D water hydrogen bonded network is an ideal platform to allow an efficient proton transport in the channels of the titanium-based inorganic solid. As a further step, we used an ab initio MD approach to provide a microscopic picture of the proton transfer in this material. These calculations unambiguously confirmed that POH groups act as the proton source. The proton being transferred from this functional group to the water molecules through the hydrogen-bonded network is evidenced in Figure 7.

The hydronium ion then moves toward a second water molecule, resulting in a proton transfer from one guest molecule to another (Figure 7c). This leads to the formation of a Zundel ($H_5O_2^+$) species as evidenced by the analysis of the radial distribution function between the oxygen atom of the hydronium species with the oxygen atom of the water molecules, which shows the existence of a peak at 2.45 Å (see Figure S12), a value comparable to that typically reported for an isolated Zundel species in gas phase (2.40 Å).[79] At the last step, the proton originating from the hydronium ion moves toward a bridging oxygen atom of the framework (Figure 7e) to form a bridging μ_2−OH function. Such an illustration provides a microscopic picture of the Grotthuss-like mechanism[80] at the origin of the proton transfer in this water-mediated proton-conducting solid.

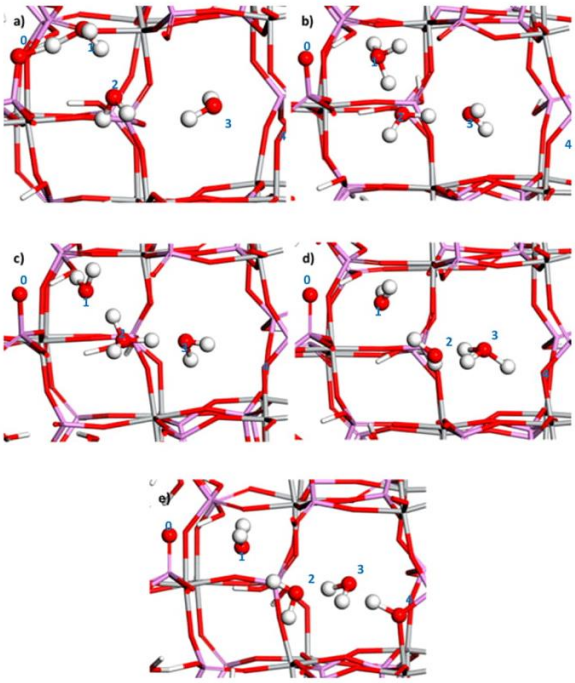

Figure 7. Illustration of the proton transfer in the hydrated $Ti^{IV}Ti^{IV}(HPO_4)_4$ gained from the ab initio molecular dynamics calculations: proton transfer from the terminal POH group of pore 1 and the water molecule of pore 3 (a), the resulting hydronium species located in pore 3 (b), proton transfer from the hydronium species and the neighboring water molecule of pore 3 (c), proton transfer between the water molecules located in pore 3 and pore 2 (d), and proton transfer from the water molecule of pore 2 and the bridging O atom of the pore 2 wall (e).

Figure 8 reports the time evolution of index associated with the protonated species in the porous solid calculated from the ab initio MD trajectory. Index 0 is assigned to the POH group located in pore 1; indexes 1, 2, and 3 refer to the first, second, and third water molecule, respectively, involved in the proton shuttling described in Figure 7, and index 4 characterizes the bridging O atom of pore 2. This result shows that the pore1/pore2 proton transfer, i.e., from the POH group to the water molecule, occurs over a short period of about 1.5 ps, a time scale comparable to the one observed for the migration of an excess proton in pure water.[70,81−84] The same conclusion can be drawn for the proton exchange from the water molecule of pore 2 to the oxygen bridging the Ti and P atoms of pore 2 wall. In contrast, the proton migration through the water/water pairs connecting pores 2 and 3 is significantly longer (about 10 ps).

■ CONCLUSIONS

The proton conductivity performance of the 3D titanium phosphate $Ti^{IV}Ti^{IV}(HPO_4)_4$ was shown to strongly depend on the relative humidity. When exposed to 95% RH, this inorganic solid exhibits conductivity that exceeds 10^{-3} S cm^{-1} even at room temperature, which competes well with other inorganic or hybrid materials. Interestingly, the activation energy of the process is very low (0.13 eV) and comparable to the value observed in Nafion, which makes $Ti^{IV}Ti^{IV}(HPO_4)_4$ one of the best candidates for an efficient proton transfer. The micro-

DOI: 10.1021/acs.chemmater.7b01850
Chem. Mater. 2017, 29, 7263−7271

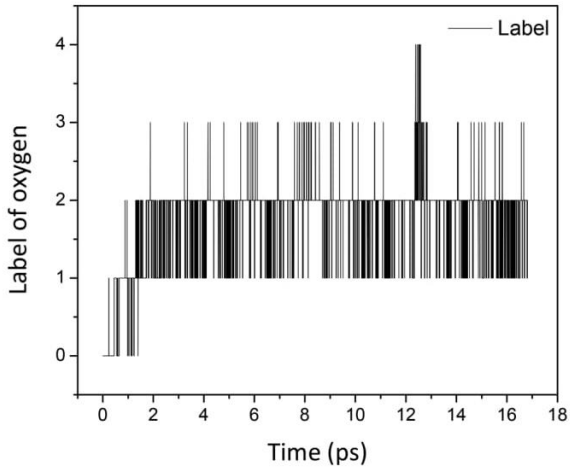

Figure 8. Time evolution of the protonated indexed species calculated from 17 ps of an ab initio MD trajectory at 273 K. Index 0 refers to the proton of the terminal POH species; indexes 1, 2, and 3 are associated with hydronium species located in pore 3, 3, and 2, respectively, and index 4 corresponds to proton connected to the bridging O of the pore 2 wall.

scopic mechanism was further elucidated using force field-based and ab initio molecular dynamics simulations. These calculations revealed that the preferential conformation of the confined water molecules forms a 3D hydrogen bonded network starting from the proton source of $Ti^{IV}Ti^{IV}(HPO_4)_4$ (i.e., POH groups) and resulting in the connection of the different channels of the solid via the water molecules. This leads to optimal conditions for transferring the proton at long distances. Propitiously, this work paves the way toward a further exploration of such a family of materials as proton-based sensors or electrolytes in fuel-cell type applications.

■ ASSOCIATED CONTENT

Supporting Information

The Supporting Information is available free of charge on the ACS Publications website at DOI: 10.1021/acs.chemmater.7b01850.

Details on the characterization of $Ti^{IV}Ti^{IV}(HPO_4)_4$, impedance measurement and analysis, and modeling (PDF)

■ AUTHOR INFORMATION

Corresponding Author

*E-mail: sabine.devautour-vinot@umontpellier.fr.

ORCID

Nathalie Steunou: 0000-0002-7049-7388

Philip L. Llewellyn: 0000-0001-5124-7052

Sabine Devautour-Vinot: 0000-0002-3812-7379

Author Contributions

T.K., N.S., and C.S. synthesized and characterized $Ti^{IV}Ti^{IV}(HPO_4)_4$; V.B. and P.L.L. collected the water adsorption isotherm; S.D.-V. performed the conductivity measurements; P.G.M.M., R.S., and G.M were in charge of the molecular simulations, and P.G.M.M., S.D.-V., and G.M. wrote the manuscript.

Funding

P.G.M.M. thanks the National Counsel of Technological and Scientific Development (CNPQ) for the scholarship. G.M. thanks the Institut Universitaire de France for its support.

Notes

The authors declare no competing financial interest.

■ REFERENCES

(1) Yamada, T.; Otsubo, K.; Makiura, R.; Kitagawa, H. Designer Coordination Polymers: Dimensional Crossover Architectures and Proton Conduction. *Chem. Soc. Rev.* **2013**, *42*, 6655.

(2) Yoon, M.; Suh, K.; Natarajan, S.; Kim, K. Proton Conduction in Metal-Organic Frameworks and Related Modularly Built Porous Solids. *Angew. Chem., Int. Ed.* **2013**, *52*, 2688−2700.

(3) Ramaswamy, P.; Wong, N. E.; Shimizu, G. K. H. MOFs as Proton Conductors − Challenges and Opportunities. *Chem. Soc. Rev.* **2014**, *43*, 5913−5932.

(4) Horike, S.; Umeyama, D.; Kitagawa, S. Ion Conductivity and Transport by Porous Coordination Polymers and Metal−Organic Frameworks. *Acc. Chem. Res.* **2013**, *46*, 2376−2384.

(5) Meng, X.; Wang, H.-N.; Song, S.-Y.; Zhang, H.-J. Proton-Conducting Crystalline Porous Materials. *Chem. Soc. Rev.* **2017**, *46*, 464−480.

(6) Taylor, J. M.; Mah, R. K.; Moudrakovski, I. L.; Ratcliffe, C. I.; Vaidhyanathan, R.; Shimizu, G. K. H. Facile Proton Conduction via Ordered Water Molecules in a Phosphonate Metal−Organic Framework. *J. Am. Chem. Soc.* **2010**, *132*, 14055−14057.

(7) Taylor, J. M.; Dawson, K. W.; Shimizu, G. K. H. A Water-Stable Metal-Organic Framework with Highly Acidic Pores for Proton-Conducting Applications. *J. Am. Chem. Soc.* **2013**, *135*, 1193−1196.

(8) Kim, S.; Dawson, K. W.; Gelfand, B. S.; Taylor, J. M.; Shimizu, G. K. H. Enhancing Proton Conduction in a Metal-Organic Framework by Isomorphous Ligand Replacement. *J. Am. Chem. Soc.* **2013**, *135*, 963−966.

(9) Bazaga-García, M.; Colodrero, R. M. P.; Papadaki, M.; Garczarek, P.; Zoń, J.; Olivera-Pastor, P.; Losilla, E. R.; León-Reina, L.; Aranda, M. A. G.; Choquesillo-Lazarte, D.; Demadis, K. D.; Cabeza, A. Guest Molecule-Responsive Functional Calcium Phosphonate Frameworks for Tuned Proton Conductivity. *J. Am. Chem. Soc.* **2014**, *136*, 5731−5739.

(10) Bao, S. S.; Li, N. Z.; Taylor, J. M.; Shen, Y.; Kitagawa, H.; Zheng, L. M. Co-Ca Phosphonate Showing Humidity-Sensitive Single Crystal to Single Crystal Structural Transformation and Tunable Proton Conduction Properties. *Chem. Mater.* **2015**, *27*, 8116−8125.

(11) Bao, S. S.; Otsubo, K.; Taylor, J. M.; Jiang, Z.; Zheng, L. M.; Kitagawa, H. Enhancing Proton Conduction in 2D Co-La Coordination Frameworks by Solid-State Phase Transition. *J. Am. Chem. Soc.* **2014**, *136*, 9292−9295.

(12) Ramaswamy, P.; Wong, N. E.; Gelfand, B. S.; Shimizu, G. K. H. A Water Stable Magnesium MOF That Conducts Protons over 10^{-2} S cm^{-1}. *J. Am. Chem. Soc.* **2015**, *137*, 7640−7643.

(13) Colodrero, R. M. P.; Papathanasiou, K. E.; Stavgianoudaki, N.; Olivera-Pastor, P.; Losilla, E. R.; Aranda, M. A. G.; León-Reina, L.; Sanz, J.; Sobrados, I.; Choquesillo-Lazarte, D.; García-Ruiz, J. M.; Atienzar, P.; Rey, F.; Demadis, K. D.; Cabeza, A. Multifunctional Luminescent and Proton-Conducting Lanthanide Carboxyphosphonate Open-Framework Hybrids Exhibiting Crystalline-to-Amorphous-to-Crystalline Transformations. *Chem. Mater.* **2012**, *24*, 3780−3792.

(14) Grohol, D.; Subramanian, M. A.; Poojary, D. M.; Clearfield, A. Synthesis, Crystal Structures, and Proton Conductivity of Two Linear-Chain Uranyl Phenylphosphonates. *Inorg. Chem.* **1996**, *35*, 5264−5271.

(15) Colodrero, R. M. P.; Olivera-Pastor, P.; Losilla, E. R.; Aranda, M. a. G.; Leon-Reina, L.; Papadaki, M.; McKinlay, A. C.; Morris, R. E.; Demadis, K. D.; Cabeza, A. Multifunctional Lanthanum Tetraphosphonates: Flexible, Ultramicroporous and Proton-Conducting Hybrid Frameworks. *Dalt. Trans.* **2012**, *41*, 4045.

DOI: 10.1021/acs.chemmater.7b01850
Chem. Mater. 2017, 29, 7263−7271

(16) Costantino, F.; Donnadio, A.; Casciola, M. Survey on the Phase Transitions and Their Effect on the Ion-Exchange and on the Proton-Conduction Properties of a Flexible and Robust Zr Phosphonate Coordination Polymer. *Inorg. Chem.* **2012**, *51*, 6992−7000.

(17) Colodrero, R. M. P.; Olivera-Pastor, P.; Losilla, E. R.; Hernández-Alonso, D.; Aranda, M. A. G.; Leon-Reina, L.; Rius, J.; Demadis, K. D.; Moreau, B.; Villemin, D.; Palomino, M.; Rey, F.; Cabeza, A. High Proton Conductivity in a Flexible, Cross-Linked, Ultramicroporous Magnesium Tetraphosphonate Hybrid Framework. *Inorg. Chem.* **2012**, *51*, 7689−7698.

(18) Bazaga-García, M.; Papadaki, M.; Colodrero, R. M. P.; Olivera-Pastor, P.; Losilla, E. R.; Nieto-Ortega, B.; Aranda, M. Á. G.; Choquesillo-Lazarte, D.; Cabeza, A.; Demadis, K. D. Tuning Proton Conductivity in Alkali Metal Phosphonocarboxylates by Cation Size-Induced and Water-Facilitated Proton Transfer Pathways. *Chem. Mater.* **2015**, *27*, 424−435.

(19) Begum, S.; Wang, Z.; Donnadio, A.; Costantino, F.; Casciola, M.; Valiullin, R.; Chmelik, C.; Bertmer, M.; Kärger, J.; Haase, J.; Krautscheid, H. Water-Mediated Proton Conduction in a Robust Triazolyl Phosphonate Metal-Organic Framework with Hydrophilic Nanochannels. *Chem. - Eur. J.* **2014**, *20*, 8862−8866.

(20) Pili, S.; Argent, S. P.; Morris, C. G.; Rought, P.; Garcia-Sakai, V.; Silverwood, I. P.; Easun, T. L.; Li, M.; Warren, M. R.; Murray, C. A.; Tang, C. C.; Yang, S.; Schröder, M. Proton Conduction in a Phosphonate-Based Metal-Organic Framework Mediated by Intrinsic "free Diffusion inside a Sphere. *J. Am. Chem. Soc.* **2016**, *138*, 6352−6355.

(21) Jaimez, E.; Hix, G. B.; Slade, R. C. T. A Phosphate−phosphonate of titanium(IV) Prepared from Phosphonomethyliminodiacetic Acid: Characterisation, N-Alkylamine Intercalation and Proton Conductivity. *Solid State Ionics* **1997**, *97*, 195−201.

(22) Jaimez, E.; Hix, G. B.; Slade, R. C. T. The Titanium (IV) Salt of N,N-(Diphosphonomethyl)glycine: Synthesis, Characterisation, Porosity and Proton Conduction. *J. Mater. Chem.* **1997**, *7*, 475−479.

(23) Donnadio, A.; Nocchetti, M.; Costantino, F.; Taddei, M.; Casciola, M.; da Silva Lisboa, F.; Vivani, R. A Layered Mixed Zirconium Phosphate/Phosphonate with Exposed Carboxylic and Phosphonic Groups: X-Ray Powder Structure and Proton Conductivity Properties. *Inorg. Chem.* **2014**, *53*, 13220−13226.

(24) Umeyama, D.; Horike, S.; Inukai, M.; Itakura, T.; Kitagawa, S. Inherent Proton Conduction in a 2D Coordination Framework. *J. Am. Chem. Soc.* **2012**, *134*, 12780−12785.

(25) Horike, S.; Umeyama, D.; Inukai, M.; Itakura, T.; Kitagawa, S. Coordination-Network-Based Ionic Plastic Crystal for Anhydrous Proton Conductivity. *J. Am. Chem. Soc.* **2012**, *134*, 7612−7615.

(26) Jin, Y. G.; Qiao, S. Z.; Xu, Z. P.; Yan, Z.; Huang, Y.; da Costa, J. C.; Lu, G. Q. Phosphonic Acid Functionalized Silicas for Intermediate Temperature Proton Conduction. *J. Mater. Chem.* **2009**, *19*, 2363−2372.

(27) Firmino, A. D. G.; Mendes, R. F.; Antunes, M. M.; Barbosa, P. C.; Vilela, S. M. F.; Valente, A. A.; Figueiredo, F. M. L.; Tomé, J. P. C.; Paz, F. A. A. Robust Multifunctional Yttrium-Based Metal−Organic Frameworks with Breathing Effect. *Inorg. Chem.* **2017**, *56*, 1193−1208.

(28) Inukai, M.; Horike, S.; Itakura, T.; Shinozaki, R.; Ogiwara, N.; Umeyama, D.; Nagarkar, S.; Nishiyama, Y.; Malon, M.; Hayashi, A.; Ohhara, T.; Kiyanagi, R.; Kitagawa, S. Encapsulating Mobile Proton Carriers into Structural Defects in Coordination Polymer Crystals: High Anhydrous Proton Conduction and Fuel Cell Application. *J. Am. Chem. Soc.* **2016**, *138*, 8505−8511.

(29) Pan, J.; Wang, S.; Xiao, M.; Hickner, M.; Meng, Y. Layered Zirconium Phosphate Sulfophenylphosphonates Reinforced Sulfonated Poly (Fluorenyl Ether Ketone) Hybrid Membranes with High Proton Conductivity and Low Vanadium Ion Permeability. *J. Membr. Sci.* **2013**, *443*, 19−27.

(30) Schuster, M.; Rager, T.; Noda, A.; Kreuer, K. D.; Maier, J. About the Choice of the Protogenic Group in PEM Separator Materials for Intermediate Temperature, Low Humidity Operation: A Critical Comparison of Sulfonic Acid, Phosphonic Acid and Imidazole Functionalized Model Compounds. *Fuel Cells* **2005**, *5*, 355−365.

(31) Gagnon, K. J.; Perry, H. P.; Clearfield, A. Conventional and Unconventional Metal−Organic Frameworks Based on Phosphonate Ligands: MOFs and UMOFs. *Chem. Rev.* **2012**, *112*, 1034−1054.

(32) Zhu, Y.-P.; Ma, T.-Y.; Liu, Y.-L.; Ren, T.-Z.; Yuan, Z.-Y. Metal Phosphonate Hybrid Materials: From Densely Layered to Hierarchically Nanoporous Structures. *Inorg. Chem. Front.* **2014**, *1*, 360.

(33) Troup, J. M.; Clearfield, A. Mechanism of Ion Exchange in Zirconium Phosphates. 20. Refinement of the Crystal Structure of alpha-Zirconium Phosphate. *Inorg. Chem.* **1977**, *16*, 3311−3314.

(34) Poojary, D. M.; Shpeizer, B.; Clearfield, A. X-Ray Powder Structure and Rietveld Refinement of γ-Zirconium Phosphate, $Zr(PO_4)(H_2PO_4)2H_2O$. *J. Chem. Soc., Dalton Trans.* **1995**, *1*, 111−113.

(35) Clearfield, A.; Smith, G. D. Crystallography and Structure of.alpha.-Zirconium Bis(monohydrogen Orthophosphate) Monohydrate. *Inorg. Chem.* **1969**, *8*, 431−436.

(36) Alberti, G.; Cardini-Galli, P.; Costantino, U.; Torracca, E. Crystalline Insoluble Salts of Polybasic metals—I Ion-Exchange Properties of Crystalline Titanium Phosphate. *J. Inorg. Nucl. Chem.* **1967**, *29*, 571−578.

(37) Christensen, A. N.; Andersen, E. K.; Andersen, I. G. K.; Alberti, G.; Nielsen, M.; Lehmann, M. S.; Tokii, T. X-Ray Powder Diffraction Study of Layer Compounds. The Crystal Structure of Alpha-$Ti(HPO_4)_2{\cdot}H_2O$ and a Proposed Structure for Gamma-$Ti(H_2PO_4)$-$(PO_4)).2H_2O$. *Acta Chem. Scand.* **1990**, *44*, 865−872.

(38) Poojary, D. M.; Bortun, A. I.; Bortun, L. N.; Clearfield, A. Synthesis and X-Ray Powder Structures of Three Novel Titanium Phosphate Compounds. *J. Solid State Chem.* **1997**, *132*, 213−223.

(39) Ekambaram, S.; Sevov, S. C. Organically Templated Mixed-Valent Ti(III)/Ti(IV) Phosphate with an Octahedral-Tetrahedral Open Framework. *Angew. Chem., Int. Ed.* **1999**, *38*, 372−375.

(40) Ekambaram, S.; Serre, C.; Férey, G.; Sevov, S. C. Hydrothermal Synthesis and Characterization of an Ethylenediamine-Templated Mixed-Valence Titanium Phosphate. *Chem. Mater.* **2000**, *12*, 444−449.

(41) Fu, Y.; Liu, Y.; Shi, Z.; Zou, Y.; Pang, W. Hydrothermal Synthesis and Structural Characterization of Two New Three-Dimensional Oxyfluorinated Titanium Phosphates-$Ti_4(HPO_4)_2(PO_4)_4F_2{\cdot}C_4N_2H_{12}{\cdot}H_2O$ and $Ti_4(HPO_4)_2(PO_4)_4F_2{\cdot}C_2N_2H_{10}{\cdot}H_2O$. *J. Solid State Chem.* **2001**, *162*, 96−102.

(42) Liu, Y.; Shi, Z.; Fu, Y.; Chen, W.; Li, B.; Hua, J.; Liu, W.; Deng, F.; Pang, W. Hydrothermal Synthesis and Structural Characterizatino of Three Organically Templated Titanium Phosphates: $Ti_2(HPO_4)_2(PO_4)_2{\cdot}C_2N_2H_{10}$, $Ti_3(H_2PO_4)(HPO_4)_{3.5}(PO_4)_2{\cdot}C_2N_2H_{10}$, and $Ti_7(HPO_4)_6(PO4)_6{\cdot}C_3N_2H_{12}$. *Chem. Mater.* **2002**, *14*, 1555−1563.

(43) Serre, C.; Taulelle, F.; Ferey, G. Rational Design of Porous Titanophosphates. *Chem. Commun.* **2003**, *22*, 2755−2757.

(44) Wloka, M.; Troyanov, S. I.; Kemnitz, E. Synthesis and Crystal Structures of Zirconium Phosphate Fluorides with New 2D and 3D Structure Types. *J. Solid State Chem.* **2000**, *149*, 21−27.

(45) Kemnitz, E.; Wloka, M.; Trojanov, S.; Stiewe, A. $[(enH_2)_{0.5}]$-$[Zr_2(PO_4)F]{\cdot}H_2O$: A Unique Zirconium Fluoride Phosphate with a Cavity Structure. *Angew. Chem., Int. Ed. Engl.* **1996**, *35*, 2677−2678.

(46) Dong, J.; Liu, L.; Li, J.; Li, Y.; Baerlocher, C.; McCusker, L. B. Synthesis, Characterization and Crystal Structure Analysis of an Open-Framework Zirconium Phosphate. *Microporous Mesoporous Mater.* **2007**, *104*, 185−191.

(47) Krogh Andersen, A. M.; Norby, P.; Hanson, J. C.; Vogt, T. Preparation and Characterization of a New 3-Dimensional Zirconium Hydrogen Phosphate, τ-$Zr(HPO_4)_2$. Determination of the Complete Crystal Structure Combining Synchrotron X-Ray Single-Crystal Diffraction and Neutron Powder Diffraction. *Inorg. Chem.* **1998**, *37*, 876−881.

(48) Perdew, J. P.; Burke, K.; Ernzerhof, M. Generalized Gradient Approximation Made Simple. *Phys. Rev. Lett.* **1996**, *77*, 3865−3868.

(49) Perdew, J. P.; Burke, K.; Ernzerhof, M. Generalized Gradient Approximation Made Simple [Phys. Rev. Lett. 77, 3865 (1996)]. *Phys. Rev. Lett.* **1997**, *78*, 1396.

DOI: 10.1021/acs.chemmater.7b01850
Chem. Mater. 2017, 29, 7263−7271

(50) VandeVondele, J.; Krack, M.; Mohamed, F.; Parrinello, M.; Chassaing, T.; Hutter, J. Quickstep: Fast and Accurate Density Functional Calculations Using a Mixed Gaussian and Plane Waves Approach. *Comput. Phys. Commun.* **2005**, *167*, 103−128.
(51) Hutter, J.; Iannuzzi, M.; Schiffmann, F.; VandeVondele, J. cp2k: Atomistic Simulations of Condensed Matter Systems. *Wiley Interdiscip. Rev. Comput. Mol. Sci.* **2014**, *4*, 15−25.
(52) Weigend, F.; Ahlrichs, R. Balanced Basis Sets of Split Valence, Triple Zeta Valence and Quadruple Zeta Valence Quality for H to Rn: Design and Assessment of Accuracy. *Phys. Chem. Chem. Phys.* **2005**, *7*, 3297.
(53) Krack, M. Pseudopotentials for H to Kr Optimized for Gradient-Corrected Exchange-Correlation Functionals. *Theor. Chem. Acc.* **2005**, *114*, 145−152.
(54) Goedecker, S.; Teter, M.; Hutter, J. Separable Dual-Space Gaussian Pseudopotentials. *Phys. Rev. B: Condens. Matter Mater. Phys.* **1996**, *54*, 1703−1710.
(55) Hartwigsen, C.; Goedecker, S.; Hutter, J. Relativistic Separable Dual-Space Gaussian Pseudopotentials from H to Rn. *Phys. Rev. B: Condens. Matter Mater. Phys.* **1998**, *58*, 3641−3662.
(56) Berendsen, H. J. C.; Postma, J. P. M.; van Gunsteren, W. F.; Hermans, J. Interaction Models for Water in Relation to Protein Hydration. *Intermolecular Forces* **1981**, *14*, 331−342.
(57) Ramachandran, C. E.; Chempath, S.; Broadbelt, L. J.; Snurr, R. Q. Water Adsorption in Hydrophobic Nanopores: Monte Carlo Simulations of Water in Silicalite. *Microporous Mesoporous Mater.* **2006**, *90*, 293−298.
(58) Demontis, P.; Stara, G.; Suffritti, G. Molecular Dynamics Simulation of Water Confined in Zeolites. *Stud. Surf. Sci. Catal.* **2002**, *142*, 1931−1938.
(59) Maris, T.; Vlugt, T. J. H.; Smit, B. Simulation of Alkane Adsorption in the Aluminophosphate Molecular Sieve AlPO4 −5. *J. Phys. Chem. B* **1998**, *102*, 7183−7189.
(60) Delley, B. An All-Electron Numerical Method for Solving the Local Density Functional for Polyatomic Molecules. *J. Chem. Phys.* **1990**, *92* (508), 508.
(61) Delley, B. From Molecules to Solids with the DMol3 Approach. *J. Chem. Phys.* **2000**, *113*, 7756−7764.
(62) Hehre, W. J.; Ditchfield, R.; Pople, J. A. Self—Consistent Molecular Orbital Methods. XII. Further Extensions of Gaussian—Type Basis Sets for Use in Molecular Orbital Studies of Organic Molecules. *J. Chem. Phys.* **1972**, *56*, 2257−2261.
(63) Vlugt, T. J. H.; García-Pérez, E.; Dubbeldam, D.; Ban, S.; Calero, S. Computing the Heat of Adsorption Using Molecular Simulations: The Effect of Strong Coulombic Interactions. *J. Chem. Theory Comput.* **2008**, *4*, 1107−1118.
(64) Nosé, S. A Molecular Dynamics Method for Simulations in the Canonical Ensemble. *Mol. Phys.* **1984**, *52*, 255−268.
(65) Nosé, S. A Unified Formulation of the Constant Temperature Molecular Dynamics Methods. *J. Chem. Phys.* **1984**, *81*, 511−519.
(66) Todorov, I. T.; Smith, W.; Trachenko, K.; Dove, M. T. DL_POLY_3: New Dimensions in Molecular Dynamics Simulations via Massive Parallelism. *J. Mater. Chem.* **2006**, *16*, 1911.
(67) Alberti, G.; Grassi, A.; Lombardo, G. M.; Pappalardo, G. C.; Vivani, R. Derivation of Force Field Parameters, and Force Field and Quantum Mechanical Studies of Layered α- and γ-Zirconium Phosphates. *Inorg. Chem.* **1999**, *38*, 4249−4255.
(68) Borges, D. D.; Devautour-Vinot, S.; Jobic, H.; Ollivier, J.; Nouar, F.; Semino, R.; Devic, T.; Serre, C.; Paesani, F.; Maurin, G. Proton Transport in a Highly Conductive Porous Zirconium-Based Metal-Organic Framework: Molecular Insight. *Angew. Chem., Int. Ed.* **2016**, *55*, 3919−3924.
(69) Mileo, P. G. M.; Devautour-Vinot, S.; Mouchaham, G.; Faucher, F.; Guillou, N.; Vimont, A.; Serre, C.; Maurin, G. Proton-Conducting Phenolate-Based Zr Metal−Organic Framework: A Joint Experimental−Modeling Investigation. *J. Phys. Chem. C* **2016**, *120*, 24503−24510.
(70) Markovitch, O.; Chen, H.; Izvekov, S.; Paesani, F.; Voth, G. A.; Agmon, N. Special Pair Dance and Partner Selection: Elementary Steps in Proton Transport in Liquid Water. *J. Phys. Chem. B* **2008**, *112*, 9456−9466.
(71) Alberti, G.; Casciola, M. *Proton Conductors*; Colomban, P., Ed.; Cambridge University Press: Cambridge, 1992.
(72) Alberti, G.; Boccali, L.; Casciola, M.; Massinelli, L.; Montoneri, E. Protonic Conductivity of Layered Zirconium Phosphonates Containing —SO_3H Groups. III. Preparation and Characterization of γ-Zirconium Sulfoaryl Phosphonates. *Solid State Ionics* **1996**, *84*, 97−104.
(73) Kawakami, Y.; Miyayama, M. Proton Conducting Properties of Layered Metal Phosphate Hydrates. *Electroceramics in Japan Ix* **2006**, *320*, 267−270.
(74) Adani, F.; Casciola, M.; Jones, D. J.; Massinelli, L.; Montoneri, E.; Rozière, J.; Vivani, R. Electrochemical and Spectroscopic Characterisation of Barium Acid Salts of 3,5-Disulfophenylphosphonic Acid. *J. Mater. Chem.* **1998**, *8*, 961−964.
(75) Jaimez, E.; Hix, G. B.; Slade, R. C. T. The titanium(I) Salt of N,N-(Diphosphonomethyl)glycine: Synthesis, Characterisation, Porosity and Proton Conduction. *J. Mater. Chem.* **1997**, *7*, 475−479.
(76) Cappadonia, M.; Erning, J. W.; Niaki, S. M. S.; Stimming, U. Conductance of Nafion 117 Membranes as a Function of Temperature and Water Content. *Solid State Ionics* **1995**, *77* (C), 65−69.
(77) Lu, Z.; Polizos, G.; Macdonald, D. D.; Manias, E. State of Water in Perfluorosulfonic Ionomer (Nafion 117) Proton Exchange Membranes. *J. Electrochem. Soc.* **2008**, *155*, B163.
(78) Rastogi, A.; K, A.; Suresh, S. Hydrogen Bond Interactions Between Water Molecules in Bulk Liquid, Near Electrode Surfaces and Around Ions. In *Thermodynamics - Physical Chemistry of Aqueous Systems*; InTech, 2011.
(79) Cao, Z.; Peng, Y.; Yan, T.; Li, S.; Li, A.; Voth, G. A. Mechanism of Fast Proton Transport along One-Dimensional Water Chains Confined in Carbon Nanotubes. *J. Am. Chem. Soc.* **2010**, *132*, 11395−11397.
(80) de Grotthuss, C. J. T. Sur La Décomposition de l'Eau et Des Corps qu'Elle Tient En Dissolution À l'Aide de l'Electricité Galvanique. *Ann. Chim. Phys.* **1806**, *58*, 54−74.
(81) Vuilleumier, R.; Borgis, D. Transport and Spectroscopy of the Hydrated Proton: A Molecular Dynamics Study. *J. Chem. Phys.* **1999**, *111*, 4251.
(82) Schmitt, U. W.; Voth, G. a The Computer Simulation of Proton Transport in Water. *J. Chem. Phys.* **1999**, *111*, 9361−9381.
(83) Izvekov, S.; Voth, G. A. Ab Initio Molecular-Dynamics Simulation of Aqueous Proton Solvation and Transport Revisited. *J. Chem. Phys.* **2005**, *123*, 44505.
(84) Wu, Y.; Chen, H.; Wang, F.; Paesani, F.; Voth, G. A. An Improved Multistate Empirical Valence Bond Model for Aqueous Proton Solvation and Transport †. *J. Phys. Chem. B* **2008**, *112*, 467−482.

DOI: 10.1021/acs.chemmater.7b01850
Chem. Mater. 2017, 29, 7263−7271

Article 3

JACS JOURNAL OF THE AMERICAN CHEMICAL SOCIETY
Communication
Cite This: J. Am. Chem. Soc. 2018, 140, 13156−13160
pubs.acs.org/JACS

Achieving Superprotonic Conduction with a 2D Fluorinated Metal–Organic Framework

Paulo G. M. Mileo,[†,§] Karim Adil,[‡,§] Louisa Davis,[†] Amandine Cadiau,[‡] Youssef Belmabkhout,[‡] Himanshu Aggarwal,[‡] Guillaume Maurin,[†] Mohamed Eddaoudi,*[,‡] and Sabine Devautour-Vinot*[,†]

[†]Institut Charles Gerhardt Montpellier, UMR 5253 CNRS, UM, ENSCM, Université Montpellier, Place E. Bataillon, 34095 Montpellier cedex 5, France

[‡]Functional Materials Design, Discovery & Development Research Group (FMD_3), Advanced Membranes & Porous Materials Center, Division of Physical Sciences and Engineering, King Abdullah University of Science and Technology (KAUST), Thuwal 23955-6900, Kingdom of Saudi Arabia

Supporting Information

ABSTRACT: A hydrolytically stable metal−organic framework (MOF) material, named KAUST-7′, was derived from a structural phase change of KAUST-7 upon exposure to conditions akin to protonic conduction (363 K/95% relative humidity). KAUST 7′ exhibited a superprotonic conductivity as evidenced by the impedance spectroscopic measurement revealing an exceptional conductivity up to 2.0×10^{-2} S cm^{-1} at 363 K and under 95% RH, a performance maintained over 7 days. *Ab initio* molecular dynamics simulations suggested that the water-mediated proton transport mechanism is governed by water assisted reorganization of the H-bond network involving the fluorine moieties in KAUST-7′ and the guest water molecules. The notable level of performances combined with a very good hydrolytic stability positions KAUST-7′ as a prospective proton-exchange membrane alternative to the commercial benchmark Nafion. Furthermore, the remarkable RH sensitivity of KAUST-7′ conductivity, substantially higher than previously reported MOFs, offers great opportunities for deployment as a humidity sensor.

Fuel cell technology is recognized as a powerful source of energy for a large variety of applications. Electrolyte allowing fast proton conduction is a key component in fuel cells development.[1] Besides the standard solid electrolyte Nafion, the search for alternative proton conductive solids that incorporate a high concentration of proton sources and highly mobile proton carriers is of growing interest. Metal Organic Frameworks (MOFs),[2] a relatively new class of porous materials, have received great attention as solid-state proton conductors because of (i) their tunable functionality for the creation of diverse proton sources and (ii) their crystalline nature that allows a regular spatial distribution of mobile proton carriers such as water, amphiprotic organic molecules or acid molecules contained in the pores.[3] Recently, a series of water stable fluorinated MOFs has been reported with outstanding separation performances for gas mixtures of great interest in oil and gas industry.[4] Typically, the 3D-**pcu** KAUST-7, based on the 2-periodic square grid, Ni-$(pyrazine)_2$, bridged by the $(NbOF_5)^{2-}$ pillars via the axial oxygen and fluorine centers, showed great promise for the selective molecular exclusion of propane from propylene.[4e] Investigation of the stability of KAUST-7 in operating condition pertaining to protonic conduction, i.e., 363 K/95% relative humidity (RH), revealed a structural phase change leading to a 2D-MOF, named KAUST-7′, that has dense and periodic arrays of water coordinated to the Ni^{2+} Lewis acid sites in a highly confined environment. This novel KAUST-7′ is potentially an efficient water-mediated proton conductor owing to (i) the presence of acidic coordinated water as proton sources; (ii) a crystalline tunnel-like architecture associated with an ultrasmall porosity, to favor the formation of an orientated hydrogen-bonded network of the guest water molecules; and (iii) a good hydrolytic stability to ensure that the proton conductivity performances can be maintained over cycles. Impedance spectroscopy measurements confirmed that KAUST-7′ shows a superprotonic conductivity up to 2.0×10^{-2} S cm^{-1} at 363 K and under 95% RH with the crystal structure maintained over 7 days of experiments. The combination of an exceptional performance and very good water stability makes this material as a solid alternative to the commercial benchmark Nafion for further applications as proton-exchange membranes,[5] key components in diverse energy and environmental related technologies including water electrolyzers, fuel cells, redox flow batteries and humidity sensors. This experimental finding is further supported by an in-depth exploration of the proton migration mechanism using advanced molecular simulations.

KAUST-7 was initially prepared following the reported procedure[4e] in a hydrofluoric acid aqueous solution containing a mixture of $Ni(NO_3)_2{\cdot}6H_2O$, Nb_2O_5 and pyrazine. This material was further treated under 95% RH and at different temperatures. Powder X-ray diffraction (PXRD) patterns showed that KAUST-7 is irreversibly transformed into a new material, named KAUST-7′. They also revealed that a structural change appears at 348 K leading to a new phase that is present with only a negligible amount of the starting material at 363 K (Figure 1c). The structure of the new phase, called KAUST-7′, was solved from PXRD data. The indexation, conducted using Mc Maille software[6] and confirmed by

Received: June 27, 2018
Published: September 18, 2018

ACS Publications © 2018 American Chemical Society

DOI: 10.1021/jacs.8b06582
J. Am. Chem. Soc. 2018, 140, 13156−13160

Journal of the American Chemical Society Communication

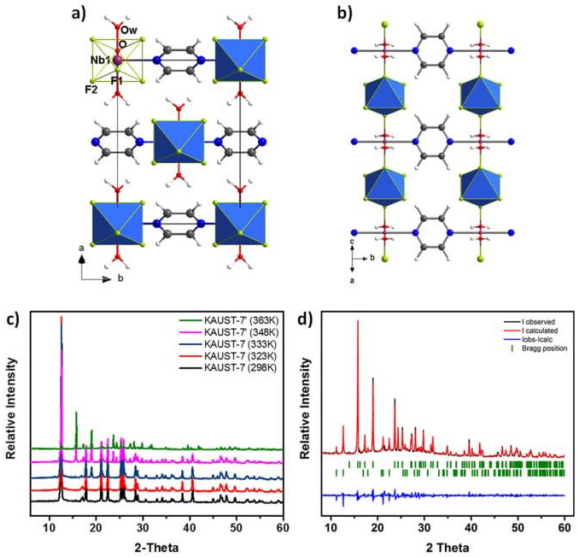

Figure 1. (a) Crystal structure of KAUST-7′ along [001] and (b) along [101]. (c) Variable temperature of KAUST-7 under 95% RH showing that KAUST-7′ appears at 348 K (d) Rietveld refinement of KAUST-7′.

applying the Le Bail methodology,[7] led to a monoclinic unit cell (a = 11.1827(1) Å, 7.0429(1) Å, 7.6093(1) Å, β = 123.36(1)°) with the $C2/m$ space group (see Table S1).

This material was found to be isostructural to a fluorinated pyrazine-based analogue, i.e., $CuNbOF_5(H_2O)_2(pyz)$.[8] Accordingly, the atomic positions of this material were taken as structure solution by replacing Cu^{2+} by Ni^{2+} cations and a Rietveld refinement was performed (Figure 1d) leading to good reliability factors (Rbragg = 4.79%, Rf = 3.68%). The structure can be described as two-dimensional sheets resulting from the connection of one-dimensional Ni-pyrazine chains pillared by $(NbOF_5)^{2-}$octahedra. The coordination sphere of Ni^{2+} cations is completed with two water molecules (Figure 1a,b) leading to the chemical formula $NiNbOF_5(H_2O)_2(pyr)$ as deduced from the elemental analysis (see Supporting Information).

ac impedance measurements were recorded on this material in a powdered form from 363 to 298 K at 95% RH, after 24 h equilibration time between temperatures. The Nyquist plots are shown in Figure 2a. They correspond to very low impedances and result in a linear tail end of semicircles at high frequency and a subsequent capacitive tail due to the ionic-blocking electrodes at lower frequencies at low temperature. The total impedance was extrapolated from the linear region to the real axis. The corresponding conductivity values increase from 6.7×10^{-3} to 2.0×10^{-2} S cm^{-1} upon heating from 298 to 363 K. KAUST-7′ exhibits conductivity values at least five times higher than KAUST-7 in the temperature range 298−323 K (see Table S3). Interestingly, KAUST-7′ surpasses the benchmark of 10^{-2} S·cm^{-1} proton conductivity and further competes with the best water-mediated proton conducting MOFs.[9]

Moreover, this remarkable performance is maintained over 1 week (Figure S4), while the solid preserves its crystal structure integrity under the operating conditions, as confirmed by the inspection of the PXRD pattern collected on the sample after

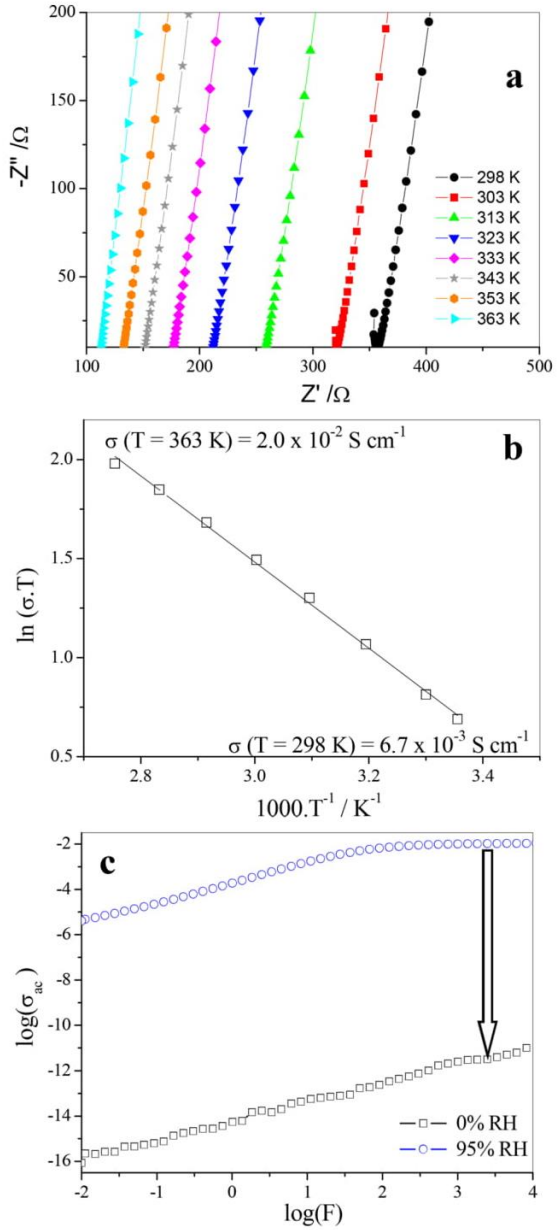

Figure 2. (a) Nyquist plot from *ac* impedance data recorded at 95% RH from 363 to 298 K for KAUST-7′. (b) Corresponding Arrhenius type plot of the conductivity of KAUST-7′. The line corresponds to the linear least-squares fit. (c) Real part of the conductivity as a function of the frequency, recorded at 298 K for the hydrated (RH = 95%) and the anhydrous (RH = 0%) KAUST-7′.

the conductivity measurements (Figure S1). These findings further support the robustness and high water stability of KAUST-7′. The Arrhenius plot ($\ln(\sigma \times T) = f(1/T)$) is illustrated in Figure 2b and it leads to an activation energy Ea of 0.19 eV. This value lies within the range of Ea < 0.4 eV, which suggests a Grotthus like mechanism[10] involving the proton transfer through a hydrogen-bond network, while water is expected to assist the proton displacement.

DOI: 10.1021/jacs.8b06582
J. Am. Chem. Soc. 2018, 140, 13156−13160

To further evidence the key role of water in the proton transport mechanism, impedance measurements were equally carried out at room temperature under different humidity conditions. Figure S5 clearly demonstrates the conductivity dependence on RH, because σ drastically increases from 2.9×10^{-8} to 6.7×10^{-3} S cm^{-1} for RH raising from 40% to 95%. This evolution follows the increasing of the water uptake as a function of the relative water pressure as shown by the adsorption isotherm (Figure S6). This further confirms that protons are involved in the water assisted conductivity process.[11]

More interestingly, a Bode representation of the electrical response, i.e., $\sigma_{ac} = f(f)$, where f is the frequency of the electrical field (see Supporting Information) allowed us to reveal that KAUST-7′ switches from a superionic conductor behavior toward an insulator one under dehydration as illustrated by the change of the σ_{ac} profile depicted in Figure 2c. The electrical conductivity profile of the hydrated sample is dominated by the dc plateau associated with the long-range transport of the proton species. It is accompanied by the Maxwell–Wagner Sillars polarization present at low frequency, due to the accumulation of the ionic charge carriers at the sample/electrodes interface. The later corresponds to the capacitive tail observed in the Nyquist plot (Figure 2a). For the anhydrous sample, the scenario drastically differs because the dc plateau completely vanishes, giving rise to a continuous increase of σ_{ac} with the frequency in the whole explored domain, characteristic of the polarization conductivity $\sigma'(\omega)$. Noteworthy, this behavior is typical of an extremely poor conductor, i.e., an insulator, consistent with the low values of $\sigma'(\omega)$ ($<10^{-10}$ S cm^{-1}). It equally turns out that the conductivity recorded at 5000 Hz and 298 K drastically drops by 9 orders of magnitude when RH decreases from 95 to 0%, i.e., $\sigma = 6.7 \times 10^{-3}$ S cm^{-1} and $\sigma = 4.0 \times 10^{-12}$ S cm^{-1} for the hydrated and the anhydrous solids, respectively. This sharp conductivity change with RH suggests that KAUST-7′ may have great potential as an active sensing material for the design of impedance-type humidity sensors, with sensitivity even surpassing that of MOFs based devices already reported in the literature.[12]

Quantum-based molecular simulations were further performed to shed light on the water-mediated proton transport mechanism at the atomistic scale. The fully hydrated KAUST-7′ structure, containing 2 water molecules per unit formula, consistent with the water adsorption uptake determined at saturation from the adsorption isotherm (see Figure S6) was first geometry optimized at the DFT-D3 level using the PBE GGA functional[13] combined with a Gaussian basis set,[14] the GTH pseudopotentials[15] and the Grimme's DFT-D3 semi-empirical dispersion corrections[16] as implemented in the CP2K package[17] (see Supporting Information for details). The corresponding DFT-optimized structure (Figure S7) clearly evidenced the formation of a hydrogen-bonded network highly orientated along the layer that involves water adsorbed between the layers (H_2O_w), fluorine atoms (F) of the inorganic node and water coordinated to Ni^{2+} (H_2O_c) with separating distances for the pairs F–H_c, F–H_w and O_w–H_c below 1.9 Å (see Figure S8). *Ab initio* molecular dynamics (AIMD) simulations were further performed to explore the dynamics of the fully hydrated KAUST-7′ using the same functional/basis set as mentioned above. These simulations were run with a time step of 1 fs for 20 ps at 298 K, in order to collect enough statistics to describe the main features of the microscopic proton conduction mechanism. This calculation revealed that the H-bonded network is characterized by a continuous evolution that implies ever-changing cleavage/formation of hydrogen-bond interactions between H_2O_w, F and H_2O_c species. An illustration of the local dynamics of this H-bonded network is provided in Figure 3. Typically, H_2O_w which initially interacts with the 2 fluorine atoms labeled as F1 and F2 (Figure 3a), can rotate to form an extra-interaction with H_2O_c and another fluorine atom labeled as F3, while keeping the hydrogen-bond with F1 (Figure 3b). This local rearrangement of H_2O_w can further induce a reorientation of H_2O_c in such a way to create an H-bond with a fluorine atom labeled as F4 that belongs to another inorganic node (Figure 3c). Such a global H_2O_w-assisted reorganization of the H-bond network generates favorable pathways for the proton propagation at the origin of the excellent conduction properties of this material.

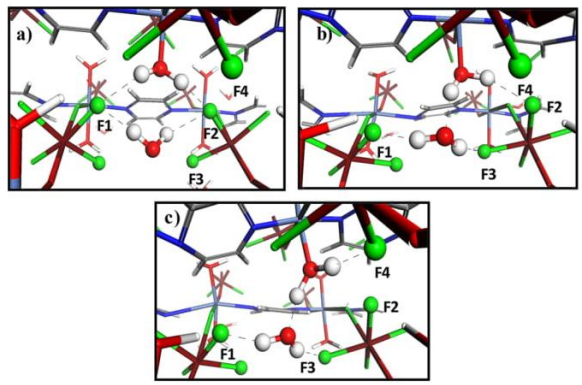

Figure 3. Illustration of the hydrogen-bond network rearrangement after 0.009 ps (a), 1.072 ps (b) and 1.879 ps (c) of the AIMD calculation run. The atoms are represented as follows: F, green; C, gray; O, red; N, blue; Ni, Nb, brown and H, white. The representation is provided along [101].

In summary, we discovered a new water stable lamellar Ni^{2+} based MOF, called KAUST-7′, with exceptional proton conductivity performances exceeding 10^{-2} S cm^{-1} at 363 K and 95% RH. This makes this novel material one of the most practical alternative materials to the commercial benchmark Nafion for further ion-exchange membrane applications. The origin of this remarkable conductivity was elucidated by molecular simulations, which showed that the acidic protons were issued from the coordinated water and further transferred within the material through an extended and efficient water H-bonded network along the interlayer. Moreover, KAUST-7′ shows a spectacular behavior by switching from a supeconductor toward an insulator upon dehydration, with a huge conductivity drop, i.e. 9 orders of magnitude, beneficial for candidate humidity sensor materials.

■ ASSOCIATED CONTENT

Supporting Information

The Supporting Information is available free of charge on the ACS Publications website at DOI: 10.1021/jacs.8b06582.

Details on the solid characterization, impedance measurements and modeling (PDF)

DOI: 10.1021/jacs.8b06582
J. Am. Chem. Soc. 2018, 140, 13156–13160

AUTHOR INFORMATION

Corresponding Authors
*sabine.devautour-vinot@umontpellier.fr
*mohamed.eddaoudi@kaust.edu.sa

ORCID
Youssef Belmabkhout: 0000-0001-9952-5007
Mohamed Eddaoudi: 0000-0003-1916-9837
Sabine Devautour-Vinot: 0000-0002-3812-7379

Author Contributions
[§]These authors contributed equally.

Notes
The authors declare no competing financial interest.

ACKNOWLEDGMENTS

The research leading to these results has received funding from the King Abdullah University of Science and Technology (KAUST) under Center Partnership Fund Program (CPF 2910). P.G.M. thanks the National Counsel of Technological and Scientific Development (CNPQ) for the scholarship. G.M. thanks the Institut Universitaire de France for its support.

REFERENCES

(1) Zhang, H.; Shen, P. K. *Chem. Soc. Rev.* **2012**, *41*, 2382−2394.
(2) (a) Zhou, H. C.; Long, J. R.; Yaghi, O. M. *Chem. Rev.* **2012**, *112*, 673−674. (b) Zhou, H. C.; Kitagawa, S. *Chem. Soc. Rev.* **2014**, *43*, 5415−5418. (c) Eddaoudi, M.; Sava, D. F.; Eubank, J. F.; Adil, K.; Guillerm, V. *Chem. Soc. Rev.* **2015**, *44*, 228−249. (d) Maurin, G.; Serre, C.; Cooper, A.; Ferey, G. *Chem. Soc. Rev.* **2017**, *46*, 3104−3107.
(3) (a) Horike, S.; Umeyama, D.; Kitagawa, S. *Acc. Chem. Res.* **2013**, *46*, 2376−2384. (b) Yamada, T.; Otsubo, K.; Makiura, R.; Kitagawa, H. *Chem. Soc. Rev.* **2013**, *42*, 6655−6669. (c) Ramaswamy, P.; Wong, N. E.; Shimizu, G. K. H. *Chem. Soc. Rev.* **2014**, *43*, 5913−5932. (d) Meng, X.; Wang, H. N.; Song, S. Y.; Zhang, H. *Chem. Soc. Rev.* **2017**, *46*, 464−480. (e) Li, A. L.; Gao, Q.; Xu, J.; Bu, X. H. *Coord. Chem. Rev.* **2017**, *344*, 54−82. Bao, S. S.; Shimizu, G. K. H.; Zheng, L. M. *Coord. Chem. Rev.* **2017**, DOI: 10.1016/j.ccr.2017.11.029.
(4) (a) Nugent, P.; Belmabkhout, Y.; Burd, S. D.; Cairns, A. J.; Luebke, R.; Forrest, K.; Pham, T.; Ma, S.; Space, B.; Wojtas, L.; Eddaoudi, M.; Zaworotko, M. J. *Nature* **2013**, *495*, 80−84. (b) Shekhah, O.; Belmabkhout, Y.; Chen, Z.; Guillerm, V.; Cairns, A.; Adil, K.; Eddaoudi, M. *Nat. Commun.* **2014**, *5*, 4228. (c) Shekhah, O.; Belmabkhout, Y.; Adil, K.; Bhatt, P. M.; Cairns, A. J.; Eddaoudi, M. *Chem. Commun.* **2015**, *51*, 13595−13598. (d) Elsaidi, S. K.; Mohamed, M. H.; Schaef, H. T.; Kumar, A.; Lusi, M.; Pham, T.; Forrest, K. A.; Space, B.; Xu, W.; Halder, G. J.; Liu, J.; Zaworotko, M. J.; Thallapally, P. K. *Chem. Commun.* **2015**, *51*, 15530−15533. (e) Cadiau, A.; Adil, K.; Bhatt, P. M.; Belmabkhout, Y.; Eddaoudi, M. *Science* **2016**, *353*, 137−140. (f) Bhatt, P. M.; Belmabkhout, Y.; Cadiau, A.; Adil, K.; Shekhah, O.; Shkurenko, A.; Barbour, L. J.; Eddaoudi, M. *J. Am. Chem. Soc.* **2016**, *138*, 9301−9307. (g) Adil, K.; Belmabkhout, Y.; Pillai, R. S.; Cadiau, A.; Bhatt, P. M.; Assen, A. H.; Maurin, G.; Eddaoudi, M. *Chem. Soc. Rev.* **2017**, *46*, 3402−3430. (h) Adil, K.; Bhatt, P. M.; Belmabkhout, Y.; Abtab, S. M. T.; Jiang, H.; Assen, A. H.; Mallick, A.; Cadiau, A.; Aqil, J.; Eddaoudi, M. *Adv. Mater.* **2017**, *29*, 1702953. (i) Kumar, A.; Hua, C.; Madden, D. G.; O'Nolan, D.; Chen, K. J.; Keane, L. A. J.; Perry, J. J., IV; Zaworotko, M. *Chem. Commun.* **2017**, *53*, 5946−5949. (j) Scott, H. S.; Shivanna, M.; Bajpai, A.; Madden, D. G.; Chen, K. J.; Pham, T.; Forrest, K. A.; Hogan, A.; Space, B.; Perry IV, J. J.; Zaworotko, M. J. *ACS Appl. Mater. Interfaces* **2017**, *9*, 33395−33400. (k) Cadiau, A.; Belmabkhout, Y.; Adil, K.; Bhatt, P. M.; Pillai, R. S.; Shkurenko, A.; Martineau-Corcos, C.; Maurin, G.; Eddaoudi, M. *Science* **2017**, *356*, 731−735.
(5) Sone, Y.; Ekdunge, P.; Simonsson, D. *J. Electrochem. Soc.* **1996**, *143*, 1254−1259.
(6) Le Bail, A. *Powder Diffr.* **2004**, *19*, 249−254.
(7) Le Bail, A.; Duroy, H.; Fourquet, J. L. *Mater. Res. Bull.* **1988**, *23*, 447−452.
(8) Hu, B.; Li, J. R.; Huang, X. Y. *Jiegou Huaxue* **2011**, *30*, 678−684.
(9) (a) Ponomareva, V. G.; Kovalenko, K. A.; Chupakhin, A. P.; Dybtsev, D. N.; Shutova, E. S.; Fedin, V. P. *J. Am. Chem. Soc.* **2012**, *134*, 15640−15643. (b) Kim, S. R.; Dawson, K. W.; Gelfand, B. S.; Taylor, J. M.; Shimizu, G. K. H. *J. Am. Chem. Soc.* **2013**, *135*, 963−966. (c) Phang, W. J.; Lee, W. R.; Yoo, K.; Ryu, D. W.; Kim, B. S.; Hong, C. S. *Angew. Chem., Int. Ed.* **2014**, *53*, 8383−8387. (d) Zhao, X.; Mao, C. Y.; Bu, X. H.; Feng, P. Y. *Chem. Mater.* **2014**, *26*, 2492−2495. (e) Nagarkar, S. S.; Unni, S. M.; Sharma, A.; Kurungot, S.; Ghosh, S. K. *Angew. Chem., Int. Ed.* **2014**, *53*, 2638−2642. (f) Ramaswamy, P.; Wong, N. E.; Gelfand, B. S.; Shimizu, G. K. H. *J. Am. Chem. Soc.* **2015**, *137*, 7640. (g) Phang, W. J.; Jo, H.; Lee, W. R.; Song, J. H.; Yoo, K.; Kim, B.; Hong, C. S. *Angew. Chem., Int. Ed.* **2015**, *54*, 5142−5146. (h) Nguyen, N. T. T.; Furukawa, H.; Gandara, F.; Trickett, C. A.; Jeong, H. M.; Cordova, K. E.; Yaghi, O. M. *J. Am. Chem. Soc.* **2015**, *137*, 15394−15397. (i) Tu, T. N.; Phan, N. Q.; Vu, T. T.; Nguyen, H. L.; Cordova, K. E.; Furukawa, H. *J. Mater. Chem. A* **2016**, *4*, 3638−3641. (j) Yang, F.; Xu, G.; Dou, Y.; Wang, B.; Zhang, H.; Wu, H.; Zhou, W.; Chen, B.; Li, J. R. *Nature Energy* **2017**, *2*, 877−883. (k) Li, X. M.; Dong, L. Z.; Li, S. L.; Xu, G.; Liu, J.; Zhang, F. M.; Lu, L. S.; Lan, Y. Q. *ACS Energy Lett.* **2017**, *2*, 2313−2318. (l) Lai, X.; Liu, Y.; Yang, G.; Liu, S.; Shi, Z.; Lu, Y.; Luo, F.; Liu, S. *J. Mater. Chem. A* **2017**, *5*, 9611−9617. (m) Wu, H.; Yang, F.; Lv, X. L.; Wang, B.; Zhang, Y. Z.; Zhao, M. J.; Li, J. R. *J. Mater. Chem. A* **2017**, *5*, 14525−14529. (n) Fard, Z. H.; Wong, N. E.; Malliakas, C. D.; Ramaswamy, P.; Taylor, J. M.; Otsubo, K.; Shimizu, G. K. H. *Chem. Mater.* **2018**, *30*, 314−318. (o) Nguyen, M. V.; Lo, T. H. N.; Luu, L. C.; Nguyen, H. T. T.; Tu, T. N. *J. Mater. Chem. A* **2018**, *6*, 1816−1821. (p) Kim, S. R.; Joarder, B.; Hurd, J. A.; Zhang, J.; Dawson, K. W.; Gelfand, B. S.; Wong, N. E.; Shimizu, G. K. H. *J. Am. Chem. Soc.* **2018**, *140*, 1077−1082. (q) Phang, W. J.; Lee, R. W.; Yoo, K.; Ryu, D. W.; Kim, B. S.; Hong, S. C. *Angew. Chem., Int. Ed.* **2014**, *53*, 8383. (r) Pili, S.; Argent, S. P.; Morris, C. G.; Rought, P.; Garcia-Sakai, V.; Silverwood, I. P.; Easun, T. L.; Li, M.; Warren, M. R.; Murray, C. A.; Tang, C. C.; Yang, S.; Schroder, M. *J. Am. Chem. Soc.* **2016**, *138*, 6352. (s) Ye, Y.; Wu, X.; Yao, Z.; Wu, L.; Cai, Z.; Wang, L.; Ma, X.; Chen, Q.-H.; Zhang, Z.; Xiang, S. *J. Mater. Chem. A* **2016**, *4*, 4062. (t) Ye, Y.; Guo, W.; Wang, L.; Li, Z.; Song, Z.; Chen, J.; Zhang, Z.; Xiang, S.; Chen, B. *J. Am. Chem. Soc.* **2017**, *139*, 15604. (u) Park, S. S.; Rieth, A. J.; Hendon, C. H.; Dinca, M. *J. Am. Chem. Soc.* **2018**, *140*, 2016.
(10) (a) de Grotthuss, C. J. T. *Ann. Chim.* **1806**, *58*, 54−74. (b) Kreuer, K. D.; Rabenau, A.; Weppner, W. *Angew. Chem., Int. Ed. Engl.* **1982**, *21*, 208−209.
(11) Donnadio, A.; Nocchetti, M.; Costantino, F.; Taddei, M.; Casciola, M.; da silva Lisboa, F.; Vivani, R. *Inorg. Chem.* **2014**, *53*, 13220−13226.
(12) (a) Achmann, S.; Hagen, G.; Kita, J.; Malkowsky, I. M.; Kiener, C.; Moos, R. *Sensors* **2009**, *9*, 1574−1589. (b) Zhang, Y.; Chen, Y.; Zhang, Y.; Cong, H.; Fu, B.; Wen, S.; Ruan, S. *J. Nanopart. Res.* **2013**, *15*, 2014. (c) Weiss, A.; Reimer, N.; Stock, N.; Tiemann, M.; Wagner, T. *Phys. Chem. Chem. Phys.* **2015**, *17*, 21634−21642. (d) Weiss, A.; Reimer, N.; Stock, N.; Tiemann, M.; Wagner, T. *Microporous Mesoporous Mater.* **2016**, *220*, 39−43. (e) Zhang, J.; Sun, L.; Chen, C.; Liu, M.; Dong, W.; Guo, W. J.; Ruan, S. *J. Alloys Compd.* **2017**, *695*, 520−525. (f) Gao, Y.; Jing, P.; Yan, N.; Hilbers, M.; Zhang, H.; Rothenberg, G.; Tanase, S. *Chem. Commun.* **2017**, *53*, 4465−4468.
(13) Perdew, J. P.; Burke, K.; Ernzerhof, M. *Phys. Rev. Lett.* **1996**, *77*, 3865−3868.
(14) VandeVondele, J.; Hutter, J. *J. Chem. Phys.* **2007**, *127*, 114105.
(15) Goedecker, S.; Teter, M.; Hutter, J. *Phys. Rev. B: Condens. Matter Mater. Phys.* **1996**, *54*, 1703−1710.
(16) Grimme, S.; Antony, J.; Ehrlich, S.; Krieg, H. *J. Chem. Phys.* **2010**, *132*, 154104.
(17) (a) VandeVondele, J.; Krack, M.; Mohamed, F.; Parrinello, M.; Chassaing, T.; Hutter, J. *Comput. Phys. Commun.* **2005**, *167*, 103−

DOI: 10.1021/jacs.8b06582
J. Am. Chem. Soc. 2018, 140, 13156−13160

Journal of the American Chemical Society Communication

128. (b) Hutter, J.; Iannuzzi, M.; Schiffmann, F.; VandeVondele, J. *WIREs Comput. Mol. Sci.* **2014**, *4*, 15−25.

DOI: 10.1021/jacs.8b06582
J. Am. Chem. Soc. 2018, 140, 13156−13160

CHAPTER 4

Computation exploration of water adsorption in MOFs

I. Introduction and contribution

This chapter presents the computational approach that was undertaken to explore the water adsorption mechanism in a series of MOFs that have been revealed as promising candidates for heat-transfer application, i.e. CUK-1(Me) (Me = Ni, Co, Mg), MIL-100(Fe) and MOF-801(Zr). These materials were shown to be attractive due to their high water uptake and sharp step-like isotherm in favorable regions of water relative pressure (P/P_0). Our collaborators in KRICT evidenced that these MOFs are among the best adsorbents for chiller applications as illustrated in Figure 4.1, which reports their Coefficient of Performances under the operating conditions T_{EVAP} = 5°C and T_{des} = 30°C.

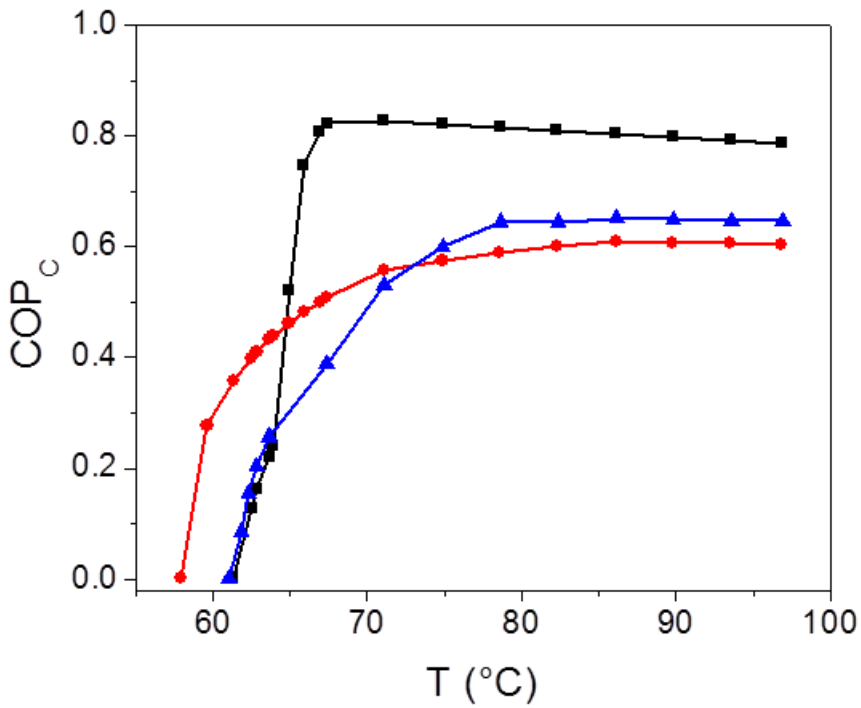

Figure 4.1 – Coefficient of performances (COP_c) plots for chiller conditions (T_{EVAP} = 5°C, T_{des} = 30°C) as a function of desorption temperature for CUK-1(Co) (-■-), MIL-100(Fe) (-●-) and MOF-801(Zr) (-▲-).

From a fundamental standpoint, these candidates have been also selected for their peculiarities in terms of water adsorption behaviors: (i) the isostructural series of CUK-1(Me), a MOF with 1D diamond-shaped pores and the asymmetric linker 2,4-pyridine dicarboxylate, was found to display a mildly hydrophobic character that can be tuned by changing the nature of the metal ion of the inorganic building units; (ii) the MOF-801(Zr), a

Zr-based MOF incorporating fumarate linkers, showed a remarkable difference in terms of water uptake and shape of the adsorption isotherm between its single crystal and powder forms [1], its water adsorption performance depending on the concentration of missing linkers in its structure and (iii) the MIL-100(Fe), a hydrophilic mesoporous MOF including coordinatively unsaturated sites (CUS) showed a complex step-wise water adsorption isotherm [2,3]. Here classical GCMC calculations have been employed not only to calculate the water adsorption isotherms and energetics of these MOFs but also to explain the peculiarities of their water adsorption behaviors in light of a careful analysis of the microscopic mechanisms in play.

It is to be noted that while GCMC simulations can be nowadays applied to accurately reproduce the adsorption behavior of porous materials with respect to simple molecules such as noble gases or light hydrocarbons, this is far more challenging once it deals with water [4]. First, despite the simple structure of the water molecule and the myriad of force fields reported in the literature (see Chapter 2), there is still no universal force field that can accurately capture all the unusual physical properties of water in confined environments. In addition, the dipole moment of water depends on the confinement degree and it can change continuously during the adsorption process. This further complicates the problem, although most of the water models treat this property as a constant [4]. Second, the simulations of water adsorption in porous materials including MOFs and zeolites converge extremely slowly, as pointed out in many publications [5–8]. Some strategies have been attempted to accelerate the simulation convergence, including the pre-tabulated energy grid method [7], pre-insertion of water molecules [8], orientational-bias moves [9], biased translational "jump moves" [8] canonical replica-exchange Monte Carlo or parallel tempering methods [10]. Other MC algorithms can be envisaged, like the energy-bias insertion moves [11] and continuous fractional component (CFC) Monte Carlo [12] to accelerate the calculations. Zhang and Snurr [4] have recently reported success in this goal using such algorithms.

In this thesis, the water adsorption isotherms on MOFs were simulated using mostly the 4-site model TIP4P/2005 [13], which was specifically developed to reproduce both the temperature of maximum density and the vaporization enthalpy of water [14]. These calculations employed a classical Monte Carlo algorithm implementing the calculation of the

interactions accelerated by making use of a grid of 0.25 Å to interpolate electrostatic and van der Waals forces. All these MC simulations were carried out with a large number of steps (at least 2×10^8 production steps preceded by 10^7 equilibration steps) which is mandatory in order to achieve equilibrium configurations for each point of the simulated isotherms.

Since these structures have pore dimensions exceeding significantly the kinetic diameter of the water molecules and they do not undergo guest-induced structural transformations, we assumed that the local rearrangements on the host framework play a minor role in the adsorption process and we thus used structural models where the host atoms are kept fixed in their initial positions. The adsorption enthalpy (ΔH_{ads}) for water was calculated using the revised Widom's test particle insertion method [15]. In the case of CUK-1(Me) and MOF-801(Zr), a conventional approach was used to model the non-bonded potentials between water molecules and the porous materials with the use of a Coulombic and LJ 12-6 potential terms to represent the electrostatic and the van der Waals interactions respectively. In this approach, the LJ 12-6 parameters assigned to each atom of the MOF were taken from generic forcefields such as the UFF [16] and DREIDING [17]. These parameters were then mixed with that of the water model using the Lorentz Berthelot mixing rule to represent the H_2O/MOF interactions. In the MC calculations, these short-range dispersion forces described by LJ 12-6 potentials were truncated at a cut-off radius of 12 Å while the Ewald summation approach was used to estimate the Coulombic contribution.

This approach to describe the MOF/water interactions is not anymore valid when one deals with specific cases like the presence of CUS sites that induce strong interactions with water. This is typically the scenario encountered for MIL-100(Fe). Here we have deployed an alternative strategy that consists of deriving the interacting energy of the water – CUS Fe(III) from *ab initio* calculations followed by a fitting of the corresponding data using an appropriate analytical function. In this specific case, we compared the results obtained from the consideration of the TIP4P/2005 water model with that using the TIP4P-Ew water model [18]. The following sections present the description of the global computational strategy and the main outcomes gained for the 3 studies.

II. CUK-1(Me)

The CUK-1(Me) is formed by the coordination of two independent metal ions (Me1 and Me2; Me = Ni, Co or Mg) to one 2,4-pdc ligand and one hydroxyl group in a distorted octahedral conformation forming 1D channels as shown in Figure 4.2a-c. The lattice connectivity of these frameworks is identical, however the space group of the as-synthesized CUK-1(Mg) differs ($P2_1/c$ in the Mg- versus C2/c in the Ni- and Co-based materials). The CUK-1(Me) framework presents diamond-like 1D pores of approximately 6 Å of accessible size, as seen in the calculated Pore Size Distribution of Figure 4.2d. In our calculations, the CUK-1(Ni), CUK-1(Co) and CUK-1(Mg) frameworks were modelled considering the crystal structures reported previously [19,20]. These structures were geometry optimized at the DFT level maintaining the experimental unit cell parameters fixed. These calculations employed a PBE GGA functional [21,22] combined with the double numerical basis set containing polarization functions (DNP) on all atoms, as implemented in the $Dmol^3$ module [23,24]. The partial charges of each atom of the framework were estimated using the REPEAT fitting approach (see Table 4.1) [25], the atom types being provided in Figure 4.3. The interactions between the MOF frameworks and water were modelled using LJ 12-6 and Coulombic potentials for the van der Waals and electrostatic contributions. To that purpose, the LJ 12-6 parameters for the atoms of the organic linker and inorganic were taken from the generic force field DREIDING [17] and UFF [16] respectively. The interactions between the H_2O molecules themselves were treated by a LJ 12-6 term and a Coulombic contribution as defined in the microscopic models employed to describe them.

As indicated in the introduction, the water molecule was described using the TIP4P/2005 model [13]. The simulation boxes were made of 12 conventional unit cells (3×2×2).

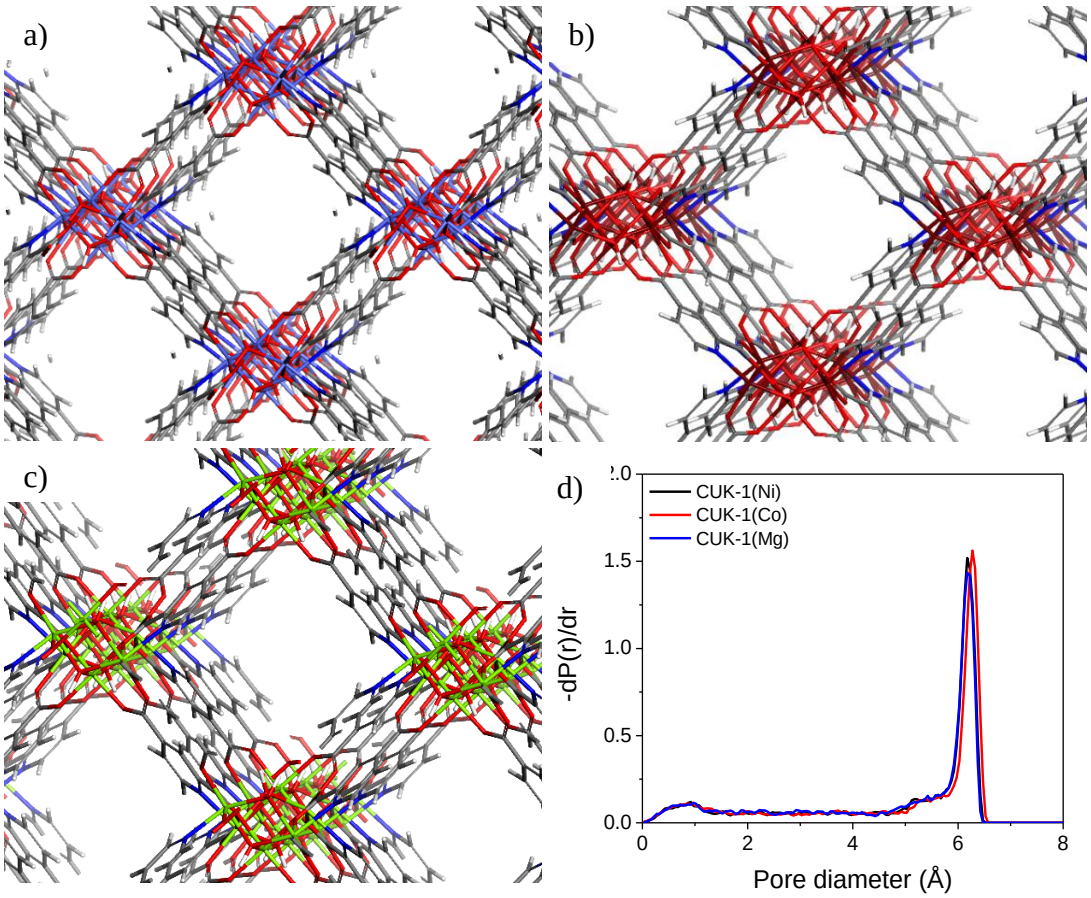

Figure 4.2 – Comparison of the DFT-optimized structures of the CUK-1(Ni) (a), CUK-1(Co) (b) and CUK-1(Mg) (c) along the a-axis and (d) Pore size distribution (PSD) of these three structures calculated using geometric parameters of the UFF forcefield to represent the atoms diameters. In grey, white, red, blue, light blue, burgundy, and green are represented respectively C, H, O, N, Ni, Co and Mg atoms.

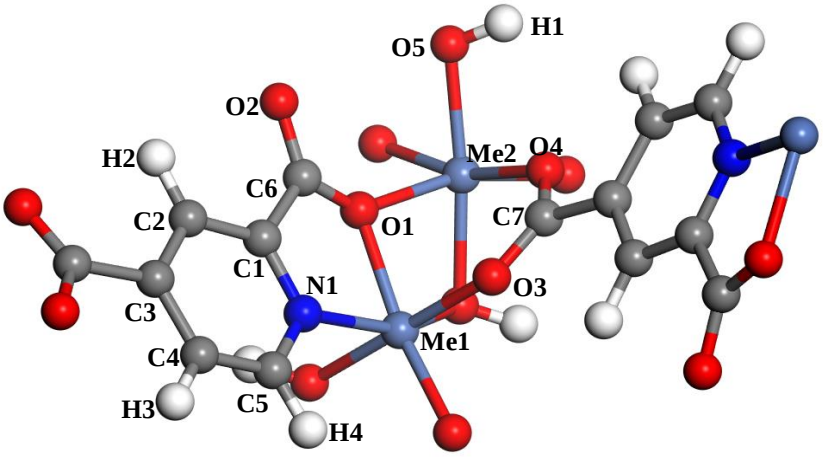

Figure 4.3 – Identification of the atoms types in the CUK-1, where Me stands for the metal in the cluster: Ni, Co or Mg, respectively in the CUK-1(Ni), CUK-1(Co) and CUK-1(Mg).

Table 4.1 – Atomic partial charges for each of the CUK-1(Me) frameworks.

Atom type	$q_{CUK-1(Ni)}$ (e)	$q_{CUK-1(Co)}$ (e)	$q_{CUK-1(Mg)}$ (e)
C1	0.4149	0.4364	0.4806
C2	-0.3901	-0.4163	-0.4388
C3	0.1351	0.1723	0.2215
C4	-0.2366	-0.2699	-0.2949
C5	0.1445	0.1719	0.2230
C6	0.2858	0.2868	0.3581
C7	0.7005	0.6565	0.6515
O1	-0.4051	-0.4046	-0.5425
O2	-0.4408	-0.4539	-0.5271
O3	-0.6391	-0.6266	-0.6784
O4	-0.6382	-0.5975	-0.6801
O5	-0.9634	-0.9040	-1.1055
H1	0.4051	0.3994	0.3984
H2	0.1923	0.1994	0.2017
H3	0.1437	0.1497	0.1537
H4	0.0599	0.0530	0.0408
N1	-0.3389	-0.3389	-0.4720
Ni1	0.9865	-	-
Ni2	1.1680	-	-
Co1	-	1.0082	-
Co2	-	1.0620	-
Mg1	-	-	1.2971
Mg2	-	-	1.4260

As mentioned above, CUK-1(Me) exhibits a singular facet regarding its water adsorption profile. Our collaborators in KRICT evidenced that changing the nature of the metal, even though without noticeable changes in the topology and pore size of this MOF, impacts significantly its hydrophilicity. As one notice from Figure 4.4a, the adsorption profiles of the nickel and copper based CUK-1 are quite similar, exhibiting a step-like shape with a pore filling at $P/P_0 = 0.12$, while in the magnesium based material the step occurs at higher pressure ($P/P_0 = 0.25$). The CUK-1(Mg) shows a higher uptake expressed in weight%, mostly due to the lighter mass of magnesium compared to nickel or copper. Indeed, the number of molecules adsorbed at saturation for all materials remains nearly the same (~30 molecules/unit cell).

As one can notice in Figure 4.4b, the trend experimentally observed for the adsorption of water in the three CUK-1 frameworks was successfully reproduced by our GCMC simulations with the confirmation that the Mg-version shows a higher hydrophobicity compared to the two other analogues.

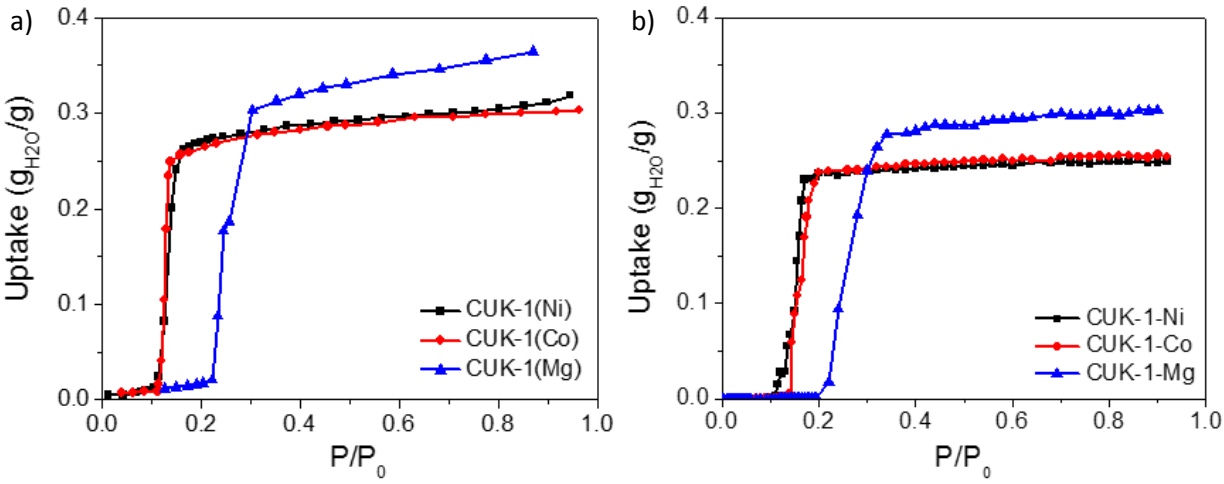

Figure 4.4 – Experimental (a) and simulated (b) water adsorption isotherm at 303 K in all CUK-1 frameworks.

The water adsorption mechanism was further explored to explain the origin of the metal dependence of the water adsorption behaviors. We evidenced that at low coverage the water molecules interact preferentially with the hydroxyl groups of the MOF framework, as one can notice in Figure 4.5a showing a sharp peak in the radial distribution function (RDF) between the oxygen of these hydroxyl groups (O_{OH}) and the oxygen of the water molecules (O_W) with a mean O_w-O_{OH} distance around 2.8 Å, a value commonly associated with the formation of a strong hydrogen bond. This conclusion was also supported by the analysis of the density probability of water calculated at low coverage which revealed that the guest molecules are located at the vicinity of the hydroxyl groups in all CUK-1 frameworks (Figure 4.6). Once the water molecules interact with these hydrophilic centers, they trigger the clustering of other molecules, forming an extensive network of water throughout the pore. One can further notice from Figure 4.5a that the RDF (O_w-O_{OH}) peak is of significantly lower intensity for CUK-1(Mg) as compared with the two other analogues, in line with a lower probability for the water molecules to interact with the hydroxyl groups. This different behavior can be supported by the analysis of the RDF between H_2O and the N atoms of the

CUK-1 framework present in the organic node. Figure 4.5b clearly emphasizes that the water molecules tend to be also located at the vicinity of these N atoms in the case of CUK-1(Mg) as shown by the presence of a well-defined peak at about 3.2 Å. This behavior can be explained by a significantly higher negative charge carried out by the N atoms in the Mg-analogue (see Table 4.1) that tends to attract the water molecules and thus diminishes the probability to find water interacting with the hydrophilic OH groups. This peculiarity of the Mg analogue is illustrated in Figure 4.6c which clearly shows a larger distribution of water in the region nearby the organic linker compared to that involved in the Ni and Cu based materials.

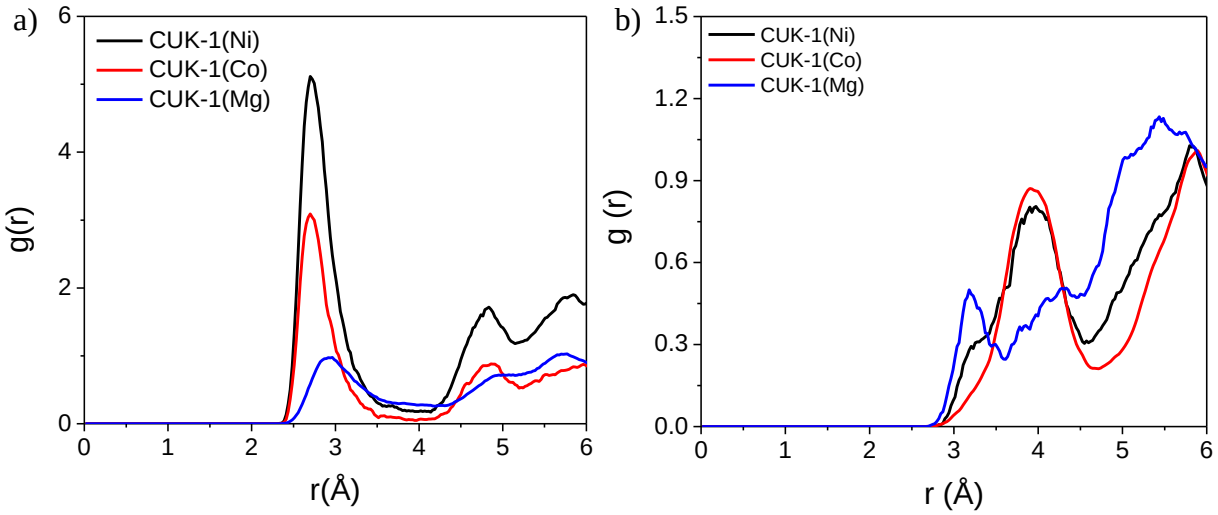

Figure 4.5 – RDFs calculated at low coverage (1 molecule per simulation box) between the oxygen of the water molecules (Ow) and (a) the oxygen of the hydroxyl groups of all CUK-1 (O_{OH}) and (b) the nitrogen (N) atoms of all CUK-1.

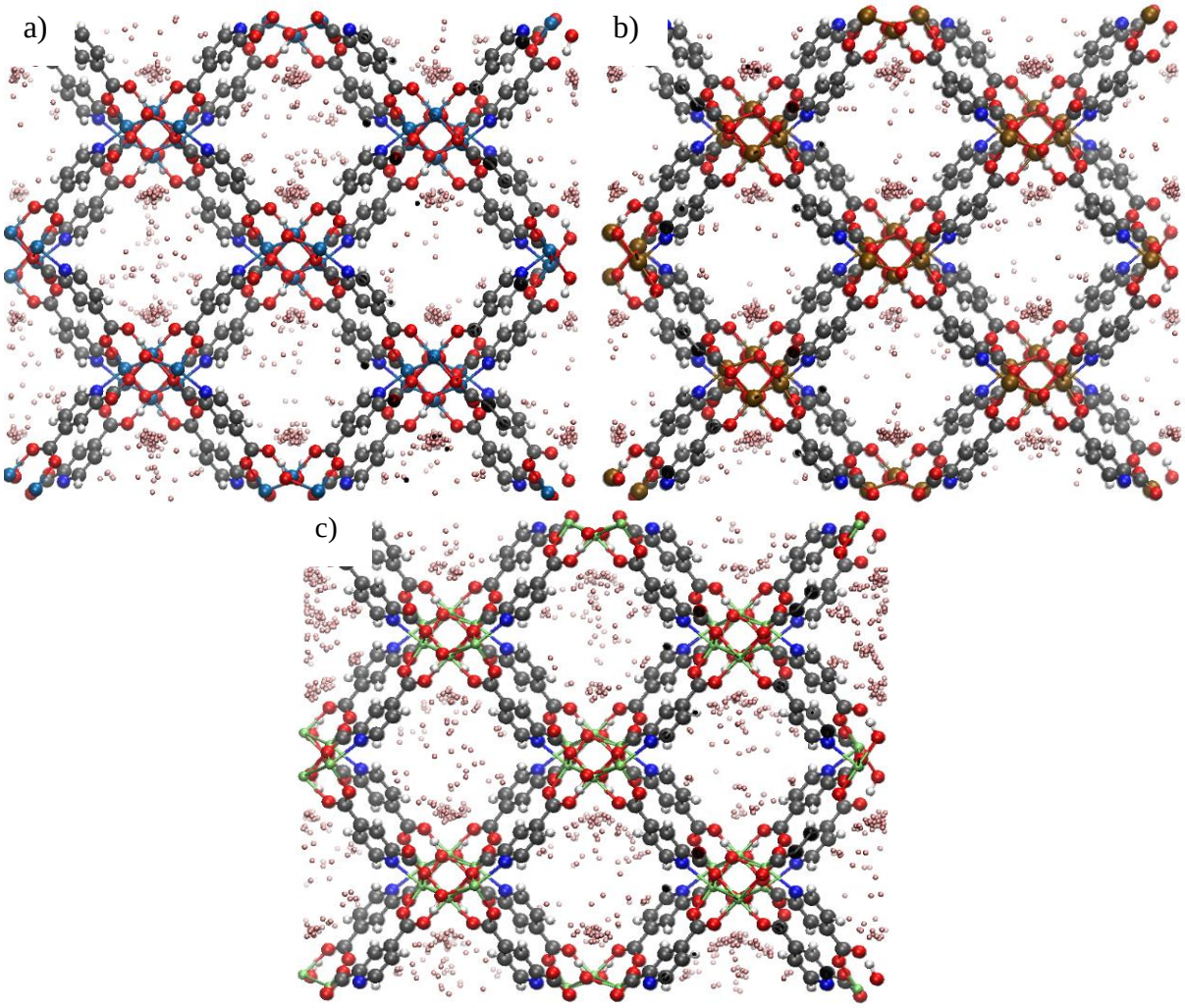

Figure 4.6 – Center of mass distribution of water molecules at low loading – 1 molecule per simulation box, before the step in the isotherm – in the CUK-1(Ni) (a), CUK-1(Co) (b) and CUK-1(Mg) (c). Representation along the *a*-axis.

Indeed, such a dual interaction between H_2O and the CUK-1(Mg) framework seems to decrease the affinity of the MOF framework to water as supported by the lower water adsorption enthalpy calculated at very low coverage for this solid as compared to the two other analogues. Figure 4.7 shows that this trend holds true in the whole range of P/P_0.

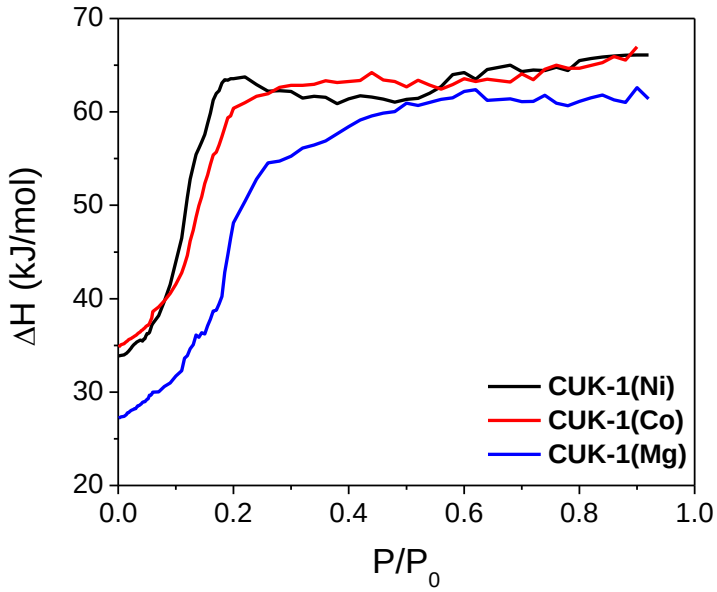

Figure 4.7 – Water Adsorption enthalpies computed for the CUK-1(Me) frameworks at 303K as a function of the relative pressure.

We further showed that the simulated water arrangement at saturation in CUK-1(Mg) reproduces very well the experimental scheme reported in the literature obtained from *in-situ* X-Ray Powder Diffraction [20] in terms of spatial distribution and conformation (see Figure 4.8). A similar adsorption behavior was also obtained for the CUK-1(Ni) and CUK-1(Co) showing that the overall arrangement of confined water in the pores is similar for the three solids at saturation, in agreement with the similar water uptake at saturation observed in all the frameworks.

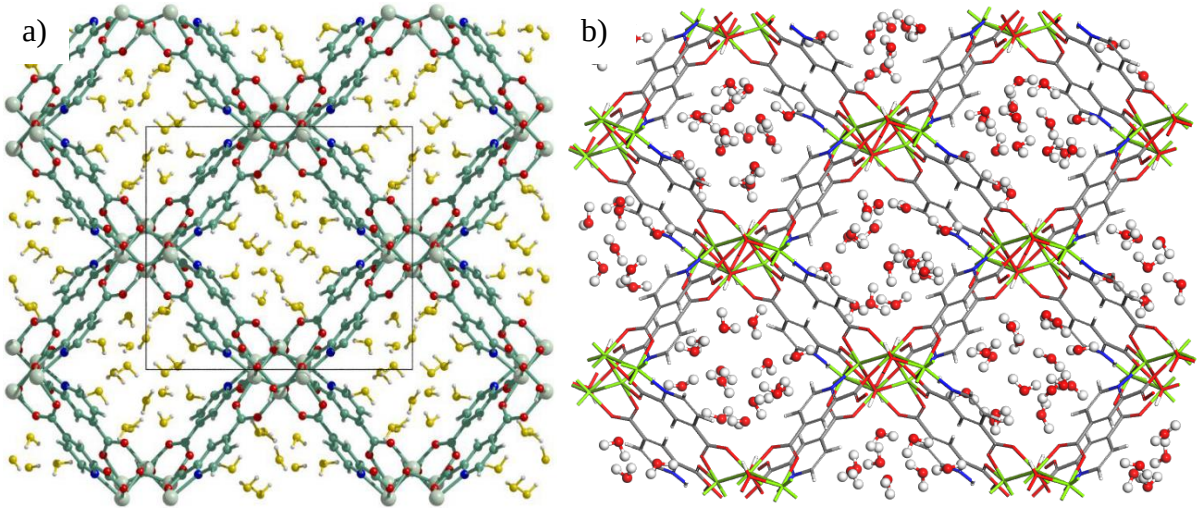

Figure 4.8 – Comparison between the simulated (a) and experimental [20] (b) distribution of water at saturation in CUK-1 (Mg). Representation along the *a*-axis.

The similarity of the water arrangement in all CUK-1 frameworks at saturation was further confirmed by an analysis of the water clustering size. The average cluster sizes are very similar for the three frameworks constituted by 15 to 18 molecules for CUK-1(Ni) and CUK-1(Mg) respectively. This value is in excellent agreement with previous experimental findings [20]. In the representative snapshot of Figure 4.9a, two of these clusters are represented in a single pore of the CUK-1(Mg).

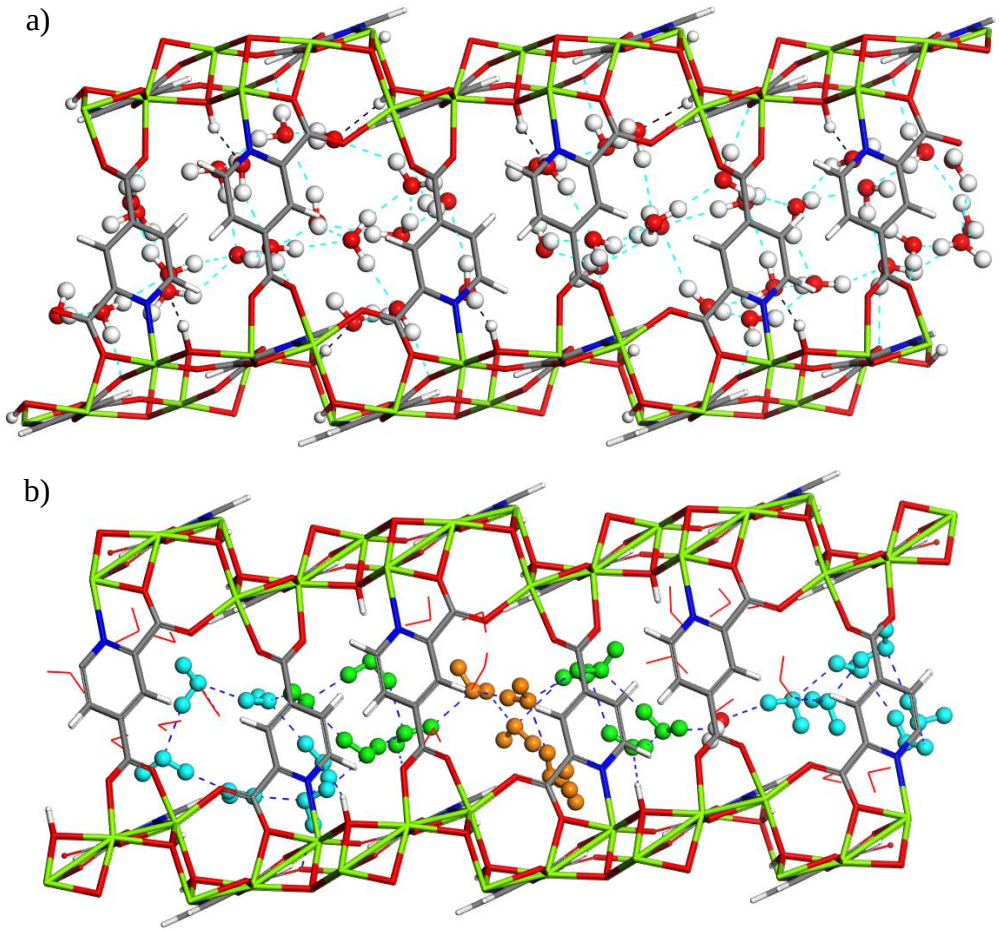

Figure 4.9 – Representative snapshots obtained from GCMC water adsorption simulations at 303 K and at saturation in a pore of CUK-1(Mg) showing the formation of (a) two independent water clusters containing about 18 molecules and (b) the arrangement of the water molecules as interconnected rings (molecules in blue, orange and green form respectively rings of 6, 5 and 4 molecules). Blue dashed lines represent hydrogen bonds among neighbor water molecules. Black dashed lines denote hydrogen bonds between water molecules and the hydroxyl groups of the MOF framework. Representation along the *c*-axis.

The GCMC simulations further evidenced that the pore size of CUK-1 is large enough to accommodate the formation of water in cycles. Most of these cycles are formed by 4 to 7 molecules (cf. Figure 4.9b) either sharing edges or linked through single water molecules, a geometry in good agreement with the pentameric drums experimentally observed in CUK-1(Mg) [20].

Another aspect that was considered is the degree of hydrogen-bond connectivity of the water molecules adsorbed in the pores of the framework, here depicted by the number of hydrogen bonds per water molecule (N_{HB}). As seen in Figure 4.10a, at saturation, the water molecules arrange themselves with a high level of connectivity (N_{HB} ~ 3.5) very close to the value observed in bulk water (3.6). This high number of hydrogen bonds per molecule has a significant contribution of the interactions with the oxygen and nitrogen atoms of the pore wall (about 1 h-bond per water molecule), since the self-association of water molecules reaches a value of N_{HB} of ~ 2.5 (cf. Figure 4.10b). At low loading, it was also observed that N_{HB} is significantly lower in CUK-1(Mg), in relation with the lower interaction energy between this MOF and the water molecules. Finally, the similar N_{HB} number found at high loading for all structures suggests that the water molecules arrange themselves similarly in all CUK-1.

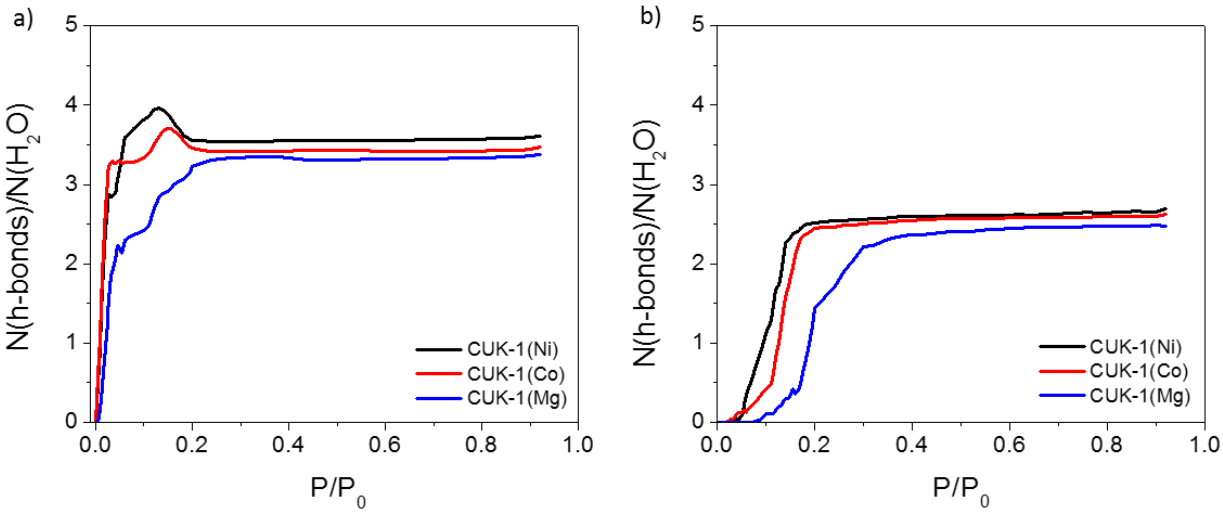

Figure 4.10 – Total number of hydrogen bonds per water molecule (a) and number of hydrogen bonds per molecules considering only the self-interactions between water molecules (b).

III. MOF-801(Zr)

The MOF-801(Zr) presents a Zr-based inorganic node– $Zr_6(\mu_3\text{-}O)_4(\mu_3\text{-}OH)_4$ – coordinated to twelve fumarate linkers, forming three symmetry-independent cavities, two with similar diameter (4.8 and 5.6 Å) and tetrahedral shape and a third octahedral-shaped one with a larger diameter (7.4 Å) (cf. Figure 4.11). In a perfectly crystallized form, i.e. without the presence of any defects, this MOF shows the following chemical composition $Zr_6O_4(OH)_4(fumarate)_6$. However this material presents defects after activation, as suggested by the elemental chemical analysis [26], which revealed a carbon and hydrogen concentration for the activated sample lower than the theoretical value calculated for the perfect MOF-801(Zr) structure. As in other Zr-based MOFs (e.g. UiO-66) [27,28], most of these defects are assumed to occur in the form of missing linkers.

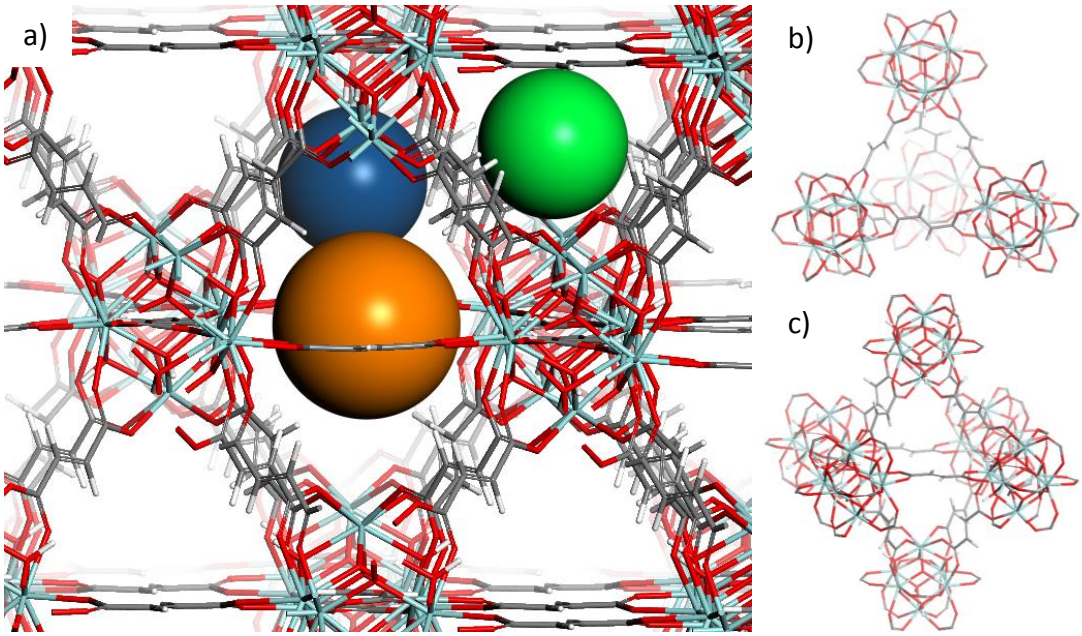

Figure 4.11 – (a) Perfect crystalline framework of the MOF-801(Zr). The blue and green balls indicate the inner space formed by two similar tetrahedral cages while the orange ball designates the space formed by the octahedral cage of this solid. In (b) and (c) one of the tetrahedral cavities and the octahedral cavity are illustrated respectively.

The crystal structure of MOF-801(Zr) was previously solved from XRPD data [29]. During the course of our work on this material, a molecular simulation study was reported on a defective MOF-801(Zr) [1]. In this work, the authors supported that a crystal structure containing four missing linkers per unit cell would be the best model to represent the water

adsorption properties of the real MOF-801(Zr) sample. However, the quality of the reproduction of the experimentally water adsorption isotherm was still not entirely satisfactory. Particularly in terms of hydrophilicity/hydrophobicity of the material, their simulations led to an adsorption of water at significantly higher P/P_0 compared to the experimental scenario (cf. Figure 4.12).

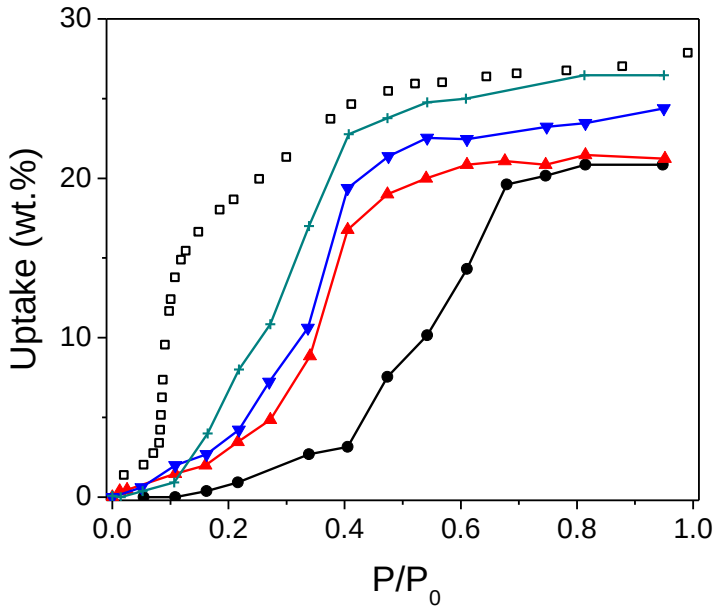

Figure 4.12 – Comparison between GCMC water adsorption isotherms in an ideal MOF-801(Zr) framework (black curve) and defect structures made by Choi *et al.* [1] with 1 (red curve), 2 (blue curve), and 4 (dark cyan curve) defects compared with experimental water adsorption isotherm reported by Furukawa *et al.* [26] in a single crystal (empty squares).

Indeed, we complemented this previous work by developing a more general strategy to get an extensive molecular level characterization of the defects on the MOF-801(Zr) and their impacts on the water adsorption behavior. From a perfect crystalline structure, we created defects by randomly removing the linkers of this MOF. Different structures with pending Zr metallic atoms in the inorganic nodes were created by removing 2, 4, 8 and 12 linkers of the unit cell. These vacancies were saturated by considering the addition of 1 H_2O molecule and 1 OH group for each neighbor Zr pair in a similar way that it was previously proposed by a first-principle simulation of the defective UiO-66 [28]. Each of these defectives structure models as well as the non-defective model (called as ideal in the rest of the section) were geometry-optimized at the DFT level maintaining the experimental unit cell

parameters fixed employing a PBE-GGA functional [21,22] combined with the double numerical basis set containing polarization functions (DNP) on all atoms, as implemented in the Dmol^3 module [23,24]. The resulting DFT-optimized frameworks are reported in Figure 4.13. The partial charges of each atom of the framework were calculated using representative cluster models cleaved for each structure (cf. Figure 4.14) with the ESP fitting approach (see Table 4.2) [25].

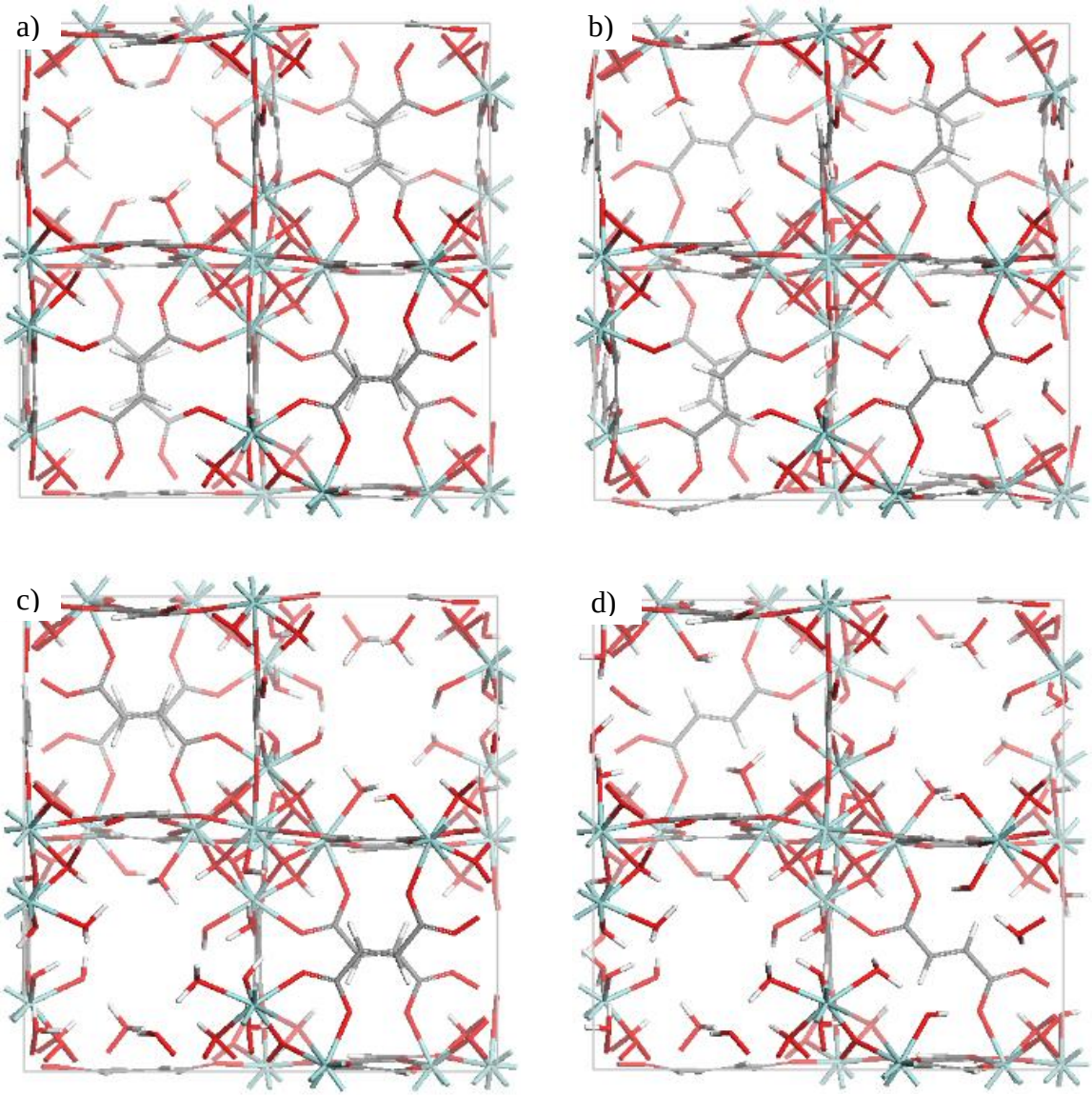

Figure 4.13 – DFT-optimized structural models developed to represent the MOF-801(Zr) structure with 2 (a), 4 (b), 8 (c), and 12 (d) missing linkers. The metallic vacancies are saturated with both OH groups and H_2O molecules.

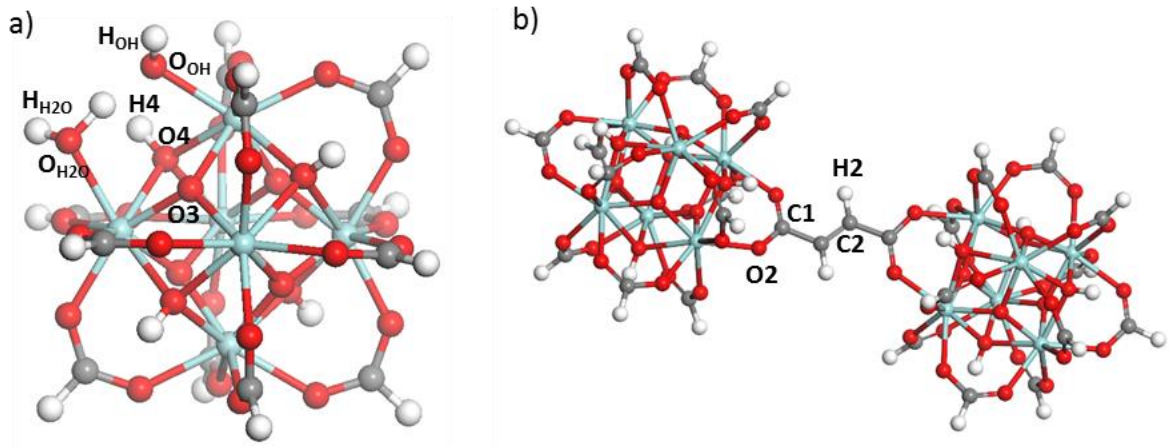

Figure 4.14 – Example of representative clusters cleaved from DFT optimized structures used in the derivation of ESP charges from the inorganic node (a) and organic linker (b) atoms. The atom types used in the derivation of those charges are indicated as labels.

Table 4.2 – Atomic partial charges of the MOF-801(Zr) derived for an ideal crystal (id) and for defective structures missing 2 (D2), 4 (D4), 8 (D8) and 12 (D12) linkers.

Atom types	Ideal	Defective models			
	q_{id} (e)	q_{d2} (e)	q_{d4} (e)	q_{d8} (e)	q_{d12} (e)
Zr	2.446	2.465	2.319	2.331	2.302
O2	-0.701	-0.679	-0.675	-0.677	-0.677
O3	-1.179	-0.963	-1.096	-1.056	-0.970
O4	-1.085	-1.377	-1.044	-1.054	-1.186
H4	0.428	0.551	0.489	0.466	0.501
C1	0.928	0.842	0.846	0.844	0.845
C2	-0.303	-0.289	-0.284	-0.286	-0.286
H2	0.166	0.164	0.169	0.167	0.167
O_{OH}	-	-0.993	-0.972	-0.986	-0.978
H_{OH}	-	0.417	0.407	0.417	0.412
O_{H2O}	-	-0.852	-0.844	-0.861	-0.833
H_{H2O}	-	0.422	0.423	0.418	0.414

The LJ 12-6 parameters of the atoms in the inorganic nodes and organic linkers of the framework were respectively taken from the generic force fields DREIDING [17] and UFF [30]. GCMC simulations of the adsorption isotherms using the ideal and defective structure models were then carried out at 298 K. The simulation boxes were made of 8 conventional unit cells (2×2×2).

One first observation of the introduction of defects in the MOF-801(Zr) was the modification of the pore volume available for the water adsorption on the MOF. This can be seen in the calculated pore size distribution (PSD) of Figure 4.15. In the ideal structure model, we can easily identify three clear peaks associated to the pores of the MOF, two of similar diameter (i.e. 4.4 and 4.7 Å) corresponding to the tetrahedral cages and another of larger diameter (6.7 Å) associated with the octahedral cages. With the introduction of defects, other peaks appear in the PSD plot. These peaks are associated with intermediary diameters between the ones associated with the ideal tetrahedral and octahedral cages and could be assigned to the defective cages formed with the random introduction of defects in the MOF's ideal structure model. The higher diameter of these cages compared to the tetrahedral cages indicate a gain in the pore volume with the introduction of defects.

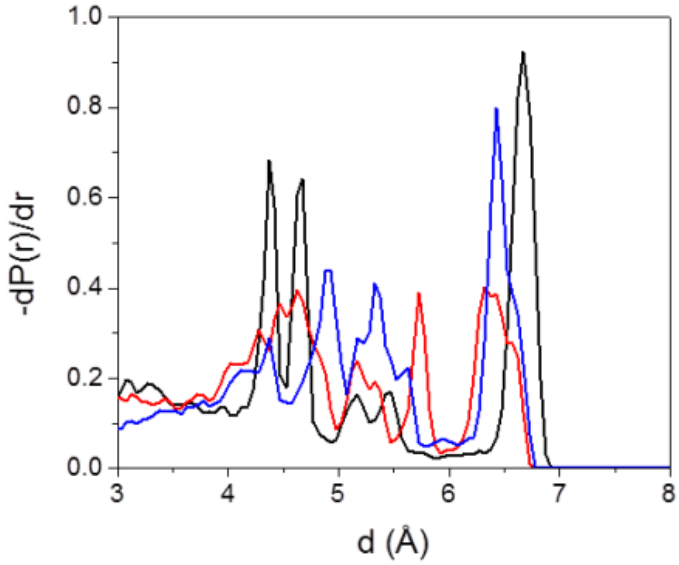

Figure 4.15 – Calculated pore size distribution for the ideal structure model of the MOF-801(Zr) (black line) compared to the ones obtained on structure models with 4 (red line) and 12 (blue line) missing linkers per unit cell.

The simulated adsorption isotherms for the so-built structure models were compared to the corresponding experimental data reported by Furukawa *et al.* [26] on single crystal and powder samples, as well as those collected by our collaborators in KRICT on a powder sample they recently synthesized. Inspecting the resulting isotherms reported in Figure 4.16, we can observe that the simulations performed with an ideal structure show a much more

hydrophobic character than the experimental water isotherms. It is required to use structure models containing 4 defects and 12 defects per unit cell to reproduce the water adsorption isotherms reported respectively for single crystal and powder samples [26]. This first observation suggests that (i) the higher the quantity of defects, the higher the hydrophilicity of the MOF, as shown by the shift on the step-wise of the isotherms to lower P/P_0, (ii) the concentration of defects on the MOFs-801(Zr) strongly depends on the synthesis conditions, since the simulated adsorption isotherms with 4 and 12 defects matches with the experimental ones obtained respectively on the single crystal and powder samples. However the simulations led to an underestimation of the water uptake obtained from our collaborators in KRICT.

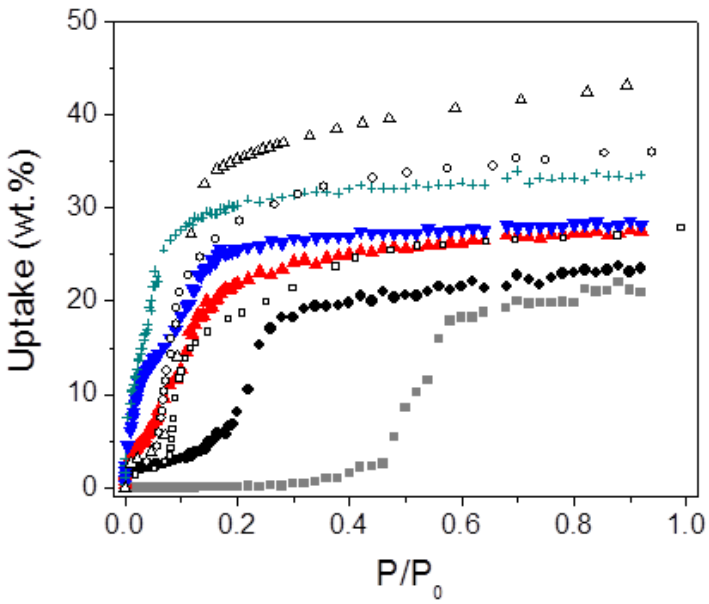

Figure 4.16 – Water adsorption isotherms on MOF-801(Zr) at 298 K calculated from GCMC simulations using an ideal crystal model (gray squares) and defective structural models with 2 (black circles), 4 (red triangles), 8 (blue reverse triangles), and 12 (dark cyan crosses) defects per unit cell. These isotherms are compared to experimental water adsorption isotherms reported by Furukawa *et al.* [26] from single crystals (empty squares) and powder samples (empty circles), and an isotherm obtained in this work (empty triangles) in a powder sample.

We further tested the hypothesis that the discrepancy between our simulations and the experimental data from KRICT would be assigned to a more efficient activation of the sample that would lead to the release of the water molecules coordinating the Zr atoms.

Indeed, as reported in Figure 4.17, considering the coordinated water of our structure models as part of the adsorbed molecules, the maximum theoretical adsorption uptake with a framework containing 12 defects per unit cell matches perfectly the maximum uptake obtained experimentally. This is an indication that our hypothesis is valid, especially considering that the release of a water molecule from the vacancy sites of the MOF-801(Zr) would not be so energetically demanding, because, as suggested by previous calculations reported in the literature [28], an intermediate bridging μ_2-OH species that form between two neighbors Zr would stabilize the vacancies.

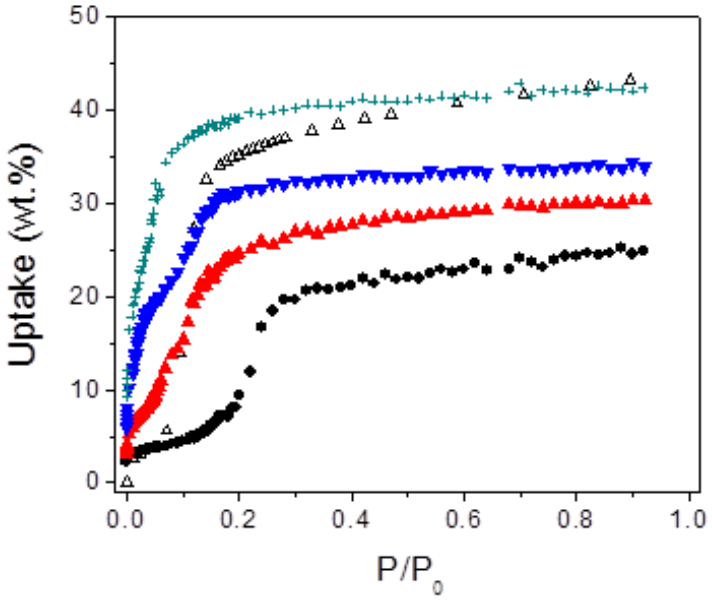

Figure 4.17 – GCMC calculated water adsorption isotherm at 298K on MOF-801(Zr) model with 2 (filled circles), 4 (filled triangles), 8 (filled inverse triangles) and 12 (crosses) defects per unit cell, considering the water molecules adsorbed in the vacancy sites as adsorbed molecules. These calculated isotherms are compared to experimental adsorption isotherms obtained in this work by our collaborators in KRICT (open triangles).

Using X-ray and neutron diffraction data, Furukawa *et al.* [26] studied the main adsorption sites of water in MOF-801(Zr). Considering the single crystal sample, they reported adsorption sites in the tetrahedral cages of the framework at low loading, associated with the connection of the water molecules to the μ_2-OH groups (site 1) (cf. Figure 4.18a-b) as well as another site formed by the water molecules of the first interacting shell, which would arrange themselves in cubic clusters (site 2) (cf. Figure 4.18b) and finally in the octahedral cages of the framework, resulting from a self-association of the water molecules at

higher loading (site 3) (cf. Figure 4.18c). The same analysis conducted on the powder sample identified a fourth adsorption site at the center of the tetrahedral cages (site 4) (cf. Figure 4.18d-e). Since the structure models of the MOF-801(Zr) framework with 4 and 12 defects were the most representative in the fitting of the adsorption behavior of respectively single crystal and powder samples, we used these models to correlate the water arrangements predicted from our GCMC simulations to the results obtained experimentally by Furukawa *et al.* [26]. For sake of comparison, we also studied the water arrangements in the ideal crystal structural model.

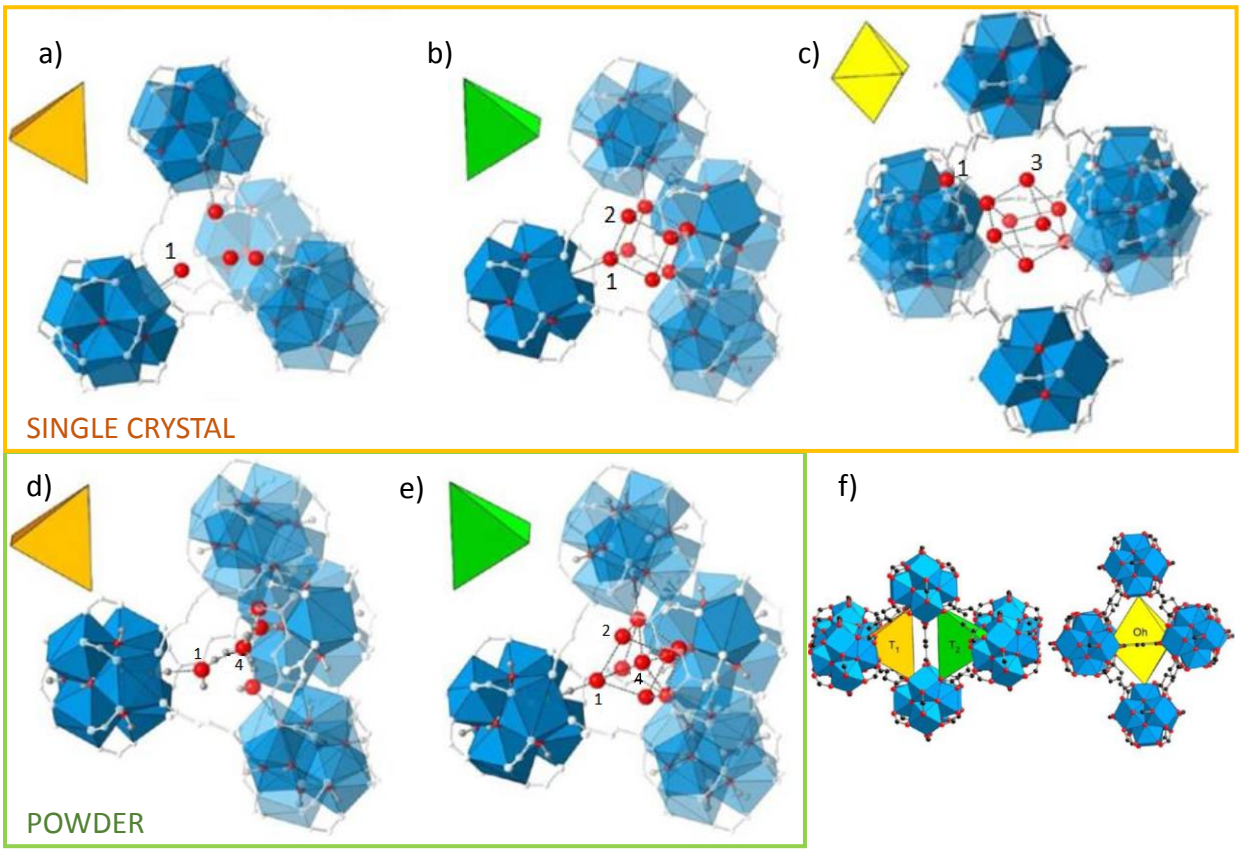

Figure 4.18 – Reinterpretation of the adsorption sites of water molecules in the MOF-801(Zr) made by Furukawa *et al.* [26] from XRPD experiments at 363 K in a single crystal sample (a-c) and from neutron powder diffraction data at room temperature in a powder sample (d-e). In (f), the tetrahedral and octahedral cavities of the MOF are evidenced. Figure adapted from ref. [26].

To study the organization of the water molecules in the pores of the MOF-801(Zr), we first used representative snapshots of the adsorption of water molecules in the structures. In an ideal framework, we observed a similar trend as evidenced in the experimental sitting

analysis. At low loadings, one notices that the water molecules are first adsorbed at the vicinity of the μ_3-OH groups of the SBUs in the tetrahedral cavities (site 1, cf. Figure 4.19a). With a minor increase in the water loading, one can observe the water molecules arrange themselves in cuboid clusters in these cavities (site 2, cf. Figure 4.19b). Up to this point the octahedral cages are unoccupied. However, at high loadings these octahedral cages are filled (site 3) having the cuboid clusters in the tetrahedral cavities as hydrogen bond anchoring points from where the pore filling occurs (see Figure 4.19c).

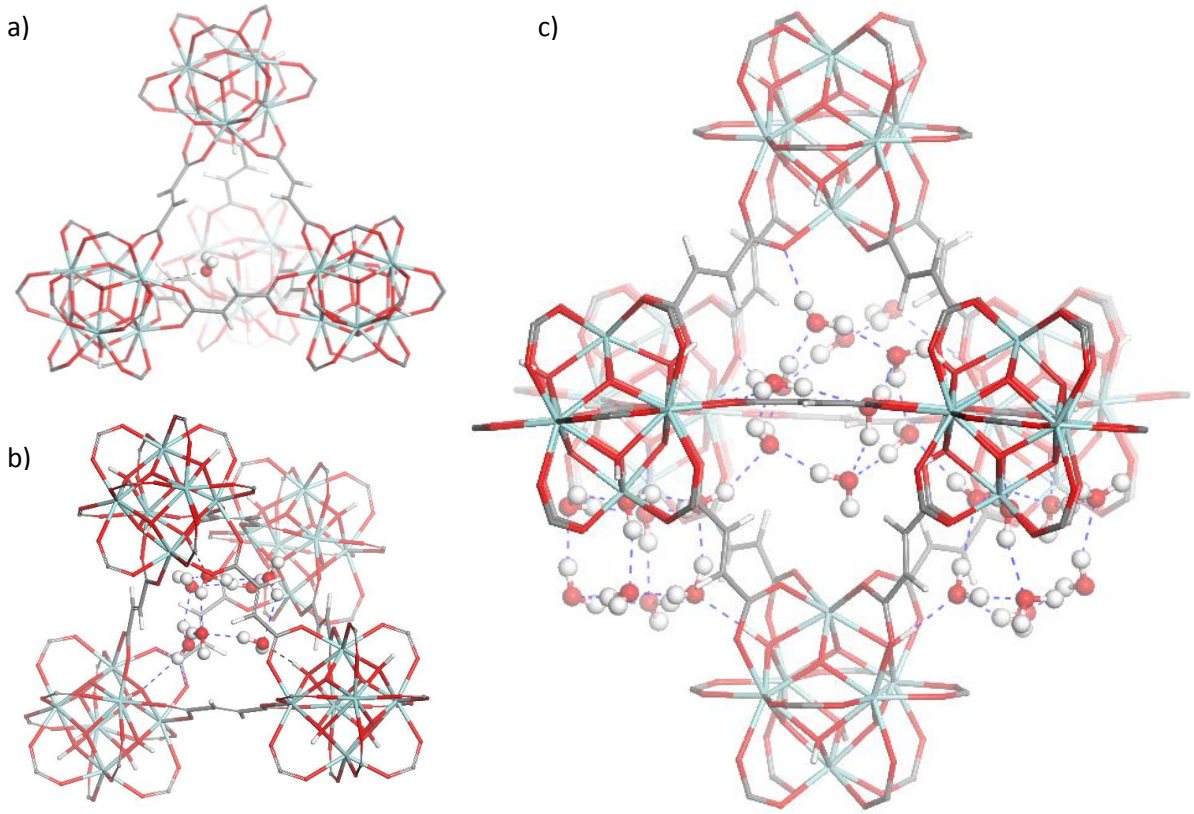

Figure 4.19 – Details of the snapshots from GCMC calculations of the water adsorption in the ideal MOF-801(Zr) framework model at 298 K. Water adsorption sites in the structure are evidenced at very low (a), intermediate (b) and high loading conditions (c).

Although this findings are consistent with the description made by Furukawa *et al.* [26] using single crystal data, they do not allow to explain the existence of the fourth site obtained reported using powder data. We further explored the impact of the defects of the framework on the water distribution by considering as typical illustration the structure model containing 4 defects per unit cell.

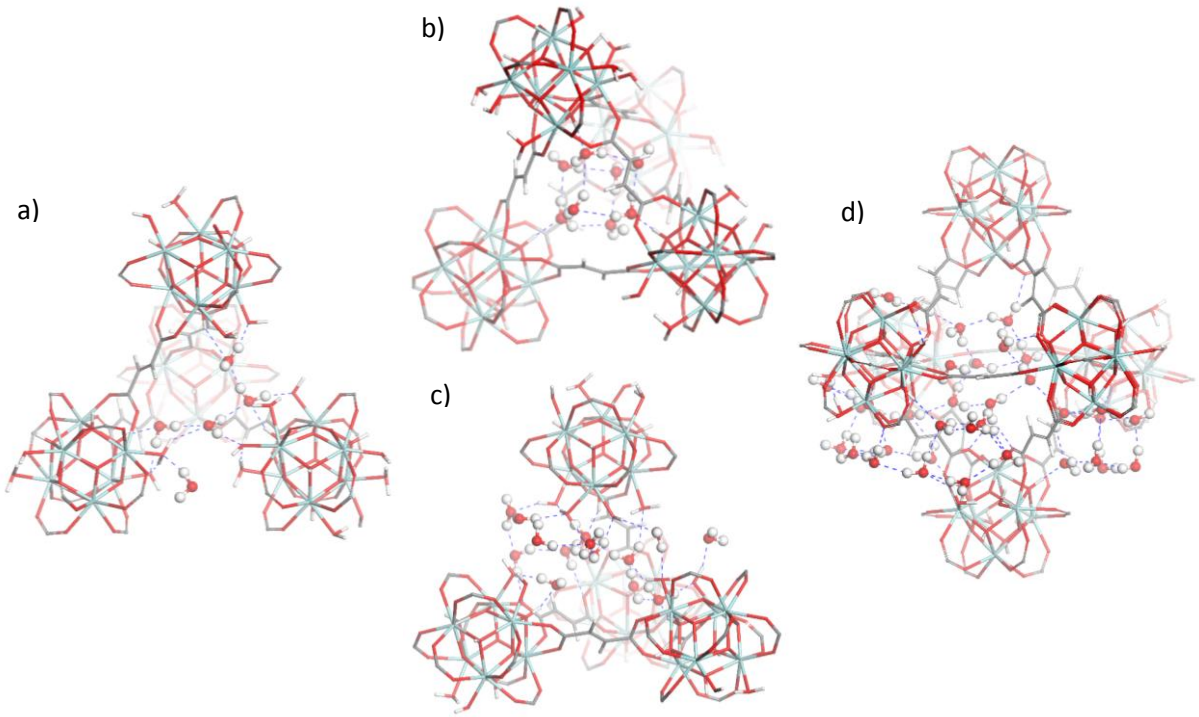

Figure 4.20 – Details of snapshots from GCMC simulations of the water adsorption at 298 K in a defective framework of MOF-801(Zr) with 4 missing linkers per unit cell. Water adsorption sites in the structure are evidenced at very low (a), intermediate (b,c) and high loading conditions (d).

On the contrary to the ideal framework, in the defective structure at low loading the water molecules are initially preferentially located in the tetrahedral cavities next to both the μ_2-OH groups and the terminal groups connected to the Zr atoms, i.e. the hydroxyl groups (OH_C) and coordinated water molecules (H_2O_C) (cf. Figure 4.20a). The formation of hydrogen bonds between the adsorbed water molecules and these hydrophilic sites coordinated to the Zr atoms are the main reason behind the gain in hydrophilicity of the framework with the introduction of defects (cf. Figure 4.16 and 4.17). The RDFs reported in Figure 4.21a-c showed that there is a hierarchy in the strength of the H-bonds between H_2O molecules and these sites. This is clearly seen by the distinct equilibrium distances of the oxygen atoms of the water molecules (O_w) and the ones from each hydrophilic group. This allowed us to classify the hydrophilic groups according to the strength of their hydrogen bonds with the water molecules in the following manner: OH_C > μ_2-OH > H_2O_C. The respective equilibrium distance of the interactions between these groups and the water molecules – 2.55, 2.65 and 2.75 Å – are all substantially shorter than the water – water

interactions in the pores of the framework (2.88 Å) (cf. Figure 4.21d). It is important to notice that the relative order of strength of the H-bonds does not mean that the water molecules interact with one of these sites on the detriment of the others. On the contrary, as seen in Figure 4.20a, the water molecules interact with one, two or three of these sites concomitantly. Consequently, they are located in an intermediate position between the hydrophilic groups (cf. Figure 4.20a), consistent with the site 1 previously identified experimentally [26].

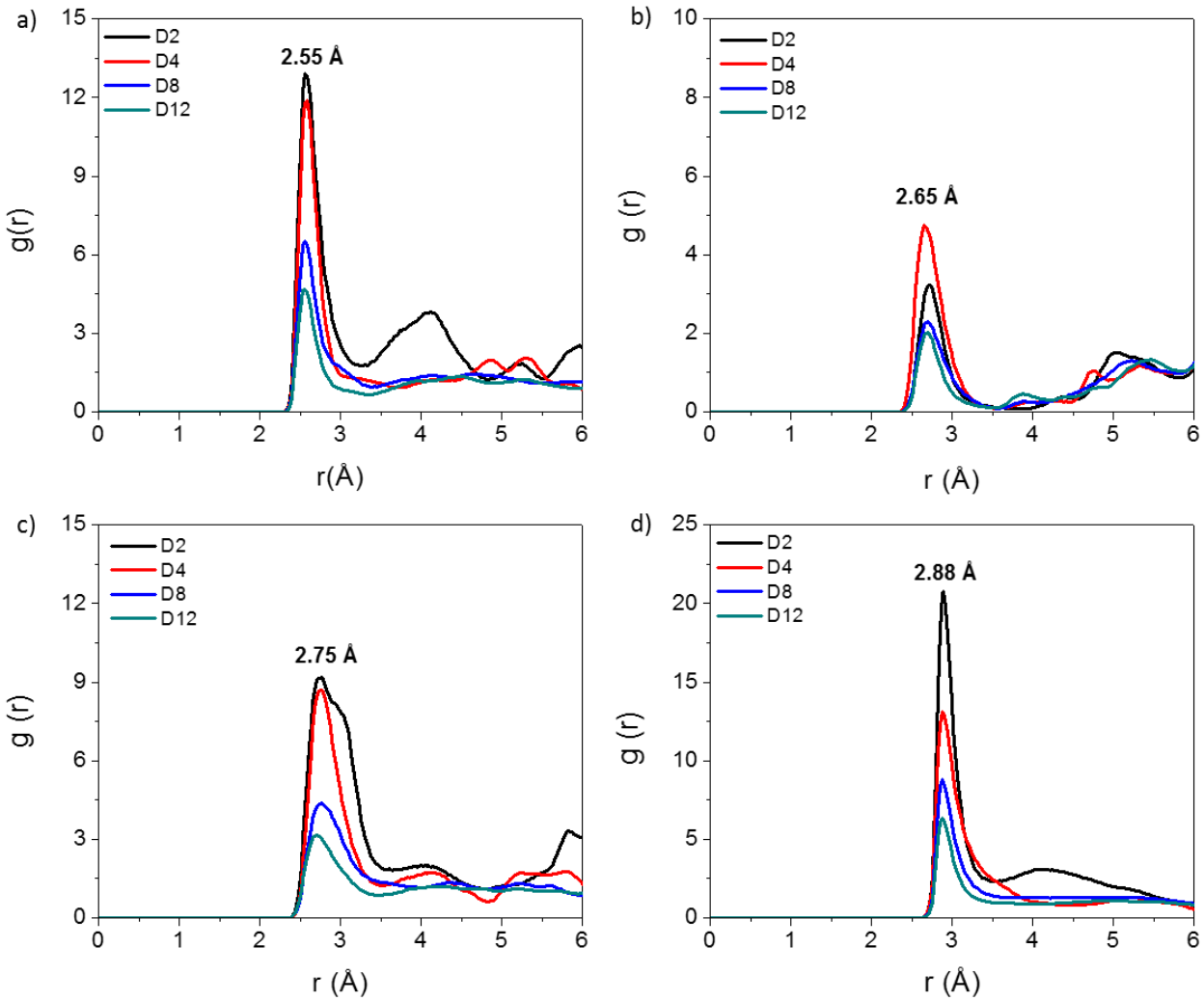

Figure 4.21 – RDFs between the pairs O_w – $O(OH_C)$ (a), O_w – $O(\mu_3\text{-}OH)$ (b), O_w – $O(H_2O_C)$ (c) and O_w – O_w (d) obtained from GCMC water adsorption calculations in structural models of the MOF-801(Zr) with 2 (black lines), 4 (red lines), 8 (blue lines) and 12 (green lines) defects per unit cell at 298K and a relative pressure of 0.05.

When the concentration of water increases, the molecules arrange themselves in cuboid clusters in the tetrahedral cages which do not present defects, i.e. site 2, (cf. Figure 4.20b). Alternatively, in tetrahedral cages presenting defects, the water molecules form clusters with similar number of molecules as before (8-12), but they do not arrange themselves in a specific geometric conformation, in relation with the fact that the cage is no more centrosymmetric with the introduction of defects (cf. Figure 4.20c). This configuration is likely to correspond to the fourth site experimentally identified in the powder sample, since the latter was assumed to contain a larger concentration of defects, as estimated from the comparison between the experimental and theoretical adsorption isotherms (cf. Figure 4.16 and 4.17).

In a more general perspective, we have explored the impact of the presence of defects on the organization of the water molecules in clusters. As seen in Figure 4.22, two regimes of cluster formation can be clearly identified: the first is the formation of small clusters which incorporate about eight molecules, i.e. the cuboid clusters in the ideal tetrahedral cavities and the distorted clusters near the hydrophilic groups. At higher loadings, these clusters start to interconnect, leading to the creation of a relatively large percolating water cluster reaching up to 200 molecules. As the concentration of defects on the framework increases, the average size of the small clusters grows from ~6 molecules in the ideal framework model to 8-12 molecules in the defective structure with 12 missing linkers per unit cell. This is consistent with the larger pore volume available in the defective structures, as observed in the calculated PSD of Figure 4.15. Moreover, as the concentration of defects increases, the relative pressures at which the formation of clusters occurs is progressively shifted towards smaller values, in agreement with the enhancement of the hydrophilicity of the framework (cf. Figure 4.22).

Now we consider the occupation of the octahedral cages. Just like in the ideal framework, the octahedral cages are only occupied at large uptake. Also similarly to what was observed in the ideal framework, the occupation of these cavities by water molecules is anchored by their hydrogen bonding with water clusters in the tetrahedral cage. As seen in Figure 4.20d, both the organized clusters from the ideal tetrahedral cages and the distorted clusters present in the defective cavities participate in this process. The full occupation of

these cavities may be taken as the bridge to the formation of the percolating clusters seen at saturation conditions.

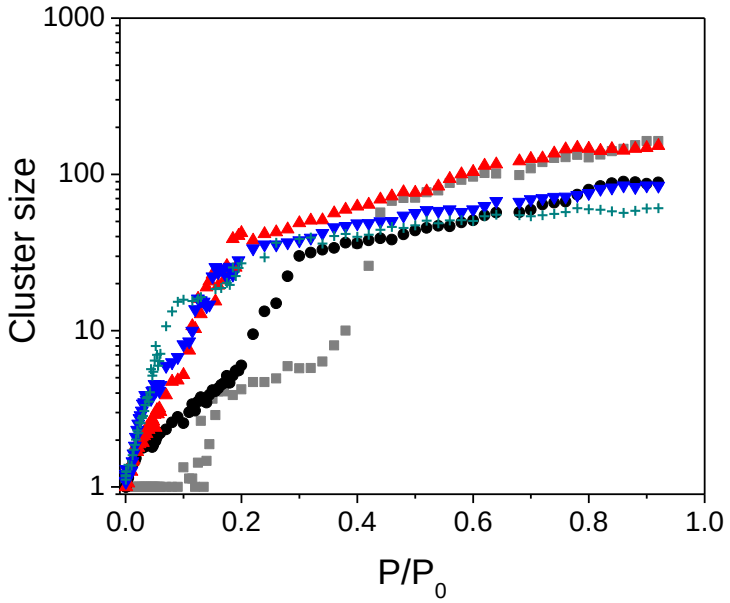

Figure 4.22 – Average water cluster sizes obtained from the GCMC simulations of the water adsorption on the MOF-801(Zr) in an ideal crystal (grey squares) and in structure models with 2 (black circles), 4 (red triangles), 8 (blue reverse triangles) and 12 (dark cyan crosses) defects per unit cell.

Another important parameter to assess the preferential interactions between the hydrophilic sites and the water molecules described in this section is the amount of hydrogen bonds each of the hydrophilic groups (OH_c, H_2O_c, μ-OH) are able to form with the adsorbed water. We thus calculated the number of hydrogen bonds per hydrophilic group at different relative pressures for the defective frameworks. In Figure 4.23, it is clear that each of the groups connected to Zr forms a number of hydrogen bonds almost twice higher than μ_2-OH. Moreover, in general the number hydrogen bonds are seen to be sharply increased with the step in water isotherm, a clear reflex of the increase in the mutual association of the water molecules during this process. Furthermore, as the concentration of defects introduced in the MOF-801(Zr) increases, we observed a clear increase of the number of hydrogen bonds formed by each of the adsorbed water molecules. For instance, in the structure model with 2 defects per unit cell, each water molecules makes about 2 hydrogen bonds each, in a model with 12 defects this number reaches almost 3, a high value considering the relatively confined environment of this MOF. This increase in the hydrogen bond connectivity of the

adsorbed water molecules can then be attributed to the more hydrophilic environment of the pore wall caused by the polar groups occupying the Zr vacancies on the defective framework models.

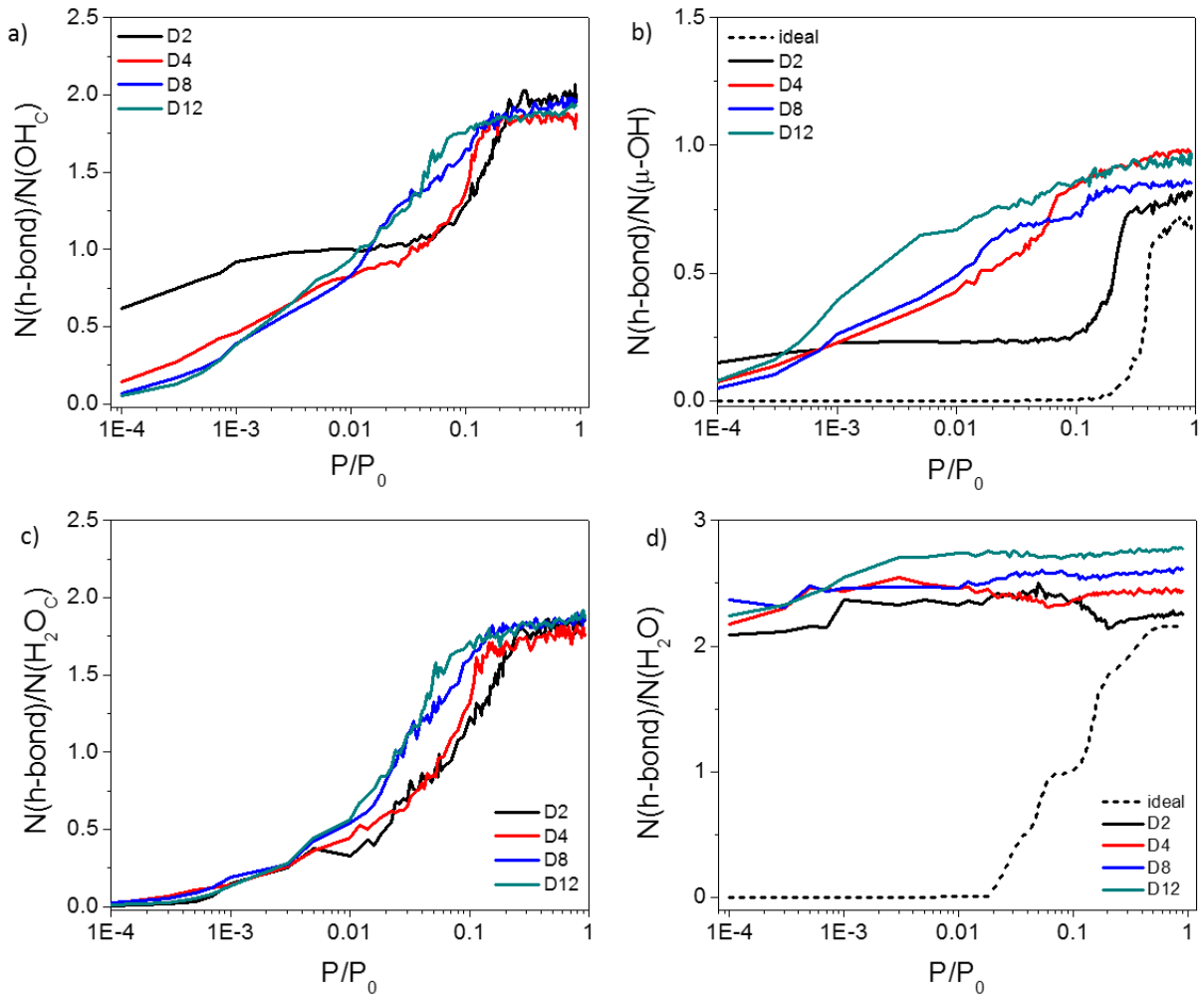

Figure 4.23 – Number of hydrogen bonds per hydrophilic groups - OH_C (a), μ-OH (b), and H_2O_c (c) – and per adsorbed water molecules (d) obtained from GCMC calculations in the interval of P/P_0 from 1×10^{-4} to 1 for the structure models of the MOF-801(Zr) with 2 (black lines), 4 (red lines), 8 (blue lines) and 12 (dark cyan lines) missing linkers per unit cell.

We finally explored the strength of the water interactions in the MOF by comparing the simulated adsorption enthalpies with the experimental isosteric heat of adsorption (Q_{st}). The isosteric heat of adsorption previously reported for water in this MOF varies in the range of 55 – 60 kJ.mol^{-1} [31,32] which is also consistent with the value determined by our collaborators (~52 kJ.mol^{-1}). This value remains significantly lower than in zeolites (~70 kJ.mol^{-1}) [33] characterized by a high interaction between water and the extra-framework

cations. Using an ideal crystal model, we have obtained a simulated adsorption enthalpy ranging from 30 to 40 kJ.mol^{-1} (cf. Figure 4.24), consistent with the higher P/P_0 of the step of the water isotherm obtained in such non-defective framework. On the other hand, the simulated values considering defective structure models (50 – 60 kJ.mol^{-1}) (cf. Figure 4.24) fit well with the experimental findings. This is clearly related to higher hydrophilicity of the framework induced by the interaction of the defective hydrophilic sites with the adsorbent.

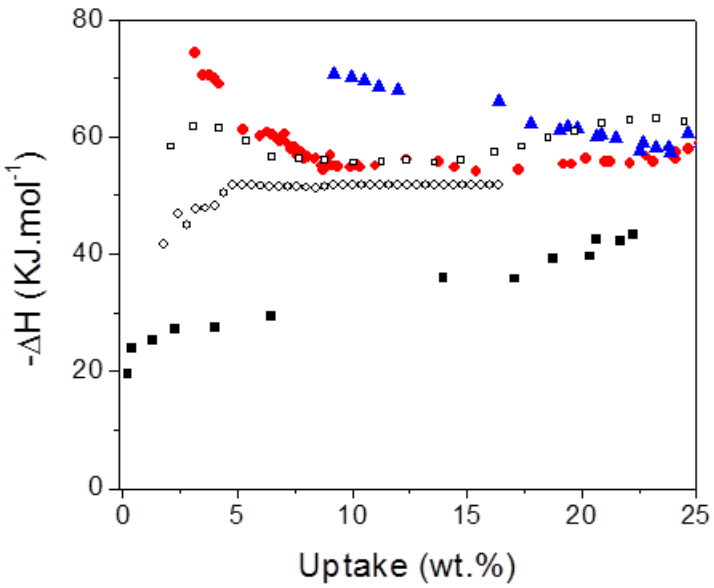

Figure 4.24 – Comparison between experimental isosteric heat of adsorption from the literature [32] (empty squares) and obtained in this work by our collaborators in the KRICT (empty circles) with adsorption enthalpies obtained from GCMC calculations at 298 K as function of the water uptake in an ideal crystal model of the MOF-801(Zr) (black squares) and in defective models with 4 (red circles) and 12 (blue triangles) missing linkers per unit cell.

IV. MIL-100(Fe)

MIL-100(Fe) is built from the assembly of trimers of Fe(III) octahedra and trimesate carboxylates [34]. This association of ligand/inorganic nodes leads to the formation of supertetrahedra of *ca.* 9.5 Å. These supertetrahedra further assemble themselves into a MTN zeolitic architecture delimiting two mesoporous cages of 25 Å and 29 Å free apertures accessible through windows of 5.5 and 8.6 Å [35] (cf. Figure 4.25). In its pristine form, each inorganic trimer of MIL-100(Fe) contains 2 Fe^{III} coordinated to H_2O and 1 Fe(III) bounded to 1 terminal –OH group. The activation allows the evacuation of the coordinated water leading to 2 Fe(III) coordinated unsaturated sites [36].

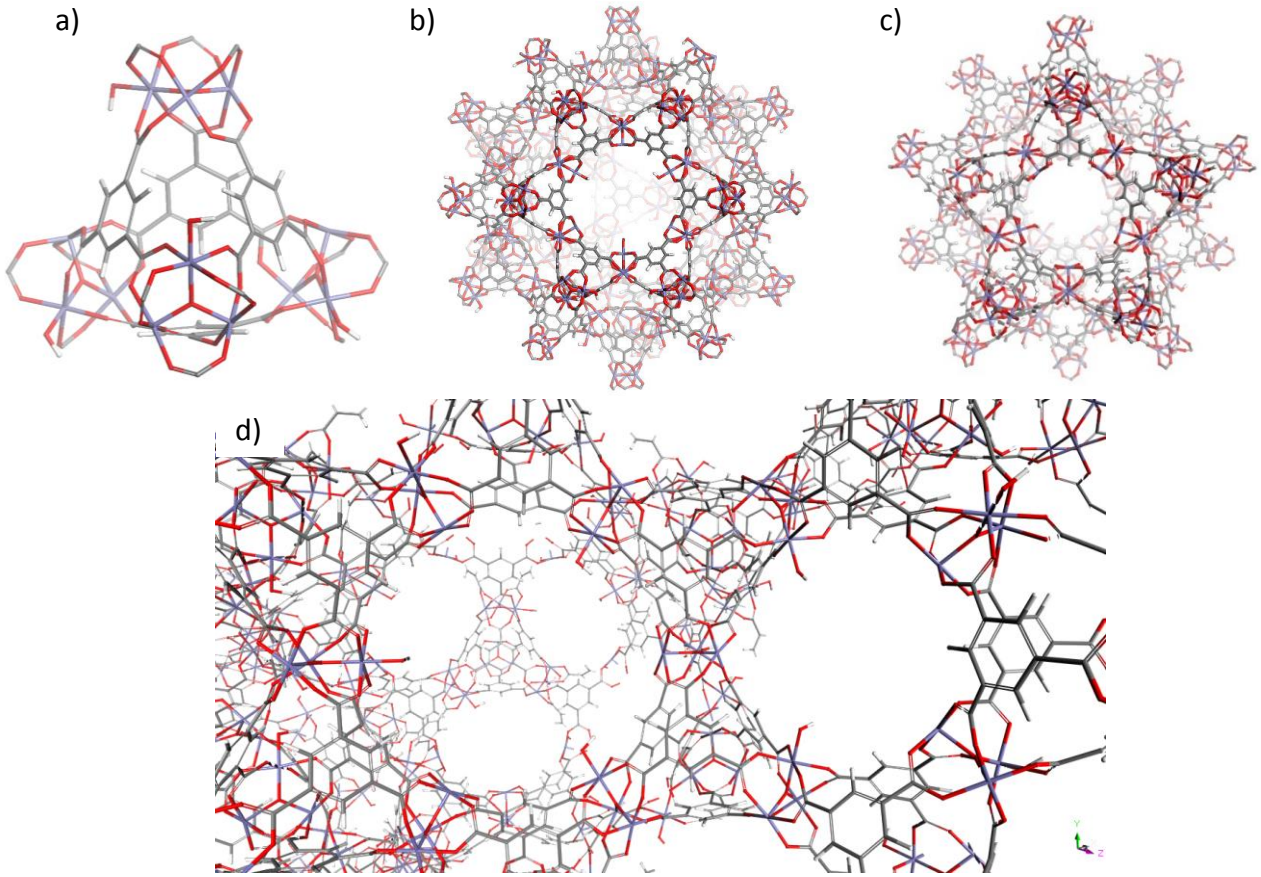

Figure 4.25 – Framework model of the MIL-100(Fe), evidencing the supertetrahedra structure formed by the association of a Fe_3O cluster – containing 2 CUS Fe(III) sites and 1 terminal OH group – with trimesate ligands (a) and the association of these structures in larger cavities showing hexagonal and pentagonal windows (b) and only pentagonal windows (c). These cavities are then interconnected forming a continuous 3D network (d).

The MIL-100(Fe) framework was modelled in its OH-version using a crystal structure previously elucidated by X-ray diffraction [35]. 1 OH group per Fe_3O trimer was added to the exposed Fe sites to be consistent with the experimental observation. The atomic positions were first geometry optimized by a forcefield-based energy minimization as implemented in the Forcite module of the BIOVIA software package Materials Studio (MS) [37], in which the framework atoms of the inorganic and organic nodes were described by the UFF [16] and DREIDING [17] forcefields respectively while the charges were treated in a first approximation using the electronegativity equalization method. Two representative clusters (Figure 4.26) of the inorganic and organic nodes of the MOF were cleaved from the optimized framework and saturated with hydrogen atoms in order to calculate the partial atomic charges in MIL-100(Fe) at the Density Functional Theory (DFT) level employing the GGA/PBE [21] functional combined with a double numerical basis set containing polarization functions (DNP), as implemented in the $Dmol^3$ module [38]. The partial charges (see Table 4.3) were derived using the ESP fitting approach [39].

Table 4.3 – Atomic partial charges attributed to the atomic partial charges for each atom type (defined in Figure 4.26).

Atom type	q (e)
Fe1	1.3872
Fe2	1.2487
C1	0.5450
C2	0.1387
C3	-0.2152
O1	-0.7023
O2	-0.5912
O3	-0.5236
O_{OH}	-0.6673
H_{OH}	0.3767
H1	0.1638

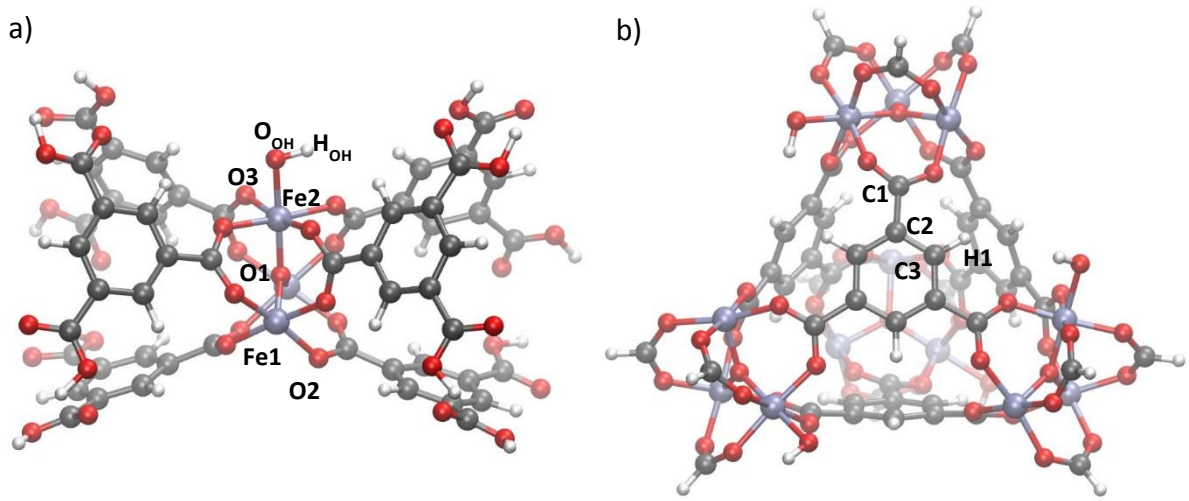

Figure 4.26 – Selected cluster models representing the atoms of the inorganic node (Fe1, Fe2, O1, O2, O3, O_{OH}, and H_{OH}) (a) and the organic linker (C1, C2, C3, H1) (b) considered in the calculation of the ESP partial charges in the OH- version of the MIL-100(Fe).

A small cluster (SC) containing the inorganic Fe_3O node saturated by formate (Figure 4.27) was further used to calculate the interaction energy for H_2O as a function of the distance separating this guest and the CUS Fe(III) sites at the DFT level. The geometry optimization of this small cluster containing 1 H_2O adsorbed molecule was first performed using spin-unrestricted calculations. This calculation was performed using the Quantum Espresso package [40,41] with plane wave functions as basis set and the GGA PBE functional [21]. The ion cores were described by Vanderbilt ultrasoft pseudopotentials [42] with a kinetic energy cutoff of 60 Ry and a density cutoff of 600 Ry. A gamma centered k-sampling of the reciprocal space was performed with a Gaussian smearing of 0.005 Ry broadening. The ground spin states of the central metallic atoms in these clusters were checked, showing that all the Fe(III) are high spin (sextet) with a lowest energy spin configuration of (+5,-5,+5), thus a total spin value of the cluster S = 5 (sextet). The Fe-H_2O energy potential was then obtained from single-point energy calculations at different Fe-H_2O distances. The interaction energy was calculated using the following expression: $E_{int} = E_{SC+H2O} - (E_{SC} + E_{H2O})$, where E_{SC+H2O} corresponds to the energy of the optimized guest-loaded cluster while E_{SC} and E_{H2O} are the energies of the SC model and the guest molecule considered as single species respectively. The resulting interaction energy curve is plotted in Figure 4.28. One can observe that the minimum corresponds to an interaction energy of -70

kJ.mol^{-1} which matches well with the experimental isosteric heat of adsorption measured at low coverage (-80 kJ.mol^{-1}) (c.f. Figure 4.31).

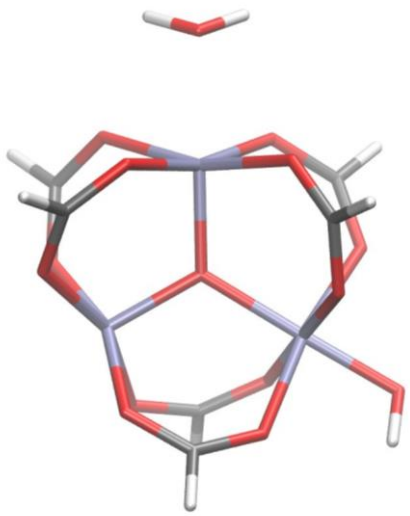

Figure 4.27 – Small cluster (SC) used for the parameterization of the Fe – H_2O interactions. In blue, red, gray and white are represented respectively Fe, O, C and H atoms.

In our GCMC simulations the interactions between MIL-100(Fe) framework and H_2O were thus treated as a sum of a van der Waals contribution and a Coulombic term.

(1) The interactions between H_2O and all the atoms of the framework with the exception of the uncoordinated Fe(III) atoms (CUS Fe(III)) were modelled using a LJ 12-6 and a Coulombic potentials to model the van der Waals and electrostatic interactions respectively (Equation 4.1). The LJ 12-6 parameters were taken from the generic forcefields DREIDING [17] and UFF [16] for the atoms present in the organic and inorganic nodes respectively while the ESP charges derived above were considered for all constitutive atoms. In this work we decided to compare two different four-site models to represent the water: TIP4P/2005 [13] and TIP4P-Ew [18] corresponding to one LJ site centered in the oxygen atom and three charged sites (see chapter 2, section I.6).

(2) The interactions between H_2O and the CUS Fe(III) atoms were described by a Buckingham potential and a Coulombic term (Equation 4.2). The parameterization of the repulsion (A and B) and dispersive (C) coefficients of the Buckingham potential was carried

out by fitting the DFT-calculated CUS Fe(III) – H_2O interaction energy ($E_{Fe\text{-}H2O}$). This curve was obtained by subtracting to the quantum-derived total interaction energy (E_{int}), the LJ 12-6 (E_{LJ}) and Coulombic (E_Q) contributions between the H_2O molecules and the rest of the atoms of the cluster, i.e. $E_{Fe–H2O} = U_{BE} – U_{LJ} - U_Q$. The charges obtained for the cluster atoms were the same applied to the rest of the framework with a slight change for the charges of the terminal hydrogen atoms so that the total cluster charge is zero.

The overall interatomic potential to describe the H_2O/MIL-100(Fe) interaction thus shows the following analytical formula:

$$E(r_{ij}) = \begin{cases} \sum_{i,j} \frac{1}{4\pi\varepsilon_0}\frac{q_i q_j}{r_{ij}} + 4\varepsilon_{ij}\left[\left(\frac{\sigma_{ij}}{r_{ij}}\right)^{12} - \left(\frac{\sigma_{ij}}{r_{ij}}\right)^{6}\right], i \neq CUS\ Fe(III) & (4.1) \\ \sum_{i,j} \frac{1}{4\pi\varepsilon_0}\frac{q_i q_j}{r_{ij}} + \left[Ae^{-\mathrm{B}r_{ij}} - \frac{\mathrm{C}}{{r_{ij}}^6}\right], i = CUS\ Fe(III) & (4.2) \end{cases}$$

Where r_{ij} stands for the distance separating atoms of the MOF and of water (respectively i and j), ε_{ij} and σ_{ij} for the crossed LJ 12-6 parameters between these sites and q_i for the partial charge of center i.

The subtraction of the LJ 12-6 and Coulombic contributions on the DFT energy curve results in similar $E_{Fe\text{-}H2O}$ energy profiles using both TIP4P/2005 and TIP4P-Ew models (cf. Figure 4.28). The resulting Buckingham potential parameters are summarized in Table 4.4. The comparisons between the DFT- and the forcefield derived curves are reported in Figure 4.29. The so-obtained excellent agreement between these two sets of data emphasizes the quality of fitting.

Table 4.4 – Buckingham parameters associated to the interactions of the CUS Fe(III) atoms and the models of water studied herein.

Buckingham parameters	TIP4P/2005	TIP4P-Ew
A ($kJ.mol^{-1}$)	969868	1130550
B ($Å^{-1}$)	4.731	4.952
C ($kJ.mol^{-1}.Å^6$)	5905.7	4907

The interactions between the H_2O molecules themselves were treated by a LJ 12-6 term and a Coulombic contribution as defined in the microscopic models employed to describe them.

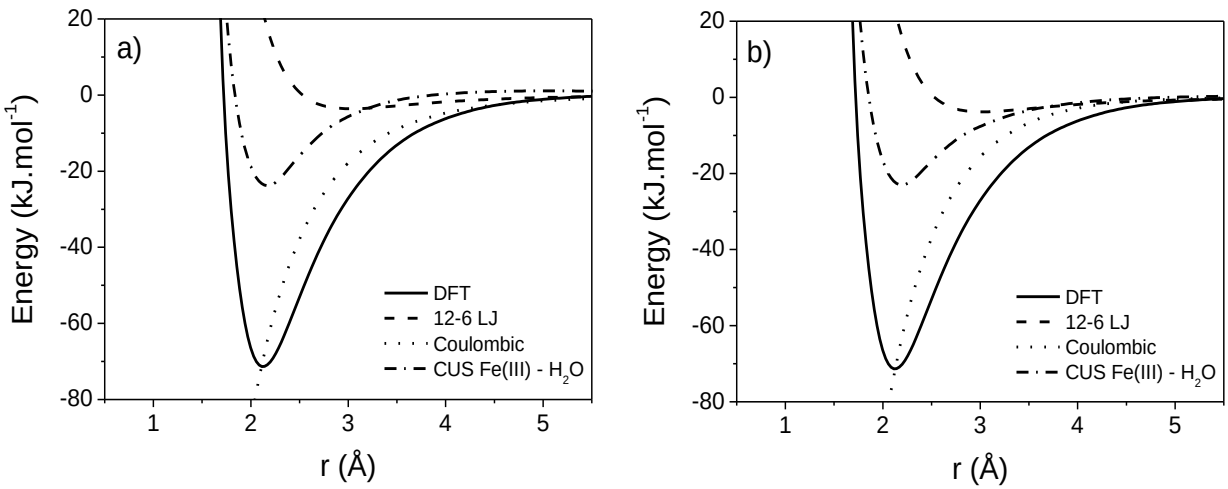

Figure 4.28 – Total binding energy versus H_2O – Fe(III) distances (solid lines) obtained from the DFT calculations between the SC cluster and a water molecule and the deconvolution of this curve into LJ 12-6 (dashed lines), Coulombic (dotted lines) and the CUS Fe(III) – H_2O (dotted-dashed lines) contributions using the TIP4P/2005 (a) and TIP4P-Ew (b) models of water.

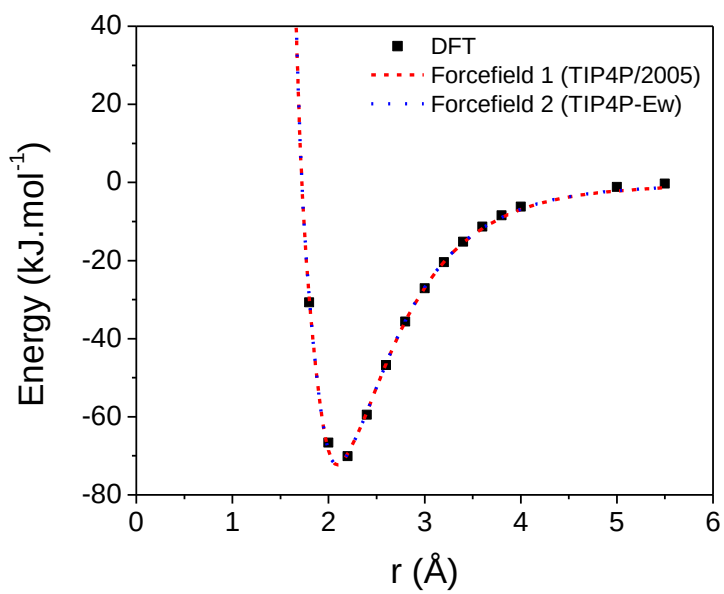

Figure 4.29 – Comparison between the total binding energy curves derived from DFT (black dots) and the forcefield approach using the water models TIP4P/2005 (red dashed line) and TIP4P-Ew (blue dotted line) versus the Fe – H_2O distance in the SC cluster.

These force fields were then implemented in a GCMC scheme to predict the water adsorption at 298 K in MIL-100(Fe) using a simulation box with a single unit cell.

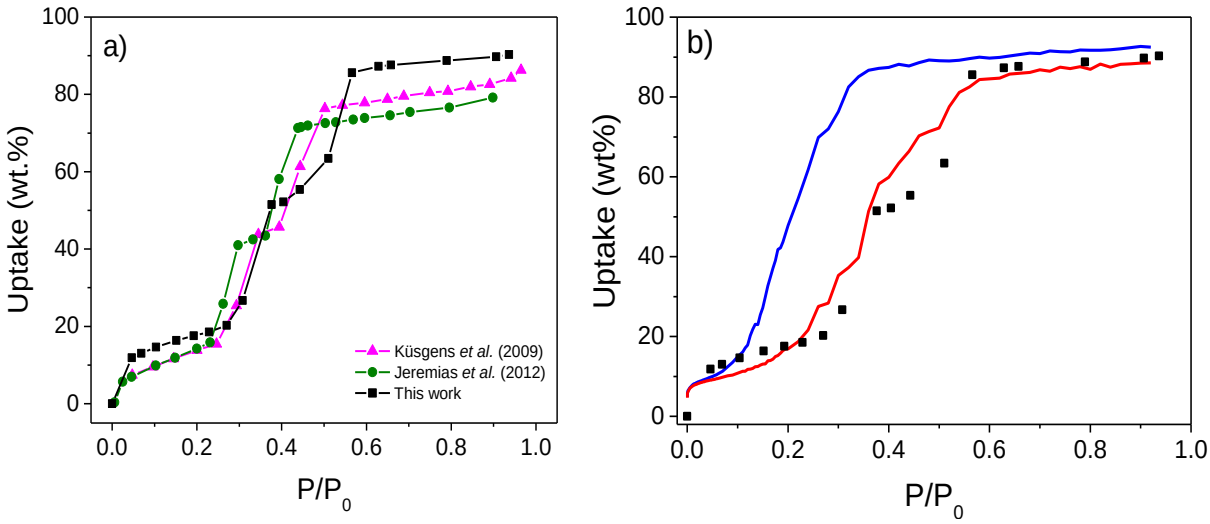

Figure 4.30 – (a) Comparison between the experimental water adsorption isotherm collected by our collaborators in KRICT (-■-) and those reported by Küsgens *et al.* (-▲-) and Jeremias *et al.* (-●-) at 298 K. (b) Comparison between the experimental (black symbol) and the simulated water adsorption isotherm: simulations using TIP4P-Ew (red line) and TIP4P/2005 (blue line) models for water.

The experimental adsorption isotherms and enthalpies were first used to verify the validity of the microscopic models (charges, force field parameters…) used in the GCMC simulations. As seen in Figure 4.30, the experimental water adsorption isotherm of MIL-100(Fe) obtained from our collaborators in KRICT exhibits a particular shape, with a gain in uptake at very low partial pressures ($P/P_0 < 0.05$) which gradually increases until $P/P_0 = 0.2$-0.3. At this stage, the water loading increases abruptly in two steps with the second step occurring at $P/P_0 \approx 0.5$ before observing a saturation regime at $P/P_0 = 0.6$. Such a shape of the water isotherm is very close that reported by previous works conducted in the same domain of temperature [2,3] (cf. Figure 4.30a). One can however notice that the water saturation uptake is slightly higher most probably due to a more efficient activation of the sample prior to the adsorption measurements. Figure 4.30b clearly evidences that the GCMC simulated adsorption isotherm using the water model TIP4P-Ew fits better the corresponding experimental data both in shape and in amount adsorbed. On the other hand, the TIP4P/2005 model clearly overestimates the uptake in the whole P/P_0 range, with the exception of $P/P_0 <$ 0.05. This disparity is due to the fact that these models predict different water-water

interactions, which are mainly involved in the pore filling process observed experimentally at $P/P_0 > 0.2$ (as explained later). This result reinforces the system-dependence of the water models to the description of the water adsorption in different pore topologies, since so far the TIP4P/2005 was revealed to be more adequate to describe the water adsorption in the other MOFs presented in this chapter. Furthermore, a good agreement was also obtained between the GCMC calculated adsorption enthalpy at low coverage using the TIP4P-Ew model and the experimental heat of adsorption (76 $kJ.mol^{-1}$ and 80 $kJ.mol^{-1}$ respectively). One can also observe that the experimental isosteric heat is well reproduced in the whole range of water loading (see Figure 4.31). This excellent agreement on macroscopic data fully validated the microscopic models used to describe the H_2O/MIL-100(Fe) system, a crucial requirement to further get reliable insight into the microscopic adsorption mechanism in play.

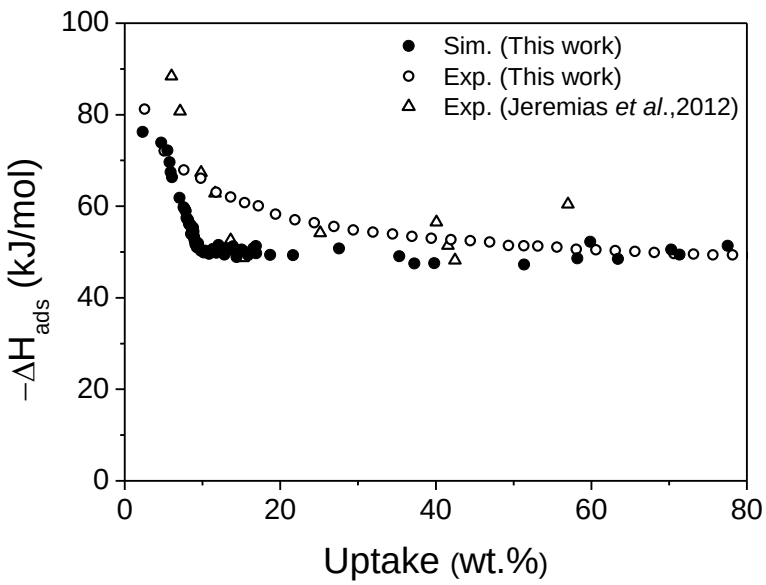

Figure 4.31 – Heat of water adsorption obtained experimentally (open symbols) compared to the simulated water adsorption enthalpy using TIP4P-Ew (filled symbols). The results obtained in this work (circles) are compared with the experimental results previously reported by Jeremias *et al.*[2].

It is expected that the CUS Fe(III) sites would be the first to be occupied by the water molecules, this high affinity leading to the sharp increase in the uptake observed at very low P/P_0. This is clearly confirmed by the GCMC simulations which evidenced that for a relative pressure of $5x10^{-4}$, the amount of water adsorbed is equivalent to the concentration of CUS sites (136 atoms/unit cell or 3.25×10^{-3} $mmol.g^{-1}$). In this domain of pressure, the RDF for the

CUS Fe(III)-oxygen atoms of the water molecules (O_W) (Figure 4.32a) shows a sharp peak at the equilibrium distance of 2.10 Å. The integration of this peak shows a value of N(r) ≈ 1, indicating that all CUS sites are coordinated by water.

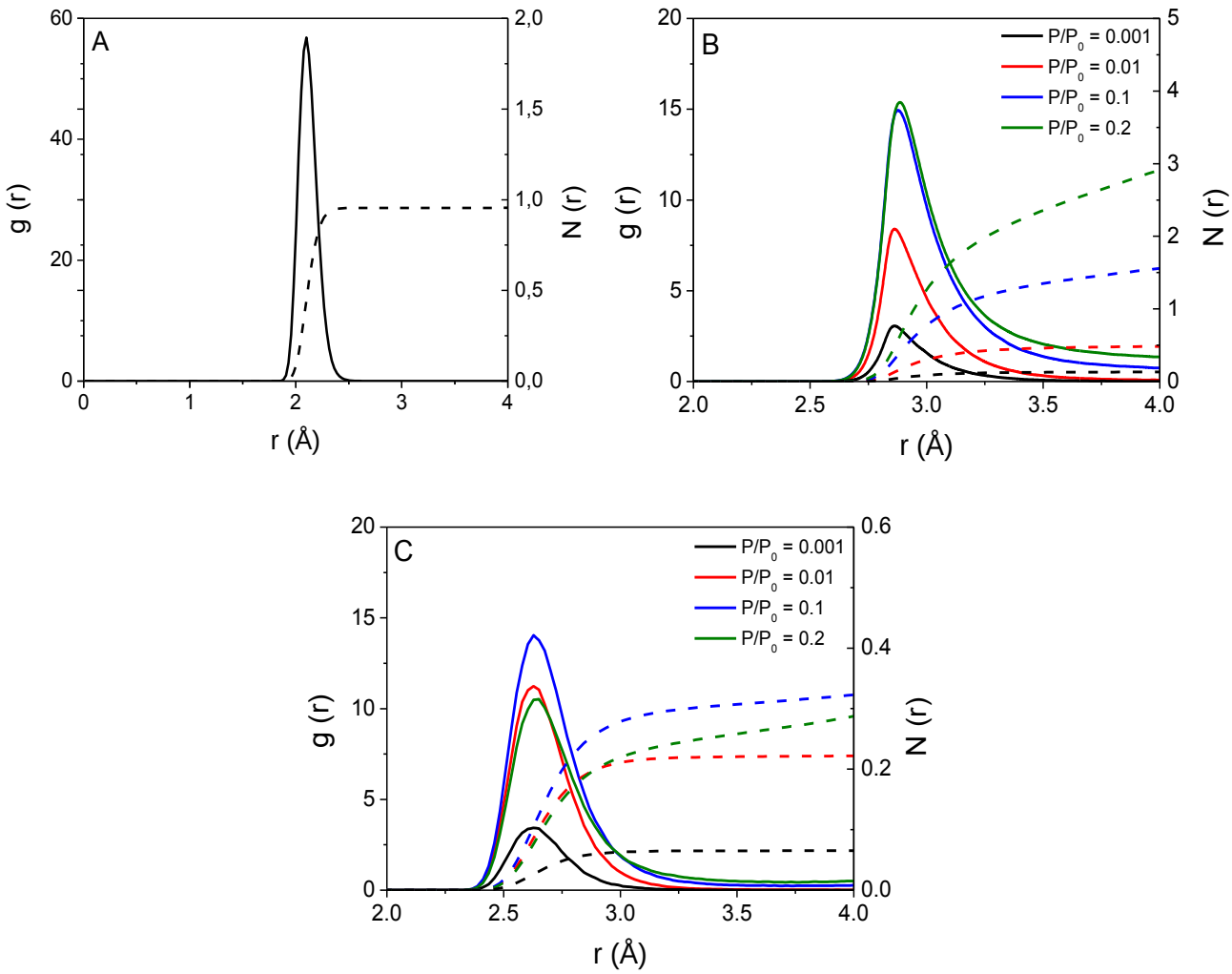

Figure 4.32 – RDFs (solid lines) and their integration (dashed lines) for the pair CUS Fe(III) – O_W at $P/P_0 = 5x10^{-4}$ (a) and the pairs O_W – O_W (b) and O_W – O_{-OH} (c) at the partial pressures of 0.001 (black lines), 0.01 (red line), 0.1 (blue line), 0.2 (green line).

Once the CUS sites are fully coordinated by water, a second adsorption regime takes place. In such regime, a gradual increase in the uptake is observed up to P/P_0 = 0.2. This region is assigned to the interactions between the adsorbed water molecules and both the water molecules coordinated to the CUS Fe(III), labelled as H_2O_C, which henceforth act as a hydrophilic group, and the terminal -OH groups bounded to the Fe. This statement is supported by the RDFs plotted in Figure 4.32b and 4.32c, which unambiguously show an

increase of the number of interactions between the water molecules and these groups as the partial pressure increases as attested by the increase of the intensity of the corresponding RDF peaks.

An in-depth analysis of the snapshots over the whole relative pressure allowed us to identify sequential water adsorption regimes. The first is the water coordination of the CUS Fe(III) sites at very low pressures as discussed above and identified in Figures 4.33a and 4.33b. At this stage, the water molecules interact mostly with the CUS Fe(III) and only a few molecules interact with the rest of the MOF framework. As the pressure increases (P/P_0 = 0.01), the extra H_2O molecules form hydrogen bonds with the H_2O_C molecules and the terminal OH groups more effectively in the pentagonal windows but also in the hexagonal ones (see in Figure 4.33c and 4.33d). When the relative pressure increases, the adsorbed water molecules start clustering in the pentagonal windows (P/P_0 = 0.1), as seen in Figures 4.33e and 4.33f. This clustering continues as pressure increases up to a point where all the pentagonal windows are occupied by the H_2O molecules (P/P_0 = 0.2). At this stage, it is remarkable that this clustering also takes place in the hexagonal windows (Figures 4.33g and 4.33h). From this point, the water molecules start to populate the cages of the MOF framework in a pore filling mechanism corresponding to the first step observed at $P/P_0 > 0.2$. However, the H_2O molecules do not fill both cages of the MOF uniformly. At P/P_0 = 0.3, a comparison between Figures 4.33i and 4.33j shows that the smaller cages of the framework are filled first while the larger cages, the only ones containing hexagonal windows, remain practically unoccupied. This observation is consistent with the fact that the most confined environment corresponds to the preferential water adsorption. Such a scenario further changes at $P/P_0 > 0.5$, where the population of the larger cages (Figures 4.33k and 4.33l) corresponds to the second step observed in the adsorption isotherm at P/P_0 = 0.55.

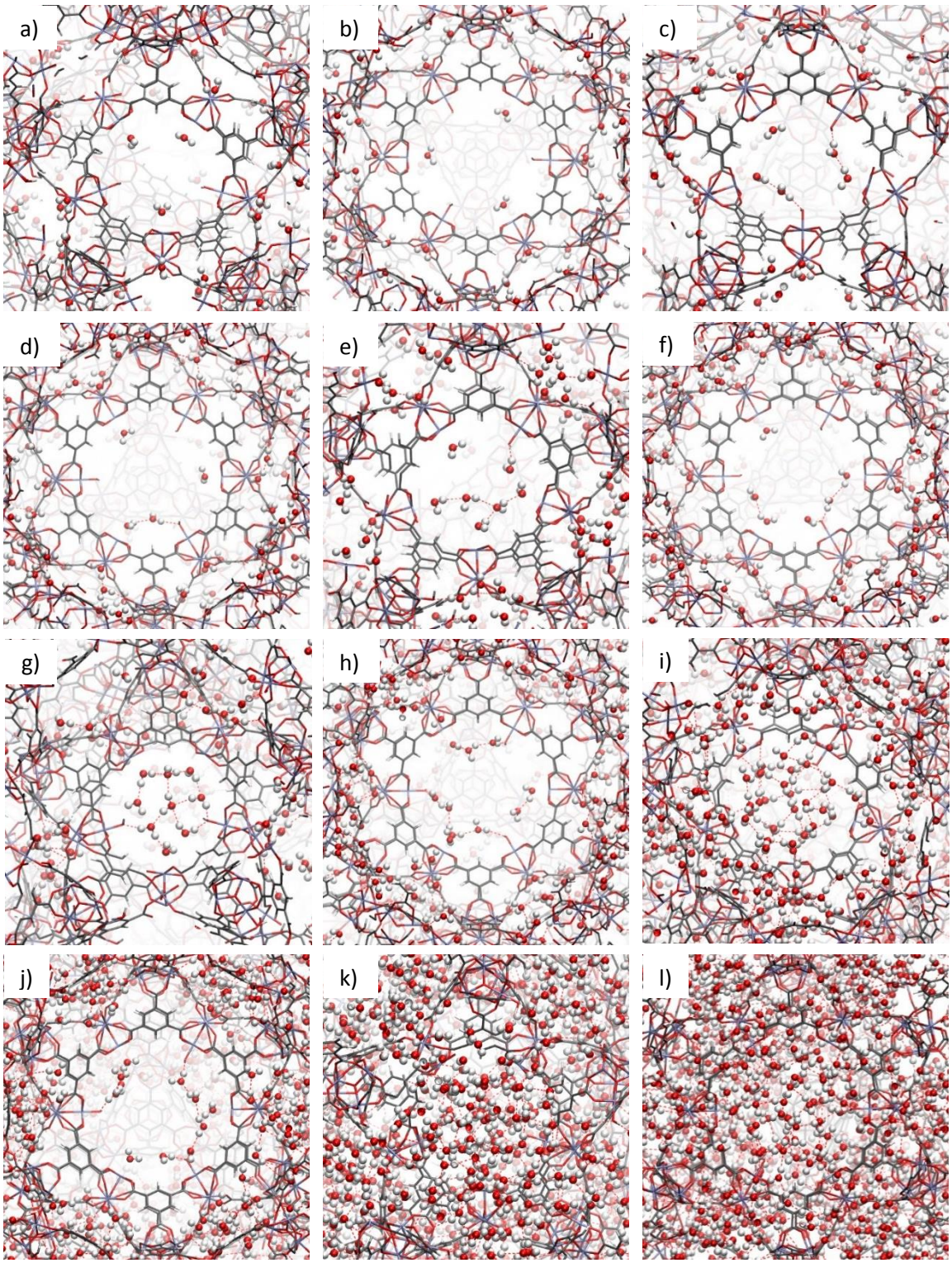

Figure 4.33 – Representative snapshots showing the simulated preferential adsorption sites of water in the pentagonal (a, c, e, g, I and k) and hexagonal (b, d, f, h, j and l) windows of MIL-100(Fe) at P/P_0 = 0.001 (a, b), 0.01 (c, d), 0.1 (e, f), 0.2 (g, h), 0.3 (i, j) and 0.5 (k, l).

As a further step, a careful analysis of the hydrogen bonding of the water molecules was also considered. Figure 4.34 reports the evolution of the number of hydrogen bonds between each hydrophilic group of the MOF framework (H_2O_c and –OH terminal) and the adsorbed water molecules as a function of the water loading. This plot clearly shows a larger fraction of terminal -OH groups involved in the hydrogen bonding vs H_2O_C in the range $P/P_0 < 0.2$, for which the filling of the smaller pores is achieved. This observation is consistent with the higher intensity of the RDF corresponding to the terminal-OH / H_2O pair (Figure 4.32b) compared to that of the H_2O_C /H_2O pair (Figure 4.32c). When $P/P_0 = 0.2$ is reached, then the fraction of both hydrogen bonds towards terminal-OH and H_2O_C becomes similar, each species establishing 1 hydrogen bond in average. Once this stage is achieved, we observe a sudden increase of the fraction of hydrogen bonds which follows the same trend than the adsorption isotherm, with a plateau of 2 hydrogen bonds per group attained at a $P/P_0 > 0.5$.

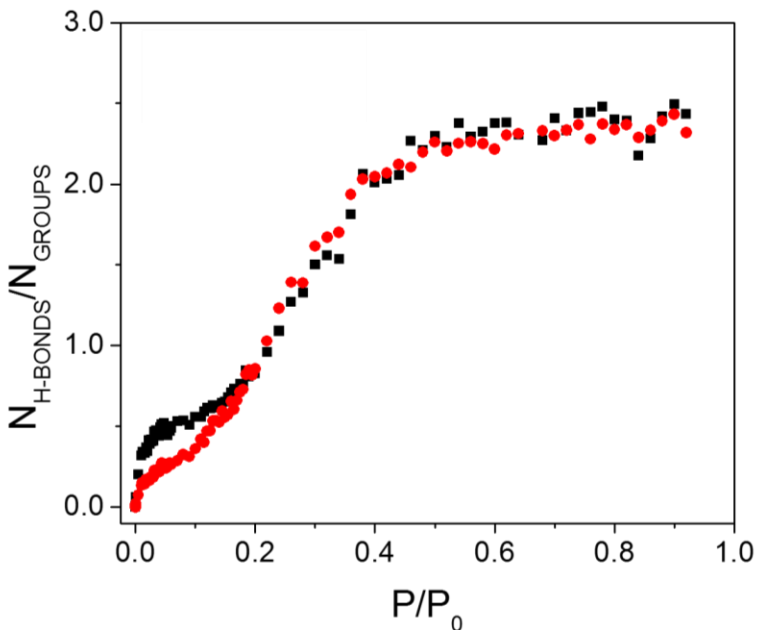

Figure 4.34 – Evolution of the number of terminal -OH – H_2O hydrogen bonds per -OH group (black squares) and the number of H_2O_C – H_2O hydrogen bonds per H_2O_C molecule (red circles) as a function of the relative pressure.

During the population of the cages which occurs in the range $0.2 < P/P_0 < 0.5$, it is clearly stated that the number of hydrogen bonds per –OH and H_2O_C increases significantly up to reach a value of 2.5. In Figures 4.35a-d, this evolution of the hydrogen bonds involving -OH groups and H_2O_C molecules is illustrated by representative snapshots considered at the beginning ($P/P_0 = 0.24$, Figures 4.35a and 4.35b) and in the middle of the filling process ($P/P_0 = 0.44$, Figures 4.35c and 4.35d). The participation of the -OH and H_2O_C groups in the filling process is reinforced by their involvement in the cluster formed by the H_2O within the cages of the MOF (cf. Figure 4.35c and 4.35d).

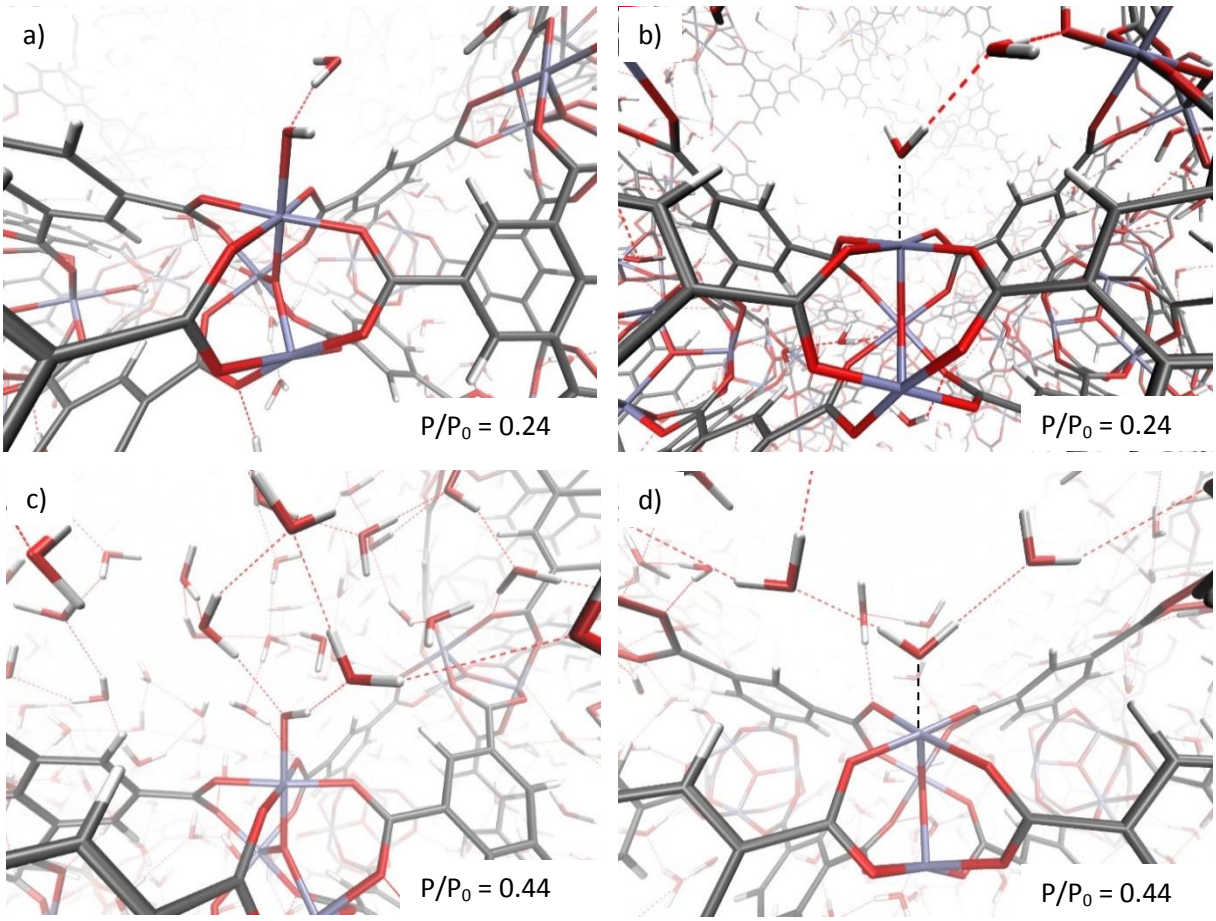

Figure 4.35 – Snapshots showing the hydrogen bonds (red dashed lines) between the H_2O molecules and the -OH groups (a, c) and the H_2O_C molecules (b, d) at the partial pressures of 0.24 and 0.44. At the beginning of the filling process, each hydrophilic group is in average hydrogen bonded to one H_2O molecule. With the progress of the pore filling, the number of H_2O molecules connected to these sites is doubled.

V. Conclusion

This chapter described the main computational results obtained on the water adsorption behavior of three MOFs – CUK-1(Me), MOF-801(Zr) and MIL-100(Fe) – which have been presented as potential candidates for adsorption-based heat reallocation applications. These materials have shown peculiar water adsorption mechanisms that have not been fully disclosed in the literature, such as the tuning of the material hydrophobicity by changing the nature of the metal in the inorganic node (CUK-1), the influence of both defects (MOF-801) and unsaturated metal sites (MIL-100) in the water adsorption profile. Classical calculations using generic and quantum derived potentials were then used to explain the origin of the peculiar water adsorption behavior in these MOFs from an in-depth analysis at the microscopic scale, i.e. the preferential adsorption sites, the spatial distribution of water, and the hydrogen bond and cluster organization in these frameworks. We were able to (i) determine the influence of the SBU metal partial charge on the arrangement of water in the pore of CUK-1(Me) that controls the hydrophilicity of the corresponding solid (ii) identify the key role played by defects in the adsorption behavior of the MOF-801(Zr) not only in terms of hydrophilicity but also in terms of water uptake and (iii) reveal the impact of the presence of the CUS sites on the step-wise adsorption behavior of MIL-100(Fe); in this later case we evidenced that the use of a different water model can slightly impact the resulting adsorption isotherms.

The unraveling of the particular mechanisms involved in the water adsorption on the aforementioned materials may be directly used to develop strategies for tuning the isotherm profile adequate for adsorption-based heat reallocation applications.

REFERENCES

[1] J. Choi, L.-C. Lin, J.C. Grossman, Role of Structural Defects in the Water Adsorption Properties of MOF-801, J. Phys. Chem. C. 122 (2018) 5545–5552. doi:10.1021/acs.jpcc.8b00014.

[2] F. Jeremias, A. Khutia, S.K. Henninger, C. Janiak, MIL-100(Al, Fe) as water adsorbents for heat transformation purposes—a promising application, J. Mater. Chem. 22 (2012) 10148–10151. doi:10.1039/C2JM15615F.

[3] P. Küsgens, M. Rose, I. Senkovska, H. Fröde, A. Henschel, S. Siegle, S. Kaskel, Characterization of metal-organic frameworks by water adsorption, Microporous Mesoporous Mater. 120 (2009) 325–330. doi:10.1016/j.micromeso.2008.11.020.

[4] H. Zhang, R.Q. Snurr, Computational Study of Water Adsorption in the Hydrophobic Metal–Organic Framework ZIF-8: Adsorption Mechanism and Acceleration of the Simulations, J. Phys. Chem. C. 121 (2017) 24000–24010. doi:10.1021/acs.jpcc.7b06405.

[5] L. Sarkisov, A. Centineo, S. Brandani, Molecular simulation and experiments of water adsorption in a high surface area activated carbon: Hysteresis, scanning curves and spatial organization of water clusters, Carbon N. Y. 118 (2017) 127–138. doi:10.1016/j.carbon.2017.03.044.

[6] P. Ghosh, K.C. Kim, R.Q. Snurr, Modeling Water and Ammonia Adsorption in Hydrophobic Metal–Organic Frameworks: Single Components and Mixtures, J. Phys. Chem. C. 118 (2014) 1102–1110. doi:10.1021/jp410758t.

[7] S. Paranthaman, F.-X. Coudert, A.H. Fuchs, Water adsorption in hydrophobic MOF channels, Phys. Chem. Chem. Phys. 12 (2010) 8123. doi:10.1039/b925074c.

[8] A. Di Lella, N. Desbiens, A. Boutin, I. Demachy, P. Ungerer, J.-P. Bellat, A.H. Fuchs, Molecular simulation studies of water physisorption in zeolites, Phys. Chem. Chem. Phys. 8 (2006) 5396. doi:10.1039/b610621h.

[9] R.F. Cracknell, D. Nicholson, N.G. Parsonage, H. Evans, Rotational insertion bias: a novel method for simulating dense phases of structured particles, with particular application to water, Mol. Phys. 71 (1990) 931–943. doi:10.1080/00268979000102241.

[10] C. Beauvais, A. Boutin, A.H. Fuchs, A Numerical Evidence for Nonframework Cation Redistribution Upon Water Adsorption in Faujasite Zeolite, ChemPhysChem. 5 (2004) 1791–1793. doi:10.1002/cphc.200400195.

[11] R.Q. Snurr, A.T. Bell, D.N. Theodorou, Prediction of adsorption of aromatic hydrocarbons in silicalite from grand canonical Monte Carlo simulations with biased insertions, J. Phys. Chem. 97 (1993) 13742–13752. doi:10.1021/j100153a051.

[12] W. Shi, E.J. Maginn, Continuous fractional component Monte Carlo: An adaptive biasing method for open system atomistic simulations, J. Chem. Theory Comput. 3 (2007) 1451–1463. doi:10.1021/ct7000039.

[13] J.L. Abascal, C. Vega, A general purpose model for the condensed phases of water: TIP4P/2005., J. Chem. Phys. 123 (2005) 234505. doi:10.1063/1.2121687.

[14] C. Vega, J.L.F. Abascal, I. Nezbeda, Vapor-liquid equilibria from the triple point up to the critical point for the new generation of TIP4P-like models: TIP4P/Ew, TIP4P/2005, and TIP4P/ice, J. Chem. Phys. 125 (2006) 1–9. doi:10.1063/1.2215612.

[15] T.J.H. Vlugt, E. García-Pérez, D. Dubbeldam, S. Ban, S. Calero, Computing the Heat of Adsorption using Molecular Simulations: The Effect of Strong Coulombic Interactions, J. Chem. Theory Comput. 4 (2008) 1107–1118. doi:10.1021/ct700342k.

[16] A.K.K. Rappé, C.J.J. Casewit, K.S.S. Colwell, W.A. Goddard III, W.M. Skiff, UFF, a Full Periodic Table Force Field for Molecular Mechanics and Molecular Dynamics Simulations, J. Am. Chem. Soc. 114 (1992) 10024–10035. doi:10.1021/ja00051a040.

[17] S.L. Mayo, B.D. Olafson, W. a G. Iii, E. Eb, E. a E.T. El, DREIDING: A Generic Force Field for Molecular Simulations, J. Phys. Chem. 101 (1990) 8897–8909. doi:10.1021/j100389a010.

[18] H.W. Horn, W.C. Swope, J.W. Pitera, J.D. Madura, T.J. Dick, G.L. Hura, T. Head-Gordon, Development of an improved four-site water model for biomolecular simulations: TIP4P-Ew, J. Chem. Phys. 120 (2004) 9665–9678. doi:10.1063/1.1683075.

[19] S.M. Humphrey, J.S. Chang, S.H. Jhung, J.W. Yoon, P.T. Wood, Porous cobalt(II)-organic frameworks with corrugated walls: Structurally robust gas-sorption materials, Angew. Chemie - Int. Ed. 46 (2007) 272–275. doi:10.1002/anie.200601627.

[20] B. Saccoccia, A.M. Bohnsack, N.W. Waggoner, K.H. Cho, J.S. Lee, D.Y. Hong, V.M. Lynch, J.S. Chang, S.M. Humphrey, Separation of P-Divinylbenzene by selective room-temperature adsorption inside Mg-CUK-1 prepared by aqueous microwave synthesis, Angew. Chemie - Int. Ed. 54 (2015) 5394–5398. doi:10.1002/anie.201411862.

[21] J.P. Perdew, K. Burke, M. Ernzerhof, Generalized Gradient Approximation Made Simple, Phys. Rev. Lett. 77 (1996) 3865–3868. doi:10.1103/PhysRevLett.77.3865.

[22] J.P. Perdew, K. Burke, M. Ernzerhof, Generalized Gradient Approximation Made Simple [Phys. Rev. Lett. 77, 3865 (1996)], Phys. Rev. Lett. 78 (1997) 1396. doi:10.1103/PhysRevLett.78.1396.

[23] B. Delley, An all-electron numerical method for solving the local density functional for polyatomic molecules, 508 (2005). doi:10.1063/1.458452.

[24] B. Delley, From molecules to solids with the DMol 3 approach From molecules to solids with the DMol 3 approach, 7756 (2014). doi:10.1063/1.1316015.

[25] C. Campañá, B. Mussard, T.K. Woo, C. Campañá, B. Mussard, T.K. Woo, Electrostatic Potential Derived Atomic Charges for Periodic Systems Using a Modified Error Functional, J. Chem. Theory Comput. 5 (2009) 2866–2878. doi:10.1021/ct9003405.

[26] H. Furukawa, F. Gándara, Y.-B. Zhang, J. Jiang, W.L. Queen, M.R. Hudson, O.M. Yaghi, Water Adsorption in Porous Metal–Organic Frameworks and Related Materials, J. Am. Chem. Soc. 136 (2014) 4369–4381. doi:10.1021/ja500330a.

[27] C.A. Trickett, K.J. Gagnon, S. Lee, F. Gándara, H.-B. Bürgi, O.M. Yaghi, Definitive Molecular Level Characterization of Defects in UiO-66 Crystals, Angew. Chemie Int. Ed. 54 (2015) 11162–11167. doi:10.1002/anie.201505461.

[28] S. Ling, B. Slater, Dynamic acidity in defective UiO-66, Chem. Sci. 7 (2016) 4706–4712. doi:10.1039/C5SC04953A.

[29] G. Wißmann, A. Schaate, S. Lilienthal, I. Bremer, A.M. Schneider, P. Behrens, Modulated synthesis of Zr-fumarate MOF, Microporous Mesoporous Mater. 152 (2012) 64–70. doi:10.1016/j.micromeso.2011.12.010.

[30] A.K.K. Rappé, C.J.J. Casewit, K.S.S. Colwell, W.A. Goddard III, W.M.M. Skiff, A.K. Rappe, C.J.J. Casewit, K.S.S. Colwell, W.A. Goddard, W.M.M. Skiff, UFF, a Full Periodic Table Force Field for Molecular Mechanics and Molecular Dynamics Simulations, J. Am. Chem. Soc. 114 (1992) 10024–10035. doi:10.1021/ja00051a040.

[31] M.V. Solovyeva, L.G. Gordeeva, T.A. Krieger, Y.I. Aristov, MOF-801 as a promising material for adsorption cooling: Equilibrium and dynamics of water adsorption, Energy Convers. Manag. 174 (2018) 356–363. doi:10.1016/j.enconman.2018.08.032.

[32] M.F. de Lange, K.J.F.M. Verouden, T.J.H. Vlugt, J. Gascon, F. Kapteijn, Adsorption-Driven Heat Pumps: The Potential of Metal–Organic Frameworks, Chem. Rev. 115 (2015) 12205–12250. doi:10.1021/acs.chemrev.5b00059.

[33] H. Kim, H.J. Cho, S. Narayanan, S. Yang, H. Furukawa, S. Schiffres, X. Li, Y.-B. Zhang, J. Jiang, O.M. Yaghi, E.N. Wang, Characterization of Adsorption Enthalpy of Novel Water-Stable Zeolites and Metal-Organic Frameworks, Sci. Rep. 6 (2016) 19097. doi:10.1038/srep19097.

[34] P.L. Llewellyn, S. Bourrelly, C. Serre, A. Vimont, M. Daturi, L. Hamon, G. De Weireld, J. Chang, D. Hong, Y. Kyu Hwang, S. Hwa Jhung, G. Férey, High Uptakes of CO 2 and CH 4 in Mesoporous Metal Organic Frameworks MIL-100 and MIL-101, Langmuir. 24 (2008) 7245–7250. doi:10.1021/la800227x.

[35] P. Horcajada, S. Surblé, C. Serre, D.-Y. Hong, Y.-K. Seo, J.-S. Chang, J.-M. Grenèche, I. Margiolaki, G. Férey, Synthesis and catalytic properties of MIL-100(Fe), an iron(III) carboxylate with large pores, Chem. Commun. 100 (2007) 2820–2822. doi:10.1039/B704325B.

[36] A. Vimont, J.-M. Goupil, J.-C. Lavalley, M. Daturi, S. Surblé, C. Serre, F. Millange, G. Férey, N. Audebrand, Investigation of Acid Sites in a Zeotypic Giant Pores Chromium(III) Carboxylate, J. Am. Chem. Soc. 128 (2006) 3218–3227. doi:10.1021/ja056906s.

[37] Dassault Systèmes BIOVIA, Materials Studio, (2017).

[38] B. Delley, From molecules to solids with the DMol3 approach, J. Chem. Phys. 113 (2000) 7756–7764. doi:10.1063/1.1316015.

[39] H. Heinz, U.W. Suter, Atomic Charges for Classical Simulations of Polar Systems, J. Phys. Chem. B. 108 (2004) 18341–18352. doi:10.1021/jp048142t.

[40] P. Giannozzi, S. Baroni, N. Bonini, M. Calandra, R. Car, C. Cavazzoni, D. Ceresoli, G.L. Chiarotti, M. Cococcioni, I. Dabo, A. Dal Corso, S. de Gironcoli, S. Fabris, G. Fratesi, R. Gebauer, U. Gerstmann, C. Gougoussis, A. Kokalj, M. Lazzeri, L. Martin-Samos, N. Marzari, F. Mauri, R. Mazzarello, S. Paolini, A. Pasquarello, L. Paulatto, C. Sbraccia, S. Scandolo, G. Sclauzero, A.P. Seitsonen, A. Smogunov, P. Umari, R.M. Wentzcovitch, QUANTUM ESPRESSO: a modular and open-source software project for quantum simulations of materials, J. Phys. Condens. Matter. 21 (2009) 395502. doi:10.1088/0953-8984/21/39/395502.

[41] P. Giannozzi, O. Andreussi, T. Brumme, O. Bunau, M. Buongiorno Nardelli, M. Calandra, R. Car, C. Cavazzoni, D. Ceresoli, M. Cococcioni, N. Colonna, I. Carnimeo, A. Dal Corso, S. de Gironcoli, P. Delugas, R.A. DiStasio, A. Ferretti, A. Floris, G. Fratesi, G. Fugallo, R. Gebauer, U. Gerstmann, F. Giustino, T. Gorni, J. Jia, M. Kawamura, H.-Y. Ko, A. Kokalj, E. Küçükbenli, M. Lazzeri, M. Marsili, N. Marzari, F. Mauri, N.L. Nguyen, H.-V. Nguyen, A. Otero-de-la-Roza, L. Paulatto, S. Poncé, D. Rocca, R. Sabatini, B. Santra, M. Schlipf, A.P. Seitsonen, A. Smogunov, I. Timrov, T. Thonhauser, P. Umari, N. Vast, X. Wu, S. Baroni, Advanced capabilities for materials modelling with Quantum ESPRESSO, J. Phys. Condens. Matter. 29 (2017) 465901. doi:10.1088/1361-648X/aa8f79.

[42] D. Vanderbilt, Soft self-consistent pseudopotentials in a generalized eigenvalue formalism, Phys. Rev. B. 41 (1990) 7892–7895. doi:10.1103/PhysRevB.41.7892.

CHAPTER 5

Conclusions and perspectives

This thesis was devoted to the combination of quantum- and force-field based computational tools to unravel the microscopic behavior of water confined in porous materials, showing outstanding performances for proton conduction or adsorption-driven heat transfer (AHT) applications. The materials of interest were selected during the course of the PhD by an experimental screening approach that was applied to a large series of solids with features pre-requisite for both applications. We mostly focused on the MOF materials owing to their great advantages in terms of tuneable functionality, topology and pore size/shape, which make them very attractive for proton conduction and AHT applications among others. The objective was to examine the organization and/or dynamics of the confined water and its interactions with the host framework, in order to identify the key features that govern the water-assisted proton conduction and the water adsorption mechanisms in play in porous solids.

The description of the water-mediated proton conduction mechanisms was firstly investigated using porous solids presenting key features as proton electrolytes, i.e. a high water stability, sources of acidic protons and an ordered arrangement of confined species (i.e. water) acting as proton media. Two MOFs, the 3D MIL-163(Zr) and the 2D KAUST-7', and one porous 3D titanium phosphate $Ti^{IV}Ti^{IV}(HPO_4)_4$ were thus considered. Apart from their different topology, these solids also differ from the nature of their proton source with phenolate, phosphate and coordinated water molecules for MIL-163(Zr), $Ti^{IV}Ti^{IV}(HPO_4)_4$ and KAUST-7', respectively. A panel of computational techniques was considered for exploring the fully hydrated solids that allowed to gain insight into the proton migration mechanism at different levels, starting from the simple illustration of the proton pathway through the H-bonded network involving water molecules with classical MC and MD simulations up the description of the proton transfer resulting in a series of bonds breaking/formation with more advanced quantum calculations. MIL-163(Zr) was firstly examined as model system, since a rigid framework was considered in the MC calculations performed in the NVT ensemble to describe the fully hydrated solid. The proton conduction mechanism was discussed by examining the water molecules arrangement inside the MOF porosity, which was demonstrated to form a percolating hydrogen bond network, connecting the proton sources through the water molecules. This configuration was assumed to offer an optimal scenario for

the proton propagation inside the MOF. As a second step, the more complex KAUST-7' was investigated. To take into account the highly confined environment of the adsorbed water molecules in this solid and the resulting water-assisted structural rearrangements of the MOF framework, AIMD calculations were adopted. In addition to taking into account the framework flexibility, the AIMD strategy provides direct insight into the proton conduction mechanism since it allows the description of bond breaking/formation. For KAUST-7', the AIMD calculations evidenced the local dynamics of the adsorbed water molecules, resulting in a H-bonded network characterized by a continuous evolution that implies ever-changing cleavage/formation of hydrogen-bonds between the adsorbed water molecules, the fluorine species present in this material and the coordinated water molecules. Such a reorganization of the H-bond network generates favorable pathways for the proton propagation at the origin of the excellent conduction properties of this material experimentally evidenced. Finally, a similar strategy was deployed to investigate the purely inorganic $Ti^{IV}Ti^{IV}(HPO_4)_4$, but starting with the implementation of a flexible forcefield in the classical MD simulations to describe the local relaxation of the phosphate groups (POH) in the water-saturated solid, prior to elucidate the proton migration by AIMD calculations. These calculations revealed that the preferential conformation of the confined water molecules forms a 3D hydrogen bonded network starting from the proton source (i.e. POH groups) and resulting in the connection of the different pores of the solid via the water molecules, leading to optimal conditions for transferring the proton at long distances. Compared to KAUST-7', these calculations allowed to gain additional information on the proton solvation structure, which involves the interconversion between hydronium and Zundel cation species.

It then turns out that the Grotthus-like mechanism experimentally evidenced in the so-studied water-mediated proton conducting porous solid is:

- Only partly described using classical force-field based approaches, which gives a static representation of the H-bonded network connecting the proton source and the mediated carriers.
- Fully characterized using an AIMD strategy, with a complete illustration of the proton transfer through the rearrangement of the H-bonded network resulting from

the local dynamics of the species, with for instance the evidence of the hydronium/Zundel interconversion.

The second part of this thesis was dedicated to the description of the water adsorption mechanism in MOFs materials, which were selected for their promising properties as water adsorbents for AHT applications, based on their COP performances. The impact of the metal nature incorporated in the inorganic node, the presence of missing linkers as defects and the existence of unsaturated metal sites on the water adsorption isotherm profile was examined through the respective investigation of CUK-1(Me), MOF-801(Zr) and MIL-100(Fe) as typical examples. From a technical point of view, the adsorption of water was modeled with classical MC calculations using generic or quantum derived potentials depending on the complexity of the solid. The analysis of the simulated and the experimental water adsorption isotherm provided information in terms of water uptake at saturation and hydrophilicity (illustrated by the P/P0 position of the first step-wise of the adsorption isotherm), being both crucial features regarding the AHT applications. In addition, a peculiar attention was devoted to develop an in-depth analysis to fully describe at the microscopic level the preferential adsorption sites of water, their spatial distribution and more specifically the hydrogen bond network and the water cluster organization.

From this computational effort, we successfully correlated the chemical features of the so-investigated MOFs with their specific water adsorption behaviors. In the case of CUK-1(Me), we evidenced that the hydrophilicity of the solid can be tuned by changing the metal nature of the inorganic node, due to specific atomic charge redistributions on the polarizable nitrogen atoms of the organic linkers. This point is particularly relevant, keeping in mind the versatility in replacing the metal center of the MOFs, while most of the structures ever tested for AHT purposes were restrictive to the investigation of only one type of the metal center. For MOF-801(Zr), a full understanding of the role of the defective missing linkers on the water adsorption properties was achieved via a deep examination of the water arrangements inside the different cages of the MOF, according to the water loading. It was shown that the missing linker introduces attractive sites (-OH or -H_2O molecules) that anchor the first adsorbed water molecules, increasing the hydrophilicity of the MOF at low loading, illustrated by the shift of the water adsorption step-wise towards lower P/P_0 values compared

to the non-defective material, while the water uptake at saturation rises with the defects increase, due to a larger pore volume. This prediction confirms the tremendous interest in controlling the design of defective MOFs for improving their performances in specific domains such as the AHT application through the control of the hydrophilicity. Finally, the adsorption of water in MIL-100(Fe) was examined using first DFT calculations to derive the potential energy curve corresponding to the interactions between the coordinated unsaturated Fe(III) sites and water, which was further implemented in GCMC calculations. A detailed analysis of the water adsorption isotherm in terms of multi-steps profile was elucidated. As expected, the first water molecules have a strong affinity with the CUS sites, resulting in the creation of coordinated waters, which further play as anchor sites for the following water molecules as the water loading increases. Then, a water clustering occurs in both types of cages of the MIL-100(Fe), resulting in the pore filling mechanism of the smaller cages followed by that of the larger cages with increasing P/P_0.

We are convinced that the systematic strategy we applied with a strong interplay between our simulation and experimental data delivers a solid microscopic description of the water arrangement inside porous solids as well as the water-assisted proton migration in this challenging family of solids. This work led to the publications of 7 articles in the most recognized journals in Physical Chemistry and 3 more are currently being submitted. There is however much effort to be deployed to rationalize the performances of this series of materials with respect to the two targeted applications. This is far more complex than other adsorption related applications such as CO_2 capture for which the domain is quite mature to be able to anticipate the requirements in terms of chemical and topological features of the optimal adsorbents to favor a thermodynamic-based or molecular sieving separation with respect to other gases such as CH_4 and N_2. More specifically in the field of proton conductive materials, the experimental screening evidenced that even for materials that integrate *a priori* the optimal features to ensure a high proton conduction, the performances were not as good as expected. This is one of the most challenging issues that will be needed to be tackled in the future to pave the way towards the development of new and outperforming materials.

ANNEXES

Dalton Transactions

PAPER

View Article Online
View Journal | View Issue

Check for updates

Cite this: Dalton Trans., 2017, 46, 15208

Confined methanol within InOF-1: CO_2 capture enhancement†

Elí Sánchez-González, ‡[a] Paulo G. M. Mileo,‡[b] J. Raziel Álvarez,[a] Eduardo González-Zamora,[c] Guillaume Maurin*[b] and Ilich A. Ibarra*[a]

Received 24th July 2017,
Accepted 14th August 2017

DOI: 10.1039/c7dt02709e

rsc.li/dalton

The CO_2 capture performance of InOF-1 was optimised by confining small amounts of MeOH within its micropores (MeOH@InOF-1). In comparison with fully activated InOF-1, MeOH@InOF-1 shows a 1.30 and 4.88-fold increase in CO_2 capture capacity for kinetic and static isothermal CO_2 adsorption experiments respectively. Density functional theory calculations coupled with forcefield based-Monte Carlo simulations revealed that such an enhancement is assigned to an increase of the degree of confinement felt by the CO_2 molecules resulting from the formation of a lump at the vicinity of the μ_2-OH groups since MeOH strongly interacts with these adsorption sites and is thus highly localized in this region.

Introduction

Current studies have demonstrated how the confinement of different solvents, within porous materials, can significantly enhance the gas solubility in comparison with the values expected by using Henry's law, *i.e.* considering a linear evolution of the concentration of a dissolved gas with respect to its partial pressure above the solvent.[1] This phenomenon is well described in the literature as "gas-oversolubility".[2] In fact, the oversolubility of different confined-solvents can dramatically modify the characteristic physicochemical properties such as the density, viscosity, specific heat and dielectric constant.[3] A remarkable example was recently presented by Garcia-Garibay and co-workers[4] who demonstrated a striking increase by 4 orders of magnitude of the dynamic viscosity of confined DMF within UCLA-R3. Luzar and Bratko[5] predicted, by Monte Carlo calculations, the oversolubility of N_2 and O_2 up to a 10-fold increase when water molecules are confined in hydrophobic mesopores. Pera-Titus *et al.*[1,6] demonstrated how the confinement of $CHCl_3$, n-C_6H_{14}, H_2O, and EtOH in mesostructured materials considerably enhances H_2 solubility. By confining *N*-methyl-2-pyrrolidone, in the mesopores of MCM-41, Pellenq[7] showed an outstanding 6-fold increment in CO_2 solubility. Farrusseng[8] confined, within MIL-101(Cr), high amounts of *n*-hexane, *i.e.* 60% of the pore volume, affording an extraordinary 22-fold enhancement in H_2 uptake. In the context of CO_2 capture where solvents are confined in metal–organic frameworks (MOFs), the corner-stone investigation was presented by Chang and Llewellyn.[9] When 40 wt% of H_2O is confined within the mesopores of MIL-100(Fe), a significant 5-fold increase of CO_2 uptake is achieved.[9]

It is worth emphasizing that gas oversolubility, as presented in the previous examples, was observed only in mesoporous materials. In fact, when referring to gas oversolubility it is required to incorporate *via* pre-adsorption or impregnation, high amounts of solvents before any gas uptake. On the other hand, when high quantities of solvents are confined within the micropores of MOF materials, it is not possible to enhance their CO_2 adsorption properties as demonstrated in UiO-66,[9] InOF-1,[10] NOTT-400[11] and NOTT-401[12] since gas oversolubility does not occur in microporous MOFs. However, when small amounts of solvents are confined within these microporous materials, an effective and efficient CO_2 capture enhancement was undoubtedly accomplished.[13]

Typically, Walton and co-workers[14] showed CO_2 capture enhancements in microporous MOF materials by confining small amounts of H_2O. Recently, our research group showed the relevance of confining small amounts of pre-adsorbed H_2O within microporous MOFs in order to enhance their CO_2 capture properties.[15] In addition to H_2O, we explored the confinement of other solvents within MOFs: DMF,[16] EtOH,[17] MeOH[18] and i-PrOH.[18] We evidenced the positive impact of all

[a]Laboratorio de Fisicoquímica y Reactividad de Superficies (LaFReS), Instituto de Investigaciones en Materiales, Universidad Nacional Autónoma de México, Circuito Exterior s/n, CU, Del. Coyoacán, 04510 Ciudad de México, Mexico. E-mail: argel@unam.mx

[b]Institut Charles Gerhardt Montpellier, UMR-5253, Université de Montpellier, CNRS, ENSCM, Place E. Bataillon, 34095 Montpellier cedex 05, France. E-mail: guillaume.maurin@univ-montp2.fr; Fax: +52(55) 5622-4595

[c]Departamento de Química, Universidad Autónoma Metropolitana-Iztapalapa, San Rafael Atlixco 186, Col. Vicentina, Iztapalapa, C. P. 09340 Ciudad de México, Mexico

† Electronic supplementary information (ESI) available: TGA data, PXRD data, activation protocol, isosteric enthalpy of adsorption data and theoretical calculations. See DOI: 10.1039/c7dt02709e

‡ These authors contributed equally to this work.

This journal is © The Royal Society of Chemistry 2017

these confined solvents on the CO_2 adsorption performances of a few microporous MOF materials.[15–18] Particularly, for EtOH[17a] and DMF,[16] the interactions of these confined solvents with the InOF-1 MOF material that afforded a considerably enhanced CO_2 capture for this MOF were possible to visualise by single crystal X-ray diffraction.

Continuing with the progress of new CO_2 capture technologies,[19] the uninterrupted development of hybrid MOF materials with high adsorption capacity, fast sorption kinetics and mild regeneration conditions,[20,21] can contribute to the "the twelve principles of CO_2 chemistry" proposed by Poliakoff.[22] Here, we present the preparation of a hybrid solvent-loaded MOF material (MeOH@InOF-1) for CO_2 capture by confining small amounts of methanol (MeOH). In addition, the MeOH adsorption properties of InOF-1[23] are discussed along with the enhanced CO_2 adsorption properties of MeOH@InOF-1. Analysis of the preferential adsorption sites and the energetics in play for both MeOH and CO_2 as single components and a binary mixture is provided by a subtle combination of periodic Density Functional Theory (DFT) and force field-based Monte Carlo (MC) simulations. This computational work allows an understanding at the molecular level of the origin of the enhancement of the affinity of InOF-1 towards CO_2 in the presence of MeOH.

Experimental section

Synthetic preparations

InOF-1 was synthesised according to the procedure published previously by Hong and co-workers.[23] Thermogravimetric analysis (see Fig. S1, ESI†) and bulk powder X-ray diffraction patterns (see Fig. S2, ESI†) of the as-synthesised InOF-1 confirmed the structure of this microporous MOF material. Samples of the as-synthesised InOF-1 were acetone exchanged[24] and activated at 453 K for two hours (either under 10^{-3} bar, static experiments, or with a constant flow of N_2 gas, dynamic experiments). N_2 adsorption isotherms for activated InOF-1, at 77 K, were performed to estimate a BET area ($0.01 < P/P_0 < 0.04$) of 1065 $m^2\ g^{-1}$ and a pore volume of 0.37 $cm^3\ g^{-1}$.

Sorption isotherms for N_2, CO_2 and MeOH

N_2 sorption isotherms (up to 1 bar and 77 K) were performed on a Belsorp mini II analyser under vacuum (10^{-3} bar). CO_2 adsorption–desorption isotherms, up to 1 bar and 196 K, were carried out on a Belsorp HP (High Pressure) analyser. MeOH isotherms were recorded in a DVS Advantage 1 instrument from Surface Measurement Systems. Ultra-pure grade (99.9995%) N_2 and CO_2 gases were purchased from PRAXAIR.

Kinetic CO_2 uptake experiments

Kinetic CO_2 capture experiments were carried out on a thermobalance (Q500 HR, from TA) at 303 K with a constant CO_2 flow of 60 mL min^{-1}.

Computational details

Periodic Density Functional Theory (DFT) calculations were first performed to optimize the geometry of the empty InOF-1, CO_2@InOF-1 and MeOH@InOF-1 structures starting with the crystal structure of InOF-1 previously published[23] and using the PBE functional[25] combined with the DNP basis set[26] as implemented in Dmol3. We considered for both CO_2 and MeOH the loading explored experimentally, *i.e.* 5.3 wt% and 2 wt% respectively.

Monte Carlo simulations in the NVT ensemble were carried out at 303 K to predict the adsorption behavior of CO_2 and MeOH as single components and a mixture in InOF-1. The same loadings than in the DFT calculations were considered for both molecules, and the simulation box was made of 8 (2 × 2 × 2) unit cells of the MOF. The host/guest and guest/guest interactions were treated using Lennard–Jones (LJ) potential and coulombic contributions. All-atom charged models were selected for both CO_2[27] and MeOH[28] while the atoms of the MOF framework were described by LJ charged sites with parameters extracted from the generic force field UFF[29] (inorganic node) and Dreiding[30] (organic node). The corresponding LJ parameters and partial charges are described in the ESI (Table S1 and Fig. S1†).

Results and discussion

Methanol sorption studies

Methanol (MeOH) adsorption–desorption analyses were studied for InOF-1. A sample of the acetone-exchanged InOF-1 was positioned in an analyser cell (DVS Advantage 1 instrument) and activated (see Synthetic preparations, static experiments). After the activated InOF-1 sample was cooled down to 303 K, a methanol adsorption–desorption isotherm was performed from $\%P/P_0$ = 0 to 90 (Fig. 1), where P_0 is the saturated vapour pressure of methanol at the working temperature (12.88 and 21.76 kPa at 293 and 303 K respectively).

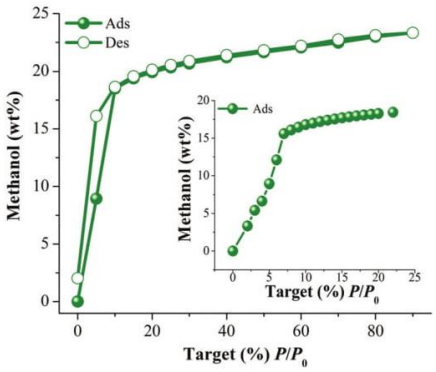

Fig. 1 Methanol (MeOH) adsorption isotherm at 303 K of InOF-1 from $\%P/P_0$ = 0 to 90. Solid circles represent adsorption, and open circles show desorption. The inset shows the MeOH adsorption isotherm at 303 K from $\%P/P_0$ = 0 to 22.

In Fig. 1 it is possible to observe a rapid MeOH uptake from the beginning of the experiment up to approximately $\%P/P_0$ = 10 (18.49 MeOH wt%). Above this pressure, we observe a quasi-plateau associated with a very slow uptake increase up to $\%P/P_0$ = 85 with a total MeOH adsorbed amount of ~23.3 wt%. The steep increase of the adsorption uptake at low pressure clearly indicates that InOF-1 shows a high affinity towards MeOH.

This was further confirmed by the evaluation of the isosteric heat of adsorption (ΔH = −41 kJ mol^{-1}, at low MeOH coverage) that was obtained from the consideration of adsorption isotherms calculated at two different temperatures and the application of the Clausius–Clapeyron equation (303 and 293 K see Fig. S3 and S4 ESI†).

Usually for MOF materials, the use of the Clausius–Clapeyron and Viral equations is very well known and we, previously, successfully used these mathematical approaches.[31] This calculation is also fully consistent with the MC-simulated adsorption enthalpy for MeOH (−40.8 kJ mol^{-1}), both values being slightly higher than the molar enthalpy of vaporisation for MeOH[32] (−38.28 kJ mol^{-1}). Finally, the ΔH for MeOH is in good agreement with the value already reported for MOFs that show bridging μ_2-OH functional groups.[33]

The lack of an inflexion point in the shape of the isotherms (Fig. 1 and 2), suggests only one domain of adsorption.[11] The overall MeOH isotherm-shape shows a characteristic type-I isotherm (IUPAC) and a minor hysteresis loop (at 303 K and $\%P/P_0$ = 0–10) was observed with marked stepped profiles in the desorption branch (Fig. 1, open circles). The pore diameter of InOF-1 (~7.5 Å)[23] is considerably larger than the kinetic diameter of MeOH (3.6 Å). Thus, this hysteresis cannot be correlated with the arguments of "kinetic trapping", as suggested by many research groups for other materials (see ref. 34 for some representative examples). Instead, the observed hysteresis might be due to the relatively strong host–guest interactions mentioned above.

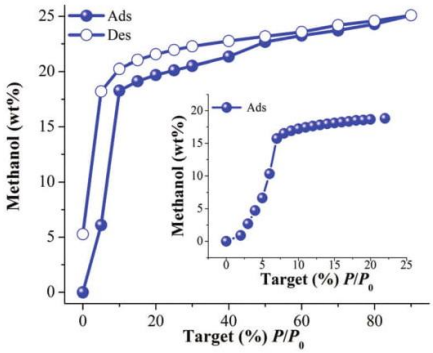

Fig. 2 Methanol (MeOH) adsorption isotherm at 293 K of InOF-1 from $\%P/P_0$ = 0 to 90. Solid circles represent adsorption, and open circles show desorption. The inset shows the MeOH adsorption isotherm at 293 K from $\%P/P_0$ = 0 to 22.

The MeOH isotherm at 293 K was similar to the sorption experiment at 303 K with two main differences: the total uptake at $\%P/P_0$ = 90 (~25.1 MeOH wt%) is slightly higher (~23.3 wt%) and the hysteresis is much more pronounced. These results are consistent with the lower operational temperature (293 K); when reducing the temperature of the experiment, a more efficient packing of the molecules can be favored by a more localized interaction between MeOH and the μ_2-OH functional groups. Thus, a slightly higher total uptake and more pronounced hysteresis are expected as previously observed for EtOH at 293 K in InOF-1.[17a]

The DFT-optimized structure of MeOH@InOF-1 (Fig. 3a) evidences a preferential sitting of the guest molecules at the vicinity of the μ_2-OH groups that leads to the formation of a hydrogen bond between O(MeOH) and H(μ_2-OH) associated with a characteristic distance of 1.90 Å (Fig. 3a), similarly to what was previously reported for ethanol (EtOH)[17a] in the same MOF. The same adsorption behavior was also observed in our MC simulations (Fig. 2b). The center of mass distribution averaged over all the configurations generated by MC simulations for a low CH_3OH loading (2 wt%) reveals that the arrangement of the guest is highly localized near the μ_2-OH groups (Fig. 3b) consistent with a strong host/guest interaction as suggested by the relatively high calculated and experimental adsorption enthalpy.

CO_2 capture studies

Dynamic and isothermal kinetic CO_2 capture experiments were carried on the acetone-exchanged samples of InOF-1. These samples were activated (see Synthetic preparations, static

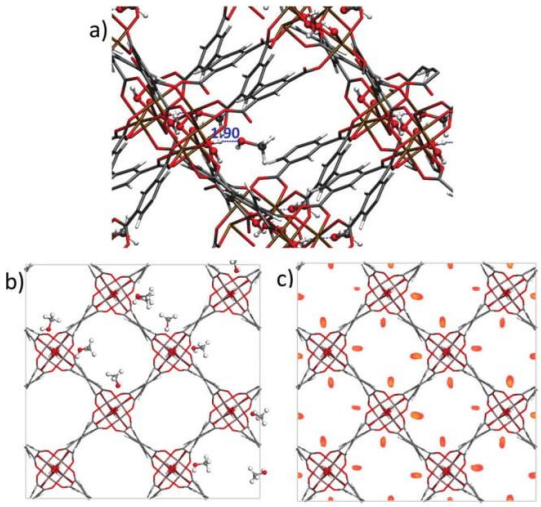

Fig. 3 DFT-optimized structure for MeOH@InOF-1 showing the preferential adsorption of the guest towards the μ_2-OH groups. (a) Illustration of the preferential adsorption sites evidenced by MC simulations (b) and the map of the center of mass distribution of MeOH averaged over all the configurations generated by MC simulations.

 This journal is © The Royal Society of Chemistry 2017

experiments) on a thermobalance Q500 HR. After the activated sample was cooled down to 303 K (under a N_2 flow), the N_2 purge flow was switched to 60 mL min^{-1} of CO_2. Fig. 4 shows the kinetic CO_2 uptake experiment at 303 K for activated InOF-1. The maximum weight percentage gain corresponds to the maximum amount of CO_2 captured. This amount of 5.2 wt% was quickly reached after only 5 min and it was constant until the end of the experiment (10 min), Fig. 4 (InOF-1).

The DFT-optimized structure of CO_2@InOF-1 (Fig. S6†) evidences that similarly to MeOH, CO_2 preferentially adsorbs at the vicinity of the μ_2-OH groups however with an interacting distance which is much longer (2.95 Å). This is consistent with a much lower adsorption enthalpy calculated by MC (−21 kJ mol^{-1}) for this guest as compared to MeOH (−40.8 kJ mol^{-1}) and a much more scattered distribution of the center of mass of the CO_2 in the pores of the MOF framework (Fig. S3†).

An acetone-exchanged sample of InOF-1 was activated (*vide supra*), cooled down to 303 K (under N_2) and fully saturated with MeOH (see the ESI†). By following an activation protocol (see the ESI†) the residual amount of confined MeOH was equal to 2 wt%. In order to corroborate the reproducibility of the activation protocol for InOF-1, we carried out 5 independent experiments (see the ESI†) which provided us, approximately, the same residual amount of MeOH. Hereinafter, this sample will be referred to as MeOH@InOF-1.

We decided to work only with small amounts of confined MeOH, within InOF-1, motivated by our previous experimental work on EtOH (2.6 wt%) confined in the micropores of InOF-1,[17a] which led to the formation of hydrogen bonds with the μ_2-OH groups and to a significant improvement of the overall CO_2 capture (2.7 fold increase).[17a]

The effect of the μ_2-OH groups present in different MOFs on the strength of interactions with solvent molecules is also well documented from a computational standpoint.[35–37]

A kinetic CO_2 adsorption experiment (303 K) was performed on a MeOH@InOF-1 sample. The total amount of CO_2 adsorbed was equal to 6.9 wt%. This CO_2 uptake was achieved at ∼4 min and remained constant until the last part of the experiment (10 min) (Fig. 4, MeOH@InOF-1). The samples of MeOH@InOF-1 were synthesised with anhydrous methanol (<0.005% water) and methanol (reagent alcohol, 95%). The kinetic CO_2 capture experiments exhibit no difference. Other residual amounts of MeOH (3%, 4% and 5%) were tested and the best result was obtained with 2 wt% of confined MeOH. Thus, the dynamic CO_2 capture, at 303 K, was approximately 1.3-fold improved (from 5.2 wt% to 6.9 wt%), after confining small amounts of MeOH within InOF-1. Since ethanol is a bigger molecule than methanol, it provides a stronger confinement effect which enhances the CO_2 capture even more.

Continuing with the investigation of the CO_2 adsorption properties of MeOH@InOF-1, static and isothermal CO_2 adsorption experiments (increasing the partial pressure from 0 to 1 bar at 196 K) were carried out. The adsorption of CO_2 at 303 K is rather complicated since it is very close to the critical temperature of CO_2.[33] At 303 K the density (δ_{CO_2}) of CO_2 adsorbed is difficult to estimate because the CO_2 saturation pressure is really high and therefore the range of P/P_0 is limited to only 0.02 at sub-atmospheric pressures.[38] Additionally, it has been postulated that adsorption in well-defined micropores occurs by a pore-filling mechanism rather than surface coverage.[38,39] For example, N_2 molecules (77 K) can fill micropores in a liquid-like fashion at very low relative pressures under 0.01. Conversely, CO_2 adsorbed at ambient temperatures can only form a monolayer on the walls of microporous materials.[39] Thus, in order to achieve pore-filling micropores and a much better and precise description of the CO_2 adsorption properties of these MOFs, CO_2 gas adsorption experiments at 196 K are highly desired.[40]

For this purpose, a CO_2 static sorption-experiment at 196 K was performed on an activated (see Synthetic preparations, static experiments) sample of InOF-1 with a total CO_2 uptake of 24.2 wt%, (Fig. 5, InOF-1). Then, a MeOH@InOF-1 sample was quickly mounted in a high-pressure cell (Belsorp HP) and carefully evacuated to eliminate any absorbed moisture. The CO_2 adsorption–desorption experiment from 0 to 1 bar and 196 K showed a CO_2 uptake at low pressure (approximately

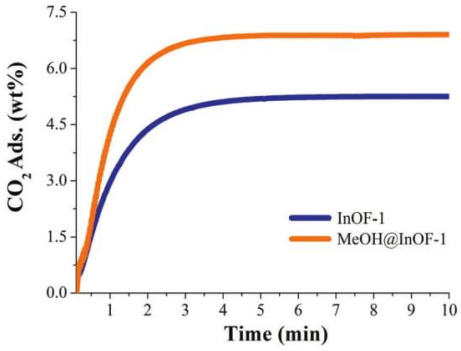

Fig. 4 Kinetic CO_2 uptake experiments performed at 303 K with a CO_2 flow of 60 mL min^{-1} in InOF-1 (blue curve) and MeOH@InOF-1 (orange curve).

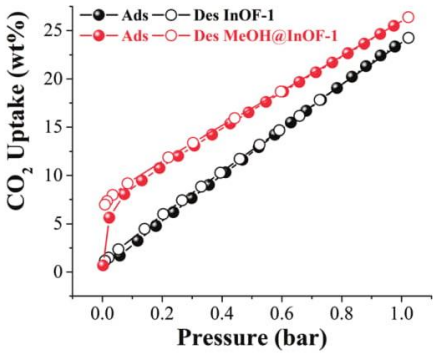

Fig. 5 Static CO_2 adsorption–desorption performed from 0 to 1 bar at 196 K on InOF-1 (black circles) and MeOH@InOF-1 (red circles).

Table 1 Adsorption properties of InOF-1 loaded with different solvents

Sample	BET surface area (m^2 g^{-1})	pore volume (cm^3 g^{-1})	Solvent loading (wt%)	CO_2 uptake (wt%)	
				Kinetic[a] (303 K)	Static[b] (196 K)
InOF-1	1066	0.37	0.00	5.24	1.14
MeOH@InOF-1	720	0.34	2	6.9	5.59
DMF@InOF-1[16]	628	0.32	4.2	8.06	7.14
EtOH@InOF-1[17a]	514	0.28	2.6	14.14	—

[a] CO_2 uptake at 1 bar and 60 mL min^{-1} flux. [b] CO_2 uptake at 0.026 bar.

0.026 bar) of 5.59 wt%, (Fig. 5, MeOH@InOF-1). Conversely, the CO_2 uptake of InOF-1 at the same pressure was equal to 1.14 wt%. This result is interesting since at very low pressure, the CO_2 uptake is considerably enhanced (4.88-fold increase) by confining small amounts of MeOH. The total CO_2 uptake of MeOH@InOF-1 at 1 bar was 26.0 wt%, which in comparison with the InOF-1 sample, corresponds only to a small improvement (1.07-fold increase) (see Fig. 5). Both BET area (720 m^2 g^{-1}) and pore volume (0.34 cm^3 g^{-1}) obtained for MeOH@InOF-1 are lower than the values for the empty InOF-1 (1065 m^2 g^{-1} and 0.37 cm^3 g^{-1} respectively). These observations are consistent with other confined solvents (EtOH and DMF) @InOF-1 (see Table 1).[16]

Molecular simulations were further performed to gain insight into the adsorption behaviors of MeOH and CO_2 at the molecular level. The MC calculations evidenced that the μ_2-OH groups are the most preferential adsorption sites for both guests as mentioned above. However, since the adsorption enthalpy for MeOH (−40.8 kJ mol^{-1}) is significantly higher than for CO_2 (−21 kJ mol^{-1}) as single components, MeOH is favorably adsorbed around the μ_2-OH groups in a binary mixture and this geometry tends to screen the CO_2/μ_2-OH interactions as can be observed from Fig. 6.

Fig. S8† shows that the presence of MeOH leads to a small enhancement of the strength of CO_2/InOF-1 interactions from −21 kJ mol^{-1} to −23 kJ mol^{-1}. The comparison between the van der Waals surface area plotted for the DFT-optimized empty InOF-1 and MeOH@InOF-1 structures demonstrates

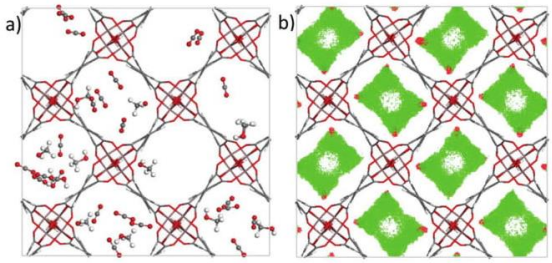

Fig. 6 Illustration of the preferential adsorption sites simulated by MC for both guests as a binary mixture in InOF-1 (a) and the map of the center of mass distribution of CO_2 (green region)/MeOH (red region) as a binary mixture averaged over all the configurations generated by MC simulations (b).

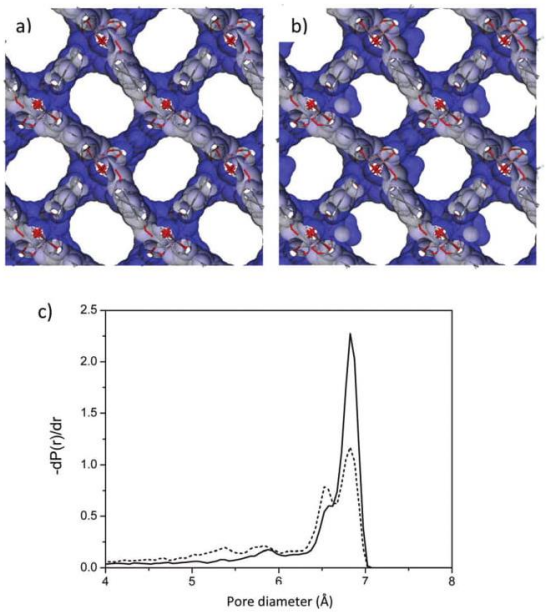

Fig. 7 van der Waals surface area plotted for the DFT-optimized empty InOF-1 (a) and MeOH@InOF-1 (b) structures. Comparison of the pore size distribution calculated for the two structures (empty InOF-1 solid lines and MeOH@InOF-1 dashed lines) (c).

that the presence of MeOH induces a decrease of the accessible porosity for CO_2, consistent with the experimental findings, by forming a lump at the vicinity of the μ_2-OH groups (Fig. 7b). This is also reflected in the plot of the pore size distribution for the two InOF-1 (Fig. 7c). This observation supports that the slightly higher CO_2 affinity of MeOH@InOF-1 as compared to the empty InOF-1 and hence the higher uptake is most probably caused by the higher degree of confinement felt by the adsorbed CO_2 in the presence of MeOH rather than a mutual energetic effect between the two guests.

Conclusions

The MeOH adsorption properties of InOF-1, a microporous In(III)-based MOF material, were first investigated. Rapid MeOH

 This journal is © The Royal Society of Chemistry 2017

uptakes and hysteresis loops at low loadings (%P/P_0 = 0 to 10) at 303 and 293 K demonstrated a high affinity towards MeOH. This MeOH affinity was experimentally quantified by the evaluation of the isosteric heat of adsorption (ΔH = −41 kJ mol^{-1}) and confirmed by force field-based MC simulations (ΔH = −40.8 kJ mol^{-1}) while DFT geometry optimizations evidenced the formation of a relatively strong hydrogen bond between O(MeOH) and H(μ_2-OH).

Kinetic isotherm CO_2 experiments showed a CO_2 uptake of 5.2 wt% for fully activated InOF-1. After confining small amounts of MeOH (2 wt%) within its micropores, the CO_2 capture, for MeOH@InOF-1, increased to 6.9 wt% corresponding to a 1.3-fold improvement. Static and isothermal CO_2 experiments (~0.026 bar and 196 K) exhibited a remarkable 4.88-fold CO_2 capture increase (from 1.14 wt%, for fully activated InOF-1 to 5.59 wt%, for MeOH@InOF-1).

MC calculations showed that MeOH forms a lump at the vicinity of the μ_2-OH groups that tends to increase the degree of confinement felt by CO_2, most probably at the origin of the higher CO_2 uptake observed in the low domain of pressure for MeOH@InOF-1 as compared to the empty solid.

Conflicts of interest

There are no conflicts to declare.

Acknowledgements

The authors thank Dr A. Tejeda-Cruz (X-ray; IIM-UNAM), PAPIIT UNAM (IN101517) and CONACyT (1789) Mexico for financial support. E. G.-Z. thanks CONACyT (236879), Mexico for financial support. Thanks to U. Winnberg (ITAM) for scientific discussions. P. G. M. Mileo thanks the National Counsel of Technological and Scientific Development (CNPQ) for the scholarship. G. M. thanks the Institut Universitaire de France for its support.

Notes and references

1 S. Miachon, V. V. Syakaev, A. Rakhmatullin, M. Pera-Titus, S. Caldarelli and J.-A. Dalmon, *ChemPhysChem*, 2008, **9**, 78.

2 (*a*) S. Clauzier, L. N. Ho, M. Pera-Titus, D. Farrusseng and B. Coasne, *J. Phys. Chem. C*, 2014, **118**, 10720; (*b*) L. N. Ho, Y. Schuurman, D. Farrusseng and B. Coasne, *J. Phys. Chem. C*, 2015, **119**, 21547.

3 (*a*) F. Volino, H. Gérard and S. Miachon, *Ann. Phys.*, 1997, **22**, 43; (*b*) K. Morishige and M. Shikimi, *J. Chem. Phys.*, 1998, **108**, 7821; (*c*) M. O. Kimball and F. M. Gasparini, *Phys. Rev. Lett.*, 2005, **95**, 165701; (*d*) U. Zammit, M. Marinelli, F. Mercuri and S. Paoloni, *J. Phys. Chem. B*, 2009, **113**, 14315.

4 X. Jiang, H.-B. Duan, S. I. Khan and M. A. Garcia-Garibay, *ACS Cent. Sci.*, 2016, **2**, 608.

5 (*a*) A. Luzar and D. Bratko, *J. Phys. Chem. B*, 2005, **109**, 22545; (*b*) D. Bratko and A. Luzar, *Langmuir*, 2008, **24**, 1247.

6 (*a*) M. Pera-Titus, R. El-Chahal, V. Rakotovao, S. Miachon and J.-A. Dalmon, *ChemPhysChem*, 2009, **10**, 2082; (*b*) M. Pera-Titus, S. Miachon and J.-A. Dalmon, *AIChE J.*, 2009, **55**, 434; (*c*) V. Rakotovao, R. Ammar, S. Miachon and M. Pera-Titus, *Chem. Phys. Lett.*, 2010, **485**, 299.

7 (*a*) N. L. Ho, J. Perez-Pellitero, F. Porcheron and R. J.-M. Pellenq, *J. Phys. Chem. C*, 2012, **116**, 3600; (*b*) N. L. Ho, J. Perez-Pellitero, F. Porcheron and R. J.-M. Pellenq, *Langmuir*, 2011, **27**, 8187; (*c*) N. L. Ho, F. Porcheron and R. J.-M. Pellenq, *Langmuir*, 2010, **26**, 13287.

8 S. Clauzier, L. N. Ho, M. Pera-Titus, B. Coasne and D. Farrusseng, *J. Am. Chem. Soc.*, 2012, **134**, 17369.

9 E. Soubeyrand-Lenoir, C. Vagner, J. W. Yoon, P. Bazin, F. Ragon, Y. K. Hwang, C. Serre, J.-S. Chang and P. L. Llewellyn, *J. Am. Chem. Soc.*, 2012, **134**, 10174.

10 R. A. Peralta, B. Alcántar-Vázquez, M. Sánchez-Serratos, E. González-Zamora and I. A. Ibarra, *Inorg. Chem. Front.*, 2015, **2**, 898.

11 J. R. Álvarez, R. A. Peralta, J. Balmaseda, E. González-Zamora and I. A. Ibarra, *Inorg. Chem. Front.*, 2015, **2**, 1080.

12 E. Sánchez-González, J. R. Álvarez, R. A. Peralta, A. Campos-Reales-Pineda, A. Tejeda-Cruz, E. Lima, J. Balmaseda, E. González-Zamora and I. A. Ibarra, *ACS Omega*, 2016, **1**, 305.

13 E. González-Zamora and I. A. Ibarra, *Mater. Chem. Front.*, 2017, **1**, 1471.

14 (*a*) H. Jasuja, Y.-G. Huang and K. S. Walton, *Langmuir*, 2012, **28**, 16874; (*b*) H. Jasuja, J. Zang, D. S. Sholl and K. S. Walton, *J. Phys. Chem. C*, 2012, **116**, 23526; (*c*) J. B. DeCoste, G. W. Peterson, H. Jasuja, T. G. Glover, Y.-G. Huang and K. S. Walton, *J. Mater. Chem. A*, 2013, **1**, 5642; (*d*) N. C. Burtch, H. Jasuja and K. S. Walton, *Chem. Rev.*, 2014, **114**, 10575; (*e*) G. E. Cmarik, M. Kim, S. M. Cohen and K. S. Walton, *Langmuir*, 2012, **28**, 15606.

15 (*a*) M. R. Gonzalez, J. H. González-Estefan, H. A. Lara-García, P. Sánchez-Camacho, E. I. Basaldella, H. Pfeiffer and I. A. Ibarra, *New J. Chem.*, 2015, **39**, 2400; (*b*) H. A. Lara-García, M. R. Gonzalez, J. H. González-Estefan, P. Sánchez-Camacho, E. Lima and I. A. Ibarra, *Inorg. Chem. Front.*, 2015, **2**, 442; (*c*) M. Sánchez-Serratos, P. A. Bayliss, R. A. Peralta, E. González-Zamora, E. Lima and I. A. Ibarra, *New J. Chem.*, 2016, **40**, 68; (*d*) A. Zárate, R. A. Peralta, P. A. Bayliss, R. Howie, M. Sánchez-Serratos, P. Carmona-Monroy, D. Solis-Ibarra, E. González-Zamora and I. A. Ibarra, *RSC Adv.*, 2016, **6**, 9978.

16 E. Sánchez-González, E. González-Zamora, D. Martínez-Otero, V. Jancik and I. A. Ibarra, *Inorg. Chem.*, 2017, **56**, 5863.

17 (*a*) R. A. Peralta, A. Campos-Reales-Pineda, H. Pfeiffer, J. R. Álvarez, J. A. Zárate, J. Balmaseda, E. González-Zamora, A. Martínez, D. Martínez-Otero, V. Jancik and I. A. Ibarra, *Chem. Commun.*, 2016, **52**, 10273; (*b*) J. R. Álvarez, E. Sánchez-González, E. Pérez,

E. Schneider-Revueltas, A. Martínez, A. Tejeda-Cruz, A. Islas-Jácome, E. González-Zamora and I. A. Ibarra, *Dalton Trans.*, 2017, **46**, 9192.

18 G. A. González-Martínez, J. A. Zárate, A. Martínez, E. Sánchez-González, J. R. Álvarez, E. Lima, E. González-Zamora and I. A. Ibarra, *RSC Adv.*, 2017, **7**, 24833.

19 (*a*) D. M. D'Alessandro, B. Smit and J. R. Long, *Angew. Chem., Int. Ed.*, 2010, **49**, 6058; (*b*) K. Sumida, D. L. Rogow, J. A. Mason, T. M. McDonald, E. D. Bloch, Z. R. Herm, Z. T.-H. Bae and J. R. Long, *Chem. Rev.*, 2012, **112**, 724.

20 (*a*) S. Yang, G. S. B. Martin, J. J. Titman, A. J. Blake, D. R. Allan, N. R. Champness and M. Schröder, *Inorg. Chem.*, 2011, **50**, 9374; (*b*) S. Yang, X. Lin, A. J. Blake, G. S. Walker, P. Hubberstey, N. R. Champness and M. Schröder, *Nat. Chem.*, 2009, **1**, 487; (*c*) A. J. Nuñez, L. N. Shear, N. Dahal, I. A. Ibarra, J. W. Yoon, Y. K. Hwang, J.-S. Chang and S. M. Humphrey, *Chem. Commun.*, 2011, **47**, 11855; (*d*) I. A. Ibarra, J. W. Yoon, J.-S. Chang, S. K. Lee, V. M. Lynch and S. M. Humphrey, *Inorg. Chem.*, 2012, **51**, 12242; (*e*) X. Lin, A. J. Blake, C. Wilson, X. Z. Sun, N. R. Champness, M. W. George, P. Hubberstey, R. Mokaya and M. Schröder, *J. Am. Chem. Soc.*, 2006, **128**, 10745; (*f*) P. Nugent, Y. Belmabkhout, S. D. Burd, A. J. Cairns, R. Luebke, K. Forrest, T. Pham, S. Ma, B. Space, L. Wojtas, M. Eddaoudi and M. J. Zaworotko, *Nature*, 2013, **495**, 80; (*g*) O. Shekhah, Y. Belmabkhout, Z. Chen, V. Guillerm, A. Cairns, K. Adil and M. Eddaoudi, *Nat. Commun.*, 2014, **5**, 522; (*h*) W. M. Bloch, A. Burgun, C. J. Coghlan, R. Lee, M. L. Coote, C. J. Doonan and C. J. Sumby, *Nat. Chem.*, 2014, **6**, 906; (*i*) K. Okada, R. Ricco, Y. Tokudome, M. J. Styles, A. J. Hill, M. Takahashi and P. Falcaro, *Adv. Funct. Mater.*, 2014, **24**, 1969; (*j*) H. Li, M. R. Hill, R. Huang, C. Doblin, S. Lim, A. J. Hill, R. Babarao and P. Falcaro, *Chem. Commun.*, 2016, **52**, 5973; (*k*) K. Sumida, N. Moitra, J. Reboul, S. Fukumoto, K. Nakanishi, K. Kanamori, S. Furukawa and S. Kitagawa, *Chem. Sci.*, 2015, **6**, 5938; (*l*) K. Hirai, S. Furukawa, M. Kondo, H. Uehara, O. Sakata and S. Kitagawa, *Angew. Chem., Int. Ed.*, 2011, **50**, 8057.

21 (*a*) T. Tozawa, J. T. A. Jones, S. I. Swamy, S. Jiang, D. J. Adams, S. Shakespeare, R. Clowes, D. Bradshaw, T. Hasell, S. Y. Chong, C. Tang, S. Thompson, J. Parker, A. Trewin, J. Bacsa, A. M. Z. Slawin, A. Steiner and A. I. Cooper, *Nat. Mater.*, 2009, **8**, 973; (*b*) R. Dawson, D. J. Adams and A. I. Cooper, *Chem. Sci.*, 2011, **2**, 1173; (*c*) W. M. Bloch, R. Babarao, M. R. Hill, C. J. Doonan and C. J. Sumby, *J. Am. Chem. Soc.*, 2013, **135**, 10441; (*d*) J. A. Mason, K. Sumida, Z. R. Herm, R. Krishna and J. R. Long, *Energy Environ. Sci.*, 2011, **4**, 3030; (*e*) R. Babarao, C. J. Coghlan, D. Rankine, W. M. Bloch, G. K. Gransbury, H. Sato, S. Kitagawa, C. J. Sumby, M. R. Hill and C. J. Doonan, *Chem. Commun.*, 2014, **50**, 3238; (*f*) I. A. Ibarra, A. Mace, S. Yang, J. Sun, S. Lee, J.-S. Chang, A. Laaksonen, M. Schröder and X. Zou, *Inorg. Chem.*, 2016, **55**, 7219; (*g*) A. López-Olvera, E. Sánchez-González, A. Campos-Reales-Pineda, A. Aguilar-Granda, I. A. Ibarra and B. Rodríguez-Molina, *Inorg. Chem. Front.*, 2017, **4**, 56.

22 M. Poliakoff, W. Leitner and E. S. Streng, *Faraday Discuss.*, 2015, **183**, 9.

23 J. Qian, F. Jiang, D. Yuan, M. Wu, S. Zhang, L. Zhang and M. Hong, *Chem. Commun.*, 2012, **48**, 9696.

24 I. A. Ibarra, S. Yang, X. Lin, A. J. Blake, P. J. Rizkallan, H. Nowell, D. R. Allan, N. R. Champness, P. Hubberstey and M. Schröder, *Chem. Commun.*, 2011, **47**, 8304.

25 (*a*) J. P. Perdew, K. Burke and M. Ernzerhof, *Phys. Rev. Lett.*, 1996, **77**, 3865; (*b*) J. P. Perdew, K. Burke and M. Ernzerhof, *Phys. Rev. Lett.*, 1997, **78**, 1396.

26 (*a*) B. Delley, *J. Chem. Phys.*, 1990, **92**, 508; (*b*) B. Delley, *J. Chem. Phys.*, 2000, **113**, 7756.

27 J. G. Harris and K. H. Yung, *J. Phys. Chem.*, 1995, **99**, 12021.

28 D. F. Plant, G. Maurin and R. Bell, *J. Phys. Chem. B*, 2007, **111**, 2836.

29 A. K. K. Rappé, C. J. J. Casewit, K. S. S. Colwell, W. A. Goddard III and W. M. Skiff, *J. Am. Chem. Soc.*, 1992, **114**, 10024.

30 S. L. Mayo, B. D. Olafson and W. A. Goddard III, *J. Phys. Chem.*, 1990, **101**, 8897.

31 (*a*) I. A. Ibarra, X. Lin, S. Yang, A. J. Blake, G. S. Walker, S. A. Barnett, D. R. Allan, N. R. Champness, P. Hubberstey and M. Schröder, *Chem. – Eur. J.*, 2010, **16**, 13671; (*b*) I. A. Ibarra, T. W. Hesterberg, B. J. Holliday, V. M. Lynch and S. M. Humphrey, *Dalton Trans.*, 2012, **41**, 8003; (*c*) I. A. Ibarra, P. A. Bayliss, E. Pérez, S. Yang, A. J. Blake, H. Nowell, D. R. Allan, M. Poliakoff and M. Schröder, *Green Chem.*, 2012, **14**, 117; (*d*) A. M. Bohnsack, I. A. Ibarra, V. I. Bakhmutov, V. M. Lynch and S. M. Humphrey, *J. Am. Chem. Soc.*, 2013, **135**, 16038; (*e*) A. J. Nuñez, M. S. Chang, I. A. Ibarra and S. M. Humphrey, *Inorg. Chem.*, 2014, **53**, 282.

32 D. R. Lide, *Handbook of Chemistry and Physics*, CRC Press LLC, 84th edn, 2004.

33 M. F. de Lange, K. J. F. M. Verouden, T. J. H. Vlugt, J. Gascon and F. Kapteijn, *Chem. Rev.*, 2015, **115**, 12205.

34 (*a*) X. B. Zhao, B. Xiao, A. J. Fletcher, K. M. Thomas, D. Bradshaw and M. J. Rosseinsky, *Science*, 2004, **306**, 1012; (*b*) H. J. Choi, M. Dincă and J. R. Long, *J. Am. Chem. Soc.*, 2008, **130**, 7848; (*c*) O. M. Linder-Patton, W. M. Bloch, C. J. Coghlan, K. Sumida, S. Kitagawa, S. Furukawa, C. J. Doonan and C. J. Sumby, *CrystEngComm*, 2016, **18**, 4172.

35 G. R. Medders and F. Paesani, *J. Phys. Chem. Lett.*, 2014, **5**, 2897.

36 V. Haigis, F.-X. Coudert, R. Vuilleumier and A. Boutin, *Phys. Chem. Chem. Phys.*, 2013, **15**, 19049.

37 F. Salles, S. Bourrelly, H. Jobic, T. Devic, V. Guillerm, P. Llewellyn, C. Serre, G. Férey and G. Maurin, *J. Phys. Chem. C*, 2011, **115**, 10764.

38 F. Rouquerol, J. Rouquerol, K. S. W. Sing, P. Llewellyn and G. Maurin, *Adsorption by Powders and Porous Solids; Principles, Methodology and Applications*, Elsevier Press, 2014.

 This journal is © The Royal Society of Chemistry 2017

39 J. Garrido, A. Linares-Solano, J. M. Martín-Martínez, M. Molina-Sabio, F. Rodríguez-Reinoso and R. Torregrosa, *Langmuir*, 1987, **3**, 76.

40 (*a*) H. J. Park and M. P. Sun, *Chem. – Eur. J.*, 2008, **14**, 8812; (*b*) S. M. Humphrey, J.-S. Chang, S. H. Jhung, J. W. Yoon and P. T. Wood, *Angew. Chem., Int. Ed.*, 2007, **46**, 272; (*c*) J. Lee, N. W. Waggoner, L. Polanco, G. R. You, V. M. Lynch, S. K. Kim, S. M. Humphrey and J. L. Sessler, *Chem. Commun.*, 2016, **52**, 8514; (*d*) A. Aguilar-Granda, S. Pérez-Estrada, E. Sánchez-González, J. R. Álvarez, J. Rodríguez-Hernández, M. Rodríguez, A. E. Roa, S. Hernández-Ortega, I. A. Ibarra and B. Rodríguez-Molina, *J. Am. Chem. Soc.*, 2017, **139**, 7549.

This journal is © The Royal Society of Chemistry 2017

THE JOURNAL OF PHYSICAL CHEMISTRY C

Article

Cite This: J. Phys. Chem. C 2018, 122, 5566−5577

pubs.acs.org/JPCC

Adsorption of 1-Propanol in the Channel-Like InOF-1 Metal−Organic Framework and Its Influence on the CO_2 Capture Performances

J. Raziel Álvarez,[†,⊥] Paulo G. M. Mileo,[‡,⊥] Elí Sánchez-González,[†] J. Antonio Zárate,[†] Joelis Rodríguez-Hernández,[§] Eduardo González-Zamora,[∥] Guillaume Maurin,*[,‡] and Ilich A. Ibarra*[,†]

[†]Laboratorio de Fisicoquímica y Reactividad de Superficies (LaFReS), Instituto de Investigaciones en Materiales, Universidad Nacional Autónoma de México, Circuito Exterior s/n, CU, 04510 Delegación Coyoacán, Ciudad de México, Mexico

[‡]Institut Charles Gerhardt Montpellier, UMR-5253, Université de Montpellier, CNRS, ENSCM, Place E. Bataillon, 34095 Montpellier cedex 05, France

[§]Departamento de Materiales Avanzados, Centro de Investigación en Química Aplicada, Blvd. Enrique Reyna No. 140, 25294 Saltillo, Coahuila, Mexico

[∥]Departamento de Química, Universidad Autónoma Metropolitana-Iztapalapa, San Rafael Atlixco 186, Col. Vicentina, C. P. 09340 Delegación Iztapalapa, Ciudad de México, Mexico

Supporting Information

ABSTRACT: The *n*-PrOH adsorption properties of the one-dimensional-channel-like metal−organic framework InOF-1 were first explored and evidenced a high affinity for this host−guest system owing to the shape of the adsorption isotherms at a low relative pressure, the presence of a hysteresis loop during the desorption process, and a relatively high isosteric heat of adsorption. Monte Carlo simulations revealed that this thermodynamic behavior is related to a preferential interaction between *n*-PrOH and the μ_2-OH groups of the InOF-1 surface at low loading, whereas *n*-PrOH self-aggregates at higher guest concentration to first form dimers and then clusters. In complement to this thermodynamic exploration, the kinetics of *n*-PrOH were further characterized and the mobility of the guests was shown to be slow most probably due to the formation of these guest clusters. Finally, we revealed that in contrast to other solvents we have reported in the past, the *n*-PrOH confinement does not enhance the CO_2 capture in InOF-1. This observation was supported by grand canonical Monte Carlo simulations. Finally, we observed that the filling of the micropores of InOF-1 by CO_2 inhibits the adsorption of *n*-PrOH, demonstrating the absence of oversolubility of *n*-PrOH in the presence of CO_2.

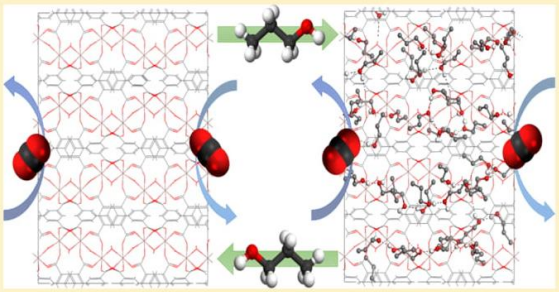

INTRODUCTION

Metal−organic frameworks (MOFs), a well-known class of crystalline hybrid porous three-dimensional materials, are constructed from metal ions and bridging organic ligands, which exhibit a huge collection of topologies.[1−5] Owing to the large diversity of the organic ligands and the high versatility of the inorganic building blocks, the design and construction of MOFs containing multifunctional sites and associated with a high chemical stability, has demonstrated the great potential of this family of porous materials in a large variety of fields.[6−9] Among them, energy-related applications from energy storage to transformation represent one of the most studied and promising research fields for MOFs.[10,11] Typically, MOFs have shown very interesting properties of H_2 storage,[12−14] CO_2 capture,[15−19] and diverse gas separations.[20−23] Recently, MOFs have been also suggested for adsorption-driven heat pump/chiller applications,[24−26] where the selection of a suitable working pair, i.e., working fluid (alcohol, water, ammonia) and adsorbent is, indeed, a key to design the optimal system. Interestingly, besides the thermodynamic adsorption capacity and affinity, the diffusivity of the working fluids through the pores of MOFs is of importance and experimental information is, however, still scarce.[27−29]

The confinement of guest molecules within the porous materials exemplifies a new and interesting approach to enhance their CO_2 capture performances.[30−32] The physical properties of guest molecules remarkably depend on the system scale; the confinement of these molecules within nanomaterials significantly transforms their density, viscosity, specific heat, and dielectric constant.[33−36] Uncommon confinement effects of the guest molecules located within the channels have been observed previously for single-walled carbon nanotubes.[37,38] However, these effects have been much scarcely investigated for MOFs materials.[39] For example, by confining large amounts of guest

Received: January 8, 2018
Revised: February 9, 2018
Published: February 13, 2018

ACS Publications © 2018 American Chemical Society

DOI: 10.1021/acs.jpcc.8b00215
J. Phys. Chem. C 2018, 122, 5566−5577

The Journal of Physical Chemistry C Article

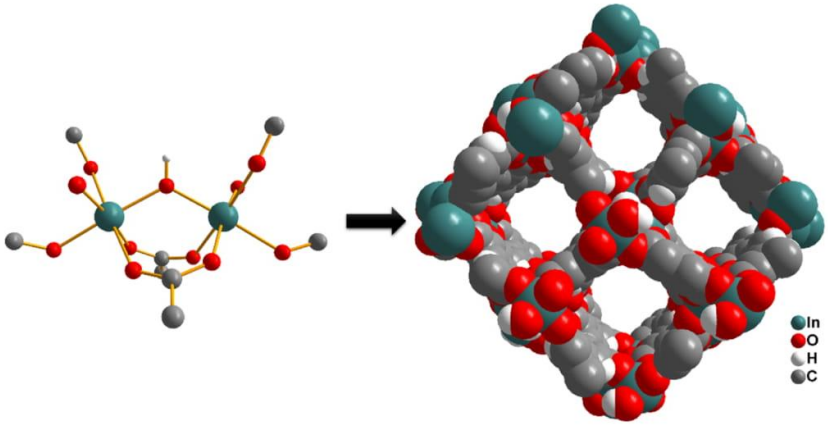

Figure 1. (Left) View of the binuclear building block of two metal ions oxygen octahedra bridged by a μ_2-hydroxyl group and (right) the crystal structure of InOF-1 along the *c*-axis showing channels of 7.50 Å pore dimension.

molecules (H_2O) in a mesoporous MOF material (MIL-100(Fe)), Llewellyn et al.[40] showed a 5-fold enhancement in the CO_2 capture. Conversely, Walton et al.[41−43] confined small amounts of H_2O within microporous MOF materials showing (i) augmented CO_2 capture performances of the corresponding MOFs and (ii) key role of the hydroxyl (−OH) functional groups in the interactions with H_2O to favor an efficient and ordered packing of the guests inside the pores. Our research groups have, systematically, confined small amounts of H_2O within microporous MOF materials to enhance their CO_2 capture capacities.[44,45] By taking the advantage of commensurate adsorption,[46] where the molecular size and shape of the guest molecule (e.g., H_2O) lead to a particular orientation that is compatible with the crystalline pore structure of the porous materials, these guest molecules can be accommodated more efficiently with a more ordered distribution.[47−49] Concisely, the hydroxyl (μ_2-OH) functional groups that are incorporated within the selected MOF materials (e.g., NOTT-400,[50] NOTT-401,[51] MIL-53(Al),[52] and InOF-1[53]) can "pin" H_2O via relatively strong hydrogen-bonding interactions.[54,55] In addition to H_2O, we investigated the confinement of different guest molecules, e.g., *N*,*N*-dimethylformamide (DMF),[56] EtOH,[57,58] MeOH,[59,60] and *i*-PrOH.[59] In this paper, we explore a complementary route via confining 1-propanol (*n*-PrOH) within the pores of InOF-1, an indium-based channel-like MOF of 7.50 Å pore dimension, with In(III) octahedral linked to four O-donors from four different $BPTC^{4-}$ ligands (H_4BPTC = biphenyl-3,3′,5,5′-tetracarboxylic acid)[61] and two μ_2-OH functional groups (Figure 1) to gain a full fundamental understanding of its solvent-controlled CO_2 adsorption performances. This joint experimental−computational study explores the influence of *n*-PrOH on the CO_2 adsorption performances of InOF-1 as compared to other solvents previously investigated. In addition to this, a special attention is dedicated to understand the adsorption and kinetic behaviors of *n*-PrOH in the pores of this MOF.

■ EXPERIMENTAL SECTION

Chemicals. Biphenyl-3,3′,5,5′-tetracarboxylic acid (H_4BPTC), indium nitrate ($In(NO_3)_3$), *N*,*N*-dimethylformamide (DMF), acetonitrile (CH_3CN), and nitric acid (65%, HNO_3) were acquired from Sigma-Aldrich and used as received.

Material Synthesis. InOF-1 = [$In_2(OH)_2$(BPTC), BPTC = biphenyl-3,3′,5,5′-tetracarboxylate] was synthesized following a previously reported recipe:[61] $In(NO_3)_3$ (156 mg, 0.40 mmol) and H_4BPTC (33 mg, 0.10 mmol) were mixed and dissolved in CH_3CN (5 mL), DMF (5 mL), and HNO_3 (65%, 0.2 mL) and finally sealed in a glass pressure tube. The clear solution was heated up at 358 K in an oil bath for 72 h. The pressure tube was cooled down to room temperature over a period of 12 h and the colorless crystalline product was separated by filtration, washed with DMF (5 mL), and dried in air, leading to a yield of 74% (based on ligand). Thermogravimetric analysis and powder X-ray diffraction were performed to control the nature and purity of the synthesized material (see the Supporting Information, Figures S1 and S2). The as-synthesized InOF-1 sample was acetone-exchanged and activated at 453 K for 2 h (either under 10^{-3} bar, static experiments, or with a constant flow of N_2 gas, dynamic experiments).

Adsorption Isotherms for N_2, CO_2, and *n*-PrOH. The N_2 sorption isotherms (77 K and up to 1 bar) were carried out on a Belsorp mini II analyzer under a high vacuum in a clean system with a diaphragm pumping system. The estimated Brunauer−Emmett−Teller area ($0.01 < P/P_0 < 0.04$) and pore volume were 1063 $m^2\ g^{-1}$ and 0.37 $cm^3\ g^{-1}$, respectively, consistent with previous findings for InOF-1.[60,61] Single-component CO_2 adsorption isotherms in the presence of *n*-PrOH up to 1 bar at 196 and 303 K were performed on a Belsorp HP (High Pressure) analyzer. Ultrapure grade (99.9995%) N_2 and CO_2 gases were purchased from Praxair. Single-component *n*-PrOH isotherms were recorded in a DVS Advantage 1 instrument from Surface Measurement System at 293 and 303 K.

Molecular Simulations. Grand canonical Monte Carlo (GCMC) simulations were carried out at 196 and 303 K to predict the adsorption isotherms for CO_2 as the single component and in mixture with 2 wt % *n*-PrOH in InOF-1 using a simulation box made of 8 (2 × 2 × 2) unit cells of the MOF (2 wt % *n*-PrOH corresponds to 6 molecules per simulation box). Additional MC simulations in the canonical (NVT) ensemble were performed at 303 K for *n*-PrOH as single component at low (1 molecule per simulation box), intermediate (6 and 24 molecules per simulation box), and high loading (47 molecules per simulation box corresponding to the experimental saturation capacity) to identify the most preferential sitting sites/

DOI: 10.1021/acs.jpcc.8b00215
J. Phys. Chem. C 2018, 122, 5566−5577

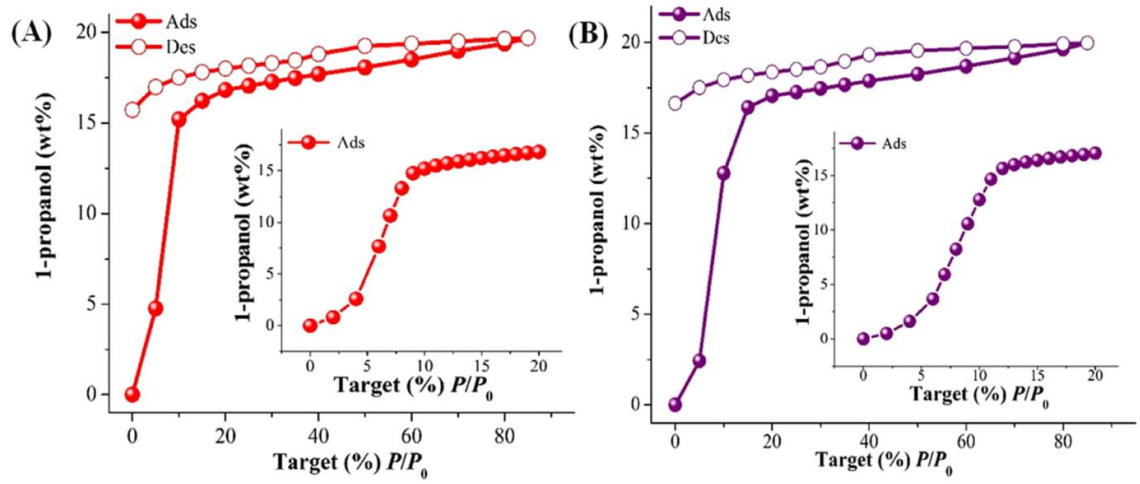

Figure 2. 1-Propanol (*n*-PrOH) adsorption isotherms of InOF-1 from % P/P_0 = 0−85 at 303 K (A) and 293 K (B). Solid and open circles correspond to the adsorption and desorption branches, respectively. The insets show the *n*-PrOH adsorption isotherms from % P/P_0 = 0−20.

interactions with the MOF pore wall, whereas the *n*-PrOH adsorption enthalpy at low coverage was simulated using the revised Widom's test particle insertion method.[62] The host−guest and guest−guest interactions were treated using a 12−6 Lennard-Jones (LJ) potential and Coulombic contributions. The EPM2[63] and united-atom TraPPE[64] models were selected for CO_2 and *n*-PrOH, respectively, whereas the atoms of the MOF framework were described by the LJ charged sites with parameters extracted from the generic force field UFF[65] and Dreiding[66] for the inorganic and organic nodes, respectively, and the partial charges taken from our previous study.[60] The Coulombic interactions were calculated using the Ewald summation technique with 10^{-6} precision and a 12 Å cutoff radius was considered to evaluate the short-range dispersion interactions. For each state point of these simulations, 2×10^7 Monte Carlo steps following 10^7 equilibration steps have been used. The analysis of the preferential interactions/locations of the guest species was performed through the plots of the radial distribution functions (RDFs) between different MOF/guest pairs and the center-of-mass distribution of the guests averaged over all of the configurations generated by MC simulations.

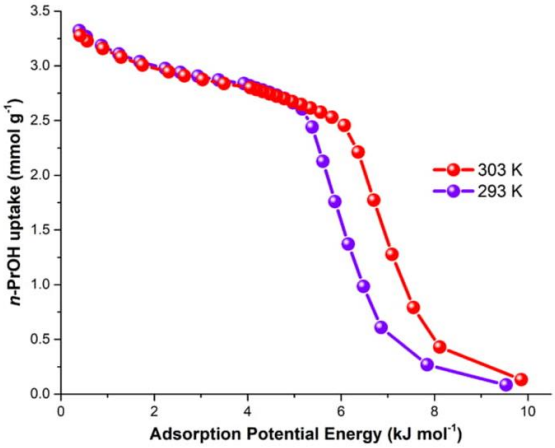

Figure 3. Plot of *n*-PrOH uptake as a function of ε (adsorption potential energy) at 293 K (violet) and 303 K (red).

■ RESULTS AND DISCUSSION

1-Propanol Sorption Studies. 1-Propanol (*n*-PrOH) sorption experiments were carried out on InOF-1. First, an acetone-exchanged InOF-1 sample was loaded into an analyzer cell (DVS Advantage 1 instrument) and activated at 453 K for 2 h. After the activation was completed, the analyzer cell (containing the activated InOF-1 sample) was cooled down to 303 K, and *n*-PrOH sorption isotherm was performed from % P/P_0 = 0−85 (Figure 2A). P_0 is the saturated vapor pressure of *n*-PrOH at the working temperature (2.02 and 3.86 kPa at 293 and 303 K, respectively). Figure 2A shows the *n*-PrOH isotherm at 303 K, where a steep increase in the *n*-PrOH uptake from % P/P_0 = 0 up to approximately % P/P_0 = 10 (15.20 *n*-PrOH wt %) was observed. From this pressure up to the end of the experiment (% P/P_0 = 85), the uptake slightly increases and reaches a quasi-plateau corresponding to a total amount of ∼19.70 *n*-PrOH wt %.

The sharp increase in the adsorption uptake of *n*-PrOH at low pressure indicates a relatively high affinity between InOF-1 and the guest molecule. In addition, the hysteresis loop observed along the desorption branch confirms this relatively strong host−guest interaction because this cannot be attributed to a "kinetic trapping" effect as suggested in other systems (see refs 67 and 68 for some representative examples). The so-called kinetic trap effect usually occurs when the pore dimensions of the adsorbent are close to the kinetic diameter (critical diameter) of the guest molecule. Here, as mentioned earlier, the pore dimension of InOF-1 (∼7.50 Å)[61] is significantly larger than the kinetic diameter of *n*-PrOH (4.7 Å).

The relatively high affinity between InOF-1 and *n*-PrOH was corroborated by the assessment of the isosteric heat of adsorption (ΔH = −53.30 kJ mol^{-1}, at low *n*-PrOH coverage), which was calculated from the adsorption isotherms measured at three different temperatures (303, 293, and 283 K) using the Clausius−Clapeyron equation (see the Supporting Information, Figures S3−S5).[69−71] This value is very well reproduced by the simulated adsorption enthalpy (−50.70 kJ mol^{-1}), and they both are higher than the molar enthalpy of vaporization for *n*-PrOH

DOI: 10.1021/acs.jpcc.8b00215
J. Phys. Chem. C 2018, 122, 5566−5577

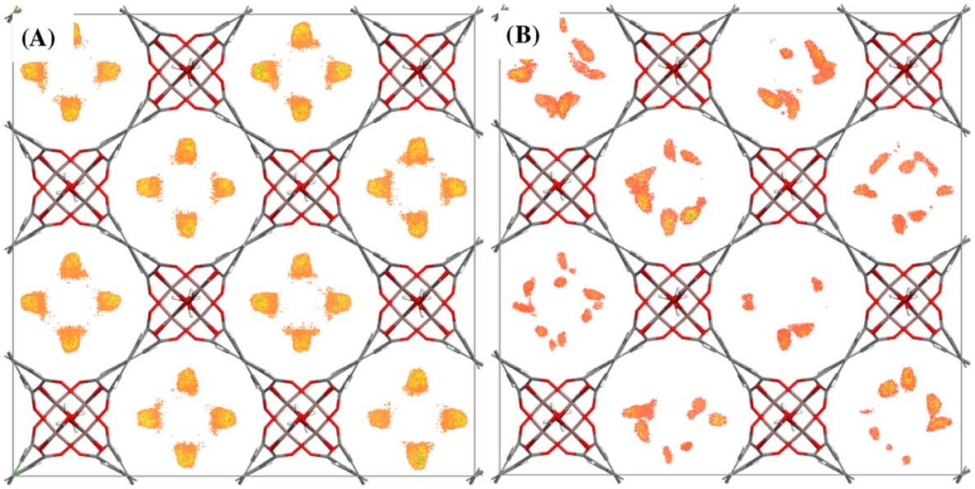

Figure 4. Center-of-mass distribution of *n*-PrOH in InOF-1 averaged over the Monte Carlo configurations obtained at 303 K for a loading of 1 guest molecule per simulation box (A) and 47 guest molecules per simulation box (B).

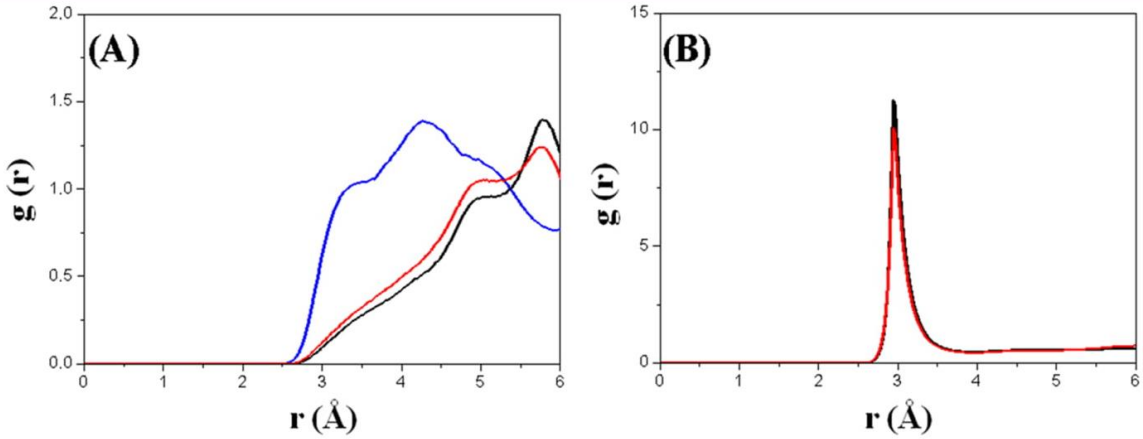

Figure 5. Radial distribution functions (RDFs) averaged over the Monte Carlo configurations at 303 K between (A) the oxygen atom of *n*-PrOH molecules and the oxygen atom of μ_2-OH of InOF-1 at low (1 guest molecule per simulation box, blue line), intermediate (6 guest molecules per simulation box, black line), and high loading (47 guest molecule per simulation box, red line). (B) The oxygen atoms of *n*-PrOH molecules at intermediate and high loadings.

(−47.45 kJ mol^{-1} at 298 K). It is worth mentioning that the so-obtained ΔH for *n*-PrOH is within the same range of value than those reported for the same molecule in μ_2-OH-containing MOFs.[72]

The *n*-PrOH sorption isotherm at 293 K is similar, as expected, to the adsorption−desorption experiment at 303 K (Figure 2B). The tiny dissimilarities are the total *n*-PrOH uptake (19.96 vs 19.68 *n*-PrOH wt %) and the hysteresis loop, which is slightly more pronounced. This behavior can be attributed to the fact that a lower operational temperature (293 K) might favor a more efficient packing of the *n*-PrOH guest molecules in the pores.

We further applied the Polanyi theory[73] to deeper understand the *n*-PrOH adsorption process within InOF-1. The adsorption potential energy (ε) represents the work required to change the states between *n*-PrOH in the adsorbed space to the adsorptive state. For one mole of an ideal gas, the potential theory establishes[73]

$$\varepsilon = \Delta F = \int_P^{P_0} V \, dP = RT \ln \frac{P_0}{P} \quad (1)$$

where ΔF is the free energy, V is the volume, and R is the universal gas constant equal to 8.3145 J K^{-1} mol^{-1}. The *n*-PrOH uptake as a function of the adsorption potential energy ε of InOF-1 (Figure 3) shows two distinct regions: first, at higher uptakes, the relationship is independent of the temperature and governed by the interactions between *n*-PrOH molecules themselves. This is related to a pore volume filling process, where the guest−guest interactions are dominant. The second region at low uptake shows a deviation between the curves at 293 and 303 K. This temperature-dependent profile is most probably associated with a relatively strong interaction between *n*-PrOH molecules and the pore wall of InOF-1.

To shed light on the adsorption behavior of *n*-PrOH at the microscopic scale, Monte Carlo simulations were performed at 303 K for different *n*-PrOH loading to identify their most

DOI: 10.1021/acs.jpcc.8b00215
J. Phys. Chem. C 2018, 122, 5566−5577

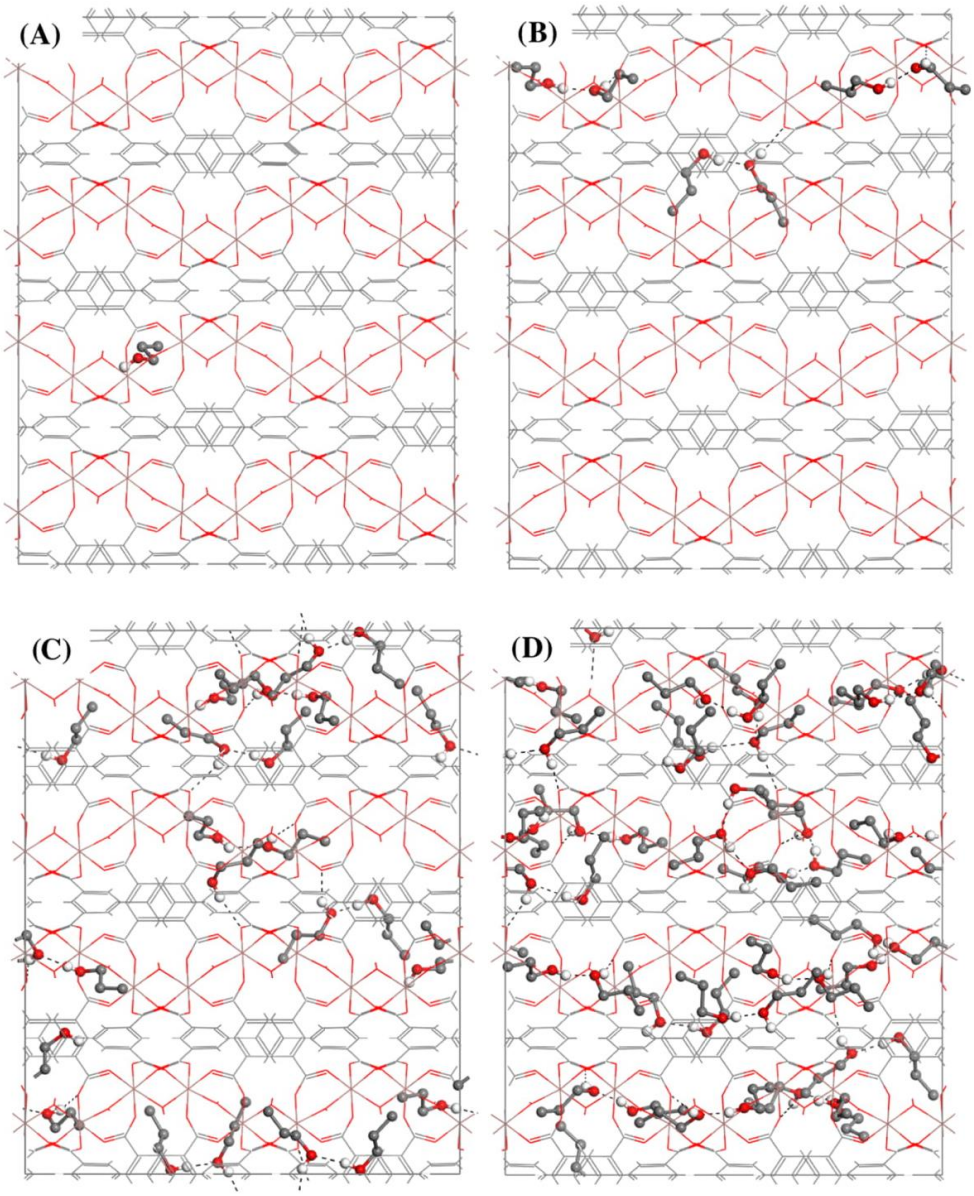

Figure 6. Monte Carlo configurations generated at 303 K showing different aggregation degrees of *n*-PrOH inside the pores of InOF-1 ((A), (B), (C), and (D) corresponding to 1, 6, 24, and 47 *n*-PrOH molecules per simulation box).

preferential adsorption sites and arrangements in the pores. The center-of-mass density map of *n*-PrOH plotted at low loading (Figure 4A) clearly supports a preferential interaction between *n*-PrOH and the μ_2-OH groups, as also evidenced by the presence of a shoulder at about 3.2 Å in the radial distribution function (RDF) for the corresponding $O_{\mu_2\text{-OH}}-O_{n\text{-PrOH}}$ pair (Figure 5A). When the loading increases, the location of *n*-PrOH is much less localized (Figure 4B) due to the *n*-PrOH−*n*-PrOH interactions as demonstrated by the sharp peak in the RDF for the corresponding $O_{n\text{-PrOH}}-O_{n\text{-PrOH}}$ pair (Figure 5B).

A further in-depth analysis of the MC configurations generated at different loadings revealed that when the loading increases, *n*-PrOH self-aggregates to first form dimers and then clusters (Figure 6).

Adsorption isobar experiments were further performed to characterize the sorption equilibrium phenomenon as a function of temperature.[74,75] Figure 7 shows that *n*-PrOH uptake increases with temperature. In zeolites and activated carbon materials it is characteristic to observe a decrease on gas and/or vapor uptake upon increasing temperature. However, for InOF-1 the n-PrOH adsorption isobar did not show such behavior.[76] This atypical behavior[75] of InOF-1 is most probably attributed to the need of overcoming a relatively high potential barrier to initiate the adsorption process. This is consistent with the

DOI: 10.1021/acs.jpcc.8b00215
J. Phys. Chem. C 2018, 122, 5566−5577

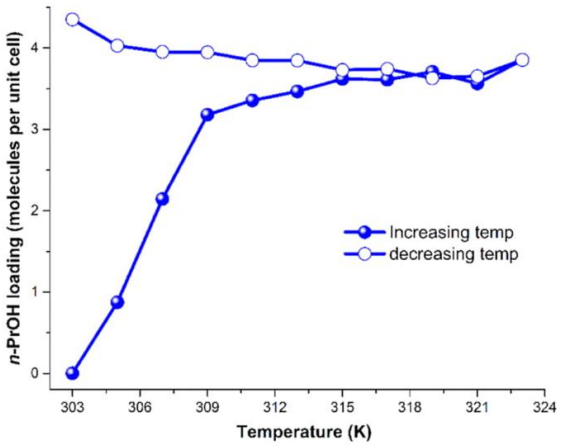

Figure 7. Sorption isobar plot of *n*-PrOH on InOF-1 at $0.02P/P_0$.

relatively strong interactions between *n*-PrOH molecules and the pore wall of InOF-1.

Experimental Kinetics Studies. The diffusion coefficient for *n*-PrOH, was further estimated by an uptake macroscopic method. Thus, a small amount of InOF-1 (~35 mg) was placed in a DVS Advantage 1 instrument to a step change in the partial pressure of *n*-PrOH (2, 5, 10, and 30% P/P_0), and adsorption was followed gravimetrically (Figure 8A). The diffusion coefficient was determined by matching the adsorption kinetic curves to the solution of diffusion equation for our boundary conditions. Considering (i) the small time regions, (ii) a diffusion coefficient independent of the position, (iii) a radial isothermal flux, and (iv) a constant *n*-PrOH concentration, the solution to the diffusion equation is equal to[77]

$$\frac{M_t}{M_\infty} \cong \frac{6}{r_p}\sqrt{\frac{\mathcal{D}t}{\pi}} - \frac{3\mathcal{D}t}{r_p^2} \text{ for } \frac{M_t}{M_\infty} < 0.8 \quad (2)$$

where M_t/M_∞ is the ratio of the amount adsorbed in time t and the mass adsorbed at infinite time (equilibrium adsorption mass), r_p is the experimental particle radius (see the Supporting Information), and $\mathcal{D}$ is the diffusion coefficient of *n*-PrOH. Due to the correlation between P/P_0 and the diffusion coefficient (Figure 8B), it is possible to refer this correlation as a transport diffusion phenomenon. In this diffusion process, the origin of the *n*-PrOH flux is due to the concentration gradient, i.e., the experimental boundary condition of the adsorbed molecules. In the low-pressure region, the main free path of the *n*-PrOH molecules considerably increases, so the probability of these molecules to collide with the pore walls is greater than that among themselves. This process is characterized by a very slow dynamic in the 0.02 and 0.05 P/P_0 region (see Figure 8B), where the diffusion coefficients were estimated to be 3.62×10^{-15} and 9.79×10^{-15} $cm^2\ s^{-1}$, respectively. These values are smaller in comparison to other MOFs (see the Supporting Information), which can be attributed to the strong host/guest interactions.

The diffusion regime within InOF-1 can be considered as configurational dynamics[77] due to the very slow mobility and strong concentration dependence (see Figure 8B). Thus, we can describe the dynamics of this guest as a combination of activated molecular jumps of *n*-PrOH between the preferential hydroxo functional groups and translational motions along the channel.

We can thus expect two mass transfer driving effects: (i) the preferential adsorption of *n*-PrOH molecules around the μ_2-OH groups of the InOF-1 and (ii) the cluster formation due to guest−guest interactions. Because the operational temperature is lower than the critical temperature of *n*-PrOH (T_c = 536.8 K), this leads to the possibility of dimers formation between the *n*-PrOH molecules as mentioned earlier based on our Monte Carlo predictions. Although it is expected that the aggregation of *n*-PrOH molecules induces a lower mobility than that of free *n*-PrOH molecules, the relatively small dimensions of the InOF-1 channels produce a constraint to the cluster formation. This constrain induces a high host−guest interaction and increases the main free path of the *n*-PrOH. For these reasons, we obtained an increase in the transport diffusion coefficients with P/P_0 (Figure 8B). Although an additional mass transfer resistance is probably due to the small crystallite dimensions of InOF-1 (see the Supporting Information, Figures S5−S6), we can expect a minimum intercrystalline resistance from the diffusion of adsorbed *n*-PrOH molecules through the particles because the observed particle size (see the Supporting Information, Figure S5) was relatively small.

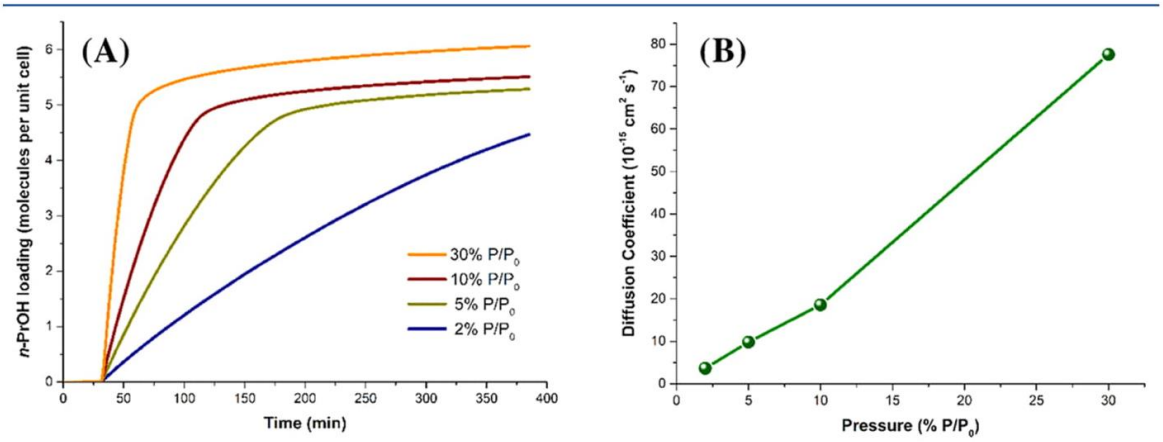

Figure 8. (A) Adsorption kinetics curves at different P/P_0 of *n*-PrOH in InOF-1. (B) Variation of transport diffusion coefficients of *n*-PrOH in InOF-1 at 303 K as a function of P/P_0 of *n*-PrOH.

DOI: 10.1021/acs.jpcc.8b00215
J. Phys. Chem. C 2018, 122, 5566−5577

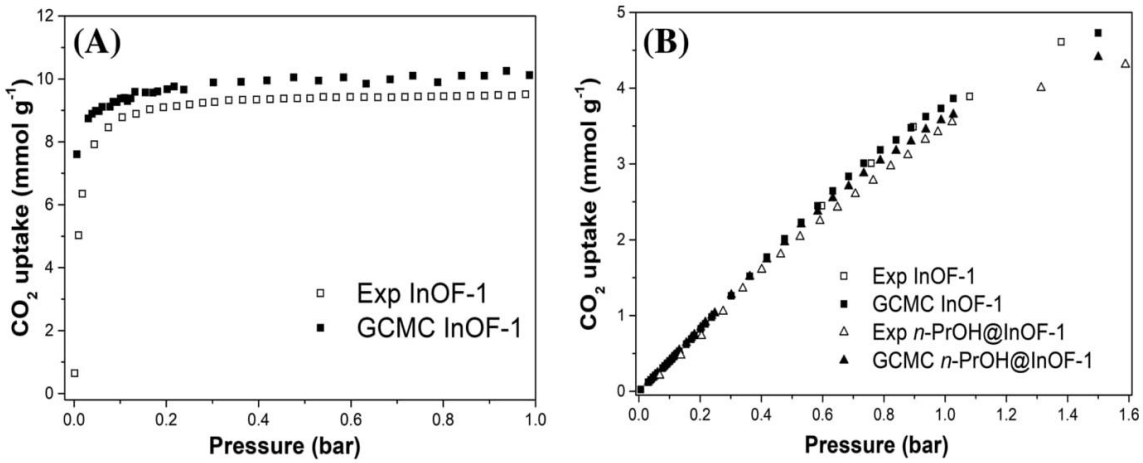

Figure 9. Experimental (empty symbols) and GCMC simulated (filled symbols) CO_2 adsorption isotherms of InOF-1 at 196 K (A) and of InOF-1 and *n*-PrOH@InOF-1 at 303 K (B).

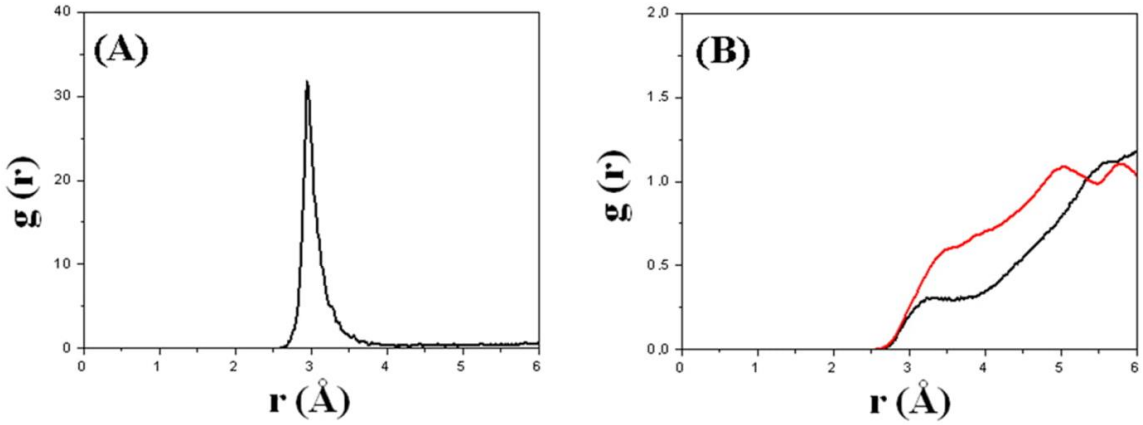

Figure 10. Radial distribution functions (RDFs) averaged over the grand canonical over the Monte Carlo configurations obtained at 303 K and 1 bar for the adsorption of CO_2 in *n*-PrOH@InOF-1 between (A) the oxygen atoms of *n*-PrOH molecules and (B) the oxygen atom of *n*-PrOH molecules (red line), the oxygen atom of CO_2 (black line), and the oxygen atom of μ_2-OH of InOF-1.

CO_2 Adsorptions Properties. An acetone-exchanged sample of InOF-1 was placed on a sample holder of a thermobalance Q500 HR and fully activated (453 K for 2 h and under a constant flow of N_2 of 60 mL min^{-1}), cooled down to 303 K (under N_2), and fully saturated with *n*-PrOH (see the Supporting Information). Later, by performing a specific activation protocol for this *n*-PrOH saturated sample (see the Supporting Information), the residual amount of confined *n*-PrOH was equal to 2 wt %. To confirm the reproducibility of this activation protocol for InOF-1, five different experiments were performed (see the Supporting Information), which corroborated the same residual (confined) amount of *n*-PrOH. Hereinafter, this sample will be referred to as *n*-PrOH@InOF-1.

First, to validate our modeling approach, we performed the CO_2 sorption experiments on a fully activated sample of InOF-1, which evidenced a total CO_2 uptake of 9.5 mmol g^{-1} (41.8 wt %) at 196 K (see Figure 9A). One observes a good agreement between the GCMC simulated and experimental adsorption isotherms, which validates the microscopic model and the force field parameters used to describe both the MOF structure and CO_2 and the MOF/CO_2 interactions. The CO_2 adsorption properties of *n*-PrOH@InOF-1 were then explored by performing static and isothermal CO_2 adsorption experiments at 303 K from 0 to 1 bar.

Static and dynamic (isothermal) CO_2 experiments on *n*-PrOH@InOF-1 samples did not show any improvement in the CO_2 capture (see Figure 9B and the Supporting Information, Figure S8). We reported earlier that by confining small amounts of H_2O,[53] EtOH,[57] MeOH,[60] and DMF[56] within the micropores of InOF-1, the CO_2 uptake was considerably enhanced. In this case, the confinement of *n*-PrOH did not augment the CO_2 adsorption properties of InOF-1. Interestingly, this trend was confirmed by our GCMC simulations at 303 K, which evidenced that the CO_2 amount adsorbed remains almost unchanged up to 0.6 bar and only slightly decreases up to 1 bar once InOF-1 is impregnated with 2 wt % of *n*-PrOH (see Figure 9B).

An in-depth analysis of the simulated preferential settings of *n*-PrOH and CO_2 in a mixture evidenced that in contrast to MeOH, which was predicted to form well-localized single adducts with the μ_2-OH groups, *n*-PrOH tends to preferentially

DOI: 10.1021/acs.jpcc.8b00215
J. Phys. Chem. C 2018, 122, 5566−5577

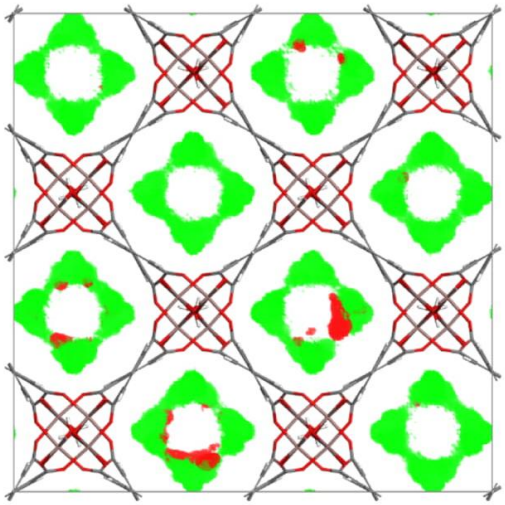

Figure 11. Center-of-mass distribution of CO_2 (green) and *n*-PrOH (red) in *n*-PrOH@InOF-1 averaged over the Monte Carlo configurations obtained at 303 K and 1 bar.

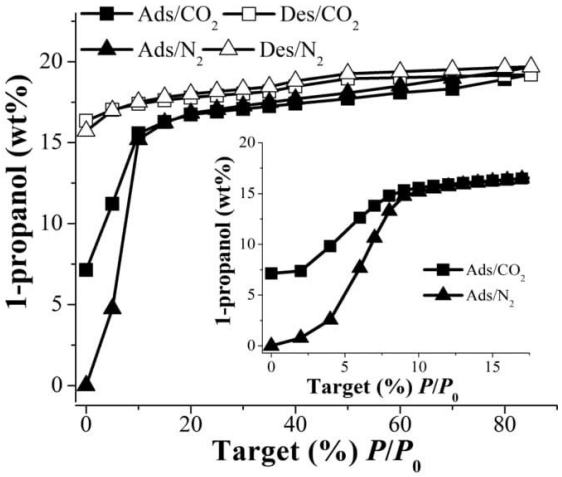

Figure 13. *n*-PrOH adsorption isotherms at 303 K of InOF-1 from % P/P_0 = 0−85 with two different gas carriers: solid triangles correspond to the N_2 carrier (100 mL min^{-1}); solid squares correspond to the CO_2 carrier (100 mL min^{-1}). Solid symbols represent adsorption and open symbols show desorption. The inset shows the *n*-PrOH adsorption isotherms (N_2 and CO_2 carriers) at 303 K from % P/P_0 = 0−18.

form clusters in a similar way than for the single-component adsorption of *n*-PrOH, leading to much weaker interactions between this guest and the μ_2-OH groups. This is illustrated in the RDFs plotted in Figure 10 at 1 bar and 303 K, which clearly show the presence of a sharp peak for the $O_{n\text{-PrOH}}-O_{n\text{-PrOH}}$ pair at a relatively short distance of 2.95 Å (Figure 10A), characteristic of a relatively strong hydrogen bond association of the *n*-PrOH molecules, whereas the probability of the *n*-PrOH/μ_2-OH interactions is much lower (Figure 10B).

The center-of-mass density map of both guest molecules *n*-PrOH@InOF-1 plotted in Figure 11 for the *n*-PrOH@InOF-1 system confirms a much less localized setting of *n*-PrOH as compared to MeOH and this leads to a much higher degree of blocking of the pores.

This is further illustrated in the van der Waals surface plot obtained for *n*-PrOH@InOF-1 (Figure 12), which evidences that the organization of *n*-PrOH in the pores leads to a significant decrease in the accessible porosity by creating an exclusion zone for the adsorption of CO_2. This scenario, which is consistent with a decrease in the CO_2 uptake for *n*-PrOH@InOF-1, strongly differs with that of MeOH@InOF-1, for which we previously evidenced a more localized distribution of the guest, leading to the formation of a lump at the vicinity of the μ_2-OH groups, thus increasing the confinement effect and an increase in the CO_2 uptake.[60]

Although the confinement of *n*-PrOH did not enhance the CO_2 capture properties of InOF-1, it provided us the curiosity of exploring a different alternative. Certainly, we have previously

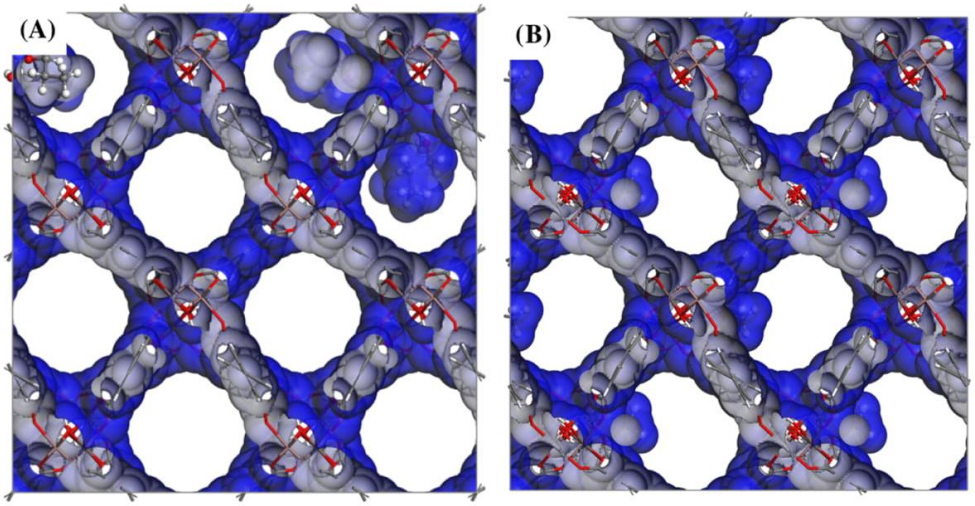

Figure 12. Comparison of the van der Waals surface plots of the *n*-PrOH@InOF-1 (A) and the MeOH@InOF-1 (B).

DOI: 10.1021/acs.jpcc.8b00215
J. Phys. Chem. C 2018, 122, 5566−5577

demonstrated that the confinement of small amounts of polar solvents in microporous MOFs can considerably enhance the CO_2 capture.[44,45] Conversely, when large amounts of these solvents were confined, the CO_2 capture properties were drastically diminished.[53,56,57] Up to this point, we have only investigated the confinement of polar solvents within InOF-1 to enhance the capture of CO_2. But what about the other way round? Indeed, the physicochemical properties in nanometer confining porous scales of condensed matter are considerably different to what is observed at the macroscopic level. Some recent investigations have demonstrated that the confinement of solvents in porous materials considerably enhances the gas solubility. This improvement is known as "oversolubility".[78−81] The oversolubility of confined solvents considerably modifies their viscosity, density, dielectric constant, and specific heat.[37,38] As an example, Garcia-Garibay[82] showed in a MOF material entitled UCLA-R3 that the confinement of DMF significantly enhanced the viscosity of this solvent up to 4 orders of magnitude.

Thus, we investigated the feasibility of confining CO_2 (within the micropores of InOF-1) to oversolubilize *n*-PrOH. First, we placed an acetone-exchanged sample of InOF-1 into an analyzer cell (DVS Advantage 1 instrument). This sample was fully activated (453 K for 2 h) and the temperature reduced to 303 K to carry out a *n*-PrOH adsorption isotherm from % P/P_0 = 0−85 (Figure 13). The particularity of this experiment was the use of CO_2 as a carrier (100 mL min^{-1}) of *n*-PrOH vapor. For comparison, we also reported the *n*-PrOH adsorption isotherm performed with N_2 (solid triangles) as a carrier (100 mL min^{-1}). Thus, the first interesting phenomenon occurs at the low loading of *n*-PrOH (from 0 to approximately 10% P/P_0), where the isotherms using either CO_2 or N_2 as carriers significantly differ (see the inset of Figure 13). The material is initially saturated with the corresponding gas carrier. When using N_2 at 303 K, it has been already demonstrated that InOF-1 did adsorb small amounts of this guest at 1 bar and, thus, the material can be considered as an empty InOF-1.[53] Conversely, when using CO_2, the total uptake at 303 K and 1 bar was approximately 7.1 wt % (see the inset of Figure 13).

This scenario where the micropores of InOF-1 are saturated by CO_2 can prove if confined CO_2 is able to further oversolubilize *n*-PrOH. Figure 13 shows that this adsorption isotherm significantly deviates with that obtained upon N_2 carrier in the range of relative pressure 0−10% P/P_0 (Figure 13). By adjusting the mathematical equations to both isotherms in this low domain of pressure, we can describe the adsorption behavior of InOF-1 in these two situations, and the slope of these equations can indicate the affinity of *n*-PrOH toward the material under different gas carriers (see the Supporting Information, Figure S9). Based on this, we observe a steeper slope and indeed a higher affinity for the adsorption of *n*-PrOH for the N_2-carrier InOF-1 (corresponding to the empty InOF-1) than for the CO_2-carrier InOF-1. This result suggests that when the micropores of InOF-1 are filled with CO_2 molecules, this makes more complex the adsorption of *n*-PrOH molecules. At a higher relative pressure from 10 to 85% P/P_0, the isotherms of N_2-carrier InOF-1 and CO_2-carrier InOF-1 (Figure 13) reached the same maximum amount of *n*-PrOH adsorbed, demonstrating that there is no oversolubility effect of *n*-PrOH in CO_2.

■ CONCLUSIONS

The exploration of the adsorption behavior of *n*-PrOH in the channel-like MOF InOF-1 evidences a relatively strong host−guest interaction that led to a sudden increase in the adsorption isotherm at low pressure, as well as the presence of a hysteresis loop during the desorption process. This experimental evidence was supported by macroscopic and microscopic modeling, typically Monte Carlo simulations revealed that *n*-PrOH preferentially sits around the μ_2-OH groups of InOF-1 at low alcohol loading, while *n*-PrOH self-aggregates to first form dimers and then clusters at higher loading. It was further shown that the adsorption kinetics of this guest is slow due to the confinement and the aggregation of the molecules.

From previous studies in this material, we have demonstrated the improvement in the CO_2 adsorption capacity by the formation of a well-localized single adducts between polar molecules and μ_2-OH groups ("bottleneck effect"). However, here the *n*-PrOH confinement did not enhance the CO_2 capture in InOF-1. This trend was also confirmed by GCMC simulations, which revealed that the preferential distribution of *n*-PrOH in mixture with CO_2 considerably decreases the accessibility of the porosity by creating an exclusion zone for the adsorption of CO_2. Finally, we explored the possibility of confining CO_2 to oversolubilize *n*-PrOH. Our results showed that when the micropores of InOF-1 are filled with CO_2, this inhibits the adsorption of *n*-PrOH, demonstrating the absence of oversolubility of *n*-PrOH in the presence of CO_2.

■ ASSOCIATED CONTENT

Supporting Information

The Supporting Information is available free of charge on the ACS Publications website at DOI: 10.1021/acs.jpcc.8b00215.

Thermogravimetric analysis, sample preparation and activation of InOF-1, isosteric enthalpy of adsorption calculations, scanning electron micrograph, affinity determination, and carbon dioxide diffusion are provided (PDF)

■ AUTHOR INFORMATION

Corresponding Authors

*E-mail: guillaume.maurin@univ-montp2.fr (G.M.).
*E-mail: argel@unam.mx. Fax: +52(55) 5622-4595 (I.A.I.).

ORCID

Elí Sánchez-González: 0000-0002-5440-329X
Guillaume Maurin: 0000-0002-2096-0450
Ilich A. Ibarra: 0000-0002-8573-8033

Author Contributions

⊥J.R.Á. and P.G.M.M. contributed equally to this work.

Author Contributions

The manuscript was written through contributions of all of the authors. All of the authors have given approval to the final version of the manuscript.

Notes

The authors declare no competing financial interest.

■ ACKNOWLEDGMENTS

The authors thank Dr. A. Tejeda-Cruz (powder X-ray; IIM-UNAM), CONACyT Mexico (1789), PAPIIT UNAM Mexico (IN101517) for financial support. E.G.-Z. thanks CONACyT (236879), Mexico for financial support. Thanks to U. Winnberg (ITAM) for scientific discussions. P.G.M.M. thanks the National Council of Technological and Scientific Development (CNPQ) for the scholarship. G.M. thanks the Institut Universitaire de France for its support. J.R.Á. acknowledges CONACyT Mexico

DOI: 10.1021/acs.jpcc.8b00215
J. Phys. Chem. C 2018, 122, 5566−5577

(Grant No. 276862). E.S.-G. thanks CONACyT Mexico (Grant No. 289042).

REFERENCES

(1) Hoskins, B. F.; Robson, R. Infinite Polymeric Frameworks Consisting of Three Dimensionally Linked Rod-Like Segments. *J. Am. Chem. Soc.* **1989**, *111*, 5962−5964.

(2) Kondo, M.; Yoshitomi, T.; Matsuzaka, H.; Kitagawa, S.; Seki, K. Three-Dimensional Framework with Channeling Cavities for Small Molecules: $\{[M_2(4,4'\text{-bpy})_3(NO_3)_4]\cdot xH_2O\}_n$ (M = Co, Ni, Zn). *Angew. Chem., Int. Ed.* **1997**, *36*, 1725−1727.

(3) Férey, G. Microporous Solids: From Organically Templated Inorganic Skeletons to Hybrid Frameworks... Ecumenism in Chemistry. *Chem. Mater.* **2001**, *13*, 3084−3098.

(4) Rowsell, J. L. C.; Yaghi, O. M. Metal−organic Frameworks: A New Class of Porous Materials. *Microporous Mesoporous Mater.* **2004**, *73*, 3−14.

(5) Férey, G. Hybrid Porous Solids: Past, Present, Future. *Chem. Soc. Rev.* **2008**, *37*, 191−214.

(6) Kuppler, R. J.; Timmons, D. J.; Fang, Q.-R.; Li, J.-R.; Makal, T. A.; Young, M. D.; Yuan, D.; Zhao, D.; Zhuang, W.; Zhou, H.-C. Potential Applications of Metal-Organic Frameworks. *Coord. Chem. Rev.* **2009**, *253*, 3042−3066.

(7) Czaja, A. U.; Trukhan, N.; Müller, U. Industrial Applications of Metal−organic Frameworks. *Chem. Soc. Rev.* **2009**, *38*, 1284−1293.

(8) Sánchez-Serratos, M.; Álvarez, J. R.; González-Zamora, E.; Ibarra, I. A. Porous Coordination Polymers (PCPs): New Platforms for Gas Storage. *J. Mex. Chem. Soc.* **2016**, *60*, 43−57.

(9) Maurin, G.; Serre, C.; Cooper, A.; Férey, G. The New Age of MOFs and of Their Porous-Related Solids. *Chem. Soc. Rev.* **2017**, *46*, 3104−3107.

(10) Li, S.-L.; Xu, Q. Metal−Organic Frameworks as Platforms for Clean Energy. *Energy Environ. Sci.* **2013**, *6*, 1656−1683.

(11) Bon, V. Metal-Organic Frameworks for Energy-Related Applications. *Curr. Opin. Green Sustainable Chem.* **2017**, *4*, 44−49.

(12) Dincă, M.; Long, J. R. Hydrogen Storage in Microporous Metal-Organic Frameworks with Exposed Metal Sites. *Angew. Chem., Int. Ed.* **2008**, *47*, 6766−6779.

(13) Thomas, K. M. Adsorption and Desorption of Hydrogen on Metal-Organic Framework Materials for Storage Applications: Comparison with Other Nanoporous Materials. *Dalton Trans.* **2009**, 1487−1505.

(14) Langmi, H. W.; Ren, J.; North, B.; Mathe, M.; Bessarabov, D. Hydrogen Storage in Metal-Organic Frameworks: A Review. *Electrochim. Acta* **2014**, *128*, 368−392.

(15) Hou, L.; Shi, W.-J.; Wang, Y.-Y.; Guo, Y.; Jin, C.; Shi, Q.-Z. A Rod Packing Microporous Metal-Organic Framework: Unprecedented *ukv* Topology, High Sorption Selectivity and Affinity for CO_2. *Chem. Commun.* **2011**, *47*, 5464−5466.

(16) Sumida, K.; Rogow, D. L.; Mason, J. A.; McDonald, T. M.; Bloch, E. D.; Herm, Z. R.; Bae, T.-H.; Long, J. R. Carbon Dioxide Capture in Metal−Organic Frameworks. *Chem. Rev.* **2012**, *112*, 724−781.

(17) Liu, J.; Thallapally, P. K.; McGrail, B. P.; Brown, D. R.; Liu, J. Progress in Adsorption-Based CO_2 Capture by Metal-Organic Frameworks. *Chem. Soc. Rev.* **2012**, *41*, 2308−2322.

(18) Wang, H.-H.; Hou, L.; Li, Y.-Z.; Jiang, C.-Y.; Wang, Y.-Y.; Zhu, Z. Porous MOF with Highly Efficient Selectivity and Chemical Conversion for CO_2. *ACS Appl. Mater. Interfaces* **2017**, *9*, 17969−17976.

(19) Li, X.-Y.; Li, Y.-Z.; Yang, Y.; Hou, L.; Wang, Y.-Y.; Zhu, Z. Efficient Light Hydrocarbon Separation and CO_2 Capture and Conversion in a Stable MOF with Oxalamide-Decorated Polar Tubes. *Chem. Commun.* **2017**, *53*, 12970−12973.

(20) Li, J.-R.; Kuppler, R. J.; Zhou, H.-C. Selective Gas Adsorption and Separation in Metal-Organic Frameworks. *Chem. Soc. Rev.* **2009**, *38*, 1477−1504.

(21) Li, J.-R.; Sculley, J.; Zhou, H.-C. Metal−Organic Frameworks for Separations. *Chem. Rev.* **2012**, *112*, 869−932.

(22) Adil, K.; Belmabkhout, Y.; Pillai, R. S.; Cadiau, A.; Bhatt, P. M.; Assen, A. H.; Maurin, G.; Eddaoudi, M. Gas/Vapour Separation Using Ultra-Microporous Metal-Organic Frameworks: Insights into the Structure/Separation Relationship. *Chem. Soc. Rev.* **2017**, *46*, 3402−3430.

(23) Cadiau, A.; Belmabkhout, Y.; Adil, K.; Bhatt, P. M.; Pillai, R. S.; Shkurenko, A.; Martineau-Corcos, C.; Maurin, G.; Eddaoudi, M. Hydrolytically Stable Fluorinated Metal-Organic Frameworks for Energy-Efficient Dehydration. *Science* **2017**, *356*, 731−735.

(24) Henninger, S. K.; Jeremias, F.; Kummer, H.; Janiak, C. MOFs for Use in Adsorption Heat Pump Processes. *Eur. J. Inorg. Chem.* **2012**, *2012*, 2625−2634.

(25) Cadiau, A.; Lee, J. S.; Damasceno Borges, D.; Fabry, P.; Devic, T.; Wharmby, M. T.; Martineau, C.; Foucher, D.; Taulelle, F.; Jun, C.-H.; et al. Design of Hydrophilic Metal Organic Framework Water Adsorbents for Heat Reallocation. *Adv. Mater.* **2015**, *27*, 4775−4780.

(26) Henninger, S. K.; Ernst, S. J.; Gordeeva, L.; Bendix, P.; Fröhlich, D.; Grekova, A. D.; Bonaccorsi, L.; Aristov, Y.; Jaenchen, J. New Materials for Adsorption Heat Transformation and Storage. *Renewable Energy* **2017**, *110*, 59−68.

(27) Jobic, H.; Rosenbach, N.; Ghoufi, A.; Kolokolov, D. I.; Yot, P. G.; Devic, T.; Serre, C.; Férey, G.; Maurin, G. Unusual Chain-Length Dependence of the Diffusion of *n*-Alkanes in the Metal-Organic Framework MIL-47(V): The Blowgun Effect. *Chem. - Eur. J.* **2010**, *16*, 10337−10341.

(28) Canepa, P.; Nijem, N.; Chabal, Y. J.; Thonhauser, T. Diffusion of Small Molecules in Metal Organic Framework Materials. *Phys. Rev. Lett.* **2013**, *110*, No. 026102.

(29) Yu, Z.; Deschamps, J.; Hamon, L.; Karikkethu Prabhakaran, P.; Pré, P. Modeling Hydrogen Diffusion in Hybrid Activated Carbon-MIL-101(Cr) Considering Temperature Variations and Surface Loading Changes. *Microporous Mesoporous Mater.* **2017**, *248*, 72−83.

(30) Ho, N. L.; Porcheron, F.; Pellenq, R. J.-M. Experimental and Molecular Simulation Investigation of Enhanced CO_2 Solubility in Hybrid Adsorbents. *Langmuir* **2010**, *26*, 13287−13296.

(31) Ho, L. N.; Perez Pellitero, J.; Porcheron, F.; Pellenq, R. J.-M. Enhanced CO_2 Solubility in Hybrid MCM-41: Molecular Simulations and Experiments. *Langmuir* **2011**, *27*, 8187−8197.

(32) Ho, N. L.; Perez-Pellitero, J.; Porcheron, F.; Pellenq, R. J.-M. Enhanced CO_2 Solubility in Hybrid Adsorbents: Optimization of Solid Support and Solvent Properties for CO_2 Capture. *J. Phys. Chem. C* **2012**, *116*, 3600−3607.

(33) Volino, F.; Gérard, H.; Miachon, S. Non-Extensive Visco-Elastic Theory II. First Experimental Tests of the Simple Theory with Rotational Modes. *Ann. Phys.* **1997**, *22*, 43−82.

(34) Morishige, K.; Shikimi, M. Adsorption Hysteresis and Pore Critical Temperature in a Single Cylindrical Pore. *J. Chem. Phys.* **1998**, *108*, 7821−7824.

(35) Kimball, M. O.; Gasparini, F. M. Universality and Finite-Size Scaling of the Specific Heat of $^3He-^4He$ Mixtures. *Phys. Rev. Lett.* **2005**, *95*, No. 165701.

(36) Zammit, U.; Marinelli, M.; Mercuri, F.; Paoloni, S. Effect of Confinement and Strain on the Specific Heat and Latent Heat over the Nematic−Isotropic Phase Transition of 8CB Liquid Crystal. *J. Phys. Chem. B* **2009**, *113*, 14315−14322.

(37) Hernández-Rojas, J.; Calvo, F.; Bretón, J.; Gomez Llorente, J. M. Confinement Effects on Water Clusters Inside Carbon Nanotubes. *J. Phys. Chem. C* **2012**, *116*, 17019−17028.

(38) Chakraborty, S.; Kumar, H.; Dasgupta, C.; Maiti, P. K. Confined Water: Structure, Dynamics, and Thermodynamics. *Acc. Chem. Res.* **2017**, *50*, 2139−2146.

(39) Jayasinghe, A. S.; Unruh, D. K.; Kral, A.; Libo, A.; Forbes, T. Z. Structural Features in Metal−Organic Nanotube Crystals That Influence Stability and Solvent Uptake. *Cryst. Growth Des.* **2015**, *15*, 4062−4070.

(40) Soubeyrand-Lenoir, E.; Vagner, C.; Yoon, J. W.; Bazin, P.; Ragon, F.; Hwang, Y. K.; Serre, C.; Chang, J. S.; Llewellyn, P. L. How Water Fosters a Remarkable 5-Fold Increase in Low-Pressure CO_2 Uptake within Mesoporous MIL-100(Fe). *J. Am. Chem. Soc.* **2012**, *134*, 10174−10181.

DOI: 10.1021/acs.jpcc.8b00215
J. Phys. Chem. C 2018, 122, 5566−5577

(41) Jasuja, H.; Huang, Y.; Walton, K. S. Adjusting the Stability of Metal−Organic Frameworks under Humid Conditions by Ligand Functionalization. *Langmuir* **2012**, *28*, 16874−16880.
(42) Jasuja, H.; Zang, J.; Sholl, D. S.; Walton, K. S. Rational Tuning of Water Vapor and CO_2 Adsorption in Highly Stable Zr-Based MOFs. *J. Phys. Chem. C* **2012**, *116*, 23526−23532.
(43) DeCoste, J. B.; Peterson, G. W.; Jasuja, H.; Glover, T. G.; Huang, Y.; Walton, K. S. Stability and Degradation Mechanisms of Metal−Organic Frameworks Containing the $Zr_6O_4(OH)_4$ Secondary Building Unit. *J. Mater. Chem. A* **2013**, *1*, 5642−5650.
(44) González-Zamora, E.; Ibarra, I. A. CO_2 Capture Under Humid Conditions in Metal−Organic Frameworks. *Mater. Chem. Front.* **2017**, *1*, 1471−1484.
(45) Benoit, V.; Chanut, N.; Pillai, R. S. S.; Benzaqui, M.; Beurroies, I.; Davautour-Vinot, S.; Serre, C.; Steunou, N.; Maurin, G.; Llewellyn, P. L. A Promising Metal-Organic Framework (MOF), MIL-96(Al) for CO_2 Separation Under Humid Conditions. *J. Mater. Chem. A* **2018**, 2081−2090.
(46) Wu, H.; Gong, Q.; Olson, D. H.; Li, J. Commensurate Adsorption of Hydrocarbons and Alcohols in Microporous Metal Organic Frameworks. *Chem. Rev.* **2012**, *112*, 836−868.
(47) Olson, D. H.; Kokotailo, G. T.; Lawton, S. L.; Meier, W. M. Crystal Structure and Structure-Related Properties of ZSM-5. *J. Phys. Chem.* **1981**, *85*, 2238−2243.
(48) Smit, B.; Maesen, T. L. M. Commensurate 'freezing' of Alkanes in the Channels of a Zeolite. *Nature* **1995**, *374*, 42−44.
(49) Olson, D.; Lan, A.; Seidel, J.; Li, K.; Li, J. Metal Organic Frameworks Showing Hydrocarbon Adsorption Properties Commensurate with Their Pore Structure. *Adsorption* **2010**, *16*, 559−565.
(50) Álvarez, J. R.; Peralta, R. A.; Balmaseda, J.; González-Zamora, E.; Ibarra, I. A. Water Adsorption Properties of a Sc(III) Porous Coordination Polymer for CO_2 Capture Applications. *Inorg. Chem. Front.* **2015**, *2*, 1080−1084.
(51) Sánchez-González, E.; Álvarez, J. R.; Peralta, R. A.; Campos-Reales-Pineda, A.; Tejeda-Cruz, A.; Lima, E.; Balmaseda, J.; González-Zamora, E.; Ibarra, I. A. Water Adsorption Properties of NOTT-401 and CO_2 Capture under Humid Conditions. *ACS Omega* **2016**, *1*, 305−310.
(52) Sánchez-Serratos, M.; Bayliss, P. A.; Peralta, R. A.; González-Zamora, E.; Lima, E.; Ibarra, I. A. CO_2 Capture in the Presence of Water Vapour in MIL-53(Al). *New J. Chem.* **2016**, *40*, 68−72.
(53) Peralta, R. A.; Alcántar-Vázquez, B.; Sánchez-Serratos, M.; González-Zamora, E.; Ibarra, I. A. Carbon Dioxide Capture in the Presence of Water Vapour in InOF-1. *Inorg. Chem. Front.* **2015**, *2*, 898−903.
(54) Burtch, N. C.; Jasuja, H.; Walton, K. S. Water Stability and Adsorption in Metal−Organic Frameworks. *Chem. Rev.* **2014**, *114*, 10575−10612.
(55) Cmarik, G. E.; Kim, M.; Cohen, S. M.; Walton, K. S. Tuning the Adsorption Properties of UiO-66 via Ligand Functionalization. *Langmuir* **2012**, *28*, 15606−15613.
(56) Sánchez-González, E.; González-Zamora, E.; Martínez-Otero, D.; Jancik, V.; Ibarra, I. A. Bottleneck Effect of *N*,*N*-Dimethylformamide in InOF-1: Increasing CO_2 Capture in Porous Coordination Polymers. *Inorg. Chem.* **2017**, *56*, 5863−5872.
(57) Peralta, R. A.; Campos-Reales-Pineda, A.; Pfeiffer, H.; Álvarez, J. R.; Zárate, J. A.; Balmaseda, J.; González-Zamora, E.; Martínez, A.; Martínez-Otero, D.; Jancik, V.; et al. CO_2 Capture Enhancement in InOF-1 via a Bottleneck Effect of Confined Ethanol. *Chem. Commun.* **2016**, *52*, 10273−10276.
(58) Álvarez, J. R.; Sánchez-Gonzalez, E.; Pérez, E.; Schneider-Revueltas, E.; Martínez, A.; Tejeda-Cruz, A.; Islas-Jácome, A.; González-Zamora, E.; Ibarra, I. A. Structure Stability of HKUST-1 towards Water and Ethanol and Their Effect on Its CO_2 Capture Properties. *Dalton Trans.* **2017**, *46*, 9192−9200.
(59) González-Martínez, G. A.; Zárate, J. A.; Martínez, A.; Sánchez-González, E.; Álvarez, J. R.; Lima, E.; González-Zamora, E.; Ibarra, I. A. Confinement of Alcohols to Enhance CO_2 Capture in MIL-53(Al). *RSC Adv.* **2017**, *7*, 24833−24840.
(60) Sánchez-González, E.; Mileo, P. G. M.; Álvarez, J. R.; González-Zamora, E.; Maurin, G.; Ibarra, I. A. Confined Methanol within InOF-1: CO_2 Capture Enhancement. *Dalton Trans.* **2017**, *46*, 15208−15215.
(61) Qian, J.; Jiang, F.; Yuan, D.; Wu, M.; Zhang, S.; Zhang, L.; Hong, M. Highly Selective Carbon Dioxide Adsorption in a Water-Stable Indium−Organic Framework Material. *Chem. Commun.* **2012**, *48*, 9696−9698.
(62) Vlugt, T. J. H.; García-Pérez, E.; Dubbeldam, D.; Ban, S.; Calero, S. Computing the Heat of Adsorption using Molecular Simulations: The Effect of Strong Coulombic Interactions. *J. Chem. Theory Comput.* **2008**, *4*, 1107−1118.
(63) Harris, J. G.; Yung, K. H. Carbon Dioxide's Liquid-Vapor Coexistence Curve and Critical Properties as Predicted by a Simple Molecular Model. *J. Phys. Chem.* **1995**, *99*, 12021−12024.
(64) Chen, B.; Potoff, J. L.; Siepmann, J. I. Monte Carlo Calculations for Alcohols and Their Mixtures with Alkanes. Transferable Potentials for Phase Equilibria. 5. United-Atom Description of Primary, Secondary, and Tertiary Alcohols. *J. Phys. Chem. B* **2001**, *105*, 3093−3104.
(65) Rappé, A. K.; Casewit, C. J.; Colwell, K. S.; Goddard, W. A., III; Skiff, W. M. UFF, a Full Periodic Table Force Field for Molecular Mechanics and Molecular Dynamics Simulations. *J. Am. Chem. Soc.* **1992**, *114*, 10024−10035.
(66) Mayo, S. L.; Olafson, B. D.; Goddard, W. A., III DREIDING: A Generic Force Field for Molecular Simulations. *J. Phys. Chem.* **1990**, *94*, 8897−8909.
(67) Zhao, X.; Xiao, B.; Fletcher, A. J.; Thomas, K. M.; Bradshaw, D.; Rosseinsky, M. J. Hysteretic Adsorption and Desorption of Hydrogen by Nanoporous Metal-Organic Frameworks. *Science* **2004**, *306*, 1012−1015.
(68) Choi, H. J.; Dincă, M.; Long, J. R. Broadly Hysteretic H_2 Adsorption in the Microporous Metal−Organic Framework Co(1,4-Benzenedipyrazolate). *J. Am. Chem. Soc.* **2008**, *130*, 7848−7850.
(69) Ibarra, I. A.; Yang, S.; Lin, X.; Blake, A. J.; Rizkallah, P. J.; Nowell, H.; Allan, D. R.; Champness, N. R.; Hubberstey, P.; Schröder, M. Highly Porous and Robust Scandium-Based Metal-Organic Frameworks for Hydrogen Storage. *Chem. Commun.* **2011**, *47*, 8304−8306.
(70) Nuñez, A. J.; Chang, M. S.; Ibarra, I. A.; Humphrey, S. M. Tuning the Host−Guest Interactions in a Phosphine Coordination Polymer through Different Types of Post-Synthetic Modification. *Inorg. Chem.* **2014**, *53*, 282−288.
(71) Ibarra, I. A.; MacE, A.; Yang, S.; Sun, J.; Lee, S.; Chang, J. S.; Laaksonen, A.; Schröder, M.; Zou, X. Adsorption Properties of MFM-400 and MFM-401 with CO_2 and Hydrocarbons: Selectivity Derived from Directed Supramolecular Interactions. *Inorg. Chem.* **2016**, *55*, 7219−7228.
(72) de Lange, M. F.; Verouden, K. J. F. M.; Vlugt, T. J. H.; Gascon, J.; Kapteijn, F. Adsorption-Driven Heat Pumps: The Potential of Metal−Organic Frameworks. *Chem. Rev.* **2015**, *115*, 12205−12250.
(73) Yang, R. T. *Gas Separation by Adsorption Processes*; Butterworth: Stoneham, 1987.
(74) Ibach, H. *Physics of Surfaces and Interfaces*; Springer: Berlin, 2006.
(75) Lemaire, E.; Decrette, A.; Bellat, J. P.; Simon, J. M.; Méthivier, A.; Jolimaître, E. Adsorption and Diffusion of Linear and Dibranched C_6 Paraffins in a ZSM-5 Zeolite. *Stud. Surf. Sci. Catal.* **2002**, *142*, 1571−1578.
(76) Tedds, S.; Walton, A.; Broom, D. P.; Book, D. Characterisation of Porous Hydrogen Storage Materials: Carbons, Zeolites, MOFs and PIMs. *Faraday Discuss.* **2011**, *151*, 75−94.
(77) Roque-Malherbe, R. M. A. *Adsorption and Diffusion in Nanoporous Materials*; CRC Press: Boca Raton, 2007.
(78) Miachon, S.; Syakaev, V. V.; Rakhmatullin, A.; Pera-Titus, M.; Caldarelli, S.; Dalmon, J. A. Higher Gas Solubility in Nanoliquids? *ChemPhysChem* **2008**, *9*, 78−82.
(79) Rakotovao, V.; Ammar, R.; Miachon, S.; Pera-Titus, M. Influence of the Mesoconfining Solid on Gas Oversolubility in Nanoliquids. *Chem. Phys. Lett.* **2010**, *485*, 299−303.
(80) Ho, L. N.; Clauzier, S.; Schuurman, Y.; Farrusseng, D.; Coasne, B. Gas Uptake in Solvents Confined in Mesopores: Adsorption versus Enhanced Solubility. *J. Phys. Chem. Lett.* **2013**, *4*, 2274−2278.

DOI: 10.1021/acs.jpcc.8b00215
J. Phys. Chem. C 2018, 122, 5566−5577

(81) Hu, Y.; Huang, L.; Zhao, S.; Liu, H.; Gubbins, K. E. Effect of Confinement in Nano-Porous Materials on the Solubility of a Supercritical Gas. *Mol. Phys.* **2016**, *114*, 3294−3306.
(82) Jiang, X.; Duan, H. B.; Khan, S. I.; Garcia-Garibay, M. A. Diffusion-Controlled Rotation of Triptycene in a Metal-Organic Framework (MOF) Sheds Light on the Viscosity of MOF-Confined Solvent. *ACS Cent. Sci.* **2016**, *2*, 608−613.

DOI: 10.1021/acs.jpcc.8b00215
J. Phys. Chem. C 2018, 122, 5566−5577

Journal of
Materials Chemistry A

PAPER

View Article Online
View Journal | View Issue

Check for updates

Cite this: *J. Mater. Chem. A*, 2018, **6**, 16900

Highly reversible sorption of H_2S and CO_2 by an environmentally friendly Mg-based MOF†

Elí Sánchez-González,‡[a] Paulo G. M. Mileo,‡[b] Mónica Sagastuy-Breña,[a] J. Raziel Álvarez,[a] Joseph E. Reynolds, III,[c] Aline Villarreal,[d] Aída Gutiérrez-Alejandre,[d] Jorge Ramírez,[d] Jorge Balmaseda,[a] Eduardo González-Zamora,[e] Guillaume Maurin,*[b] Simon M. Humphrey*[c] and Ilich A. Ibarra*[a]

Received 7th June 2018
Accepted 14th August 2018

DOI: 10.1039/c8ta05400b

rsc.li/materials-a

Mg-CUK-1, an ecologically friendly material synthesised in water is found to be a high-capacity, highly reversible adsorbent for acidic gases including H_2S and CO_2. Furthermore, Mg-CUK-1 is demonstrated to retain long-range crystallinity upon sorption cycling; its sorption performance is maintained over multiple cycles, even in the presence of high relative humidity (95%). Reversible H_2S adsorption by Mg-CUK-1 is rare among MOFs studied for this purpose to date. The joint experimental and computational studies presented here show that Mg-CUK-1 is an effective solid adsorbent for applications in the field of acid gas capture, an application that is highly relevant for the purification of many industrial gas streams.

Introduction

The development of new functional materials for environmental remediation applications such as the capture of toxic gaseous by-products is an important issue for many large-scale industrial processes.[1] There is a continuing need to improve the performance of such materials, as well as to determine ways to manufacture them using environmentally sensitive and realistically scalable methods. Metal–Organic Frameworks (MOFs) are a topical class of crystalline solids[2a] that can be synthesised with 3-D microporous structures, making them ideal candidates for toxic gas remediation applications.[2c,b] MOFs have already shown promise in the selective capture of a variety of pollutants of direct relevance to air quality, climate change, and human health in modern society.[3] By tailoring the chemical functionality of the MOF pore environment, the sorption behaviour of a given MOF can be fine-tuned for highly selective storage and/or separation of specific gaseous pollutants, including CO_2,[4] H_2S,[5] SO_2,[6] NH_3,[7] NO_x,[8] and volatile organic compounds (VOCs).[3,5a,9,10] Despite their potential utility, the vast majority of MOFs must be synthesised using harmful organic solvents (*e.g.*, *N*,*N'*-dimethylformamide, DMF),[11] in direct conflict with the primary motivations of using such materials to address environmental issues. Thus, the preparation of functional MOFs using green synthetic strategies, *i.e.*, using water as a solvent and non-toxic metal and organic components, is of timely importance.[12]

Hydrogen sulfide (H_2S) is a toxic species present in natural gas and biogas; the desulphurisation process of different gas streams, (*e.g.*, oil refineries) is a primary source of H_2S emissions.[5b] H_2S is a colourless gas, which is highly corrosive, flammable and poisonous to humans. At concentrations over 100 ppm, H_2S can be lethal since this molecule is quickly absorbed into the blood stream, limiting O_2 uptake at the cellular level.[13] Therefore, the selective capture of H_2S is essential in many industrial processes. However, only very few porous materials have been comprehensively studied in H_2S capture to date.[5a,b] Representative studies reported by De Weireld,[14] Zou[15] and Eddaoudi[16] indicate that most of the MOFs undergo decomposition upon adsorption of H_2S, while it is difficult for some others to desorb H_2S due to relatively strong host-guest binding in the pores either *via* strong physisorption or even by chemisorption. In this case, desorption of H_2S is therefore accompanied by an impractically large energy penalty.[17] The identification of new MOFs that are capable of highly cyclable H_2S sequestration under industrially feasible pressure-swing desorption conditions[18a] remains an important,

[a]*Laboratorio de Fisicoquímica y Reactividad de Superficies (LaFReS), Instituto de Investigaciones en Materiales, Universidad Nacional Autónoma de México, Circuito Exterior s/n, CU, Del. Coyoacán, 04510, Ciudad de México, Mexico. E-mail: argel@unam.mx; Fax: +52(55)-5622-4595*

[b]*Institut Charles Gerhardt Montpellier, UMR-5253, Université de Montpellier, CNRS, ENSCM, Place E. Bataillon, 34095 Montpellier cedex 05, France. E-mail: guillaume.maurin@univ-montp2.fr*

[c]*Department of Chemistry, The University of Texas at Austin, Welch Hall 2.204, 105 East 24th St., Stop A5300, Austin, Texas 78712-1224, USA. E-mail: smh@cm.utexas.edu*

[d]*UNICAT, Departamento de Ingeniería Química, Facultad de Química, Universidad Nacional Autónoma de México (UNAM), Coyoacán, Ciudad de México, Mexico*

[e]*Departamento de Química, Universidad Autónoma Metropolitana-Iztapalapa, San Rafael Atlixco 186, Col. Vicentina, Iztapalapa, C. P. 09340, Ciudad de México, Mexico*

† Electronic supplementary information (ESI) available: TGA data, PXRD data, SEM micrographs, breakthrough plots, DRIFT-FTIR spectra and molecular simulations. See DOI: 10.1039/c8ta05400b

‡ These authors contributed equally to this work.

This journal is © The Royal Society of Chemistry 2018

unsolved problem. CO_2 is another topical acidic gas that is commonly present alongside H_2S in industrial gas streams (*e.g.*, in natural gas and syngas).[18b] Thus, there is a critical need to design new adsorbents that can reversibly capture both H_2S and CO_2 with high capacities, under industrially realistic conditions.

Perhaps the most vitally important consideration regarding the potential use of MOFs as H_2S and CO_2 adsorbents under industrially realistic conditions relates to their stability in the presence of ambient moisture. Effluent gas streams that require scrubbing for H_2S and other toxic molecules commonly contain high relative humidity (% RH). This presents a major problem to MOFs that are susceptible to hydrolysis.[19a] As a potential solution to this problem, it has been shown that MOFs constructed using highly polarizing and high-valent metal cations (*e.g.*, Mg^{2+}, Cr^{3+}, Al^{3+}, Ti^{4+}, and Zr^{4+}) exhibit enhanced chemical stability in the presence of moisture.[19b,c] Other examples of water-stable MOFs include those recently reported by Dincă *et al.*,[19d] Eddaoudi *et al.*[19e] and Uribe-Romo *et al.*[19f] which showed outstanding water adsorption performances. Such hydrolytic stable MOFs could also be employed in a number of other critical large-scale applications, as adsorbents in heat-pumps and chillers,[20] in storage technologies for arid environments,[21] in low-cost water capture and abatement,[22] and in water-mediated proton conductors.[23]

In this contribution, we show that an environmentally friendly Mg(II)-based MOF can reversibly adsorb H_2S and CO_2 gases with high storage capacities, between 0 and 1 bar. The MOF, called Mg-CUK-1 [24] (CUK = Cambridge University–KRICT), originally reported by Humphrey and co-workers, can be prepared rapidly (30 min) in large quantities under microwave-assisted heating, using only water as solvent.[24] Mg-CUK-1 is also of relatively low toxicity, since it is only comprised of Mg(II) ions coordinated to the commercially available organic ligand 2,4-pyridinedicarboxylic acid (2,4-pdcH_2; C_5H_3N-2,4-CO_2H) and hydroxide ions (OH^-). Mg-CUK-1 was shown to be unusually thermally stable (>500 °C) owing to the presence of infinite chains of edge- and vertex-sharing $[Mg_3(\mu_3\text{-OH})]^{5+}$ triangles that support corrugated 1-D channels with a cross-sectional accessible opening of 8.1 × 10.6 Å (Fig. 1).[24] Based on the solvent of synthesis, Mg-CUK-1 is inherently water-stable and it can be rehydrated by direct immersion in aqueous media.

In this work, to test the viability of Mg-CUK-1 in the reversible capture of the acidic gases CO_2 and H_2S as well as the adsorption of CO_2 in the presence of relative humidity, we carefully characterised the following features: (i) the H_2O adsorption–desorption properties to evaluate the impact of humidity on the material; (ii) the CO_2 capture properties under controlled RH; and, (iii) the H_2S sequestration performance upon multiple cycles of adsorption and desorption. To support these application-focused experimental studies, we have employed advanced computational methods to gain fundamental insights into the mechanisms responsible for the observed reversible sorption of H_2S and CO_2 by Mg-CUK-1 under operating conditions.

Experimental section

Chemicals

2,4-Pyridinedicarboxylic acid (2,4-pdcH_2), magnesium nitrate hydrate ($Mg(NO_3)_2$) and potassium hydroxide (KOH) were purchased from Sigma-Aldrich and used as received. In-house deionised water was used to prepare all solutions. For sorption studies, ultra-high purity (99.9995+%) N_2 and CO_2 gases as well as H_2S (15.0% vol. diluted in N_2) were obtained from Praxair.

Material synthesis

Mg-CUK-1, $[Mg_3(\mu_3\text{-OH})_2(2,4\text{-pdc})_2]$, was synthesised following a previously reported procedure.[24] In brief, 2,4-pdc (170 mg; 1.0 mmol) was dissolved in H_2O (4.0 cm^3) by the addition of KOH (2.0 M; 2.0 cm^3), to which was added a second solution of $Mg(NO_3)_2$ hydrate (380 mg; 1.5 mmol) in H_2O (4 cm^3) to give a viscous, opaque white slurry. The mixture was transferred into a Teflon-lined Easy-Prep (CEM Corp.) vessel and heated at 573 K

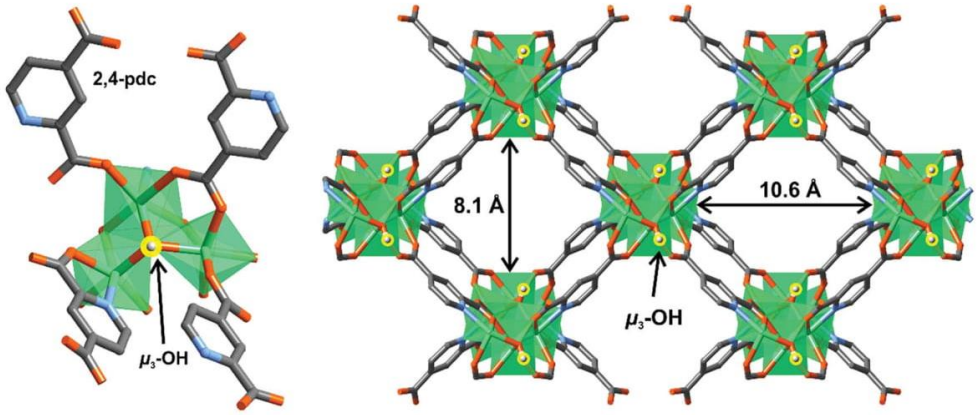

Fig. 1 (left) view of the trinuclear building block of three Mg(II) metal ions oxygen-octahedra bridged by a μ_3-hydroxyl group, through the *b* axis, and (right) the crystal structure of Mg-CUK-1 along *c* axis showing 8.1 × 10.6 Å channels.

for 35 min in a MARS microwave reactor (CEM Corp.). The reaction temperature was controlled using a fiber-optic sensor. After cooling to room temperature (15–30 min), the crystalline solid was purified by short (3 × 20 s) cycles of sonication in fresh H_2O, followed by decanting off the amorphous suspension. Large, colourless prismatic crystals were isolated (average yield = 124 mg, 42%). Thermogravimetric analysis (TGA) and powder X-ray diffraction (PXRD) of the sample were carried out to confirm phase purity of the Mg-CUK-1 (Fig. S1 and S2†).

Adsorption isotherms for CO_2 and H_2O

CO_2 sorption isotherms (196 K and up to 1 bar) were obtained on a Belsorp HP analyser under high vacuum in a clean system. The estimated BET area ($0.005 < P/P_0 < 0.15$) was equal to 604 $m^2\ g^{-1}$ with a corresponding pore volume of 0.22 $cm^3\ g^{-1}$ (Fig. S3†). These textural properties are in good agreement with the previously reported data.[24,25] This correlation confirmed the correct activation of the material. High pressure CO_2 adsorption isotherms (0–6 bar, and 303 K) were collected on a Belsorp HP analyser. H_2O vapour isotherms were recorded by a dynamic method, using air gas as carrier gas, using a DVS Advantage 1 instrument from Surface Measurement Systems (mass sensitivity: 0.1 μg, Relative Humidity (RH), accuracy: 0.5% RH, vapour pressure accuracy: 0.7% P/P_0. Mg-CUK-1 samples were activated at 373 K for 1 hour under flowing N_2. The H_2O uptake in weight percent (wt%) units was calculated as [(adsorbed amount of water)/(amount of adsorbent) × 100], consistent with established procedures. Water cycling experiments were performed at 303 K; for the adsorption phase, RH = 95% was maintained for 8 hours. Then, the sample was exposed to a dry air flow for a further 8 hours to ensure complete desorption prior to re-adsorption. CO_2 adsorption experiments at fixed RH were performed on the hydrated Mg-CUK-1 (13% RH). The material was activated as described above and then exposed to this constant RH for 1 hour. The water-impregnated sample was then transferred to a Belsorp HP analyser cell for the CO_2 adsorption.

H_2S adsorption–desorption studies

Dynamic adsorption experiments were performed at 303 K using a tubular quartz adsorber (internal diameter = 7 mm) filled with Mg-CUK-1 (Scheme S1†). Before beginning the H_2S adsorption tests, samples were activated *in situ* at 373 K for 1 hour with a constant flow of dry N_2 gas and then slowly cooled to 303 K. Samples were exposed to synthetic H_2S/N_2 gas mixtures at $p = 0.689$ bar with a total flow rate = 30 $cm^3\ min^{-1}$. A HP-5890 gas chromatograph equipped with an HP-PLOT 1 column and a TCD was used to analyse the H_2S concentration. Adsorption experiments at different H_2S concentrations were performed using 6, 9, 12 and 15% vol H_2S/N_2 gas mixtures (see ESI† for the corresponding breakthrough curves). The adsorption capacities were obtained by integrating the areas above the breakthrough curves. At the end of each experiment, the Mg-CUK-1 sample was exposed to a constant flow of dry N_2 gas, after which the sample was put through a Temperature Swing Reactivation (TSR) cycle (under N_2 gas) at 373 K using the standard protocol (*vide supra*) prior to changing the H_2S vol%.

DRIFTS

Diffuse-reflectance infrared Fourier-transform spectroscopy (DRIFTS) of Mg-CUK-1 samples in powder form were performed using a Nicolet 380 spectrometer (DTGS detector) with 4 cm^{-1} resolution equipped with a diffuse reflectance vacuum cell fitted with KBr windows. DRIFT spectra were collected on an activated Mg-CUK-1 sample (373 K for 1 h and ~6×10^{-3} torr), as well as of the same sample after exposure to five cycles of H_2S adsorption–desorption. To do so, the as-synthesised Mg-CUK-1 was first activated and exposed to H_2S using the protocol described above; after the fifth reactivation, the powder was transferred to a quartz cell and briefly evacuated at 6×10^{-3} torr at 303 K before collecting the spectrum.

Scanning electron microscopy (SEM)

Morphology studies were carried out on a JEOL Benchtop Scanning Electron Microscope, Neoscope JCM-6000 using secondary electrons at 15 kV current, in a high vacuum, and the processing of the images was carried out using Neoscope software.

Computational details

The crystal structure of Mg-CUK-1 [24] (CCDC-1024710) was geometry-optimised at the density functional theory (DFT) level while keeping the experimental cell parameter fixed. These calculations employed a PBE functional[26] combined with a double numeric basis set containing polarisation functions (DNP),[27a] as implemented in the Dmol[3] package. The same settings were employed to geometry-optimise the H_2S-loaded Mg-CUK-1 at different guest concentrations. The partial charges (Fig. S6†) for each atom in the MOF were derived from the REPEAT strategy (see ESI†).[27b]

The microscopic models of the three guest molecules were defined as follows: (i) CO_2 was described by the EPM2 model,[28] corresponding to a rigid and linear molecule representation with 3 charged Lennard-Jones (LJ) sites and a C=O bond length of 1.149 Å; (ii) H_2O was represented by the TIP4P/2005 model,[29] a four-site model, with a single LJ site centered in the oxygen position and three charged sites, two centered in the hydrogen positions and one located 0.1546 Å below the hydroxyl-O atom in the molecule bisector axis, having an O–H bond length of 0.9572 Å; and (iii) H_2S was represented by the model reported by Kamath *et al.* (2005),[30] *i.e.*, using a model with three charged LJ sites centered in the atomic position, a S–H bond of 1.34 Å, and an H–S–H bond angle = 92.5°. Regarding Mg-CUK-1, the 12-6 LJ parameters for the inorganic and organic moieties were taken from the UFF[31] and DREIDING[32] force fields, respectively. The Mg-CUK-1/guest interactions were described using a 6-12 LJ potential and a coulombic contribution. Following a general approach adopted in previous studies,[33] the H atom of the μ_3-OH groups interacts with the guests only through electrostatic interactions. The LJ crossed parameters between the MOF and the guests were calculated using the Lorentz–Berthelot mixing rules. The LJ contribution had a cut-off distance of 12 Å, while long-range electrostatic interactions were handled using the Ewald summation technique.[34]

 This journal is © The Royal Society of Chemistry 2018

Next, Grand Canonical Monte Carlo (GCMC) simulations were carried out at 303 K to predict the adsorption behaviour of Mg-CUK-1 for H_2O, CO_2 and H_2S as single components. A simulation box made of 12 unit cells (3 × 2 × 2) was employed, by fixing all atoms of the framework in their initial positions. The adsorption enthalpies at low coverage were calculated using the revised Widom test particle insertion method.[35] As a further step, in order to gain insight into the CO_2 adsorption properties of Mg-CUK-1 in the presence of H_2O, GCMC simulations were performed for a MOF framework loaded with 1 H_2O molecule per unit cell (corresponding to the experimental water loading at 13% RH). In the case of H_2S, additional MC simulations were performed in the canonical ensemble (NVT) to identify the preferential adsorption sites for the guest molecules at low, intermediate and high pressures. This exploration involved the analysis of the radial distribution functions plotted between different MOF/guest pairs calculated from hundreds of MC configurations.

Results and discussion

Fig. 2A shows the water adsorption isotherm of Mg-CUK-1 between 0 and 95% P/P_0, obtained at 303 K. The isotherm corresponds to a Type-V adsorption behaviour: at low pressure (0–20% P/P_0) H_2O adsorption is very gradual (Fig. 2A, inset); then, there is a rapid increase in H_2O uptake between 20 and 35% P/P_0; above 35% P/P_0 the uptake remained basically constant corresponding to a maximum H_2O uptake of 34.4 wt% (19.1 mmol g^{-1} at 95% P/P_0). This performance is among the best MOF performances reported so far (adsorption uptake ranging from 25 to 40 wt%)[21,36,37] for low-cost atmospheric water generation, although the material Co_2Cl_2BTDD has achieved 96 wt%.[38]

These experimental data obtained for Mg-CUK-1 are in excellent agreement with the GCMC-predicted adsorption isotherm (Fig. 2A; solid line), which provides a solid validation of the microscopic model (LJ parameters and charges) employed in our simulations for the CUK-1 framework. Such a shape of the adsorption isotherm is due to the mildly hydrophilic character of Mg-CUK-1, as confirmed by a moderate simulated adsorption enthalpy for H_2O at very low coverage (−42.6 kJ mol^{-1}) which then increases up to −60 kJ mol^{-1} above $P/P_0 = 0.20$. Furthermore, one can observe a well-pronounced hysteresis loop upon desorption (Fig. 2A; open circles) mostly caused by the presence of strong H-bonding between the H_2O adsorbates and the hydroxyl groups that are present once the pore starts to be filled.[39] Since the accessible pore openings of Mg-CUK-1 (8.1 × 10.6 Å)[24] are significantly larger than the kinetic diameter of H_2O (2.7 Å), the observed hysteresis is unlikely to be due to the `kinetic trapping' behaviour.[40–42]

To investigate the H_2O adsorption–desorption cyclability of Mg-CUK-1, a set of eight H_2O sorption isotherms were measured continuously on the same sample at 303 K (Fig. 2B). This study showed no apparent decrease in the total capacity, indicating that Mg-CUK-1 can be repeatedly fully dehydrated. Water was successfully removed between each cycle by simply flowing dry N_2 through the sample, without the need to use additional external heating. This method of regeneration is highly beneficial from an energy economy perspective. PXRD analysis of the same Mg-CUK-1 sample after eight adsorption–desorption experiments confirmed retention of bulk crystallinity (Fig. 3; blue data). Additionally, a CO_2 adsorption isotherm at 196 K was collected on the sample that underwent 8 water adsorption cycles to assess the retention of its surface area under this operating condition (Fig. S4†). The estimated BET area was equal to 586 m^2 g^{-1}, which is very similar to the value obtained for the pristine material (604 m^2 g^{-1}), *i.e.* only a 3% loss of surface area. This emphasises the exceptional stability of Mg-CUK-1 in the presence of water vapour.

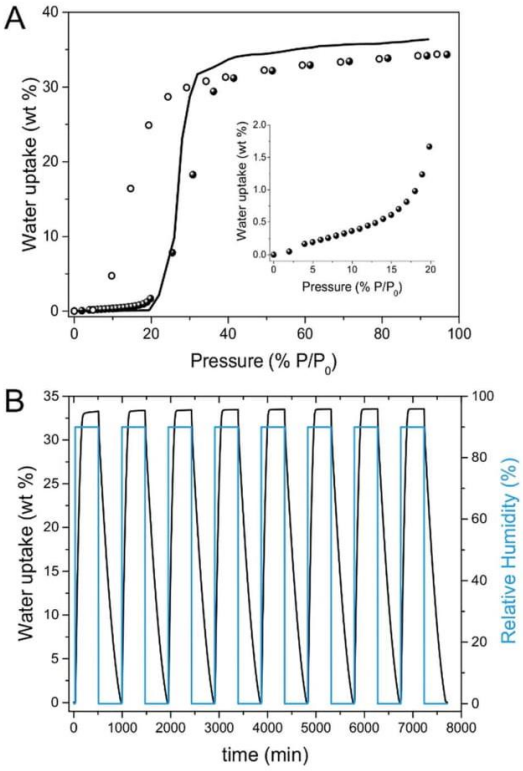

Fig. 2 (A) Water adsorption isotherm at 303 K of Mg-CUK-1 from % $P/P_0 = 0$ to 95. Solid and open circles represent experimental adsorption and desorption branches, respectively, and the solid line represents the GCMC simulations of the adsorption. The inset shows the H_2O adsorption isotherm at 303 K from % $P/P_0 = 0$ to 20. (B) Water adsorption–desorption uptake obtained from 8 cycles on Mg-CUK-1 at 303 K.

CO_2 adsorption studies

Next, isothermal CO_2 adsorption experiments were performed on Mg-CUK-1 as a function of % RH. A comparison of the CO_2 adsorption isotherms at 303 K obtained for the fully dehydrated Mg-CUK-1 *versus* Mg-CUK-1 rehydrated to 13% RH is presented in Fig. 4. The total adsorbed amount of CO_2 was very similar in both cases between 0 and 0.3 bar. At higher partial pressures,

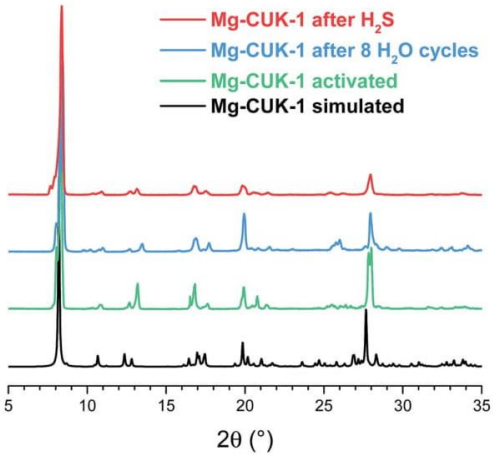

Fig. 3 PXRD patterns of the Mg-CUK-1 simulated pattern from the crystal structure (black line), activated sample (green line), after H_2O sorption cycling (blue line), and after H_2S sorption (red line).

there was a slight enhancement in CO_2 uptake for the sample at 13% RH, which reaches 3.37 mmol g^{-1} at 1 bar (*cf.* 3.03 mmol g^{-1} for the anhydrous sample at the same pressure; Fig. 4). At elevated pressures (2–6 bar of CO_2), the uptake difference remained approximately constant, reaching a total uptake of 5.89 and 6.39 mmol g^{-1} for the anhydrous and partially hydrated samples, respectively. Both experimental adsorption isotherms were very well reproduced by our GCMC simulations, from which we were also able to extract a relatively high CO_2 adsorption enthalpy of −35 and −36.5 kJ mol^{-1} for the anhydrous and partially hydrated samples, respectively; these magnitudes are in-line with what has been reported

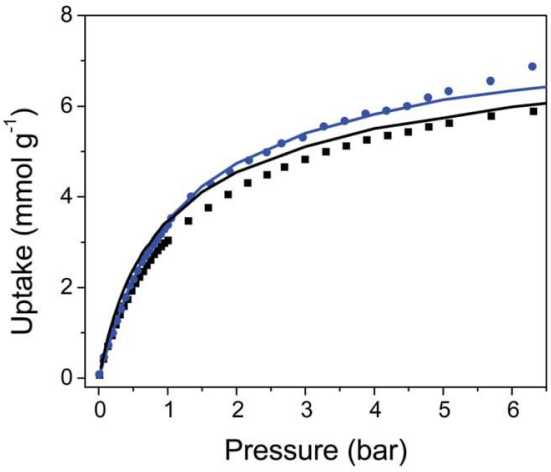

Fig. 4 Experimental CO_2 adsorption isotherm for fully dehydrated Mg-CUK-1 (black squares) and Mg-CUK-1 in the presence of 13% RH (blue circles); the corresponding simulated adsorption isotherms are represented as solid lines. All data are reported at 303 K.

experimentally and theoretically for other μ_3-OH-decorated MOFs that show specific interactions between these hydroxyl groups and the CO_2 molecules.[43] Interestingly, these results clearly demonstrated that the CO_2 adsorption properties of Mg-CUK-1 in terms of both CO_2 uptake and affinity are retained in the presence of humidity. This is in sharp contrast with some other CO_2 adsorbents which show a drastic drop of their performances in the presence of humidity.[44] We can assume that the adsorbed water binds to the μ_3-OH groups that create additional adsorption sites for CO_2 molecules and hence contribute to slightly enhance both CO_2 adsorption capacity and affinity as previously observed.[39] This renders Mg-CUK-1 as an attractive adsorbent to operate the capture of CO_2 under real conditions.

H_2S adsorption studies

The adsorption of H_2S by Mg-CUK-1 was assessed by a series of breakthrough experiments (see ESI†). The adsorption capacities obtained are shown in Fig. S8.† At the lowest H_2S concentration studied (6% vol H_2S), the gas uptake was equal to 1.41 mmol H_2S g^{-1}, which corresponds to 45.5 cm^3 H_2S g^{-1}. This value is approximately the same as the N_2 adsorption capacity observed at the same pressure.[24] The H_2S uptake by Mg-CUK-1 was approximately 40% higher than the performances of a number of well-studied MOFs (experiments with low H_2S concentrations *ca.* 1–6 kPa), including MIL-100(Fe),[15] MIL-53(Fe),[14] HKUST-1,[15] MOF-5,[15] MIL-53(Cr),[14] Ga-soc-MOF[16] and MIL-125(Ti),[45] all of which show H_2S capacities of approximately 1 mmol g^{-1}. Similar H_2S capacities have been reported for Zn-MOF-74 (1.64 mmol g^{-1})[15] and Cu(BDC)$(TED)_{0.5}$ (1.65 mmol g^{-1}).[15] Notably, of this entire list of MOFs, only MIL-53(Cr) and Ga-soc-MOF were able to reversibly adsorb H_2S in addition to Mg-CUK-1, which is an essential condition for their potential use in practical applications. In order to validate our experimental H_2S breakthrough adsorption results, we evaluated the H_2S adsorption performances of MOF-74, HKUST-1 and MIL-101(Cr), which were previously explored using H_2S breakthrough experiments. Our home-made experimental setup revealed very similar H_2S capture performances to the existing data (see Fig. S9 and Table S2†), demonstrating the reliability of our measurements.

Interestingly, Mg-CUK-1 also exhibited a two-fold increase in its H_2S adsorption capacity as the H_2S feed gas concentration was increased from 6 to 15% vol (reaching 3.1 mmol H_2S g^{-1}); 15 vol% is the maximum feed concentration that could be practically measured (equivalent to 0.1 bar of H_2S). In order to investigate the H_2S regeneration-capacity and the structural stability of Mg-CUK-1, cycling H_2S experiments at 15% vol H_2S were then performed on the same Mg-CUK-1 sample; this was accompanied by PXRD and scanning electron microscopy (SEM) analyses of the products to confirm retention of the crystal structure (Fig. 3 red data and Fig. S13†). First, cycling adsorption–desorption results showed that the H_2S adsorption capacity remained constant during the five adsorption–desorption cycles (3.2 ± 0.2 mmol g^{-1}, Fig. 5A), which suggests that H_2S was completely desorbed when the sample was re-activated. A comparison of the DRIFTS data for the as-synthesised Mg-CUK-1

 This journal is © The Royal Society of Chemistry 2018

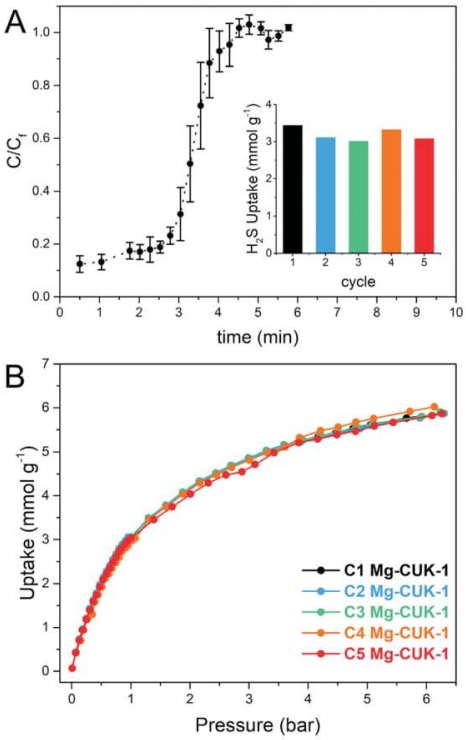

Fig. 5 (A) Breakthrough curves of H_2S adsorption by Mg-CUK-1 at 303 K using a feed H_2S concentration of 15% vol. The total H_2S/N_2 rate flow was 30 cm^3 min^{-1}. The inset shows the comparative adsorption capacities for each cycle. (B) The CO_2 adsorption isotherms for Mg-CUK-1 after H_2S sorption cycling, measured at 303 K and up to 6.5 bar.

and H_2S-cycled Mg-CUK-1 samples after re-activation (at 373 K for 1 h under flowing N_2 gas) led to spectra that were essentially indistinguishable (Fig. S15†), confirming that this re-activation condition allows full removal of H_2S. Since the adsorption capacity did not change after several adsorption–desorption cycles, Mg-CUK-1 appears to be very stable upon repeated H_2S exposure at room temperature. This is a desirable property for highly H_2S stable MOFs; previous studies of a series of related MIL materials (MIL-47(V), MIL-53(Al, Cr),[14] and MIL-125(Ti))[45] led to the hypothesis that H_2S stability is enhanced for MOFs that do not contain open metal sites, which cannot undergo M–SH_2 ligation. Additionally, CO_2 adsorption isotherms at 196 and 303 K were measured after each H_2S exposure, prior to a TSR step (Fig. S10†). These experiments confirmed the retention of both the surface area (592.4 ± 7.6 m^2 g^{-1}, Fig. S12†) and the CO_2 adsorption capacity of the Mg-CUK-1 (5.93 ± 0.12 mmol g^{-1}, Fig. 5B).

As shown previously, Mg-CUK-1 demonstrates a 'soft crystalline' behaviour, being flexible in the solid-state;[46] the pores relax upon H_2O adsorption/desorption.[24] Thus, we decided to investigate such a flexible behaviour when H_2S molecules are adsorbed in the pores of Mg-CUK-1. First, a fully dehydrated Mg-CUK-1 was saturated with H_2S (15% vol H_2S). Later, this sample was incompletely re-activated (by only flowing dry N_2 gas at 303 K for 10 minutes) to achieve a partially H_2S saturated sample. When PXRD experiments were performed, a shift in the position of the low-angle reflections (between 8 and 9° 2θ) was observed (see Fig. 6A). This suggested the flexible character of the structure upon H_2S adsorption/desorption, since the PXRD pattern (partially H_2S saturated) matched neither with the fully activated sample nor the water saturated sample (Fig. 6).

In order to gain a better understanding of the degree of flexibility of Mg-CUK-1 upon H_2S loading, the experimental PXRD patterns collected at different H_2S loadings were analysed

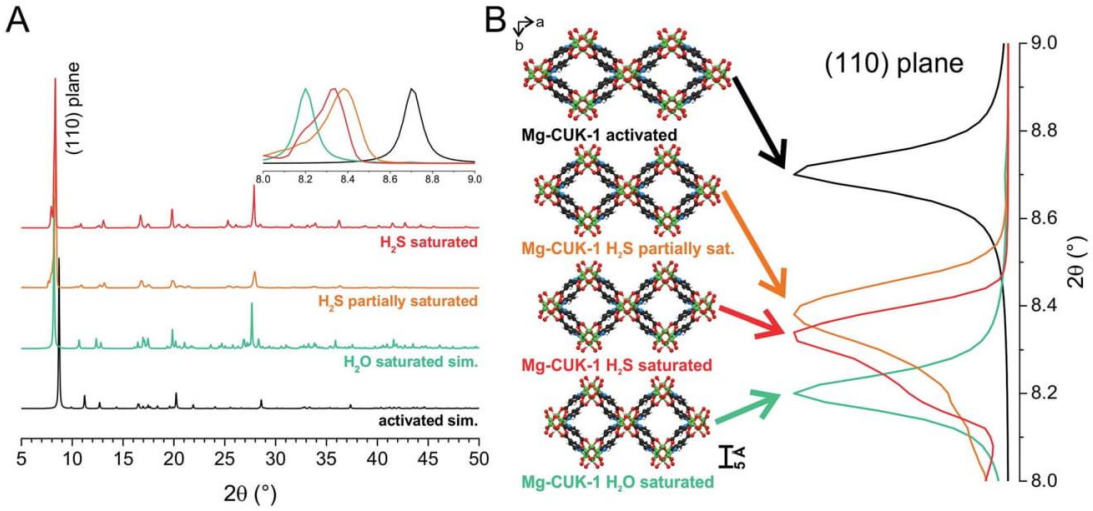

Fig. 6 (A) PXRD experiments on samples of Mg-CUK-1 with different molecule loadings. The inset shows the two-theta shifting of the 110 plane. (B) Representation of the Mg-CUK-1 cell deformation as a visual aid to explain the two-theta shifting.

molecular H_2S interactions tend to become slightly weaker (Fig. 7E and 8B). This finding can be attributed to a certain degree of interaction of the H_2S molecules with the MOF pore-wall, which acts to prevent H_2S condensation inside the micropores, as shown in MIL-47(V).[14b]

Conclusions

The environmentally friendly synthesised Mg-CUK-1 was demonstrated to be a highly robust MOF for acid gas remediation applications. Its chemical stability towards H_2O and H_2S (retention of the framework crystallinity and total gas adsorption capacity) was experimentally established by powder X-ray diffraction and adsorption–desorption (H_2O and H_2S) experimental cycles. Mg-CUK-1 is one of the best performing H_2S breakthrough materials showing remarkable H_2S reversibility, under temperature swing re-activation (TSR) conditions. Remarkably the CO_2 adsorption properties of Mg-CUK-1 remain unchanged upon exposure to H_2O and H_2S. Mg-CUK-1 was shown to exhibit a 'soft crystalline' behaviour when small amounts of H_2S are confined within its micropores. Molecular simulations complemented our experimental evidence and more importantly, provided us the preferential adsorption sites for the CO_2 and H_2S molecules inside the channels of Mg-CUK-1. Particularly, the calculated moderate adsorption enthalpy for H_2S (-23.3 kJ mol^{-1}) in comparison to exiting MOF materials confirmed the regeneration viability of Mg-CUK-1, under mild conditions. In summation, Mg-CUK-1 has been demonstrated to be an exceptional candidate for the capture of CO_2, even under humid conditions, as well as a remarkably stable adsorbent for the reversible sorption of H_2S.

Conflicts of interest

There are no conflicts of interest.

Acknowledgements

The authors thank Dr A. Tejeda-Cruz (powder X-ray; IIM-UNAM) for analytical assistance, U. Winnberg (ITAM) for scientific discussions and G. Ibarra-Winnberg for conceptualising the design of this contribution. Financial support for this work was provided by PAPIIT UNAM Mexico (IN101517), CONACyT under grant No. 1789 (I. A. I.), 236879 (E. G.-Z.), 276862 (J. R. Á.) and 289042 (E. S.-G.), a scholarship from the National Counsel of Technological and Scientific Development CNPQ (P. G. M. M.), the Institut Universitaire de France (G. M.), and the Welch Foundation (F-1738, J. E. R. & S. M. H.).

Notes and references

1 P. Kumar, K.-H. Kim, E. E. Kwon and J. E. Szulejko, *J. Mater. Chem. A*, 2016, **4**, 345.

2 (*a*) G. Maurin, C. Serre, A. Cooper, G. Férey and S. L. James, *Chem. Soc. Rev.*, 2017, **46**, 3104; (*b*) S. L. James, *Chem. Soc. Rev.*, 2003, **32**, 276; (*c*) J. L. C. Rowsell and O. M. Yaghi, *Microporous Mesoporous Mater.*, 2004, **73**, 3.

3 N. M. Padial, E. Quartapelle Procopio, C. Montoro, E. López, J. E. Oltra, V. Colombo, A. Maspero, N. Masciocchi, S. Galli, I. Senkovska, S. Kaskel, E. Barea and J. A. R. Navarro, *Angew. Chem., Int. Ed.*, 2013, **52**, 8290.

4 (*a*) K. Sumida, D. L. Rogow, J. A. Mason, T. M. McDonald, E. D. Bloch, Z. R. Herm, T. H. Bae and J. R. Long, *Chem. Rev.*, 2012, **112**, 724; (*b*) J. Liu, P. K. Thallapally, B. P. McGrail, D. R. Brown and J. Liu, *Chem. Soc. Rev.*, 2012, **41**, 2308; (*c*) D. Andirova, C. F. Cogswell, Y. Lei and S. Choi, *Microporous Mesoporous Mater.*, 2016, **219**, 276.

5 (*a*) E. Barea, C. Montoro and J. A. R. Navarro, *Chem. Soc. Rev.*, 2014, **43**, 5419; (*b*) M. S. Shah, M. Tsapatsis and J. I. Siepmann, *Chem. Rev.*, 2017, **117**, 9755.

6 (*a*) D. Britt, D. Tranchemontagne and O. M. Yaghi, *Proc. Natl. Acad. Sci. U. S. A.*, 2008, **105**, 11623; (*b*) C. A. Fernandez, P. K. Thallapally, R. K. Motkuri, S. K. Nune, J. C. Sumrak, J. Tian and J. Liu, *Cryst. Growth Des.*, 2010, **10**, 1037; (*c*) T. G. Glover, G. W. Peterson, B. J. Schindler, D. Britt and O. M. Yaghi, *Chem. Eng. Sci.*, 2011, **66**, 163; (*d*) S. Yang, J. Sun, A. J. Ramirez-Cuesta, S. K. Callear, W. I. F. David, D. P. Anderson, R. Newby, A. J. Blake, J. E. Parker, C. C. Tang and M. Schröder, *Nat. Chem.*, 2012, **4**, 887; (*e*) K. Tan, P. M. Canepa, W. Gong, J. Liu, D. H. Johnson, A. Dyevoich, P. K. Thallapally, T. Thonhauser, J. Li and Y. J. Chabal, *Chem. Mater.*, 2013, **25**, 4653; (*f*) W. P. Mounfield III, C. Han, S. H. Pang, U. Tumuluri, Y. Jiao, S. Bhattacharyya, M. R. Dutzer, S. Nair, Z. Wu, R. P. Lively, D. S. Sholl and K. S. Walton, *J. Phys. Chem. C*, 2016, **120**, 27230; (*g*) K. Tan, S. Zuluaga, H. Wang, P. M. Canepa, K. Soliman, J. Cure, J. Li, T. Thonhauser and Y. J. Chabal, *Chem. Mater.*, 2017, **29**, 4227; (*h*) S. Glomb, D. Woschko, G. Makhloufi and C. Janiak, *ACS Appl. Mater. Interfaces*, 2017, **9**, 37419.

7 (*a*) K. Vikrant, V. Kumar, K.-H. Kim and D. Kukkar, *J. Mater. Chem. A*, 2017, **5**, 22877; (*b*) J. F. Van Humbeck, T. M. McDonald, X. Jing, B. M. Wiers, G. Zhu and J. R. Long, *J. Am. Chem. Soc.*, 2014, **136**, 2432; (*c*) A. J. Rieth and M. Dincă, *J. Am. Chem. Soc.*, 2018, **140**, 3461.

8 (*a*) X. Zhang, W. Chen, W. Shi and P. Cheng, *J. Mater. Chem. A*, 2016, **4**, 16198; (*b*) A. C. McKinlay, B. Xiao, D. S. Wragg, P. S. Wheatley, I. L. Megson and R. E. Morris, *J. Am. Chem. Soc.*, 2008, **130**, 10440; (*c*) M. J. Ingleson, R. Heck, J. A. Gould and M. J. Rosseinsky, *Inorg. Chem.*, 2009, **48**, 9986; (*d*) A. C. McKinlay, J. F. Eubank, S. Wuttke, B. Xiao, P. S. Wheatley, P. Bazin, J.-C. Lavalley, M. Daturin, A. Vimont, G. De Weireld, P. Horcajada, C. Serre and R. E. Morris, *Chem. Mater.*, 2013, **25**, 1592; (*e*) S. R. Miller, E. Alvarez, L. Fradxourt, T. Devic, S. Wuttke, P. S. Wheatley, N. Steunou, C. Bonhomme, C. Gervais, D. Laurencin, R. E. Morris, A. Vimont, M. Daturi, P. Horcajada and C. Serre, *Chem. Commun.*, 2013, **49**, 7773; (*f*) R. R. Haikal, C. Hua, J. J. Perry IV, D. O'Nolan, I. Syed, A. Kumar, A. H. Chester, M. J. Zaworotko, M. H. Yacoub and M. H. Alkordi, *ACS Appl. Mater. Interfaces*, 2017, **9**, 43520.

9 (*a*) L. Zhou, X. Zhang and Y. Chen, *Mater. Lett.*, 2017, **197**, 224; (*b*) K. Vellingiri, J. E. Szulejko, P. Kumar, E. E. Kwon, K.-H. Kim, A. Deep, D. W. Boukhvalov and R. J. C. Brown, *Sci. Rep.*, 2016, **6**, 27813.

10 (*a*) J.-R. Li, R. J. Kuppler and H.-C. Zhou, *Chem. Soc. Rev.*, 2009, **38**, 1477; (*b*) D. Banerjee, A. J. Cairns, J. Liu, R. K. Motkuri, S. K. Nune, C. A. Fernandez, R. Krishna, D. M. Strachan and P. K. Thallapally, *Acc. Chem. Res.*, 2015, **48**, 211; (*c*) K. Adil, Y. Belmabkhout, R. S. Pillai, A. Cadiau, P. M. Bhatt, A. H. Assen, G. Maurin and M. Eddaoudi, *Chem. Soc. Rev.*, 2017, **46**, 3402.

11 R. P. Pohanish, *Sittig's Handbook of Toxic and Hazardous Chemicals and Carcinogens*, William Andrew Publishing, New York, USA, 2008.

12 P. T. Anastas and J. C. Warner, *Green Chemistry: Theory and Practice*, Oxford University Press, Oxford, U.K., 1998.

13 (*a*) R. O. Beauchamp, J. S. Bus, J. A. Popp, C. J. Boreiko, D. A. Andjelkovich and P. Leber, *CRC Crit. Rev. Toxicol.*, 1984, **13**, 25; (*b*) P. K. Moore and M. Whiteman, *Chemistry, Biochemistry and Pharmacology of Hydrogen Sulfide*, Handbook of Experimental Pharmacology, Springer International Publishing, Switzerland, 2015.

14 (*a*) L. Hamon, C. Serre, T. Devic, T. Loiseau, F. Millange, G. Férey and G. De Weireld, *J. Am. Chem. Soc.*, 2009, **131**, 8775; (*b*) L. Hamon, H. Leclerc, A. Ghoufi, L. Oliviero, A. Travert, J.-C. Lavalley, T. Devic, C. Serre, G. Férey, G. De Weireld, A. Vimont and G. Maurin, *J. Phys. Chem. C*, 2011, **115**, 2047.

15 J. Liu, Y. Wei, P. Li, Y. Zhao and R. Zou, *J. Phys. Chem. C*, 2017, **121**, 13249.

16 Y. Belmabkhout, R. S. Pillai, D. Alezi, O. Shekhah, P. M. Bhatt, Z. Chen, K. Adil, S. Vaesen, G. De Weireld, M. Pang, M. Suetin, A. J. Cairns, V. Solovyeva, A. Shkurenko, O. El Tall, G. Maurin and M. Eddaoudi, *J. Mater. Chem. A*, 2017, **5**, 3293.

17 R.-T. Yang, in *Gas Separation by Adsorption Processes*, Imperial College Press, London, 1997, ch. 2, pp. 9–26.

18 (*a*) G. Liu, V. Chernikova, Y. Liu, K. Zhang, Y. Belmabkhout, O. Shekhah, C. Zhang, S. Yi, M. Eddaoudi and W. J. Koros, *Nat. Mater.*, 2018, **17**, 283; (*b*) M. Tagliabue, D. Farrusseng, S. Valencia, S. Aguado, U. Ravon, C. Rizzo, A. Corma and C. Mirodatos, *Chem. Eng. J.*, 2009, **155**, 553.

19 (*a*) E. González-Zamora and I. A. Ibarra, *Mater. Chem. Front.*, 2017, **1**, 1471; (*b*) T. Devic and C. Serre, *Chem. Soc. Rev.*, 2014, **43**, 6097; (*c*) A. J. Howarth, Y. Liu, P. Li, Z. Li, T. C. Wang, J. T. Hupp and O. K. Farha, *Nat. Rev. Mater.*, 2016, **1**, 15018; (*d*) C. R. Wade, T. Corrales-Sanchez, T. C. Narayan and M. Dincă, *Energy Environ. Sci.*, 2013, **6**, 2172; (*e*) S. M. T. Abtab, D. Alezi, P. M. Bhatt, A. Shkurenko, Y. Belmabkhout, H. Aggarwal, Ł. J. Weselinski, N. Alsadun, U. Samin, M. N. Hedhili and M. Eddaoudi, *Chem*, 2018, **4**, 94; (*f*) M. W. Logan, J. D. Adamson, D. Le and F. J. Uribe-Romo, *ACS Appl. Mater. Interfaces*, 2017, **9**, 44529.

20 (*a*) F. Meunier, *Appl. Therm. Eng.*, 2013, **61**, 830; (*b*) C. Janiak and S. K. Henninger, *Chimia*, 2013, **67**, 419.

21 H. Furukawa, F. Gándara, Y.-B. Zhang, J. Jiang, W. L. Queen, M. R. Hudson and O. M. Yaghi, *J. Am. Chem. Soc.*, 2014, **136**, 4369.

22 (*a*) J. Liu, F. Zhang, X. Zou, G. Yu, N. Zhao, S. Fan and G. Zhu, *Chem. Commun.*, 2013, **49**, 7430; (*b*) M. Sánchez-Serratos, P. A. Bayliss, R. A. Peralta, E. González-Zamora, E. Lima and I. A. Ibarra, *New J. Chem.*, 2016, **40**, 68.

23 (*a*) M. Sadakiyo, T. Yamada and H. Kitagawa, *J. Am. Chem. Soc.*, 2014, **136**, 13166; (*b*) M. Sadakiyo, T. Yamada, K. Honda, H. Matsui and H. Kitagawa, *J. Am. Chem. Soc.*, 2014, **136**, 7701; (*c*) P. Ramaswamy, N. E. Wong and G. K. H. Shimizu, *Chem. Soc. Rev.*, 2014, **43**, 5913; (*d*) P. Ramaswamy, N. E. Wong, B. S. Gelfand and G. K. H. Shimiz, *J. Am. Chem. Soc.*, 2015, **137**, 7640; (*e*) S. S. Nagarkar, S. M. Unni, A. Sharma, S. Kurungot and S. K. Ghosh, *Angew. Chem.*, 2014, **126**, 2676; (*f*) D. D. Borges, S. Devautour-Vinot, H. Jobic, J. Ollivier, F. Nouar, R. Semino, T. Devic, C. Serre, F. Paesani and G. Maurin, *Angew. Chem., Int. Ed.*, 2016, **55**, 3919; (*g*) P. G. M. Mileo, S. Devautour-Vinot, G. Mouchaham, F. Faucher, A. Vimont and G. Maurin, *J. Phys. Chem. C*, 2016, **120**, 28374.

24 B. Saccoccia, N. W. Waggoner, K. Cho, S. Lee, D. Hong, M. Alisha, V. M. Lynch, J. Chang and S. M. Humphrey, *Angew. Chem., Int. Ed.*, 2015, **54**, 5394.

25 J. Woong, S. H. Jhung, Y. K. Hwang, S. M. Humphrey, P. T. Wood and J.-S. Chang, *Adv. Mater.*, 2007, **19**, 1830.

26 J. P. Perdew, K. Burke and M. Ernzerhof, *Phys. Rev. Lett.*, 1996, **77**, 3865.

27 (*a*) W. J. Hehre, J. A. Ditchfield and J. A. Pople, *J. Chem. Phys.*, 1972, **56**, 2257; (*b*) C. Campañá, B. Mussard and T. K. Woo, *J. Chem. Theory Comput.*, 2009, **5**, 2866.

28 J. G. Harris and K. H. Yung, *J. Phys. Chem.*, 1995, **99**, 12021.

29 J. L. F. Abascal and C. Vega, *J. Chem. Phys.*, 2005, **123**, 234505.

30 G. Kamath, N. Lubna and J. J. Potoff, *J. Chem. Phys.*, 2005, **123**, 124505.

31 A. K. Rappe, C. J. Casewit, K. S. Colwell, W. A. Goddard and W. M. Skiff, *J. Am. Chem. Soc.*, 1992, **114**, 10024.

32 S. L. Mayo, B. D. Olafson and W. A. Goddard, *J. Phys. Chem.*, 1990, **94**, 8897.

33 (*a*) E. Sánchez-González, P. G. M. Mileo, J. R. Álvarez, E. González-Zamora, G. Maurin and I. A. Ibarra, *Dalton Trans.*, 2017, **46**, 15208; (*b*) D. D. Borges, P. Normand, A. Permiakova, R. Babarao, N. Heymans, D. S. Galvão, C. Serre, G. De Weireld and G. Maurin, *J. Phys. Chem. C*, 2017, **121**, 26822.

34 (*a*) O. N. Osychenko, G. E. Astrakharchik and J. Boronat, *Mol. Phys.*, 2012, **110**, 227; (*b*) J. Kolafa and J. W. Perram, *Mol. Simul.*, 1992, **9**, 351.

35 T. J. H. Vlugt, E. García-Perez, D. Dubbeldam, S. Ban and S. Calero, *J. Chem. Theory Comput.*, 2008, **4**, 1107.

36 (*a*) H. Kim, S. R. Rao, E. A. Kapustin, L. Zhao, S. Yang, O. M. Yaghi and E. N. Wang, *Nat. Commun.*, 2018, **9**, 1191; (*b*) H. Kim, S. Yang, S. R. Rao, S. Narayanan, E. A. Kapustin, H. Furukawa, A. S. Umans, O. M. Yaghi and E. N. Wang, *Science*, 2017, **356**, 430.

37 A. Cadiau, J. S. Lee, D. D. Borges, P. Fabry, T. Devic, M. T. Wharmby, C. Martineau, D. Foucher, F. Taulelle, C.-H. Jun, Y. K. Hwang, N. Stock, M. F. De Lange, F. Kapteijn, J. Gascon, G. Maurin, J.-S. Chang and C. Serre, *Adv. Mater.*, 2015, **27**, 4775.

38 A. J. Rieth, S. Yang, E. N. Wang and M. Dincă, *ACS Cent. Sci.*, 2017, **3**, 668.

39 (*a*) J. R. Álvarez, R. A. Peralta, J. Balmaseda, E. González-Zamora and I. A. Ibarra, *Inorg. Chem. Front.*, 2015, **2**, 1080;

 This journal is © The Royal Society of Chemistry 2018

(*b*) E. Sánchez-González, J. R. Álvarez, R. A. Peralta, A. Campos-Reales-Pineda, A. Tejeda-Cruz, E. Lima, J. Balmaseda, E. González-Zamora and I. A. Ibarra, *ACS Omega*, 2016, **1**, 305; (*c*) R. A. Peralta, B. Alcántar-Vázquez, M. Sánchez-Serratos, E. González-Zamora and I. A. Ibarra, *Inorg. Chem. Front.*, 2015, **2**, 898.

40 (*a*) X. Zhao, B. Xiao, A. J. Fletcher, K. M. Thomas, D. Bradshaw and M. J. Rosseinsky, *Science*, 2004, **306**, 1012; (*b*) H. J. Choi, M. Dincă and J. R. Long, *J. Am. Chem. Soc.*, 2008, **130**, 7848.

41 R. Roque-Malherbe, *Microporous Mesoporous Mater.*, 2000, **41**, 227.

42 R. A. Peralta, A. Campos-Reales-Pineda, H. Pfeiffer, J. R. Álvarez, J. A. Zárate, J. Balmaseda, E. González-Zamora, A. Martínez, D. Martínez-Otero, V. Jancik and I. A. Ibarra, *Chem. Commun.*, 2016, **52**, 10273.

43 (*a*) D.-M. Chen, X.-P. Zhang, W. Shi and P. Cheng, *Inorg. Chem.*, 2015, **54**, 5512; (*b*) G. E. Cmarik, M. Kim, S. M. Cohen and K. S. Walton, *Langmuir*, 2012, **28**, 15606; (*c*) D.-M. Chen, N.-N. Zhang, C.-S. Liu, Z.-H. Jiang, X.-D. Wang and M. Du, *Inorg. Chem.*, 2017, **56**, 2379.

44 (*a*) A. C. Kizzie, A. G. Wong-Foy and A. J. Matzger, *Langmuir*, 2011, **27**, 6368; (*b*) J. A. Mason, T. M. McDonald, T.-H. Bae, J. E. Bachman, K. Sumida, J. J. Dutton, S. S. Kaye and J. R. Long, *J. Am. Chem. Soc.*, 2015, **137**, 4787; (*c*) V. Benoit, N. Chanut, R. S. Pillai, M. Benzaqui, I. Beurroies, S. Devautour-Vinot, C. Serre, N. Steunou, G. Maurin and P. L. Llewellyn, *J. Mater. Chem. A*, 2018, **6**, 2081.

45 S. Vaesen, V. Guillerm, Q. Yang, A. D. Wiersum, B. Marszalek, B. Gil, A. Vimont, M. Daturi, T. Devic, P. L. Llewellyn, C. Serre, G. Maurin and G. De Weireld, *Chem. Commun.*, 2013, **49**, 10082.

46 Y. Hijikata, S. Horike, D. Tanaka, J. Groll, M. Mizuno, J. Kim, M. Takata and S. Kitagawa, *Chem. Commun.*, 2011, **47**, 7632.

47 (*a*) Y. Laligant, A. Le Bail and F. Goutenoire, *J. Solid State Chem.*, 2001, **159**, 223; (*b*) T. Riosnel, J. Gonzalez-Platas and J. Rodriguez-Carvajal, *WinPlotr and FullProf suite program, version 3.00*, 2015, https://www.ill.eu/sites/fullprof, (june, 2017).

48 Q. Yang, S. Vaesen, M. Vishnuvarthan, F. Ragon, C. Serre, A. Vimont, M. Daturi, G. De Weireld and G. Maurin, *J. Mater. Chem.*, 2012, **22**, 10210.

This journal is © The Royal Society of Chemistry 2018

ROYAL SOCIETY OF CHEMISTRY View Article Online
DOI: 10.1039/C8DT03365J

Dalton Transactions

Paper

Humidity-induced CO_2 capture enhancement in Mg-CUK-1

Received 00th January 20xx,
Accepted 00th January 20xx

DOI: 10.1039/x0xx00000x

www.rsc.org/

Mónica Sagastuy-Breña,[a†] Paulo G. M. Mileo,[b†] Elí Sánchez-González, [a] Joseph E. Reynolds III,[c] Tamara Jurado-Vázquez,[a] Jorge Balmaseda,[a] Eduardo González-Zamora,[d] Sabine Devautour-Vinot,[b] Simon M. Humphrey,[c,*] Guillaume Maurin,[b,*] and Ilich A. Ibarra [a,*]

Kinetic CO_2 adsorption measurements in the water-stable and permanently microporous Metal-Organic Framework material, Mg-CUK-1, reveal a 1.8-fold increase in CO_2 capture from 4.6 wt% to 8.5 wt% in the presence of 18% relative humidity. Thermodynamic CO_2 uptake experiments corroborate this enhancement effect, while grand canonical Monte Carlo simulations also support the phenomenon of a humidity-induced increase in the CO_2 sorption capacity in Mg-CUK-1. Molecular simulations were implemented to gain insight into the microscopic adsorption mechanism responsible for the observed CO_2 sorption enhancement. These simulations indicate that the cause of increasing CO_2 adsorption enthalpy in the presence of H_2O is due to favorable intermolecular interactions between the co-adsorbates confined within the micropores of Mg-CUK-1.

Introduction

The continuous rising levels of atmospheric carbon dioxide that result from anthropogenic emissions is one of the greatest environmental threats to our civilization. For example, in 2017, worldwide CO_2 emissions from fossil fuel combustion increased by about 2% compared to the previous two years.[1] Such a dramatic increase contributed to the current total world record of 36.8 Gt of CO_2 in the atmosphere.[2] Undoubtedly, identifying ways to significantly reduce atmospheric CO_2 levels is critical to alleviate the threat that global warming presents to our planet. At present, national governments are working together on a world-wide basis to promote the development of new technologies for more efficient and effective CO_2 capture.[3] In addition to existing CO_2 capture technologies (*e.g.* alkanolamine aqueous solutions or alkaline solid adsorbents), potential replacement technologies are currently being investigated at a more fundamental level. This includes the use of porous solid-state materials for adsorption-desorption based processes.[4] Therefore, new porous materials with high chemical and thermal stability, high CO_2 adsorption capacities, and that enable fast CO_2 sorption kinetics and desorption under mild conditions, are actively being sought.[4,5]

Metal-organic frameworks (MOFs) are microporous materials whose topologies and sorption properties can be more broadly tuned than classical mesoporous materials (*e.g.*, zeolites). MOFs are therefore among the most promising candidates for CO_2 capture and separation: their sorption selectivity to CO_2 with respect to many other common gases (*e.g.,* CH_4 and N_2) can be controlled by modulation of the micropore topology and volume, and by chemical functionalization of the pore surfaces.[4-7] In addition to size-exclusion mechanisms that favor the selective capture of CO_2 over larger molecules, thermodynamic separations can also be envisaged, whereby sorption selectivity is enhanced by promoting certain host-guest (*i.e.*, MOF-adsorbate) interactions.

Current synthetic approaches to achieve these aims include the incorporation of open metal sites that provide sites of stronger molecular sorption,[7] and by functionalizing the organic linker with Lewis basic groups (*e.g.,* amines, alcohols).[7,8] More recently, intensive studies are also being made to enhance the CO_2 uptake of MOFs by exploiting the synergistic effects engendered by pre-confining small amounts of polar molecules in the pores.[9,10a,b] For example, Eddaoudi and co-workers[11] found that the recyclable and moisture-stable MOF SIFSIX-3-Cu could achieve enhanced CO_2 uptake and selectivity in highly diluted gas streams. Walton *et al.*[12] showed that pre-adsorption of sparing amounts of H_2O vapor inside MOFs decorated with hydroxyl functional groups in their pore walls led to a dramatic enhancement of the CO_2 uptake.[10c-e] In a similar fashion, we previously demonstrated that confinement of small amounts of H_2O in a series of MOFs consistently resulted in improved CO_2 capture properties.[13] Specifically, we found that μ_2-OH functional groups present in these MOFs (NOTT-400,[14] NOTT-401,[15] MIL-53(Al),[16]InOF-1[17]) can 'pin' H_2O adsorbates *via* relatively strong hydrogen bonding interactions.[13] These sequestered H_2O molecules are well ordered in the pore-structure of the MOFs and serve as preferential adsorption sites for subsequent CO_2 molecules.[18]

[a.] *Laboratorio de Fisicoquímica y Reactividad de Superficies (LaFReS), Instituto de Investigaciones en Materiales, Universidad Nacional Autónoma de México, Circuito Exterior S/N, CU, Coyoacán, 04510, Ciudad de México, México. E-mail: argel@unam.mx; Fax: +52(55) 5622-4595.*
[b.] *Institut Charles Gerhardt Montpellier, UMR-5253, Université de Montpellier, CNRS, ENSCM, Place E. Bataillon, 34095 Montpellier cedex 05, France. E-mail: guillaume.maurin@univ-montp2.fr*
[c.] *Department of Chemistry, The University of Texas at Austin, Welch Hall 2.204, 105 East 24th St., Stop A5300, Austin, Texas 78712-1224, United States. E-mail: smh@cm.utexas.edu*
[d.] *Departamento de Química, Universidad Autónoma Metropolitana-Iztapalapa, San Rafael Atlixco 186, Col. Vicentina, Iztapalapa, 09340, Ciudad de México, México.*
† These authors contributed equally to this work.
Electronic Supplementary Information (ESI) available: TGA data, PXRD data water adsorption isotherm and kinetic CO_2 experiments. See DOI: 10.1039/x0xx00000x

In related studies, Liu *et al.*[18d] and Chen *et al.*[18e] reported a moderate enhancement of the CO_2 uptake under 10% relative humidity (RH) in MIL-101 using experimental and computational approaches, respectively. Snurr and co-workers[18b] also provided a comprehensive simulation-analysis of the interactions between the quadrupole moment of gaseous CO_2 and the electric field created by H_2O molecules, which was the responsible for CO_2 capture enhancement in HKUST-1. Le Van *et al.*[18c] experimentally demonstrated that a small amount of H_2O increased the CO_2 adsorption capacity in the same material. More recently, Benoit *et al.* experimentally showed and corroborated by molecular simulations how the CO_2 adsorption properties were maintained for MIL-96(Al) under 10% RH.[10c]

In this context, our present study sought to explore the performance of an environmentally-friendly MOF Mg-CUK-1[19] (CUK for Cambridge University–KRICT), in the capture of CO_2 under humid conditions. This MOF can be considered to be environmentally-friendly, since it is rapidly synthesized under microwave-assisted heating in hydrothermal H_2O as the only solvent; it is also prepared using biologically-compatible Mg^{2+} ions and the low-toxicity organic ligand 2,4-pyridinedicarboxylate acid, $(NC_5H_3\text{-}2,4\text{-}(CO_2)_2)^{2-}$. The X-ray crystal structures of hydrated Mg-CUK-1 including positions of all H_2O solvates in the as-synthesized material, and its fully desolvated version have been published elsewhere; Mg-CUK-1 contains infinite 1-D rhombus-shaped microchannels with accessible openings of approximately 8.1 x 10.6 Å (see Figure 1).[19] The Mg^{2+} centres in Mg-CUK-1 are octahedrally-coordinated as $[Mg_3(\mu_3\text{-}OH)]^{5+}$ triangles, which are bridged into infinite edge- and vertex-sharing 1-D chains that provide the MOF with structural robustness, even when the microchannels are devoid of guests. Besides this application-orientated exploration, advanced experimental and computational tools have allowed us to gain an unprecedented fundamental insight into the adsorption and co-adsorption mechanisms between H_2O and CO_2 in this MOF, which in turn help to explain the origins of CO_2 capture enhancement.

Experimental Details

Chemicals.

2,4-Pyridinedicarboxlic acid, magnesium nitrate hydrate ($Mg(NO_3)_2$) and potassium hydroxide (KOH) were obtained from Sigma-Aldrich and used as received.

Material Synthesis.

Mg-CUK-1 = $[Mg_3(OH)_2(2,4\text{-}PDC)_2$, 2,4-PCD = 2,4-pyridinecarboxylate], was synthesized following the previously reported procedure:[19] 2,4-Pyridinedicarboxlic acid (170 mg, 1.0 mmol) and KOH (2.0 $_M$, 2.0 cm^3) in H_2O were added to a stirred solution of $Mg(NO_3)_2$, (380 mg, 1.5 mmol) in H_2O (3 cm^3) to give a viscous, opaque slurry mixture. The reaction mixture was placed inside a 23 cm^3 Teflon-lined autoclave and heated at 483 K for 15 h and then cooled down for 6 h. The crystalline solid was purified by short (3 x 20 s) cycles of sonication in fresh H_2O, followed by decanting of the slurry supernatant. Large, colorless prismatic crystals were isolated (average yield: 124 mg). TGA and PXRD were carried out and confirmed the nature of the synthesized material and its purity (see Fig. S1 and Fig. S2, respectively, SI).

Adsorption Isotherms for CO_2 and H_2O.

View Article Online DOI: 10.1039/C8DT02265J

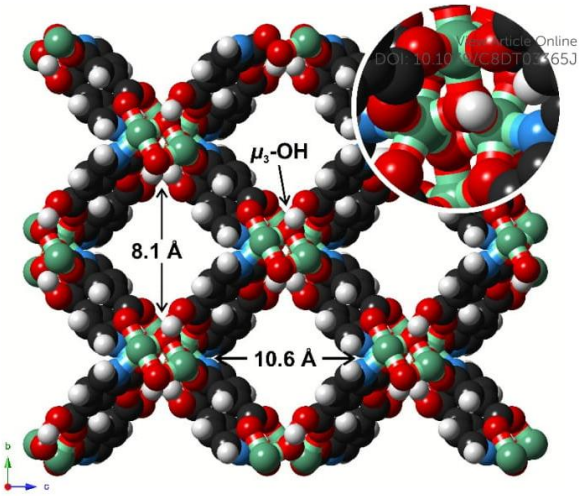

Figure 1. Crystal structure of Mg-CUK-1viewed along the crystallographic *a*-axis, depicting the one-dimensional channels with the hydroxyl group in the *b*-direction. Inset, trinuclear Mg(II) building block with the hydroxyl group pointing towards the center of the channel.

Ultra-pure grade (99.9995%) CO_2 gas was purchased from Praxair. CO_2 adsorption-desorption isotherms at 196 K and between 0–1 bar were carried out on a Belsorp mini II analyzer under high vacuum.

The calculated BET area ($0.01 < P/P_0 < 0.04$) based on the CO_2 adsorption data was approximately 600 $m^2\ g^{-1}$ with an associated pore volume of 0.21 $cm^3\ g^{-1}$. CO_2 adsorption–desorption isotherms were further collected up to 1 bar and 303 K on a Belsorp HP analyzer. An H_2O vapor isotherm was recorded by a dynamic method in a DVS Advantage 1 instrument from Surface Measurement System (mass sensitivity: 0.1 µg; RH accuracy: 0.5 %RH, vapor pressure accuracy: 0.7% P/P_0. Mg-CUK-1 samples were activated at 373 K for 1 hour under flowing N_2 prior to H_2O adsorption experiments.

Kinetic CO_2 Capture Experiments.

Kinetic CO_2 uptake experiments were carried out on a thermobalance (Q500 HR, from TA) at room temperature (303 K) with a constant CO_2 flow (60 mL min^{-1}). Prior to these measurements, Mg-CUK-1 samples were placed inside the thermobalance and activated by heating from room temperature to 373 K for 1h and under a N_2 gas flow. With the aid of a humidity-controlled thermobalance (Q5000 SA; TA Instruments), kinetic uptake experiments at 303 K with a constant CO_2 flow (60 mL min^{-1}) were carried out on activated Mg-CUK-1 samples. Additionally, these kinetic CO_2 experiments were performed in a DVS Advantage 1 instrument (Surface Measurement Systems; mass sensitivity: 0.1 µg, RH accuracy: 0.5% RH, vapor pressure accuracy: 0.7% P/P_0.

Computational Details.

The previously reported crystal structure of Mg-CUK-1[19] was geometry optimized at the density functional theory (DFT) level while keeping the experimental cell parameters fixed. Calculations employed the PBE functional[20] combined with a double numeric basis set containing polarization functions (DNP)[21] as implemented in the Dmol³ package. The partial charges of each atom of the Mg-

 This journal is © The Royal Society of Chemistry 20xx

View Article Online
DOI: 10.1039/C8DT03365J

CUK-1 framework were derived using an ESP fitting strategy applied to a cluster model cleaved from the periodic structure (see Supporting Information). The 12-6 Lennard-Jones (LJ) parameters of the inorganic and organic moieties of the MOF were taken from the UFF[24] and DREIDING[25] force fields, respectively. Following a general approach adopted in previous studies,[26] the hydrogen of the μ_3-OH groups interacts with the guests only through electrostatic interactions.

The microscopic models of the two guest molecules were defined as follows: (*i*) CO_2 was described by the EPM2 model[22] corresponding to 3 charged Lennard-Jones (LJ) sites centered on the atoms of CO_2; and, (*ii*) H_2O was represented by the TIP4P/2005 model[23] (a 4-site model) with 1 LJ site centered in the oxygen position and 3 charged sites, two centered in the hydrogen positions, and one situated 0.1546 Å below the oxygen atom in the molecular bisector axis.

Grand Canonical Monte Carlo (GCMC) simulations were carried out at 303 K to predict the adsorption behavior of Mg-CUK-1or H_2O and CO_2 as single components. We employed a simulation box comprised of 12-unit cells (3×2×2), maintaining all atoms of the framework in their initial positions. The Mg-CUK-1/guest interactions were described by a 6-12 LJ potential and a coulombic contribution. The LJ crossed parameters between the MOF and the guests were calculated using the Lorentz-Berthelot mixing rules. The LJ contribution was evaluated using a cut-off distance of 12 Å while the long-range electrostatic interactions were accounted for using the Ewald summation technique.[27] The adsorption enthalpies at low coverage for each single guest were calculated using the revised Widom's test particle insertion method.[28] As a further step, in order to gain insight on the CO_2 adsorption properties of Mg-CUK-1 in the presence of H_2O, GCMC were performed for a MOF loaded with 1 molecule of H_2O per unit cell, which gives a good approximation to the experimental uptake, *i.e.*, 0.99 wt% H_2O loading (corresponding to that of 18% RH).

Additional Monte Carlo simulations were performed in the NVT ensemble to identify the preferential adsorption sites for the guest molecules at low, intermediate and high pressures for the single components. This exploration implied the analysis of radial distribution functions plotted between different MOF/guest pairs, energy histograms and center of mass (COM) density plots calculated from hundreds of MC configurations.

Results and Discussion

Experimental

Figure 2 reports the H_2O adsorption isotherm for Mg-CUK-1 measured between % P/P_0 = 0–95 at 303 K. As previously reported,[29] Mg-CUK-1 proved to be water-stable and eight H_2O adsorption-desorption cycles were also performed at 303 K, (see Fig. S3, SI). In addition, PXRD experiments confirmed the water-stability (see Fig. S4, SI) of Mg-CUK-1 after the H_2O sorption isotherm (*vide infra*).

The experimental static CO_2 adsorption isotherm (thermodynamic analysis, see Figure 3) first demonstrated an enhancement of the CO_2 capture in the presence of 18% RH. Following this observation, we decided to further investigate the kinetic evolution of CO_2 uptake (CO_2 capture *versus* time) as a function of H_2O content RH over the range 5– 20% RH experimentally. These RH values were selected based on the H_2O adsorption isotherm (see Fig. 2), since they are located in the lower H_2O uptake region, where the uptake slowly increases with increasing % P/P_0. With this in mind, kinetic CO_2 experiments were

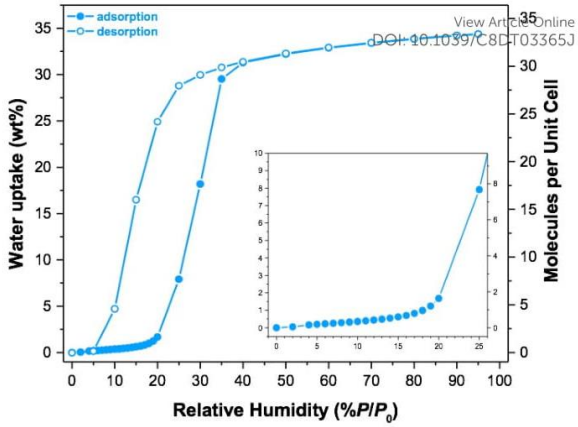

Figure 2. Water adsorption isotherm of Mg-CUK-1 at 303 K from %P/P_0 = 0 to 95, the inset shows water loadings range from %P/P_0 = 0 to 25.

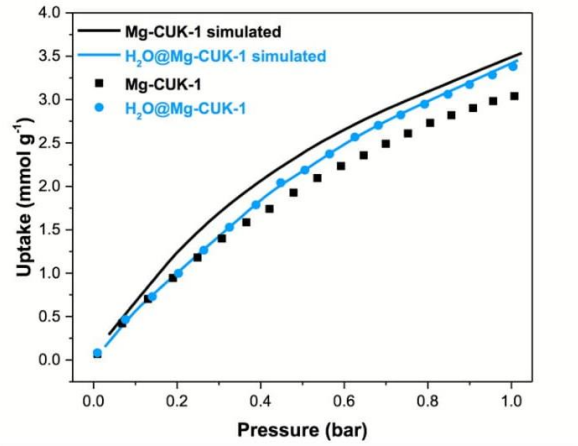

Figure 3. CO_2 adsorption isotherm at 303 K for fully dehydrated Mg-CUK-1 (black squares) and Mg-CUK-1 in the presence of 18% RH (blue circles); the corresponding simulated adsorption isotherms are represented as solid lines.

first performed at 303 K with a constant CO_2 flow of 60 mL min^{-1} (Figure 4).

Under anhydrous conditions and 303 K, the maximum CO_2 capture was estimated to be 4.6 wt%, which was reached after only 10 min; after this period of time, the CO_2 loading remained constant (30 min). Next, a kinetic CO_2 isotherm experiment at 303 K was carried out under the same range of RH values. Table 1 and Figure 4 showed the corresponding CO_2 experiments' kinetic results under different relative humidities. These kinetic results confirmed that at 18% RH, the CO_2 capture was considerably enhanced to a maximum CO_2 uptake (see Table 1 and Figure 4) that is internally consistent with the prior thermodynamics observations.

Figure 5 (right) reports the kinetic CO_2 adsorption at constant % RH in two distinct regimes: (i) the pre-adsorption of only H_2O (see Figure 4, right-blue line); and, (ii) the CO_2 adsorption in the presence of this H_2O within the pore of Mg-CUK-1 (see Figure 5, right-red line). When we imposed 18 %RH (only adsorption of H_2O), the sample weight rapidly increased (Figure 5, right; blue data). A steady-state with respect to CO_2 loading was achieved after 10 min and was fully stabilized at ~20 min. Then, from 20 min to 40 min the H_2O uptake remained constant at 0.9 wt%,

View Article Online
DOI: 10.1039/C8DT03365J

which is consistent with the H_2O uptake obtained from the adsorption isotherm at 303 K (0.99 wt%, see Fig. 2). At 40 min, CO_2 flow (60 mL min^{-1}) was initiated, resulting in a rapid weight increase (H_2O+CO_2), which reached stability at approximately 70 min, (Figure 5, right; red data). Then, the maximum amount of CO_2 captured (considering the H_2O uptake of 0.9 wt%) was equal to 8.5 wt%. Ultimately, CO_2 capture by Mg-CUK-1 in the presence of 18% RH was increased by a factor of 1.8 due to the presence of favorable CO_2···H_2O interactions inside the microchannels (from 4.6 wt% to 8.5 wt%).

This magnitude was confirmed by performing kinetic CO_2 experiments in a DVS Advantage 1 instrument (SMS). This equipment has a much higher measurement sensitivity, enabling H_2O pre-adsorption in Mg-CUK-1 to be completed in 20 min timeframe (Figure S5), resulting in a total H_2O capture of approximately 0.85 wt%. Subsequently, CO_2 adsorption (60 mL min^{-1}) was recorded from 20 min to the end of the experiment (160 min), to reach a total CO_2 capture of ~8.4 wt% (Figure S5). Thus, the enhancement of the CO_2 uptake in the presence of humidity was even more pronounced in the case of the breakthrough curves (kinetic analysis) than at the thermodynamic level.

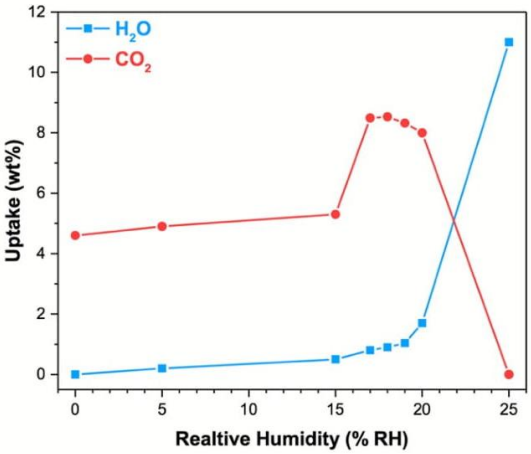

Figure 4. Mg-CUK-1 individual uptake of pre-adsorbed H_2O and CO_2 capture (from kinetic experiments) for different relative humidities at 303 K.

Table 1. Uptake data from the kinetic CO_2 isotherm experiments at 303 K at different relative humidities.

Relative Humidity (RH%)	Uptake (wt%)		Molecules per Unit Cell		Molecules per μ_3-OH group	
	H_2O	CO_2	H_2O	CO_2	H_2O	CO_2
0	-	4.6	-	1.827	-	0.228
5	0.2	4.9	0.194	1.946	0.024	0.243
15	0.5	5.3	0.485	2.105	0.061	0.263
17	0.8	8.49	0.776	3.372	0.097	0.422
18	**0.9**	**8.53**	**0.874**	**3.388**	**0.109**	**0.424**
19	1.04	8.32	1.009	3.305	0.126	0.413
20	1.7	8	1.650	3.178	0.206	0.397

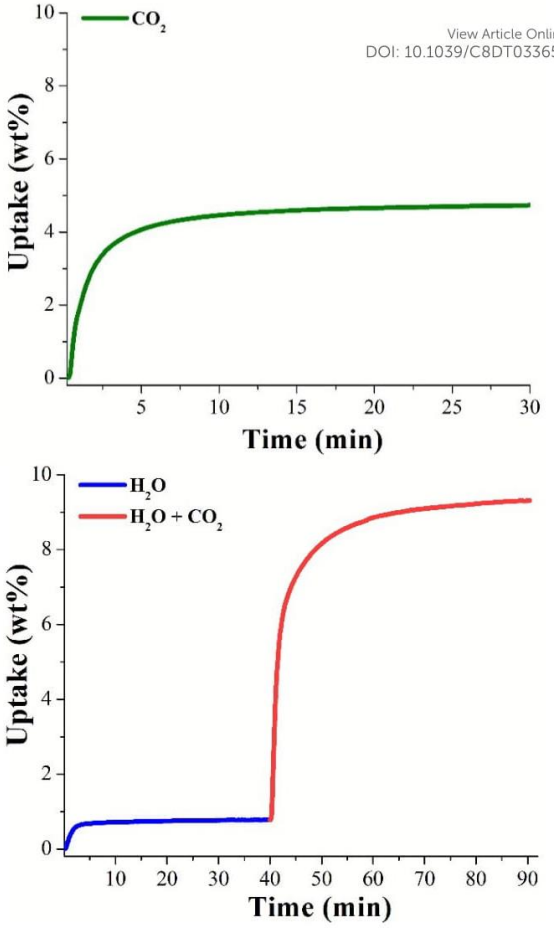

Figure 5. (top) kinetic CO_2 uptake experiment performed at 303 K with a CO_2 flow of 60 mL min^{-1}; (bottom) kinetic CO_2 uptake experiments carried out at 18 %RH at 303 K; H_2O (blue line) and H_2O+CO_2 (red line).

Molecular simulations

The simulated H_2O adsorption isotherm for Mg-CUK-1 was first compared to the corresponding experimental data. Close agreement between the two sets of data over the entire pressure range provided validation of the microscopic models for both Mg-CUK-1 (LJ parameters and charges) and H_2O, to accurately reproduce the adsorption behaviour in this MOF. This is also supported when the consideration of the fully desolvated MOF in the whole range of water relative pressure is a reasonable approximation to capture the water adsorption behaviour of Mg-CUK-1. We have evidenced that H_2O preferentially interacts with the hydroxyl groups that project into the MOF microchannels, while only a small fraction of adsorbed H_2O is located in the vicinity of the organic linker as illustrated by the Center-of-Mass density plot calculated for 1 H_2O/u.c. (see Figure 6).

The experimental CO_2 adsorption isotherm (from 0 to 1 bar and 303 K, see Figure 3) was also very well reproduced by our GCMC simulations, which indicated a relatively high adsorption enthalpy of –35 kJ/mol; this magnitude is in-line with what has been reported elsewhere for interactions between CO_2 and MOFs containing hydroxyl groups.[30] Analysis of the configurations generated by our

This journal is © The Royal Society of Chemistry 20xx

View Article Online
DOI: 10.1039/C8DT03365J

MC simulations at low loading indicated that the CO_2 molecules predominantly interact with the hydroxyl groups, and to a lesser extent with the conjugated organic moieties. This is supported by RDFs plots of the corresponding pairs (Figure 7A), which show that the average distances between the oxygen of CO_2 (O_{CO_2}), the hydrogen of the hydroxyl groups (H_{OH}) and the hydrogen of the organic linkers (H_{PDC}) are 2.2 and 3.1 Å respectively. These overall host/guest interactions are illustrated by a representative MC snapshot reported in Figure 7B.

As a further step, our simulations confirmed a slight enhancement of the CO_2adsorption uptake for the H_2O loaded Mg-CUK-1 (18% RH) as compared to the pristine Mg-CUK-1 (see Figure 3). In the presence of humidity, GCMC simulations evidenced that the CO_2 molecules interact, not only with the sites described above, but also with the H_2O molecules, as shown in the snapshot in Figure 8B. However, such $H_2O\cdots CO_2$ interactions are relatively weak as revealed by the RDF plot for the corresponding pair (Figure 8A), which shows that the most preferential interacting distances are above 3 Å. This observation is also supported by a relatively small increase of the CO_2 adsorption enthalpy at low coverage in the presence of H_2O (–36.5 kJ/mol) vs the anhydrous scenario (-35 kJ/mol).

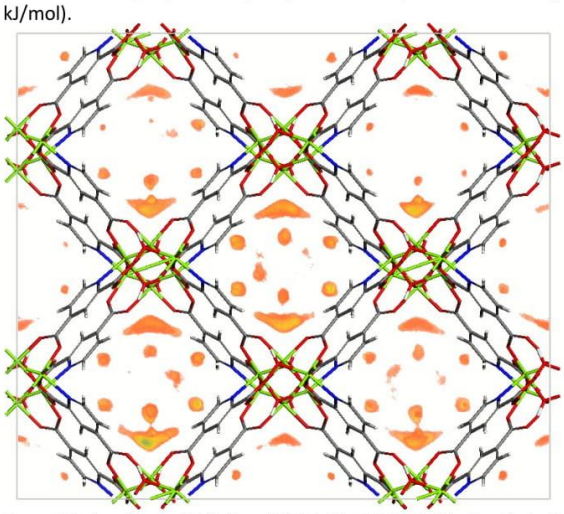

Figure 6. Center of mass distribution of H_2O in Mg-CUK-1 calculated by Monte Carlo simulations considering the case of 1 H_2O molecule /u.c. at 303 K.

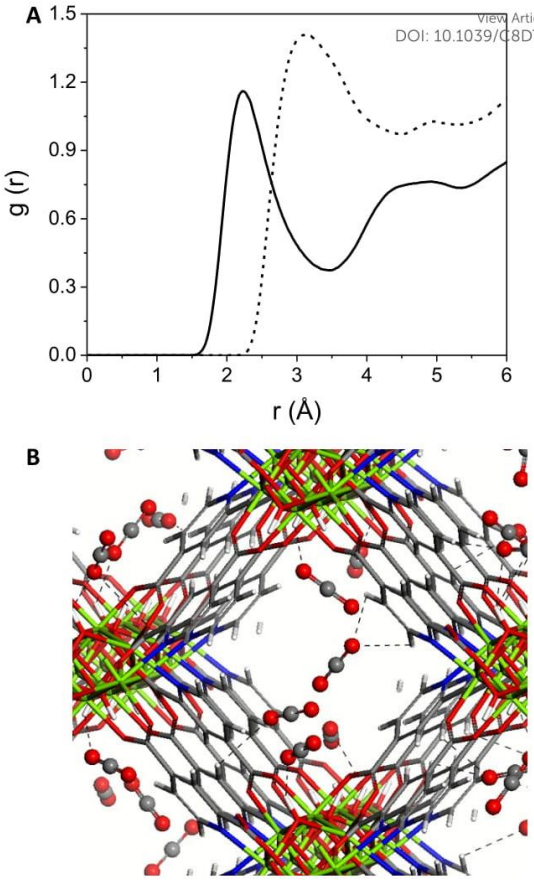

Figure 7. **A.** Radial distribution functions calculated by GCMC simulations at 1 bar and 303 K for the pairs $O_{CO_2} \cdots H_{\mu_3\text{-}OH}$ (solid line) and $O_{CO_2} \cdots H_{PDC}$ (dashed line) for Mg-CUK-1. **B.** Representative snapshot illustrating the interactions between CO_2 and the atoms of the MOF pore wall. The dashed lines in the snapshots denote interactions between the CO_2 molecules and the surrounding atoms at distances bellow 3 Å.

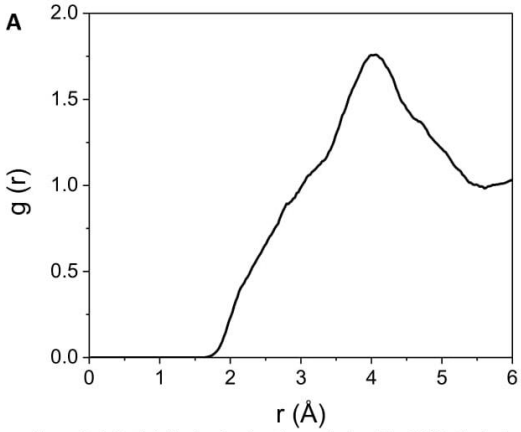

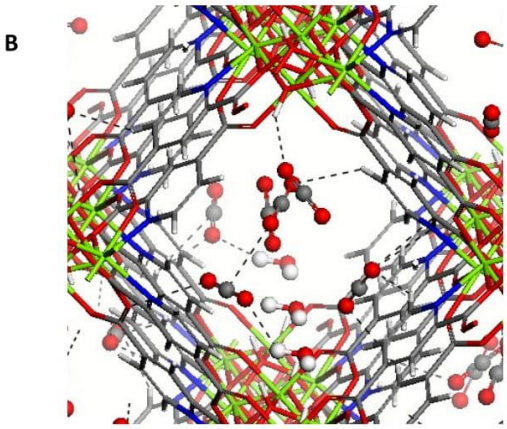

Figure 8. **A.** Radial distribution functions calculated by GCMC simulations at 1 bar and 303 K for the pair O_{CO2}–H_w for hydrated Mg-CUK-1. **B.** Representative snapshot showing the interactions between CO_2 and the atoms of the MOF pore wall. The dashed lines in the snapshots denote interactions between the CO_2 molecules and the surrounding atoms at distances bellow 3 Å.

View Article Online
DOI: 10.1039/C8TA08351

Conclusions

Kinetic CO_2 uptake experiments revealed a significant enhancement of the CO_2 capture performances for the water-stable MOF Mg-CUK-1, *i.e.*, 1.8-fold increased, from 4.6 wt% to 8.5 wt% CO_2 uptake) under 18% RH. This trend was also confirmed by thermodynamic measurements and GCMC simulations. The phenomenon of H_2O--induced CO_2 uptake enhancement was highly pronounced in measurements conducted under thermodynamic control. The underlying kinetics responsible for this process are more difficult to understand and measure directly, but supporting molecular simulations allowed us to gain additional insights into the microscopic adsorption mechanisms at play. In particular, theory suggests that an increase in the CO_2 adsorption enthalpy, in the presence of H_2O, is due to favourable intermolecular interactions between CO_2 and H_2O which are confined within Mg-CUK-1. The fundamental understanding gained from this joint experimental/computation study paves the way towards the design of new and more efficient CO_2 capture systems under humidly (*i.e.*, realistic, ambient) conditions.

Conflicts of interest

There are no conflicts of interest.

Acknowledgements

The authors thank Dr. A. Tejeda-Cruz (powder X-ray; IIM-UNAM), CONACyT Mexico (1789), PAPIIT UNAM Mexico (IN101517) for financial support. E.G-Z. thanks CONACyT (236879), Mexico for financial support. Thanks to U. Winnberg (ITAM) and G. Ibarra-Winnberg for scientific discussions. P.G.M. Mileo thanks the National Counsel of Technological and Scientific Development (CNPQ) for the scholarship. G.M. thanks the Institut Universitaire de France for its support. E. S.-G. thanks CONACyT Mexico (grant No. 289042).

Notes and references

1. National Oceanic and Atmospheric Administration (NOAA) https://www.esrl.noaa.gov/gmd/ccgg/trends/?utm_source=www.uoota.com (accessed May 30, 2018).
2. Intergovernmental Panel on Climate Change (IPCC) https://www.ipcc.ch/publications_and_data/publications_ipcc_fourth_assessment_report_wg1_report_the_physical_science_basis.htm (accessed may 30, 2018).
3. (a) I. S. Thakura, M. Kumara, S. J. Varjanib, Y. Wuc, E. Gnansounoud and S. Ravindrane, *Bioresource Technology.* 2018, **256**, 478–490. b) M. H. Ibrahim, M. H. El-Naas, Z. Zhang and B. Van der Bruggen, *Energy Fuels*, 2018, **32**, 963–978.
4. (a) S. L. James, *Chem. Soc. Rev*. 2003, **32**, 276–288. (b) J. L. C. Rowsell and O. M. Yaghi, *Microporous Mesoporous Mater.* 2004, **73**, 3–14. (c) S. Choi, J. H. Drese and C. W. Jones, *ChemSusChem* 2009, **2**, 796–854. (d) J. Wang, L. Huang, R. Yang, Z. Zhang, J. Wu, Y. Gao, Q. Wang, D. O'Hareb and Z. Zhong, *Energy Environ. Sci.* 2014, **7**, 3478–3518. (e) B. Dou, C. Wang, Y. Song, H. Chen, B. Jiang, M. Yang and Y. Xu, *Renew. Sustain. Energy Rev.* 2016, **53**, 536–546.
5. N. M. Padial, E. Quartapelle Procopio, C. Montoro, E. López, J. E. Oltra, V. Colombo, A. Maspero, N. Masciocchi, S. Galli, I. Senkovska, S. Kaskel, E. Barea, and J. A. R. Navarro, *Angew. Chemie - Int. Ed*. 2013, **52**, 8290–8294.
6. (a) S.-L. Li, and Q. Xu, *Energy Environ. Sci.* 2013, **6**, 1656–1683. (b) V. Bon, *Curr. Opin. Green Sustain. Chem.* 2017, **4**, 44–49.
7. (a) M. Dincă and J. R. Long, *Angew. Chemie - Int. Ed.* 2008, **47**, 6766–6779. (b) K. M. Thomas, *Dalt. Trans.* 2009, **9**, 1487–1505. (c) H. W. Langmi, J. Ren, B. North, M. Mathe and D. Bessarabov, *Electrochim. Acta* 2014, **128**, 368–392.
8. (a) K. Sumida, D. L. Rogow, J. A. Mason, T. M. McDonald, E. D. Bloch, Z. R. Herm, T.-H. Bae, and J. R. Long, *Chem. Rev.* 2012, **112**, 724–781. (b) J. Liu, P. K. Thallapally, B. P. McGrail, D. R. Brown and J. Liu, *Chem. Soc. Rev.* 2012, **41**, 2308–2322. (c) D. Andirova, C. F. Cogswell, Y. Lei and S. Choi, *Microporous Mesoporous Mater.* 2016, **219**, 276–305; (d) D. Y. Hong, Y. K. Hwang, C. Serre, G. Férey and J. S. Chang, *Adv. Funct. Mater.* 2009, **19**, 1537–1552; (e) W. Bloch, R. Babarao, M. R Hill, C. J Doonan and C. Sumby, *J. Am. Chem. Soc.* 2013, **135**, 10441-10448.
9. (a) J. J. Low, A. I. Benin, P. Jakubczak, J. F. Abrahamian, S. A. Faheem and R. R. Willis, *J. Am. Chem. Soc.* 2009, **5**, 15834–15842; (b) J. Canivet, A. Fateeva, Y. Guo, B. Coasne and D. Farrusseng, *Chem. Soc. Rev.* 2014, **43**, 5594–5617; (c) J. Canivet, J. Bonnefoy, C. Daniel, A. Legrand, B. Coasne, and D. Farrusseng, *New J. Chem.* 2014, **38**, 3102–3111.
10. (a) M. R. Gonzalez, J. H. Gonzalez-Estefan, H. A. Lara-Garcia, P. Sanchez-Camacho, E. I. Basaldella, H. Pfeiffer and I. A. Ibarra, 2015, **39**, 2400-2403; (b) H. A. Lara-García, M. R. Gonzalez, J. H. González-Estefan, P. Sánchez-Camacho, E. Lima and I. A. Ibarra, *Inorg. Chem. Front.* 2015, **2**, 442–447. (c) V. Benoit, N. Chanut, R. S. Pillai, M. Benzaqui, I. Beurroies, S. Devautour-Vinot, C. Serre, N. Steunou, G. Maurin and P. L. Llewellyn, *J. Mater. Chem. A* 2018, **6**, 2081–2090. (d) M. Benzaqui, R. S. Pillai, A. Sabetghadam, V. Benoit, P. Normand, J. Marrot, N. Menguy, D. Montero, W. Shepard, A. Tissot, C. Martineau-Corcos, C. Sicard, M. Mihaylov, F. Carn, I. Beurroies, P. L. Llewellyn, G. De Weireld, K. Hadjiivanov, J. Gascon, F. Kapteijn, G. Maurin, N. Steunou and C. Serre, *Chem. Mater.* 2017, **29**, 10326–10338. (e) J. W. Yoon, Y. K. Seo, Y. K. Hwang, J. S. Chang, H. Leclerc, S. Wuttke, P. Bazin, A. Vimont, M. Daturi, E. Bloch, P. L. Llewellyn, C. Serre, P. Horcajada, J. M. Grenèche, A. E. Rodrigues and G. Férey, *Angew. Chemie - Int. Ed.*, 2010, **49**, 5949–5952.
11. P. Nugent, Y. Belmabkhout, S. D. Burd, A. J. Cairns, R. Luebke, K. Forrest, T. Pham, S. Ma, B. Space, L. Wojtas, M. Eddaoudi and M. J. Zaworotko, *Nature,* 2013, **495**, 80–84.
12. (a) H. Jasuja, Y. G. Huang and K. S. Walton, *Langmuir*, 2012, **28**, 16874–16880. (b) H. Jasuja, J. Zang, D. S. Sholl and K. S. Walton, *J. Phys. Chem. C*, 2012, **116**, 23526–23532. (c) J. B. DeCoste, G. W. Peterson, H. Jasuja, T. G. Glover, Y. Huang and K. S. Walton, *J. Mater. Chem. A*, 2013, **1**, 5642. (d) P. M. Schoenecker, C. G. Carson, H. Jasuja, C. J. J. Flemming and K. S. Walton, *Ind. Eng. Chem. Res.*, 2012, **51**, 6513–6519. (e) N. C. Burtch, H. Jasuja and K. S. Walton, *Chem. Rev.*, 2014, **114**, 10575–10612. (f) G. E. Cmarik, M. Kim, S. M. Cohen and K. S. Walton, *Langmuir*, 2012, **28**, 15606–15613.
13. E. González-Zamora and I. A. Ibarra, *Mater. Chem. Front.*, 2017, **1**, 1471–1484.

 This journal is © The Royal Society of Chemistry 20xx

14. J. R. Álvarez, R. A. Peralta, J. Balmaseda, E. González-Zamora and I. A. Ibarra, *Inorg. Chem. Front.*, 2015, **2**, 1080–1084.
15. E. Sánchez-González, J. R. Álvarez, R. A. Peralta, A. Campos-Reales-Pineda, A. Tejeda-Cruz, E. Lima, J. Balmaseda, E. González-Zamora and I. A. Ibarra, *ACS Omega*, 2016, **1**, 305–310.
16. M. Sánchez-Serratos, P. A. Bayliss, R. A. Peralta, E. González-Zamora, E. Lima and I. A. Ibarra, *New J. Chem.*, 2016, **40**, 68–72.
17. R. A. Peralta, B. Alcántar-Vázquez, M. Sánchez-Serratos, E. González-Zamora and I. A. Ibarra, *Inorg. Chem. Front.*, 2015, **2**, 898–903.
18. (a) H. Wu, Q. Gong, D. H. Olson and J. Li, *Chem. Rev.*, 2012, **112**, 836–868. (b) A. Ö. Yazaydin, A. I. Benin, S. A. Faheem, P. Jakubczak, J. J. Low, R. W. Richard and R. Q. Snurr, *Chem. Mater.*, 2009, **21**, 1425–1430. (c) J. Liu, Y. Wang, A. I. Benin, P. Jakubczak, R. R. Willis and M. D. LeVan, *Langmuir,* 2010, **26**, 14301–14307. (d) Q. Liu, L. Ning, S. Zheng, M. Tao, Y. Shi and Y. He, *Sci. Rep.* 2013, **3**, 2916-2921. (e) Y. F. Chen, R. Babarao, S. I. Sandler and J. W. Jiang, *Langmuir*, 2010, **26**, 8743–8750.
19. B. Saccoccia, A. M. Bohnsack, N. W. Waggoner, K. H. Cho, J. S. Lee, D. Y. Hong, V. M. Lynch, J. S. Chang and S. M. Humphrey, *Angew. Chemie - Int. Ed.*, 2015, **54**, 5394–5398.
20. J. P. Perdew, K. Burke and M. Ernzerhof, *Phys. Rev. Lett.* 1996, **77**, 3865–3868.
21. W. J. Hehre, J. A. Ditchfield, and J. A. Pople, *J. Chem. Phys.* 1972, **56**, 2257–2261.
22. J. G. Harris, and K. H. Yung, *Phys. Chem.* 1995, **99**, 12021-12024.
23. J. L. F. Abascal and C. A. Vega, *J. Chem. Phys*. 2005, **123**, 234505–234512.
24. A. K. Rappe, C. J. Casewit, K. S. Colwell, W. A. Goddard and W. M. Skiff, *J. Am. Chem. Soc*. 1992, **114**, 10024–10035.
25. S. L. Mayo, B. D. Olafson and W. A. Goddard, *J. Phys. Chem.* 1990, **94**, 8897–8909.
26. (a) E. Sanchez-Gonzalez, P. G. M. Mileo, J. J. R. Alvarez, E. Gonzalez-Zamora, G. Maurin and I. A. Ibarra, *Dalton Trans.*, 2017, **46**, 15208-15215. (b) D. D. Borges, P. Normand, A. Permiakova, R. Babarao, N. Heymans, D. S. Galvão, C. Serre, G. Weireld and G. Maurin, *J. Phys. Chem. C*, 2017, **121**, 26822–26832.
27. (a) O. N. Osychenko, G. E. Astrakharchik and J. Boronat, *Mol. Phys.* 2012, **110**, 227-247. (b) J. Kolafa and J. W. Perram, *Mol. Sim*., 1992, **9,** 351-368.
28. T. J. H. Vlugt, E. García-Perez, D. Dubbeldam, S. Ban and S. Calero, *J. Chem. Theory Comput*. 2008, **4**, 1107–1118.
29. E. Sánchez-González, P. G. M. Mileo, M. Sagastuy-Breña, J. R. Álvarez, J. E. Reynolds, A. Villarreal, A. Gutiérrez-Alejandre, J. Ramírez, J. Balmaseda, E. González-Zamora, G. Maurin, S. M. Humphrey and I. A. Ibarra, *J. Mater. Chem. A*, 2018, **6**, 16900–16909.
30. (a) D.-M. Chen, X.-P. Zhang, W. Shi and P. Cheng, *Inorg. Chem.* 2015, **54**, 5512; (b) G. E. Cmarik, M. Kim, S. M. Cohen and K. S. Walton, *Langmuir*, 2012, **28**, 15606; (c) D.-M. Chen, N.-N. Zhang, C.-S. Liu, Z.-H. Jiang, X.-D. Wang and M. Du, *Inorg. Chem.* 2017, **56**, 2379.
31. (a) R. A. Peralta, A. Campos-Reales-Pineda, H. Pfeiffer, J. R. Álvarez, J. A. Zárate, J. Balmaseda, E. González-Zamora, A. Martínez, D. Martínez-Otero, V. Jancik and I. A. Ibarra, *Chem. Commun.*, 2016, **52**, 10273–10276. (b) E. Sánchez-González, E. González-Zamora, D. Martínez-Otero, V. Jancik and I. A. Ibarra, *Inorg. Chem.*, 2017, **56**, 5863–5872.

View Article Online
DOI: 10.1039/C9DT03365J

Dalton Transactions

View Article Online
DOI: 10.1039/C8DT03365J

Mg-CUK-1 showed a 1.8-fold increase in CO_2 capture from (4.6 wt% to 8.5 wt%) in the presence of 18% RH. Grand canonical Monte Carlo simulations demonstrated that the cause of increasing CO_2 capture, in the presence of H_2O, is due to favorable intermolecular interactions between the co-adsorbates confined within the micropores of Mg-CUK-1.

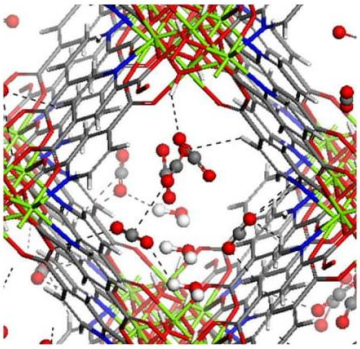

List of Articles

Title	Journal	Year
Achieving Superprotonic Conduction with a 2D Fluorinated Metal–Organic Framework	Journal of the American Chemical Society	2018
Humidity-induced CO_2 capture enhancement in Mg-CUK-1	Dalton Transactions	2018
Adsorption of 1-Propanol in the Channel-Like InOF-1 Metal–Organic Framework and Its Influence on the CO_2 Capture Performances	The Journal of Physical Chemistry C	2018
Highly reversible sorption of H2S and CO_2 by an environmentally friendly Mg-based MOF	Journal of Materials Chemistry A	2018
Confined methanol within InOF-1: CO_2 capture enhancement	Dalton Transactions	2017
Highly Efficient Proton Conduction in a Three-Dimensional Titanium Hydrogen Phosphate	Chemistry of Materials	2017
Proton-Conducting Phenolate-Based Zr Metal–Organic Framework: A Joint Experimental–Modeling Investigation	The Journal of Physical Chemistry C	2016

List of Conferences

Conference	Nature	Year
Journée de l'école doctorale Chimie Balard	Poster	2017
2nd European Conference on Metal Organic Frameworks and Porous Polymers	Poster	2017
11th International Symposium on the Characterization of Porous Solids (COPS-XI)	Poster	2017
253rd American Chemical Society, Advanced Materials, Technologies, Systems & Processes	Oral	2017
2nd School on Biological Soft Matter: from molecular interactions to engineered materials	Poster	2017
Journées de l'Association Française de l'Adsorption	Poster	2017
I Workshop on rational design for improved functionalities of porous inorganic materials	Oral	2016
5th international Conference on Metal-Organic Frameworks & Open Framework Compounds	Oral	2016
EMN meeting on Metal-Organic Frameworks, Energy Materials Nanotechnology	Oral	2016
Fundamentals of Adsorption	Poster	2016
38ème Réunion GFZ	Poster	2016

Abstract

The objective of this PhD thesis was to gain insight into the proton dynamics and water adsorption mechanisms in novel porous materials that have been identified experimentally as promising candidates for low temperature proton conduction and adsorption-based heat reallocation-related applications. This was achieved by combining advanced computational tools at the electronic (Density Functional Theory) and atomic (force field_based Monte Carlo and Molecular Dynamics) levels to (i) reveal the water-assisted proton migration pathway through the pores of the hybrid metal organic frameworks MIL-163(Zr) and KAUST-7'and the inorganic phosphate $Ti^{IV}Ti^{IV}(HPO_4)_4$ materials at the origin of their outstanding proton conduction performances and (ii) explain the water adsorption behaviors of a series of metal organic frameworks CUK-1(Me), MOF-801(Zr) and MIL-100(Fe) that can be tuned by changing the nature of the metal center, creating defects and incorporating coordinatively unsaturated sites. Such a fundamental understanding is expected to pave the way towards a more efficient development of materials for the two explored applications.

Keywords: Proton conduction, adsorption based heat reallocation, porous materials, water adsorption, proton dynamics, molecular simulations.

Résumé

L'objectif de la thèse a été de comprendre la dynamique protonique et l'adsorption d'eau dans de nouveaux matériaux poreux identifiés expérimentalement comme des candidats prometteurs pour des applications dans le domaine de la conduction protonique et du transfert de chaleur par adsorption. Dans ce contexte, des simulations à l'échelle électronique (Théorie de la fonctionnelle de la Densité) et atomique (Monte Carlo et Dynamique Moléculaire classique) ont permis (i) d'élucider les mécanismes de conduction protonique assistées par l'eau de deux matériaux hybrides de type MOFs, MIL-163(Zr) et KAUST-7', et d'un phosphate de titane, $Ti^{IV}Ti^{IV}(HPO_4)_4$ à l'origine de leurs performances exceptionnelles et (ii) d'interpréter les comportements d'adsorption de l'eau d'une série de matériaux hybrides CUK-1(Me), MOF-801(Zr) and MIL-100(Fe) qui peuvent être modulées par la nature de leur centre métallique, la création de défauts et l'incorporation de sites de coordination insaturés. Cette connaissance fondamentale devrait permettre de voir émerger de façon plus efficace des matériaux pour les deux applications visées.

Mots clefs: Conduction protonique, transfert de chaleur par adsorption, matériaux poreux, adsorption d'eau, dynamique protonique, simulations moléculaires.